Technische Universität München

Fakultät für Chemie

Degradation Mechanisms of Layered Oxides Used as Cathode Active Materials in Lithium-Ion Batteries

Benjamin Strehle

Vollständiger Abdruck der von der Fakultät für Chemie der
Technischen Universität München zur Erlangung des akademischen Grades eines

Doktors der Naturwissenschaften (Dr. rer. nat.)

genehmigten Dissertation.

Vorsitzender:	Priv.-Doz. Dr. Friedrich Esch
Prüfer der Dissertation:	1. Prof. Dr. Hubert A. Gasteiger
	2. Prof. Dr. Thomas F. Fässler
	3. Prof. Jeff Dahn, Ph.D. (Dalhousie University, Canada)

Diese Dissertation wurde am 25.04.2022 bei der Technischen Universität München eingereicht und durch die Fakultät für Chemie am 08.07.2022 angenommen.

Abstract

The development of new cathode active materials (CAMs) is primarily motivated by increasing the energy density and reducing the cost of lithium-ion batteries (LIBs); however, the commercial application equally depends on their durability during battery operation. Therefore, it is the aim of this thesis to identify important degradation mechanisms of layered transition-metal oxide CAMs and to precisely quantify their impact on the electrochemical performance and capacity fading. In order to differentiate between degradation modes occurring at the surface and within the bulk of the materials, we employed on-line electrochemical mass spectrometry (OEMS) as well as X-ray (XPD) and neutron powder diffraction (NPD) in conjunction with several electrochemical and physicochemical analysis techniques.

The main part of this thesis focuses on Li- and Mn-rich layered oxides, which are considered as next-generation CAM, but the here discussed challenges have prevented their commercialization until now. First, the comparison of differently synthesized CAMs revealed important material metrics governing the electrochemical performance right from the pristine state. Following this, we carefully examined the oxygen release during the initial cycles and the consequent surface degradation of the materials as a function of the over-lithiation and the activation temperature. Furthermore, the structural origins of the inherent voltage hysteresis and voltage fading were investigated on the basis of the lattice parameter variations and a critical evaluation of the transition-metal migration. In the last part, we systematically compared the capacity fading mechanisms of a state-of-the-art NCM-811 cathode operated either at ambient or elevated temperature over the duration of up to 1000 cycles. While the bulk structure is largely preserved, we could show that surface instabilities caused by oxygen release lead to the gradual formation of an electrochemically inactive and resistive surface layer around the primary NCM-811 particles.

Kurzfassung

Die Entwicklung neuer Kathodenaktivmaterialien zielt in erster Linie darauf ab, die Energiedichte von Lithium-Ionen-Batterien zu erhöhen und deren Kosten zu senken, aber die kommerzielle Anwendung hängt in gleicher Weise von deren Lebensdauer im Batteriebetrieb ab. Daher soll diese Arbeit einen Beitrag dazu leisten, wichtige Alterungsmechanismen in Übergangsmetall-Schichtoxiden zu verstehen und deren Einfluss auf das elektrochemische Verhalten und den Kapazitätsverlust exakt zu bestimmen. Um die Alterungsprozesse an der Oberfläche von denen im Inneren der Materialien zu unterscheiden, verwenden wir on-line elektrochemische Massenspektrometrie (OEMS) sowie Röntgen- (XPD) und Neutronenpulverdiffraktion (NPD) in Verbindung mit weiteren elektrochemischen und physikalisch-chemischen Analysetechniken.

Der Hauptteil dieser Arbeit beschäftigt sich mit Lithium- und Mangan-reichen Schichtoxiden, die als zukünftige Kathodenaktivmaterialien betrachtet werden, aber die hier untersuchten Probleme verhindern bis jetzt deren Kommerzialisierung. Zunächst legt der Vergleich unterschiedlich hergestellter Materialien wichtige Materialeigenschaften offen, die von Anfang an das elektrochemische Verhalten bestimmen. Im Anschluss quantifizieren wir die Sauerstoffreisetzung innerhalb der ersten Zyklen und die daraus resultierende Oberflächendegradation in Abhängigkeit der Überlithiierung und der Aktivierungstemperatur. Außerdem werden die strukturellen Ursachen der den Materialien innewohnenden Spannungshysterese und des Spannungsverlusts anhand der Veränderung der Gitterparameter und einer kritischen Bewertung der Übergangsmetallbewegung untersucht. Im letzten Teil wenden wir uns dem Kapazitätsverlust von state-of-the-art NCM-811 Kathoden zu, deren Alterungsmechanismen beim Betrieb bei Raum- und erhöhter Temperatur systematisch über die Dauer von bis 1000 Zyklen miteinander verglichen werden. Wir können zeigen, dass die Bulkstruktur größtenteils erhalten bleibt, aber die durch den Sauerstoffausbau ausgelöste Instabilität der Oberfläche führt zu der langsamen Bildung einer elektrochemisch inaktiven und resistiven Oberflächenschicht um die NCM-811 Primärpartikel.

Table of Contents

List of Abbreviations

Abbreviation	**Description**
AAM	anode active material
BET	Brunauer-Emmett-Teller
BEV	battery electric vehicle
BJH	Barrett-Joyner-Halenda
CAM	cathode active material
CE	Coulombic efficiency
CC	constant current
CCCV	constant current/constant voltage
CE	counter-electrode
CEI	cathode electrolyte interphase
CV	constant voltage
DEC	diethyl carbonate
DLS	dynamic laser scattering
DMC	dimethyl carbonate
EC	ethylene carbonate
EG	ethylene glycol
EIS	electrochemical impedance spectroscopy
EMC	ethyl methyl carbonate
FIB	focused argon-ion beam
FEC	fluoroethylene carbonate
GHG	greenhouse gas
GWRE	gold wire reference-electrode
HRTEM	high-resolution transmission electron microscopy
ICE(V)	internal combustion engine (vehicle)
ICP-AES	inductively coupled plasma atomic emission spectroscopy
LEDC	lithium ethylene dicarbonate
LCO	lithium cobalt oxide ($LiCoO_2$)
LFP	lithium iron phosphate ($LiFePO_4$)
LMO	lithium manganese oxide ($LiMn_2O_4$)
LMR-NCM	lithium- and manganese-rich NCM ($Li[Li_xM_{1-x}]O_2$)

LNMO	lithium nickel manganese oxide ($LiNi_{0.5}Mn_{1.5}O_4$)
LP57	EC:EMC solvent mixture (3:7 by weight) with 1M $LiPF_6$
LP57-2	LP57 electrolyte with 2% VC
LTO	lithium titanate ($Li_4Ti_5O_{12}$)
MIP	mercury intrusion porosimetry
NCA	lithium nickel cobalt aluminum oxide ($Li[Ni_{1-x-y}Co_xAl_y]O_2$)
NCM-abc	lithium nickel cobalt manganese oxide ($Li[Ni_aCo_bMn_c]O_2$, $a + b + c = 1$)
NMP	*N*-methyl-2-pyrrolidone
NMR	nuclear magnetic resonance
NPD	neutron powder diffraction
OCV	open circuit voltage
OEM	original equipment manufacturer
OEMS	on-line electrochemical mass spectrometry
PVDF	polyvinylidene difluoride
RE	reference-electrode
SEI	solid electrolyte interphase
SEM	scanning electron microscopy
SEM	secondary electron multiplier
SHE	standard hydrogen electrode
SOC	state of charge
SRM	standard reference material
(S)TEM	(scanning) transmission electron microscopy
STP	standard temperature (0°C) and pressure (1 bar)
TM	transition-metal
UHV	ultra-high vacuum
VC	vinylene carbonate
WE	working-electrode
WPPF	whole powder pattern fitting
XAS	X-ray absorption spectroscopy
XPD	X-ray powder diffraction
XPS	X-ray photoelectron spectroscopy

1 Introduction

Since their commercialization by Sony in 1991,[1] lithium-ion batteries (LIBs) have become a key technology in our modern and fast-paced society, because many people are dependent on LIB-powered portable electronic devices such as mobile phones and laptops in everyday life.[2] This success story only had been possible through profound, long-lasting research efforts, both before and after Sony's milestone in 1991, which is why John B. Goodenough, M. Stanley Whittingham, and Akira Yoshino undoubtedly are well-deserved laureates of the Nobel Prize in Chemistry 2019, honored "for the development of lithium-ion batteries".[3]

Whittingham laid the foundation by the invention of the TiS_2/Li battery in the 1970s.[4] Since its operating voltage of ≈2.2 V vs. Li^+/Li is relatively low, limiting the energy density of the cell, researchers were looking for other cathode active materials and Goodenough discovered in 1980 the potential of layered metal oxides, from which $LiCoO_2$ (LCO) showed good structural stability during lithium de-/intercalation at much higher voltages of >4.0 V vs. Li^+/Li.[5] However, to make lithium-ion batteries a viable and safe product, the metallic lithium anode also had to be replaced, because non-uniformly deposited lithium dendrites could lead to short circuits and even to the explosion of the cell. It was Yoshino's merit to combine LCO with a carbon material, which resulted in the first LIB purely based on intercalation compounds in 1985.[6] From there, it obviously did not take a long time until their commercialization in 1991.

The first-generation lithium-ion batteries provided a gravimetric energy density of 80 Wh/kg,[1] which already surpassed the practical energy density of well-developed lead-acid batteries (40 Wh/kg) and which was on the same level as nickel-metal hydride batteries (80 Wh/kg) that had been commercialized one year earlier.[2,7] However, LIBs are appealing compared to the other battery technologies due to

their lower toxicity as well as their much better Coulombic and energy efficiencies.[2,7] Furthermore, the low molecular weight of lithium (7 g/mol) and its low standard reduction potential ($E^0(Li^+/Li)$ = −3.04 V vs. SHE) afford the possibility to reach higher energy densities by constantly optimizing the cell chemistry.[8]

In recent years, the development of lithium-ion batteries is mainly promoted by the automotive industry.[6,9] Since transport vehicles emit roughly one quarter of the global energy-related greenhouse gas (GHG) emissions,[9] internal combustion engine (ICE)-powered vehicles (ICEVs) have to be replaced by battery electric vehicles (BEVs), which in turn have to be charged from renewable energy sources to reduce the CO_2 emissions and thus to decarbonize the transportation sector. In 2020, 10.9 million electric vehicles had been on the streets worldwide,[10] which accounted, despite significant growth rates, only for about 1% of the global car stock.[11] With the signing of the Paris Agreement in 2016 for reducing global GHG emissions and consequent legislative regulations in many countries and regions,[12,13] however, almost all major car manufacturers have committed to developing and releasing electrified vehicles. For example, General Motors announced in January 2021 to sell only emission-free cars by 2035, while the most ambitious and verifiable targets of a traditional original equipment manufacturer (OEM) probably have been defined by Volvo, who wants to reach a sales share of 50% fully electrified cars by 2025.[14] Just founded in 2003, Tesla is a pioneer in the field of electric mobility, who still takes the leading role with almost 500,000 sold BEVs in 2020, closely followed by Volkswagen with 422,000 sales of fully and partially electrified cars.[10] Tesla's Model 3 is the most successful BEV, offering a usable battery energy of 50 kWh at a base price of roughly 44,000 € in the Standard Plus version.[15] The implemented battery covers an average driving range of 335 km at a consumption of about 15 kWh per 100 km.[15]

To be unconditionally compatible with gasoline-fueled ICEVs and to reach mass market penetration, lithium-ion batteries for automotive applications still require further improvements such as (i) higher energy densities to achieve longer driving ranges, (ii) faster charging rates, and (iii) lower costs.[16,17] State-of-the-art LIBs have energy contents of 260 Wh/kg and 700 Wh/L at cell level, but the US Department

of Energy estimated that automotive batteries have to deliver 350 Wh/kg and 750 Wh/L to enable the targeted driving range of at least 500 km at acceptable costs.[7,18] The current sales-weighted battery pack price of 156 US$/kWh[11] has to drop below 100 US$/kWh (corresponding to roughly 75 US$/kWh on the battery cell level) to reach cost parity between ICEVs and BEVs.[18] Since the cathode is typically the most significant component by both weight (≈50%) and cost (≈33%) in a battery cell, the development of new cathode active materials (CAMs) is a key challenge to fulfill the above targets.[16,18]

All commercially used cathode active materials are compounds containing 3d transition-metals (Mn, Fe, Co, Ni) as active redox centers. Within this group, cobalt is by far the most critical raw material due to its high price (≈53 US$/kg)[19,20] and it further faces ethical problems due to hazardous and non-sustainable mining conditions.[21,22] For these reasons, LCO was gradually replaced by nickel-based layered oxides, that is, $Li[Ni_aCo_bMn_c]O_2$ (a + b + c = 1; NCM-abc) and $Li[Ni_{1-x-y}Co_xAl_y]O_2$ (NCA), which became the preferred choice for automotive applications in recent years.[9,18] Since the raw metal price of nickel (≈16 US$/kg) is by a factor of 3 lower compared to cobalt (≈53 US$/kg),[19] Ni-rich CAMs with limited Co content (e.g., NCM-811) drastically reduced the costs of the battery cell. Furthermore, they deliver higher capacities at a given upper cut-off voltage than less Ni-rich variants, which also increases the energy density of the cell.[23,24] To reach the cell-level energy target of 350 Wh/kg, the cathode active material is expected to contribute at least 800 Wh/kg on the material level, which pushes the layered transition-metal oxides close to their fundamental limits due to structural instabilities at high delithiation levels.[24,25] This raises concern with respect to their safety and durability—two other key parameters, which have to be delicately balanced with the energy and cost requirements.[18]

In the search of alternative CAMs, there are also a lot of research activities invested in the development of Li- and Mn-rich layered oxides (LMR-NCM), which could further decrease the cathode costs due to the even lower price of Mn (≈2 US$/kg)[26] and which offer higher reversible capacities than conventional layered oxides.[27] Despite these benefits, the class of over-lithiated CAMs still has to overcome several serious obstacles before they can be actually used in real applications such as

powering battery electric vehicles.[28,29] For this reason, it is the main scope of this thesis to develop a mechanistic understanding of important degradation processes happening both at the surface and within the bulk structure of over-lithiated CAMs, which limit their initial performance, but also their long-term stability. Since Ni-rich layered oxides keep dominating the battery market, this thesis will further elucidate the capacity fading mechanisms of an NCM-811 CAM operated until high delithiation levels and at different temperatures.

1.1 The Working Principle of Lithium-Ion Batteries

State-of-the-art lithium-ion batteries are based on the so-called "rocking chair" concept, because the lithium-ions are shuttled back and forth between the electrodes. Figure 1 shows the example of an LCO/graphite full-cell during the discharge reaction, which resembles the first lithium-ion battery introduced by Sony in 1991.[1] The electrodes consist of intrinsically stable intercalation materials, which are capable of reversibly storing the lithium-ions in their host structure. Here, the electrode with the lower lithiation potential is the negative electrode, which is by convention in the lithium-ion battery research also termed "anode", independent of the reaction direction (i.e., oxidation or reduction). On the other hand, the electrode with the higher lithiation potential is the positive electrode, which is also referred to as "cathode". The micrometer-sized active material particles are fixed with a polymer binder onto current collector metal foils (copper for the anode, aluminum for the cathode) with an optimized thickness of 8-12 µm.[6] In order to prevent a short circuit, the electrodes are separated by a porous polyolefin separator with a typical thickness of 12-25 µm.[6] The pores of the separator as well as of the electrodes are filled with a non-aqueous electrolyte containing a dissociated lithium salt to enable sufficient Li-ion mobility. Once the electrodes are connected by an external circuit, the electrochemical reactions take place in tandem. During discharge, the graphite anode releases Li-ions and electrons by forming a variety of Li_xC_6 phases (from x = 1 to 0) according to:

$$Li_xC_6 \rightarrow C_6 + x\,Li^+ + x\,e^- \quad (1)$$

After traveling through the electrolyte and the external circuit, respectively, the LCO cathode takes them up in the layered structure by the following reaction:

$$Li_{1-x}CoO_2 + x\,Li^+ + x\,e^- \rightarrow LiCoO_2 \quad (2)$$

whereby Co^{4+} (for x = 1) gets reduced to Co^{3+} (for x = 0), i.e., the Co^{3+}/Co^{4+} redox couple is responsible for charge compensation during charge/discharge of the cell. Consequently, the overall reaction looks as follows:

$$Li_xC_6 + Li_{1-x}CoO_2 \underset{Charge}{\overset{Discharge}{\rightleftharpoons}} C_6 + LiCoO_2 \quad (3)$$

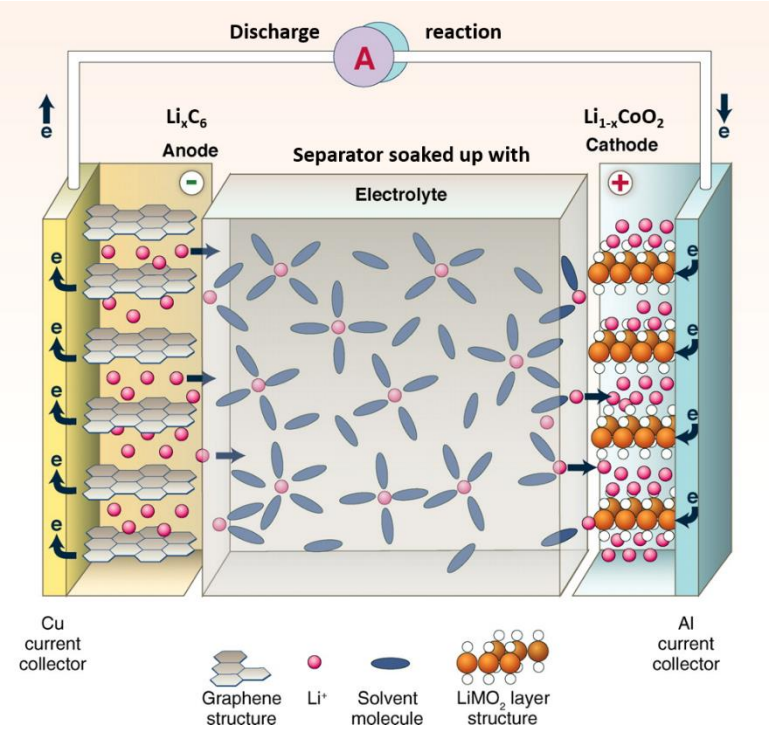

Figure 1. Schematic illustration of the main components and the working principle of lithium-ion batteries, using the example of an LCO/graphite full-cell during discharge. Reproduced from ref. 8 with permission from AAAS (Copyright 2011).

Designed as energy storage device, a battery converts chemical energy directly into electrical energy and vice versa. Since the Li-ions prefer to be intercalated in the cathode due to its higher potential, the discharge reaction proceeds voluntarily and releases the stored chemical energy, while the charge reaction has to be forced by applying electrical power and the afore-described redox reactions occur in reverse direction. The energy is simply the product of the cell voltage (potential difference of the two electrodes) and the cell capacity (extent of the reactions, which is expressed as x in the above equations). Therefore, the gravimetric energy density (Wh/kg) normalized to the mass and the volumetric energy density (Wh/L) normalized to the volume of a rechargeable battery mainly depend on the specific capacities (mAh/g) and the operating potentials (V) of the selected anode and cathode active materials. According to the applied notation, the energy densities refer to the pack, cell, electrode, or material level of the battery. The round-trip energy efficiency of a charge/discharge cycle ($\eta = E_{Discharge}/E_{Charge}$) is less than 100% and decreases with increasing current density due the internal cell resistance, which has ohmic, kinetic, and mass transport-related contributions and thus dissipates some of the energy as heat.

1.2 Electrolyte Solutions

The electrolyte is responsible for the Li-ion transport between the electrodes. Since the voltage range covers more than 4 V, exceeding the stability limit of aqueous electrolytes (≈1.2 V), lithium-ion batteries rely on aprotic solvents, which must be capable of dissolving a lithium salt. Standard solvents are the cyclic ethylene carbonate (EC) in combination with linear carbonates such as dimethyl (DMC), diethyl (DEC), and ethylmethyl carbonate (EMC).[30] Here, EC ensures the dissolution of the salt due to its high dielectric constant, while the linear carbonates decrease the electrolyte viscosity and the freezing point, thus enabling fast Li-ion transport.[30] $LiPF_6$ is the most common electrolyte salt because of the proper balance between several properties, including its high solubility and conductivity (maximum at concentrations of 0.8-1.5 mol/L),[7,31] its ability to passivate the aluminum cathode current collector, and its compatibility with graphite anodes.[30] However, the use of $LiPF_6$ limits the battery operation to temperature below 60°C, because $LiPF_6$ disproportionates increasingly into insoluble LiF and highly reactive PF_5 at higher temperatures.

The reductive stability of the electrolyte is limited to potentials above ≈0.8 V vs. Li^+/Li, where EC starts to decompose mainly into lithium ethylene dicarbonate (LEDC) and gaseous ethylene.[32–34] LEDC forms, together with other decomposition products such as Li_2CO_3 and LiF, a so-called solid electrolyte interphase (SEI) on the graphite surface,[35,36] whose thickness is on the order of ≈50 nm for an EC/EMC/$LiPF_6$ blend.[33] This SEI layer serves as a protective film that blocks the electron transfer between the anode and the electrolyte, thus inhibiting further electrolyte decomposition, while allowing the Li-ions to travel through in order to get de-/intercalated into the graphite host structure. The linear carbonates are less passivating than EC, as they get reduced at lower potentials into the respective lithium alkyl carbonates, carbon monoxide, and soluble lithium alkoxides, which trigger the trans-esterification of unreacted solvent molecules.[37,38]

To improve the SEI properties, especially with respect to the long-term cycling stability of the cell,[39] additives are dosed to the base electrolyte.[40] These additives are generally being reduced at higher potentials than the actual solvents, so that their effectiveness can be evaluated based on the decrease of ethylene gassing

(from EC reduction) and on the extent of trans-esterification (from EMC reduction).[34] The most common SEI-forming additives are vinylene carbonate (VC) and fluoroethylene carbonate (FEC), which both release carbon dioxide and form organic polymer species upon reduction.[41,42] The concentration of additives is typically less than 5 wt% to not significantly alter the bulk electrolyte properties.[7] In case of VC, too high concentrations would increase the irreversible capacity loss and the anode impedance;[43,44] however, FEC can also be used as co-solvent without deteriorating the cell performance.[27,45]

The stability of carbonate-based electrolytes towards electrochemical oxidation is sufficient up to potentials of ≈4.7-4.8 V vs. Li^+/Li.[44,46] Again, VC constitutes an exception, as it already gets oxidized at ≈4.3 V vs. Li^+/Li, which could lead to a significant impedance build-up on the cathode side, especially at elevated temperatures.[44] For this reason, VC should be completely consumed on the graphite anode during the formation cycles, or otherwise be omitted for high-voltage applications. On the other hand, the use of EC-based electrolytes is problematic, because layered oxides evolve oxygen at high delithiation levels.[25,47] The oxygen release causes a chemical oxidation of the electrolyte,[48] to which in particular EC is vulnerable to.[49] Therefore, EC-free electrolytes are currently the preferred choice for high-voltage batteries. These electrolytes either consist of a linear carbonate with a few weight percent of an SEI-forming additive (also called enabler)[50] or they use fluorinated co-solvents such as FEC.[46]

1.3 Anode Active Materials

Li-ion batteries predominantly rely on carbonaceous materials as anode active material (AAM), in particular graphite as well as amorphous (hard and soft) carbons.[6,7] Sony's first LIB from 1991 used a soft carbon material with a discharge capacity of ≈220 mAh/g, but already one year later it was replaced by a hard carbon electrode (which, in contrast to a soft carbon, cannot be graphitized at high temperatures). Back then, the hard carbon provided a capacity of ≈320 mAh/g, which increased the energy density of these second-generation cells from 80 to 120 Wh/kg.[1] The hard carbon material could be further optimized and offers specific capacities of up to 550 mAh/g, which is significantly more than the ≈350 mAh/g provided by graphite. On a volumetric basis, this difference is however much smaller, because graphite possesses a higher density (≈2.2 g/cm^3) than that of hard carbon (≈1.5 g/cm^3). Furthermore, hard carbon has a sloping voltage curve and a poor initial Coulombic efficiency, so that graphite became quickly the favored anode active material.[1,51] Graphite has a low and flat working potential of ≈0.1 V vs. Li^+/Li and the intercalation of lithium into Li_xC_6 occurs in several stages, from which LiC_{12} and LiC_6 are the major compounds (the latter corresponds to a theoretical capacity of 372 mAh/g).[52] On the downside, the low potential with respect to Li^+/Li limits the fast-charging capability of graphite anodes because of the risk of lithium plating. This process can be caused by liquid (electrolyte) and solid phase (graphite) mass-transport limitations and/or by retarded charge-transfer kinetics for lithium intercalation, so that the anode potential drops locally below 0 V vs. Li^+/Li.[53] Since lithium plating consumes active lithium and further bears the risk of lithium dendrite formation, eventually leading to short circuits, it should be avoided under all circumstances, which restricts, e.g., the charging rate, the low-temperature operation, and the application of thick electrodes in today's lithium-ion batteries.[54]

As far as safety is concerned, LTO ($Li_4Ti_5O_{12}$) would be a promising alternative to graphite anodes. Its high working potential of 1.55 V vs. Li^+/Li avoids the formation of an SEI film and of lithium dendrites on the electrode surface,[9] so that the application of nano-sized LTO materials allows for an excellent rate capability and low-temperature operation.[55] Moreover, the spinel structure is very stable with

only 0.2% volume changes during de-/lithiation (thus also referred to as zero-strain material), resulting in a long cycle-life.[56] However, the high working potential goes along with two major drawbacks: (i) in combination with the limited specific capacity of only 175 mAh/g (lithiation until $Li_7Ti_5O_{12}$), the energy density of LTO-containing batteries is significantly lower compared to the ones with graphite. Aiming at increasing the cell voltage, this would call for pairing LTO with high-voltage cathodes, but (ii) LTO anodes further face gassing issues. In the absence of a protecting SEI layer, trace water contaminants and protons formed during electrolyte oxidation at high voltages are easily reduced to H_2.[57] Therefore, LTO is currently not considered to be used in automotive applications, but the long cycle-life makes it attractive for stationary battery storage systems.

Since intercalation compounds cannot provide significantly higher capacities than graphite, alloy- and conversion-type materials are another research focus for the anode side.[58] Within this group, silicon is the most interesting future AAM, because the alloying with lithium to $Li_{15}Si_4$ provides a theoretical capacity of ≈3590 mAh/g,[59] which is almost tenfold higher than that of graphite. Additionally, the average working potential of ≈0.4 V vs. Li^+/Li is rather low, thus enabling high energy densities. However, the alloying process is accompanied by very large volume changes (>300% vs. ≈10% in case of graphite), which induces mechanical stress and particle disintegration.[9] As the SEI layer cannot withstand the expansion/contraction of the silicon particles, this process causes a continuous consumption of electrolyte and lithium inventory on the freshly exposed surface area. On a cell level, the silicon degradation manifests itself in low Coulombic efficiencies and rapid capacity fading. Practical mitigation strategies are blending silicon with graphite in different ratios[59] or limiting the cut-off potentials,[60] such that the anode degradation can be minimized at the expense of its usable capacity. Silicon-graphite composite electrodes are already applied in state-of-the-art lithium-ion batteries (e.g., in Tesla's Model 3).[7,9]

1.4 Cathode Active Materials

Since TiS_2 was predominantly used in its delithiated form,[61] the active lithium that is shuttled between the electrodes had to be provided by the metallic lithium counter-electrode in the first TiS_2/Li batteries introduced by Whittingham.[4] By replacing sulfur in the MX_2 chalcogenide structure with oxygen, Goodenough and co-workers managed to synthesize the lithiated $LiCoO_2$ (LCO) in 1980,[5] which can be paired with a graphite anode and thus does not require a lithium anode. Starting from there, the cathode active material is the active lithium source and consequently governs the capacity of the full-cell. In order to increase the energy density of the cell, as it is desired for extending the driving range of battery electric vehicles, the CAM should have a high reversible capacity and/or a high operating potential.

$LiCoO_2$ belongs to the class of layered transition-metal oxides with the general formula unit $LiMO_2$. Here, the monovalent Li^+ and the trivalent Co^{3+} (M^{3+}) reside in octahedral sites and they are separated in alternating layers within a cubic close-packed array of oxide ions.[62] This layered structure is also referred to as O3 stacking (ABCABC stacking sequence of the oxide lattice).[63] The Li-ion diffusion in the lithium plane occurs via tetrahedral voids that share faces with the native octahedral sites, thus enabling a good Li-ion conductivity. At the same time, LCO features a high electronic conductivity, as it becomes metallic upon delithiation.[62] The theoretical capacity for complete lithium extraction amounts to 274 mAh/g, but the practical capacity was limited for a long time to ≈140 mAh/g,[62] because LCO experiences several phase transitions upon delithiation,[64] which finally lead to the irreversible transformation into an O1 structure (ABAB stacking) and the loss of oxygen from the lattice.[65] At an average voltage of ≈3.9 V vs. Li^+/Li,[29] the material-level energy density of ≈545 Wh/kg would be far below the targeted 800 Wh/kg for automotive applications;[18] however, coating and doping strategies enabled the development of high-voltage LCO with >190 mAh/g (>740 Wh/kg) in recent years.[29,64] Despite these improvements, the limited resources and the high price of cobalt (≈53 US$/kg)[19] render LCO unsuitable for powering battery electric vehicles, but it is still the most prevalent battery technology for consumer electronics[2,9] that only require small amounts of CAM, and for which LCO is advantageous due to its

safety and high volumetric energy density (from the high electrode density).[29] Attempts to replace cobalt in the layered structure by cheaper transition-metals such as manganese (≈2 US$/kg)[26] and iron (≈0.2 US$/kg)[26] failed, because $LiMnO_2$ and $LiFeO_2$ do not crystallize in the O3-type structure during high-temperature calcination.[62] Alternatively, manganese and iron were successfully implemented in two other types of Co-free CAMs, namely (i) spinel oxides with the general formula unit LiM_2O_4 and (ii) phospho-olivines with the general formula unit $LiMPO_4$.

The most common spinel oxide is $LiMn_2O_4$ (LMO), which was first reported by Thackeray and Goodenough in 1983.[66] Here, Mn^{3+}/Mn^{4+} occupies octahedral sites, while Li^+ is placed in tetrahedral sites of the spinel oxide framework.[67] Three-dimensional diffusion channels via neighboring octahedral voids enable a high Li-ion conductivity and better rate capability compared to layered materials with two-dimensional diffusion pathways.[9] The theoretical capacity for $1 > x_{Li} > 0$ in $Li_xMn_2O_4$ amounts to 148 mAh/g, but it is practically restricted to 110 mAh/g.[29] At an operating voltage of ≈4.0 V vs. Li^+/Li, the material-level energy density of 440 Wh/kg is relatively low and LMO further suffers from poor high-temperature performance because of its instability towards protons in the electrolyte, leading to Mn dissolution from the cathode due to the disproportionation reaction of Mn^{3+} into Mn^{2+} and Mn^{4+}. While Mn^{4+} remains in the solid phase, Mn^{2+} dissolves into the electrolyte and deposits on the anode,[68] where the concomitant SEI degradation leads to a capacity fading of the full-cell.[69] For these reasons, LMO is not the exclusive CAM in LIB-powered BEVs, but it is blended in composite cathodes, where LMO contributes high power on acceleration, while the other CAM (typically NCM) offers a high energy density for long driving ranges.[9]

Replacing manganese partially by nickel gives rise to the high-voltage spinel $LiNi_{0.5}Mn_{1.5}O_4$ (LNMO), for which the mean voltage at $1 > x_{Li} > 0$ is shifted from ≈4.0 V to ≈4.7 V vs. Li^+/Li.[70,71] At a reversible capacity of 135 mAh/g,[62] LNMO has a ≈1.4-fold higher energy density of ≈635 Wh/kg compared to LMO. Moreover, the charge compensation is modified, because manganese remains in its inactive and more stable Mn^{4+} state, while nickel gets oxidized from Ni^{2+} at $x_{Li} = 1$ to Ni^{4+} at $x_{Li} = 0$.[72] Since LNMO operates at the oxidative stability limit of carbonate-based electrolytes, the thus generated protons could still attack the spinel structure,

leading to the same capacity fading mechanism than for LMO. Consequently, novel high-voltage electrolytes have to be developed and LNMO is not expected to penetrate the BEV market until the late 2020s at the earliest.[18]

The application of phospho-olivines as cathode active material was discovered by Padhi and Goodenough in 1997,[73] where $LiFePO_4$ (LFP) is the most important and commercially relevant representative. LFP stands out due to its low costs, environmental friendliness, and long cycle-life. Since oxygen is covalently bonded in the phosphate anion, the structural and thermal stability gives LFP an enhanced safety compared to the other types of CAMs.[9] The olivine structure exhibits one-dimensional channels for Li-ion transport, which results in a slow solid-state lithium diffusion and low electronic conductivity;[74] however, the rate capability of LFP can be significantly increased by the use of nanoscale particles (100-500 nm) with an electronically conductive carbon coating at the surface.[75,76] These strategies bring the achievable capacity to ≈160 mAh/g (theoretical capacity of 170 mAh/g). Unfortunately, the low voltage plateau of ≈3.4 V vs. Li^+/Li limits the gravimetric energy density to ≈545 Wh/kg and, owing to its low electrode density, the volumetric energy density of LFP is even more inferior to that of LCO.[29] For this reason, OEMs started to concentrate on other CAMs with a higher energy content for the application in electrified vehicles.[9,18] Nevertheless, LFP is suitable for heavy-duty applications (e.g., buses and trucks) and stationary battery storage systems, where its low costs and longevity are more important than energy density.

Among the presented groups of cathode active materials, spinel oxides and phospho-olivines already exploit the maximum capacity for lithium extraction/insertion ($1 > x_{Li} > 0$), which barely allows for further improvements in terms of energy density (without running into stability issues of the electrolyte at higher voltages; see LNMO). In contrast, layered transition-metal oxides get not fully delithiated upon cycling, so that their energy density can be still pushed further; however, LCO is in conflict with the cost requirements in the automotive industry. As the raw materials contribute by more than 50% to the CAM cost,[77] even the partial substitution of cobalt by cheaper metals can have a big impact.[18] On the research level, this development was initiated around 2000, when cobalt was either mixed with nickel and manganese,[78] or with nickel and aluminum,[79] resulting in the

well-known class of NCM and NCA materials.[80] The first commercialized NCM material was NCM-111 ($Li[Ni_{0.33}Co_{0.33}Mn_{0.33}]O_2$, e.g., employed in the first-generation BMW i3[16]), which provides a reversible capacity of ≈160 mAh/g until an upper cut-off voltage of 4.3 V vs. Li^+/Li.[23] NCM materials with a higher Ni content offer a larger share of their capacity at a given voltage, e.g., NCM-622 has a capacity of ≈185 mAh/g and NCM-811 has a capacity of ≈210 mAh/g until 4.3 V vs. Li^+/Li. Their theoretical capacity amounts to 275-278 mAh/g and is thus virtually identical to that of LCO; however, the cooperation of several transition-metals suppresses the bulk phase transitions known for LCO at high SOCs. Each TM is believed to contribute specific properties to the NCM material. Being the main redox active species, it is the common understanding that nickel offers high capacity but poor cycling and thermal stability, while cobalt provides structural stability and faster kinetics, and the electrochemically inactive manganese is a spectator ion, which improves the cycle-life and safety by stabilizing the structure.[23,61]

With regard to the cycling stability, however, Ni-rich layered oxides are not fundamentally inferior to their lower-Ni variants.[18,24] For a long time, the contrary conception was based on comparative studies where NCM materials with different nickel content were charged to the same upper cut-off voltages,[23,81] but this leads to a vastly different Li utilization (as can be seen for the above given capacities). Consequently, all of the layered oxides face the same problems when operated at a high level of delithiation, irrespective of the Ni fraction or charging voltages; a fact that is primarily related to their surface instability. Starting at an SOC of ≈80% (relative to the pristine state, i.e., $x_{Li} \leq 0.2$), NCMs evolve lattice oxygen from the near-surface region,[25,82] which gradually transforms into a spinel- or rocksalt-type surface layer with an increased charge-transfer resistance.[83,84] The concomitant evolution of CO and CO_2 can be explained by the chemical reaction of the electrolyte with the released oxygen,[49] because it is, at least partially, highly reactive singlet oxygen.[47] Furthermore, the layered oxides experience a strong anisotropic volume contraction upon delithiation, which is again a universal phenomenon almost entirely dependent on the Li utilization;[85] however, it becomes more manifest in Ni-rich layered oxides, as they are intentionally operated to a higher degree of delithiation by cycling them to the same upper cut-off potential (e.g., volume contraction of ≈1% for NCM-111 vs. ≈5% for NCM-811 until 4.3 V vs. Li^+/Li).[24] The

repeated volume change during cycling leads to cracking of the agglomerated NCM particles.[86,87] On the one hand, this could diminish the electrical contact between the individual crystallites,[88,89] and on the other hand, it might enhance the surface-related degradation mechanisms, as the electrolyte infiltrates into the interior of the secondary agglomerates.[87,90] From a bulk perspective, the irreversible migration of transition-metals from the TM layer into the emptied Li layer at high SOCs may reduce the solid-state lithium diffusion, which finds expression in an increased impedance of the cathode.[91] This so-called cation mixing is considered to be more relevant for Ni-rich layered oxides.[92,93] In section 3.4, we investigate the capacity fading of the Ni-rich NCM-811 during long-term cycling, whereby we put special emphasis on the quantification and interrelation of these intrinsic degradation mechanisms of the cathode active material.

Indeed, layered oxides with a nickel content of about 80% currently belong to the most Ni-rich CAMs with proven cycling stability.[9,18,80] At an upper cut-off voltage of 4.3 V vs. Li^+/Li, equivalent to the most common end-of-charge voltage of 4.2 V in a full-cell,[6,94] the reversible capacities of 210 mAh/g obtained from NCM-811 ($Li[Ni_{0.80}Co_{0.10}Mn_{0.10}]O_2$) and of 200 mAh/g obtained from NCA-80 ($Li[Ni_{0.80}Co_{0.15}Al_{0.05}]O_2$) translate into a material-level energy density of ≈800 Wh/kg and 760 Wh/kg, respectively.[29] As these values already touch the targeted energy density for BEVs, NCM and NCA materials will soon prevail the battery market. This is shown in Table 1, where the here discussed CAMs are compared with respect to their basic electrochemical properties and market share. In 2018, the CAM volume was about 350,000 tons worldwide and the sum of NCM and NCA market share was 50%.[95] It is forecasted that the total volume will grow to more than 1,670,000 tons in 2030, which is predominantly driven by the vehicle electrification, and the Ni-rich layered oxides will almost entirely replace the other commercialized CAMs with a joint market share of 93%. Here, the vast majority of OEMs is expected to focus on NCM materials, while Tesla is assumed to keep NCA chemistry.[18,95] Although the two Ni-rich CAMs deliver similar practical capacities and energy densities, manganese and aluminum dopants also induce subtle differences. NCM-811 offers a better thermal stability (stabilizing effect of Mn) and slightly lower costs (less complex synthesis), while NCA-80 is advantageous with

respect to its power characteristics (Al facilitates Li-ion diffusion) and cycle-life (Mn is especially detrimental due to its dissolution and deposition on anode).[9,80]

Table 1. Electrochemical characteristics[29,62] and market share[95] of commercialized and so-called emerging cathode active materials for lithium-ion batteries. The electrochemical data refer to the material level and thus represent the most optimisitc values, which can be obtained in a half-cell measurement at a slow rate. For the layered oxides, the upper cut-off voltage vs. Li^+/Li is chosen at 4.3 V (NCM = NCM-811, NCA = NCA-80), 4.45 V (high-voltage LCO), and 4.7 V (LMR-NCM), respectively. The theoretical capacity of Li- and Mn-rich layered oxides depends on the degree of over-lithiation.[27] The market share includes their usage in portable electronic devices, battery electric vehicles, and industrial as well as stationary applications; however, the forecasted values for 2030 are mainly driven by the automotive sector.[95] The market launch of LNMO and LMR-NCM is not expected to be before the late 2020s at the earliest.[18]

CAM	Theoretical capacity [mAh/g]	Practical capacity [mAh/g]	Average voltage [V vs. Li^+/Li]	Gravimetric energy density [Wh/kg]	Market share in 2018 [95]	Projected market share in 2030 [95]
Commercialized						
LCO	274	190	3.9	740	11%	2%
LMO	148	110	4.0	440	5%	—
LFP	170	160	3.4	545	34%	5%
NCM	275	210	3.8	800	41%	87%
NCA	279	200	3.8	760	9%	6%
Emerging						
LNMO	147	135	4.7	635	—	—
LMR-NCM	350-380	250	3.6	900	—	—

At the moment, most R&D efforts are invested in increasing the nickel content as much as possible. For example, Tesla might utilize this year a hybrid NCMA cathode active material with 90% Ni and less than 5% Co for its Model Y produced at the Gigafactory Shanghai,[96] which further combines the beneficial properties of Mn and Al dopants.[97] In the end, this trend could culminate in pure lithium nickel oxide ($LiNiO_2$, LNO), which was already explored in the early 1990s by Dahn and co-workers,[98] but back then LNO suffered from too many drawbacks, such as an off-stoichiometric composition after synthesis, multiple phase transitions during de-/lithiation, and its high sensitivity towards surface impurities at ambient storage.[99] Now, these obstacles might potentially be overcome by the incorporation of ≤5% dopants.[100,101]

This development raises the fundamental question about the need to investigate CAMs other than NCM and NCA, that is, high-manganese cathodes such as LNMO or Li- and Mn-rich layered oxides (LMR-NCM; mentioned in the beginning and also shown in Table 1). Focusing on LMR-NCM, the gravimetric energy density of 900 Wh/kg is indeed higher than that of NCM-811 and NCA-80; however, this benefit gets lost on a volumetric basic due to the lower electrode density (2.7 vs. 3.2-3.4 g/cm^3), resulting in ≈2400 Wh/L for LMR-NCM versus ≈2600 Wh/L for the two Ni-rich CAMs.[29] On a cell level, the energy densities of the different CAMs are very similar as well, independent of the selected anode material.[16] Furthermore, Li- and Mn-rich layered oxides fall short on several other frontiers, e.g., energy efficiency, rate capability, and cycling stability, such that it still awaits commercial success despite intensive efforts in both academia and industry.[28,29] Hence, Volkswagen surprised many market observers during its Power Day event in March 2021,[102] where VW announced to incorporate high-manganese cathodes such as LNMO and LMR-NCM into its mainstream cathode chemistry.[103] Even though all CAMs will eliminate Co sooner or later, the main reason to roll out high-manganese cathodes is the even ≈8-fold lower metal price of Mn (≈2 US$/kg)[26] compared to Ni (≈16 US$/kg),[19] which might yield a material cost saving of ≈20% for LMR-NCM cathodes compared to NCM-811 and NCA-80.[7] Beyond that, Mn is ≈10 times more abundant than Ni and widely distributed over many countries and regions, thus posing no risk for the supply chain.[103] Since apparently a lot of hopes are pinned on LMR-NCM cathodes, but the material still suffers from many drawbacks, the next section will examine it more closely.

1.5 Li- and Mn-Rich Layered Oxides and Their Challenges to Commercialization

At a first glance, Li- and Mn-rich NCMs closely resemble the afore-noted NCMs such as NCM-811, because they also possess a layered structure with alternating lithium and transition-metal layers within the oxide lattice, but some of the transition-metals are intentionally replaced by lithium (see Figure 3a,b). Starting from the known formula unit $LiMO_2$ with an ideal Li:M ratio of 1:1, this over-lithiation can be either expressed as $Li_{1+x}M_{1-x}O_2$ or $Li[Li_xM_{1-x}]O_2$. The first notation might be preferably used for regular layered oxides (e.g., $Li_{1+x}[Ni_{0.8}Co_{0.1}Mn_{0.1}]_{1-x}O_2$), because it does not alter the transition-metal composition in the square brackets, by which NCM (and NCA) materials are commonly abbreviated in the literature. These materials also have a small off-stoichiometry after synthesis, which typically amounts to $|x| \leq 0.05$.[24,104] The usage of the absolute value indicates that the materials can either have excess lithium, as it is the case for commercial LCO cathodes,[105] or excess transition-metal (TM), as it is commonly reported for the opposite end member LNO.[106,107] In addition, the mixed compounds such as NCM tend to cation mixing between the lithium and transition-metal layer,[61] which can be expressed as $Li_{1-x}M_x[Li_xM_{1-x}]O_2$ (assuming a Li:M ratio of 1:1) and which is on the same order of magnitude with $x \leq 0.05$ after synthesis (here only positive values).[108] Both phenomena could affect the electrochemical performance of regular layered oxides, because the occupation of TMs (mostly Ni^{2+}) in the lithium layer blocks free Li sites und further reduces the Li-ion solid-state diffusion;[91] however, the general characteristics such as the shape of the voltage curve remain fairly unaltered if the extent of off-stoichiometry and/or cation mixing is small.[61,109] Later, it will be discussed how the composition of a layered oxide can be measured by an elemental analysis of the pristine CAM powder (see section 2.3), while the cation mixing can be accessed by powder diffraction and Rietveld refinement (see section 2.2).

Archetypical Li_2MnO_3.—The second notation $Li[Li_xM_{1-x}]O_2$ highlights the structural modification of LMR-NCMs, because the progressive substitution of excess Li^+ for M^{3+} takes place in the transition-metal layer. In order to maintain the overall 3+ charge, the remaining M elements have an increasing share of M^{4+} following the equation $Li[Li_x^+M_{2x}^{4+}M_{1-3x}^{3+}]O_2$, so that the maximum Li content in the TM layer

amounts to x = 1/3.[28] Several elements can crystallize in the Li-rich $Li[Li_{1/3}M_{2/3}]O_2$ structure type (M = Mn, Ni,[110] Ru,[111] Sn,[111,112] Ir,[112] etc.), alternatively denoted Li_2MO_3, but Li_2MnO_3 is the most prominent and best studied compound among this group.[113–119] Its crystallographic motif is based on the O3-type layered structure already known from $LiMO_2$; however, the Li:Mn ratio of 1:2 energetically favors their ordered arrangement in the TM layer. While the transition-metals are randomly distributed in regular NCM materials, one LiO_6 octahedron is ideally surrounded by six MnO_6 octahedra to form a honeycomb pattern in Li_2MnO_3. This in-plane ordering reduces the symmetry from the rhombohedral system of $LiMO_2$ (space group $R\bar{3}m$) to the monoclinic system (space group $C2/m$), but the additional superstructure reflections in the X-ray diffractogram are often broad and weak due to the presence of extended stacking faults (resulting from planar shifts of the TM layer) and microstructural defects (such as Li_2O vacancies), which both heavily depend on the synthesis conditions.[116,118]

Historical aspects.—The development of Li- and Mn-rich layered oxides can be dated back to the early 1990s, where Li_2MnO_3 was considered to be electrochemically inactive, but then Thackeray et al. found out that $Li_{2-x}MnO_{3-x/2}$ phases ($0 < x < 2$) could be used as cathode active material.[113] These phases were prepared by acid leaching of Li_2O from Li_2MnO_3 and they delivered capacities of up to 200 mAh/g upon relithiation in a lithium cell. In 1997, Numata et al. reported that $Li(Li_{x/3}Mn_{2x/3}Co_{1-x})O_2$ phases ($0 \leq x \leq 1$) can be synthesized as a solid solution between the two end members, $LiCoO_2$ and Li_2MnO_3.[120] Due to their structural compatibility, the inert Li_2MnO_3 component could effectively stabilize the electrochemically active $LiCoO_2$ during cycling to an upper cut-off voltage of 4.3 V vs. Li^+/Li, at the expense of lowering the discharge capacity from ≈160 mAh/g for x = 0 (LCO) to ≈90 mA/g for x = 0.3.[121] In 1999, Kalyani et al. reported for the first time that Li_2MnO_3 can be electrochemically activated by charging until 4.5 V vs. Li^+/Li.[114] Then, Lu and Dahn synthesized and characterized a series of $Li[M_xLi_{1/3-2x/3}Mn_{2/3-x/3}]O_2$ compounds ($0 < x \leq 0.5$) with M being Ni[122–124] or Cr,[125] while Park and co-workers reported the Co-based counterparts.[126] Following the expected sloping voltage curve until 4.4 V vs. Li^+/Li, these materials can access additional capacity during an irreversible voltage plateau at 4.5 V vs. Li^+/Li, which was overlooked by Numata et al. and which increases with decreasing x (i.e., with

more lithium in the TM layer). The materials exceeded 300 mAh/g during the first charge and offered a reversible capacity of more than 225 mAh/g in the following cycles.

Crystal structure.—The interest in such materials was driven by the aim of stabilizing the layered $LiMnO_2$, which was already around 2000 to be considered to be a cost-competitive alternative to LCO and LNO, while delivering higher capacities than the spinel LMO.[127] However, the direct synthesis is not possible due the similar radii of Li^+ and Mn^{3+}, and also the ion-exchanged $LiMnO_2$ (prepared from the layered $NaMnO_2$) readily converts into the more stable spinel structure upon delithiation, resulting in a poor electrochemical performance.[28] Therefore, the above research groups and others tried to stabilize the layered structure by introducing an $LiMO_2$ component (with M being a single or several TMs) into the structurally related Li_2MnO_3.[127,128] In 2004, Thackeray and colleagues at the Argonne National Laboratory started to use this formal two-phase notation, $x\ Li_2MnO_3 \cdot (1\text{-}x)\ LiMO_2$, to describe Li- and Mn-rich CAMs as a structurally integrated "layered-layered" composite,[109,129] while others headed by Dahn et al. think of these materials as a solid solution using the equivalent notation $Li[Li_{x/(2+x)}M'_{2/(2+x)}]O_2$ (with M' = Mn + M).[130,131] Here, the over-lithiation typically amounts $x \approx 0.3\text{-}0.5$, translating into ≈13-20% lithium in the TM layer.[27,131] Since this is less than the 33% lithium residing in the TM layer in Li_2MnO_3, the vivid and in part controversial debate about the original structure of Li- and Mn-rich layered oxides addresses the cation ordering in the TM layer, forming either segregated, nm-seized M and honeycomb-like Li/Mn clusters (see Figure 2a), or a homogeneous TM distribution with long-range Li ordering (see Figure 2b).

A comprehensive review by Hu et al. concluded that about 30% of the literature reports support the two-phase composite model (with $R\bar{3}m$ + $C2/m$ phases), while 70% favor the solid solution model of either $R\bar{3}m$ or $C2/m$ symmetry.[131] To corroborate their findings, researchers employed various experimental techniques such as XPD,[130,132] NMR,[133,134] XAS,[134,135] and TEM;[136,137] however, their conclusions might often not be reliable, as they are drawn for a single material and/or from selected techniques. This is especially the case for the composite model due to the structural similarity between the two phases and the lack of a defined reference

structure.[131] Using a solution-based combinatorial approach, McCalla et al. studied large arrays of compositions in the Li-Mn-Co and Li-Mn-Ni oxide pseudo-ternary systems.[138–140] For the Li-Mn-Co oxide system,[138] they observed solid solutions over the entire composition line between $LiCoO_2$ and Li_2MnO_3 when the samples were quenched from either 800 or 900°C. Upon slow cooling (1°C/min), however, the structures separate on the 2-10 nm length scale with both domains lying on the same lattice, as evidenced through a rigorous analysis of the peak broadening in the XPD patterns. Similarly, the phase separation in the Li-Mn-Ni oxide system strongly depends on the calcination conditions (e.g., temperature, atmosphere, and cooling rate)[139] and metal site vacancies may promote the formation of a solid solution.[140] Hong et al. point out that a nanocomposite can be hardly distinguished from a solid solution when each domain just contains a few atoms and approaches a size of less than 1 nm.[141] Due to this complexity and the diversity of opinions in the literature, we will use both notations interchangeably throughout this work, even though diffraction data are solely treated with a single-phase structural model, giving preference to the $R\bar{3}m$ symmetry (see section 3.3).

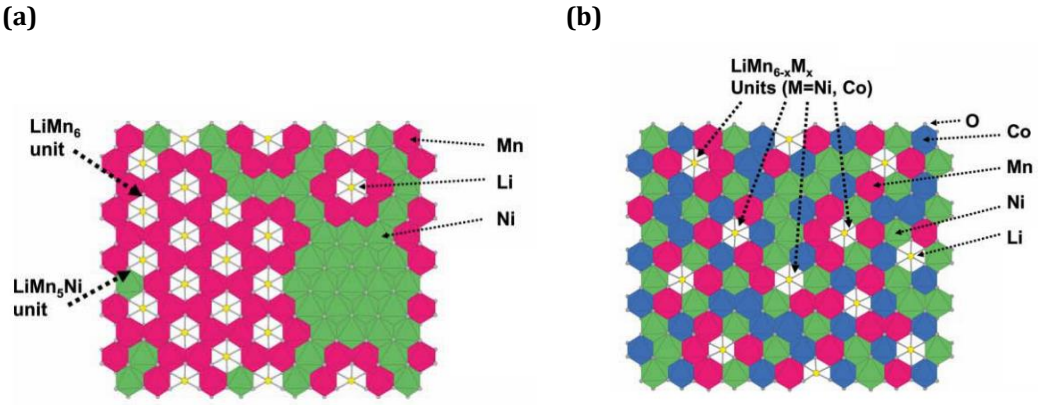

Figure 2. Schematic structural illustrations of the TM layer in Li- and Mn-rich layered oxides. **(a)** $Li_{1+x}(Mn_{0.5}Ni_{0.5})_{1-x}O_2$ with $x \approx 0.1$, where the Li-ions remain clustered to the Mn-ions, forming preferentially $LiMn_6$ units in a honeycomb pattern, so that the material can be described as a Li_2MnO_3-$LiNiO_2$ nanocomposite structure according to the two-phase notation. **(b)** $Li_{1+x}(Mn_{0.33}Ni_{0.33}Co_{0.33})_{1-x}O_2$ with $x \approx 0.1$, where the partial replacement of Mn by Co makes it difficult to preserve $LiMn_6$ units with distinct short-range order, thus forming $LiMn_{6-x}M_x$ units, so that the material can be considered as a solid solution with long-range Li ordering. Reproduced from ref. 109 with permission of The Royal Society of Chemistry (Copyright 2007).

Charge compensation mechanism.—More importantly, the debate about the proper structural model also governed the understanding of the redox processes in Li- and Mn-rich layered oxides. Figure 3c,d show typical charge/discharge voltage curves of a regular NCM-811 and of an over-lithiated $Li[Li_{0.17}Ni_{0.19}Co_{0.10}Mn_{0.54}]O_2$,

which can alternatively be written as 0.42 $Li_2MnO_3 \cdot 0.58\ Li[Ni_{0.39}Co_{0.20}Mn_{0.41}]O_2$, during the first two cycles in a half-cell. In case of the NCM-811 CAM, the cationic framework can compensate for the exchanged capacity when the transition-metals get oxidized until their 4+ state (see dashed black lines). Note that this TM-mediated capacity is slightly less than the theoretical capacity of 274 mAh/g for complete lithium extraction due to the 1% over-lithiation, but sufficiently more than the ≈236 mAh/g reached within the first charge until 4.5 V vs. Li^+/Li. In contrast, the TMs could only account for less than half of the ≈317 mAh/g obtained until 4.8 V vs. Li^+/Li for LMR-NCM cathode (theoretical capacity of 350 mAh/g if all lithium is extracted from the material). In fact, the cationic redox is responsible for the sloping part of the first charge curve,[142,143] where the material behaves like a regular layered oxide,[144,145] but it cannot explain the extended voltage plateau afterwards. Thus, researchers debated several possibilities, where the extra capacity might come from, such as TM over-oxidation,[114,146] Li^+/H^+ exchange,[115] or oxygen extraction/re-insertion.[147]

Based on the two-phase notation, there was the wide-spread belief that the Li_2MnO_3 phase becomes activated during the plateau according to $Li_2MnO_3 \rightarrow 2Li^+ + 2e^- + MnO_2 + 0.5O_2$, so that the newly formed MnO_2 phase could be reversibly cycled in addition to the already active Li_xMO_2 component in the following cycles.[109,129,148] This reaction would imply that lattice oxygen is irreversibly lost from the bulk structure, as was attempted to prove, e.g., by the detection of intermediate Li_2O on the cathode surface (using surface-enhanced Raman spectroscopy)[149] or of oxygen-deficient structures in the charged state (using XPD and NPD).[124,150] Furthermore, several groups detected O_2 upon charging by mass spectrometry;[151–154] however, they either used a staircase voltage profile[151] or linear voltage ramps,[152,153] so that the gas release could not be correlated to the voltage plateau. In 2014, Castel et al. were most likely the first ones who quantified the evolved O_2 and CO_2 during a constant current charge, but they were focusing on follow-up reactions in the electrolyte.[154] Therefore, we will present in section 3.2 several on-line electrochemical mass spectrometry (OEMS; see section 2.1) studies,[27,155] which for the first time showed that the oxygen release happens after the voltage plateau and, more importantly, that the evolved oxygen is far too little to explain the extra

capacity according to the until then assumed Li_2MnO_3 activation that was described above.

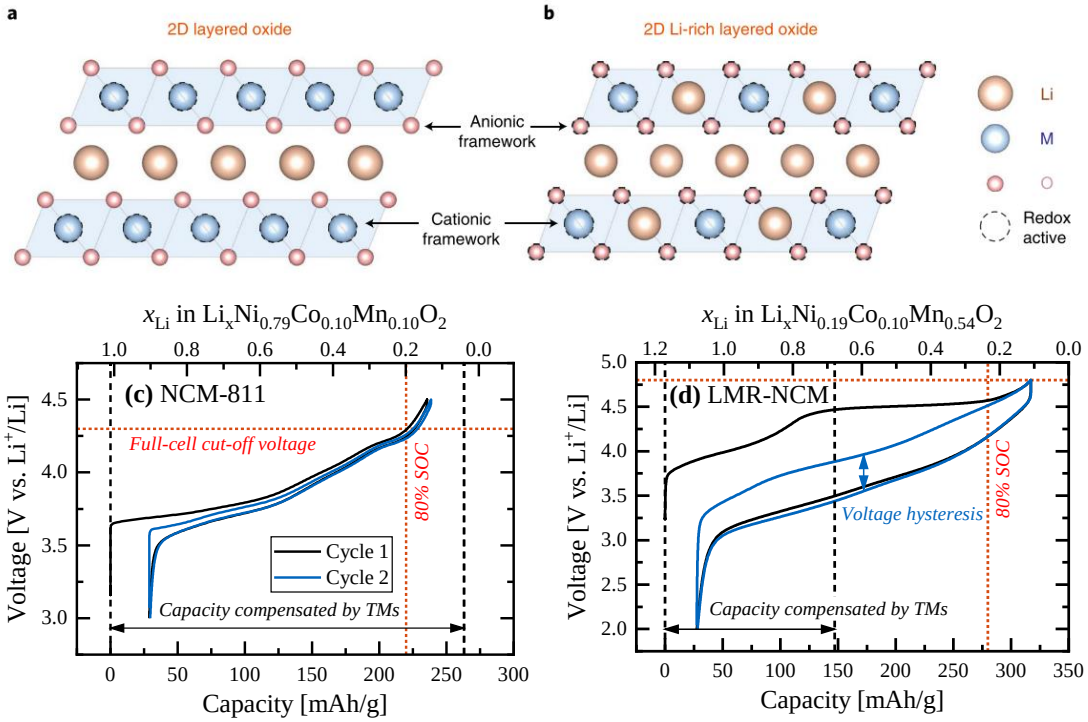

Figure 3. Crystal structure and electrochemical properties of layered oxides: **(a)** structure of a regular layered oxide, such as NCM-811, and **(b)** of an over-lithiated layered oxide, such as $Li[Li_{0.17}Ni_{0.19}Co_{0.10}Mn_{0.54}]O_2$ (corresponding to 0.42 Li_2MnO_3), which incorporates additional lithium in the TM layer (cationic framework) and further uses the anionic framework as an active redox center. Reproduced from ref. 156 with permission from Springer Nature (Copyright 2018). **(c,d)** Comparison of the corresponding voltage profiles within the first two charge/discharge cycles. The electrode voltages were measured at 25°C and at a C-rate of C/10 against a metallic lithium CE in the voltage window of either 3.0-4.5 V (NCM-811) or 2.0-4.8 V vs. Li^+/Li (LMR-NCM). The exchanged capacity is also referred to the lithium content in the layered oxides (top x-axis).

Now, it is generally accepted in the literature, on the basis of complementary theoretical[157,158] and experimental works (using XAS and XPS),[142,143,159] that the extraordinary capacity during the voltage plateau originates from a reversible O^{2-}/O^{n-} redox ($n < 2$) of the anionic framework, which is independent of the cationic redox and which also persists after the activation charge. The principles of the anionic redox are reviewed in detail by Assat and Tarascon.[156] In short, all three oxygen 2p orbitals are engaged in M-O bond formation in regular layered oxides $LiMO_2$, while the higher O:M ratio in over-lithiated materials leads to an O 2p non-bonding state due the weak interaction with the Li 2s orbital. This O non-bonding state offers a second band, besides the usual M-O anti-bonding band, for removing electrons and thus gaining capacity, but it exhibits sluggish kinetics compared to the fast cationic redox.[143] Its position in the band structure of the oxide determines

the ratio of reversible versus irreversible anionic redox, whereby the latter leads to oxygen release from the near-surface region of the CAM particles, as will be also shown in section 3.2.[27,155] For Li- and Mn-rich layered NCMs, the reversible contribution in the bulk is however the dominating process.[142] Interestingly, it was recently shown that the archetypical Li_2MnO_3 indeed releases O_2 as a $4e^-/O_2$ process (accounting for ≈70% of the first charge capacity),[119] as expected for the above activation reaction. Since the first charge capacity of Li_2MnO_3 increases with the available surface area,[117] the oxygen release is a surface-driven process.

Oxygen release and its implications.—The same holds true, albeit to a much lower extent, for the here investigated Li- and Mn-rich NCMs. The oxygen vacancies promote a transition-metal migration to form a reconstructed spinel-like surface layer,[160] as evidenced by (S)TEM measurements.[161–163] Since the loss of lattice oxygen is accompanied by the reduction of surface TM-ions,[164] the entire process is not expected to provide any electrons for the external circuit und is thus analogous to the surface degradation known from regular layered oxides.[25,83,84] Both stoichiometric and over-lithiated layered oxides were intensively studied by OEMS in our group.[25,27,47,82,155] Table 2 summarizes the oxygen release from in total six CAMs during the initial cycles (in the form of O_2, CO, and CO_2). They were deliberately charged to an SOC of 87-94% (relative to the total amount of lithium in the pristine composition; corresponding to different upper cut-off voltages) to trigger the oxygen release starting at ≈80% SOC. To evaluate which class of materials is more prone to surface instabilities at high delithiation levels, the gas amounts have to be compared in the surface-normalized unit of µmol/m² (using the BET surface area of the pristine CAMs). Surprisingly, the stoichiometric CAMs appear to release significantly more oxygen; however, we will show in section 3.4.2 that the cracking of NCM particles increases their surface area by a factor of ≈10 in the charged state compared to the ≈0.3 m²/g in the pristine state, while the high surface area of ≥6 m²/g of the over-lithiated CAMs remains essentially unaltered during cycling. Hence, the intrinsic oxygen release from regular NCMs closely corresponds to that of the over-lithiated CAM with 0.33 Li_2MnO_3 content, amounting to ≈23-27 µmol/m². Increasing the Li_2MnO_3 content leads to considerably more gassing (by a factor of up to 5 for the 0.50 Li_2MnO_3 CAM), because the increasing share of anionic compared to cationic redox enhances its

instability, so that the oxygen depletion zone can penetrate deeper into the active material particles. The subsequent surface reconstruction diminishes the rate capability of the LMR-NCM cathodes due to the high charge-transfer resistance of the spinel-like surface layer.[27,145]

Table 2. Oxygen release from stoichiometric[25] and over-lithiated layered oxides,[27] as determined during the initial 2-4 cycles at 25°C by on-line electrochemical mass spectrometry. The CAMs were intentionally delithiated beyond the onset of oxygen release at an SOC of ≈80% (see uppermost SOC at the upper cut-off voltage; onset voltage also provided), whereby the SOC is referenced to the total amount of lithium in the materials. The evolved amounts of O_2, CO, and CO_2 are referenced to the CAM mass (µmol/g) and the sum is also normalized to the BET surface area of the pristine CAMs (µmol/m²). Measurement conditions: Stoichiometric CAMs: 4 cycles, graphite CE, $LiPF_6$/EC electrolyte. The full-cell voltages were converted into the ≈0.1 V higher voltages versus Li^+/Li. Over-lithiated CAMs: 2 cycles, lithium CE, $LiPF_6$/FEC/DEC electrolyte.

CAM	A_{BET}	Voltage		SOC	Gas evolution				
	[m²/g]	[V vs. Li^+/Li]		[%]	[µmol/g]				[µmol/m²]
		Onset	Cut-off	Cut-off	O_2	CO	CO_2	Σ	Σ
Stoichiometric[25]									
NCM-111	0.26	≈4.67	≈4.9	94	2.3	21	47	≈70	≈270
NCM-622	0.35	≈4.64	≈4.9	92	2.1	28	60	≈90	≈255
NCM-811	0.18	≈4.30	≈4.5	87	1.4	13	31	≈45	≈250
Over-lithiated[27]									
0.33 Li_2MnO_3	6.5	4.6	4.8	92	6	n.d.	140	≈146	≈23
0.42 Li_2MnO_3	6.5	4.6	4.8	92	180	n.d.	125	≈305	≈50
0.50 Li_2MnO_3	6.0	4.6	4.8	91	550	n.d.	145	≈695	≈115

Table 2 allowed for a mechanistic comparison of the oxygen release from the different CAMs; however, in real applications the regular layered oxides are typically operated until a full-cell voltage of 4.2 V,[6,94] corresponding to ≈4.3 V vs. Li^+/Li. Thus, NCM-111 and NCM-622 are not expected to evolve any oxygen (onset potential >4.6 V vs Li^+/Li; see Table 2), while NCM-811 is close to the SOC threshold of 80% under this condition (see red dotted lines in Figure 3c). In contrast, the over-lithiated layered oxides have to be cycled until a full-cell voltage of 4.7 V in the first cycle (4.6 V in the following cycles) in order to reach their full capacity, so that they run inevitably into the oxygen release regime (see Figure 3d). This might raise safety concerns, especially for large-format pouch cells, because the cathode becomes another gassing source next to the SEI-related anode gassing. In Table 3, we compare their gassing contributions for state-of-the-art NCM-811/graphite and

LMR-NCM/graphite full-cells within the first cycle(s). Here, the oxygen release from the NCM-811 CAM leads to a projected gas volume of <1 mL/Ah, which is negligibly small compared to the anode gassing of ≈11-14 mL/Ah (comprising C_2H_4, H_2, and CO from the EC-based electrolyte).[25] The decomposition of surface carbonate impurities (typically ≈0.1 wt% Li_2CO_3, releasing CO_2) might add up to ≈2 mL/Ah more gassing from the cathode side,[25,165] but the total gassing is almost exclusively restricted to the first cycle. Applying a single degassing step during the first discharge, ≈6 Ah NCA-81/graphite multi-layer pouch cells could be operated for more than 1500 cycles until an end-of-charge voltage of even 4.3 V, without facing any gassing issues.[166,167]

Table 3. Comparison of the anode (due to SEI formation) versus cathode gassing (due to oxygen release) in state-of-the-art NCM-811/graphite[25] and LMR-NCM/graphite[166] full-cells with their optimized electrolyte systems until an end-of-charge voltage of 4.2 V and 4.7/4.6 V (first/following cycles), respectively. The gas amounts are referenced to the CAM mass (µmol/g) and they are further expressed as a projected gas volume per full-cell capacity (mL/Ah; evaluated at 25°C and 1 bar). The anode/cathode areal capacity balancing amounts to 1.2/1.0 in both cases. The anode gassing of the NCM-811/graphite full-cell represents the range measured for several NCM/graphite cells by Jung et al.[25] To change the gassing ratio between cycle 1 and cycle 2-4, the LMR-NCM/graphite cells were either activated at 25 or 45°C, while the following cycles were measured consistently at 25°C. The gassing in cycle 2-4 was not separated into its contributions originating from anode and cathode.

Setup	Cycle 1				Cycle 2-4	
Temperature	Anode gassing		Cathode gassing		Full-cell gassing	
[°C]	[µmol/g]	[mL/Ah]	[µmol/g]	[mL/Ah]	[µmol/g]	[mL/Ah]
NCM-811/graphite, EC-based electrolyte, until 4.2 V[25]						
25	≈80-100	≈11-14	<10	<1	—	—
LMR-NCM (0.33 Li_2MnO_3)/graphite, FEC-based electrolyte, until 4.7/4.6 V[166]						
25+25	≈90	≈9	≈160	≈16	≈125	≈12
45+25	≈105	≈11	≈220	≈22	≈60	≈6

This established NCA-81/graphite cell chemistry served as reference for ≈7 Ah LMR-NCM/graphite cells, whose gassing behavior is also shown Table 3 (as estimated from OEMS measurements). Here, the anode evolves ≈9 mL/Ah at 25°C in an FEC-based electrolyte (mainly CO_2 and H_2), which is fairly similar to the NCM-811/graphite cell. Since the BET surface area of both graphite types amounts to ≈4 m^2/g, the small variation in anode gassing originates mainly from the different reduction mechanisms in EC-based versus FEC-based electrolytes.[34,41,42]

The cathode consists of a 0.33 Li_2MnO_3 CAM, which showed the least oxygen release in Table 2, but the projected gas volume of ≈16 mL/Ah is almost twice as much as from the anode side and the gassing continues on a similar level in the following cycles (most likely also caused by the cathode). To prevent the pouch cells from burst opening due to the excessive cathode gassing, the formation strategy had to be modified by (i) increasing the activation temperature from 25 to 45°C (in order to shift as much gassing as possible into the first cycle; see Table 2) and (ii) by a adding a second degassing step (in order to split the contributions from anode and cathode).[166]

Aside from the sheer quantity of gas, the concomitant evolution of CO_2 (and CO) indicates the chemical oxidation of the electrolyte caused by reactive oxygen species, which were initially proposed to be superoxide radicals,[154,168,169] but more recent results by our group point towards the importance of singlet oxygen in this process.[47,49] In the case of EC-based electrolytes, the electrolyte degradation would lead to a rapid rollover failure of LMR-NCM/graphite full-cells due a resistance build-up, probably caused by organic surface deposits;[46] more stable cycling performance is obtained with the here employed FEC-based electrolyte, but its drawback is the limited thermal stability of FEC in combination with $LiPF_6$ salt.[170] In either instance, the generation of protons leads to TM dissolution,[171,172] from which especially manganese damages the SEI layer and consumes active lithium on the graphite anode.[69,173,174]

The gas evolution owing to the FEC decomposition is the most likely reason why the ≈7 Ah LMR-NCM/graphite pouch cells got ruptured after ≈250 cycles, so that the tests had to be stopped for safety reasons.[167] To conclude, the gassing of LMR-NCM cathodes remains a serious challenge, which compromises safety, cost, and energy density and still awaits proper mitigation strategies.

Coulombic efficiency.—Several review articles comment on the first cycle Coulombic efficiency (CE) being a major drawback of Li- and Mn-rich layered oxides with reported values of ≤80%.[29,131,175] However, the comparison in Figure 3c,d shows that an NCM-811 and LMR-NCM cathode can possess fairly similar irreversible capacity losses of ≈27-29 mAh/g (CE of 88% and 91%, respectively). For regular layered oxides, the lowered Li-ion solid-state diffusion[176] and the high

charge-transfer resistance[177] at high degrees of lithiation limit the full occupation of the Li layer during discharge, while the irreversible removal of the Li-ions from the TM layer during the first charge is another influence factor for over-lithiated oxides.[178] On a full-cell level, Schreiner et al. reported slightly lower CE values of 85% and 84% for the NCA-81 and 0.33 Li_2MnO_3 CAM, respectively, but they are again almost identical. Since graphite anodes typically have an initial Coulombic efficiency of ≈92%,[29] the extra lithium from an LMR-NCM cathode might serve as a reservoir to compensate for the active lithium loss due to TM (Mn) dissolution upon cycling, but for a yet unknown reason, only half of the lithium from the irreversible capacity loss of the LMR-NCM cathode reaches the anode side.[27]

CAM morphology.—One of the key aspects to achieve both high discharge capacity and high initial CE is the particle morphology of the CAM. State-of-the-art LMR-NCM materials consist of loosely packed, porous agglomerates (diameter of ≈10 µm) with relatively small primary particles (diameter of ≈0.05-0.2 µm) and a high surface area (≥5 m^2/g; see Table 2).[166] This morphology is beneficial with respect to the electrochemical characteristics, because the short Li-ion diffusion length in the solid and the high exposed CAM surface area for lithium de-/intercalation facilitate the rate capability.[131] On the downside, the high surface area triggers the formation of surface hydroxide and carbonate impurities, which compromise the cell performance due to side reaction with the electrolyte.[179,180] Moreover, the loosely packed agglomerates possess a high internal porosity, as visualized in the cross-sectional SEM image in Figure 4a, which reduces the industrially important tap density of the CAM powders to ≤2 g/cm^3 (compared to ≈2.5 g/cm^3 for a commercial NCM-622 CAM[181]).[29]

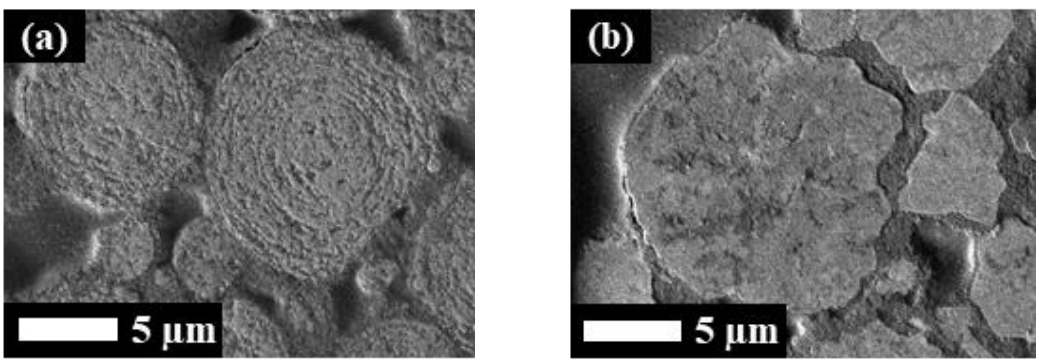

Figure 4. Cross-sectional SEM images of **(a)** a porous and **(b)** a dense 0.33 Li_2MnO_3 CAM, which will be characterized in more detail in section 2.3.

Schreiner et al. could show that this internal porosity cannot be removed during the calendering of the electrode sheets, because severe defects such as the embossing of the aluminum foil would set in before the breakage of the particles, so that the electrodes could only be compacted to a porosity of 42% (electrode density of 2.3 g/cm^3).[166] As a consequence, LMR-NCM cathodes would miss the material-level requirement of the volumetric energy density defined in section 1.4 (calling for an electrode density of 2.7 g/cm^3, which requires a porosity of 32%). Since the additional pore volume has to be filled with electrolyte, it further adds weight on the cell level. This calls for an optimization of the synthesis process, either during the co-precipitation of the TM precursors and/or during the subsequent calcination with the lithium source, in order to obtain more densely packed CAMs with low internal porosity and high tap density, as exemplarily shown in Figure 4b for a differently synthesized LMR-NCM material.[182,183] In section 2.3, we will introduce several techniques to determine the morphology of cathode active materials. These techniques will be then applied in section 3.1, where we compare state-of-the-art porous CAMs with new dense CAMs with regard to their physical and electrochemical properties.

Voltage hysteresis.—Following the first activation cycle, the combination of cationic and anionic redox offers a large reversible capacity of more than 250 mAh/g (see Figure 3d). In comparison to the second cycle voltage curve of the NCM-811 CAM (see Figure 3c), however, it is immediately apparent that the charge and discharge profile of the LMR-NCM cathode are largely separated, amounting to more than 400 mV in the mid-SOC regime (see blue arrow). For most intercalation compounds, this voltage hysteresis could be explained by polarization effects originating, e.g., from poor charge-transfer kinetics and/or slow solid-state diffusion (both is also the case for LMR-NCM cathodes[145,184]), so that the hysteresis should vanish under open circuit voltage (OCV) conditions (i.e., at zero current and after sufficient relaxation). To examine this aspect, Figure 5 shows similar C/10 cycles as in Figure 3 for the already introduced large-format LMR-NCM and NCA-81 full-cells, which were recorded with and without intermittent OCV breaks for 1 h.[167] As expected, the charge/discharge curves of the NCA-81/graphite cell join up to a single OCV curve in between them, thus containing only resistive contributions. Here, the OCV curve is a direct measure of the cell's state of charge. In contrast, the

LMR-NCM/graphite cell maintains a large fraction of the voltage hysteresis under OCV conditions, which even persists at extremely low rates (C/300),[185] at high temperatures (55°C),[186] and after long relaxation periods (100 h).[185] This has several practical implications: First, the OCV path dependence complicates the SOC management, because the battery management system typically determines the SOC of the battery pack by the measured cell voltage. Second, the area between the charge/discharge curves corresponds to lost electrical energy, which diminishes the round-trip energy efficiency (η) and which is dissipated as heat. For the NCA-81 full-cell, the lost energy amounts only to ≈16 mWh/g at C/10 (η = 98%), while the LMR-NCM full-cell loses ≈128 mWh/g at C/10 (η = 87%), with ≈37% contributed from the current-independent OCV hysteresis.[167] The polarization effects make the situation even worse at higher C-rates, so that the higher amount of generated heat leads to a drastic increase of the surface temperature of the LMR-NCM/graphite pouch cells (53°C at 3C compared to 33°C for the NCA-81/graphite cell). This puts high requirements on the thermal management when utilizing Li- and Mn-rich cathode active materials.

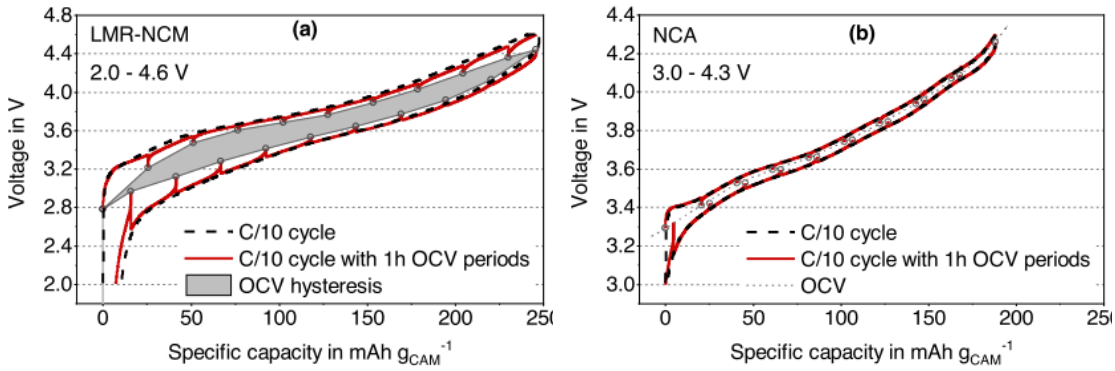

Figure 5. Voltage profiles of **(a)** ≈7 Ah LMR-NCM (0.33 Li_2MnO_3)/graphite and **(b)** ≈6 Ah NCA-81/graphite multi-layer pouch cells at C/10 and 25°C after formation. The C/10 cycles were either conducted with (red) or without (black) 1 h OCV rest periods in the voltage window of 2.0-4.6 V (LMR-NCM, rest periods every 25 mAh/g) or 3.0-4.3 V (NCA-81, rest periods every 20 mAh/g). Reprinted from ref. 167 under a Creative Commons Attribution 4.0 License.

The OCV hysteresis is an intrinsic bulk property of over-lithiated materials, which is of thermodynamic rather than kinetic origin.[156] Voltage window-opening experiments demonstrated an intra-cycle hysteresis on the order of ≈1 V for up to ≈12% of the reversibly de-/intercalated lithium-ions, i.e., this share of Li-ions is extracted at the end of charge, but only inserted back at the end of discharge.[144,187] The hysteresis is induced by the activation process in the first cycle, where the irreversibly removed Li-ions in the TM layer leave behind vacancies,[178] which in

turn might facilitate the transition-metal migration into the Li layer, as initially proposed by Gallagher, Croy, and co-workers.[188,189] According to this most prevalent theory, the reversible TM migration into tetrahedral sites of the Li layer causes the voltage hysteresis (more precisely, OCV hysteresis), while their irreversible capture in the octahedral sites of the Li layer leads to the so-called voltage fading. Researchers tried to confirm the correlation to TM migration, e.g., by NPD,[150] TEM,[190] and solid-state ^{6}Li NMR,[187] but it remains an open debate in the literature whether such a correlation implies causation, or if the voltage hysteresis is rather linked to the anionic redox.[143,156] In section 3.3.1, we will evaluate these theories on the basis of the lattice parameter evolution within the initial cycles.[191] Furthermore, we will attempt to determine the metal occupancies on the Li/TM layers by a combination of XPD and NPD.

Voltage fading.—The accumulation of transition-metals on the Li layer over the course of 100 cycles will be studied by *in situ* synchrotron XPD in section 3.3.2.[192] This process transforms the layered bulk structure gradually into a spinel-like cation arrangement,[150,193,194] whereby the degree of transformation depends on the type and oxidation state of the transition-metals.[141] The irreversible change in lithium site energy leads to the so-called voltage fading, which effectively reduces the operating voltage during charge and discharge. Thus, the voltage fading has to be distinguished from a resistance build-up, which increases the mean charge voltage, but lowers the mean discharge voltage. Both phenomena are illustrated in Figure 6 for a lab-scale LMR-NCM/graphite full-cell, which was operated in regular intervals at three different C-rates for in total 500 cycles. At the lowest C-rate of C/10 (a), both the mean charge voltage and the mean discharge voltage decrease upon cycling, i.e., the observed process is indeed governed by the voltage fading. In contrast, the mean voltages run counter at the highest C-rate of 3C (c), and the reduction of the mean discharge voltage is twice as big than at C/10 (≈0.62 vs. ≈0.31 mV/cycle) due to the dominant resistance build-up at high currents. The intermediate C-rate of 1C (b) falls in between these two extreme cases and thus is a mixed regime of voltage fading and resistance build-up.

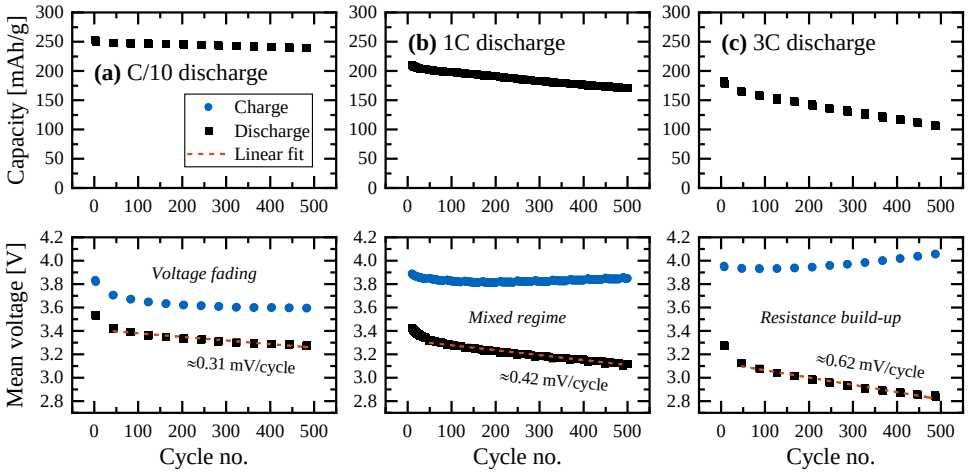

Figure 6. Cycling stability of an LMR-NCM (0.33 Li_2MnO_3)/graphite full-cell with regards to their specific capacity (**upper panels**) and mean cell voltage during charge and discharge (**lower panels**). The laboratory test cell was operated at 25°C in the voltage window of 2.0-4.6 V at three different C-rates. The constant current (CC) discharge was mainly done at 1C **(b)** with additional check-up cycles at C/10 **(a)** and fast cycles at 3C **(c)**, respectively. The charge was either performed in CC mode at C/10 (check-up cycles) or in constant current/constant voltage (CCCV) mode (CC at C/2, CV until C/10; regular and fast cycles). The reduction of the mean discharge voltage is approximated through a linear fit in the cycle range of cycle ≈45 to ≈500.

Reported values for the voltage fading span over a wide range from ≈0.7 to ≈10 mV/cycle (raising no claim of completeness) and typically refer to the change of the mean discharge voltage in a half-cell measurement over not more than 100 cycles.[141,195] The voltage fading is often considered to be one, if not the major challenge of over-lithiated CAMs, because it reduces the energy density, complicates the battery management system, and is often linked to their capacity decay during prolonged cycling. Zheng et al. reviewed several mitigation strategies including an improved cation uniformity, lattice doping, and surface modifications.[29] However, the recent study by Kraft et al. has shown that the mean discharge voltage of the ≈7 Ah LMR-NCM/graphite pouch cells drops only by ≈0.6 mV/cycle at C/2 (compared to ≈0.2 mV/cycle for the reference NCA-81/graphite cells, and on a similar level than for the lab-scale full-cell in Figure 6), reducing the energy density by less than 5% over the duration of 250 cycles.[167] Furthermore, the concomitantly observed capacity decay of ≈18% is independent of the applied C-rate and thus dominated by the loss of active lithium. The authors assume that the electrolyte degradation at the high end-of-charge voltage at 4.6 V and its follow-up reactions are the main fading mechanism, so that future research efforts should primarily attempt (i) to mitigate the oxygen release and (ii) to develop more stable electrolyte systems.

2 Experimental Methods

2.1 On-Line Electrochemical Mass Spectrometry

On-line electrochemical mass spectrometry (OEMS) is a powerful tool to study batteries, because the gas analysis provides quantitative and mechanistic insights about the underlying reactions. Initially designed by Tsiouvaras et al. to investigate the charging process of Li-O_2 batteries,[196] the OEMS setup at the Chair of Technical Electrochemistry at TUM was quickly adapted to Li-ion batteries, and since then is one of the most frequently used devices in our group, which addresses an increasing amount of research questions.

In this respect, the 2-compartment cell with an aluminum edge-sealed Li-ion conductive glass ceramic between the working-electrode and the counter-electrode was an important development by Metzger et al.[197,198] As both compartments are hermetically sealed from each other, the gas evolution (and consumption) from the working-electrode in the upper compartment can be exclusively measured by OEMS. This approach is used, e.g., to investigate the reductive[42] or oxidative stability[197] of electrolytes on carbon model electrodes and the impact of electrolyte additives[34] or transition-metal ions[69] on the SEI formation of graphite anodes. Crosstalk phenomena between anode and cathode can be examined by comparing the gassing results from 1-compartment versus 2-compartment cells.[198] In the absence of any electrochemical reaction, our group also studied the chemical reactivity of ethylene carbonate towards nucleophilic species such as hydroxides, which are either deliberately added to the electrolyte[179] or which are present as surface impurities on cathode active materials.[199] Other cell designs, which were developed over time, can be used to investigate the thermal decomposition of the $LiPF_6$ salt[200] and the reactivity of carbonate solvents with singlet oxygen.[49]

Singlet oxygen is evolved from delithiated layered transition-metal oxides within the initial cycles;[47] however, most of the oxygen release can be readily detected as O_2 and CO_2 by OEMS. The oxygen release from Li- and Mn-rich CAMs is the main application of the OEMS setup in this thesis (see section 3.2). The experiments rely on the 1-compartment cell design, whose assembly comprises a Ø 17 mm counter-electrode, two porous polyolefin separators (Celgard, USA) with a diameter of 28 mm, a Ø 15 mm working-electrode, and 100-120 µL electrolyte. In contrast to electronically conductive carbon/graphite electrodes, which are typically coated on separators, a stainless steel mesh (SS316, aperture 26 µm, wire diameter 25 µm, The Mesh Company, UK) is used as current collector for the cathode coatings. The narrow aperture of the mesh and the compression of the electrodes (2.5 t, 20 s) ensure a sufficient in-plane conductivity, while the released gases can permeate through the porous substrate into the headspace of the cell. In order to stick onto the mesh, the cathode slurry needs to be very viscous (solid content of ≈70 wt%). The wet-film thickness of 20 µm results in a loading of ≈8-10 mg_{CAM}/cm^2. The counter-electrode is either metallic lithium or partially delithiated and capacitively over-sized LFP. LFP is preferably used in the temperature-dependent gassing study (see section 3.2.3), because any gas consumption is excluded at the low and constant LFP voltage plateau of ≈3.5 V vs. Li^+/Li (where neither electrolyte oxidation nor reduction reactions are expected to occur).

The assembled cell is placed inside a temperature-controlled chamber and connected to the mass spectrometer. As schematically shown in Figure 7, the evolved gases are sampled into the mass spectrometer via a crimped capillary leak with a calibrated leak rate of ≈$2 \cdot 10^{-5}$ atm·cm^3/s (≈1 µL/min, Vacuum Technology Inc., USA). Here, the pressure reduction works in a single step from ambient pressure (≈1 bar within the cell) to ≈10^{-5} mbar. Since the OEMS cell is an otherwise closed system with a headspace volume of ≈10 mL, the continuous sampling decreases the pressure inside the cell. This limits the overall time of a single measurement (sum of the rest phase and the actual experiment) to less than 40 h (pressure drop of ≈25%); however, intermittent purging with argon could be used to establish the original base pressure and thus enables several consecutive measurements (at the expense of detecting the potential consumption of gases evolved in the prior step). The mass spectrometer itself is a QMA 410 system

(Pfeiffer Vacuum, Germany), which is equipped with a closed cross-beam ionization chamber, a quadrupole mass analyzer, and an off-axis secondary electron multiplier (SEM) detector. At the detector, the operating pressure amounts to ≈10^{-7} mbar due to a turbo pump, and the SEM can quantify gas concentrations down to the low ppm level. Some rather recent modifications concern our attempts to reduce the background signals. While the OEMS cell can be operated from 0 to 80°C (adjusted by the climate chamber, standard at 25°C), heating cords and insulation tapes hold the mass spectrometer constantly at 120°C, such that solvent molecules can easily detach from the walls. This heating was extended to the high surface area corrugated tube, which is placed between the capillary and the ceramic insulation. Beyond that, the formerly used rotary vane pump (pre-evacuating the tube after cell connection) was replaced by an oil-free membrane pump, because back diffusion of oil residuals could also increase the background signals.

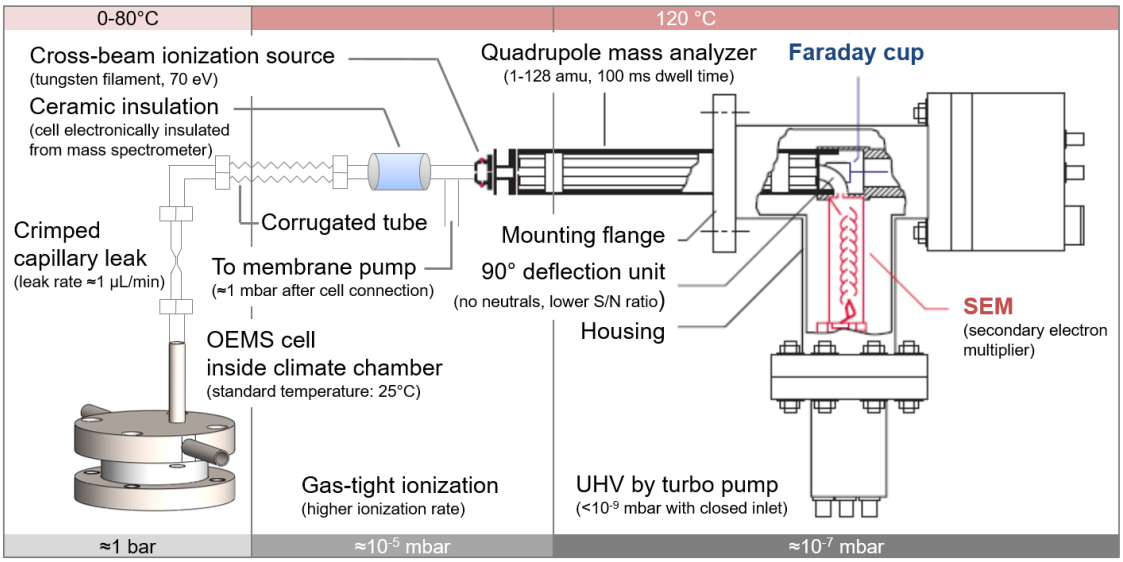

Figure 7. Schematic illustration of the OEMS setup. The gases that are evolved during the (electro)chemical reaction within the OEMS cell are sampled through the crimped capillary leak and subsequently analyzed in the mass spectrometer system. Here, the most important steps are the ionization in the crossbeam ionization source, the m/z separation in the quadrupole mass analyzer, and the detection by the SEM. The figure is adapted from the references 196 and 201.

Figure 8 shows a characteristic measurement routine of an OEMS experiment, where the ion currents m/z are plotted as a function of time. The raw signals are divided by the ion current of the ^{36}Ar isotope (m/z = 36) to compensate for any temperature/pressure fluctuations, and the normalized signals are further smoothed with a Savitzky-Golay function. The cell is initially purged with argon for 2 min to remove any residual gases from the glove box atmosphere. Afterwards, the

cell is rested for 4 h, which allows the electrolyte solvents to re-establish their gas-liquid equilibrium. The equilibrated background signals are either fitted with a second order exponential decay function or a combined exponential/linear function. This function is then extrapolated to the actual electrochemical measurement and subtracted from the normalized signals to correct for the electrolyte background. The released gases are finally quantified in the calibration step, where the cell is successively purged with argon, a calibration gas mixture, and again with argon for 30 min each. The argon flushing removes the accumulated gases and is used to interpolate the remaining electrolyte background by a second order exponential decay function. The signal rise in the middle part corresponds to a concentration of 2000 ppm of either H_2 (analyzed at m/z = 2), C_2H_4 (26), CO (28), O_2 (32), CO_2 (44) in the calibration gases (Westfalen, Germany). The calibration factor is determined by a linear fit of the baseline-corrected signal during the last ≈15 min; however, no smoothing is applied (typical values are reported in reference 34). The relative concentrations of the released gases in ppm, representing their volume fraction in the head space, can be converted in absolute amounts in units of µmol by using the cell volume, pressure, and temperature during the respective experiment. Normalization by the active material mass (µmol/g) or surface area (µmol/m²) gives the common units used in our publications (see section 3.2).

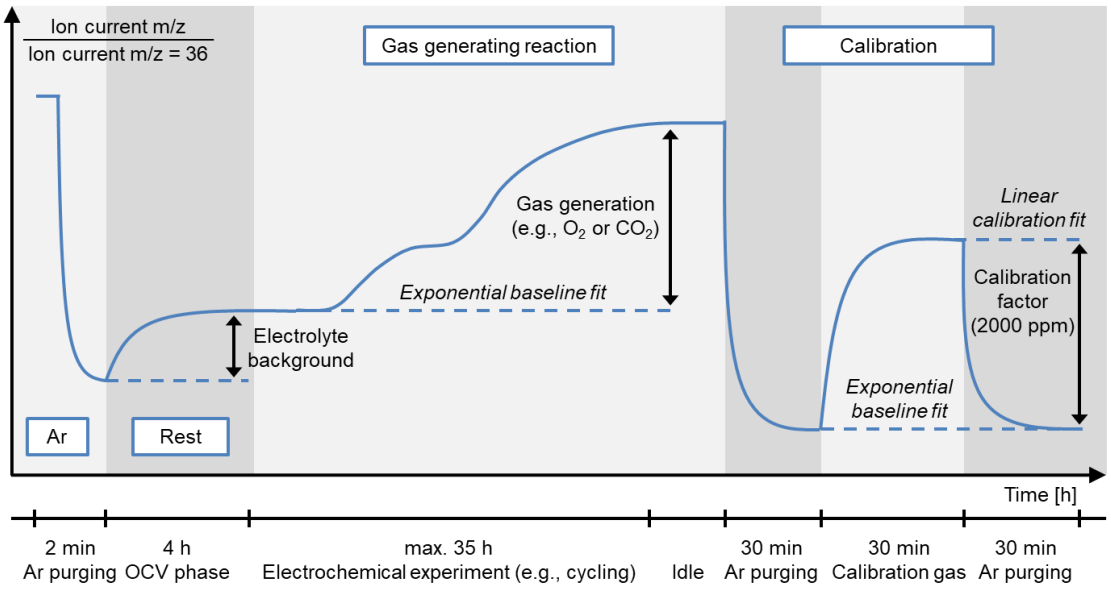

Figure 8. Schematic illustration of the OEMS raw data and its treatment, as described by Metzger.[201] After connection to the mass spectrometer system, the cell is initially purged with argon, followed by a rest phase for signal equilibration and the actual (electro)chemical experiment. To quantify the evolved gases, the measurement routine is completed by a calibration step.

2.2 Powder Diffraction

Powder diffraction is probably one of the most widely used non-electrochemical characterization tools in the field of lithium-ion battery research. Using the example of Ni-rich layered oxides, there are numerous *in situ* and/or *operando* studies in the literature, which apply X-ray powder diffraction (XPD) to investigate, e.g., the formation of CAMs from their precursors during calcination,[202] the lithium de-/intercalation process during cycling,[24,101,203,204] and the failure mechanisms of fatigued CAMs.[101,205,206] These advanced application possibilities reveal the importance of atomic-level structure information in understanding, designing, and optimizing established as well as new battery active materials.

Theoretical background.—Let us start with the principles of X-ray powder diffraction by looking at the diffraction pattern of a pristine NCM-811 CAM in Figure 9a (measured *ex situ* as powder sample). The diffractogram shows several reflections of the sample, which can be analyzed with respect to their position, profile, and (integrated) intensity (see Figure 9b). Since X-rays are scattered at the lattice planes of a crystal, the number of reflections and their position define the symmetry of the structure (the so-called space group) and the dimensions of the unit cell, allowing for qualitative phase identification. This relationship finds expression in Bragg's law:

$$n\lambda = 2d_{\mathrm{hkl}} \sin\theta \qquad (4)$$

where λ is the wavelength of the incident X-ray beam, d_{hkl} is the inter-planar spacing of parallel lattice planes, and θ is the angle between the incident beam and the respective lattice planes. Bragg's law is only satisfied when the scattered waves interfere constructively, i.e., when the difference between the path lengths of two waves is equal to an integer multiple of the wavelength (n, typically n = 1), so that the scattered waves remain in phase. Each reflection is related to the diffraction along a particular set of lattice planes, which are further defined by the Miller indices (*hkl*). For the hexagonal symmetry, which layered oxides such as NCM-811 belong to with their $R\bar{3}m$ space group, the lattice parameters a and c are calculated as follows from the d_{hkl} spacing and the Miller indices:

$$\frac{1}{d_{hkl}^2} = \frac{4}{3}\frac{h^2 + hk + k^2}{a^2} + \frac{l^2}{c^2} \quad (5)$$

while the other lattice parameters of the unit cell are constrained to be $b = a$, $\alpha = \beta = 90°$, and $\gamma = 120°$, respectively. The lattice parameters a and c strongly depend on the lithium content (x_{Li}) of the CAM during charge/discharge cycling.[24,85,188,207] This correlation will be used in section 3.3.1 to investigate the structural origin of hysteresis phenomena in Li- and Mn-rich layered oxides.[191] Furthermore, the determination of a precise $c/a = f(x_{Li})$ calibration curve for the Ni-rich NCM-811 CAM is the centerpiece of the long-term degradation studies in section 3.4,[208,209] because it allows for quantifying different capacity loss terms of the CAM.

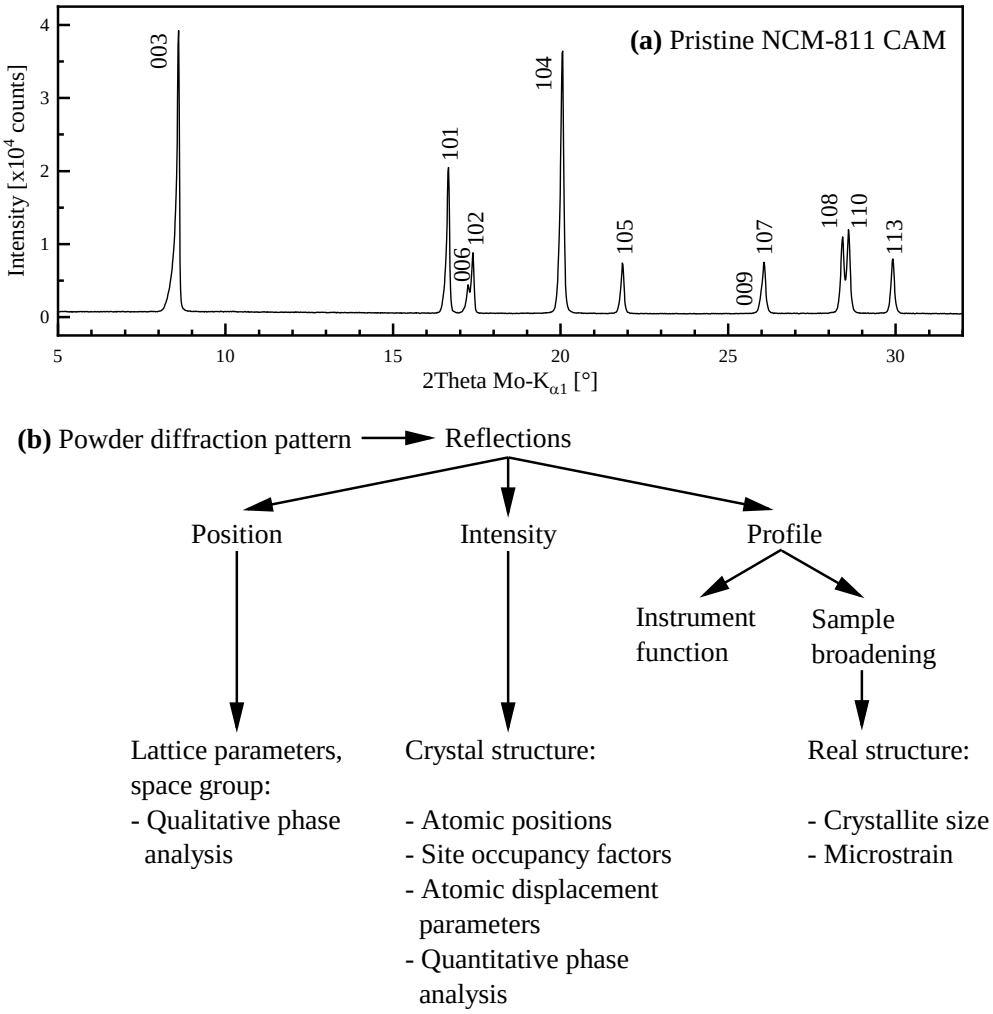

Figure 9. (a) X-ray powder diffraction pattern of a pristine NCM-811 CAM ($Li[Ni_{0.8}Co_{0.1}Mn_{0.1}]O_2$), which was measured as a powder sample at a laboratory diffractometer equipped with Mo-$K_{\alpha1}$ radiation ($\lambda = 0.7093$ Å). The individual reflections are labeled with their respective Miller indices (*hkl*) from the $R\bar{3}m$ space group of the layered transition-metal oxide. **(b)** Overview of the various structural information that can be deduced from the position, intensity, and profile of the reflections (adopted from reference 210).

The reflection profile (including the peak shape and width) is governed by the instrument function and sample-related broadening effects, from which real structure information can be extracted. Here, the instrument function is usually measured with highly crystalline standard reference materials (SRMs), which are assumed to create no peak broadening and which are further used for the angular correction of laboratory diffractometers (zero error) or for the wavelength determination of beamlines. Within this thesis, Si, CeO_2, and $Na_2Ca_3Al_2F_{14}$ SRMs were employed at different diffractometers. Fixing the instrument function afterwards, the two contributions from sample broadening can be separated by their different θ-dependence in a so-called Williamson-Hall analysis.[211] While the crystallite size broadening (for crystallites smaller than ≈200 nm) scales with $1/\cos\theta$, the microstrain broadening increases with $\tan\theta$ and is caused by crystallographic defects such as vacancies, antisite disorder and dislocations.[212,213] The Williamson-Hall analyses carried out in sections 3.3.2 and 3.4.1 reveal that the reflection broadening of CAMs can be fairly well described by the smooth functions of the diffraction angle in the discharged (lithiated) state. In the charged (delithiated) state, however, the microstrain contribution becomes anisotropic with respect to the Miller indices (*hkl*) of the reflections,[214,215] which can be treated by a phenomenological model proposed by Stephens (see section 3.4.1).[216]

The proper modeling of the peak broadening is crucial for obtaining crystal structure information from the intensity of the reflections by means of a Rietveld refinement. The Rietveld method comprises the entire information content of a powder pattern by fitting each intensity data point with a model whose parameters are refined using a least squares regression routine to optimize the fit. In contrast to former fitting procedures, which relied on the integrated intensity of the reflections, this approach introduced by Rietveld intrinsically accounts for the overlap of independent diffraction peaks.[217] In order to extract crystallographic parameters, the intensities of a calculated structure model ($y_{calc,i}$) are compared to the intensities of the observed diffraction pattern ($y_{obs,i}$) at each data point *i*. According to the method of least squares, the squared sum of differences between $y_{obs,i}$ and $y_{calc,i}$ is subjected to minimization:[210]

$$\sum_i \left(w_\mathrm{i} \left(y_\mathrm{obs,i} - y_\mathrm{calc,i} \right)^2 \right) \rightarrow Min \tag{6}$$

where w_i is a weighting factor derived from the variance of $y_\mathrm{obs,i}$ as $1/\sigma^2(y_\mathrm{obs,i})$. The calculated intensity $y_\mathrm{calc,i}$ is described by various contributions as:[210]

$$y_\mathrm{calc,i} = \sum_p \left(S_\mathrm{p} \sum_{\boldsymbol{s}(p)} \left(\left| F_\mathrm{calc,\boldsymbol{s},p} \right|^2 \Phi_\mathrm{\boldsymbol{s},p,i} Corr_\mathrm{\boldsymbol{s},p,i} \right) \right) + Bkg_\mathrm{i} \tag{7}$$

Here, the outer sum runs over all crystalline phases p, while the inner sum runs over all Bragg reflections $\boldsymbol{s}$ = (hkl) of a phase. The scaling factor S_p is proportional to the weight fraction of phase p in a composite sample (e.g., CAM and conductive graphite mixed in the cathode electrode; see section 3.4.2), which is the basis for a quantitative phase analysis. $Corr_\mathrm{\boldsymbol{s},p,i}$ represents the sum of several correction factors, e.g., due to the diffraction geometry (Lorentz-polarization factor, multiplicity, axial divergence, absorption), $\Phi_\mathrm{\boldsymbol{s},p,i}$ describes the profile function, and the background at position i is denoted as Bkg_i. The reflection intensities are governed by the structure factors $F_\mathrm{calc,\boldsymbol{s},p}$, which contains all relevant crystallographic parameters of the phase (viz., atomic positions within the unit cell, site occupancy factors, and atomic displacement parameters). For layered transition-metal oxides, the site occupancy factors are of particular interest, because many studies aim at determining the cationic mixing between the lithium and transition-metal layer,[93,100,150,159] which is mostly computed as a paired anti-site defect (e.g., $Li_{1-x}M_x[Li_xM_{1-x}]O_2$ for a fully lithiated stoichiometric CAM).[218,219] The same holds true within this thesis, as will be shown in detail for Li- and Mn-rich layered oxides in section 3.3 (investigating the influence of cationic mixing on voltage hysteresis and voltage fading) and for the Ni-rich NCM-811 CAM in section 3.4 (investigating its impact on long-term capacity fading).

Since the Rietveld method involves many contributions from both the sample and the instrument, the initial starting values of all parameters need to be a close approximation of the final structure, whose optimized parameters are the outcome of the refinement. The quality of the refinement can be accessed visually by evaluating the difference plot between the measured and calculated intensities, but their difference can be also expressed in statistical agreement factors (the so-called

R-factors, e.g., R_{wp}, R_{bragg}, and χ^2).[220] *R*-factors are helpful to follow the effect of small changes in the structural model (e.g., when adding a new refinement parameter), but they are difficult to compare for different samples or measurement setups.[221] Estimated standard deviations of all refined parameters are based on the diagonal elements of the inverse correlation matrix and will be reported according to the notation of Schwarzenbach et al. (e.g., 1.23±0.04 is expressed as 1.23(4)).[222] Except for section 3.3.2 where Karin Kleiner used the freely available FullProf suite for data analysis,[223,224] all other refinements within this thesis are performed with the commercial software package TOPAS (Coelho, Version 6, 2016).[225,226] The unique scripting language of TOPAS makes it possible to easily implement more sophisticated models,[210] e.g., the joint Rietveld refinement of X-ray and neutron powder diffraction data. Furthermore, multi-pattern datasets from *in situ* and/or *operando* XPD can be analyzed rapidly by doing sequential refinements. Since, e.g., the lattice parameters change only gradually within a charge/discharge cycle, the refined parameters of one diffraction pattern are used as starting value for the following pattern in an automated manner.

In situ cell design and measurement setup.—Within this thesis, it is the primary goal to investigate structural changes by *in situ* techniques, because this approach allows for characterizing battery active materials under real operating conditions. In combination with the simultaneously measured electrochemical data, the relationship between the structure and the electrochemical properties could be elucidated much easier than under *ex situ* (or *post-mortem*) conditions, where the harvesting and further treatment of the electrode might potentially lead to deviations from the original state of the material (e.g., changes in the state of charge of the CAM). The first choice to be made when planning an *in situ* XPD study concerns the cell design. In the literature, there are numerous cell designs reported, which span from modified coin cells[204,206,227] to single-layer pouch cells[24,89] to custom-made cells.[228,229] In order to allow the X-ray beam to penetrate the cell in a Debye-Scherrer (transmission) geometry, the casing of common coin cells has to be either thinned by using, e.g., laser technology,[206] or the casing has to be replaced by an X-ray transmissive and sealed window such as beryllium,[204] glassy carbon,[229] glass,[228] or a polyimide film.[227] Based on the preliminary work by Irmgard Buchberger in our group,[230] single-layer pouch cells are used for the *in situ* XPD

measurements in this thesis. Here, the electrode stack is encased in a thin polymer-coated aluminum foil (the so-called pouch bag), which has the advantage that the cell is directly suitable for XPD experiments in transmission mode. Next to coin cells and Swagelok®-type T-cells, single-layer[46,89] and multi-layer pouch cells[94,231] are further established as laboratory test cells for electrochemical characterization. However, the huge variety of pouch cells with respect to the dimension and arrangement of the individual components goes along with more complex manufacturing steps compared to the other cell designs, including the cutting of electrodes/separators (using cutting dies and a hydraulic press), the contacting of the electrodes to the current collector tabs (by ultrasonic welding), as well as the assembly and sealing (with a vacuum sealer) in the glove box.[230]

Figure 10 provides an overview about two of the three pouch setups developed and employed in this thesis. All setups share the same dimensions for the cathode working-electrode (WE, 30x30 mm^2; contacted by an Al tab), the counter-electrode (CE, 33x33 mm^2; contacted by a Ni tab), and the glass-fiber (GF) separators (36x36 or 38x38 mm^2). The half-cell pouch setup with a metallic lithium CE in Figure 10a is exclusively used for *in situ* XPD experiments at our in-house STOE STADI P diffractometer (STOE, Germany), which is equipped with a Mo-$K_{\alpha1}$ source (λ = 0.7093 Å), a Ge(111) monochromator, and a Mythen 1K detector. In order to increase the intensity from the NCM CAM phase in the diffraction pattern, the cathode electrode has a high loading of ≈15-20 mg/cm^2, while the contribution from side phases is minimized by using a relatively thin pouch foil (12 µm-thick Al layer), metallic lithium as CE, and only one GF separator soaked up with 400 µL electrolyte. The measurements are restricted to a maximum of three charge/ discharge cycles, whereby the cell is controlled by a portable potentiostat (SP-200, Biologic, France). Since the experiments are performed at slow C-rates with geometrical current densities below 1 mA/cm^2, there is no risk of an internal short due to lithium dendrites. Furthermore, the pouch cells need no external compression at such low current densities (and few cycles) to obtain the same capacities than in other cell formats, so that the cell holder consists only of two thin Al plates used for fixation. The broad X-ray beam requires a hole of at least 10 mm in diameter, i.e., the irradiated area would not be compressed anyways. The measurements at the laboratory diffractometer are referred to as “L-XPD”

experiments in the sections 3.3.1 and 3.4.1 and they target at monitoring the lattice parameters of the different CAMs within the initial cycles. This can be either done in *in situ* mode by recording the entire diffractogram during intermittent rest phases (in capacity steps of 10-25 mAh/g) or in *operando* mode by recording only small 2θ ranges during cycling (alternating measurement of the (003) and (110) reflections, corresponding to capacity intervals of ≈4 mAh/g). While the first method allows for correlating the lattice parameters to the open circuit voltage of the CAM (with up to 25 data points per charge/discharge step), the second method generates sufficient data points for an accurate c/a = f(x_{Li}) calibration curve (with up to 60 data points per charge/discharge step).

(a) Half-cell pouch setup and cell holder (Ø 10-15 mm hole, no compression)

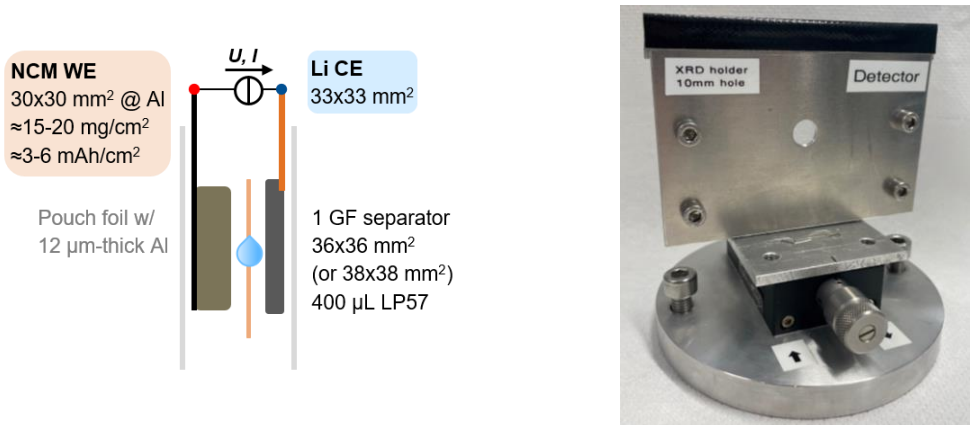

(b) Full-cell pouch setup with lithium reference-electrode and cell holder (Ø 1.5 mm hole, ≈2 bar compression, equipped with 2 cells)

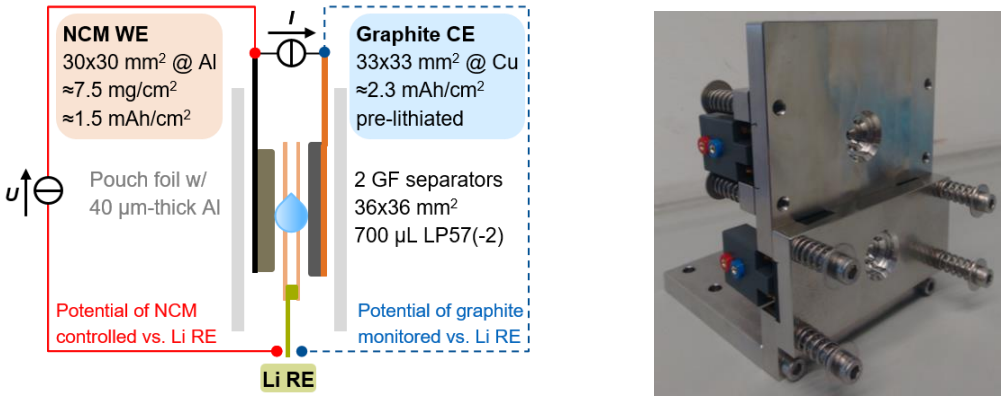

Figure 10. Schematic drawing of the single-layer pouch cells (left) and the corresponding cell holders (right) used for *in situ* X-ray powder diffraction: **(a)** half-cell pouch setup for short experiments (up to three cycles) at our laboratory diffractometer and **(b)** full-cell pouch setup for long-term measurements (up to 1000 cycles) at the LDE facility of beamline I11, Diamond Light Source.[232]

The observation of structural changes during long-term cycling requires a full-cell pouch setup with an intrinsically stable graphite CE, which was developed within

the scope of Franziska Friedrich's Master's Thesis[233] and which is depicted in Figure 10b. However, this approach is accompanied by (i) additional side phases from the graphite CE (C_6, LiC_{12}, and LiC_6) and its copper current collector foil, (ii) an intensified side phase from aluminum due to the usage of the regular pouch foil (with a 40 µm-thick Al layer, being impermeable for moisture and increasing the stiffness of the pouch foil), and (iii) a complex background from two GF separators with 700 µL electrolyte and from the polymers in the pouch foil. Therefore, these experiments were conducted at a synchrotron facility (beamline I11, Diamond Light Source, UK) and are denoted as "S-XPD" in the Results section. Powder diffraction data collected at synchrotron sources have numerous advantages over L-XPD data, including a superior signal-to-noise ratio, better resolution, tunable wavelength, and faster acquisition times.[219,234] The high intensity of S-XPD data enables a lower NCM-811 cathode loading of ≈7.5 mg/cm² at a reasonable acquisition time of 5 min in section 3.4.1, avoiding SOC inhomogeneities across the thickness of the electrode during C/2 cycling,[235] and the lower wavelength of λ ≈ 0.494 Å (25 keV) minimizes absorption effects. The cells are compressed at ≈2 bar by a home-made spring-loaded cell holder, which only requires a 1.5 mm hole in diameter for the small X-ray beam at the synchrotron (200x200 µm²), so that the compression of the irradiated hole region is maintained by the stiffness of the pouch foil. Moreover, the beamline I11 provides a special long-duration experiment (LDE) facility, where the cells are mounted on a stage that is moved once a week into the beam to record the diffraction patterns on a 2D Pixium area detector (for more details see reference 232). Hence, the cells remain connected to the battery cycler (Arbin, USA), while maintaining their alignment in the diffraction geometry during the automated data collection. For each cell, two diffraction patterns are measured under OCV conditions in the completely discharged and charged state of the CAM (separated by a few hours). In order to focus exclusively on the NCM-811 CAM, the graphite CE is partially lithiated by performing its formation versus metallic lithium beforehand in a separate pouch cell. In so doing, the graphite CE is equipped with a sufficient lithium reservoir of ≈0.7 mAh/cm² (compared to ≈1.5 mAh/cm² from the NCM-811 cathode) to exclude any capacity fading from the anode due to the loss of active lithium, and the potential of the cathode WE can be controlled versus the

additionally added lithium RE. As shown in section 3.4.1, these pouch cells could be cycled and analyzed for up to 1000 cycles at room temperature.

Comparison of several diffractograms.—Figure 11 shows exemplary diffraction patterns from the two *in situ* pouch cell designs in Figure 10 with an NCM-811 cathode, in comparison to *ex situ* data of an NCM-811 CAM powder measured at the laboratory diffractometer and at the neutron powder diffraction (NPD) beamline SPODI of the research reactor FRM II. Focusing first on the three XPD datasets in the panels (a,c,d), the data treatment becomes increasingly complicated when moving from *ex situ* L-XPD of the CAM powder (only NCM phase present; see (a)) to *in situ* L-XPD measured in the half-cell pouch setup (three phases present; see (c)) and then to *in situ* S-XPD measured in the full-cell pouch setup (six phases present; see (d)). The presence of several side phases considerably reduces the number of structural parameters that can be freely refined for the targeted NCM phase. In case of the phase-pure *ex situ* dataset in Figure 11a, the performed Rietveld refinement includes all relevant information such as the lattice parameters (*a* and *c*) and crystallographic parameters (Li-Ni mixing, *z*-coordinate of oxygen, three site-specific atomic displacement parameters), from which the Li-Ni mixing amounts to 3.1(1)% for the pristine NCM-811 CAM.

For the two *in situ* datasets, the calculated intensity of the NCM phase is highlighted by the green area. Its contribution to the overall pattern is smaller than the contribution from aluminum (WE current collector and pouch foil) and copper (CE current collector foil in the full-cell), which further overlap with several of the NCM reflections. For this reason, the NCM phase obtained from *in situ* L-XPD is treated by means of structure-independent whole powder pattern fitting (WPPF).[210] Neglecting the crystal structure of the phase, the intensity of each reflection is calculated individually either by the Pawley method or by the Le Bail method, so that only the lattice parameters can be extracted from these fits. The WPPF approach is also applied for the metal foils due to preferred orientation effects. In case of the *in situ* S-XPD dataset, the NCM phase is actually refined with a structural model; however, we fix the Li-Ni mixing to the value of the pristine NCM-811 CAM powder (due to an otherwise unreasonable scatter of up to 4%).

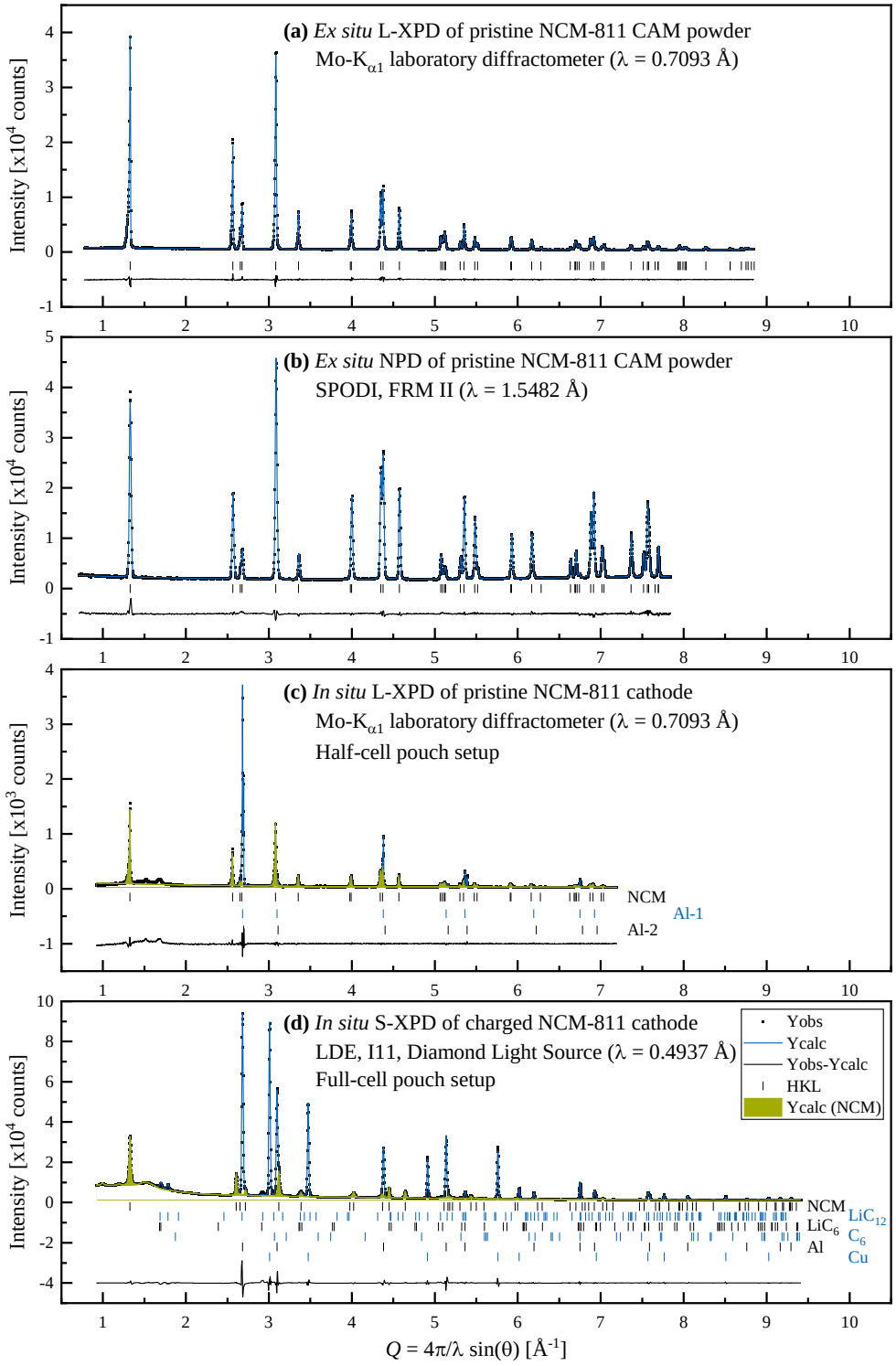

Figure 11. Comparison of different diffraction data of the NCM-811 CAM: **(a)** *ex situ* L-XPD of the pristine CAM powder measured in a 0.3 mm borosilicate capillary, **(b)** *ex situ* NPD of the pristine CAM powder measured in a 10 mm vanadium can at the SPODI beamline (FRM II), **(c)** *in situ* L-XPD of the pristine NCM-811 cathode measured in the half-cell pouch setup, and **(d)** *in situ* S-XPD of a charged NCM-811 cathode measured in the full-cell pouch setup at beamline I11 (Diamond Light Source). To compensate for the different wavelengths of the diffractometers, the diffraction angle is converted into *Q* space. The observed (black points), calculated (blue lines), and difference diffraction profiles (black lines) are shown together with the position of the Bragg peaks of the phases. For the *in situ* data, the calculated intensity of the NCM-811 CAM phase is highlighted by the green area.

Consequently, we failed in our initial attempt to monitor the evolution of the Li-Ni mixing *in situ* during cycling and instead, we focus on the lattice parameter changes (see section 3.4.1). Alternatively, the Li-Ni mixing will be determined by *ex situ* L-XPD from harvested NCM-811 cathodes, which is also an equally valid and simple approach to track the lattice parameters for a limited number of cycled samples (see section 3.4.2). To avoid any change and/or contamination of the sample, the rest phase after reaching the desired state of the cell should be kept short (on the order of hours or less to minimize self-discharge effects, especially at high SOCs) and the cells are opened inside the glovebox. The scratched off cathode material is directly loaded and air-tightly sealed into a 0.3 mm borosilicate capillary (Hilgenberg, Germany), which is measured on the same day.

In contrast to the above studies about the Ni-rich NCM-811 CAM, we manage to follow the Li-Ni mixing of a Li- and Mn-rich CAM by *in situ* S-XPD in section 3.3.2.[192] This is due to the fact that we employ a modified half-cell pouch setup (without the interfering side phases from graphite and especially copper) at the synchrotron facility. To exclude the risk of lithium dendrite growth, we cycle a low-loaded cathode with ≈6.3 mg/cm^2 at a slow C-rate of C/5, resulting in a geometrical current density of only ≈0.3 mA/cm^2, and we also utilize four GF separators (with 1.5 mL electrolyte). These cells could be operated over the duration of 100 charge/discharge cycles, where the Li-Ni mixing increases notably by ≈3%. However, this approach could not be transferred to the other studies, because the NCM-811 CAM has to be cycled for several hundreds of cycles to observe a similar increase (at an elevated cycling temperature of 45°C), but half-cells would experience a rapid capacity fading after ≈200-300 cycles.[233]

Based on these experiences, we recommend *ex situ* L-XPD in the future for Rietveld refinements of pristine CAM powders and harvested cathode electrodes when targeting to obtain crystallographic information such as the Li-Ni mixing, while *in situ* L-XPD in the half-cell pouch setup should be used for monitoring lattice parameter changes within a charge/discharge cycle. For the latter, the diffraction data can be treated by whole powder pattern fitting (WPPF), which is also applied in section 3.1 to determine real structure information (crystallite size and microstrain) from pristine CAM powders.[236] Even though the *ex situ* analysis of

harvested cathodes requires their proper handling to avoid erroneous results (e.g., lower lithium content due to self-discharge), we conclude that it generates as authoritative results (and beyond) as those obtained from *in situ* diffraction, which is biased by the presence of several side phases. Comparing the accuracy of L-XPD and S-XPD data (see also section 3.3.1), synchrotron data would actually not be required for our purposes, but this might be different for other research questions, which either need special diffraction geometries[234,235] and/or the highest possible data quality.[219,237]

Neutron powder diffraction and co-refinement.—Due to the similar ionic radii of Li^+ and Ni^{2+},[23,218] cationic mixing is mainly refined as Li-Ni mixing in stoichiometric layered oxides (as also done for the NCM-811 CAM within this thesis); however, the situation becomes different in over-lithiated Mn-rich CAMs, where also Mn is considered to move into the Li layer during cycling.[150,238,239] Moreover, Li can be de-intercalated both from the Li and the TM layer.[178,240] Since X-rays interact with the electron cloud, the scattering factor is proportional to the number of electrons in an atom, as can be seen in Figure 12 for the most common elements existing in lithium-ion batteries. As a consequence, XPD has a low contrast for elements close in atomic number (such as Ni and Mn) and it poorly resolves light elements (such as Li and O) in the presence of heavier elements. Due to the spatial delocalization of the electron density, the X-ray scattering factor (also referred to as X-ray atomic form factor) falls off with increasing scattering vector (Q; exemplarily shown for 0, 5, and 10 $Å^{-1}$ in Figure 12) and it further depends on the oxidation state of an element, so that the contribution from redox-active elements will depend on the state of charge of the CAM.[218,219] Neutron powder diffraction (NPD) does not have these difficulties, because the scattering of neutrons involves the interaction with the atomic nuclei. The neutron scattering length (equivalent to the X-ray scattering factor) varies irregularly with the atomic number (and isotope) and is not Q-dependent (see Figure 12). The latter can be easily seen by comparing the two diffractograms of the pristine NCM-811 CAM powder in Figure 11a,b. While the intensity decreases exponentially for the XPD pattern (a), it remains high also at high Q values in case of the NPD pattern (b), which makes NPD a better approach than XPD to determine atomic displacement parameters.[218,219]

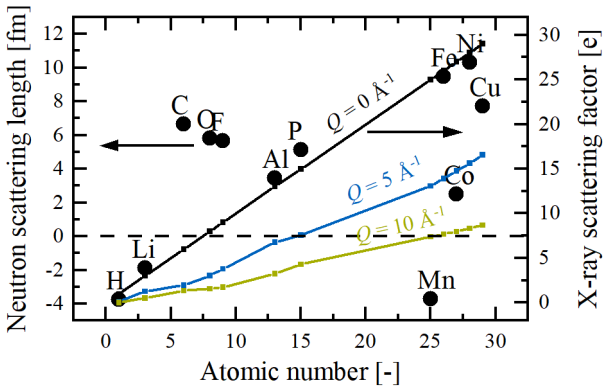

Figure 12. Comparison of the neutron scattering length[225] (data points; left y-axis) and X-ray scaterring factor[241] (data points with interpolated lines; right y-axis) of several elements which can be found in the active materials, electrolyte, and current collector foils of lithium-ion batteries. The X-ray scattering factor is expressed as the number of electrons contributing to the scattering event and is given for the neutral atoms at three different Q values of 0, 5, and 10 Å^{-1}, respectively. At Q = 0, the X-ray scattering factor is equivalent to the total number of electrons in the atom.

The variability of the neutron scattering lengths (Mn < Li < Co < O < Ni, with Mn and Li having negative values; see Figure 12) can help to unravel the structural complexity of Li- and Mn-rich CAMs. However, since diffraction probes the scattering power of crystallographic sites and not of their individual constituents (up to four elements on the metal layers in our case), the number of simultaneously refined site occupancy factors is restricted to the number of complementary diffraction datasets. Therefore, we apply a joint Rietveld refinement approach[238,242] of *ex situ* L-XPD and NPD data from the identical sample in section 3.3.1.[191] The NPD data were measured at the high-resolution neutron powder diffractometer SPODI of the research reactor FRM II (Germany), and the CAM powder required in the gram scale was harvested from custom-made multi-layer pouch cells. Regarding the data treatment during the co-refinement, some parameters (e.g., instrumental correction factors and peak broadening) are optimized independently on a local level for each diffraction pattern, while the lattice parameters and crystallographic parameters are refined jointly on a global level for both diffractograms. This approach enables a maximum of two elements to be refined on the same site,[219] but there are several limitations (e.g., the simultaneous refinement of Li and Mn), which will be critically discussed in section 3.3.1.

2.3 Material Characterization

The electrochemical characterization of a newly synthesized or supplied cathode active material should be always accompanied by an extensive material characterization on a powder level. The knowledge of important material properties can already indicate some of the electrochemical performance characteristics of the CAM in a battery cell, because both are often correlated with each other in a property-performance relationship (as presented in section 3.1).[29,182,243] While the previous section 2.2 highlighted the application possibilities of (X-ray) powder diffraction to determine structural information of the CAM, such as the microstrain and the Li-Ni mixing, this chapter will discuss experimental techniques, from which the stoichiometry and the morphology of a CAM can be evaluated.

CAM composition.—The stoichiometry with respect to the metal composition can be determined by an elemental analysis of the as-received CAM powder; however, there are two important considerations to be made: First, the metal composition of the entire CAM sample does not necessarily represent the metal composition of the actual layered oxide due to the presence of surface impurities, which are either left over from the synthesis process and/or are formed during ambient storage.[199,244] Second, the Li:M ratio of stoichiometric layered oxides such as NCM-811 is not exactly 1:1,[24,104] because an excess of the lithium source is mixed with the transition-metal precursor prior to the calcination step to compensate for the loss of lithium as volatile Li_2O at high temperatures.[99,245] In the case of NCM-811, this off-stoichiometry can be expressed as $Li_{1+x}[Ni_{0.8}Co_{0.1}Mn_{0.1}]_{1-x}O_2$ or, in a more general notation applicable to every NCM-based CAM, as $Li[Li_xNi_aCo_bMn_c]O_2$ where the sum of x, a, b, and c equals 1. Here, the additional lithium (equivalent to x) is placed on the TM layer and typically amounts to $0 \leq x \leq 0.05$ for "stoichiometric" layered oxides.

For the NCM-811 CAM investigated in section 3.4, it was necessary to determine its exact composition in order to know the lithium content of the pristine material and the theoretical capacity for complete lithium extraction. Therefore, we sent the CAM powder, which was permanently stored under argon atmosphere in our laboratory, to the Mikroanalytisches Labor Pascher (Remagen, Germany). For elemental

analysis, the CAM powder was dissolved by pressurized acid digestion in *aqua regia* and the mass fractions of Li, Ni, Co, and Mn were determined by inductively coupled plasma atomic emission spectroscopy (ICP-AES). The measured weight percentages of the metals and of the residual mass, which could be ideally assigned to lattice oxygen in the layered oxide, are summarized in Table 4. In order to correct these values for the most common surface contaminants, viz., Li_2SO_4,[246] Li_2CO_3,[199] and $TMCO_3$,[199] the Mikroanalytisches Labor Pascher further determined the sulfur content also by ICP-AES and the carbonate content (more specifically, carbon as CO_3^{2-} (CO_3-C)) by quantifying CO_2 after washing the CAM powder in a mild acid.[165] Li_2CO_3 and $TMCO_3$ can be separated by measuring the CO_3-C content of the as-received CAM (containing both carbonate versions) and of a calcined CAM which was heated to 600°C under argon in a tube furnace, so that $TMCO_3$ gets completely decomposed (starting at temperatures of 120-320°C, depending on the type of transition-metal) but Li_2CO_3 remains stable.[199] The impurities amount to 0.89 wt% Li_2SO_4, 0.55 wt% Li_2CO_3, and 0.59 wt% $TMCO_3$ (assuming a Ni:Co:Mn ratio of 8:1:1) and were subtracted from the mass fractions of the respective components, e.g., reducing the weight percentages of lithium and of the residual in the case of Li_2SO_4 by 0.11 wt% (−2Li) and 0.78wt% ($-SO_4$), respectively.

Table 4. Elemental analysis of an as-received NCM-811 CAM powder by ICP-AES, where the measured weight percentages of the metals (and the residual mass) are corrected for common impurities such as Li_2SO_4, Li_2CO_3, and $TMCO_3$, in order to calculate the exact stoichiometry of the layered transition-metal oxide ($Li[Li_\delta Ni_a Co_b Mn_c]O_z$). Note that the Li_2CO_3 content was determined from the calcined CAM powder (>600°C), whereas the $TMCO_3$ content was derived from the remaining CO_3-C weight percent of the as-received sample (<600°C) after subtracting the CO_3-C share of the calcined sample.

Weight percent	**Li**	**Ni**	**Co**	**Mn**	**Residual**	**Comment**
Measured	7.35	46.9	5.96	5.60	34.21	
Li_2SO_4	−0.11				−0.78	0.26 wt% S
Li_2CO_3	−0.10				−0.45	0.09 wt% CO_3-C (>600°C)
$TMCO_3$		−0.23	−0.03	−0.03	−0.30	0.06 wt% CO_3-C (<600°C)
Calculated	7.13	46.67	5.93	5.57	32.68	
$Li[Li_xNi_aCo_bMn_c]O_z$	**Li**	**Ni**	**Co**	**Mn**	**"O"**	x + a + b + c = 1
Measured	1.028	0.775	0.098	0.099	2.075	
Calculated	1.015	0.786	0.099	0.100	2.018	

The newly calculated weight percentages should now correspond to the actual layered oxide, whose formula unit $Li[Li_xNi_aCo_bMn_c]O_z$ (assuming x + a + b + c = 1 on the TM layer) is shown in Table 4 and compared to that of the originally measured weight percentages of the entire CAM. The quality of the above approach can be evaluated by the oxygen content of the layered oxide, which is inferred from the residual mass and should be equal to z = 2. Taking the surface species into account reduces the z value from 2.075 to 2.018 and brings it thus reasonably close to the ideal value of 2. Within the accuracy of the elemental analysis (≈0.01 wt% for each element), we report the composition of the NCM-811 layered oxide used in section 3.4 to be $Li[Li_{0.01}Ni_{0.79}Co_{0.10}Mn_{0.10}]O_2$, which agrees almost perfectly to the targeted stoichiometry. This gives a theoretical capacity of 280 mAh/g_{NCM} purely for the layered oxide and 274 mAh/g_{CAM} for the entire CAM (including the surface impurities) for complete lithium extraction of 1.01.

The over-lithiated NCM material (with the mid-lithium content) presented in section 3.3.1 was analyzed by the same method, because the metal composition is an essential input parameter for the Rietveld refinements in this study. Here, the composition was determined as $Li[Li_{0.17}Ni_{0.19}Co_{0.10}Mn_{0.54}]O_2$, whereby the calculation includes ≈1 wt% of the above contaminants. In order to assign the residual mass stoichiometrically to lattice oxygen (z = 2), however, there has to be at least another ≈2 wt% of unassigned impurities. This gives a theoretical capacity of 361 mAh/g_{NCM} and 350 mAh/g_{CAM} (including ≈3 wt% of surface impurities) for complete lithium extraction of 1.17.

CAM morphology.—Poly-crystalline CAMs are µm-sized secondary agglomerates, which are composed of smaller primary crystallites. The packing of the individual crystallites can be either loose or dense, depending on the applied synthesis route. In the following, the morphology of poly-crystalline CAMs will be evaluated and compared by various techniques, using the example of porous versus dense Li- and Mn-rich layered oxides. To get a first qualitative impression, SEM images of a porous CAM (shown in the black box) and of a dense CAM (shown in the blue box) are presented in Figure 13a,b. The SEM analysis was performed with a JEOL scanning electron microscope (JSM-7500F, JEOL, Japan) in the backscattering mode at an accelerating voltage of either 1 or 5 kV, and the measurements were done in

cooperation with Katia Rodewald from the Wacker-Chair of Macromolecular Chemistry at TUM. Figure 13a1-a4 show top-view images of the pristine CAM powders, which reveal the size (on the order of ≈10 µm) and the shape of the secondary agglomerates. While the CAM in the upper panels (a1,a2) possesses a uniform, spherical shape, the agglomerates of the CAM in the lower panels (a3,a4) are much more irregularly formed and edged. Furthermore, the higher magnification level (with the 1 µm scale bar) shows faceted crystals on the outer surface of the spherical CAM (a2), which originate most likely from surface impurities as discussed above.

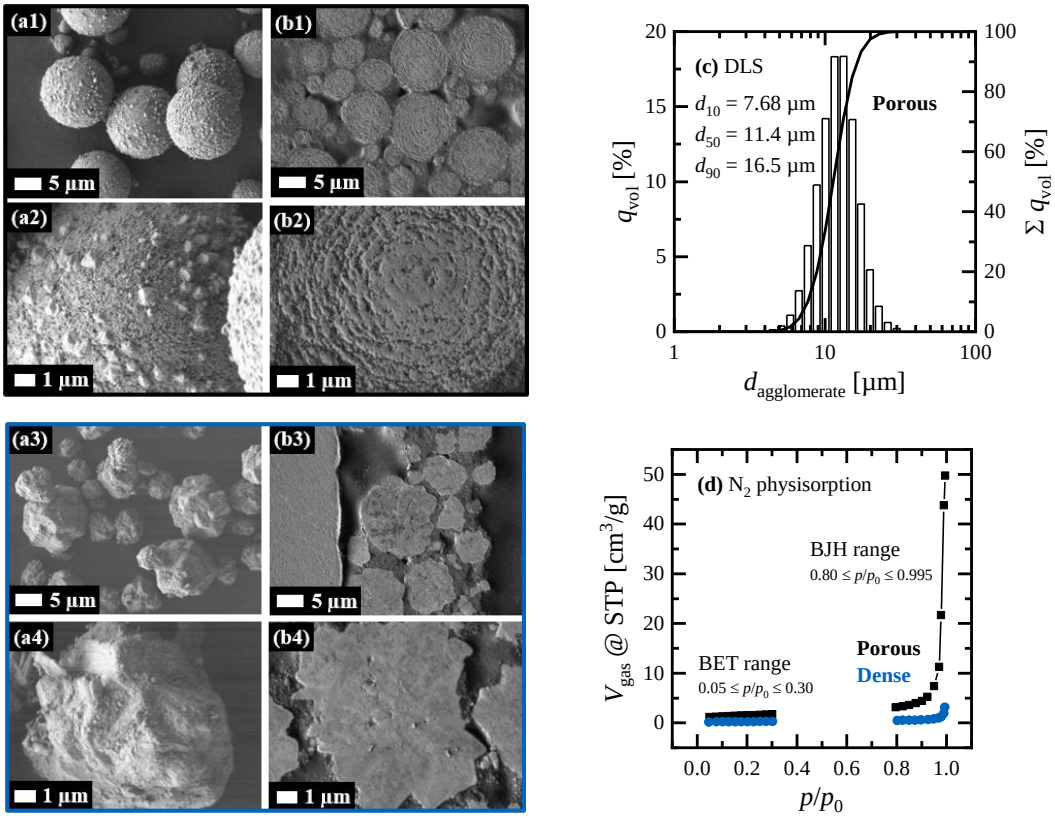

Figure 13. Evaluation of the morphology of two Li- and Mn-rich layered oxides, whose particles are either pourous (data shown in black) or densely packed (data shown in blue). The applied techniques are: **(a)** top-view SEM images of the CAM powders to visualize the outer shape of the secondary agglomerates; **(b)** cross-sectional SEM images of the compressed cathode electrodes to illustrate the packing of the primary crystallites inside the agglomerates; **(c)** dynamic laser scattering (DLS) to measure the particle size distribution (exemplarily shown for the porous CAM); and **(d)** N_2 physisorption to determine the specific surface area (in the BET range) and the intra-particular pore volume of the CAMs (in the BJH range). The SEM images are either shown at a magnification level of 2500x (5 µm scale bar) or 10000x (1 µm scale bar). The left side of the image (b3) shows the smooth current collector foil after mechanical polishing of the electrode.

Cross-sectional SEM images can be prepared either by mechanical polishing[208] or by focused argon-ion beam (FIB) milling of cathode electrodes.[90] Since our laboratory has only been equipped recently with a FIB cross-section polisher

(IB-19530 CP, JEOL, Japan), the cross-sectional images in Figure 13b depict mechanically polished cathode electrodes. For that purpose, 1x1 cm^2 pieces were punched out of pristine, compressed electrodes and they were embedded in epoxy resin (EpoThin 2 resin and hardener, Buehler, USA). The hardened resin block was first ground on SiC paper in two steps (grade P320 and P1200, CarbiMet S, Buehler) and subsequently polished with 9 and 3 µm diamond polishing pastes (MetaDi Supreme Polycrystalline Diamond Suspensions, Buehler). The final polishing step was done with a 0.05 µm Al_2O_3 agent (MasterPrep Alumina Suspension, Buehler), which is small enough to get smooth cross-sections at the desired magnifications (as illustrated for the aluminum current collector foil at the left side of (b3)). The cross-sections show the interior of the secondary agglomerates and thus reveal the packing of the primary crystallites. In case of the CAM in the upper panels (b1,b2), the primary crystallites are only loosely connected with each other, resulting in a fluffy, "porous" structure with a lot of pore volume in between the crystallites. This gives reason to expect a high specific surface area for the porous material. On the other hand, the CAM in the lower panels (b3,b4) is much more closely packed, which should result in a low specific surface area. For this "dense" CAM, the individual crystallites appear to be fused together and there is barely any pore space between them.

Based on this first qualitative impression from SEM images acquired in top-view and cross-sectional mode, morphological properties such as the particle size distribution, the specific surface area and the intra-particular pore volume will be now quantified by applying dynamic laser scattering (DLS), gas physisorption, and mercury intrusion porosimetry (MIP), respectively.

CAM particle size distribution.—Dynamic laser scattering (DLS) relies on the Mie scattering theory and measures the particle size distribution on a volume basis. For that purpose, one tip of a spatula of the pristine CAM powders was dispersed in ethanol by sonication and then analyzed in a flow-through cell at our DLS device (HORIBA LA-960, Retsch Technology, Germany). The measurements were evaluated with a real part refractive index of 1.36 for ethanol and of 2.11 for the CAM (assuming MnO as reference material). The volumetric particle size distribution of the porous CAM is depicted in Figure 13c. Here, the diameter of the

secondary agglomerates is shown on a logarithmic scale, while the relative particle number is either shown as bar chart per diameter segment (on the left y-axis) or as accumulated signal (on the right y-axis). The commonly reported d_{50} value splits the distribution with half below and half above this diameter and amounts to 11.4 µm for the porous CAM (12.1 µm for the dense CAM). The distribution width can be expressed by the so-called "span" and is computed according to $(d_{90}-d_{10})/d_{50}$. The span amounts to 0.77 and 0.74 for the porous and dense CAM, respectively, which is a narrow distribution (span < 1). Even though being rather similar for these two CAMs, the particle size and its distribution depend on several synthesis parameters and further affect the tap density of the CAM powder.[182]

Specific surface area.—The specific surface area of the pristine CAM powders can be determined with a gas sorption analyzer (Autosorb-iQ, Quantachrome, USA). The adsorption of a gas (the so-called adsorbate) on the surface of a solid sample (the so-called adsorbent) is typically described through an isotherm, which measures the quantity of a gas taken up during adsorption (or released during desorption) at a constant temperature and as a function of the gas pressure. Prior to the actual measurement, the surface has to be cleaned, which is done by outgassing the CAM powders at 120°C for 12 h under dynamic vacuum. The most convenient approach is N_2 physisorption conducted at the temperature of liquid nitrogen (boiling point of 77 K at atmospheric pressure). Figure 13d shows sections of the adsorption isotherms of the two Li- and Mn-rich layered oxides. Here, the quantity of adsorbed N_2 is expressed as gas volume (V_{gas}) at standard temperature and pressure (STP: 0°C and 1 bar) normalized to the sample mass, while the relative pressure (p/p_0) corresponds to the actual gas pressure divided by the saturated vapor pressure of N_2 at 77 K. For the evaluation of the surface area, the Brunauer-Emmet-Teller (BET) theory is the most widely accepted procedure, which relies on the concept of multilayer adsorption. Measuring eleven data points in the relative pressure range of $0.05 \leq p/p_0 \leq 0.30$ used for BET analysis (see Figure 13d), the specific surface area is obtained from a linear fit through the $1/(V_{gas}\cdot(p_0/p-1))$ versus p/p_0 representation of the adsorption isotherm. For our example, the BET surface area (A_{BET}) amounts to 5.3 m^2/g for the porous CAM (in black) and to 0.37 m^2/g for the dense CAM (in blue), respectively.

In order to estimate whether the surface area of the primary particles or that of the secondary agglomerates was measured by N_2 physisorption, it is helpful to translate these A_{BET} values into an average particle diameter (d_{avg}) by assuming solid spheres and by using the crystallographic density of the CAMs ($\rho_{cryst} \approx 4.35$ g/cm^3). According to $d_{avg} = 6/(\rho_{cryst} \cdot A_{BET})$, the 5.3 m^2/g of the porous CAM correspond to 0.26 µm, which reflects the size of its primary crystallites in agreement to the SEM cross-sections (see Figure 13b). On the other hand, the average diameter of 3.7 µm from the 0.37 m^2/g of the dense CAM matches the size of the secondary agglomerates. Note that the estimated 3.7 µm are smaller than the d_{50} value of 12.1 µm due to the non-spherical shape and surface roughness of the agglomerates.

Since N_2 physisorption requires an absolute surface area of the sample of ≈2.5-5.0 m^2, it can readily be applied to CAM powders which are typically available in the gram scale; however, it cannot be used to track the surface area evolution of the CAM during battery operation (the cathode electrode mass is in the mg scale for small lab cells). This requires krypton as adsorbate. Kr has the advantage over N_2 to be much more sensitive due to its ≈300 times lower saturation pressure at liquid nitrogen temperature, which minimizes the void volume correction and hence enables the analysis of low surface area samples. Kr physisorption was used in section 3.4.2 for NCM-811 cathode electrodes cycled for up to 700 cycles at 45°C. Before the gas physisorption measurement, the cycled electrodes have to be washed in several steps in organic solvents to remove residuals of the conductive salt (which would otherwise block pores and reduce the surface area).[90] Furthermore, the surface area contribution of the conductive additives in the electrode (carbon and/or graphite) has to be subtracted from the actually measured surface area of the entire electrode.[90]

In summary, BET measurements are not just a facile tool to determine the specific surface area of CAMs, but also to evaluate their morphology. For the µm-sized poly-crystalline CAMs investigated within this thesis, surface areas of ≤1 m^2/g are indicative for densely packed particles, where the gas is only adsorbed to the outer surface of the secondary agglomerates. In analogy to the gas molecules, this holds true for the liquid electrolyte when the CAM is utilized in a battery, i.e., only the outer surface of the CAM particles is wetted with the electrolyte. If the surface area

amounts to ≥3 m^2/g, the agglomerates are expected to be very porous, such that the inner surface of the primary particles is in contact to the gas (during gas physisorption) and to the electrolyte (within the battery).

Intra-particular pore volume.—The internal porosity of a cathode active material critically affects its volumetric and gravimetric energy density on a cell level, because the additional pore volume cannot be easily reduced by calendering the cathode electrodes and thus requires more electrolyte to be filled into the cell.[166] For this reason, the internal pore volume is an important figure of merit of a CAM, which can be quantified by mercury intrusion porosimetry (MIP). Generally speaking, MIP measures the pore size distribution of a powder or solid sample, which corresponds to the distribution of pore volume with respect to pore size. Since mercury does not wet most substances and will not penetrate pores by capillary action, it has to be forced to fill open pore space by applying an external pressure. According to the Washburn equation:

$$d_{\mathrm{pore}} = -\frac{4 \cdot \gamma_{\mathrm{Hg}} \cdot \cos \theta_{\mathrm{Hg}}}{p} \tag{8}$$

the pressure correlates inversely to the pore diameter (d_{pore}), at which the intruded mercury volume (v_{pore}) is determined by its capacitance change in the sample holder. Equation (8) assumes a cylindrical pore geometry and measures the largest entrance towards a pore, whereby γ_{Hg} is the surface tension of Hg (0.485 N/m at 20°C) and θ_{Hg} is the contact angle of Hg (112-142°, with 130° being the most widely accepted value without further information). MIP is frequently applied to battery electrodes, e.g., for determining the electrode porosity as a function of electrode compression,[166,247,248] but the internal porosity of a CAM can also be accessed on a powder level.

Using an AutoPore V instrument (Micromeritics, USA) in the pressure range of 0.007 to 410 MPa, pore diameters from ≈180 µm down to ≈3 nm can be reached. Figure 14a shows the porosimetry data of the two Li- and Mn-rich layered oxides. Here, the logarithmic derivative of the pore volume is plotted versus the pore diameter on a logarithmic scale (until 20 µm), so that the area under the curve is equivalent to the pore volume in the examined pore diameter range. For both CAMs, the large peak corresponds to the filling of inter-particular pore space between the

secondary agglomerates, and the respective pore diameter of ≈3 µm (at the maximum) scales with the agglomerate size (d_{50} values of ≈11-12 µm; see above). As a rule of thumb, the particle size is approximately 2 to 4 times larger compared to the measured pore size (depending on the packing structure).[249] After filling the entire void volume between the agglomerates, mercury starts to penetrate, if present, into the intra-particular pores inside the agglomerates. As expected, this process leads to an additional peak for the porous CAM (black solid line) at pore diameters smaller than 300 nm (median diameter of ≈60 nm), while the curve of the dense CAM (blue solid line, shifted upwards by 0.3 cm³/g) remains flat. The intra-particular pore volume ($v_{\mathrm{pore}}^{\mathrm{intra}}$) at ≤300 nm is summarized in Figure 14b for in total five Li- and Mn-rich layered oxides, from which the two porous CAMs have $v_{\mathrm{pore}}^{\mathrm{intra}}$ values of ≈45-70 mm³/g, while it amounts to less than 10 mm³/g for the three dense CAMs (as determined by MIP).

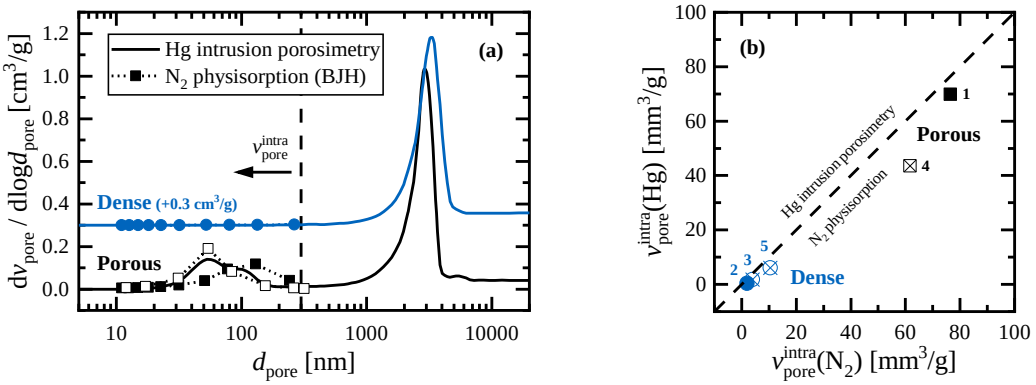

Figure 14. Determination of the internal porosity of porous vs. dense Li- and Mn-rich layered oxides eihter by using Hg intrusion porosimetry or N_2 physisorption (with the BJH method). **(a)** Logarithmic differential pore volume ($dv_{\mathrm{pore}}/d\log d_{\mathrm{pore}}$) as a funtion of the pore diamter (d_{pore}). The two presented CAMs are the same as in Figure 13. The BJH analysis is performed by default from the adsorption isotherm (closed symbols), but the gas sorption measurement was extended by the desorption branch (open symbols) in case of the porous CAM (black curves). Furthermore, the blue curves of the dense CAM are shifted upwards by 0.3 cm³/g for better visibility. **(b)** Comparison of the intra-particular pore volume ($v_{\mathrm{pore}}^{\mathrm{intra}}$, at pore diameters smaller than 300 nm) for five different CAMs (two porous and three dense CAMs, whereby no. (1) and (2) have been taken over from panel (a)) and for both introduced techniques. Note that $v_{\mathrm{pore}}^{\mathrm{intra}}(N_2)$ was derived from the highest measured relative pressure at p/p_0 = 0.995 during N_2 physisorption.

Mercury intrusion porosimetry is a very accurate and rapid method for pore structure analysis, but it is sample-destructive and Hg has to be treated with care. In this regard, N_2 physisorption offers an alternative approach to determine the internal porosity of CAM powders, as it will be anyways performed after synthesis to measure their specific surface area. Extending the adsorption isotherm by eleven

more data points at high relative pressures of $0.80 \leq p/p_0 \leq 0.995$ (see Figure 13d), the Barrett-Joyner-Halenda (BJH) theory can be used for pore structure analysis.[243] The BJH method is based on the Kelvin model of pore filling and needs to include an (arbitrarily chosen) data point where all pores are considered to be filled (typically at $p/p_0 = 0.995$). As shown in Figure 14a, the BJH method covers the same mesopore and small macropore size range of ≈10-300 nm, which is required to determine the intra-particular pore volume of the CAMs. The comparison of five different CAMs in Figure 14b shows a pretty good agreement within ≈5 mm^3/g between both techniques; only for the porous CAM (4), the BJH analysis of N_2 physisorption data delivers almost 20 mm^3/g more pore volume than MIP. Furthermore, the pore size range is shifted to higher values if the BJH analysis is performed with adsorption isotherm data (see closed squares of the porous CAM in Figure 14a). If the gas physisorption measurement is however extended by a desorption branch (see open squares), the BJH analysis and mercury intrusion porosimetry agree almost perfectly with each other.

The intra-particular porosity can be calculated as follows:

$$\varepsilon_{\text{intra}} = \frac{v_{\text{pore}}^{\text{intra}}}{v_{\text{pore}}^{\text{intra}} + \frac{1}{\rho_{\text{cryst}}}} \tag{9}$$

where ρ_{cryst} is the crystallographic density of the CAM (≈4.35 g/cm^3 for the above layered transition-metal oxides). Using the $v_{\text{pore}}^{\text{intra}}$ values from Figure 14b, the material-level porosity inside the secondary agglomerates amounts to ≈15-25% for the porous CAMs, but to less than 5% for the dense CAMs.

Comparison of several densities.—Finally, let us have a look on different densities which can be calculated from various techniques and which differ by the types of pores included into the calculation. Table 5 gives an overview of four densities for the porous CAM (4) and the dense CAM (5) from Figure 14b. The highest possible density is the crystallographic density (ρ_{cryst}) inferred from X-ray powder diffraction, because the volume is restricted to the actual solid neglecting any kind of pore. The presence of closed pores, which are encapsulated into the solid, can be determined with a gas pycnometer (service measurements done by Micromeritics with a AccuPy II 1340 instrument). This is a gas displacement method, using

typically helium or nitrogen, where the gas molecules are able to fill the minutest pore spaces and which thus measures the so-called skeletal density ($\rho_{skeletal}$). In case of the porous CAM (4), ρ_{cryst} and $\rho_{skeletal}$ coincide within the accuracy of the measurements, but their difference of 4.31 vs. 4.21 g/cm^3 implies some closed pores for the dense CAM (5). Taking the inverse of the densities, the volume of closed pores can be estimated to be (1/4.21−1/4.31) cm^3/g ≈ 6 mm^3/g. Mercury intrusion porosimetry provides two more densities: the apparent density ($\rho_{apparent}$) at the highest applied pressure (410 MPa) and the bulk density (ρ_{bulk}) usually chosen at the initial filling pressure (0.007 MPa). Since the pore penetration of mercury is restricted to pore diameters of greater than ≈3 nm (see Eq. (8)), any difference between $\rho_{skeletal}$ and $\rho_{apparent}$ is indicative for the presence of micropores (typically defined to be <2 nm). This adds an additional pore volume of ≈9 mm^3/g for the porous CAM (4) and ≈6 mm^3/g for the dense CAM (5), respectively.

Table 5. Comparison of different densities of the porous CAM (4) and the dense CAM (5) from Figure 14b. The crystallographic density (ρ_{cryst}) is inferred from from X-ray powder diffraction (XPD), whereas the sekeletal density ($\rho_{skeletal}$) is determined by N_2 pycnometry. Hg intrusion porosimetry delivers the apparent density ($\rho_{apparent}$) at the highest applied pressure and the bulk density (ρ_{bulk}) at the initial filling pressure.

Method	**XPD**	**N_2 pycnometry**	**Hg intrusion porosimetry**	
ρ [g/cm^3]	**ρ_{cryst}**	**$\rho_{skeletal}$**	**$\rho_{apparent}$**	**ρ_{bulk}**
Porous CAM (4)	4.34	4.33	4.16	1.52
Dense CAM (5)	4.31	4.21	4.11	1.30

The bulk density includes all available pore spaces within the material in the volume measurement and thus reflects the density of the freely settled CAM powder loaded into the sample holder (the mercury column of ≈1 cm only fills pores greater than ≈180 µm). The bulk density is not an intrinsic property of the material, as it depends on the sample handling, and it has to be distinguished from the industrially important tap density,[29,182] which is obtained from filling a container with the sample material and vibrating it to obtain a near optimum packing.

In section 3.1, it will be shown how the internal pore volume of the CAM powder (determined by mercury intrusion porosimetry) can be used to estimate the electrode density of LMR-NCM model electrodes (with a CAM share of 92.5 wt%). As the intra-particular porosity inside the secondary agglomerates of the CAM

cannot be reduced by electrode calendering,[166] it adds to the inter-particular porosity between the CAM agglomerates and the electrode additives (i.e., conductive carbon and binder), which is typically calendered down to ≈30%.[16,250,251] Consequently, the overall electrode porosity of the porous CAM (4) and the dense CAM (5) can be estimated to be ≈44% and ≈32%, which in turn results in an electrode density of ≈2.2 g/cm^3 and ≈2.7 g /cm^3, respectively. For both morphologies, this is less than the practical electrode density of Ni-rich CAMs (3.2-3.4 g/cm^3);[29] however, the difference to the dense CAM (5) is mainly caused by the inherently lower crystallographic density of Li- and Mn-rich layered oxides (≤4.35 vs. 4.75 g/cm^3 for NCM-811). This implies that the dense CAM (5) would reach the required electrode density of LMR-NCM cathodes defined in section 1.4.

3 Results

The following chapter presents the published articles of this PhD thesis. The journal articles are thematically grouped into four sections. Section 3.1 investigates the material properties of Li- and Mn-rich layered oxides and how they affect the initial electrochemical performance during a rate test.

Section 3.2 addresses surface-related degradation phenomena of Li- and Mn-rich layered oxides, which are initiated by oxygen release in the first cycles. Since the origin of oxygen release was controversially discussed in the literature, section 3.2.1 shows an OEMS analysis of the gas evolution during the initial charge/discharge cycles. The released amounts of O_2 and CO_2 are compared to the proposed bulk versus surface reactions, which leads to the conclusions that the gassing originates from the surface and that it leads to a reconstruction of the CAM particle surface into a spinel-like layer. Based on this finding, section 3.2.2 investigates the gas evolution from three over-lithiated NCMs with different Li_2MnO_3 content. Increasing the Li_2MnO_3 content causes more oxygen release and results in thicker spinel-like surface layers, as could be verified by HRTEM images and by electrochemical means. Finally, section 3.2.3 focuses on the temperature dependence of the oxygen release. The variation of the activation temperature significantly affects the achievable capacity in the subsequent cycles, because both the extent of oxygen release and the rate of the surface reconstruction rises with increasing temperature. Section 3.2.3 will not be published outside of this PhD thesis.

Section 3.3 turns towards degradation processes that happen in the bulk of Li- and Mn-rich layered oxides and which are investigated by diffraction techniques. In section 3.3.1, the voltage hysteresis within a charge/discharge cycle is correlated to reversible structural changes of the lattice parameters. The variation of the lattice

parameters allows conclusions about the underlying redox processes and is further analyzed as a function of the Li_2MnO_3 content and the cycling conditions. The impact of TM migration is critically discussed on the basis of jointly refined XPD and NPD data. The structural origin of the voltage fading during long-term cycling is presented in section 3.3.2 by using *in situ* synchrotron XPD. Over the duration of 100 cycles, the irreversible accumulation of transition-metals on octahedral Li-sites could explain the poor cycling stability of Li- and Mn-rich layered oxides.

Since stoichiometric NCMs are still the most widely used class of cathode active materials, section 3.4 investigates the capacity fading of the Ni-rich NCM-811 CAM. While section 3.4.1 focuses on the capacity fading at ambient temperature and uses primarily *in situ* techniques to the quantify the underlying degradation modes, section 3.4.2 examines in a comparative manner the CAM aging at elevated temperature with *ex situ* analysis tools. It turns out that the NCM-811 bulk structure is largely preserved over the course of 1000 cycles at 25°C or 700 cycles at 45°C, respectively, but oxygen release and particle cracking leads to the gradual formation of a resistive, disordered surface layer around the primary NCM-811 particles.

3.1 Material Properties Governing the Initial Performance of Li- and Mn-Rich Layered Oxides

The article "Specific Surface Area and Bulk Strain: Important Material Metrics Determining the Electrochemical Performance of Li- and Mn-Rich Layered Oxides" was submitted to the peer-reviewed *Journal of The Electrochemical Society* in March 2022 and it was published "open access" in June 2022.[236] The article was distributed under the terms of the Creative Commons Attribution 4.0 License and its permanent weblink can be found under: https://iopscience.iop.org/article/10.1149/1945-7111/ac766c.

Li- and Mn-rich layered oxides (also referred to as over-lithiated NCMs) offer high reversible capacities of more than 250 mAh/g,[28,141] which makes them a promising next-generation cathode active material for lithium-ion batteries.[7,9] Among the numerous challenges that so far have prevented their large-scale commercialization,[29] the ones with regard cost and energy density requirements could potentially be satisfied by revisiting the commonly applied synthesis conditions. Regarding the cost aspect, cobalt has to be entirely removed from the system,[20,243] while high energy densities on a cell level could be only achieved by replacing the currently used porous Li- and Mn-rich NCMs (LMR-NCMs) by more closely packed LMR-NCMs.[166,182]

To promote this transition, BASF SE provided us for this study with five Li- and Mn-rich layered oxides, which differ with respect to their morphology, applying two different (undisclosed) synthesis methods, and, in terms of the choice of transition-metals, using Co-containing and Co-free materials. The morphology of the as-received CAM powders is characterized by a series of techniques, including cross-sectional SEM images, gas physisorption measurements, and mercury intrusion porosimetry. These analyses show that one synthesis method results in loosely packed CAMs, consisting of porous agglomerates (i.e., with a morphology similar to that shown in Figure 4a), while the other yields much denser, compacted CAMs (i.e., with a morphology similar to that shown in Figure 4b). As a consequence, the BET surface area varies by a factor of ≈4-15 between the porous versus the dense CAMs.

A discharge rate test reveals that the densely packed CAMs provide up to ≈140 mAh/g less capacity at 1C than the loosely packed CAMs. However, a significant fraction of this difference can be accounted for when the mass-normalized currents (in mA/g) are divided by the BET surface area, which results in a constant, C-rate independent capacity offset among the investigated CAMs at a given surface-normalized current (in mA/m^2). In the following, we perform X-ray powder diffraction measurements of the CAM powders, whereby a size/strain analysis of the reflection broadening shows that the remaining capacity offset scales almost linearly with the extent of microstrain in the bulk material.

In summary, we identify two important material metrics which determine the electrochemical performance of Li- and Mn-rich layered oxides: (i) the surface area in contact to the electrolyte defines the effective surface-normalized current density that in turn determines the overpotential due to the charge-transfer resistance, and (ii) the microstrain within the primary crystallites affects distinct redox features that are activated during cycling.

Author contributions

B.S. conceived this study and conducted the electrochemical, structural as well as most of the morphological characterization of the CAMs. J.Y. prepared the FIB cross-sections and measured the corresponding SEM images, while F.F. was responsible for the dynamic laser scattering measurements. B.S. wrote the manuscript. All authors discussed the results and commented on the manuscript.

Journal of The Electrochemical Society, 2022 **169** 060521

Specific Surface Area and Bulk Strain: Important Material Metrics Determining the Electrochemical Performance of Li- and Mn-Rich Layered Oxides

Benjamin Strehle,*,z Jiyoung Yoon, Franziska Friedrich, and Hubert A. Gasteiger**

Chair of Technical Electrochemistry, Department of Chemistry and Catalysis Research Center, Technical University of Munich, D-85748 Garching, Germany

Li- and Mn-rich layered oxides are a promising next-generation cathode active material (CAM) for automotive applications. Beyond well-known challenges such as voltage fading and oxygen release, their commercialization also depends on practical considerations including cost and energy density. While the cost requirement for these materials could be satisfied by eliminating cobalt, the volumetric energy density requirement might imply the transition from the most widely used porous structure to a more densely packed structure. Here, we investigated five Li- and Mn-rich layered oxides which were synthesized by various routes to obtain CAMs with different morphologies (porous vs dense), transition-metal compositions (Co-containing vs Co-free), and agglomerates sizes (≈6−12 μm). The as-received materials were characterized, e.g., by gas physisorption, Hg intrusion porosimetry, as well as X-ray powder diffraction, and were electrochemically tested by a discharge rate test. Thus, we identified two important material metrics which determine the initial electrochemical performance of Li- and Mn-rich CAMs, and which might be used as performance predictors: (i) the surface area in contact with the electrolyte that defines the effective current density which is applied to the surface of the CAMs, and (ii) the microstrain in the bulk that affects distinct redox features during cycling.
 [DOI: 10.1149/1945-7111/ac766c]

Manuscript submitted March 15, 2022; revised manuscript received May 19, 2022. Published June 15, 2022.

Li- and Mn-rich layered oxides are considered as potential next-generation cathode active material (CAM) for automotive applications.[1–3] They offer exceptionally high specific capacities of about 250 mAh g^{-1} in combination with very low material cost.[4,5] The capacity increase in the over-lithiated compared to stoichiometric CAMs originates from a slight rearrangement of the layered structure, $Li[Li_{\delta}TM_{1-\delta}]O_2$.[5,6] While stoichiometric CAMs such as NCMs ($Li[Ni_{1-x-y}Co_xMn_y]O_2$) and NCAs ($Li[Ni_{1-x-y}Co_xAl_y]O_2$) are barely over-lithiated, with δ being close to zero, Li- and Mn-rich CAMs possess δ values between 0.1 and 0.2. Apart from Mn, the transition-metal (TM) mixture typically contains minor fractions of Ni and Co, but Co-free variants are also reported in the literature.[7–10] Omitting Co is important to reducing the cost, since it is the most expensive element among the three transition-metals and it is further problematic due to sustainability and geopolitical aspects.[11–13] The practical application of Li- and Mn-rich CAMs is hindered by several significant challenges,[4,14] including a pronounced voltage hysteresis within a charge-discharge cycle,[15,16] discharge voltage fading during long-term cycling,[10,17] and oxygen release within the first cycles,[18,19] which leads to both surface reconstruction[20] and electrolyte decomposition.[21] All of these problems are well-known, and numerous mitigation strategies are suggested in the literature.[5,22,23] However, implications originating from the morphology of the CAMs have gotten little attention yet.

A recent study from our university systematically compared the pilot scale production process of ≈6–7 Ah multi-layer pouch cells using either a Ni-rich CAM (NCA with 81% Ni) or a Li- and Mn-rich CAM.[24,25] Here, the latter could not be calendered to commonly used electrode porosities of ≈30%. The authors attributed this issue to the morphology of the Li- and Mn-rich CAM, which has a significant fraction of internal porosity within the secondary agglomerates. This internal porosity cannot be removed by calendering, because severe defects such as the embossing of the aluminum current collector foil set in before the breakage of the CAM particles, thereby preventing calendering on an automated production line below a porosity of ≈42%. At such a high porosity, the resulting electrode density was only ≈2.3 $g_{electrode}$ $cm^{-3}{}_{electrode}$, ≈15% lower than the initially targeted electrode density of ≈2.7 $g_{electrode}$ $cm^{-3}{}_{electrode}$ (for ≈32% porosity),[24] on which projections on the potential energy density of Li- and Mn-rich cathodes are typically based on.[14] This issue is addressed in the review articles by Zheng et al.[14] and Hy et al.[22] in view of the low tap density of Li- and Mn-rich CAM powders (typically ⩽2 g cm^{-3}). The extent of internal porosity further finds expression in the specific surface area of the pristine CAMs, which is usually on the order of ≈5 m^2 g^{-1} for over-lithiated oxides, but <1 m^2 g^{-1} for stoichiometric oxides.[21] Therefore, we conclude that most of the Li- and Mn-rich CAMs investigated in the literature feature a high internal porosity. This calls for improved or alternative synthesis routes in order to obtain more densely packed CAMs and to increase their volumetric energy density.[14,22]

Another property which will be addressed in this work is the strain in cathode active materials, or more precisely, the microstrain on an atomic level. Microstrain has its origin in crystal defects, which can be classified either as point defects (e.g., local displacements,[26] vacancies,[27] and site disorder[28]), line defects (e.g., dislocations[29]), planar defects (e.g., stacking faults[30] and twin boundaries[31]) or volume defects (e.g., voids[32]). All these defects cause a residual stress in the material that is otherwise in equilibrium with its surrounding, i.e., it does not experience any external forces or temperature gradient.[33] Consequently, the residual tensile and compressive forces have to be balanced inside the material. In this context, microstrain represents the normalized displacement of atoms from their ideal position within the lattice, especially in the vicinity of the defect site due to the acting forces. This distortion leads to line broadening in the diffraction profile of the sample and can be quantified by a size/strain analysis, e.g., with the Williamson-Hall method.[34–36] Here, size broadening (as known from the Scherrer equation) originates from extended imperfections, which split a crystal into smaller incoherently diffracting domains. Microstrain arises from more localized defects, but the differentiation between both contributions is sometimes difficult.[37] Mathematically, both scale solely with the diffraction angle θ and they can be separated according to their different θ-dependence. At high SOCs, however, the reflections of layered oxides typically vary non-monotonically with θ due to an additional *hkl* dependence. During the refinement, this anisotropic line broadening can be modeled by the phenomenological model from Stephens.[38–40] It is believed to be caused, e.g., by the

*Electrochemical Society Student Member.
**Electrochemical Society Fellow.
zE-mail: benjamin.strehle@tum.de

statistical distribution of stacking faults in layered oxides,[41] oxygen-deficient regions,[42] or a density variation of lithium atoms (either from grain to grain or even within a grain).[43] For LNO ($LiNiO_2$), the occurrence of anisotropic strain broadening and stacking faults upon delithiation could be recently monitored by operando X-ray powder diffraction (XPD).[30] Furthermore, microstrain effects are discussed as important nucleation sites for intra-granular cracking.[44]

In the present study, we investigated five Li- and Mn-rich layered oxides, which all have the same degree of over-lithiation, but which were subjected to different synthesis conditions by our cooperation partner BASF SE. Depending on the used proprietary synthesis routes, the five CAMs can be differentiated into three categories in terms of: (i) morphology, differentiating porous from dense CAMs; (ii) transition-metal composition, differentiating Co-containing from Co-free CAMs; and, (iii) secondary agglomerate size, ranging from D_{50} values of ≈6 to ≈12 μm, respectively. We characterized the as-received materials by a series of techniques, namely scanning electron microscopy, particle size analysis by laser scattering, gas physisorption, Hg intrusion porosimetry, and X-ray powder diffraction, which all target at their initial material metrics. These metrics are related to important surface and bulk properties of the CAMs, which will be then correlated in a quantitative manner to their initial electrochemical performance during a discharge rate test.

Experimental

Materials.—We investigated five Li- and Mn-rich layered oxides provided by BASF SE (Germany), which differ with respect to their morphology, transition-metal (TM) composition, and particle size. The degree of over-lithiation is similar among the five CAMs and amounts to $\delta = 0.14 \pm 0.01$ in $Li[Li_\delta TM_{1-\delta}]O_2$, which can be also written as 0.33 Li_2MnO_3 following the "x $Li_2MnO_3 \cdot (1-x)$ $LiTMO_2$" notation used by Teufl et al.[20] Throughout this work, the CAMs are abbreviated according to the "morphology-cobalt content-particle size" nomenclature serving as a CAM ID. This specifies the morphology of the secondary agglomerates as either porous (P) or dense (D), achieved by two different proprietary synthesis routes, the cobalt content as either Co-containing (wCo) or Co-free (woCo), as well as the particle size, referring to the targeted diameter of the secondary agglomerates (in μm). Consequently, the five investigated CAMs are referred to as P-wCo-10, D-wCo-10, D-wCo-6, P-woCo-6, and D-woCo-6.

In order to modify the surface (specific surface area) and bulk properties (microstrain), we further subjected the as-received D-woCo-6 CAM to a post-calcination step. Here, ≈4 g of the CAM powder were weighed into an alumina crucible (GTS Keramik, Germany) and heat-treated in a tube furnace (Carbolite, Germany) for 5 h at 1000 °C (prior heating at 10 °C min^{-1} and subsequent cooling at 2 °C min^{-1}) in an inert argon atmosphere (99.999% purity, Westfalen, Germany; flow rate of ≈1 l min^{-1}). The post-calcination temperature of 1000 °C intentionally goes beyond the original sintering temperature of ≈930 °C for the as-received CAM. Afterwards, the post-calcined sample was handled and analyzed just like the other CAMs, and it is referred to as D-woCo-6-1000C in the following.

Scanning electron microscopy (SEM).—The morphology of the CAMs was evaluated by scanning electron microscopy (JSM-7500F, JEOL, Japan) in backscattering mode at an accelerating voltage of 1 kV. We measured both top-view images of the pristine CAM powders and cross-sectional images of the pristine, compressed electrodes. The cross-sections were either prepared by mechanical polishing, following the procedure described by Friedrich et al. (i.e., the samples were embedded into epoxy resin and in the final step polished with a 0.05 μm Al_2O_3 suspension),[40] or by focused argon-ion beam (FIB) milling with a JEOL cross-section polisher (IB-19530CP, JEOL, Japan). In the latter case, the electrodes were first cut with a razor blade to create a clean cutting edge; subsequently, the electrodes were milled along this edge at a temperature of −100 °C, and in the final step with an acceleration voltage of 4 kV for 1.5–3 h (argon-ion beam alternatingly on/off for 10/10 s).

Particle size analysis.—The volumetric particle size distribution of the CAMs was measured by dynamic laser scattering (DLS; HORIBA LA-960, Retsch Technology, Germany), which is based on the Mie scattering theory. One tip of a spatula of the pristine CAM powder was dispersed in ethanol by sonication and then analyzed in a flow-through cell. The measurement was evaluated with a real part refractive index of 2.11 for the CAM (assuming MnO as reference material[45]) and of 1.36 for ethanol. We report the D_{50} values of the different CAMs.

Gas physisorption analysis.—The specific surface area of the CAMs was determined by gas physisorption (Autosorb-iQ, Quantachrome, USA) at 77 K using nitrogen as adsorbate. Beforehand, the pristine CAM powders were outgassed at 120 °C for 12 h under dynamic vacuum. The sample mass was chosen to achieve an absolute surface area of 2.5–5.0 m^2 inside the sample holder. Adsorption isotherms were measured with 11 data points in the relative pressure range of $0.05 \leqslant p/p_0 \leqslant 0.30$ (p/p_0 tolerance of −0.003 and +0.009, equilibration time of 3 min). The specific surface area was calculated according to the Brunauer-Emmet-Teller (BET) theory, whereby the ideal linear range is selected by the Micropore BET Assistant of the ASiQwin software (typically 7 out of the 11 points).[46]

Mercury intrusion porosimetry (MIP).—The pore size distribution and pore volume of the CAMs were measured with a Micromeritics AutoPore V instrument (Micromeritics, USA). The as-received CAM powders were dried overnight at 120 °C under dynamic vacuum and then loaded into the penetrometer (sample holder) with a bulb and stem volume of 3.00 and 0.412 cm^3, respectively. The sample mass was between 0.5−1.0 g, targeting at an usage of ≈60% of the stem volume filled with mercury. The penetrometer was filled at a pressure of 0.007 MPa. First, the low-pressure port measures the mercury intrusion up to a pressure of 0.35 MPa (one data point every 0.014 MPa, equilibration time of 10 s), while the subsequent high-pressure port goes all the way up to 410 MPa (>30 points per decade, equilibration rate of 5 μl $(g{\cdot}s)^{-1}$). The pore diameter (d_{pore}) is calculated with the Washburn equation:

$$d_{pore} = -\frac{4 \cdot \gamma_{Hg} \cdot \cos\theta_{Hg}}{p} \quad [1]$$

where γ_{Hg} is the surface tension of Hg (0.485 N m^{-1} at 20 °C), θ_{Hg} is the contact angle of Hg (130°), and p is the applied pressure. Consequently, the measurable pore diameter ranges from ≈180 μm to ≈3 nm.

The intruded mercury volume was corrected with a blank run of the empty penetrometer (filled only with Hg). Since the correction might not be perfect at the high-pressure end (e.g., due to heating of the hydraulic oil), we further omitted negative intrusion values (typically ⩽5 mm^3 g^{-1} at ⩽20 nm). Following our previous study,[24] we assigned the pore volume obtained for pore diameters smaller than 300 nm to that of intra-particular pores ($v_{pore,intra}$) inside the secondary agglomerates. The associated intra-particular porosity (ε_{intra}) was calculated as follows:

$$\varepsilon_{intra} = \frac{v_{pore,intra}}{v_{pore,intra} + \frac{1}{\rho_{cryst}}} \quad [2]$$

where ρ_{cryst} is the crystallographic density of the layered oxides (≈4.35 g cm^{-3}).

X-ray powder diffraction (XPD).—The pristine CAM powders were loaded into 0.3 mm borosilicate capillaries and measured in the

Journal of The Electrochemical Society, 2022 169 060521

2θ range of 5°–60° (one data point every 0.015°) for ≈14 h at our in-house STOE STADI P diffractometer (STOE, Germany). This instrument works in transmission mode using Mo-$K_{\alpha1}$ radiation (λ = 0.7093 Å), a Ge(111) monochromator, and a Mythen 1K detector. The XPD data were analyzed with the Topas software package.[47] The layered oxides were treated with the structure-independent Le Bail method using the *C*2/*m* symmetry (space group no. 12).[48] In contrast to the Rietveld method, this approach does not require the exact composition of the CAMs or any sophisticated structural model. While the Rietveld method primarily targets at extracting crystallographic information (e.g., atomic positions and site occupancy factors) by modelling the reflection intensity, the here applied Le Bail method focuses on the line broadening in order to obtain real structure information (i.e., crystallite size and microstrain).

We refined the background (Chebyshev polynomial with 12 coefficients), instrumental parameters (zero shift and axial divergence), the four lattice parameters (a, b, c, and β) as well as the intensity of each individual reflection (according to the Le Bail method). However, we were particularly interested in the line broadening of the reflections (Γ_{hkl}):

$$\Gamma_{hkl} = \Gamma_{instrument} + \Gamma_{size} + \Gamma_{strain} \quad [3]$$

which has contributions from the instrument ($\Gamma_{instrument}$) and from the sample (Γ_{size} and Γ_{strain}). The instrumental broadening was determined with a standard silicon material using the Thompson-Cox-Hastings pseudo-Voigt function (Topas command *TCHZ_Peak_Type*, parameters *U*, *W*, and *X* activated).[37] The crystallite size of the sample leads to line broadening according to the well-known Scherrer equation:

$$\Gamma_{size} = \frac{K \cdot \lambda}{L_{vol} \cdot \cos\theta} \quad [4]$$

where K is a shape factor (on the order of 1), λ is the wavelength, θ is the Bragg angle, and L_{vol} is the volume-weighted mean column length of the crystallites. Assuming spherical crystallites, their average diameter corresponds to $d_{sphere} = 4/3 \cdot L_{vol}$.[37] Note that the Scherrer equation is only applicable to sub-μm crystallites (L_{vol} less than ≈200 nm). Finally, there is a microstrain contribution of the sample:

$$\Gamma_{strain} = 4 \cdot \varepsilon_0 \cdot \tan\theta \quad [5]$$

where $\varepsilon_0 = \Delta d/d$ is the mean lattice spacing deviation. This lattice imperfection is caused by the displacement of atoms from their ideal position, e.g., due to point defects such as vacancies and interstitials.

The two contributions of the sample broadening can be separated by their θ-dependence, $\Gamma_{size} \propto 1/\cos\theta$ vs $\Gamma_{strain} \propto \tan\theta$. Another important aspect of the size/strain analysis addresses the calculation method of the line broadening. The Topas Technical Reference recommends extracting L_{vol} from the integral breadth-based $\Gamma_{size(IB)}$, while ε_0 should rely on the full width at half maximum-based $\Gamma_{strain(FWHM)}$.[37] The integral breadth of a reflection is obtained from dividing the line profile area by its height, and the crystallite size determined therefrom is fairly independent of the size distribution and shape (with K set to 1). Following this advice, we used the *LVol_FWHM_CS_G_L* and *e0_from_Strain* commands in Topas, which both comprise Lorentzian and Gaussian component convolutions. Thus, there are a total of four parameters to describe the line profile of the layered oxide, but we deactivated the parameters with a limit warning from the program (individually for each CAM). This could happen when the crystallite size is too large or the microstrain is too small to be quantifiable, which might apply only to one component (Lorentzian or Gaussian) or to the entire contribution (size or strain). Please note that the applied commands describe an isotropic line broadening, i.e., the width of the reflections scales solely with 2θ, but there is no anisotropic dependence on *hkl*. Furthermore, we did not implement an additional broadening of the superstructure reflections, because they barely affect the size/strain values extracted from the entire diffractogram.

During the review process, it was pointed out that silicon is not the best choice for calibrating the instrumental broadening of the diffractometer, as it might contribute sample-related broadening effects. Therefore, we recommend LaB_6 or $Na_2Ca_3Al_2F_{14}$ (NAC) as line profile standards in future studies. Assuming that the measured broadening originates solely from the CAMs, the size/strain analysis would yield a maximum deviation of 0.02% (absolute) higher microstrain values; however, the observed trend between the CAMs is unaffected.

Electrochemical characterization.—Cathode coatings consist of the CAM powder, conductive carbon (Super C65, Timcal, Switzerland), and polyvinylidene fluoride binder (PVDF, Kynar HSV 900, Arkema, France) at a weight ratio of 90:5:5 (for the Co-containing CAMs) or 92.5:4.0:3.5 (for the Co-free CAMs). The slurry was prepared with *N*-methyl-2-pyrrolidone (NMP, anhydrous, 99.5%, Sigma-Aldrich, Germany) in several steps in a planetary orbital mixer (Thinky, USA) and then cast onto the 15 μm thick aluminum current collector foil (MTI, USA). After drying at 50 °C in a convection oven, the loading of the cathode sheets amounts to ≈5.0–6.0 mg_{CAM} cm^{-2} (for the Co-containing CAMs) and ≈6.5–7.0 mg_{CAM} cm^{-2} (for the Co-free CAMs); the CAM loading of each electrode was determined with a precision of ±0.05 mg_{CAM} cm^{-2}. Disk-shaped electrodes with a diameter of 10 mm were punched out of the cathode sheets and compressed at 2 t for 20 s. The electrodes were dried overnight at 120 °C in a vacuum oven (Büchi, Switzerland) and then inertly transferred into an argon-filled glove box (<0.1 ppm O_2 and H_2O, MBraun, Germany).

Electrochemical testing was conducted in 3-electrode Swagelok® T-cells with a lithium metal counter-electrode (Li-CE, with Ø 11 mm of a 450 μm thick lithium foil, Albemarle, USA) and a lithium metal reference-electrode (Li-RE, with Ø 6 mm). Anode and cathode were separated by two glass-fiber separators (Ø 11 mm, glass microfiber filter 691, VWR, Germany), which were soaked with 60 μl of LP57 electrolyte (1M $LiPF_6$ in EC:EMC = 3:7 by weight, BASF SE, Germany). The cells were measured at 25 °C in a temperature-controlled chamber (Binder, Germany) with a battery cycler (Series 4000, Maccor, USA).

The cathode potential was controlled vs the Li-RE and the C-rate was based on a nominal capacity of 250 mAh g^{-1} (i.e., 1C ≡ 250 mA g^{-1}). The cycling protocol started with an activation cycle in the potential window of 2.0–4.8 V vs Li^+/Li at a C-rate of C/15 or C/10, whereby the latter was completed with a constant voltage (CV) hold at 4.8 V for 1 h. Following two subsequent stabilization cycles between 2.0–4.7 V vs Li^+/Li at C/10 (without CV hold), the cells passed a discharge rate test going in nine steps from 10C to C/50 for 2 cycles each. The potential window was fixed between 2.0−4.7 V vs Li^+/Li and the discharge was done consecutively at 10C, 5C, 2C, 1C, C/2, C/5, C/10, C/20, and C/50, respectively. The charge had a C-rate of less or equal than C/2, i.e., the charge was limited to C/2 when the discharge was faster, but both were equal at slower rates. Furthermore, each charge step was completed by a CV hold at 4.7 V vs Li^+/Li until the current dropped below C/50 (corresponding to 5 mA g^{-1}). After the rate test, we performed two more stabilization cycles, which yielded 23 cycles in total. After running into the final cut-off condition for charge or discharge, we measured the open circuit voltage (OCV) in each cycle for 10 min before continuing the measurement.

Unless otherwise stated, any specific parameters such as the specific capacity (in mAh g^{-1}) or the specific surface area (in m^2 g^{-1}) are normalized to the CAM mass, and the potential is reported in V vs Li^+/Li.

Results and Discussion

Morphology of the as-received CAMs.—As a first step, we will compare qualitatively the morphology of the cathode active

materials on the basis of SEM images. Figure 1 shows the five investigated CAMs from left to right (a−e), whereby the first two rows (1,2) depict top-view images of the pristine CAM powders and the last to rows (3,4) depict cross-sectional images of the pristine, compressed electrodes. At magnifications of 2.500x (1,3) and 10.000x (2,4), the scale bar refers to 5 μm and 1 μm, respectively. The SEM images reveal significant differences between the two porous CAMs (P-wCo-10 (a) and P-woCo-6 (d)) in comparison to the three dense CAMs (D-wCo-10 (b), D-wCo-6 (c) and D-woCo-6 (e)). Here, the top-view images illustrate the size and especially the shape of the secondary agglomerates. While the porous CAMs possess a uniform, almost perfectly spherical shape (see Figs. 1a1 and 1d1), the secondary agglomerates of the dense CAMs are irregularly formed and edged (see Figs. 1b1, 1c1, and 1e1). The higher magnifications reveal some smaller particles on the outer surface of the secondary agglomerates, from which the faceted crystals on the P-wCo-10 CAM can be clearly differentiated from the subjacent material (see Fig. 1a2). These faceted crystals have lateral dimensions of ≈0.5 μm and might potentially originate from carbonate impurities, because they were identified as the main impurity on a similar Li- and Mn-rich CAM.[49] Qualitatively, the size of the secondary agglomerates is on the order of ≈5–10 μm; a more quantitative assessment was done by dynamic laser scattering, yielding the corresponding D_{50} values that are provided at the top of Fig. 1 and in Table I. These D_{50} values agree within ≈1–2 μm with the targeted secondary agglomerate sizes of either 6 μm or 10 μm.

The cross-sectional images were prepared either by mechanical polishing (Figs. 1a3, 1a4, 1b3, 1b4, 1c3, 1c4 for the Co-containing CAMs) or by FIB milling of the cathode electrodes (Figs. 1d3, 1d4, 1e3, 1d4 for the Co-free CAMs). Note that the former approach visualizes only the CAM particles, since the electrodes were embedded into epoxy resin, while in the latter case the C65 conductive carbon also becomes visible between the CAM particles. The cross-sections highlight the interior of the secondary agglomerates. The packing of the primary particles is crucial for the differentiation into porous vs dense CAMs. In case of the porous CAMs (see Figs. 1a3, 1a4, 1d3, and 1d4), the primary crystallites are loosely connected with each other, which gives rise to a fluffy structure with significant void space between the individual crystallites. On the other hand, the dense CAMs are much more closely packed and the crystallites appear to be fused together by solid-solid grain boundaries. While the two Co-containing representatives, D-wCo-10 (see Figs. 1b3, 1b4) and D-wCo-6 (see Figs. 1c3, 1c4), exhibit virtually no void space in their interior, the D-woCo-6 CAM (see Figs. 1e3, 1e4) features some occasional pores, which however might not be connected with each other and/or to the outside.

The qualitative differences observed by SEM imaging find expression in the specific surface areas of the CAMs (A_{BET}). As shown in Fig. 1 and Table I, the A_{BET} values range by a factor of up to ≈15, from 5.3–5.4 $m^2\ g^{-1}$ for the porous CAMs to 0.37–1.3 $m^2\ g^{-1}$ for the dense CAMs. Assuming solid spheres and using the crystallographic density of ≈4.35 g cm^{-3}, these A_{BET} values can be translated into an average particle diameter according to $d_{BET} = 6/(\rho_{cryst} \cdot A_{BET})$.[50] In case of the porous CAMs, this diameter amounts to $d_{BET} \approx 0.26$ μm, which is on the order of the primary crystallites (see Figs. 1a4 and 1d4). This estimate seems reasonable. The porous network of the secondary agglomerates enables full access to the inner part of the agglomerates, so that the surface area

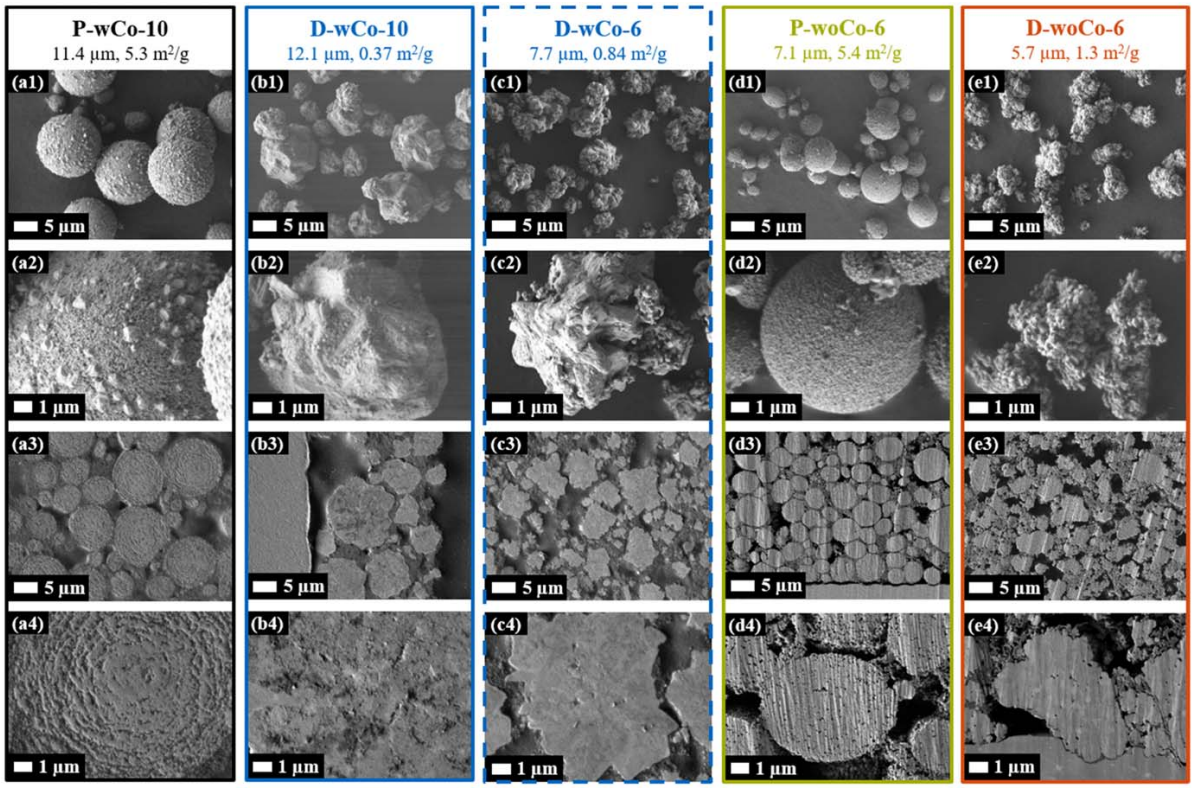

Figure 1. SEM top-view images of the pristine CAM powders (1st and 2nd row) and cross-sectional images of the pristine, compressed electrodes (3rd and 4th row). The cross-sections of the three Co-containing CAMs were prepared by mechanical polishing, while the two Co-free CAMs were treated by FIB milling (see Experimental section). Note that the scratches in the panels (d3, d4, e3, e4) come from the not optimized settings of the FIB milling, and that the internal pore volume of the P-woCo-6 CAM in panel (d4) might be partially smeared and blocked due to abrasion products. The magnifications amount to 2.500x (1st and 3rd row; 5 μm scale bar) and 10.000x (2nd and 4th row; 1 μm scale bar). At the top, the CAM ID is given together with its secondary agglomerate size (given as D_{50} diameter from dynamic laser scattering) and its A_{BET} values (from nitrogen physisorption).

Journal of The Electrochemical Society, 2022 **169** 060521

Table 1. Comparison of the five investigated Li- and Mn-rich CAMs with respect to their material properties in the pristine state and their rate test performance. Material properties are the median secondary agglomerate size (D_{50}) from dynamic laser scattering (DLS), the specific surface area (A_{BET}) from N_2 physisorption, the intra-particular pore volume ($v_{pore,intra}$) and porosity (ε_{intra}) from mercury intrusion porosimetry (MIP), as well as the crystallite size (L_{vol}) and microstrain (ε_0) from X-ray powder diffraction (XPD). The discharge capacity of the CAMs is compared at a current density of 1C (corresponding to 250 mA g^{-1}) and at 10 mA m^{-2} (after BET surface area normalization), respectively. The latter was interpolated from the rate test data; except for the D-wCo-10 CAM, which was extrapolated from the lowest current density of ≈14 mA m^{-2}. The reported errors are the standard deviation from at least two measurements (N_2 physisorption and MIP), estimated from a single measurement by the refinement program (XPD), or from two cells averaged over the two cycles at each C-rate (rate test).

CAM	DLS	N_2 physisorption	MIP		XPD		Rate test	
							Discharge capacity [mAh g^{-1}]	
	D_{50} [μm]	A_{BET} [m^2 g^{-1}]	$v_{pore,intra}$ [mm^3 g^{-1}]	ε_{intra} [%]	L_{vol} [nm]	ε_0 [%]	@ 1C	@ 10 mA m^{-2}
P-wCo-10	11.4	5.3 ± 0.2	70 ± 0.3	23.3 ± 0.1	128 ± 7	0.025 ± 0.001	222 ± 1	≈250
D-wCo-10	12.1	0.37	<1	<0.4	too large	0.181 ± 0.003	86 ± 1	(≈180)
D-wCo-6	7.7	0.84	1.8 ± 0.2	0.8 ± 0.1	too large	0.167 ± 0.003	115 ± 1	≈181
P-woCo-6	7.1	5.4 ± 0.3	44 ± 0.5	16.1 ± 0.2	97 ± 6	0.038 ± 0.002	198 ± 1	≈223
D-woCo-6	5.7	1.3 ± 0.04	6.1 ± 0.8	2.6 ± 0.3	too large	0.097 ± 0.001	152 ± 1	≈212

of all of the primary crystallites is exposed to the gas (during the gas physisorption measurement). This, presumably, also allows full access of the primary particle surfaces to the electrolyte (which infiltrates the internal pores when assembled into a battery). In contrast, the average BET-based diameter of the dense CAMs amounts to ≈3.7 μm for D-wCo-10, ≈1.6 μm for D-wCo-6, and ≈1.1 μm for D-woCo-6, which more closely reflects the size of the secondary agglomerates. Consequently, the dense CAMs expose primarily the outer surface area of the secondary agglomerates to the gas (and thus to the electrolyte). Note that the d_{BET} values of the dense CAMs are smaller than the D_{50} values (by a factor of ≈4–6), likely due to their non-spherical shape and the roughness of their outer surface. This is especially pronounced for the D-woCo-6 CAM, where the primary crystallites can actually be identified in top-view mode (see Fig. 1e2), similarly to the two porous CAMs (see Figs. 1a2 and 1d2); however, they are strongly compacted in the bulk of the agglomerates, as seen in the cross-sectional image (see Fig. 1e4).

The SEM images as well as the BET surface areas revealed large morphological differences between the dense vs porous CAMs. Based on this, we also sought to quantify their internal porosity by mercury intrusion porosimetry. Since mercury has a contact angle greater than 90° and thus does not wet most substances, it has to be forced to fill the open pore space by applying an external pressure. According to the Washburn equation (see Eq. 1 in the Experimental section), the pressure correlates inversely with the pore diameter at which the intruded mercury volume is determined by its capacitance change in the penetrometer stem. This approach can be applied to battery material powders[51] and electrodes.[24,52,53]

Figure 2 shows the porosimetry data of the five CAM powders. The pore volume is depicted as accumulative pore volume (v_{pore}) in panel (a) and as its logarithmic derivative ($dv_{pore}/d\log d_{pore}$) in panel (b), both plotted vs the pore diameter (d_{pore}) on a logarithmic scale, so that the area under the latter curve directly corresponds to the pore volume within the examined pore diameter range. As the large pores get filled first, the measurement can be divided into three sections. In the first section (see ① in Fig. 2a), the loose CAM powders are compacted without filling any of the pore space in between the secondary agglomerates, which gives rise to a linear increase of the intruded volume. Here, the D-wCo-6 (blue dashed line) and D-woCo-6 CAMs (red solid line) seem to be more loosely packed than the other CAMs. When the secondary agglomerates are arranged in a close packing, mercury starts to fill the inter-particular pore volume in between them at Hg pressures that correspond to diameters below ≈4 μm (see section ② in Fig. 2a). The pore diameter at which the peak of the differential volume has its maximum ($d_{pore,inter,max}$) clearly increases with the D_{50} diameter of the secondary agglomerates (listed Table 1). The $D_{50}/d_{pore,inter,max}$ ratio amounts to ≈3.5–4.2, which agrees well with the rule of thumb

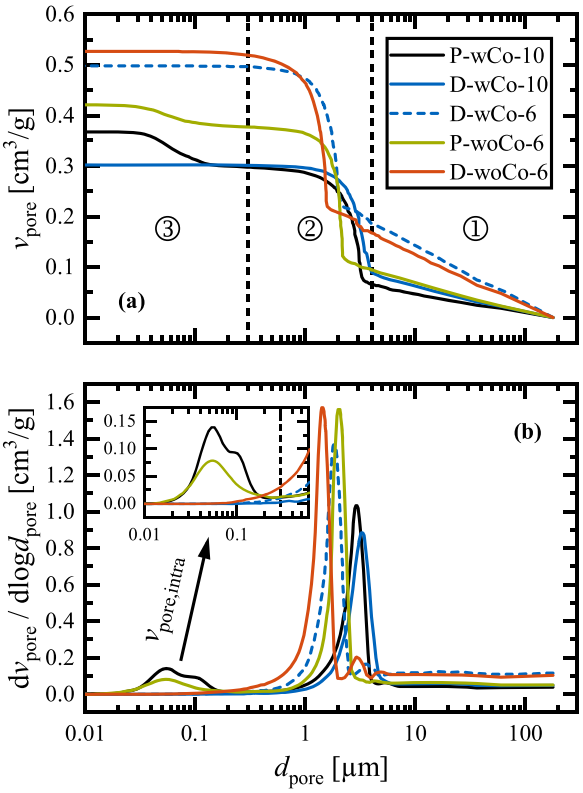

Figure 2. Mercury intrusion porosimetry of the as-received CAM powders. (a) Cumulative pore volume (v_{pore}), and (b) logarithmic differential pore volume ($dv_{pore}/d\log d_{pore}$) as a function of the pore diameter (d_{pore}) plotted on a logarithmic scale. Starting with large pores, the measurement can be divided into three sections: ① powder compaction, ② filling of inter-particular pores between the secondary agglomerates, and ③ filling of intra-particular pores inside the agglomerates, which is defined as occurring below 300 nm. We show here one measurement for each CAM, while the intra-particular pore volume and porosity reported in Table I are based on two measurements each.

reported by Giesche, namely that the effective pore size between particles is ≈2–4 times smaller than the particle diameter (the exact ratio depends on the particles packing structure).[54]

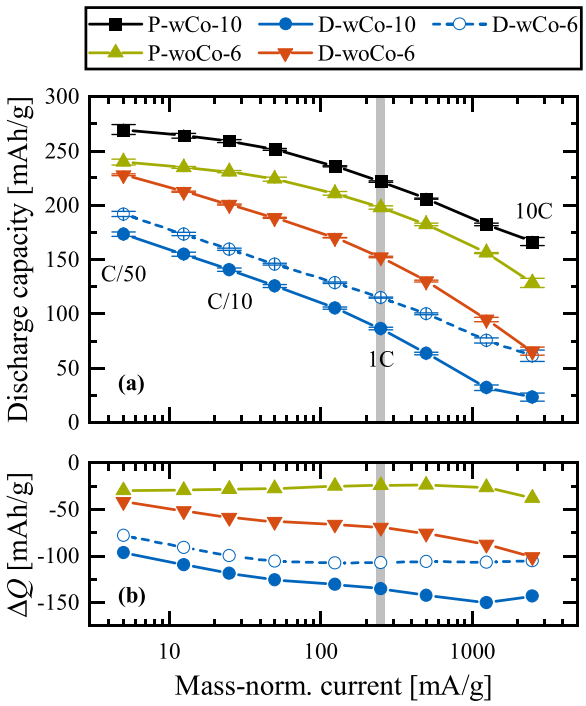

Figure 3. Discharge rate test of the five investigated Li- and Mn-rich layered oxides. After activation and two more stabilization cycles, the CAMs were cycled between cathode potentials of 2.0–4.7 V vs Li^+/Li (controlled against a Li-RE), increasing the C-rate in nine steps from 10C to C/50 during discharge, while the charge was limited to ⩽C/2 (with an additional CV hold at 4.7 V to C/50). The two cycles acquired at each C-rate were averaged for this plot from two cells measured for each CAM. The C-rate is referenced to a nominal capacity of 250 mAh g^{-1}, corresponding to a mass-normalized current of 250 mA g^{-1} at 1C. (a) Discharge capacity and (b) capacity difference (ΔQ) relative to the best-performing P-wCo-10 CAM (both in mAh/g). The discharge capacity at 1C (marked by the gray bar) is listed in Table I.

After filling the entire void volume between the agglomerates, further increasing the mercury pressure finally leads to its penetration into the intra-particular pores inside the agglomerates (see section ③ in Fig. 2a). We defined this process as occurring at pore diameters smaller than 300 nm, because the differential pore volume of the porous CAMs (P-wCo-10 (in black) and P-woCo-6 (in green) in Fig. 2b), has a minimum at this diameter between sections ② and ③ (see inset). The pore diameter of the two porous CAMs ranges from ≈200 nm down to ≈20 nm, with a median value of ≈60 nm. Based on the cross-sectional images of the porous CAMs (see Figs. 1a4 and 1d4), the large pores might mainly occur close to the surface of the secondary agglomerates, while the pores become smaller towards their interior. From the intra-particular pore volume ($v_{pore,intra}$) in section ③, we can calculate the internal porosity (ε_{intra}) according to Eq. 2, which amounts to ≈23% and ≈16% for P-wCo-10 and P-woCo-6, respectively (see Table I). The difference of ≈7% is in qualitative agreement to the cross-sectional images, because the P-wCo-10 CAM (Figs. 1a4) appears visually to be more porous than the P-woCo-6 CAM (Fig. 1d4). On the other hand, the three dense CAMs (in blue and red) feature barely any pores below 300 nm, which gives rise to the horizontal plateaus of the mercury intrusion curves in Fig. 2a. The internal porosity of the dense CAMs is less than 3%; the actual value is likely lower due to the artefact arising from an apparent minor filling of inter-particular pores at mercury pressures corresponding to pore sizes below 300 nm (see, e.g., red line of D-woCo-6 in the inset of Fig. 2b). Please note that we defined the detection limit of $v_{pore,intra}$ to be 1 mm^3 g^{-1}, which is why the upper limit of ε_{intra} is given as 0.4% for D-wCo-10 in Table I.

As discussed in our previous publication,[24] the internal porosity of porous secondary agglomerates leads to a substantially reduced electrode density, which compromises the volumetric energy density of the battery cell. For example, considering that cathode electrodes of densely packed CAMs can typically be calendered to ≈30% porosity,[1,55,56] with the porosity almost entirely due to the pore space between secondary agglomerates (i.e., $\varepsilon^*_{total} \approx \varepsilon^*_{inter} \approx 30\%$), the electrode density of the here examined dense D-woCo-6 CAM at 92.5 wt% CAM in the electrode would be ≈2.69 $g_{electrode}$ $cm^{-3}_{electrode}$ (with $\varepsilon^*_{total} = \varepsilon^*_{inter} + \varepsilon^*_{intra} \approx 32\%$). On the other hand, the electrode density would be only ≈2.22 $g_{electrode}$ $cm^{-3}_{electrode}$ for the porous P-woCo-6 counterpart with an internal porosity of $\varepsilon^*_{intra} \approx 14\%$ ($\varepsilon^*_{total} \approx 44\%$). The asterisk (*) indicates that these porosities are related to the entire electrode and not only to the CAM (see explanation and underlying equations in the Appendix). This comparison illustrates the negative impact of the internal porosity of secondary CAM agglomerates on the achievable electrode density and thus on the potential volumetric energy density of the cell.[51]

Rate test analysis.—Let us now turn towards the electrochemical characterization of the five CAMs. Figure 3 shows the results of a discharge rate test, which was conducted after the first activation cycle (see Fig. A·1 in the Appendix) and two more stabilization cycles (measuring details can be found in the Experimental section). The applied C-rates cover more than two orders of magnitude, from 10C to C/50, whereby 1C corresponds to a mass-normalized current of 250 mA g^{-1}. To avoid any capacity drop due to the kinetic overpotential of the lithium counter-electrode, especially at high C-rates (up to ≈18 mA cm^{-2} at 10C), the cathode potential was controlled vs a lithium reference-electrode between 2.0 and 4.7 V. Furthermore, the use of two glass-fiber separators with a thickness of ≈400 μm prevents an internal short due to lithium dendrites, and the concomitant electrolyte excess (≈13 $g_{electrolyte}/g_{CAM}$) avoids the deterioration of the bulk electrolyte due to its continuous reduction on the anode side. Since slow cycles have a higher charge throughput, they are expected to cause more degradation of the CAM, e.g., due to surface reconstruction[20] and impedance build-up.[57] Therefore, the fast rates were performed first, and the decreasing C-rates in the subsequent cycles counteract any potential impedance build-up, so that the entire test procedure represents in good approximation the initial material performance. The charge rate was the same as the discharge rate for ⩽C/2 and was kept at C/2 for higher discharge rates; the charge process was completed by a constant voltage hold at 4.7 V until the current dropped below C/50. This procedure ensures that the upper state of charge (SOC) limit and thus the starting point of each discharge are fairly constant during the rate test. To validate this, we added a 10 min. OCV phase after each charge and discharge step. The last OCV value after running into the upper cathode cut-off potential of 4.7 V was found to only vary within a small voltage window of ≈40 mV for each CAM, i.e., the uppermost SOC is indeed very similar throughout the entire rate test (ΔSOC estimated to be ⩽3 mAh g^{-1}). In contrast, the lower SOC limit after reaching the cathode potential of 2.0 V results in, as expected, lower open circuit voltages when decreasing the C-rate, and the OCV values in the discharged state span over more than 1 V.

As shown in Fig. 3, the porous Co-containing P-wCo-10 CAM (in black) has the best rate capability, reaching capacities from ≈166 mAh g^{-1} at 10C to ≈270 mAh g^{-1} at C/50, which agrees with similar state-of-the-art Li- and Mn-rich layered oxides that have a high BET surface area and contain cobalt.[24,58] On the other hand, the dense Co-containing D-wCo-10 CAM (solid blue line) exhibits the worst performance with only ≈23 mAh g^{-1} at 10C and ≈173 mAh g^{-1} at C/50, whereby the other dense Co-containing D-wCo-6 CAM shows only slightly better performance (dashed blue

Journal of The Electrochemical Society, 2022 **169** 060521

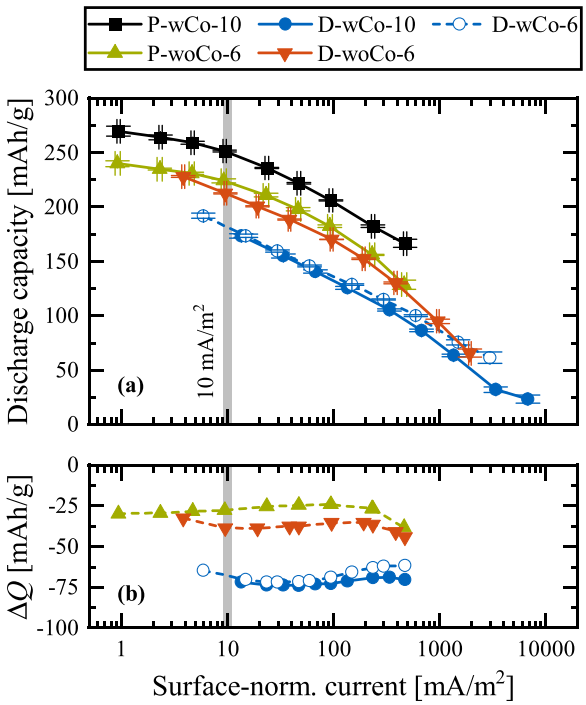

Figure 4. Rate test data of Fig. 3 re-plotted as function of the surface-normalized current, which is calculated by dividing the mass-normalized current by the BET surface of the different CAMs. (a) Discharge capacity and (b) capacity difference (ΔQ) relative to the best-performing P-wCo-10 CAM (both in mAh/g). The discharge capacity at a surface-normalized current of 10 mA m^{-2} (see gray bar) is obtained by interpolation of the available data points and is listed in Table I.

line). Since the performance of the Co-free CAMs (P-woCo-6 (in green) and D-woCo-6 (in red)) falls in between these three Co-containing CAMs, there is no obvious correlation between the accessible capacity and whether the CAMs contain cobalt or not. On the other hand, the performance of the CAMs seems to be sorted according to their BET surface area (see Table I): the porous CAMs with BET surface areas of more than 5 m^2 g^{-1} (P-wCo-10 and P-woCo-6) have the highest capacities, followed by the dense CAMs, whose capacities decrease with decreasing BET surface area, namely from D-woCo-6 with 1.3 m^2 g^{-1} to D-wCo-6 with 0.84 m^2 g^{-1}, all the way to D-wCo-10 with 0.37 m^2 g^{-1}. Furthermore, the capacity difference of the dense CAMs relative to the porous CAMs decreases as the applied C-rate becomes smaller, which is illustrated by the plot of the capacity difference of any given CAM relative to the best-performing P-wCo-10 CAM in Fig. 3b. The observed decrease of performance with decreasing BET surface area is not too surprising, as higher BET values result in more CAM surface area that is available for lithium-ion transfer across the CAM/electrolyte interface, based on the assumption that the CAM surface area measured by N_2 physisorption equals the CAM surface area that is exposed to the electrolyte during the rate test (see below discussion). This holds true as long as micropores below ≈1 nm do not contribute significantly to the BET surface area, as those could only be accessed by the nitrogen gas during BET measurements and not by solvated lithium-ions during electrochemical measurements.[59]

The current divided by the CAM surface area exposed to the electrolyte (further on referred to as the surface-normalized current) defines the actual current density that governs the charge-transfer process. Thus, assuming that the intrinsic charge-transfer resistance referenced to the CAM/electrolyte interfacial surface area (in units of $\Omega \cdot m^2$) is similar for the different CAMs, their effective charge-transfer resistance (in units of $\Omega \cdot g$) should scale linearly with their BET surface area. As the porous CAMs feature the highest BET surface area (i.e., the highest surface-to-bulk ratio), with the majority of the primary crystallites being in direct contact with the electrolyte, their effective charge-transfer resistance (in units of $\Omega \cdot g$) should be the lowest. On the other hand, in case of the dense CAMs, the primary crystallites are fused together through solid-solid grain boundaries, such that only the outer surface of the secondary agglomerates is exposed to the electrolyte. This in turn increases their effective charge-transfer resistance (in $\Omega \cdot g$), which leads to higher overpotentials at a given C-rate. Consequently, the rate test representation in Fig. 3 is not a fair comparison between the investigated CAMs, because the mass-normalized current (in mA/g) at a given C-rate does not account for the largely different CAM/electrolyte interfacial areas. Therefore, under the reasonable assumption that the intrinsic charge-transfer resistance (in units of $\Omega \cdot m^2$) is similar, the rate capability of the CAMs should be compared as a function of the surface-normalized current (in units of mA/m^2), rather than in terms of the mass-normalized current or C-rate (as was done in Fig. 3).

Such a comparison is shown in Fig. 4, where the mass-normalized current (from Fig. 3) is divided by the BET surface area of the CAMs, plotting the discharge capacities against the logarithm of the surface-normalized current. Now, the rate test data of the different CAMs are shifted along the *x*-axis: the porous CAMs reach lower surface-normalized currents (shifted to the left) than the dense CAMs (shifted to the right). This has some interesting implications. The dense and Co-containing CAMs (in blue), which differ just by agglomerate size (12.1 μm for D-wCo-10 vs 7.7 μm for D-wCo-6, see Table I), now exhibit the same discharge capacity for most of the shared surface-normalized current range in Fig. 4, while they were separated by ≈20−40 mAh g^{-1} at any given C-rate (see Fig. 3b). This means that the BET surface area (different by a factor of ≈2.3) can quantitatively explain their performance variation. In a similar manner, the performance difference between the two Co-free CAMs (P-woCo-6 (in green) and D-woCo-6 (in red)) is almost entirely compensated for by the surface area normalization (different by a factor of ≈4.2).

The porous and Co-containing P-wCo-10 CAM (in black) still outperforms the other CAMs, but the capacity offset is nearly constant within the surface-normalized current range that the materials have in common, as shown by plotting the capacity difference of the various CAMs with respect to the best-performing P-wCo-10 CAM (see Fig. 4b). There are some small deviations at high surface-normalized currents (corresponding to the two highest C-rates of 5C and 10C), where the capacity is not only governed by the CAM itself, but also by electrode properties such as loading and tortuosity. For example, the capacities of the Co-free CAMs (with ≈6.5−7.0 mg_{CAM} cm^{-2} loading) decrease faster with increasing rate compared to the Co-containing CAMs (with ≈5.0−6.0 mg_{CAM} cm^{-2} loading) due to their higher loading. The remaining offset between the CAMs indicates at least a second, yet unknown descriptor of their electrochemical performance, but the surface area obviously plays a big role. Looking at a practically relevant C-rate of 1C (see gray bar in Fig. 3), the best- and the worst-performing CAMs, i.e., P-wCo-10 and D-wCo-10, are separated by ≈136 mAh g^{-1}. After surface area normalization, the capacity offset is almost halved to ≈70 mAh g^{-1} at essentially all surface-normalized currents (see solid blue symbols in Fig. 4b). A similar reduction is achieved for the other dense CAMs, as can be checked in Table I, where the capacity values at 1C (≡ 250 mA g^{-1}) and at 10 mA m^{-2} (see gray bar in Fig. 4a) are summarized for all the here investigated CAMs.

Prior to concluding this discussion, it must be mentioned that the here used surface-normalized currents are based on the BET surface area of the as-received CAM powders, even though the actual CAM/electrolyte interfacial surface area during the rate test might increase to somewhat higher values, as reported by Oswald et al. for stoichiometric NCMs.[59] The extent of surface area increase over

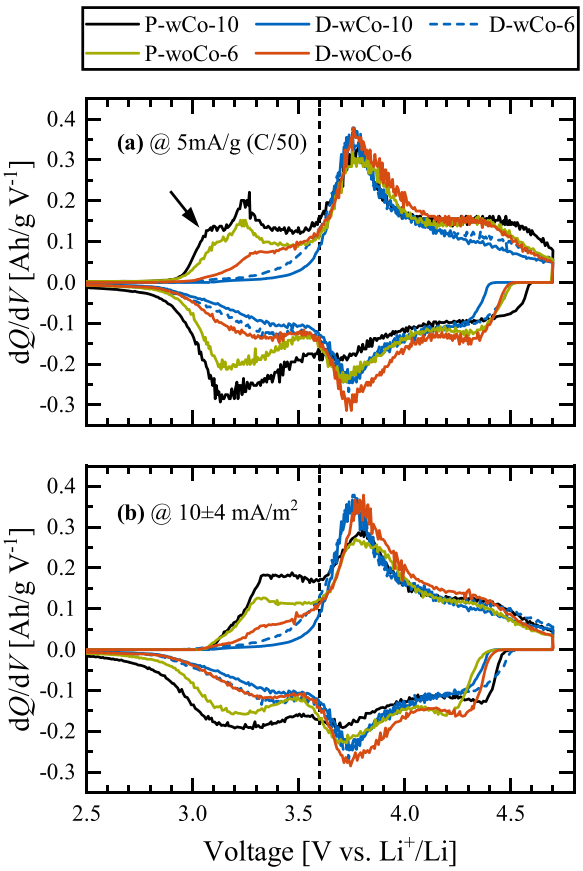

Figure 5. Differential capacity (dQ/dV) of the investigated CAMs, as measured during the rate test in Fig. 3. The CAMs are compared at two different conditions: (a) at the slowest C-rate of C/50, corresponding to a mass-normalized current of 5 mA g^{-1}, or (b) at a fixed surface-normalized current of ≈10 mA m^{-2}, which corresponds to different C-rates for each CAM due to their different surface areas (i.e., C/5 for P-wCo-10 and P-woCo-6, C/20 for D-woCo-6, and C/50 for D-wCo-10 and DwCo-6). The dashed vertical line separates the low-voltage redox feature below 3.6 V from the redox features at higher voltages. The arrow in panel (a) highlights the dQ/dV peak of a spinel layer formed around the primary particles of the porous CAMs.

the course of the test procedure (with in total 23 cycles) was examined for a porous (P-woCo-6) and a dense CAM (D-woCo-6), using the capacitance-based method developed by Oswald et al.[59] As this revealed a similar surface area increase of the porous and the dense CAM (by a factor of ≈1.4–1.6; see Appendix), the conclusions drawn from Fig. 4 still hold true (only the absolute numbers of the surface-normalized currents would change by this factor).

In order to understand where the remaining capacity offset comes from, Fig. 5 shows dQ/dV data of the CAMs during the rate test shown in Fig. 3. They are compared both at the slowest C-rate of C/50, corresponding to a mass-normalized current of 5 mA g^{-1} (see Fig. 5a), and at a similar surface-normalized current of ≈10 mA m^{-2} (see Fig. 5b). Due to the largely different CAM surface areas, the latter comparison translates into different C-rates, ranging from C/5 for the high surface area CAMs to C/50 for the low surface area CAMs. Note that the surface-normalized representation is not freely chosen (due to the pre-defined C-rates in the rate test and the different CAM surface areas), but the variation of the surface-normalized current amounts to less than 10 ± 4 mA m^{-2}. We show both representations of the dQ/dV data, because the yet unknown descriptor(s) of the accessible capacity do not necessarily have the same dependence on the effective CAM particle diameter that was implied by the above analysis based on surface-normalized currents. There, we had assigned the origin of the different observed capacities to the charge-transfer resistance, which differs at a given C-rate (in units of Ω·g), but which is expected to be identical in its intrinsic unit after surface area normalization (in units of Ω·m^2). Assuming spherical particles (reasonably consistent with the SEM images in Fig. 1), the surface area scales inversely with the effective particle diameter (i.e., $d_{particle}$ based on the actual CAM/electrolyte interfacial area), which suggests the following proportionality between the accessible capacity (Q) and $d_{particle}$: $Q \propto 1/R_{CT} \propto A_{BET} \propto 1/d_{particle}$. In case of the porous CAMs, the effective particle diameter corresponds to the primary crystallite size (on the order of ≈230−240 nm, as deduced from the A_{BET} values), whereas the dense CAMs only expose the outer surface of the secondary agglomerates to the electrolyte, so that the effective particle diameter is similar to their D_{50} values of ≈6−12 μm. Since the relevant particle diameters differ by more than one order of magnitude, it is not unreasonable to assume that the remaining capacity offset between the different CAMs at a given surface-normalized current (see Fig. 4b) might be explained by their solid-state lithium diffusion kinetics. Here, the effective diffusion time ($\tau_{diffusion}$) would scale with the solid-state lithium diffusion coefficient ($\tilde{D}_{Li}$) according to $\tau_{diffusion} = d^2_{particle}/(4\tilde{D}_{Li})$.[60,61] For the same lithium diffusion coefficient ($\tilde{D}_{Li}$), the different diffusion lengths from the surface into the core of the CAM particles (i.e., $d_{particle}/2$) result in different diffusion times, so that the accessible capacity might also have an additional dependence on the particle diameter according to $Q \propto 1/\tau_{diffusion} \propto 1/d^2_{particle}$.

We will revisit this topic; however, let us start by analyzing the dQ/dV data in Fig. 5. They can be divided into three regions: a broad low-voltage feature up to ≈3.6 V, followed by a sharp, well-defined and large peak at ≈3.8 V, which is completed by another broad high-voltage feature positive of ≈4.1 V. Independent of the two different dQ/dV comparisons (i.e., either at equal C-rate (Fig. 5a) or at equal surface-normalized current (Fig. 5b)), the investigated CAMs differ predominantly with respect to their low-voltage feature (on the left-hand side of the dashed vertical line), which is virtually absent for the D-wCo-10 CAM (solid blue line), but strongly pronounced for the P-wCo-10 CAM (solid black line). The low-voltage features of the other CAMs fall in between these two extreme cases.

Assat at al. used a series of spectroscopic techniques to investigate $Li[Li_{0.20}Ni_{0.13}Co_{0.13}Mn_{0.54}]O_2$, which features the same morphology and dQ/dV characteristics as our porous CAMs.[62] By doing so, they managed to assign the different voltage regions to specific redox activities and thus to clarify the charge compensation mechanism of post-activated Li- and Mn-rich CAMs (i.e., after their first activation cycle). The oxygen redox (O^{2-}/O^{n-} with $n < 2$) is spread over the entire voltage regime, accounting exclusively for the high-voltage feature, but being mixed in different ratios with the cationic redox for the other dQ/dV peaks. The sharp and large peak at ≈3.8 V can mainly be ascribed to the redox activity of Ni ($Ni^{2+}/Ni^{3+}/Ni^{4+}$) and, if present, of Co (Co^{3+}/Co^{4+}). Mn is originally in its inactive 4 + state in the pristine Li- and Mn-rich layered oxide, but the oxygen redox initiates some Mn redox activity (Mn^{3+}/Mn^{4+}) after activation (≈10% Mn^{3+} in the discharged state according to Assat et al.[62]), which further grows during long-term cycling.[63] This Mn redox and the accompanied anionic redox of oxygen take place in the low-voltage feature negative of ≈3.6 V.

Please note that the porous CAMs (P-wCo-10 (in black) and P-woCo-6 (in green)) show an additional shoulder at ≈3.0−3.15 V during charge at the lowest C-rate of C/50 (highlighted by the arrow in Fig. 5a). As reported by Teufl et al.,[20] this shoulder is distinctive of a spinel-like layer which is formed at the surface of the particles. Initiated by oxygen release at the end of the activation charge (see also discussion of Fig. A·1), the oxygen-depleted layered surface

Journal of The Electrochemical Society, 2022 **169** 060521

Table II. Estimation of the characteristic diffusion time for the five as-received CAMs and the post-calcined D-woCo-6-1000C CAM according to $\tau_{diffusion} = d^2_{particle}/(4\tilde{D}_{Li})$. Here, the particle diameter is derived from their BET surface area according to $d_{particle} \approx d_{BET} = 6/(\rho_{cryst} \cdot A_{BET})$ with $\rho_{cryst} \approx 4.35$ g cm^{-3}, and the solid-state lithium diffusion coefficient is assumed to be $5 \cdot 10^{-14}$ cm^2 s^{-1} for all CAMs. The materials are ordered by their BET surface area from low to high A_{BET} values, and the comparison also includes their microstrain ε_0.

CAM	A_{BET} [m^2/g]	d_{BET} [μm]	$\tau_{diffusion}$ [h]	ε_0 [%]
D-wCo-10	0.37	≈3.7	≈190	0.181
D-woCo-6-1000C	0.68	≈2.0	≈57	0.038
D-wCo-6	0.84	≈1.6	≈37	0.167
D-woCo-6	1.3	≈1.1	≈16	0.097
P-wCo-10	5.3	≈0.26	≈0.94	0.025
P-woCo-6	5.4	≈0.26	≈0.91	0.038

gradually transforms into a resistive, spinel-like layer within the first ≈20 cycles (the C/50 data shown in Fig. 5a corresponds to cycle 21 of the test procedure). The spinel feature is visible for the porous CAMs, since all primary particles are exposed to the electrolyte, yielding a relatively high surface spinel fraction (maximum of ≈5 mol% and layer thickness of ≈2 nm for the here investigated CAMs with $\delta = 0.14$).[20] For the dense CAMs, the spinel phase can be formed only at the outer surface of the secondary agglomerates, which results in a negligibly small spinel fraction. However, the spinel surface feature is small compared to the following bulk feature from Mn and O redox and is therefore not taken into consideration for the further analysis.

The presence (or absence) of specific redox activities points towards a bulk property of the CAMs as being the second descriptor of their electrochemical performance. This brings us back to the above discussion about the solid-state lithium diffusion. Croy and co-workers came to a similar conclusion, when they were investigating in detail the impedance characteristics of Li- and Mn-rich layered oxides,[64] e.g., by changing the particle morphology through the calcination conditions.[65] While the impedance at voltages greater than ≈3.6 V (≈3.5 V in their studied full-cells) is dominated by the CAM/electrolyte interface,[65] the distinct impedance rise at voltages smaller than ≈3.6 V is ascribed to local structural changes in the bulk of the CAM particles. These changes are associated with low-voltage, disordered lithium sites with slow lithium diffusion.[64] Here, the authors were also emphasizing the influence of the particle size, which affects the effective diffusion time to the second power ($\tau_{diffusion} = d^2_{particle}/(4\tilde{D}_{Li})$).

In order to roughly estimate the diffusion time of the five cathode active materials, we use the average BET-based particle diameter that differs by a factor of 5.4/0.37 ≈ 15 for the end members P-woCo-6 and D-wCo-10, or squared by a factor of $(5.4/0.37)^2 \approx 210$ (see A_{BET} and the thereof derived d_{BET} in Table II). The SOC-dependent lithium diffusion coefficient can be determined from various techniques, including the galvanostatic intermittent titration technique (GITT),[60,66] electrochemical impedance spectroscopy (EIS),[50,62] and cyclic voltammetry[67,68]; however, the reported values of $\tilde{D}_{Li}$ span over several orders of magnitude from $\approx 10^{-11}$ to $\approx 10^{-18}$ cm^2 s^{-1} for Li− and Mn-rich layered oxides. This huge scatter is a well-known problem in the literature,[61,69] and we select a median value of $\tilde{D}_{Li} \approx 5 \cdot 10^{-14}$ cm^2 s^{-1} for our calculation, which results in reasonable diffusion times as shown in Table II.

The characteristic diffusion time of the lithium-ions from the surface into the core of the particles (or in the reverse direction) ranges from ≈190 h for the D-wCo-10 CAM to only ≈1 h for the two porous CAMs. Consequently, the extent of the low-voltage redox feature below 3.6 V might be solely explained by the effective particle size, because the diffusion time of the D-wCo-10 CAM exceeds the available charge/discharge time at the lowest C-rate of C/50 during the rate test, which is why the low-voltage peak is virtually absent in the dQ/dV plots (see solid blue line in Fig. 5). On the other hand, the two porous CAMs could be operated until 1C without any diffusion limitation, resulting in a pronounced low-voltage peak at lower C-rates (see black and green lines in Fig. 5). Since the other CAMs line up in between, we assume a correlation between the increasing low-voltage redox peak and the decreasing diffusion time. The latter seems in turn to scale with the effective particle diameter. Note that the diffusion coefficient increases at higher SOCs (i.e., in the delithiated state) by a factor of ≈10–100,[50,62,66] so that the redox features at higher voltages are considerably less affected by the solid-state lithium diffusion kinetics.

In order to prove the particle size effect for the same base material, we performed a post-calcination of the D-woCo-6 CAM at 1000 °C for 5 h in argon atmosphere (see Experimental section for further details). As expected, the BET surface area of the D-woCo-6-1000C CAM is roughly 2-fold lower than that of the as-received parent due to particle growth, and the diffusion time would thus increase by a factor of ≈4 (see Table II). The rate test performance of both CAMs is compared in Fig. 6.

Surprisingly, the post-calcined CAM (dashed blue line in Fig. 6b) outperforms the as-received CAM (solid blue line in Fig. 6b) during the entire rate test. The improvement of the discharge capacity amounts to ≈66 mAh g^{-1} at the highest C-rate of 10C and still to ≈13 mAh g^{-1} at the lowest C-rate of C/50, respectively. Please note that the capacity increase would be even higher in the representation vs the surface-normalized current, as the curves are shifted along the x-axis. This unexpected trend is, at first glance, contradicting the results of Liu et al.[60] and Gutierrez et al.,[65] who observed lower capacities for CAMs calcined at higher temperatures compared to those calcined at lower temperatures.

To gain a detailed insight, Fig. 6a compares the discharge dQ/dV data of both CAMs. Focusing on the low-voltage redox peak below 3.6 V (on the left-hand side of the dashed vertical line), there are rate-dependent differences between the as-received CAM (solid lines) and the post-calcined CAM (dashed lines): (i) at C/50 (in red), the capacity share of D-woCo-6-1000C is higher than that of D-woCo-6 (see the plain area with the "+" sign); (ii) at C/2 (in green), both curves lie on top of each other; and (iii) at 2C (in blue), D-woCo-6-1000C contributes less capacity than D-woCo-6 (see the hatched area with the "–" sign). Due to the simultaneous changes at higher voltages, we can probably obtain more authoritative information by comparing the capacity contributions above ($Q_{>3.6V}$, green lines) and below 3.6 V ($Q_{<3.6V}$, red lines) for all C-rates in Fig. 6b. At the lowest C-rate of C/50, the ≈13 mAh/g higher capacity of the D-woCo-6-1000C CAM originates indeed mainly from the low-voltage peak ($\Delta Q_{<3.6V} \approx 9$ mAh g^{-1} vs $\Delta Q_{>3.6V} \approx 4$ mAh g^{-1}). Both capacity shares decrease moderately with increasing C-rate; however, starting at ≈C/2 for the as-received CAM or at ≈2C for the post-calcined CAM, $Q_{>3.6V}$ collapses, while $Q_{<3.6V}$ rises again. This is most likely a resistance effect that shifts dQ/dV features at higher voltages gradually to lower voltages during discharge. As a consequence, the clear distinction between the redox features associated with $Q_{>3.6V}$ and $Q_{<3.6V}$ becomes blurred at high C-rates.

All in all, the results from Fig. 6 question the above-assumed particle size effect on the diffusion kinetics, because the as-received D-woCo-6 CAM and the post-calcined D-woCo-6-1000C CAM ought to be interchanged during the rate test. Alternatively, there might be an additional variation of the lithium diffusion coefficient that was yet assumed to be constant among the tested CAMs. This is exactly what was reported by Liu et al. for their Li[$Li_{0.13}Ni_{0.30}Mn_{0.57}$]$O_2$ CAMs, which were calcined at sintering temperatures of either at 800, 900, or 1000 °C.[60] Increasing the sintering temperature reduced the BET surface area (from ≈5.0 to ≈0.68 m^2 g^{-1}) and increased the primary particle size (from diameters of ≈80 to ≈500 nm); however, at the same, they observed an increase of the lithium diffusion coefficient by GITT (e.g., from $\approx 1.3 \cdot 10^{-15}$ to $\approx 1.8 \cdot 10^{-14}$ cm^2 s^{-1} at 4.0 V during charge). The

Journal of The Electrochemical Society, 2022 169 060521

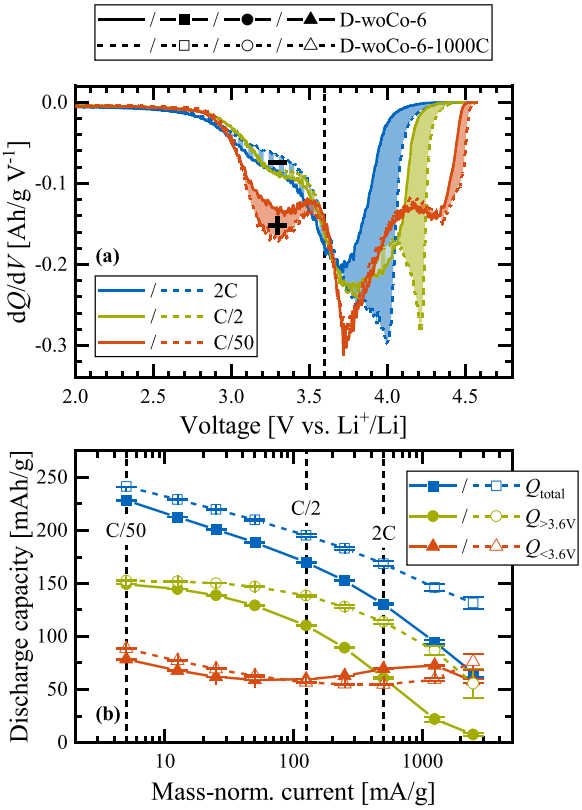

Figure 6. Rate test comparison of the as-received D-woCo-6 CAM and the post-calcined D-woCo-6-1000C CAM, which was heat-treated at 1000 °C for 5 h in argon atmosphere (see Experimental section). (a) Differential capacity (dQ/dV) of the discharge reaction at three different C-rates (viz, at 2C, C/2, and C/50). The capacity difference between both CAMs at a given C-rate is highlighted by the filled area of the same color. The plain area (see also the "+" sign) indicates a higher capacity share of the post-calcined compared to the as-received CAM, while the hatched area (see also the "–" sign) denotes a lower capacity share in the respective voltage range. (b) Discharge capacity vs the mass-normalized current for all tested C-rates. The C-rates that were analyzed in panel (a) are highlighted by dashed vertical lines. Furthermore, the discharge capacity (Q_{total}) is divided into its contributions above 3.6 V ($Q_{>3.6V}$; right-hand side of the dashed vertical line in panel (a)) and below 3.6 V ($Q_{<3.6V}$; left-hand side of the dashed vertical line in panel (a)).

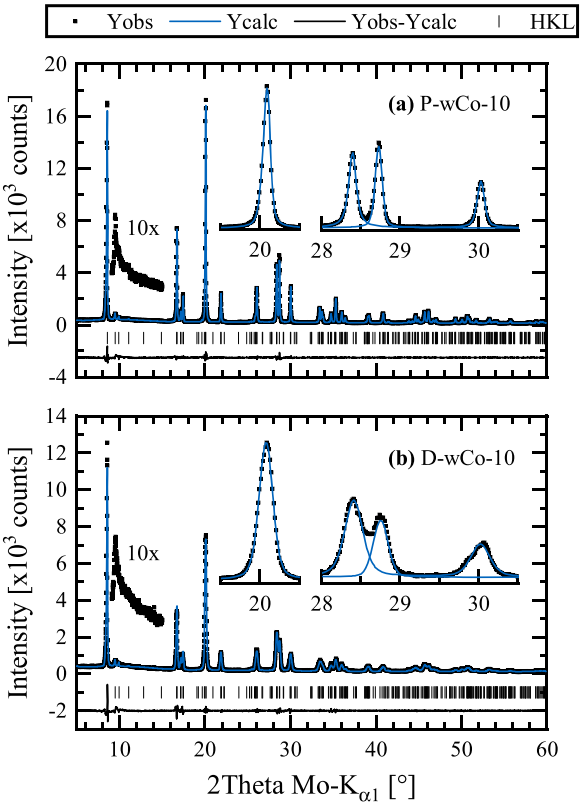

Figure 7. X-ray powder diffractograms of two exemplarily chosen as-received CAM powders acquired on our in-house Mo-diffractometer (λ = 0.7093 Å), and then refined with a structure-independent fit in the C2/m space group according to the Le Bail method, putting special emphasis on a size/strain analysis of the line broadening (see Experimental section): (a) P-wCo-10, with R_{wp} = 6.10% and χ^2 = 1.70; (b) D-wCo-10, with R_{wp} = 6.96% and χ^2 = 1.93. The observed (black points), calculated (blue lines), and difference diffraction profiles (black lines) are shown together with the position of the Bragg reflections (black ticks). The 10x magnifications of the Yobs data points between 9.1–15.0° 2θ highlight the superstructure reflections due to in-plane Li/TM ordering in the TM layer. The insets show a subset of peak which were fitted individually with a pseudo-Voigt peak function (Topas command PV_Peak_Type, using a θ-independent FWHM and Lorentzian-Gaussian mixing parameter for each peak).

authors conclude that the calcination temperature needs to be delicately balanced to obtain the optimum electrochemical performance with respect to these parameters. In their case, the solid-state lithium diffusion kinetics are more slowed down by the increasing particle size at higher temperatures than being accelerated by the increasing lithium diffusion coefficient. Regarding the dense and Co-free CAMs in Fig. 6, $\tilde{D}_{Li}$ has to rise by a factor of greater than 4 to overcompensate the particle growth of the post-calcined compared to the as-received CAM (see Table II). This sounds reasonable considering the ≈16-fold difference of $\tilde{D}_{Li}$ reported by Liu et al.

We want to point out that all these calculations have to be taken with a grain of salt, e.g., due to the approximation of spherical particles and due to the uncertainty of reported $\tilde{D}_{Li}$ values, so that it is impossible to perfectly disentangle the influence of the particle size and the lithium diffusion coefficient. This being said, we assume that the latter is the dominating parameter to explain the remaining capacity differences after surface area normalization in Fig. 4. Since Liu et al. established a connection between $\tilde{D}_{Li}$ and the microstrain of their investigated CAMs,[60] the following size/strain analysis will provide further evidence for this hypothesis.

Size/strain analysis.—We collected X-ray powder diffraction (XPD) data for every CAM in its pristine state. As an example, Fig. 7 shows the diffractograms of P-wCo-10 and D-wCo-10, which represent the best- and worst-performing of the five as-received CAMs, respectively. All of the CAM powders exhibit a well-defined layered structure, which can be indexed according to the hexagonal α-$NaFeO_2$ structure with $R\bar{3}m$ symmetry.[42,70] The over-lithiation in the TM layer ($Li[Li_\delta TM_{1-\delta}]O_2$ with δ = 0.14 ± 0.01) adds an additional honeycomb-like Li/TM ordering, which leads to superstructure reflections (see 10× magnifications between 9.1°–15.0° 2θ in Fig. 7) and allows an alternative indexing in the monoclinic *C*2/*m* space group.[48,71] However, the superstructure reflections are quite broad and have a low intensity due to the presence of stacking faults and due to the off-stoichiometric Li/TM ratio.[72,73] The top-view SEM images suggested the presence of surface impurities, especially for the P-wCo-10 CAM (see the faceted crystals on top of the secondary agglomerates in Fig. 1a2). Here, Li_2CO_3 is a common

Journal of The Electrochemical Society, 2022 **169** 060521

Table III. Individual fitting of a selection of peaks from the X-ray powder diffractograms of the P-wCo-10 and the D-wCo-10 CAM shown in Fig. 7 (see insets). The peaks cover one hkl reflection in the R−3m space group, but several in the C2/m space group. The full width at half maximum (FWHM) was determined with a pseudo-Voigt peak function (using the PV_Peak_Type command in Topas).

hbb	*hkl* reflections		FWHM [°]	
	R−3*m*	*C*2/*m*	P-wCo-10	D-wCo-10
≈20.1	104	20–2, 131	0.0886 ± 0.0006	0.200 ± 0.008
≈28.4	108	13–3, 202	0.106 ± 0.017	0.27 ± 0.03
≈28.7	110	33–1, 060	0.094 ± 0.010	0.22 ± 0.03
≈30.0	113	33–2, 222, 061, 330	0.102 ± 0.016	0.29 ± 0.04

impurity on the CAM surface, as it readily forms under ambient conditions,[49] either from the unreacted lithium source or from leaching lithium out of the layered oxide. Robert et al.[74] and Grenier et al.[75] were able to observe Li_2CO_3 on NCA samples by high-resolution synchrotron XPD, but the most intense (110) reflection at ≈9.8° 2θ (for Mo-$K_{\alpha1}$ radiation) would be superimposed by the superstructure reflections of over-lithiated samples. Furthermore, we do not observe the (−202) and (002) reflections of Li_2CO_3 at ≈14.0° and ≈14.5°; however, the signal-to-noise ratio and intensity of the laboratory diffractometer is probably too low to resolve impurity phases on the level of less than ≈1 wt%. Therefore, we still assume that carbonate impurities are the most likely source for the faceted crystals observed in the SEM images.

The most interesting observation concerns the line broadening of the reflections. The insets of Fig. 7 show a subset of peaks, which can either be described by one *hkl* reflection in the *R*−3*m* symmetry or by several reflections in the *C*2/*m* symmetry (see *hkl* assignments in Table III). Already by naked eye, it is obvious that the P-wCo-10 CAM (see Fig. 7a) has much narrower reflections than the D-wCo-10 CAM (see Fig. 7b). This finding is confirmed by an individual fitting of the peaks with a pseudo-Voigt peak function (containing Lorentzian and Gaussian contributions). The full width at half maximum (FWHM) of the peaks (corresponding to either one or two/four reflections) is listed in Table III. The selected peaks of the P-wCo-10 CAM are narrower by a factor of ≈2.3−2.8 than the peaks of the D-wCo-10 CAM, and the FWHM difference becomes larger with increasing 2θ. At a first glance, this result is in contradiction to the SEM images in Fig. 1, because the primary crystallites of the P-wCo-10 CAM are expected to be significantly smaller than that of the D-wCo-10 CAM. According to the well-known Scherrer equation (see Eq. 4), the crystallite size is inversely proportional to the line broadening, i.e., the P-wCo-10 CAM should exhibit broader reflections than the D-wCo-10 CAM. However, the microstrain (ε_0 in Eq. 5) provides a second contribution to the sample broadening, and it is a measure of the lattice imperfection in the bulk of the sample. Both contributions can be separated and quantified by their different θ-dependence. This is typically done by the so-called Williamson-Hall method, where the line broadening is individually analyzed for each reflection (in a similar manner than for the selected peaks in Fig. 7 and Table III).[34,42] Manual analysis is possible only in the *R*-3*m* space group, where each apparent peak belongs to one *hkl* reflection (strictly speaking, this was done above). Therefore, we decided to rely on the whole powder pattern fitting (WPPF) approach,[76] where all reflections can be treated together in a structure-independent fit according to the Le Bail method and which enables the use of the *C*2/*m* symmetry. Since the *C*2/*m* space group has more than double the amount of *hkl* reflections than *R*-3*m* for the same set of peaks, it can model their line broadening more accurately. The size/strain analysis, as implemented in the Topas software package,[47] uses the same base equations as the Williamson-Hall analysis (detailed information are provided in the Experimental section).

The applied model describes the observed diffraction patterns very well, as can be seen visually in Fig. 7, and also the error indices R_{wp} and χ^2 (listed in the figure caption) are reasonably low. The size/strain values of all five as-received CAMs are listed in Table I. We will first focus on the crystallite size parameter L_{vol}, which is defined as the volume-weighted mean column length of the crystallites and which can be converted into an average diameter of $d_{sphere} = 4/3 \cdot L_{vol}$ using a spherical approximation.[37] For all three dense CAMs, the L_{vol} values were too large (i.e., >200 nm) to contribute significantly to the line broadening, and they were therefore excluded from the refinement. On the other hand, the porous CAMs have L_{vol} values of ≈128 nm for P-wCo-10 and ≈97 nm for P-woCo-6, which yield spherical diameters of ≈171 nm and ≈129 nm, respectively. These results are in good qualitative agreement with the SEM images in Fig. 1, and for the porous CAMs, the XPD-based d_{sphere} values agree within a factor of ≈2 with the d_{BET} values of 260 nm approximated from their specific surface areas.

Focusing next on the microstrain parameter, one can observe that the ε_0 values vary by a factor of ≈7 for the different CAMs, viz., from ≈0.025% for the P-wCo-10 CAM to ≈0.181% for the D-wCo-10 CAM (see Table I). This range is consistent with the ε_0 values of layered oxides reported in the literature.[36,60,77] For example, Liu et al. reported ε_0 values ranging from ≈0.13% (at 800 °C) to ≈0.08% (at 1000 °C) for the $Li[Li_{0.13}Ni_{0.30}Mn_{0.57}]O_2$ CAM that was calcined at different sintering temperatures.[60] Using the classical Williamson-Hall approach, Gent et al. measured ε_0 values of ≈0.10% and ≈0.19% for pristine and partially delithiated NCM-111, respectively (the particle size of the poly-crystalline CAM remained fairly constant at ≈200 nm).[77] Fell et al. monitored the microstrain in a similar fashion for the Li- and Mn-rich $Li[Li_{0.2}Ni_{0.2}Mn_{0.6}]O_2$ during the activation cycle (excluding size-induced broadening).[36] Here, the microstrain increased from ≈0.15% in the pristine state to ≈0.32% in the middle of the first discharge. The increase of microstrain during cycling is explained by the growth of crystallographic defects such as vacancies, antisite disorder, dislocations, and stacking faults as well as large scale SOC heterogeneities. Such an increase during cycling is also expected for the here examined CAMs, but assuming that the increase scales with the ε_0 values of the pristine samples, we can try to correlate these initial values with the electrochemical performance of the CAMs. This attempt is motivated by the fact that the best- and worst-performing CAMs during the rate test (i.e., P-wCo-10 and D-wCo-10, see Figs. 3 and 4) also exhibit the lowest and highest microstrain values, respectively. To compensate for the surface area effect on the accessible capacities, Fig. 8 compares the discharge capacities at a given surface-normalized current of either 10 or 100 mA m^{-2} (both datasets were extracted after surface area normalization from Fig. 4) with the microstrain values of the CAMs.

Surprisingly, there is an almost linear relationship between the discharge capacity at a given surface-normalized current and the microstrain, with the discharge capacity decreasing by ≈40 ± 5 mAh g^{-1} per 0.1% increase in microstrain. Since the microstrain goes hand in hand with the effective particle diameter for the as-received CAMs (see Table II), this correlation does not automatically imply causation. Fortunately, the post-calcined D-woCo-6-1000C CAM forms an exception, with d_{BET} increasing from ≈1.1 to ≈2.0 μm, while ε_0 diminishes from ≈0.097% to ≈0.038% as compared to the as-received parent. The post-calcination was

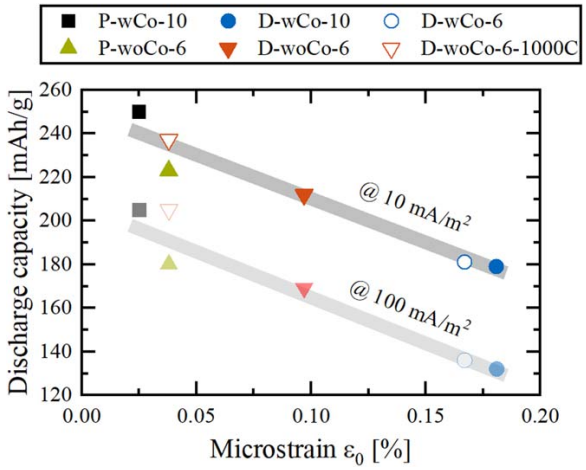

Figure 8. Correlation of the discharge capacity at two different surface-normalized currents with the microstrain of the as-received CAMs and the post-calcined D-woCo-6-1000C CAM. The discharge capacities were extracted at 10 mA m^{-2} (intensively colored data points) and 100 mA m^{-2} (transparent data points) by interpolation of the rate test data in Fig. 4 (please note that the discharge capacity of the D-wCo-10 CAM at 10 mA m^{-2} was extrapolated from the lowest current density of ≈14 mA m^{-2}). To illustrate the fairly linear relationship, the gray bars serve as a guide to the eye.

intentionally done at 1000 °C and thus beyond the original sintering temperature of ≈930 °C, so that the crystallinity is improved by healing up lattice defects. The post-calcined CAM fits perfectly into the trend lines of the as-received CAMs in Fig. 8 (see red open triangles). Therefore, we are confident that the solid-state lithium diffusion kinetics determine the accessible capacity predominantly according to the following proportionality: $Q \propto 1/\tau_{diffusion} \propto \tilde{D}_{Li} \propto 1/\varepsilon_0$. On the other hand, the initially suggested particle size effect is regarded to be of minor importance for the lithium diffusion in the solid phase.

Since the microstrain is a rather generic parameter, we would finally like to address the question which kind of lattice imperfection might be responsible for the observed differences among the here examined CAMs. In case of Li- and Mn-rich layered oxides, the degree of Li/TM ordering in the TM layer (within the *ab*-plane) and their stacking (along the *c*-direction) is an often discussed phenomenon.[72,78,79] However, the comparison of the superstructure region (see 10x magnifications in Fig. 7) reveals no significant differences between the tested CAMs. This leads us to the conclusion that the in-plane Li/TM ordering and the extent of stacking faults is comparable and thus not the main contribution to microstrain. Furthermore, we also performed some Rietveld refinements to evaluate the impact of the Li-Ni mixing (not shown here). Briefly summarized, the Ni amount on the Li layer might differ by up to ≈3% among the investigated CAMs; however, we do not observe a causal relationship to the microstrain.

Alternatively, there is increasing attention in the literature to the impact of oxygen vacancies.[27,80–83] Regarding the synthesis of the CAMs, they might play an important role in this work, because the calcination requires the infiltration of lithium and also oxygen into the TM precursors.[9,84] For the dense CAMs, the oxygen atoms thus might have much longer solid-state diffusion pathways than for the porous CAMs to reach the core of the secondary agglomerates, leading potentially to more oxygen vacancies (and consequently to more microstrain). Oxygen vacancies can be also created on purpose after calcination, e.g., chemically by a gas-solid interface reaction with CO_2 (using NH_4HCO_3 as precursor)[80,81] or electrochemically in an electrochemical reactor with a solid electrolyte separator (i.e., cathodically charging a CAM powder bed).[83] Both methods are carried out at temperatures of up to 600 °C and could hence reduce the available surface area due to agglomeration and grain growth.[83] This makes it difficult to discern the influence of oxygen vacancies from the surface area effect. Apart from that, the results in the literature are ambiguous. After introducing oxygen vacancies in the Co-free CAM $Li[Li_{0.2}Ni_{0.2}Mn_{0.6}]O_{2-z}$, Nakamura et al.[83] measured a slightly lower capacity and rate capability (for $z = 0.03$ vs $z = 0$), while Li et al.[81] observed the opposite trend (for $z = 0.07$ vs $z = 0$). Both studies have in common that the oxygen vacancies enhance the Mn redox feature at low voltages (at the expense of the Ni redox feature at higher voltages). Recently, Csernica et al.[27] quantified the oxygen loss, including bulk oxygen vacancies, from a Li- and Mn-rich layered oxide (with $\delta = 0.18$) upon cycling. After 500 charge/discharge cycles, the authors found ≈6.5 at% oxygen vacancies ($\Delta z \approx 0.13$) and they further linked the progressive oxygen release to the voltage fade of the CAM.[27] The so-called voltage fade describes the reduction of the average operating voltage of Li- and Mn-rich layered oxides during electrochemical cycling.[5] In dQ/dV plots, the voltage fade manifests in (i) the redox peak at ≈3.8 V gradually shifting to lower voltages and in (ii) the low-voltage feature also moving from ≈3.4 to ≈3.0 V.[17,27] All these results are in contradiction to our findings, where higher ε_0 values (due to more defects) strongly diminish the low-voltage feature, being virtually absent for the D-wCo-10 CAM with the highest microstrain (see Fig. 5). Thus, oxygen vacancies also seem to be an unlikely origin of microstrain in our present work.

Lastly, we want to discuss the possibility of dislocations that represent line defects by introducing extra half-planes into the lattice.[29] In contrast, the above-discussed stacking faults are classified as planar defects, which perturbs the stacking sequence of the honeycomb-like ordered TM layers along the *c*-axis, while preserving their cubic close-packed arrangement (i.e., O3 packing).[78] Singer et al. could monitor the dislocation density in single particles during cycling by operando 3D Bragg coherent diffractive imaging.[29] They found much more dislocations in the investigated Li- and Mn-rich CAM than in stoichiometric NCA (which was further in accordance with the microstrain values from bulk powder diffraction). Furthermore, the dislocations modify the local lithium environment by perturbing the O3 packing (containing only edge-sharing octahedral sites between the Li and TM layer) and by also introducing O1-like parts (with face-sharing octahedral sites).[29] This defect is another kind of stacking fault, whose energetic penalty slows down the lithium-ion diffusion, particularly at high lithium concentrations (i.e., in the discharged state). However, the authors correlated the dislocations again to the voltage fade in over-lithiated CAMs and thus to the gradual emergence of low-voltage characteristics upon cycling.

Since most of the known lattice defects (including the in-plane Li/TM ordering, stacking faults, oxygen vacancies, and dislocations) seem to contradict our observation that increasing microstrain reduces the capacity contribution at low voltages, we cannot present a conclusive theory about the origin of the microstrain, but we assume it to influence the solid-state lithium diffusion coefficient (governing especially the low-voltage redox feature, as shown in Figs. 5 and 6). Future studies on this topic should include high-resolution (scanning) transmission electron microscopy ((S)TEM) experiments, which are now capable of visualizing even light elements such as lithium and oxygen in layered transition-metal oxides,[85] and which could thus detect all different kinds of lattice imperfections on an atomic level.[31]

In summary, we could show that the BET surface area and the bulk microstrain describe the electrochemical performance of the examined Li- and Mn-rich CAMs in an almost quantitative manner. Here, the BET surface area represents the CAM/electrolyte interfacial surface area, which dictates the effective charge-transfer resistance of the cathode electrode. This effect can be compensated for by surface normalization of the currents during the discharge rate test (see Fig. 4). On the other hand, the bulk microstrain explains the remaining capacity difference at a given surface-normalized current (see Fig. 8), as it probably controls the lithium diffusion coefficient

Journal of The Electrochemical Society, 2022 **169** 060521

and thus determines the extent of the low-voltage redox features below ≈3.6 V. Finally, the post-calcination reveals a strategy to modify these important properties and thus to improve the electrochemical performance of the CAMs.

Conclusions

In this work, we investigated five different Li- and Mn-rich cathode active materials (CAMs), which differ with respect to their morphology (porous vs dense), the incorporation of cobalt (Co-containing vs Co-free), and the secondary agglomerate size (D_{50} values between ≈6 and ≈12 μm). Their initial electrochemical performance is largely different, as evidenced by a discharge rate test, providing capacities from ≈222 mAh g^{-1} down to ≈86 mAh g^{-1} at a practical C-rate of 1C (corresponding to 250 mA g^{-1}). This large variation can be traced back in a quantitative manner to important material metrics, originating both from the surface and from the bulk of the CAMs.

First, the morphology (and to a minor extent the secondary agglomerate size) affects the electrochemically active surface area and thus the effective current density under which the CAMs are operated at a given C-rate. For this reason, the current is referenced to the CAM/electrolyte interfacial surface area, represented here by the BET surface area of the as-received CAMs. In the case of porous CAMs (≈5.3 m^2 g^{-1}), virtually all primary crystallites are exposed to the electrolyte, whereas for dense CAMs (≈0.4–1.3 m^2 g^{-1}) only the outer surface of the secondary agglomerates is in contact with the electrolyte. To account for this difference, the rate test data should be analyzed on the basis of surface-normalized currents (in mA/m^2) rather than on the more commonly used basis of mass-normalized currents (in mA/g). This results in a constant capacity offset among the five investigated CAMs at a given surface-normalized current, revealing that a large fraction (≈50%) of the rate performance differences can be accounted for by their variation in BET surface area. Furthermore, as the internal porosity of the secondary agglomerates cannot easily be removed during the calendaring of the electrodes, the CAM morphology largely affects the electrode density (≈2.2 vs ≈2.7 $g_{electrode}$ $cm^{-3}{}_{electrode}$ estimated for porous and dense CAMs, respectively) and thus the volumetric energy density of the battery cell.

The remaining capacity differences were shown in turn to scale linearly with the microstrain in the bulk material, which was determined by a size/strain analysis of XPD data. Consequently, the combination of (i) surface normalization of the currents and of (ii) microstrain quantification managed to almost completely capture the achievable capacity of the here examined Li- and Mn-rich layered oxides. The origin of the microstrain remains elusive, because the most common lattice imperfections (viz., in-plane Li/TM ordering and stacking faults, oxygen vacancies, dislocations) could not explain that the capacity contribution of the low-voltage redox feature (below ≈3.6 V vs Li^+/Li) substantially decreases with increasing microstrain. The post-calcination of the D-woCo-6 CAM at 1000 °C reduced the microstrain by a factor ≈2.6, thereby also improving its rate capability in comparison to the as-received parent.

This work emphasizes the importance of a proper material characterization, because material metrics such as the specific surface area (from gas physisorption), internal porosity (from Hg intrusion porosimetry), and microstrain (from X-ray powder diffraction) are important performance predictors. They allow for predicting the electrochemical behavior of Li- and Mn-rich CAMs right from their as-received state. Furthermore, we observed no influence of the cobalt content on the performance, i.e., Co can be easily removed from the mixture of Ni-Co-Mn in order to reduce material costs. Attempting to increase the volumetric energy density, however, the replacement of porous CAMs by dense CAMs still must be optimized. The agglomerate size and surface-to-bulk ratio of dense CAMs have to be tuned in such a way that they maintain a reasonable rate capability. Finally, their microstrain in the bulk has to be minimized, which requires the understanding of the underlying lattice imperfection.

Acknowledgments

Financial support by BASF SE through its Scientific Network on Electrochemistry and Batteries is gratefully acknowledged. The authors further want to thank Tobias Käter for his preliminary work on the Co-containing CAMs, Stefan Oswald for his contribution to the capacitance measurements, Katia Rodewald from the Wacker-Chair of Macromolecular Chemistry at the Technical University of Munich for the SEM measurements, and Jordan Lampert for fruitful discussions.

Appendix

Electrode density.—The electrode density ($\rho_{electrode}$, in units of $g_{electrode}/cm^3{}_{electrode}$) can be estimated from its individual constituents i and the targeted/achieved electrode porosity (ε^*_{total}) as follows:

$$\rho_{electrode} = (1 - \varepsilon^*_{total})\cdot\rho_{solids} = (1 - \varepsilon^*_{total})\cdot\left(\sum_i \frac{\omega_i}{\rho_i}\right)^{-1} \quad [A\cdot1]$$

where ω_i is the mass fraction and ρ_i is the crystallographic or particle density of the materials used in the composite electrode. Following the publication by Schreiner et al.,[24] our model electrodes are made of 92.5 wt% CAM ($\rho_{CAM} = 4.35$ g cm^{-3}), 4.0 wt% C65 conductive carbon ($\rho_{C65} = 2.0$ g cm^{-3}), and 3.5 wt% PVDF binder ($\rho_{PVDF} = 1.76$ g cm^{-3}), resulting in an average density of the pure solids of $\rho_{solids} = 3.96$ g cm^{-3}.

The electrode porosity (ε^*_{total}) is the sum of (i) the inter-particular porosity (ε^*_{inter}) from the pore space between the secondary agglomerates of the CAM as well as the electrode additives, and of (ii) the intra-particular porosity (ε^*_{intra}) between the primary crystallites of the CAM. While ε^*_{inter} can be easily reduced to ≈30% by calendaring, ε^*_{intra} is fairly invariant upon the calendaring process, and thus increases the electrode porosity of an inherently porous CAM.[24] The asterisk (*) indicates that the porosities are based on the electrode level, as opposed to the CAM-based porosity ε_{intra} of the CAM powder that is given in Table I. The conversion of the intra-particular pore volume ($v_{pore,intra}$) obtained from the CAM powder by mercury intrusion porosimetry (see Table I) into the electrode-based intra-particular porosity (ε^*_{intra}) can be done as follows:

$$\varepsilon^*_{intra} = \frac{\omega_{CAM}\cdot v_{pore,intra}}{\omega_{CAM}\cdot v_{pore,intra} + \frac{1}{\rho_{solids}}} \quad [A\cdot2]$$

For the above electrode composition, ε^*_{intra} amounts to ≈13.8% for the porous Co-free P-woCo-6 CAM and to ≈2.2% for the dense Co-free D-woCo-6 CAM, respectively. This means that for a typically achieved inter-particular cathode electrode porosity of $\varepsilon^*_{inter} \approx 30\%$, the resulting overall electrode porosity ($\varepsilon^*_{total} = \varepsilon^*_{inter} + \varepsilon^*_{intra}$) would be ≈44% for the porous P-woCo-6 CAM, much higher than that of ≈32% for the dense D-woCo-6 CAM.

Activation cycle.—Figure A·1 shows the voltage profiles of the first activation cycle from the five Li- and Mn-rich layered oxides. As depicted in the inset, there is a substantial spread of the obtained capacities already in the first cycle, whereby the best- and worst-performing CAMs (P-wCo-10 and D-wCo-10) differ by ≈83 mAh g^{-1} during charge and by ≈132 mAh g^{-1} during discharge, respectively. Note that the CAMs are sorted according to their first-cycle discharge capacities in the same order than in the rate test that is following the activation and stabilization cycles (see Fig. 3). The first-cycle Coulombic efficiencies (CEs; see dashed lines) range from close to 90% for the porous CAMs (P-wCo-10 and P-woCo-6) to ≈80% for the D-woCo-6 CAM, all the way down to ≈60% for the dense and Co-containing CAMs (D-wCo-10 and D-wCo-6). For the here examined over-lithiated CAMs with $\delta = 0.14 \pm 0.01$, the oxygen release typically starts at a first-cycle charge

Journal of The Electrochemical Society, 2022 169 060521

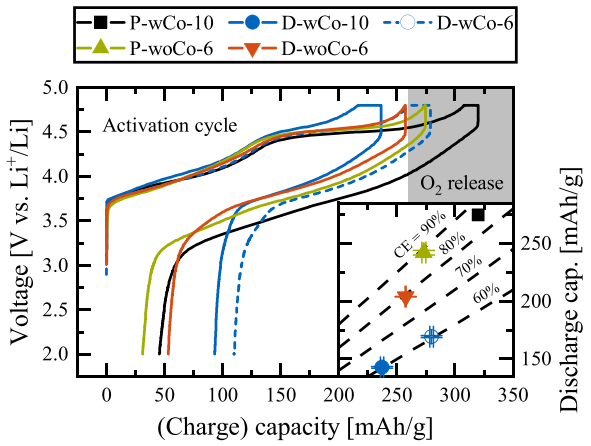

Figure A·1. Activation cycle of the five investigated Li- and Mn-rich layered oxides, which was conducted between 2.0 and 4.8 V vs Li^+/Li at a C-rate of either C/10 (with an additional 1 h CV hold at 4.8 V; applied for the Co-containing CAMs) or C/15 (without any CV hold; applied for the Co-free CAMs). Further details can be found in the Experimental section. The gray bar highlights the expected regime for oxygen release.[20,86] The inset shows the first-cycle discharge capacity (right-hand *y*-axis) as a function of the first-cycle charge capacity; the dashed lines represent different Coulombic efficiencies (CEs).

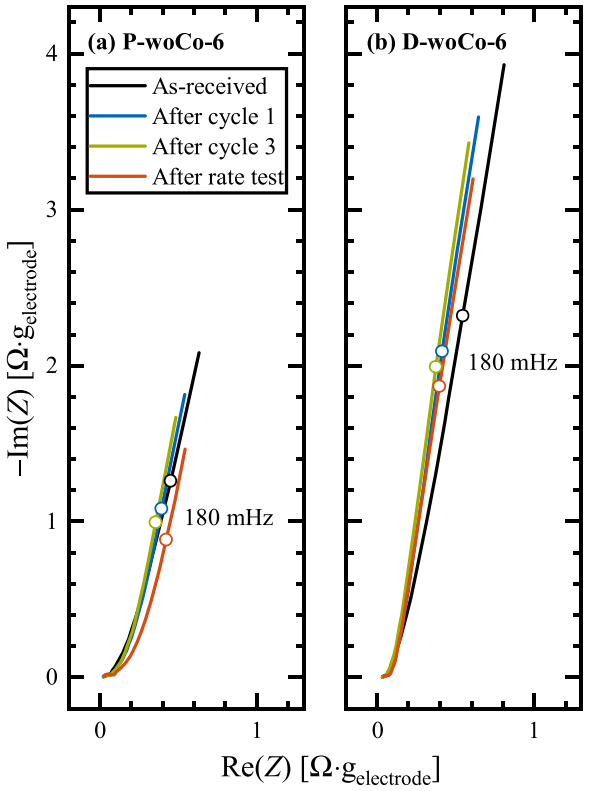

Figure A·2. Nyquist plots at selected points before and after the discharge rate test of **(a)** the P-woCo-6 CAM and of **(b)** the D-woCo-6 CAM. After an additional 1 h CV step at the lower cut-off voltage of 2.0 V, the potential-controlled EIS measurements of the modified cells with a Li/FSG counter-electrode were conducted in blocking conditions at 2.0 V and 25 °C with a VMP-300 potentiostat (BioLogic, France) in the frequency range of 100 kHz to 100 mHz and with an AC voltage perturbation of 15 mV. The frequency points at 180 mHz are indicated by empty circles.

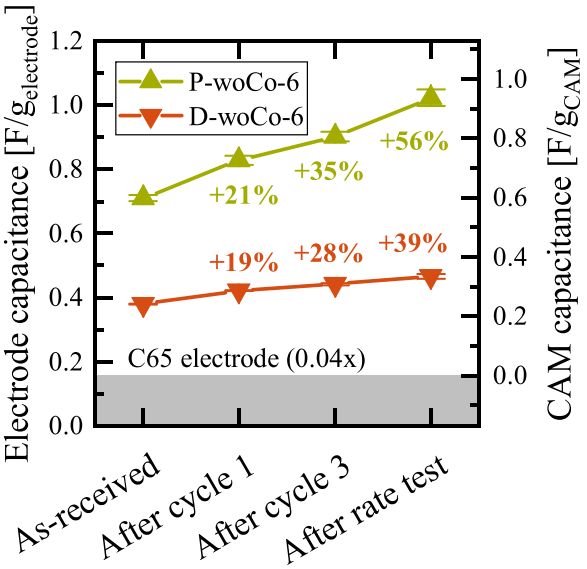

Figure A·3. Specific capacitance of the cathode electrodes over the course of the rate test procedure, as determined from the Nyquist plots in Fig. A·2 (average and min/max values from two cells for each sample). The capacitance of the entire electrode (left y-axis) is converted into the capacitance share of the Co-free CAMs (right y-axis) by subtracting the contribution of the C65 conductive carbon (3.9 F/g_{C65} from a C65 electrode multiplied by its weight fraction of 4 wt% in the actual electrode; see gray bar). The percentages refer to the increase of the CAM capacitance relative to the as-received samples.

capacity of ≈260–280 mAh g^{-1} (regime for O_2 release highlighted in gray),[20,86] so that we only expect the P-wCo-10 CAM to release lattice oxygen in larger quantities, while minor gas amounts might be evolved from the D-wCo-6 and P-woCo-6 CAMs; however, the D-wCo-10 and D-woCo-6 CAMs should ideally not release any oxygen, at least within the first activation cycle.

Capacitance analysis.—In order to monitor the evolution of the CAM/electrolyte interfacial surface area over the course of the rate test, we used electrochemical impedance spectroscopy (EIS) and applied the capacitance-based method introduced by Oswald et al.[59] For this purpose, we slightly modified the counter-electrode by placing a free-standing graphite (FSG) electrode between the lithium metal foil and the glass-fiber separator, as described by Morasch et al.[87] The impedance contribution of this Li/FSG composite electrode to the WE + CE impedance is negligibly small compared to that of the cathode electrode, so that the cell impedance largely represents the cathode impedance of the Li- and Mn-rich CAM. Electrochemical impedance spectra were measured in blocking conditions (i.e., in the fully discharged state after a constant voltage hold at 2.0 V for 1 h) for the freshly assembled cell, after the activation cycle, after two more stabilization cycles, and at the end of the entire test procedure (with in total 23 cycles). The Nyquist plots of both Co-free CAMs (P-woCo-6 and D-woCo-6) are shown in Fig. A·2. Since the CAMs have a quasi-infinite charge-transfer resistance in their fully discharged (i.e., lithiated) state, the impedance response shows only capacitive behavior, so that the capacitance is a direct measure of the electrode's surface area.[59]

Now, the cathode electrode capacitance can be determined from the imaginary impedance ($Im(Z_{f_0})$) at the frequency point of f_0 = 180 mHz according to $C \approx 1/(2\pi \cdot f_0 \cdot (-Im(Z_{f_0})))$. The electrode capacitance (in units of $F/g_{electrode}$) can be converted into the CAM capacitance (in units of F/g_{CAM}) originating solely from the Li- and Mn-rich layered oxide by subtracting the capacitance share of the C65 conductive carbon (4.0 wt% C65 and 3.9 F/g_{C65}, as determined

Journal of The Electrochemical Society, 2022 **169** 060521

from a C65 electrode (C65:PVDF 50:50 wt%) under the same conditions). The electrode and CAM capacitance of the Co-free materials are plotted in Fig. A·3.

For the as-received samples directly after cell assembly, the CAM capacitance that is proportional to the CAM/electrolyte interfacial surface area amounts to ≈0.60 F/g_{CAM} for the porous P-woCo-6 CAM (in green) and to ≈0.24 F/g_{CAM} for the dense D-woCo-6 CAM (in red), respectively. Thus, the capacitance ratio of 0.60/0.24 ≈ 2.5 is slightly lower than the BET surface area ratio of 5.4/1.3 ≈ 4.2 (see Table I), which might be related to the inability of the electrolyte to penetrate into very small pores within the secondary agglomerates of the porous CAM (see Fig. 1d4), in contrast to the penetration by nitrogen during the BET measurement. The extent of capacitance increase, however, is very similar for the porous and dense CAMs, being most pronounced within the first three cycles and amounting to ≈40%–60% increase at the end of rate test procedure.

ORCID

Benjamin Strehle https://orcid.org/0000-0001-8878-1160
Franziska Friedrich https://orcid.org/0000-0001-9400-1212
Hubert A. Gasteiger https://orcid.org/0000-0001-8199-8703

References

1. D. Andre, S.-J. Kim, P. Lamp, S. F. Lux, F. Maglia, O. Paschos, and B. Stiaszny, *J. Mater. Chem. A*, **3**, 6709 (2015).
2. R. Schmuch, R. Wagner, G. Hörpel, T. Placke, and M. Winter, *Nat. Energy*, **3**, 267 (2018).
3. Y. Ding, Z. P. Cano, A. Yu, J. Lu, and Z. Chen, *Electrochem. Energy Rev.*, **2**, 1 (2019).
4. P. Rozier and J. M. Tarascon, *J. Electrochem. Soc.*, **162**, A2490 (2015).
5. J. Hong, H. Gwon, S.-K. Jung, K. Ku, and K. Kang, *J. Electrochem. Soc.*, **162**, A2447 (2015).
6. M. M. Thackeray, S.-H. Kang, C. S. Johnson, J. T. Vaughey, R. Benedek, and S. A. Hackney, *J. Mater. Chem.*, **17**, 3112 (2007).
7. Z. Lu, L. Y. Beaulieu, R. A. Donaberger, C. L. Thomas, and J. R. Dahn, *J. Electrochem. Soc.*, **149**, A778 (2002).
8. D.-K. Lee, S.-H. Park, K. Amine, H. J. Bang, J. Parakash, and Y.-K. Sun, *J. Power Sources*, **162**, 1346 (2006).
9. W.-C. Chen, Y.-F. Song, C.-C. Wang, Y. Liu, D. T. Morris, P. A. Pianetta, J. C. Andrews, H.-C. Wu, and N.-L. Wu, *J. Mater. Chem. A*, **1**, 10847 (2013).
10. X. Zhang, X. Meng, J. W. Elam, and I. Belharouak, *Solid State Ionics*, **268**, 231 (2014).
11. E. A. Olivetti, G. Ceder, G. G. Gaustad, and X. Fu, *Joule*, **1**, 229 (2017).
12. C. Banza Lubaba Nkulu et al., *Nat. Sustain.*, **1**, 495 (2018).
13. A. H. Tkaczyk, A. Bartl, A. Amato, V. Lapkovskis, and M. Petranikova, *J. Phys. D: Appl. Phys.*, **51**, 203001 (2018).
14. J. Zheng, S. Myeong, W. Cho, P. Yan, J. Xiao, C. Wang, J. Cho, and J. Zhang, *Adv. Energy Mater.*, **7**, 1601284 (2017).
15. J. R. Croy, K. G. Gallagher, M. Balasubramanian, Z. Chen, Y. Ren, D. Kim, S.-H. Kang, D. W. Dees, and M. M. Thackeray, *J. Phys. Chem. C*, **117**, 6525 (2013).
16. H. Konishi, T. Hirano, D. Takamatsu, A. Gunji, X. Feng, S. Furutsuki, S. Takahashi, and S. Terada, *Solid State Ionics*, **300**, 120 (2017).
17. J. R. Croy, D. Kim, M. Balasubramanian, K. Gallagher, S.-H. Kang, and M. M. Thackeray, *J. Electrochem. Soc.*, **159**, A781 (2012).
18. D. Streich, A. Guéguen, M. Mendez, F. Chesneau, P. Novák, and E. J. Berg, *J. Electrochem. Soc.*, **163**, A964 (2016).
19. B. Strehle, K. Kleiner, R. Jung, F. Chesneau, M. Mendez, H. A. Gasteiger, and M. Piana, *J. Electrochem. Soc.*, **164**, A400 (2017).
20. T. Teufl, B. Strehle, P. Müller, H. A. Gasteiger, and M. A. Mendez, *J. Electrochem. Soc.*, **165**, A2718 (2018).
21. T. Teufl, D. Pritzl, P. Krieg, B. Strehle, M. A. Mendez, and H. A. Gasteiger, *J. Electrochem. Soc.*, **167**, 110505 (2020).
22. S. Hy, H. Liu, M. Zhang, D. Qian, B.-J. Hwang, and Y. S. Meng, *Energy Environ. Sci.*, **9**, 1931 (2016).
23. F. Schipper et al., *Inorganics*, **5**, 32 (2017).
24. D. Schreiner et al., *J. Electrochem. Soc.*, **168**, 030507 (2021).
25. L. Kraft, T. Zünd, D. Schreiner, R. Wilhelm, F. J. Günter, G. Reinhart, H. A. Gasteiger, and A. Jossen, *J. Electrochem. Soc.*, **168**, 020537 (2021).
26. H. Liu et al., *J. Mater. Chem. A*, **6**, 4189 (2018).
27. P. M. Csernica et al., *Nat. Energy*, **6**, 642 (2021).
28. L. Yin et al., *Chem. Mater.*, **32**, 1002 (2020).
29. A. Singer et al., *Nat. Energy*, **3**, 641 (2018).
30. M. Mock, M. Bianchini, F. Fauth, K. Albe, and S. Sicolo, *J. Mater. Chem. A*, **9**, 14928 (2021).
31. S. Ahmed, A. Pokle, M. Bianchini, S. Schweidler, A. Beyer, T. Brezesinski, J. Janek, and K. Volz, *Matter*, **4**, 3953 (2021).
32. S. Ahmed et al., *ACS Nano*, **13**, 10694 (2019).
33. P. Staron et al. (ed.), *Neutrons and Synchrotron Radiation in Engineering Materials Science* (Wiley, Weinheim, Germany) (2017).
34. G. Williamson and W. Hall, *Acta Metall.*, **1**, 22 (1953).
35. K. Kleiner, P. Jakes, S. Scharner, V. Liebau, and H. Ehrenberg, *J. Power Sources*, **317**, 25 (2016).
36. C. R. Fell, D. Qian, K. J. Carroll, M. Chi, J. L. Jones, and Y. S. Meng, *Chem. Mater.*, **25**, 1621 (2013).
37. User Manual, *TOPAS 6 Technical Reference* (Bruker AXS GmbH, Karlsruhe, Germany) (2014).
38. P. W. Stephens, *J. Appl. Crystallogr.*, **32**, 281 (1999).
39. A. O. Kondrakov, A. Schmidt, J. Xu, H. Geßwein, R. Mönig, P. Hartmann, H. Sommer, T. Brezesinski, and J. Janek, *J. Phys. Chem. C*, **121**, 3286 (2017).
40. F. Friedrich, B. Strehle, A. T. S. Freiberg, K. Kleiner, S. J. Day, C. Erk, M. Piana, and H. A. Gasteiger, *J. Electrochem. Soc.*, **166**, A3760 (2019).
41. L. Croguennec, C. Pouillerie, A. N. Mansour, and C. Delmas, *J. Mater. Chem.*, **11**, 131 (2001).
42. K. Kleiner, B. Strehle, A. R. Baker, S. J. Day, C. C. Tang, I. Buchberger, F.-F. Chesneau, H. A. Gasteiger, and M. Piana, *Chem. Mater.*, **30**, 3656 (2018).
43. F. Sigel, B. Schwarz, K. Kleiner, C. Dräger, L. Esmezjan, M. Yavuz, S. Indris, and H. Ehrenberg, *Chem. Mater.*, **32**, 1210 (2020).
44. P. Yan, J. Zheng, M. Gu, J. Xiao, J.-G. Zhang, and C.-M. Wang, *Nat. Commun.*, **8**, 14101 (2017).
45. R. D. Shannon, R. C. Shannon, O. Medenbach, and R. X. Fischer, *J. Phys. Chem. Ref. Data*, **31**, 931 (2002).
46. Gas Sorption System Operating Manual, *ASiQwin Software Version 3.01* (Quantachrome Instruments, Boynton Beach, Florida, FL) (2013).
47. A. Coelho, *TOPAS-Academic Version 6* (Coelho Software, Brisbane, Australia) (2016).
48. D. Mohanty, A. Huq, E. A. Payzant, A. S. Sefat, J. Li, D. P. Abraham, D. L. Wood, and C. Daniel, *Chem. Mater.*, **25**, 4064 (2013).
49. J. Sicklinger, H. Beyer, L. Hartmann, F. Riewald, C. Sedlmeier, and H. A. Gasteiger, *J. Electrochem. Soc.*, **167**, 130507 (2020).
50. W. Mao, G. Ai, Y. Dai, Y. Fu, X. Song, H. Lopez, and V. Battaglia, *J. Electrochem. Soc.*, **163**, A3091 (2016).
51. P.-E. Cabelguen, D. Peralta, M. Cugnet, and P. Maillet, *J. Power Sources*, **346**, 13 (2017).
52. K. Kitada, H. Murayama, K. Fukuda, H. Arai, Y. Uchimoto, Z. Ogumi, and E. Matsubara, *J. Power Sources*, **301**, 11 (2016).
53. L. Froboese, P. Titscher, B. Westphal, W. Haselrieder, and A. Kwade, *Mater. Charact.*, **133**, 102 (2017).
54. H. Giesche, *Part. Part. Syst. Charact.*, **23**, 9 (2006).
55. K. G. Gallagher et al., *J. Electrochem. Soc.*, **163**, A138 (2016).
56. A. Kwade, W. Haselrieder, R. Leithoff, A. Modlinger, F. Dietrich, and K. Droeder, *Nat. Energy*, **3**, 290 (2018).
57. T. Teufl, D. Pritzl, S. Solchenbach, H. A. Gasteiger, and M. A. Mendez, *J. Electrochem. Soc.*, **166**, A1275 (2019).
58. H. Sclar et al., *J. Electrochem. Soc.*, **167**, 110563 (2020).
59. S. Oswald, D. Pritzl, M. Wetjen, and H. A. Gasteiger, *J. Electrochem. Soc.*, **167**, 100511 (2020).
60. J. Liu, H. Chen, J. Xie, Z. Sun, N. Wu, and B. Wu, *J. Power Sources*, **251**, 208 (2014).
61. M. Chouchane, E. N. Primo, and A. A. Franco, *J. Phys. Chem. Lett.*, **11**, 2775 (2020).
62. G. Assat, D. Foix, C. Delacourt, A. Iadecola, R. Dedryvère, and J.-M. Tarascon, *Nat. Commun.*, **8**, 2219 (2017).
63. G. Assat, A. Iadecola, D. Foix, R. Dedryvère, and J.-M. Tarascon, *ACS Energy Lett.*, **3**, 2721 (2018).
64. J. Chen, A. Gutierrez, M. T. Saray, R. S. Yassar, M. Balasubramanian, Y. Wang, and J. R. Croy, *J. Electrochem. Soc.*, **168**, 080506 (2021).
65. A. Gutierrez, J. T. Kirner, M. T. Saray, M. Avdeev, L. Geng, R. S. Yassar, W. Lu, and J. Croy, *J. Electrochem. Soc.*, **169**, 020574 (2022).
66. J. Zheng, W. Shi, M. Gu, J. Xiao, P. Zuo, C. Wang, and J.-G. Zhang, *J. Electrochem. Soc.*, **160**, A2212 (2013).
67. H. Liu, W. Xiang, C. Bai, L. Qiu, C. Wu, G. Wang, Y. Liu, Y. Song, Z.-G. Wu, and X. Guo, *Ind. Eng. Chem. Res.*, **59**, 19312 (2020).
68. P. Vanaphuti, Y. Liu, X. Ma, J. Fu, Y. Lin, J. Wen, Z. Yang, and Y. Wang, *ACS Appl. Mater. Interfaces*, **13**, 22597 (2021).
69. A. Nickol, T. Schied, C. Heubner, M. Schneider, A. Michaelis, M. Bobeth, and G. Cuniberti, *J. Electrochem. Soc.*, **167**, 090546 (2020).
70. N. Yabuuchi, K. Yoshii, S.-T. Myung, I. Nakai, and S. Komaba, *J. Am. Chem. Soc.*, **133**, 4404 (2011).
71. W. E. Gent et al., *Nat. Commun.*, **8**, 2091 (2017).
72. H. Koga, L. Croguennec, P. Mannessiez, M. Ménétrier, F. Weill, L. Bourgeois, M. Duttine, E. Suard, and C. Delmas, *J. Phys. Chem. C*, **116**, 13497 (2012).
73. J. Liu, L. Yin, L. Wu, J. Bai, S.-M. Bak, X. Yu, Y. Zhu, X.-Q. Yang, and P. G. Khalifah, *Inorg. Chem.*, **55**, 8478 (2016).
74. R. Robert, C. Bünzli, E. J. Berg, and P. Novák, *Chem. Mater.*, **27**, 526 (2015).
75. A. Grenier, H. Liu, K. M. Wiaderek, Z. W. Lebens-Higgins, O. J. Borkiewicz, L. F. J. Piper, P. J. Chupas, and K. W. Chapman, *Chem. Mater.*, **29**, 7345 (2017).
76. R. E. Dinnebier, A. Leineweber, and J. S. O. Evans, *Rietveld Refinement: Practical Powder Diffraction Pattern Analysis Using TOPAS* (Walter de Gruyter GmbH, Berlin) (2019).
77. W. E. Gent et al., *Adv. Mater.*, **28**, 6631 (2016).
78. J. Bréger, M. Jiang, N. Dupré, Y. S. Meng, Y. Shao-Horn, G. Ceder, and C. P. Grey, *J. Solid State Chem.*, **178**, 2575 (2005).

79. J. Serrano-Sevillano, D. Carlier, A. Saracibar, J. M. Lopez del Amo, and M. Casas-Cabanas, *Inorg. Chem.*, **58**, 8347 (2019).
80. B. Qiu et al., *Nat. Commun.*, **7**, 12108 (2016).
81. Q. Li et al., *J. Mater. Chem. A*, **8**, 7733 (2020).
82. T. Nakamura, H. Gao, K. Ohta, Y. Kimura, Y. Tamenori, K. Nitta, T. Ina, M. Oishi, and K. Amezawa, *J. Mater. Chem. A*, **7**, 5009 (2019).
83. T. Nakamura, K. Ohta, Y. Kimura, K. Tsuruta, Y. Tamenori, R. Aso, H. Yoshida, and K. Amezawa, *ACS Appl. Energy Mater.*, **3**, 9703 (2020).
84. H. Deng, I. Belharouak, Y.-K. Sun, and K. Amine, *J. Mater. Chem.*, **19**, 4510 (2009).
85. S. Ahmed, M. Bianchini, A. Pokle, M. S. Munde, P. Hartmann, T. Brezesinski, A. Beyer, J. Janek, and K. Volz, *Adv. Energy Mater.*, **10**, 2001026 (2020).
86. T. Zünd, B. Strehle, and H. A. Gasteiger, *ECS Meet. Abstr.*, **MA2019-01**, 510 (2019).
87. R. Morasch, B. Suthar, and H. A. Gasteiger, *J. Electrochem. Soc.*, **167**, 100540 (2020).

3.2 Surface-Related Degradation of Li- and Mn-Rich Layered Oxides

3.2.1 Quantification of Oxygen Release during the Initial Cycles

This section presents the article entitled "The Role of Oxygen Release from Li- and Mn-Rich Layered Oxides during the First Cycles Investigated by On-Line Electrochemical Mass Spectrometry".[155] The manuscript was submitted to the peer-reviewed *Journal of The Electrochemical Society* in September 2016 and was published in January 2017. The article is published "open access" and distributed under the terms of the Creative Commons Attribution Non-Commercial No Derivatives 4.0 License. A permanent weblink of this article is provided under: https://iopscience.iop.org/article/10.1149/2.1001702jes.

In this study, we investigate the gassing behavior of the Li- and Mn-rich layered oxide $Li[Li_{0.17}Ni_{0.18}Co_{0.10}Mn_{0.55}]O_2$ (also written in the 2-phase notation as $0.42\ Li_2MnO_3 \cdot 0.58\ Li[Ni_{0.38}Co_{0.21}Mn_{0.41}]O_2$) by on-line electrochemical mass spectrometry (OEMS). The CAM provides a capacity of ≈320 mAh/g during the first charge until 4.8 V vs. Li^+/Li, which exceeds the charge that can be compensated by the transition-metals (≈148 mAh/g from the $LiTMO_2$ phase, assuming that all TMs get oxidized to their formal 4+ state). As many researchers detected O_2 during the first charge,[151,152,154] there was the common belief in the literature that the additional charge originates from the activation of the Li_2MnO_3 phase during the voltage plateau at ≈4.5 V vs. Li^+/Li according to the following equation: $Li_2MnO_3 \rightarrow 2Li^+ + 2e^- + MnO_2 + 0.5O_2$.[109,129,148] Here, oxygen loss would occur throughout the bulk of the material.

To check this assumption, we conducted OEMS experiments that allowed for a rigorous and quantitative analysis of the evolved gases. We show that the oxygen release sets in at ≈4.6 V vs. Li^+/Li after the voltage plateau. Even when taking the sum of evolved O_2 and CO_2, the thus determined oxygen release accounts to less than ≈20% of the oxygen amount expected from the Li_2MnO_3 activation, i.e., the lattice oxide ions contribute reversibly to charge compensation by anionic redox (O^{2-}/O^{n-}).[142,143] Alternative to the bulk oxygen loss, we suggest a structural rearrangement at the near-surface region of the LMR-NCM particles, where the

oxygen-depleted phase transforms into a spinel (M_3O_4) or rock-salt layer (MO, where M is the sum of Li and TMs). Such reactions are well-known from the thermal decomposition of delithiated layered oxides, Li_xMO_2,[252,253] whose oxygen release upon charging was investigated in parallel to this work.[25,254] We present a mathematical model, which allows to estimate the spinel (or rock-salt) fraction based on the stoichiometry $Li_xTM_yO_2$, where x is the remaining lithium content at the onset of O_2 evolution and y is the transition-metal content of the CAM. Here, the spinel fraction equals the ratio of the actually measured oxygen amount relative to the theoretically expected amount for the complete layered-to-spinel conversion. Using a spherical shell model based on the BET surface area of the CAM, the spinel fraction can further be converted into a surface layer thickness. After two cycles, we estimate the thickness of the spinel-like surface layer to be on the order of ≈2-3 nm, which agrees perfectly with previous (S)TEM studies.[161–163]

To support the main article, additional information is supplied for the benefit of the reader. The Supporting Information includes the calculations for the expected oxygen release according to the different mechanisms as well as for the surface layer thickness and also provides an overview of literature reports which identified spinel surface layers by microscopy, spectroscopy, and/or diffraction techniques.

Author contributions

B.S. designed and performed the OEMS experiments. K.K. prepared the mesh coatings and further built the cells to analyze the voltage profiles and dQ/dV curves. B.S. and R.J. developed the phase transformation model and calculated the thickness of the oxygen-depleted surface layer. B.S., K.K., H.A.G., and M.P. wrote the manuscript. All authors discussed the results and commented on the manuscript.

A400 Journal of The Electrochemical Society, 164 (2) A400-A406 (2017)

The Role of Oxygen Release from Li- and Mn-Rich Layered Oxides during the First Cycles Investigated by On-Line Electrochemical Mass Spectrometry

Benjamin Strehle,[a,*,z] Karin Kleiner,[a,*] Roland Jung,[a,*] Frederick Chesneau,[b] Manuel Mendez,[b] Hubert A. Gasteiger,[a,] and Michele Piana[a,***]**

[a]*Chair of Technical Electrochemistry, Department of Chemistry and Catalysis Research Center, Technische Universität München, D-85748 Garching, Germany*
[b]*BASF SE, GCN/EE - M311, D-67056 Ludwigshafen, Germany*

In the present work, the extent and the role of oxygen release during the first charge of lithium- and manganese-rich $Li_{1.17}[Ni_{0.22}Co_{0.12}Mn_{0.66}]_{0.83}O_2$ (also referred to as HE-NCM) was investigated with on-line electrochemical mass spectrometry (OEMS). HE-NCM shows a unique voltage plateau at around 4.5 V in the first charge, which is often attributed to a decomposition reaction of the Li-rich component Li_2MnO_3. For this so-called "activation", it has been hypothesized that the electrochemically inactive Li_2MnO_3 would convert into MnO_2 while lattice oxide ions are oxidized and released as O_2 (or even CO_2) from the host structure. However, qualitative and quantitative examination of the O_2 and CO_2 evolution during the first charge shows that the onset of both reactions is above the 4.5 V voltage plateau and that the amount of released oxygen is an order of magnitude too low to be consistent with the commonly assumed Li_2MnO_3 activation. Instead, the amount of released oxygen can be correlated to a structural rearrangement of the active material which occurs at the end of the first charge. In this process, oxygen depletion from the HE-NCM host structure leads to the formation of a spinel-like phase. This phase transformation is restricted to the near-surface region of the HE-NCM particles due to the poor mobility of oxide ions within the bulk. From the evolved amount of O_2 and CO_2, the thickness of the spinel-like surface layer was estimated to be on the order of ≈2–3 nm, in excellent agreement with previously reported (S)TEM data.

Manuscript submitted September 8, 2016; revised manuscript received November 21, 2016. Published January 5, 2017.

Since the discovery of the positive electrode material $LiCoO_2$ and its commercialization in the Li-ion technology by Sony in 1991,[1] analogous layered oxides ($LiMeO_2$, Me = Ni, Co, Mn, Al, etc.) were studied, aiming at higher intrinsic specific capacity, energy, stability, and lower costs.[2–7] Among others, $Li[Ni_{1/3}Co_{1/3}Mn_{1/3}]O_2$ (NCM-111) showed very interesting performances in terms of specific capacity and stability.[8,9] Recently, materials characterized by an increase of exploitable Li^+ charge drew a lot of attention.[10,11] These so-called Li-rich compounds result from the substitution of part of the transition metal ions by Li^+, in a structural arrangement closely related to the layered structure.[11–14]

Li_2MnO_3 (or $Li[Li_{1/3}Mn_{2/3}]O_2$) is the simplest structure in this category and crystallizes in the monoclinic system (space group *C2/m*), while the common $LiMeO_2$-based layered structures crystallize in the hexagonal system (space group *R*-3*m*).[11,13,14] The two structures are very close to each other despite this difference in symmetry, related simply to the Li^+ ordering in the transition metal sites. This similarity is evident in the structure of the Li-rich NCM $Li_{1+x}Me_{1-x}O_2$ (Me = Ni, Co, Mn), also referred to as high-energy NCM (HE-NCM), where the hexagonal symmetry of the layered structure is broken by the superstructure of Li^+ in the transition metal sites, shown by the superlattice reflections in the diffractograms.[15,16] This similarity makes the Li_2MnO_3 crystalline domains difficult to detect, for which typically the notation x Li_2MnO_3 • (1-x) $LiMeO_2$ has been used.[14,17,18]

The higher lithium content of the HE-NCM material results in an increase in specific capacity and energy. Peculiar to this material is that the amount of lithium ions that can be deintercalated is higher than the possible increase in the valence of the transition metals. This was initially rationalized by the formation of an oxygen-deficient layered oxide throughout the bulk of the material, formed by oxygen loss during the first activation cycle.[19,20] Accordingly, subsequent on-line mass spectrometry studies demonstrated the evolution of O_2 during the first charge.[21–23] The observed oxygen release was commonly attributed to Li_2MnO_3 activation and assigned to a unique plateau in the first charge of HE-NCM.[24,25] In the proposed process, lattice O^{2-} anions are oxidized to O_2 and removed from the oxide bulk structure, while the initially inactive manganese becomes electrochemically active after the first activation charge. However, very recently, an alternative view has been proposed, namely the direct involvement of lattice oxide ions by oxygen redox in the reversible charge/discharge reaction.[26,27]

The present paper will critically discuss the extent and the role of oxygen release from the HE-NCM host structure during the first activation charge. By means of quantitative on-line electrochemical mass spectrometry (OEMS) analysis of the amount of evolved oxygen and the onset potential of oxygen evolution it can be clearly shown that the O_2 release does not take place during the 4.5 V plateau in the first charge (the so-called "activation"). Instead, we provide evidence that the O_2 release occurs due to a structural rearrangement, consistent with the formation of a spinel-like surface layer observed in several (S)TEM studies.[28–30] This hypothesis is in good agreement with the amount of oxygen observed in our study, which in turn would be too low for the previously proposed Li_2MnO_3 activation.[17,24]

Experimental

All experiments were conducted with $Li_{1.17}[Ni_{0.22}Co_{0.12}Mn_{0.66}]_{0.83}O_2$ (further on referred to as HE-NCM; BET >>1 m^2 g^{-1}, BASF SE, Germany), which can also be written as 0.42 Li_2MnO_3 • 0.58 $Li[Ni_{0.38}Co_{0.21}Mn_{0.41}]O_2$. HE-NCM inks were prepared by mixing 96 wt% of HE-NCM, 2 wt% of Super C65 conductive carbon (Timcal, Switzerland), and 2 wt% of polyvinylidene fluoride binder (PVDF, Kynar HSV 900, Arkema, France) with *N*-methyl-2-pyrrolidone (NMP, anhydrous, 99.5%, Sigma-Aldrich, Germany) in a planetary orbital mixer (Thinky, USA) in several steps. In the case of standard electrodes for tests in Swagelok T-cells, the ink was coated onto an aluminum foil using a doctor blade at a wet-film thickness of 50 µm. For the OEMS measurements conducted in a specially designed cell,[31] the ink was coated on a steel mesh (SS316, aperture 26 µm, wire diameter 25 µm, The Mesh Company Ltd, UK) in order to allow access of the

*Electrochemical Society Student Member.
**Electrochemical Society Fellow.
***Electrochemical Society Member.
[z]E-mail: benjamin.strehle@tum.de

Journal of The Electrochemical Society, **164** (2) A400-A406 (2017)

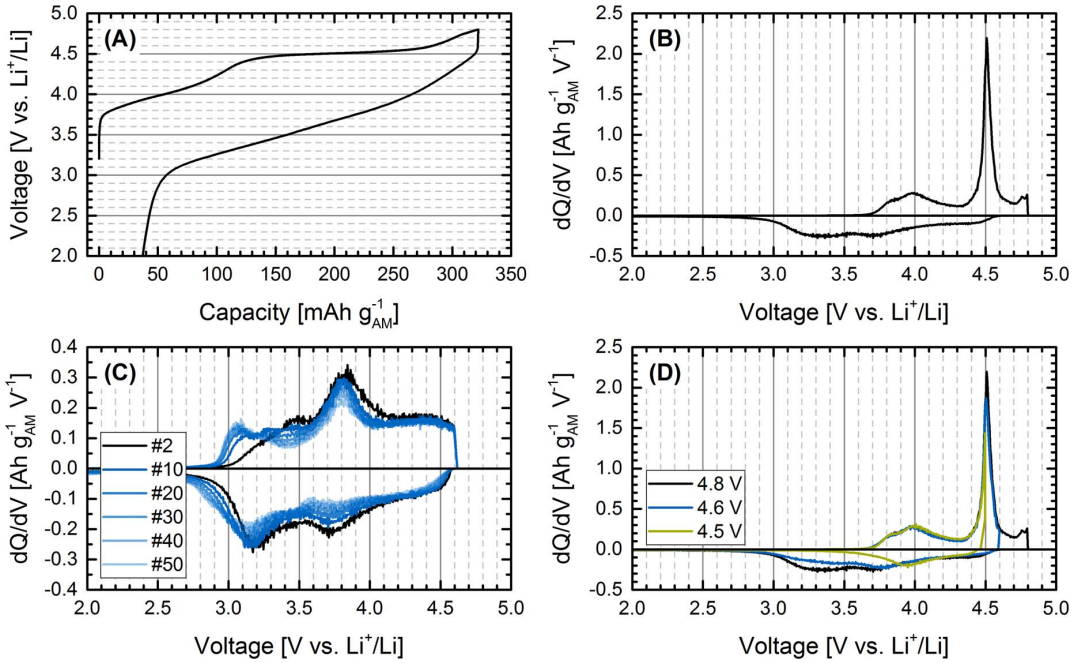

Figure 1. First cycle of HE-NCM (A) and the corresponding differential capacity (dQ/dV) plot (B). Panel C shows the differential capacity of the subsequent cycles. In panel D, the dQ/dV plot of the first cycle is shown for different upper voltage cutoffs, illustrating its influence on the discharge peaks. HE-NCM was cycled vs. metallic Li at a C-rate of C/10 and 25°C. In panel A-C, the first cycle was performed between 4.8 V and 2.0 V, while the upper cutoff voltage was 4.6 V for the subsequent cycles.

evolved gases to the capillary leading to the mass spectrometer.[32] The electrodes were punched out (loading/diameter: ≈4 mg_{AM} cm^{-2}/10 mm for T-cells and ≈10 mg_{AM} cm^{-2}/15 mm for OEMS cells), pressed for 20 s with 2.5 tons, and dried overnight at 120°C under dynamic vacuum. Swagelok T-cells were built using two glass fiber separators (glass microfiber filter, 691, VWR, Germany) and 120 µL LP57 electrolyte (1 M $LiPF_6$ in EC:EMC 3:7 by weight, <20 ppm H_2O, BASF SE). In contrast, OEMS cells were built using two porous polyolefin separators (H2013, Celgard, USA) and 100 µL LP57. Metallic lithium foil (thickness 0.45 mm, 99.9%, Rockwood Lithium, USA) was used as counter-electrode for all cells (diameter: 11 mm for T-cells and 17 mm for OEMS cells), except in one OEMS experiment, where a partially charged (delithiated) LFP counter-electrode with an areal capacity of 3.5 mAh cm^{-2} was used (from Custom Cells Itzehoe GmbH, Germany), which was charged at C/5 by 3.0 mAh cm^{-2}, corresponding to ca. $Li_{0.14}FePO_4$. Prior to cycling, the head space of the OEMS cells was purged for 2 min with argon to remove any gas traces from the glove box atmosphere. A 4 h OCV step was applied prior to starting the experiments. Conversion of the mass spectrometer currents to concentrations was done for O_2 and CO_2, using a calibration gas containing 2000 ppm of each gas in Ar (Westfalen AG, Germany). C-rates are defined based on a specific capacity of 300 mAh g^{-1}_{AM} (AM ≡ cathode active material, HE-NCM in our case).

Results and Discussion

Electrochemical characterization.—HE-NCM shows a unique activation cycle with a plateau around 4.5 V in the first charge to 4.8 V (Figure 1A), yielding an overall capacity of ca. 320 mAh g^{-1}_{AM}, which is close to the theoretical capacity of the material of ca. 360 mAh g^{-1}_{AM} (if one were to assume that all lithium could be extracted, based on $Li_{1.17}[Ni_{0.22}Co_{0.12}Mn_{0.66}]_{0.83}O_2$ with a molar mass of 86.8 g mol^{-1}). This can be seen more clearly in the differential capacity (dQ/dV) plot of the first charge/discharge cycle (Figure 1B), in which the activation plateau corresponds to a large peak at 4.5 V (HE-NCM vs. Li^+/Li). The presence of this peak is only observed in the first charge but not in the following cycles (Figure 1C). Depending on the voltage cutoff (before, on, or after the activation plateau), additional peaks appear at ca. 3.2 V and 3.7 V in the subsequent discharge cycles and at 3.0 V in the charge cycles (Figure 1C). The higher the end-of-charge voltage during the first activation cycle, the more pronounced are the additional peaks in the dQ/dV plot (Figure 1D). Apart from the electrochemical characterization, XRD patterns of the pristine material and after the first cycle are shown in the Supporting Information. The weak reflections between 9 and 12° are consistent with a two-phase rhombohedral-monoclinic system,[33] which clearly assign the material to the class of Li- and Mn-rich layered oxides (see Section 1 of the Supporting Information).

Li_2MnO_3 activation.—In the past, most authors have ascribed the origin of this so-called activation to the removal of oxygen from the bulk structure, leading to an oxygen-deficient bulk material.[17,19–21,24,25,34] Some of them attributed the activation of HE-NCM to the formation of delithiated MnO_2 according to Eq. 1,[17,24] which can be reversibly lithiated in the following discharge:

$$Li_2MnO_3 \rightarrow 2\,Li^+ + 2\,e^- + MnO_2 + 1/2\;O_2 \uparrow \qquad [1]$$

If following Eq. 1, the quantitative activation of Li_2MnO_3 in our material with the composition 0.42 Li_2MnO_3 • 0.58 $Li[Ni_{0.38}Co_{0.21}Mn_{0.41}]O_2$ (molar mass 104.8 g mol^{-1}) would lead to the release of ca. 2000 μmol_{O_2} g^{-1}_{AM}, corresponding to ca. 17% of all oxygen atoms in HE-NCM (calculation given in Section 2 of the Supporting Information). This requires transport of oxygen anions from the bulk of the material to the surface during activation, from where it could be released as molecular oxygen.

Gas evolution during first charge.—Figure 2 shows OEMS data obtained while charging HE-NCM vs. metallic Li at C/20 up to 4.8 V. Following the first constant current step (CC), one cell was held at open circuit voltage (OCV, black curve in Figure 2A) for 10 h, while

A402 Journal of The Electrochemical Society, **164** (2) A400-A406 (2017)

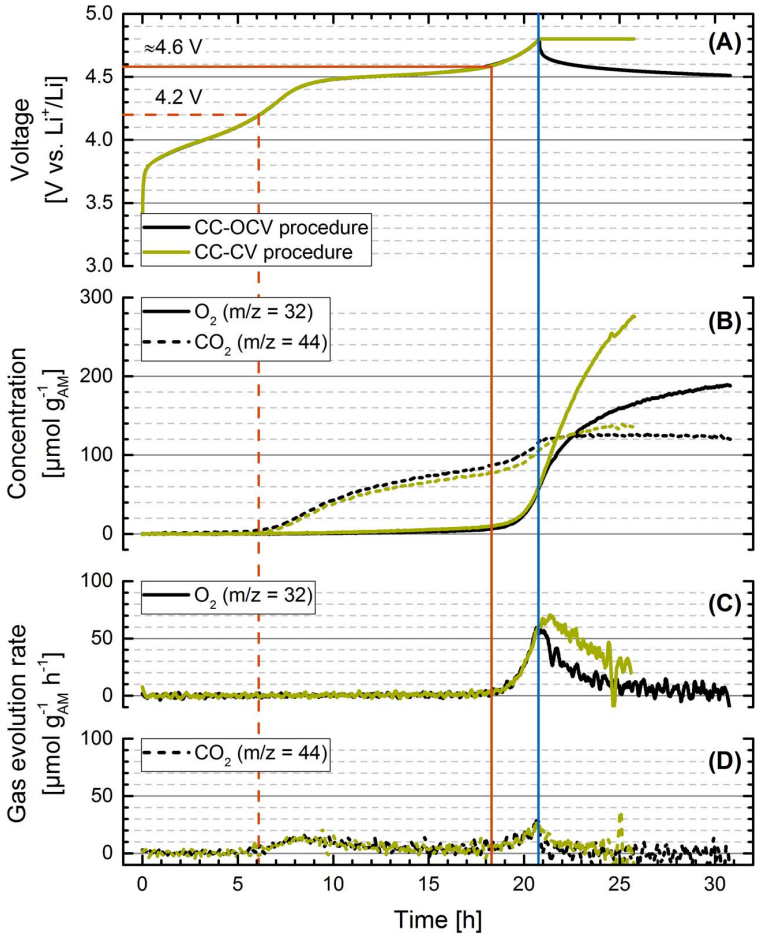

Figure 2. OEMS measurement of the first charge of HE-NCM vs. metallic Li to 4.8 V at C/20 and 25°C, followed by either an OCV step for 10 h (black curves) or a CV hold at 4.8 V for 5 h (green curves). Panel A shows the voltage curve vs. time (note that the curves are superimposed up to the upper cutoff voltage, i.e., up to ca. 21 h). Panel B illustrates the evolved amount of O_2 (solid curves) and CO_2 (dashed curves) in units of µmol g^{-1}_{AM}, whereas the O_2 and CO_2 evolution rates in units of µmol g^{-1}_{AM} h^{-1} are shown in the panels C and D, respectively. The dashed red lines indicate the initial onset potential of CO_2 evolution; the solid red lines indicate the onset potential of O_2 evolution (as well as the second onset potential for CO_2 evolution); the solid blue line marks the end of the CC charge at the cutoff voltage of 4.8 V.

another cell was held at 4.8 V in a constant voltage step (CV, green curve in Figure 2A) for 5 h, recording continuously the O_2 and CO_2 evolution in both cases (accumulated O_2 and CO_2 signals are shown in Figure 2B, while the evolution rates of O_2 and CO_2 are shown in Figure 2C and Figure 2D, respectively).

Starting with the CC-OCV experiment (black lines in Figure 2), the CO_2 evolution begins at 4.2 V (before the plateau), followed by a second increase at ≈4.6 V (after the plateau), which coincides with the onset potential for O_2 evolution. While the CO_2 release stops at the beginning of the OCV step, interestingly, the O_2 evolution goes on and does not complete within the measurement time. Let us first examine the evolution of CO_2. In agreement with Metzger et al.,[35] we attribute the initial CO_2 evolution starting at 4.2 V (marked by the dashed red lines in Figure 2) to the decomposition of carbonate impurities on the surface of the HE-NCM particles. The 4.2 V onset potential agrees with the Li_2CO_3 oxidation potential reported in the literature,[25,36,37] whereby essentially one CO_2 molecule per Li_2CO_3 is produced.[37] This first CO_2 evolution process continues up to a potential of ≈4.6 V (marked by the solid red lines in Figure 2), beyond which a second increase of the CO_2 evolution is observed. Note that the first process gradually levels off during the plateau, consistent with the consumption of an impurity which is only present in limited quantities. Up to ≈4.6 V, ≈80 μmol_{CO_2} g^{-1}_{AM} are evolved (Figure 2B), which for a 1:1 stoichiometric ratio between oxidized Li_2CO_3 and evolved CO_2 would correspond to a Li_2CO_3 content of ≈0.6 wt% (from: 80 μmol_{CO_2} g^{-1}_{AM} · 74 $g_{Li_2CO_3}$ $mol^{-1}_{Li_2CO_3}$). The calculated amount of Li_2CO_3 is to be expected on the HE-NCM particles (particularly in view of its rather high BET surface area[23]). This interpretation of the CO_2 signal is at variance with the mechanism proposed by Streich et al.[23] and by Luo et al.,[27] who concluded that the entire amount of CO_2 evolved during the initial charging of HE-NCM materials (i.e., including the CO_2 evolved between ≈4.2 and ≈4.6 V in their experiments) would originate from the attack of reactive oxygen species (e.g., superoxide radicals) released from the HE-NCM lattice on the electrolyte solvents. As evidence, Luo et al. noted the detection of $C^{16/18}O_2$ from their partially ^{18}O-labeled active material, but since their isotopic labeling process (heating the synthesized material in $^{18}O_2$-containing gas at 800°C) would also lead to the labeling of carbonate species, the formation of $C^{16/18}O_2$ can equally well be explained by the electrooxidation of Li_2CO_3 surface impurities. The latter are typically present in layered oxide materials.[38–40] However, the detection of $C^{16/18}O_2$ during the entire charging curve shows that the anodic oxidation of the electrolyte (without any involvement of the active material), which would release solely $C^{16/16}O_2$ in the experiment by Luo et al., is of minor importance for this class of materials. Thus, while we disagree with the interpretation by Streich et al.[23] and by Luo et al.[27] that the evolved CO_2 below ≈4.6 V originates from the reaction of the electrolyte with released lattice oxygen, we do believe that the second increase of the CO_2 evolution rate above 4.6 V, which coincides with the onset of O_2 evolution, is indeed caused by this reaction.

Next we will examine the O_2 evolution during the CC-OCV procedure. During the initial sloping region and during the high voltage plateau, i.e., at potentials below ≈4.6 V and a charge capacity of ≈280 mAh g^{-1}_{AM}, only minute amounts of O_2 are observed (less than 10 μmol_{O_2} g^{-1}_{AM}). This number could account for only

≈1 mAh g^{-1}_{AM} (assuming 4 electrons/O_2) and would thus be negligible compared to the overall charge capacity of ≈280 mAh g^{-1}_{AM}. Therefore, since the lattice oxygen evolution happens only after the plateau at 4.5 V, it cannot be correlated to the Li_2MnO_3 activation according to Eq. 1, as was done in some of the literature.[17,24] Only at potentials above ≈4.6 V, substantial O_2 evolution is observed, reaching a total amount of ≈60 μmol_{O_2} g^{-1}_{AM} once the positive voltage cutoff of 4.8 V is reached (see solid blue line in Figure 2). At this point, the charge capacity amounts to ≈310 mAh g^{-1}_{AM}, of which only ≈6.4 mAh g^{-1}_{AM} can be ascribed to the detected amount of O_2. The O_2 data may be compared to the study by Streich et al.,[23] who obtained 29 μmol_{O_2} g^{-1}_{AM} at a cutoff potential of 4.7 V, in excellent agreement with the ≈25 μmol_{O_2} g^{-1}_{AM} which we recorded at 4.7 V (Figure 2B). While the O_2 evolution rate (Figure 2C) is at its maximum at the positive voltage cutoff of 4.8 V, O_2 evolution continues even during the subsequent OCV period at a rate which decreases with decreasing potential. After 10 h of OCV, the potential decays to ≈4.5 V, at which point the total amount of O_2 approaches a value of ≈200 μmol_{O_2} g^{-1}_{AM} and the O_2 evolution gradually stops. Consequently, the total amount of evolved O_2 during the CC-OCV procedure amounts to only 10% of what would be predicted on the basis of Eq. 1 (i.e., of 2000 μmol_{O_2} g^{-1}_{AM}; see Section 2 of the Supporting Information). Note that the amount of O_2 dissolved in the electrolyte accounts to ca. 0.1% of the overall O_2 and is thus negligible compared to the gas phase which is detected by OEMS (calculation given in Section 3 of the Supporting Information). Even if we were to assume that all of the evolved CO_2 (≈120 μmol_{CO_2} g^{-1}_{AM}) would derive from the oxidation of the electrolyte by released lattice oxygen, as was suggested by Luo et al. (assuming the formation of 1 mol of CO_2 from 1 mol of released O_2),[27] only ≈16% of the evolved O_2 predicted by Eq. 1 would be released during the CC-OCV procedure. More likely, however, only ≈40 μmol_{CO_2} g^{-1}_{AM} derive from electrolyte oxidation by lattice oxygen (based on the above argument that CO_2 formed up to 4.6 V is due to Li_2CO_3 oxidation), so that the maximum amount of released oxygen (≈240 μmol g^{-1}_{AM}) amounts to ≈12% of what would be predicted by Eq. 1.

One remaining unresolved phenomenon in the CC-OCV data in Figure 2 is the fact that the CO_2 evolution stops very shortly after entering the OCV step (best seen by the CO_2 trace in Figure 2B), despite the fact that the amount of O_2 still increases by a factor of ≈3 (see O_2 trace in Figure 2B). This is clearly inconsistent with the above assumption that released lattice oxygen attacks the electrolyte solvents leading to CO_2 formation. As it seems to be required that charge passes the external circuit, one could hypothesize an (independent) oxidation step of the electrolyte which would be suppressed during OCV. Furthermore, as the released lattice oxygen species is not known, the absent CO_2 evolution might be explained by assuming that the oxidation of the electrolyte is largely triggered by superoxide radicals ($O_2^{\bullet-}$) rather than by molecular oxygen, which was proposed previously for alkyl carbonate-based electrolytes[41,42] as well as for the photo-assisted oxidation of organic dyes in aerated solutions.[43] At cathode potentials significantly above 3 V, superoxide radicals could only be formed by O_2 reduction at the lithium anode, where it might proceed as long as lithium is deposited (i.e., as long as a fresh lithium is being plated). Under this assumption, superoxide radicals to decompose the alkyl carbonates to CO_2 would be present during the CC step, but could not be supplied anymore during the OCV period. This will be discussed further when examining the gas evolution during the CC-CV charge.

Layered-to-spinel transformation.—Let us now summarize our observations so far: (i) almost no O_2 from the HE-NCM host structure is released during the activation plateau, (ii) the total amount of evolved gases is roughly one order of magnitude lower than what would be predicted based on Eq. 1, and (iii) the O_2 evolution continues during OCV, i.e., when no charge is passed. This provides strong evidence that the evolved O_2 is not related to the bulk oxidation of the Li_2MnO_3 phase according to Eq. 1. In contrast, the negligible amount of O_2 and the probably largely Li_2CO_3-derived CO_2 accumulated by the end of the voltage plateau (i.e., just below 4.6 V) suggests that the following oxygen release is associated with a structural rearrangement of the surface of the HE-NCM material, rather than being related to the electrochemically driven process described traditionally by Eq. 1. Such reactions are well-known from structurally related layered oxides and describe the chemical decomposition of Li_xMeO_2 into a spinel-like structure with the composition M'_3O_4 (M' = Me+Li), shown in Eq. 2.[44–46] This phase transformation is consistent with the observed phase reported in several (S)TEM studies from Li- and Mn-rich layered oxides (an overview is provided in Section 4 of the Supporting Information).[28–30,47–50] As the transition metal content in Li-rich materials is smaller than that for common layered oxides, the reaction is given in the generalized form for $Li_xMe_yO_2$. Especially in the case of Ni-rich materials,[51–55] the oxygen depletion of the near-surface region is a continuously ongoing process during cycling and/or at elevated temperatures, leading via the spinel structure to a rock-salt structure with the composition M'O (M' = Me+Li), described in Eq. 3.[44,45] The restriction of these reactions to the near-surface region can be rationalized by the low O^{2-} anion mobility within the bulk material at/near room temperature.

$$Li_xMe_yO_2 \rightarrow \frac{x+y}{3} Li_{3-\frac{3y}{x+y}} Me_{\frac{3y}{x+y}} O_4 + \frac{3-2(x+y)}{3} O_2 \uparrow, \quad \text{where } x \ll 1 \text{ and } y \leq 1 \qquad [2]$$

$$Li_xMe_yO_2 \rightarrow \frac{x+y}{3} Li_{3-\frac{3y}{x+y}} Me_{\frac{3y}{x+y}} O_4 + \frac{3-2(x+y)}{3} O_2 \uparrow$$
$$\rightarrow (x+y) Li_{1-\frac{y}{x+y}} Me_{\frac{y}{x+y}} O + \frac{2-(x+y)}{2} O_2 \uparrow \qquad [3]$$

In summary, Equations 2 and 3 present an alternative view to Eq. 1 of the oxygen evolution mechanism for HE-NCM materials during activation, assuming that oxygen is released by the conversion of a layered oxide into a spinel (or rock-salt) structure at high potentials. This picture would be by analogy with thermally induced phase transformations observed for charged layered oxide materials.[44–46,53]

In the second experiment shown in Figure 2, a C/20 activation charge to 4.8 V and then continued with a constant voltage step for 5 h was performed (see green curves). Up to the positive cutoff potential of 4.8 V, the voltage and gas evolution responses are identical with the foregoing experiment (compare green vs. black curves). The O_2 evolution rate during the 4.8 V hold period is substantially larger than during OCV (see black vs. green solid curves in Figure 2C), so that the total amount of evolved oxygen is larger at the end of the CV step (≈280 μmol_{O_2} g^{-1}_{AM} after 5 h CV compared to ≈200 μmol_{O_2} g^{-1}_{AM} after 10 h OCV, see Figure 2B). This seems to be at variance with our above assumption that the diffusion of O^{2-} anions within the bulk structure would limit the growth of the oxygen-depleted surface layer, i.e., that it would restrict the release of molecular oxygen to the near-surface region. However, since lithium deintercalation continues during the CV step (amounting to ≈20 mAh g^{-1}_{AM}), the oxide material becomes even more unstable, so that it is not unreasonable to assume that this would lead either to a slightly increased O^{2-} diffusion and/or a further conversion of the spinel layer to a rock-salt structure (Eq. 3). Both effects would be accompanied by further O_2 release. As the O_2 evolution rate during the CV step diminishes in a similar way than during OCV, we think that the oxygen depletion is still limited to the external part of the particles and does not affect the core of the particles. Note that Equation 2 and 3 describe the formation of the spinel (metal/oxygen ratio 3:4) and rock-salt structure (metal/oxygen ratio 1:1) with an ideal stoichiometry. However, it is also possible to reach stoichiometries in between in which the metal to oxygen ratio differs from the ideal case. Contrary to the CC-OCV experiment, the CO_2 evolution continues at low rate during most of the CV step, which would be consistent with an oxidation step of the alkyl carbonates or the continuous formation of superoxide radicals during lithium plating on the anode.

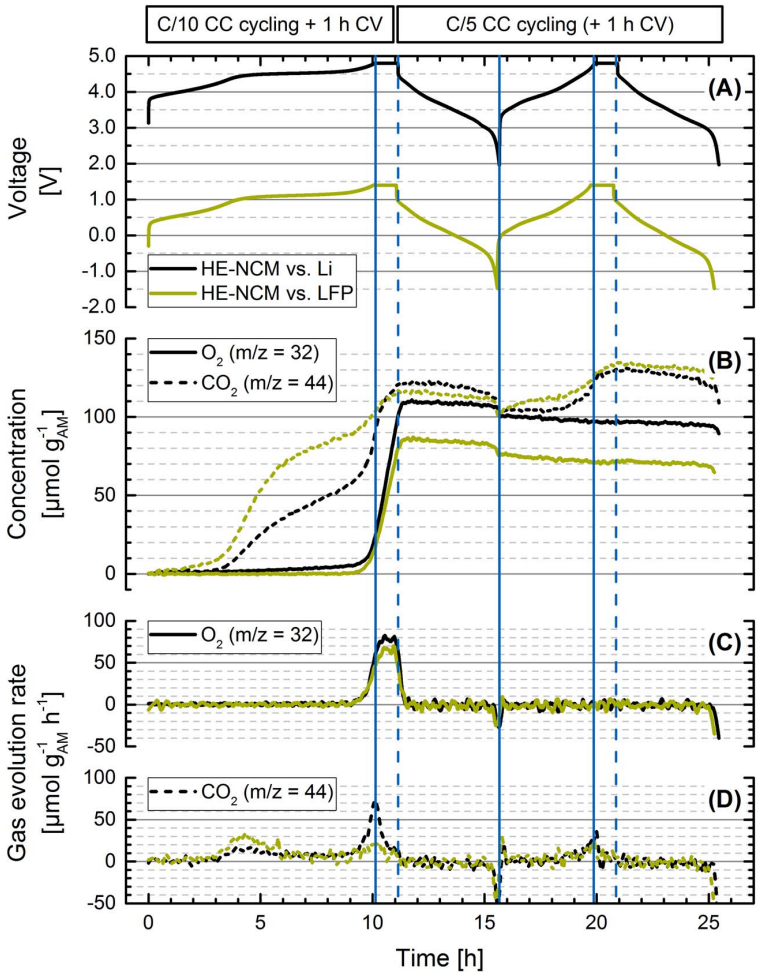

Figure 3. HE-NCM vs. Li (black curves) and HE-NCM vs. LFP (green curves), cycled at C/10 in the first charge and at C/5 in the subsequent discharge as well as the second cycle. Both measurements were performed at 25°C in the potential range of 2.0–4.8 V vs. Li^+/Li for the HE-NMC working-electrode, including a CV step of 1 h at the end of each CC charge. Panel A shows the voltage curves vs. time. Panel B illustrates the evolved amount of O_2 (solid curves) and CO_2 (dashed curves) in units of µmol g^{-1}_{AM}, whereas the O_2 and CO_2 evolution rates in units of µmol g^{-1}_{AM} h^{-1} are shown in the panels C and D, respectively. The blue solid lines indicate the end of the CC steps; the dotted blue lines show the end of the CV steps.

Gas evolution during the first two cycles.—After having examined the first activation charge, we now investigate whether O_2 release from the HE-NCM host structure also occurs in the second cycle or not (Figure 3). Therefore, using first the same electrode configuration as was used in Figure 2 (viz., HE-NCM vs. Li), we performed a C/10 charge to 4.8 V completed with a CV step of 1 h and followed by a C/5 discharge to 2.0 V, with a subsequent second cycle at C/5 (see black curves in Figure 3). Once the upper cutoff voltage is reached in this first charge at C/10, the amounts of evolved O_2 and CO_2 are lower than what we had observed at C/20 (≈25 µmol_{O_2} g^{-1}_{AM} and ≈90 µmol_{CO_2} g^{-1}_{AM} at C/10 vs. ≈60 µmol_{O_2} g^{-1}_{AM} and ≈105 µmol_{CO_2} g^{-1}_{AM} at C/20), which we ascribe to the slow kinetics of lattice oxygen release. However, at the end of the subsequent 1 h hold at 4.8 V, the amounts of evolved O_2 and CO_2 are essentially identical for first cycle activation at either C/10 or C/20 (≈110 µmol_{O_2} g^{-1}_{AM} and ≈120 µmol_{CO_2} g^{-1}_{AM} at C/10 + 1 h CV vs. ≈125 µmol_{O_2} g^{-1}_{AM} and ≈120 µmol_{CO_2} g^{-1}_{AM} at C/20 + 1 h CV). It is noteworthy that the O_2 evolution immediately stops upon switching from the CV step in the first cycle, during which O_2 is still being evolved, to the first discharge step. The rapidly vanishing O_2 evolution rate (Figure 3C) demonstrates that there is no delay between the O_2 evolution from the HE-NCM material and its detection in the OEMS. As the near-surface region is lithiated and thus stabilized first during discharge, the abrupt end of the O_2 evolution also shows that it must originate from the external part of the particles. Very surprising is the observation that there is no O_2 evolution during the second charge, even though the overall amount of evolved O_2 after the first charge at C/10 and 1 h hold at 4.8 V (≈110 µmol_{O_2} g^{-1}_{AM}) is less than what was measured in the previous experiments with a C/20 charge and 5 h hold at 4.8 V (≈280 µmol_{O_2} g^{-1}_{AM}). Consequently, any formed spinel-like surface layer in the former case should be thinner and further O_2 evolution in the second charge would be expected, contrary to what we and others[23] have observed. In order to explain this discrepancy, we hypothesize that the initially formed surface layer is modified during the first discharge, thereby preventing further oxygen release in subsequent charges. In addition, the change in the HE-NCM bulk structure upon the initial release of almost all of its lithium ions during activation (320 mAh g^{-1}_{AM} in the first charge vs. a theoretical maximum of ca. 360 mAh g^{-1}_{AM}) leads to different bulk thermodynamic properties, which might affect the oxygen release. Note that the overall capacity during the second charge decreases to ca. 275 mAh g^{-1}_{AM}. The OEMS measurement shows also a slight decrease in the O_2 and CO_2 signals once the potential decreases below 3.0 V at the end of discharge, which can be attributed to the formation of Li_2O_2 and Li_2CO_3 on the HE-NCM surface.[25,56] This newly formed Li_2CO_3 can then be oxidized in a subsequent charge, which we believe is the reason for the observed CO_2 evolution in the second charge, starting again at 4.2 V. This was already proposed previously.[56]

In order to ensure that no gaseous products are consumed on the Li counter-electrode, the same cycling procedure was applied to HE-NCM but using partially delithiated LFP as counter-electrode (green curves in Figure 3; see also in the experimental part). Neither O_2 nor CO_2 are expected to be reduced at the LFP potential.[57] Its potential was monitored in a T-cell with a Li reference-electrode to

Table I. Estimation of the molar fraction and thickness of the spinel-like surface layer for *Model A* (lattice oxygen-derived CO_2 only above ≈4.6 V) and *Model B* (CO_2 evolved prior to O_2 evolution at ≈4.6 V also due to the reaction with lattice oxygen), based on the gas evolution for the HE-NCM/Li cell data in Figure 3 (black lines). For CO_2, we assume that both oxygen atoms come from the lattice O^{2-} anions, as suggested by Luo et al.[27] The capacity is also derived from the gas evolution, assuming that four electrons are exchanged per gas molecule. For details see Section 5 and 6 of the Supporting Information.

		Model A (≥4.6 V)		*Model B* (≥4.2 V)	
Gas evolution	n [μmol g^{-1}_{AM}]	O_2	110	O_2	110
		CO_2	60	CO_2	120
Capacity ($4e^-/O_2$ & CO_2)	C_{spec} [mAh g^{-1}_{AM}]	18		25	
Fraction of spinel phase	x_{spinel} [mol.%]	5.7		7.7	
Spinel-like surface layer thickness	t_{spinel} [nm]	2.1		2.9	

determine the voltage cutoffs in the HE-NCM/LFP full-cell for the OEMS measurement (−1.45 V and 1.40 V selected as cell potential for the lower and upper voltage cutoffs). That the chosen cutoffs are reasonably comparable can be deduced from the close similarity of the charge/discharge curve features for the HE-NCM/Li and the HE-NCM/LFP cells (compare black and green curve in Figure 3A). The amount of evolved O_2 after the first cycle is slightly lower for the HE-NCM/LFP cell compared to the HE-NCM/Li cell (≈85 μmol_{O_2} g^{-1}_{AM} vs. ≈110 μmol_{O_2} g^{-1}_{AM}, respectively), but this might be due to small but finite differences in the upper voltage hold value. Regarding the CO_2 evolution, there are clear differences prior to the onset of O_2 evolution (reaching ≈90 μmol_{CO_2} g^{-1}_{AM} for HE-NCM/LFP vs. ≈60 μmol_{CO_2} g^{-1}_{AM} for HE-NCM/Li), which might be due to an inhomogeneous distribution of carbonate impurities among different electrodes. Overall, however, the differences in total gas evolution are not very large, so that any possible "cross-talk" effects between anode and cathode are either negligible or very similar.

Thickness of the spinel-like surface layer.—Assuming that the detected O_2 as well as the associated CO_2 obtained from Figure 3 derives from the formation of a near-surface spinel layer and not from the removal of oxygen from the bulk of the material, we will now estimate its thickness. The latter can be calculated by taking into account the amount of oxygen atoms which are released from the HE-NCM host structure according to Eq. 2. To perform this calculation, we will use two different models. *Model A*: We only consider the amount of gases evolved at a voltage higher than 4.6 V, i.e., once the onset of O_2 evolution is observed, which, without doubt, will derive from HE-NCM lattice oxygen. *Model B*: As some authors assume that the CO_2 observed prior to O_2 evolution (i.e., between 4.2 V and 4.6 V) originates from electrolyte oxidation by reaction with released lattice oxygen,[23,27] we will also provide an estimate for the near-surface layer thickness using the overall gas evolution (i.e., including the CO_2 evolution starting at 4.2 V), even though we believe that it is more likely due to the electrooxidation of Li_2CO_3 impurities. These two models will now be applied to the HE-NCM/Li cell data shown in Figure 3 (black lines). The formation of a spinel structure (M'_3O_4, M' = Me+Li) at 4.6 V, corresponding to a charge capacity of ≈275 mAh g^{-1}_{AM} at C/10, can be written as follows (see Supporting Information for more details):

$$Li_{0.28}Me_{0.83}O_2 \rightarrow 0.37\ Li_{0.76}Me_{2.24}O_4 + 0.26\ O_2 \uparrow \quad [4]$$

Comparing the results in Table I, the difference between the two models is less than 1 nm which is reasonably small compared to the estimated average HE-NCM particle radius of ≈110 nm (see Section 6 of the Supporting Information) and based on the approximations used for this calculation. Nevertheless, the estimated thickness of ≈2–3 nm for the spinel-like phase is in excellent agreement with recent (S)TEM results, which propose also a 2–3 nm thick surface layer formed during the first cycle.[28–30] As already mentioned in the discussion of Figure 2, it is not possible to determine whether the transformation of the near-surface region stops at the spinel structure (as described in Eq. 2) and to what extent it may proceed all the way to the rock-salt structure (as described in Eq. 3). In the latter case, the estimated thickness of the near-surface layer would be smaller by a factor of ca. 2. The overall maximum estimated capacity of ≈25 mAh g^{-1}_{AM} is five times lower than the capacity provided by HE-NCM during the plateau. However, the gas evolution does not occur during the plateau but mostly after plateau at potentials of 4.6 V and above, proceeding even if HE-NCM is hold at open circuit potential after the first charge.

Conclusions

In the present work, we show the gas evolution of HE-NCM during the first two cycles using OEMS. The gas evolution can be divided into a CO_2 evolution starting at 4.2 V and ending before 4.6 V, followed by a second CO_2 production starting at 4.6 V after the activation plateau and coinciding with the onset of the evolution of O_2. In agreement with the literature[25,35,37,56] and according to the use of a Li excess in HE-NCM synthesis, we attribute the CO_2 evolution at low voltages mainly to the electrooxidation of Li_2CO_3 impurities, while the O_2 and CO_2 evolution at voltages higher than 4.6 V are both attributed to oxygen evolved from the HE-NCM lattice. We exclude any possible gas consumption on the Li counter-electrode by comparing the results obtained with LFP as counter-electrode. The maximum recorded gas evolution due to lattice oxygen upon extended potential hold at 4.8 V (see CC-CV experiment in Figure 2), ≈420 μmol g^{-1}_{AM} (assuming that CO_2 evolution at low potentials is due to electrolyte oxidation by released lattice oxygen) or ≈340 μmol g^{-1}_{AM} (assuming that CO_2 evolution at low potentials is due to the oxidation of Li_2CO_3 impurities), is, in any case, at least 5-fold lower than what would be expected for the so-called Li_2MnO_3 activation (2000 μmol g^{-1}_{AM}) assumed in the literature.[17,24] This led us to propose an alternative reaction to the Li_2MnO_3 activation, namely, the formation of a spinel-like near-surface structure analogous to the known structural rearrangements in layered oxides. From the amount of evolved gases, we estimated the thickness of such a spinel-like surface layer on the HE-NCM particles to be on the order of ≈2–3 nm, in excellent agreement with previously observed (S)TEM data.[28–30]

Acknowledgments

The authors gratefully acknowledge BASF SE for financial support of this research through the framework of its Scientific Network on Electrochemistry and Batteries. R.J. thanks BMW AG for funding.

References

1. K. Mizushima, P. C. Jones, P. J. Wiseman, and J. B. Goodenough, *Mater. Res. Bull.*, **15**, 783 (1980).
2. C. Delmas and I. Saadoune, *Solid State Ionics*, **53–56**, 370 (1992).
3. T. Ohzuku, A. Ueda, and M. Kouguchi, *J. Electrochem. Soc.*, **142**, 4033 (1995).
4. T. Ohzuku and Y. Makimura, *Chem. Lett.*, **30**, 744 (2001).
5. J. S. Weaving, F. Coowar, D. A. Teagle, J. Cullen, V. Dass, P. Bindin, R. Green, and W. J. Macklin, *J. Power Sources*, **97–98**, 733 (2001).
6. Z. Lu, D. D. MacNeil, and J. R. Dahn, *Electrochem. Solid-State Lett.*, **4**, A200 (2001).
7. F. Zhou, X. Zhao, and J. R. Dahn, *J. Electrochem. Soc.*, **156**, A343 (2009).
8. I. Belharouak, Y.-K. Sun, J. Liu, and K. Amine, *J. Power Sources*, **123**, 247 (2003).
9. J. Choi and A. Manthiram, *J. Electrochem. Soc.*, **152**, A1714 (2005).
10. Z. Lu and J. R. Dahn, *J. Electrochem. Soc.*, **149**, A1454 (2002).
11. Z. Lu, L. Y. Beaulieu, R. A. Donaberger, C. L. Thomas, and J. R. Dahn, *J. Electrochem. Soc.*, **149**, A778 (2002).

12. Y. S. Meng, G. Ceder, C. P. Grey, W. S. Yoon, M. Jiang, J. Bréger, and Y. Shao-Horn, *Chem. Mater.*, **17**, 2386 (2005).
13. N. Tran, L. Croguennec, C. Labrugère, C. Jordy, P. Biensan, and C. Delmas, *J. Electrochem. Soc.*, **153**, A261 (2006).
14. M. M. Thackeray, S.-H. Kang, C. S. Johnson, J. T. Vaughey, R. Benedek, and S. A. Hackney, *J. Mater. Chem.*, **17**, 3112 (2007).
15. J. Bréger, M. Jiang, N. Dupré, Y. S. Meng, Y. Shao-Horn, G. Ceder, and C. P. Grey, *J. Solid State Chem.*, **178**, 2575 (2005).
16. K. A. Jarvis, Z. Deng, L. F. Allard, A. Manthiram, and P. J. Ferreira, *Chem. Mater.*, **23**, 3614 (2011).
17. J.-S. Kim, C. S. Johnson, J. T. Vaughey, M. M. Thackeray, S. A. Hackney, W. Yoon, and C. P. Grey, *Chem. Mater.*, **16**, 1996 (2004).
18. M. M. Thackeray, C. S. Johnson, J. T. Vaughey, N. Li, and S. A. Hackney, *J. Mater. Chem.*, **15**, 2257 (2005).
19. Z. Lu and J. R. Dahn, *J. Electrochem. Soc.*, **149**, A815 (2002).
20. N. Tran, L. Croguennec, M. Ménétrier, F. Weill, P. Biensan, C. Jordy, and C. Delmas, *Chem. Mater.*, **20**, 4815 (2008).
21. A. R. Armstrong, M. Holzapfel, P. Novák, C. S. Johnson, S.-H. Kang, M. M. Thackeray, and P. G. Bruce, *J. Am. Chem. Soc.*, **128**, 8694 (2006).
22. F. La Mantia, F. Rosciano, N. Tran, and P. Novák, *J. Appl. Electrochem.*, **38**, 893 (2008).
23. D. Streich, A. Guéguen, M. Mendez, F. Chesneau, P. Novák, and E. J. Berg, *J. Electrochem. Soc.*, **163**, A964 (2016).
24. H. Yu, H. Kim, Y. Wang, P. He, D. Asakura, Y. Nakamura, and H. Zhou, *Phys. Chem. Chem. Phys.*, **14**, 6584 (2012).
25. N. Yabuuchi, K. Yoshii, S.-T. Myung, I. Nakai, and S. Komaba, *J. Am. Chem. Soc.*, **133**, 4404 (2011).
26. H. Koga, L. Croguennec, M. Ménétrier, P. Mannessiez, F. Weill, C. Delmas, and S. Belin, *J. Phys. Chem. C*, **118**, 5700 (2014).
27. K. Luo, M. R. Roberts, R. Hao, N. Guerrini, D. M. Pickup, Y.-S. Liu, K. Edström, J. Guo, A. V. Chadwick, L. C. Duda, and P. G. Bruce, *Nat. Chem.*, **8**, 684 (2016).
28. A. Boulineau, L. Simonin, J.-F. Colin, E. Canévet, L. Daniel, and S. Patoux, *Chem. Mater.*, **24**, 3558 (2012).
29. A. Boulineau, L. Simonin, J.-F. Colin, C. Bourbon, and S. Patoux, *Nano Lett.*, **13**, 3857 (2013).
30. C. Genevois, H. Koga, L. Croguennec, M. Ménétrier, C. Delmas, and F. Weill, *J. Phys. Chem. C*, **119**, 75 (2015).
31. S. Meini, M. Piana, N. Tsiouvaras, A. Garsuch, and H. A. Gasteiger, *Electrochem. Solid-State Lett.*, **15**, A45 (2012).
32. N. Tsiouvaras, S. Meini, I. Buchberger, and H. A. Gasteiger, *J. Electrochem. Soc.*, **160**, A471 (2013).
33. F. Amalraj, M. Talianker, B. Markovsky, D. Sharon, L. Burlaka, G. Shafir, E. Zinigrad, O. Haik, D. Aurbach, J. Lampert, M. Schulz-Dobrick, and A. Garsuch, *J. Electrochem. Soc.*, **160**, A324 (2012).
34. J. R. Croy, K. G. Gallagher, M. Balasubramanian, Z. Chen, Y. Ren, D. Kim, S.-H. Kang, D. W. Dees, and M. M. Thackeray, *J. Phys. Chem. C*, **117**, 6525 (2013).
35. M. Metzger, B. Strehle, S. Solchenbach, and H. A. Gasteiger, *J. Electrochem. Soc.*, **163**, A798 (2016).
36. B. D. McCloskey, D. S. Bethune, R. M. Shelby, G. Girishkumar, and A. C. Luntz, *J. Phys. Chem. Lett.*, **2**, 1161 (2011).
37. S. Meini, N. Tsiouvaras, K. U. Schwenke, M. Piana, H. Beyer, L. Lange, and H. A. Gasteiger, *Phys. Chem. Chem. Phys.*, **15**, 11478 (2013).
38. K. Matsumoto, R. Kuzuo, K. Takeya, and A. Yamanaka, *J. Power Sources*, **81–82**, 558 (1999).
39. N. Mijung, Y. Lee, and J. Cho, *J. Electrochem. Soc.*, **153**, A935 (2006).
40. S.-W. Lee, H. Kim, M.-S. Kim, H.-C. Youn, K. Kang, B.-W. Cho, K. C. Roh, and K.-B. Kim, *J. Power Sources*, **315**, 261 (2016).
41. S. A. Freunberger, Y. Chen, Z. Peng, J. M. Griffin, L. J. Hardwick, F. Bardé, P. Novák, and P. G. Bruce, *J. Am. Chem. Soc.*, **133**, 8040 (2011).
42. V. S. Bryantsev, V. Giordani, W. Walker, M. Blanco, S. Zecevic, K. Sasaki, J. Uddin, D. Addison, and G. V. Chase, *J. Phys. Chem. A*, **115**, 12399 (2011).
43. M. Stylidi, D. I. Kondarides, and X. E. Verykios, *Appl. Catal. B Environ.*, **47**, 189 (2004).
44. N. Yabuuchi, Y.-T. Kim, H. H. Li, and Y. Shao-Horn, *Chem. Mater.*, **20**, 4936 (2008).
45. S.-M. Bak, K.-W. Nam, W. Chang, X. Yu, E. Hu, S. Hwang, E. A. Stach, K.-B. Kim, K. Y. Chung, and X.-Q. Yang, *Chem. Mater.*, **25**, 337 (2013).
46. S.-M. Bak, E. Hu, Y. Zhou, X. Yu, S. D. Senanayake, S.-J. Cho, K.-B. Kim, K. Y. Chung, X.-Q. Yang, and K.-W. Nam, *ACS Appl. Mater. Interfaces*, **6**, 22594 (2014).
47. A. K. Shukla, Q. M. Ramasse, C. Ophus, H. Duncan, F. Hage, and G. Chen, *Nat. Commun.*, **6**, 8711 (2015).
48. B. Qiu, M. Zhang, L. Wu, J. Wang, Y. Xia, D. Qian, H. Liu, S. Hy, Y. Chen, K. An, Y. Zhu, Z. Liu, and Y. S. Meng, *Nat. Commun.*, **7**, 12108 (2016).
49. H. Koga, L. Croguennec, P. Mannessiez, M. Ménétrier, F. Weill, L. Bourgeois, M. Duttine, E. Suard, and C. Delmas, *J. Phys. Chem. C*, **116**, 13497 (2015).
50. P. Yan, A. Nie, J. Zheng, Y. Zhou, D. Lu, X. Zhang, R. Xu, I. Belharouak, X. Zu, J. Xiao, K. Amine, J. Liu, F. Gao, R. Shahbazian-Yassar, J.-G. Zhang, and C.-M. Wang, *Nano Lett.*, **15**, 514 (2015).
51. D. P. Abraham, R. D. Twesten, M. Balasubramanian, I. Petrov, J. McBreen, and K. Amine, *Electrochem. Commun.*, **4**, 620 (2002).
52. S. Muto, Y. Sasano, K. Tatsumi, T. Sasaki, K. Horibuchi, Y. Takeuchi, and Y. Ukyo, *J. Electrochem. Soc.*, **156**, A371 (2009).
53. L. Wu, K.-W. Nam, X. Wang, Y. Zhou, J.-C. Zheng, X.-Q. Yang, and Y. Zhu, *Chem. Mater.*, **23**, 3953 (2011).
54. S.-K. Jung, H. Gwon, J. Hong, K.-Y. Park, D.-H. Seo, H. Kim, J. Hyun, W. Yang, and K. Kang, *Adv. Energy Mater.*, **4**, 1300787 (2014).
55. R. Jung, M. Metzger, F. Maglia, C. Stinner, and H. A. Gasteiger, Manuscript in preparation.
56. J. Hong, H. D. Lim, M. Lee, S. W. Kim, H. Kim, S. T. Oh, G. C. Chung, and K. Kang, *Chem. Mater.*, **24**, 2692 (2012).
57. A. Guéguen, D. Streich, M. He, M. Mendez, F. F. Chesneau, P. Novák, and E. J. Berg, *J. Electrochem. Soc.*, **163**, A1095 (2016).

Supporting Information for

The Role of Oxygen Release from Li- and Mn-Rich Layered Oxides During the First Cycles Investigated by On-Line Electrochemical Mass Spectrometry

Benjamin Strehle,[a,*,z] Karin Kleiner,[a,*] Roland Jung,[a,*] Frederick Chesneau,[b] Manuel Mendez,[b] Hubert A. Gasteiger,[a,**] and Michele Piana[a,***]

[a] *Chair of Technical Electrochemistry, Department of Chemistry and Catalysis Research Center, Technische Universität München, D-85748 Garching, Germany*

[b] *BASF SE, GCN/EE – M311, D-67056 Ludwigshafen, Germany*

* Electrochemical Society Student Member.
** Electrochemical Society Fellow.
*** Electrochemical Society Active Member.
[z] E-mail: benjamin.strehle@tum.de

1) XRD of the pristine material and after the first cycle

Figure S1 shows the XRD patterns of the pristine material and of an electrode after the first cycle. The weak reflections between 9 and 12° arise from the Li^+ ordering in the transition metal plane and are a clear indication for Li- and Mn-rich layered oxide materials. The bulk structure of the material is maintained after the first activation cycle.

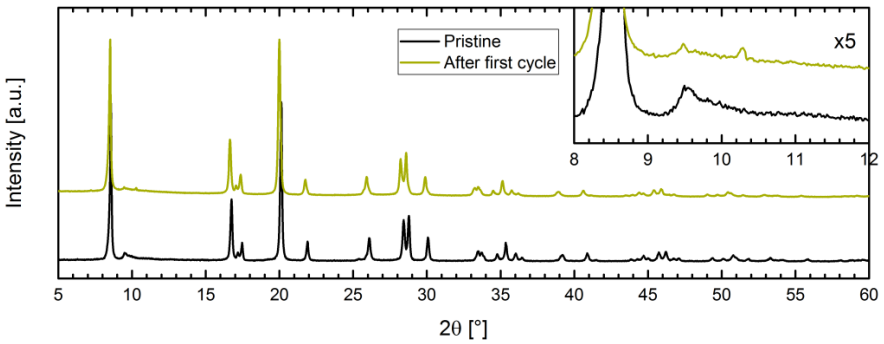

Figure S1. XRD patterns of the pristine material and from an electrode harvested in the discharged state after the first cycle. The intensity is normalized to the maximum intensity of the (003) reflection at 8.5°. The inset shows a magnification of the weak reflections between 9 and 12°. The XRD patterns were obtained in a 0.3 mm borosilicate capillary as sample holder (Debye-Scherrer geometry) with a STOE STADI P diffractometer (STOE, Germany) using Mo-$K_{\alpha 1}$ radiation (λ = 0.70932 Å, 50 kV, 40 mV) and a Mythen 1K detector.

2) Oxygen release due to Li_2MnO_3 activation

In the following section, the theoretical amount of oxygen evolved according to Eq. 1 in the main part is calculated. For this calculation, the following notation of our HE-NCM material is used: 0.42 Li_2MnO_3 • 0.58 $Li[Ni_{0.38}Co_{0.21}Mn_{0.41}]O_2$, corresponding to a molar mass of 104.8 g mol^{-1}. Assuming that the complete Li_2MnO_3 phase is converted into MnO_2, the expected amount of evolved O_2 would be

$$n^{\text{theor}}_{O_2,Li_2MnO_3} = \frac{1}{2} \cdot \frac{0.42}{104.8\ \text{g mol}^{-1}} \approx 2000\ \mu\text{mol}_{O_2}\ \text{g}^{-1}_{\text{AM}} \qquad \text{[S1]}$$

Using Faraday's law and $4e^-/O_2$, the gas evolution would lead to a charge capacity of ≈215 mAh g^{-1}_{AM}. Analogous to Eq. S1, the overall oxygen (as O_2) in the HE-NCM structure amounts to

$$n^{\text{theor}}_{O_2,\text{HE-NCM}} = \frac{1}{2} \cdot \frac{3 \cdot 0.42 + 2 \cdot 0.58}{104.8\ \text{g mol}^{-1}} \approx 11.5\ \text{mmol}_{O_2}\ \text{g}^{-1}_{\text{AM}} \qquad \text{[S2]}$$

This means that ca. 17% of the total oxygen in the HE-NCM lattice have to be extracted in case of a quantitative conversion of the Li_2MnO_3 phase according to Eq. 1.

3) O_2 and CO_2 solubility in the electrolyte

The O_2 concentration in the electrolyte can be derived from the so-called Bunsen coefficient, α. It is defined as the volume of gas, reduced to 273.15 K and 1 atm, which is adsorbed by unit volume of solvent (at the temperature of measurement) under a partial pressure of 1 atm (in units of $cm^3_{gas}\ cm^{-3}_{liquid}$).[S1] In the case of organic carbonates such as EC, PC, DMC, and DEC, measured as 1:1 binary mixtures with 1 M $LiPF_6$ at 25°C, the Bunsen coefficient of O_2 ranges from $\alpha \approx 0.05$ to 0.1.[S1] By applying the ideal gas law, this values translate to a concentration of ca. 2-4 mM O_2 in the electrolyte (which is consistent with 4.8 mM measured for 0.2 M TBATFSI in PC in a rotating ring-disk electrode study[S2]). For our electrolyte LP57 (1 M $LiPF_6$ in EC:EMC 3:7 by weight) we can suppose a similar solubility.

As the actual concentration in the electrolyte scales linearly with the applied partial pressure of O_2 (according to Henry's law), one has to find a general expression for the amount in the liquid phase, $n_{O_2,l}$, relative to the amount in the gas phase, $n_{O_2,g}$. The O_2 amount in the liquid phase is given by the Bunsen coefficient, the volume of liquid, V_l, and the molar fraction of O_2 in the gas phase, $x_{O_2,g}$,

$$n_{O_2,l} = \frac{V_{O_2,l}}{V_{m,l}} = \frac{\alpha \cdot V_l}{V_{m,l}} \cdot x_{o_2,g} \qquad [S3]$$

where $V_{m,l} = 22.414\ l\ mol^{-1}$ is the molar volume following the definition of the Bunsen coefficient (0°C and 1 atm). The molar fraction includes the partial pressure of O_2, $x_{O_2,g} = p_{O_2}/p^o$ (p^o = 1 atm).

The O_2 amount in the gas phase is defined by the cell volume, V_{OEMS}, and also $x_{O_2,g}$,

$$n_{O_2,g} = \frac{V_{O_2,g}}{V_{m,g}} = \frac{V_{OEMS}}{V_{m,g}} \cdot x_{o_2,g} \qquad [S4]$$

where $V_{m,g} = 24.465\ l\ mol^{-1}$ is the molar volume at the measurement conditions (25°C and 1 atm).

Consequently, the ratio $n_{O_2,l}/n_{O_2,g}$ can be calculated independently of the partial pressure as follows:

$$\frac{n_{O_2,l}}{n_{O_2,g}} = \frac{\alpha \cdot V_l}{V_{OEMS}} \cdot \frac{V_{m,g}}{V_{m,l}} = \frac{0.1 \cdot 100 \cdot 10^{-6}\ l}{10 \cdot 10^{-3}\ l} \cdot \frac{24.465\ l\ mol^{-1}}{22.414\ l\ mol^{-1}} = 1.1 \cdot 10^{-3} \qquad [S5]$$

Using the higher limit of the Bunsen coefficient ($\alpha = 0.1$), V_l = 100 µl, and V_{OEMS} = 10 ml, the fraction of O_2 dissolved in the electrolyte corresponds to ca. 0.1% relative to the gaseous O_2 and is thus negligible for the further analysis.

As the CO_2 solubility in the electrolyte is roughly one order of magnitude higher than O_2,[S3] the error amounts here to ca. 1%.

4) Literature overview about the formation of a spinel layer

There are several (S)TEM studies in the literature where a spinel-like surface layer was identified on Li- and Mn-rich layered oxides. A brief overview is provided in the following Table S1. Depending on the investigated conditions, a few nm thick spinel layer was either found on the pristine material,[S4] after the first cycle,[S7-S9] or during continuous cycling.[S10] Similar to the O_2 evolution at the end of the first charge, Qiu et al. have formed a ≈2 nm thick spinel/rock-salt-like phase by chemically creating oxygen vacancies on their material.[S5] Furthermore, Koga et al. have shown that the layered phase is converted into a spinel-type phase above 940°C during thermal treatment.[S6] This thermally induced phase transformation supports the analogy to the formation of a spinel surface layer through charging at high potentials.

Table S1. Overview of the literature which identified a spinel surface layer on Li- and Mn-rich layered oxides. For better comparison, the composition is given in the same way for all the materials, $Li_{1+x}Me_{1-x}O_2$. The abbreviations of the applied techniques stand for (scanning) transmission electron microscopy ((S)TEM), electron energy loss spectroscopy (EELS), X-ray energy dispersive spectroscopy (XEDS), thermal gravimetric analysis (TGA), and X-ray diffraction (XRD).

Reference	Material	Technique	Condition	Result
This work	$Li_{1.17}[Ni_{0.22}Co_{0.12}Mn_{0.66}]_{0.83}O_2$ = $Li_{1.17}Ni_{0.18}Co_{0.10}Mn_{0.55}O_2$	OEMS	After 1st charge	≈2-3 nm thick spinel-like surface layer calculated from evolved O_2 (and CO_2)
S4	$Li_{1.20}Ni_{0.13}Co_{0.13}Mn_{0.54}O_2$	STEM, EELS, XEDS	Pristine	≈2 nm thick Co- and/or Ni-rich spinel with antisite defects (on selected surface facets)
S5	$Li_{1.144-2x}Ni_{0.136}Co_{0.136}Mn_{0.544}O_{2-x}$ (with chemically created O vacancies on the surface)	(S)TEM, EELS	Pristine	≈2 nm thick spinel/rock-salt-like phase on the surface
S6	$Li_{1.20}Ni_{0.13}Co_{0.13}Mn_{0.54}O_2$	TGA, XRD	Variation of synthesis temperature	Spinel-type phase above 940°C (bulk transformation due to heat treatment)
S7, S8	$Li_{1.20}Ni_{0.18}Mg_{0.01}Mn_{0.61}O_2$ (Co replaced by Mg)	(S)TEM, EELS	After 1st charge (and discharge)	≈2-3 nm thick defect spinel phase at the edge of the particles
S9	$Li_{1.20}Ni_{0.13}Co_{0.13}Mn_{0.54}O_2$	(S)TEM	After 1st cycle	"Splayered" domains (i.e., between layered and spinel) at the external part of the particles
S10	$Li_{1.20}Ni_{0.20}Mn_{0.60}O_2$ (Co-free material)	(S)TEM, EELS, XEDS	Continuous cycling (100 cycles)	Ni-enriched surface reconstruction layer, sequential phase transition of $C2/m \rightarrow I41 \rightarrow$ Spinel

5) Oxygen release due to spinel transformation

According to the general Eq. 2, the gas evolution accompanied by the spinel transformation depends on the exact stoichiometry $Li_xMe_yO_2$, including the fraction of transition metal ions (y) and the degree of delithiation during charge (x). Regarding the first point, we consider the $Li_{1+x}Me_{1-x}O_2$ notation of the pristine material, $Li_{1.17}[Ni_{0.22}Co_{0.12}Mn_{0.66}]_{0.83}O_2$ (molar mass 86.8 g mol^{-1}), for which the theoretical delithiation capacity is ca. 360 mAh g$^{-1}_{AM}$. The degree of delithiation depends on the state of charge which was selected here at 4.6 V, where the O_2 (and CO_2) evolution due to spinel transformation starts. For the HE-NCM/Li measurement in Figure 3 (black lines), the charge capacity at 4.6 V accounts to ≈275 mAh g$^{-1}_{AM}$. Consequently, 76% of the theoretically available charge have been extracted, and if we assume that this capacity comes only from delithiation, 0.89 of the 1.17 lithium in the structure have been removed. Thus, the corresponding composition of the material at 4.6 V is $Li_{0.28}[Ni_{0.22}Co_{0.12}Mn_{0.66}]_{0.83}O_2$ ($Li_{0.28}Me_{0.83}O_2$, Me = Ni, Co, Mn), which undergoes the spinel transformation as written in Eq. 4. The theoretical amount of evolved O_2 for the complete conversion of the layered oxide of that composition into the spinel phase would be

$$n^{\text{theor}}_{O_2,\text{spinel}} = \frac{0.26}{86.8\ \text{g mol}^{-1}} \approx 3000\ \mu\text{mol}_{O_2}\ \text{g}^{-1}_{AM} \qquad [S6]$$

The molar fraction of the spinel phase, x_{spinel}, can be calculated by comparing this value to the measured gas evolution of O_2 and CO_2 derived from lattice oxygen:

$$x_{\text{spinel}} = \frac{n^{\text{meas}}_{O_2,\text{spinel}}}{n^{\text{theor}}_{O_2,\text{spinel}}} \leq 1 \qquad [S7]$$

6) Thickness of the spinel layer

Since we believe that the spinel transformation proceeds from the outer to the inner part of the HE-NCM particles, the spinel phase is formed as a spherical shell as depicted in Figure S2. In order to keep our model simple, we assume spherical primary particles. Their average radius is calculated from the BET surface area, A_{BET}, and the crystallographic density, ϱ, of the pristine material as follows:

$$r = \frac{3}{A_{\text{BET}} \cdot \varrho} \approx 110\ \text{nm} \qquad [S8]$$

We calculated the thickness of the spinel surface layer using the following geometrical relation of a spherical shell:

$$\frac{V_{\text{shell}}}{V} = \frac{r^3 - r'^3}{r^3} = 1 - \left(\frac{r'}{r}\right)^3 = x_{\text{spinel}} \leftrightarrow r' = r \cdot \left(1 - x_{\text{spinel}}\right)^{\frac{1}{3}} \qquad [S9]$$

$$t_{\text{spinel}} = r - r' \qquad [S10]$$

Taking the simplifying approximation that the density and molar mass of the layered oxide and the spinel phase are roughly the same, the volume ratio V_{shell}/V equals the molar fraction of the spinel phase, x_{spinel}.

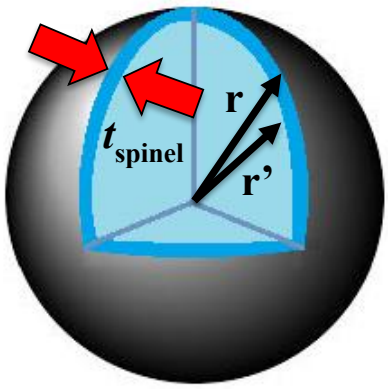

Figure S2. Schematic of the HE-NCM particles. The spinel phase is formed as a spherical shell with the thickness t_{spinel}.

References

S1. J. Read, K. Mutolo, M. Ervin, W. Behl, J. Wolfenstine, A. Driedger, and D. Foster, *J. Electrochem. Soc.*, **150**, A1351 (2003).

S2. J. Herranz, A. Garsuch, and H. A. Gasteiger, *J. Phys. Chem. C*, **116**, 19084 (2012).

S3. P. Kolář, H. Nakata, J.-W. Shen, A. Tsuboi, H. Suzuki, and M. Ue, *Fluid Phase Equilib.*, **228-229**, 59 (2005).

S4. A. K. Shukla, Q. M. Ramasse, C. Ophus, H. Duncan, F. Hage, and G. Chen, *Nat. Commun.*, **6**, 8711 (2015).

S5. B. Qiu, M. Zhang, L. Wu, J. Wang, Y. Xia, D. Qian, H. Liu, S. Hy, Y. Chen, K. An, Y. Zhu, Z. Liu, and Y. S. Meng, *Nat. Commun.*, **7**, 12108 (2016).

S6. H. Koga, L. Croguennec, P. Mannessiez, M. Ménétrier, F. Weill, L. Bourgeois, M. Duttine, E. Suard, and C. Delmas, *J. Phys. Chem. C*, **116**, 13497 (2012).

S7. A. Boulineau, L. Simonin, J.-F. Colin, E. Canévet, L. Daniel, and S. Patoux, *Chem. Mater.*, **24**, 3558 (2012).

S8. A. Boulineau, L. Simonin, J.-F. Colin, C. Bourbon, and S. Patoux, *Nano Lett.*, **13**, 3857 (2013).

S9. C. Genevois, H. Koga, L. Croguennec, M. Ménétrier, C. Delmas, and F. Weill, *J. Phys. Chem. C*, **119**, 75 (2015).

S10. P. Yan, A. Nie, J. Zheng, Y. Zhou, D. Lu, X. Zhang, R. Xu, I. Belharouak, X. Zu, J. Xiao, K. Amine, J. Liu, F. Gao, R. Shahbazian-Yassar, J.-G. Zhang, and C.-M. Wang, *Nano Lett.*, **15**, 514 (2015).

3.2.2 Surface Reconstruction Initiated by Oxygen Release

This section presents the article "Oxygen Release and Surface Degradation of Li- and Mn-Rich Layered Oxides in Variation of the Li_2MnO_3 Content".[27] The manuscript was submitted in June 2018 and published in August 2018 as peer-reviewed publication in the *Journal of The Electrochemical Society*. It is published as an "open access" article and distributed under the terms of the Creative Commons Attribution Non-Commercial No Derivatives 4.0 License. The article was presented as Paper 36 by Tobias Teufl at the 231st Meeting of the Electrochemical Society in New Orleans, Louisiana, USA (May 28-June 1, 2017). The permanent weblink of the article is: https://iopscience.iop.org/article/10.1149/2.0691811jes.

The preceding section 3.2.1 analyzed the gassing behavior of a Li- and Mn-rich layered oxide, x Li_2MnO_3 · (1-x) $LiMO_2$, with a medium degree of over-lithiation (x = 0.42). In this comparative study, we have a closer look on the oxygen release and electrochemical performance of three over-lithiated CAMs with different Li_2MnO_3 content, ranging from x = 0.33 to 0.42 to 0.50, respectively.

Increasing the Li_2MnO_3 content magnifies the reversible anionic redox through an extended voltage plateau at ≈4.5 V vs. Li^+/Li, but at the same time it also increases the irreversible oxygen loss at the end of the first charge. The evolved amount of O_2 from the CAMs increases from ≈6 µmol/g for 0.33 Li_2MnO_3 by two orders of magnitude to ≈550 µmol/g for 0.50 Li_2MnO_3. The OEMS data are complemented by electrochemical half-cell data and HRTEM images of pristine and cycled electrodes. The HRTEM analysis proves the formation of a disordered, spinel-like phase, which is restricted to a near-surface layer of ≈1-2 nm for 0.33 Li_2MnO_3 and ≈4 nm for 0.42 Li_2MnO_3, as expected from the mathematical model of the gassing data introduced in the former section.[155] For 0.50 Li_2MnO_3, however, the spinel fraction of ≈20 mol% leads to a partial collapse of the bulk structure, such that spinel-like domains also grow into the interior of the particles. This finding is the most likely explanation why previous studies, using primarily highly over-lithiated CAMs with 0.50 Li_2MnO_3, proposed the bulk oxygen release through the activation of the Li_2MnO_3 component.[109,124] The spinel phase is further identified by its characteristic dQ/dV peak at ≈3.1 V vs. Li^+/Li in the half-cell data. Here, the oxygen-depleted, highly conductive phase formed in the very first cycles transform gradually within

≈20 cycles into a densified, more resistive spinel phase. The concomitant capacity loss can be explained quantitatively by the spinel fraction estimated from the OEMS data and by considering the capacity difference between the layered oxide (250 mAh/g) and the spinel (140 mAh/g).

Finally, we investigate the full-cell performance of the three over-lithiated CAMs. Over the duration of 250 cycles, they all show virtually similar full-cell metrics, including the initial capacity, capacity retention as well as voltage and energy fading. This has two important implications: (i) The oxygen release is not related to voltage hysteresis and voltage fading, which are instead caused by bulk phenomena such as (ir)reversible transition-metal migration.[159,188,192] (ii) By combining a reasonable full-cell performance with a low gas evolution in the initial cycles, the 0.33 Li_2MnO_3 material is the preferred choice for the application in large-format cells.[166,167]

Author contributions

T.T and B.S. conducted the OEMS experiments. T.T. and M.M. were in charge of the electrochemical characterization. P.M. carried out the TEM analysis. T.T. wrote and H.A.G. edited the manuscript. All authors discussed the results and commented on the manuscript.

A2718 *Journal of The Electrochemical Society*, **165** (11) A2718-A2731 (2018)

Oxygen Release and Surface Degradation of Li- and Mn-Rich Layered Oxides in Variation of the Li_2MnO_3 Content

Tobias Teufl,[1,2,*,z] **Benjamin Strehle,**[2,*] **Philipp Müller,**[1] **Hubert A. Gasteiger,**[2,**] **and Manuel A. Mendez**[1]

[1]*BASF SE Ludwigshafen, New Battery Materials and Systems, D-67056 Ludwigshafen, Germany*
[2]*Chair of Technical Electrochemistry, Department of Chemistry and Catalysis Research Center, Technical University of Munich, D-85748 Garching, Germany*

In this study, we will show how the oxygen release depends on the Li_2MnO_3 content of the material and how it affects the actual voltage fading of the material. Thus, we compared overlithiated NCMs (x Li_2MnO_3 • (1-x) $LiMeO_2$; Me = Ni, Co, Mn) with x = 0.33, 0.42 and 0.50, focusing on oxygen release and electrochemical performance. We could show that the oxygen release differs vastly for the materials, while voltage fading is similar, which leads to the conclusion that the oxygen release is a chemical material degradation, occurring at the surface, while voltage fading is a bulk issue of these materials. We could prove this hypothesis by HRTEM, showing a surface layer, which is dependent on the amount of oxygen released in the first cycles and leads to an increase of the charge-transfer resistance of these materials. Furthermore, we could quantitatively deconvolute capacity contributions from bulk and surface regions by dQ/dV analysis and correlate them to the oxygen loss. As a last step, we compared the gassing to the base NCM ($LiMeO_2$, Me = Ni, Co, Mn), showing that surface degradation follows a similar reaction pathway and can be easily modulated by controlling the amount of Li_2MnO_3.

 [DOI: 10.1149/2.0691811jes]

Manuscript submitted June 15, 2018; revised manuscript received July 31, 2018. Published August 24, 2018. This was Paper 36 presented at the New Orleans, Louisiana, Meeting of the Society, May 28–June 1, 2017.

To face future issues, as global warming, air pollution, as well as the consumption of fossil fuels, an alternative is required to cover the future demand of energy and mobility in an environmentally friendly and sustainable way. In this context, lithium-ion batteries are viable options for large scale energy storage and for electric vehicles, as they have been used to power consumer electronics for many years.[1,2] Since graphite is an excellent anode material at potentials of ≈0.1 V vs. Li^+/Li with a roughly 2-fold higher specific capacity of about 360 mAh/g compared to currently used cathode active materials (CAMs), many efforts have been undertaken to increase the specific capacity and energy density of CAMs. As first practical cathode active material Lithium-Cobalt-Oxide (LCO) was investigated by Goodenough et al. in the 1980s, exhibiting a specific capacity of about 140 mAh/g and having a layered structure composed of lithium and transition metal layers.[3] As these layered structures showed good structural stability during lithium extraction and insertion, and therefore good capacity retention, many attempts have been undertaken to further develop alternative layered structures which would offer higher capacity. One promising attempt that led to the currently used Lithium-Nickel-Cobalt-Manganese-Oxides (NCMs) is to change the occupancy of the transition metal layer by not using exclusively cobalt, but also introducing nickel and manganese into the transition metal layer; hereby it was found that nickel shows a high redox activity, while manganese helps to stabilize the structure during lithium extraction.[4–6] By using different transition metals and metal compositions, a playground has been created that allows to tune the properties of the material: while initially a Ni:Co:Mn ratio of 1:1:1 was used (also referred to as NCM-111), trends nowadays favor the so-called Ni-rich NCMs, for example with a Ni:Co:Mn ratio of 8:1:1, which yield higher capacities at practicable potentials.[6,7] However, it has been shown that all NCM materials show structural instabilities at high state-of-charge (SOC), i.e., at a high degree of delithiation, leading to oxygen release from the near-surface region accompanied by the formation of a resistive surface layer; ultimately, this leads to rapid capacity fading and limits the practical capacity of NCM materials to <200 mAh/g. [8–10]

Therefore, in the 2000s the concept of lithium- and manganese-rich NCM materials was investigated by preparing a Li_2MnO_3 domain within an NCM material in a certain composition, leading to x Li_2MnO_3 • (1-x) $LiMeO_2$ (Me = Ni, Co, Mn), also referred to as High-Energy NCM (HE-NCM), with which high reversible capacities of ≈250 mAh/g can be achieved.[11] However, these materials exhibit serious issues that so far has hindered its commercialization, such as a decrease of the average discharge voltage over extended charge/discharge cycling (commonly referred to as voltage fading), a large hysteresis between charge and discharge voltage, as well as high impedance.[12–14] Since the discovery of this class of materials, researchers have been trying to find an explanation for these high reversible capacities, as the capacities exceed the theoretical capacity limit that could be explained by the classical view of transition metal cation redox. Initially, it was thought that during the first cycle activation plateau at ≈4.5 V vs. Li^+/Li an electrochemical activation of redox inactive Li_2MnO_3 would take place, leading to a release of bulk lattice oxygen and to an electrochemically active $LiMnO_2$ phase which could charge compensate Li extraction to capacities >200 mAh/g.[15–18] This oxygen release was ascribed to cause strong structural changes within the bulk material, ultimately leading to a layered-to-spinel transformation of the particles. This transformation of the bulk material was believed to lead to the HE-NCM specific phenomena such as voltage fading and hysteresis.[12,19–22] However, this activation was suggested to be accompanied by an oxygen release from the bulk of the material, which was suggested from XRD data by Lu et al. in 2002.[19,20] At first sight, this seemed consistent with the mass spectrometrically detected O_2 and CO_2 evolution starting during the activation plateau, which was interpreted to indicate the release of Li_2O from the bulk of the material during activation and accompanying structural changes within the bulk material.[15,17,18,23,24] However, the exact quantification of the released oxygen by Strehle et al. and Luo et al. revealed that the amount of released oxygen is an order of magnitude too low to be consistent with the assumed electrochemical oxygen release[25,26] and also that the O_2 evolution does not start until right after the activation plateau (only <10 $\mu mol_{O2}/g_{AM}$ during the plateau, but >100 $\mu mol_{O2}/g_{AM}$ following thereafter; shown by Strehle et al.).[25] Both observations suggested that the observed oxygen release cannot be ascribed to a loss of oxygen from the bulk of the material, but that the oxygen is only being released from the near-surface

*Electrochemical Society Member.
**Electrochemical Society Fellow.
[z]E-mail: tobias-maximilian.teufl@basf.com

region of the HE-NCM material.[25] While this contradicted most of the literature on the mechanistics of the HE-NCM activation process, it was in accordance with the conclusions drawn by earlier work based on careful XRD, neutron diffraction, and high-resolution transmission electron microscopy.[27–29]

Thus, more recent studies propose that bulk and surface of these overlithiated materials show distinctly different properties, rationalized by a bulk-shell model.[25,27–29] It has been suggested that oxygen release takes places in near-surface region, leading to a chemical layered-to-spinel transformation and a concomitant impedance buildup by the formed resistive surface layer. This phenomenon has also been shown to be one of the main fading mechanisms for traditional NCM materials.[10,30] In contradiction to the bulk oxygen release, the recent literature gives strong evidence that reversible anionic oxygen redox participation in the bulk material can serve for charge compensation and therefore explain the high reversible capacities within this class of materials.[31–34] Therefore, it is suggested that high degrees of delithiation and reversible oxygen redox trigger reversible and irreversible transition metal migration within the bulk material, leading to voltage fading and to the large charge/discharge voltage hysteresis due to the hindered lithium diffusion within the bulk material.[14,35–38] In contradiction to the hypothesis of bulk oxygen release and bulk structural transformation, recent studies give clear evidence that the bulk structure is preserved, while a relatively small fraction of transition metals (about 10% over 100 cycles)[35] migrate reversibly and over extended charge/discharge cycling irreversibly between the transition metal and the lithium layers, leading to changes of the bulk material thermodynamics like the charge and discharge potentials as well as to the observed voltage fading.[25,35]

In this study, we will examine the effect of oxygen release onto the bulk and the surface structure of HE-NCM and correlate it with the macroscopic electrochemical performance of the material. These studies will be conducted with HE-NCM materials with different amounts of the Li_2MnO_3 phase (x = 0.33, 0.42 and 0.50 if referenced to x Li_2MnO_3 • (1-x) $LiMeO_2$), comparing the materials in terms of their oxygen release, their half- and full-cell performance as well as their impedance growth. These data will be complemented with high-resolution transmission electron microcopy (HRTEM) analysis of pristine and charge/discharge cycled materials. By on-line electrochemical mass spectrometry (OEMS) and HRTEM we prove that oxygen release above 4.6 V vs. Li^+/Li leads to a restructuration of the near-surface region, the extent of which increases with increasing over-lithiation and with increasing amounts of oxygen released during the first few cycles. Furthermore, while large differences are observed in the amount of oxygen released for the different materials, their electrochemical performance as well as their voltage fading behavior does not correlate with the extent of oxygen release. Thus, we propose that oxygen release does not have an influence on the bulk properties of HE-NCM, but rather affects the extent of surface restructuration/degradation.

Experimental

Electrode preparation.—HE-NCM with the compositions 0.33 Li_2MnO_3 • 0.67 $LiMeO_2$, 0.42 Li_2MnO_3 • 0.58 $LiMeO_2$, and 0.50 Li_2MnO_3 • 0.50 $LiMeO_2$ was obtained from BASF SE (Germany) and synthesized by the same procedure. While the exact Ni:Co:Mn ratio of the base NCM cannot be disclosed, the $LiMeO_2$ domain was held constant for all materials used in this study, while only the amount of Li_2MnO_3 was varied from 0.00 up to 0.50. The sum formula for the materials was x Li_2MnO_3 • (1-x) $LiMeO_2$ (x = 0.00, 0.33, 0.42, 0.50), whereby the x = 0.42 material is identical what that used by Strehle et al.[25] For coin cell testing, inks for cathode electrode preparation consisted of 92.5 wt% HE-NCM (BASF SE, Germany), 3.5 wt% polyvinylidene-fluoride binder (PVDF, Solef 5130, Solvay, Belgium), 2 wt% conductive carbon (Super-C65, Timcal, Switzerland; BET area of ≈65 m^2/g), and 2 wt% graphite (SFG6L, Timcal, Switzerland; BET area of ≈17 m^2/g). The materials were dispersed in N-methyl pyrrolidine (NMP, anhydrous, Sigma-Aldrich, USA) and coated onto aluminum foil (16 μm). Dried electrodes were calendered to a density of 2.3 g/cm^3, calandered electrodes had final electrode thickness of 20 μm. For electrochemical testing, electrodes with a diameter of 14 mm were punched out, ending up with an active material loading of ≈6.5 mg/cm^2, corresponding to ≈1.6 mAh/cm^2, based on a nominal reversible capacity of 250 mAh/g.

Electrodes for OEMS measurements were prepared by dispersing 96 wt% HE-NCM or the base NCM without Li_2MnO_3 (BASF SE, Germany), 2 wt% conductive carbon (Super-C65, Timcal, Switzerland), and 2 wt% PVDF binder (Kynar HSV 900, Arkema, France) in NMP (anhydrous, Sigma-Aldrich, USA). A high solid content of 71% for the slurry was chosen to enable coating onto a porous stainless-steel mesh (SS316, aperture 26 μm, wire diameter 25 μm, The Mesh Company Ltd., UK). The slurry was coated with a wet film thickness of 20 μm onto the stainless-steel mesh, yielding a HE-NCM loading of ≈8.5 mg/cm^2, corresponding to ≈2.1 mAh/cm^2. Electrodes for OEMS experiments were punched out with a diameter of 15 mm and compressed for 20 s with 2.5 tons.

Graphite electrodes were commercial electrodes with a graphite loading of ≈6.7 mg/cm^2, corresponding to ≈2.4 mAh/cm^2 (based on a theoretical capacity of 360 mAh/g); for electrochemical testing, graphite electrodes with a diameter of 15 mm were punched out. All anode and cathode electrodes were dried overnight under vacuum in an oven within the glove box (O_2, H_2O < 0.1 ppm, MBraun, Germany) at 120°C and were not exposed to air after the drying procedure. For some experiments, graphite anodes were preformed in coin half-cells: cells were cycled for two cycles with a discharge rate of C/15 down to 0.025 V vs. Li^+/Li followed by a 1 h CV step at this potential and a subsequent charge at C/15 up to 1.5 V vs. Li^+/Li; then, the cells were disassembled at 1.5 V in a glove box (O_2, H_2O < 0.1 ppm, MBraun, Germany). These preformed graphite electrodes were used for full-cell assembly without any further washing step.

On-line electrochemical mass spectrometry (OEMS).—For OEMS experiments, electrodes coated onto a stainless-steel mesh (see above) were used to have a porous medium as current collector in order to allow diffusion from the electrode to the capillary.[25] For OEMS measurements a custom-made cell is used; the cell design as well as the OEMS setup were reported previously.[39] OEMS cells were assembled with Li metal counter electrode, two porous polyolefin separators (2500, Celgard, USA), a HE-NCM or NCM working electrode and 120 μl of electrolyte composed of FEC:DEC (2:8 g:g) and 1 M $LiPF_6$ (BASF SE, Germany). The cells were connected to the mass spectrometer, held for 4 h at OCV (open circuit voltage), and then charged to 4.8 V vs. Li^+/Li at a C/10 rate, followed by a 1 h CV step at 4.8 V vs. Li^+/Li; the discharge to 2.0 V vs. Li^+/Li and the second charge/discharge cycle were conducted at C/5 rate between 4.8 V vs Li^+/Li (+1 h CV) and 2.0 V vs Li^+/Li (C-rates here are calculated based on a nominal capacity of 250 mAh/g). For quantification of the mass spectrometer currents, a calibration gas containing H_2, O_2, CO_2, C_2H_4 (each 2000 ppm) in Argon (Linde AG, Germany) was used. All currents were normalized to the current at m/z = 36 (Ar isotope) in order to correct for effects of minor pressure and temperature deviations, and afterwards the currents m/z = 32 (O_2) and m/z = 44 (CO_2) were converted into gas concentration.

Electrochemical characterization.—Galvanostatic cycling was carried out in 2032-type coin-cells (Hohsen Corp., Japan) at 25°C in a temperature controlled oven (Binder, Germany) and using a battery cycler (Series 4000, Maccor, USA). Half-cells were assembled in an argon filled glove box (O_2, H_2O < 0.1 ppm, MBraun, Germany) using a Li metal anode with a diameter of 17 mm, three glass fiber separators (glass microfiber, GF/A, VWR, Germany), and an HE-NCM cathode (coated on Al current collector) with a diameter of 14 mm. The cells were filled with 120 μL electrolyte (FEC:DEC (2:8 g:g) with 1 M $LiPF_6$; BASF SE, Germany). For impedance measurements in symmetrical cells, charge/discharge cycled half-cells were charged to 50% SOC in the final cycle (based on the preceding complete charge-discharge cycle) and afterwards the cathodes were harvested in an argon filled glove box. Subsequently, two harvested cathodes from cells cycled with the same procedure were reassembled for impedance

A2720 Journal of The Electrochemical Society, 165 (11) A2718-A2731 (2018)

measurements into a symmetric coin cell with one thick glass fiber separator (300 μm thickness; glass microfiber filter, GF/D, VWR, Germany) and 95 μL of the same FEC:DEC electrolyte. For full-cell experiments in 2032 coin-cells, a graphite anode with a diameter of 15 mm and a cathode with a diameter of 14 mm were assembled with one polyethylene separator (2500, Celgard, USA) and with 14 μL of electrolyte based on FEC:DEC with 1 M $LiPF_6$ with an additional confidential co-solvent to improve full-cell cycling stability. For proof of reproducibility, at least two independent measurements were carried out and the here presented cycling data show the average values while the error bars reflect the maximum and minimum of the measured values.

All cells were allowed to rest for 2 hours prior to electrochemical testing and C-rates are referenced to a nominal capacity of 250 mAh/g. For half-cells, the first activation cycle was conducted at C/10 up to 4.8 V, followed by a 1 h CV-step at this potential and a discharge at C/5 to 2.0 V. The second charge/discharge cycle was conducted at C/5 and also charged up to 4.8 V, followed by 1 h CV-step at 4.8 V and a discharge at C/5 to 2.0 V (up to this point identical with the OEMS cycling procedure). The subsequent charge/discharge cycles at C/5 had a reduced upper cutoff potential of 4.7 V without a CV-step and the same lower cutoff potential of 2.0 V (CC/CC charge/discharge procedure).

Full-cells were activated in the first cycle at a C-rate of C/15 to 4.7 V (corresponding to ≈4.8 V vs. Li^+/Li, as in the half-cell and OEMS measurements), followed by a 1-hour CV-step at this potential (CCCV charge), and then discharged at C/15 to 2.0 V (CC); in subsequent cycles, the upper cutoff and CV-step potential were reduced to 4.6 V. Afterwards 4 cycles at C/10 were applied (CCCV), followed by a rate test for which the cell was charged/discharged for 3 cycles each at 0.2C (CCCV)/0.5C (CC), 0.5C (CCCV)/1C (CC), 0.5C (CCCV)/2C (CC), 0.5C (CCCV)/3C (CC), whereby all CV-steps were terminated after 1 h or when the current decreased below 0.01C. The rate test was followed by 250 cycles with a charge rate of 0.5C (CCCV) and a discharge rate of 1C (CC), the CV-step defined as above.

High-resolution transmission electron microscopy (HRTEM).— Cathodes for HRTEM measurements were obtained from half-cell coin-cells which had been cycled at C/5 for 2 or 50 cycles (see above for cell assembly and half-cell cycling procedure). The electrodes were harvested at 0% SOC (cells discharged to 2.0 V), corresponding to a fully lithiated cathode material. After cycling, cathodes were harvested in an argon filled glove-box and then washed for 5 minutes first in an FEC:DEC (2:8 g:g) solvent mixture and then in pure DEC (BASF SE, Germany). Subsequently, the electrodes were dried overnight at room temperature inside the glove box.

Samples for transmission electron microscopy (TEM) were prepared by focused ion beam (FIB) milling using a Strata 400 dualbeam machine (FEI Company, Hillsboro, USA). Samples were immediately imaged at 200 keV by HRTEM on FEI Tecnai G20 and FEI Osiris microscopes. The local crystal structure of oriented crystallites was analyzed by Fourier-analysis of the images using the Digital Micrograph software (Gatan, Pleasanton, USA: version 2.11).

Results

Electrochemical activation plateau.—Table I lists the different HE-NCM and NCM materials by their compositions, given as x Li_2MnO_3 • (1-x) $LiMeO_2$ (Me = Ni, Co, Mn) with x = 0.00, 0.33, 0.42 and 0.50. The shown total theoretical capacities (Q) are calculated for a theoretical complete delithiation using Faraday's law:

$$Q = \frac{n_{Li}\, F}{M} \qquad [1]$$

with F being the Faraday constant (96485 As/mol), M being the molar mass of the (HE-)NCM, and n_{Li} being the moles of lithium per mol of (HE-)NCM. Furthermore, the fraction of the capacity arising from the NCM domain and from the Li_2MnO_3 domain can be calculated individually from the given stoichiometry and molecular weight and is also shown in Table I. From these results, one can see that higher

Table I. Chemical formulas/compositions, theoretical capacity and BET surface areas for materials with Li_2MnO_3 content of 0.00, 0.33, 0.42 and 0.50; Li_2MnO_3 was varied with the same $LiMeO_2$ component, ending up in a constant Ni:Co ratio and a variation in the amount of Li and Mn for the different compositions. The total theoretical capacity is calculated for 100% delithiation of the material, according to Equation 1; furthermore, shown are the nominal theoretical capacities of the $LiMeO_2$ and the Li_2MnO_3 domains.

	Theoretical capacity [mAh/g]			
Composition	Total	$LiMeO_2$	Li_2MnO_3	BET [m^2/g]
0.00 Li_2MnO_3 • 1.00 $LiMeO_2$	279	279	0	0.5
0.33 Li_2MnO_3 • 0.67 $LiMeO_2$	346	174	172	6.5
0.42 Li_2MnO_3 • 0.58 $LiMeO_2$	363	148	215	6.5
0.50 Li_2MnO_3 • 0.50 $LiMeO_2$	377	126	251	6.0

Li_2MnO_3 contents lead to a higher share of capacity arising from the Li_2MnO_3 domain, but also the theoretical total capacity of the overall compound can be increased substantially with increasing lithium content. Also shown in Table I are the BET areas, which are essentially identical for the HE-NCM materials, but more than an order of magnitude lower for the NCM material. Therefore, for better comparability, gas evolution rates from OEMS experiments will be also normalized to the BET area (in units of μmol/m^2).

Figure 1 depicts the first cycle activation for all three compositions in half-cells, showing the first cycle charge-discharge curves

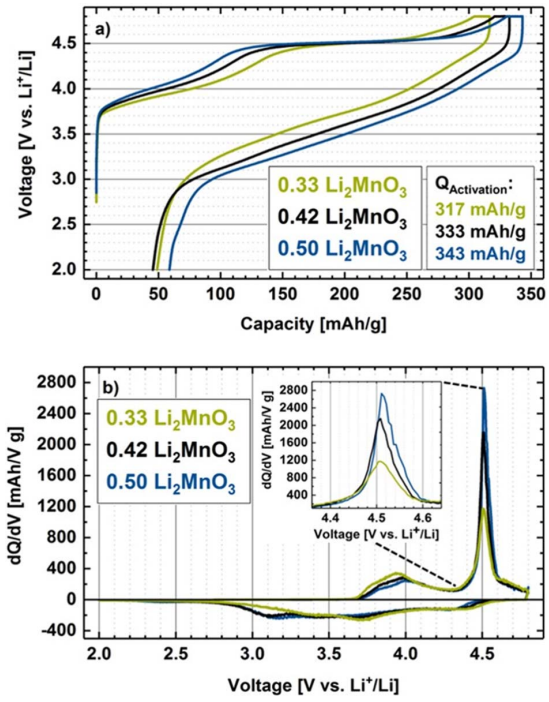

Figure 1. (a) Voltage vs. capacity for the first activation cycle in half-cells of HE-NCM with 0.33, 0.42, and 0.50 Li_2MnO_3 content (see Table I); the first charge capacity $Q_{Activation}$ is given in the figure. (b) Corresponding dQ/dV plots, show an increasing peak at 4.5 V with increasing Li_2MnO_3 contents (the inset is a zoom into the 4.5 V region). Cells were activated with metallic-Li as counter electrode at C/10 up to 4.8 V followed by a 1 h CV-step at 4.8 V and then discharged at C/5 to 2.0 V at 25°C in FEC:DEC (2:8 g:g) with 1 M $LiPF_6$.

in Figure 1a and the corresponding dQ/dV plot in Figure 1b, both showing a longer activation plateau and a higher amount of capacity in this plateau with increasing Li_2MnO_3 content. The first charge capacities are given in Figure 1a, reaching 317 mAh/g for a Li_2MnO_3 content of 0.33, 333 mAh/g for 0.42 Li_2MnO_3, and 343 mAh/g for 0.50 Li_2MnO_3. Comparing the measured capacities from Figure 1 to the total theoretical capacities listed in Table I, the apparent degree of delithiation is 92% for the materials with 0.33 and 0.42 Li_2MnO_3 and 91% for the material with 0.50 Li_2MnO_3. While the degree of delithiation is similar for different Li_2MnO_3 contents, one should note that delithiation beyond 90% of the overall amount of lithium is unique for this class of materials and cannot be achieved for classical NCM materials without irreversibly destroying the material.[10] However, this high delithiation cannot be explained by only taking cationic redox into account, given that Mn^{IV} in Li_2MnO_3 is redox inactive. Therefore, it is clear that another mechanism is responsible for charge compensation. While some groups expect electrochemical activation of Li_2MnO_3 to MnO_2 accompanied by bulk oxygen release,[11] more recent publications give strong evidence that anionic oxygen redox might serve for charge compensation at high delithiation.[26,31–33] The specific role of oxygen release HE-NCM particularly during the first activation cycle will be analyzed and discussed later on.

Focusing now on the quantitative effect of the Li_2MnO_3 on the capacity in the activation plateau, we defined the capacity gained during the plateau as the capacity gained between 4.40 V and 4.60 V. The thus obtained capacities during the activation plateau are 116 mAh/g for 0.33 Li_2MnO_3, 159 mAh/g for 0.42 Li_2MnO_3, and 190 mAh/g for the 0.50 Li_2MnO_3 content, showing a clear correlation between the Li_2MnO_3 content and the activation plateau capacity.[40] On the other hand, Figure 1a shows also that the capacity loss during the first discharge increases with increasing Li_2MnO_3 content, resulting in a comparable first-cycle irreversible capacity loss of 49 mAh/g for 0.33 and 46 mAh/g for 0.42 Li_2MnO_3, while the HE-NCM with the higher 0.50 Li_2MnO_3 content shows a much higher value of 60 mAh/g. In the discussion section, we will examine in detail the possible origins and explanations for this high irreversible capacity loss during activation, and how it influences the actual full-cell performance of the material.

Effect of the activation in full-cells.—For further analysis of the high irreversible capacity during the first charge/discharge cycle of HE-NCMs, full-cells were assembled, in the same way as the half-cells discussed in Figure 1, using a preformed graphite counter electrode instead of a lithium counter electrode. The graphite electrode was preformed in the same electrolyte in order to eliminate anode SEI losses (detailed information can be found in the experimental section). The upper cutoff potential was lowered from 4.8 V for the half-cells to 4.7 V in the full-cells, so that the upper cutoff potential of the cathode corresponded to ≈4.8 V vs. Li^+/Li in both cases. Figure 2a shows the corresponding first charge/discharge potential profiles for the different HE-NCMs. Comparable first-cycle irreversible capacities can be observed for the full-cells with preformed graphite electrodes and the Li metal half-cells (see Table II). By using preformed graphite electrodes, a capacity loss caused by the graphite anode is not expected, as a preformed SEI already exists which should prevent further electrolyte decomposition.

After the first cycle, the discharged cells were disassembled and the graphite anodes were harvested in order to determine the amount of cyclable lithium present in the graphite anode in the discharged HE-NCM//graphite full-cell. This was done by assembling half-cells with the harvested graphite electrodes with lithium counter electrodes and discharging them to 1.5 V at 0.1C in order to obtain the residual capacity in the graphite anodes, whereby this value was normalized to the mass of the cathode that was used during the full-cell activation, providing comparable results for the different cathode materials. Figure 2b shows that the residual capacity in the graphite anodes depends on the Li_2MnO_3 content of the cathode used during full-cell activation, and as one might expect, a higher Li_2MnO_3 content leads to a higher residual capacity stored in the anode. Table II compares the

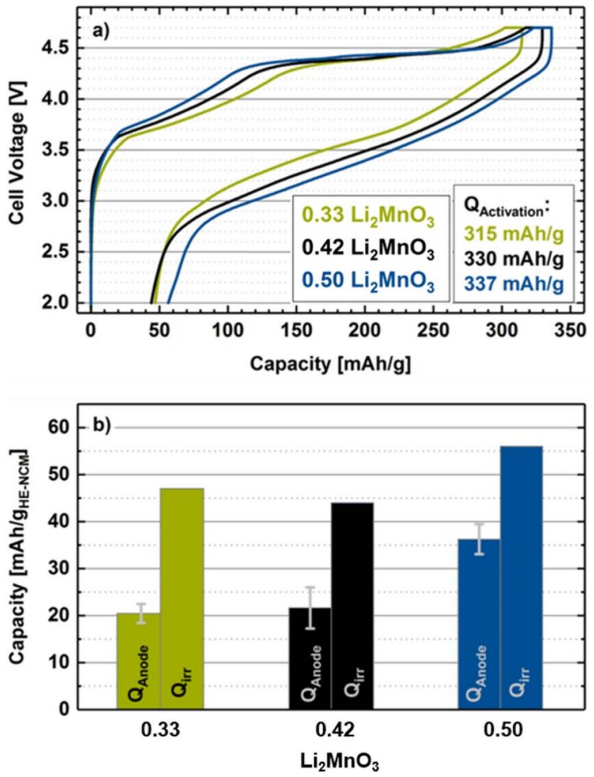

Figure 2. (a) Voltage curves for the first activation cycle in a full-cell of HE-NCM with 0.33, 0.42, and 0.50 Li_2MnO_3 content (see Table I), using preformed graphite anodes (see experimental section). (b) Residual capacity of the preformed graphite anodes after the first charge/discharge cycle (Q_{Anode}), obtained from the delithiation of harvested graphite anodes in half-cells to 1.5 V at C/10 (referenced to the cathode loading), as well as the irreversible first-cycle capacities (Q_{irr}) derived from Figure 2a (error bars for the residual capacities are derived from two independent measurements). Full-cells were charged at C/10 up to 4.7 V followed by a 1 h CV-step at 4.7 V and then discharged at C/5 to 2.0 V at 25°C in FEC:DEC (2:8 g:g) with 1 M $LiPF_6$.

first-cycle irreversible capacities measured during full-cell and half-cell activation as well as the residual capacity stored in the graphite anodes. From this it can be concluded that a higher first-cycle irreversible capacity leads to a higher amount of cyclable lithium within the graphite anode. In other words, a high irreversible capacity during the first charge does not necessarily mean that a high amount of lithium is lost irreversibly, but rather that after the HE-NMC activation not all of the extracted lithium can be reinserted into the cathode active

Table II. First-cycle irreversible capacities (Q_{irr}) during the first charge/discharge cycle for HE-NCMs with different Li_2MnO_3 content, taken from Figure 1a and Figure 2a, respectively. Also, the residual capacity obtained from preformed graphite anodes shown in Figure 2b is compared to the first-cycle irreversible capacity loss, showing an offset of ≈20 – 27 mAh/g.

	Q_{irr} [mAh/g]		
Li_2MnO_3	Half-cell	Full-cell	Residual capacity in preformed graphite [mAh/g]
0.33	49	47	20
0.42	46	44	22
0.50	60	56	36

A2722 Journal of The Electrochemical Society, 165 (11) A2718-A2731 (2018)

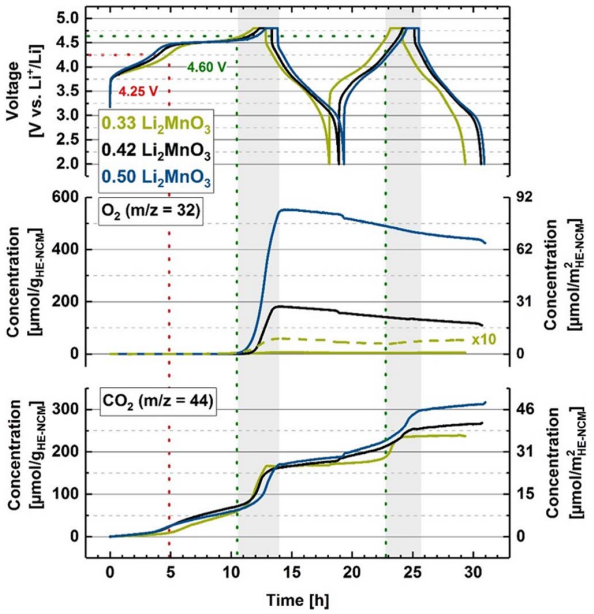

Figure 3. OEMS measurements for the first two charge/discharge cycles in a half-cell with three different HE-NCM compositions (see also Table I). Upper panel: charge/discharge voltage vs. time; middle/lower panel: evolution of the concentrations of concomitantly evolved O_2/CO_2 given in units of either $\mu mol/g_{AM}$ (left axes) or $\mu mol/m^2_{AM}$ (right axes). Cells were charged at C/10 rate to 4.8 V, followed by 1 h CV-step at 4.8 V and a consecutive discharge at C/5 to 2.0 V and another full charge/discharge cycle at C/5. Cells were composed of metallic Li counter electrode and a Celgard separator (CG2500) and experiments were conducted at 25°C in FEC:DEC (2:8 g:g) with 1 M $LiPF_6$. The vertical dashed red line indicates the first onset of CO_2 evolution, and the vertical dashed green lines mark the potential of 4.6 V where the onset of O_2 evolution occurs.

material (even though for mechanistically different reasons, an irreversible capacity loss is also observed for NCM 111).[41,42] However, for all compositions an offset between capacity loss during the first cycle and the cyclable lithium capacity in the graphite anodes of about 20 – 27 mAh/g is observed. This capacity offset must correspond to an irreversible loss of active lithium in side-reactions during the first charge/discharge cycle and cannot be assigned to typical anode SEI losses, as the SEI was already preformed on the graphite electrodes. The specific reactions leading to this phenomenon are unfortunately not clear at this time. However, Figure 2 shows that an increasing Li_2MnO_3 content leads to a higher amount of active lithium within a HE-NCM//Graphite full-cell. Thus, it is expected that this additional lithium can be utilized for SEI formation or stored in the graphite anode as lithium reservoir that can be utilized during cycling. Therefore, the full-cell performance is expected to be improved for higher Li_2MnO_3 which will be discussed later.

Oxygen release during activation.—To examine the effect of different Li_2MnO_3 onto the oxygen release of overlithiated NCM materials and to get insights if electrochemical Li_2MnO_3 activation accompanied by bulk oxygen release is feasible, results of the OEMS measurements on all three compositions are shown in Figure 3. The upper panel shows the galvanostatic charge/discharge profiles between 2.0 and 4.8 V against a Li counter electrode, and the middle/lower panels depict the concentration of the concomitantly evolved O_2/CO_2; concentrations are given in terms of both $\mu mol/g_{AM}$ (left axis) and $\mu mol/m^2_{AM}$ (right axis), whereby the latter surface normalized concentration will be used in the discussion section for comparison with the stochiometric NCM material. The first onset of CO_2 evolution can be observed at 4.2 V, followed by a rapid increase in CO_2 upon the onset of oxygen release at 4.6 V vs. Li^+/Li, i.e., at the end of the first charge activation plateau. Quite striking when comparing the different HE-NCMs is that the amount of evolved CO_2 is essentially identical for all materials, the extent of O_2 release decreases substantially with decreasing Li_2MnO_3.

However, concerning the origin of CO_2 from stochiometric and overlithiated layered oxides, there is an ongoing debate: while Luo et al.[26] suggested that the main part of CO_2 evolved from overlithiated oxides derives from electrolyte oxidation with lattice oxygen, it has been proposed by Renfrew et al.[43] that CO_2 evolution is exclusively triggered by the decomposition of Li_2CO_3 surface impurities. However, Jung et al.[8,10,44] and Strehle et al.[25] proposed another concept for stochiometric and overlithiated layered oxides, respectively, suggesting that CO_2 evolution starting at 4.2 V vs. Li^+/Li before the onset of oxygen release is produced by the oxidation of surface impurities, while the released oxygen is suggested to react with the carbonate electrolyte causing CO_2 evolution, consistent with the concomitant rapid increase in CO_2 concentration. While the exact mechanism leading to CO_2 evolution is still subject to ongoing discussions, we will here adopt the mechanistic view proposed by Strehle et al. and Jung et al. As mentioned above, a rather striking observation is the ≈100-fold variation in the amount of oxygen released by the end of the first activation charge for the different Li_2MnO_3 contents: ≈6 µmol/g (≈1 µmol/m²) for 0.33 Li_2MnO_3, ≈180 µmol/g (≈28 µmol/m²) for 0.42 Li_2MnO_3, and ≈550 µmol/g (≈85 µmol/m²) for 0.50 Li_2MnO_3 content. If compared to the amount of O_2 which would be expected for the historically proposed bulk activation of Li_2MnO_3 (1600 µmol/g for 0.33 Li_2MnO_3, 2000 µmol/g for 0.42 Li_2MnO_3, and 2350 µmol/g for 0.50 Li_2MnO_3), bulk oxygen release does not seem to be a feasible mechanism for these overlithiated materials. As already shown in a previous study, oxygen release caused by a chemical layer-to-spinel transformation leading to the formation of a resistive surface layer and concomitant oxygen release from near-surface regions can explain the phenomena of oxygen release for HE-NCMs[25] as well as for classical NCM materials.[9,10] In these reports as well as in our present study, the main part of the oxygen evolution is detected during the first charge of the material, while rather small amounts of O_2 evolution can be detected during the second cycle. The continuous oxygen consumption during the cycling procedure indicated by the decreasing O_2 concentration after the first charging cycle (see middle panel in Figure 3) is ascribed to a gradual reduction of oxygen to Li_2O_2 on the lithium counter electrode, shown by Yabuuchi et al. to occur below 3.0 V vs. Li^+/Li.[22] Furthermore, a more sudden oxygen consumption can be observed when the cathode is cycled below 3.0 V vs. Li^+/Li (e.g., at ≈19 h in Figure 3), whereby the initially formed superoxide radical causes a sharp CO_2 increase due to reaction with the electrolyte.[22] During the first charging cycle, the onset of O_2 evolution is accompanied by a rapid increase of the CO_2 evolution rate, as discussed above. However, while no further evolution of O_2 can be observed in the second cycle, further CO_2 evolution can be detected at the potential where O_2 started to evolve in the first cycle (≈4.6 V), indicating further oxygen release from the cathode material, even if no molecular O_2 evolution can be detected anymore.

Galvanostatic cycling of half-cells.—As a next step, Figure 4 shows the half-cell cycling data for all three different compositions over 50 cycles at a rather slow rate of C/5 and with a high amount of electrolyte (120 µl). Figure 4a depicts the discharge capacity retention for the materials, whereby the material with the highest Li_2MnO_3 content also shows the highest initial capacities, as expected from Table I and Figure 1. The capacity of the 0.50 Li_2MnO_3 material (blue symbols) decreases strongly during the first 20 cycles, resulting in a capacity loss of 28 mAh/g between cycle 3 and cycle 50 (253 mAh/g to 225 mAh/g), while the capacity fading of the 0.42 Li_2MnO_3 over the same cycles is much lower (255 mAh/g to 240 mAh/g), amounting to a capacity loss of 15 mAh/g. The lowest capacity fading of roughly 7 mAh/g between cycle 3 and 50 is observed for the 0.33 Li_2MnO_3 (247 mAh/g to 240 mAh/g). Comparing this with the results from Figure 3 suggests that a higher oxygen release leads to more extensive

Journal of The Electrochemical Society, 165 (11) A2718-A2731 (2018)

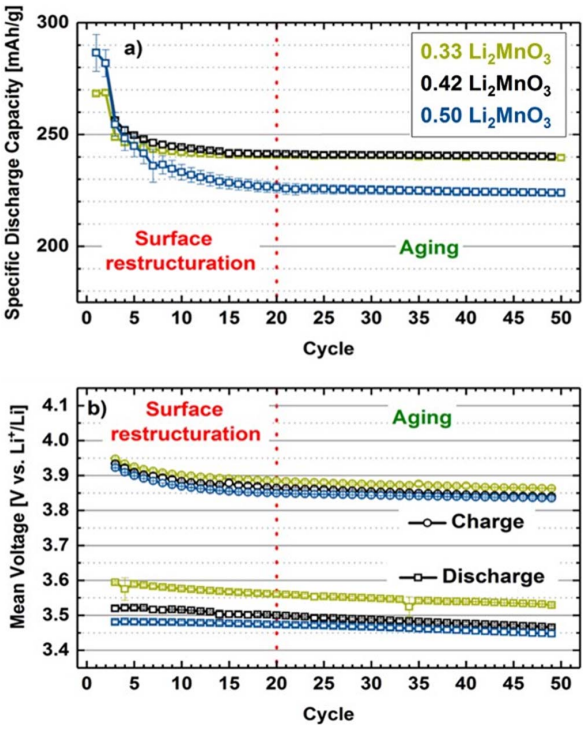

Figure 4. Electrochemical cycling at C/5 rate of the different HE-NCM compositions at 25°C using a Li counter electrode, FEC:DEC (2:8 g:g) with 1 M $LiPF_6$ electrolyte, and a glassfiber separator. The first activation cycle was carried out at C/10 to 4.8 V where the potential was held for 1 h and then the cell was discharged at C/5 to 2.0 V, followed by an analogous second activation cycle at C/5 (up to 4.8 V + 1 h CV); all further cycling (i.e., starting at the third cycle) was carried out at C/5 rate without any CV-steps (CC charge/discharge) between 2.0 V and 4.7 V. (a) shows the specific discharge capacity as a function of the cycle number (note that the first two discharge capacities are cycled up to 4.8 V followed by 1 h CV), while (b) shows the corresponding mean charge and discharge voltage (as defined by Eq. 1 in Jung et al.[10]). All data points represent the average of at least two independent measurements and the error bars reflect the maximum and minimum of the measured values.

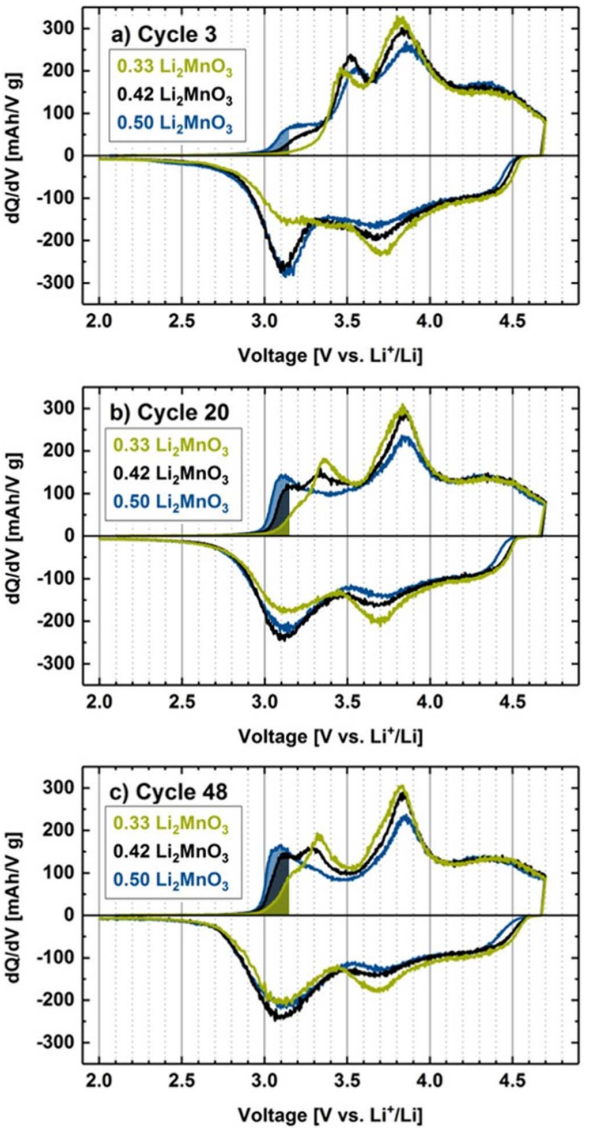

Figure 5. Electrochemical cycling of the different HE-NCM compositions at 25°C using a Li counter electrode, FEC:DEC (2:8 g:g) with 1 M $LiPF_6$ electrolyte, and a glassfiber separator. The activation and cycling procedure is that same as that shown/described in Figure 4. All dQ/dV plots were recorded at C/5 for cycle 3 (a), cycle 20 (b) and cycle 48 (c). The shaded areas in the charging cycles represent the hypothesized rocksalt-to-spinel transition.

surface degradation and a concomitant decrease of the electrochemical performance; the effect of oxygen release on active material loss will be discussed and quantified in the discussion section. As oxygen release is hypothesized to be correlated to the voltage hysteresis and the hysteresis between charge and discharge,[11,45] one might pose the question whether the large differences in oxygen release shown in Figure 3 also have such a big influence onto the voltage fading of the different materials. The mean charge and discharge voltages are shown in Figure 4b. It can be seen that the mean charge voltage fading is comparable for all three materials, showing a fading of ≈90-100 mV between cycle 3 and 50 for all materials. The same observation can be made for the mean discharge voltage fading, which does not differ largely between the different materials (≈40–70 mV). Thus, while the O_2 release increases by almost two orders of magnitude as the Li_2MnO_3 content is increased, the differences in voltage fading are rather minor, which suggests that the main cause of the voltage fading of HE-NCMs is not related directly to the oxygen release. Therefore, the oxygen release is a side reaction occurring at the HE-NCM near-surface region,[25] while reversible and irreversible transition metal migration in the bulk material cause the main voltage fading and the high hysteresis.[35,45,46]

Figure 5 depicts the dQ/dV plots for cycle 3, cycle 20, and cycle 48 extracted from the cycling data shown in Figure 4. Hereby, cycle 3 is the first C/5 cycle between 2.0 V and 4.7 V and therefore is subjected to the same cycling conditions as cycle 20 and 48. For the characterization of the mean voltages as well as the evolution of the spinel surface layer, we will focus on the charging curve of the materials, as the discharge shows very high impedances and limitations of Li diffusion within the bulk of the material, which is part of a separate study.[14] The most striking differences can be observed by a peak in the dQ/dV plot growing at roughly 3.1 V during the charge (shadowed areas in Figure 5). In Figure 5a and Figure 5b it can be seen that the area under this peak is largest for the 0.50 Li_2MnO_3 material that also has the highest O_2 release, while for the material with the lowest oxygen release (0.33 Li_2MnO_3) the area under this peak is lowest. Therefore, we suggest that this peak might be correlated to an oxygen deficient, spinel-like electrochemically active

A2724 Journal of The Electrochemical Society, 165 (11) A2718-A2731 (2018)

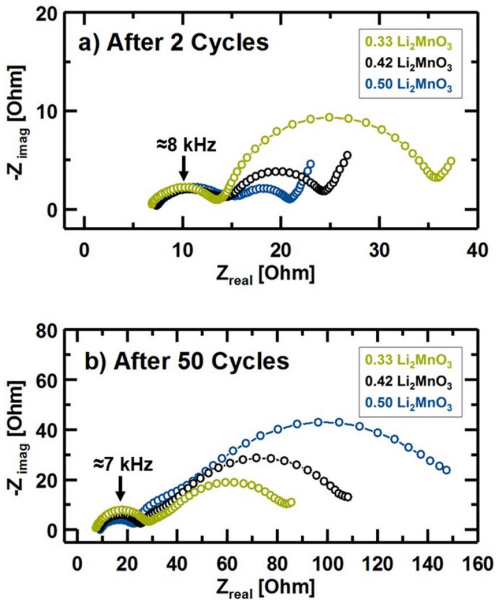

Figure 6. Impedance spectra measured in symmetric coin cells with cathodes harvested at 50% SOC (a) after the two-cycle activation procedure and (b) after a total of 50 cycles according to the procedure shown in Figure 4. Symmetric cells were built with a 300 μm glassfiber separator and with 95 μL of 1 M $LiPF_6$ in FEC:DEC (2:8 g:g) electrolyte. Impedance spectra were measured at the OCV at 50% SOC (between 300 kHz and 30 mHz with an amplitude of 10 mV).

surface structure, which would also be consistent with the observations by Bruce et al. and Thackeray, who proposed the rocksalt-to-spinel transition ($Li_2Mn_2O_4 \rightarrow LiMn_2O_4 + Li^+ + e^-$) at such potentials.[47,48] Comparing the evolution of the area under these peaks, it can be clearly seen that it increases substantially from cycle 3 to cycle 20, while it remains relatively constant between cycle 20 and cycle 48. This behavior reflects the evolution of the capacity loss with cycling, which is most pronounced during the first 20 cycles, while afterwards the capacity stays approximately constant (Figure 4a). Thus, the capacitive contribution from the first charging peak in the dQ/dV plot seems to correlate with the capacity loss, which we will further quantify in the discussion section, including the relationship of this feature with the extent of oxygen release.

Impedance spectroscopy in symmetric cells.—It has been reported in the literature that surface degradation of layered oxides, caused by oxygen release, can lead to spinel and rocksalt like structures at the surface of the cathode material, leading to drastic increases in the charge transfer resistance, which in turn might be the cause of the so-called rollover failure.[10,49] Figure 6 shows impedance spectra measured in symmetric cells for HE-NCM electrodes with the three different compositions (a) after 2 activation cycles, and (b) after another 48 cycles (total of 50 cycles) according to the procedure in Figure 4. Impedance spectra were acquired at OCV following a charge to 50% SOC (based on the preceding full charge-discharge cycle). All Nyquist plots show two distinct semi-circles, one at high frequencies that shows the same resistance for all the materials both at cycle 2 and 50 (increasing from ≈8 to ≈20 Ω), and one at lower frequencies which differs significantly for the different compositions. Previous studies have shown that the semi-circle at high frequencies for cathode electrodes can be assigned to a contact resistance at the interface of the cathode electrode with the aluminum current collector,[50,51] which can also be rationalized by considering the electrode capacitance corresponding to this first semi-circle:

$$C = \frac{1}{R\ 2\ \pi\ f_{max}} \quad [2]$$

where C is the capacitance, R is the diameter of the semi-circle (divided by two in this case of a symmetric cell), and f_{max} is the frequency corresponding to the apex of the first semi-circle. For the data shown in Figure 6a, the resistance for one electrode is R ≈8 Ω and f_{max} ≈8 kHz, equating to an electrode capacitance of ≈5 μF, which is similar for all HE-NCM compositions. To understand its origin, one may normalize it by either the surface area of the current collector (≈1.5 cm^2 for the 14 mm diameter electrodes) or by the total surface area of the cathode electrode (≈730 cm^2, based on the mass of HE-NCM and conductive carbons in the electrode multiplied by their BET surface area), yielding either ≈3.2 μF/cm^2 or ≈0.007 μF/cm^2, respectively. If compared to the typical double layer capacitance which is on the order of ≈10^1 μF/cm^2, it is clear that the first semi-circle occurs due to a contact resistance at the interface between the electrode and the current collector. Detailed studies onto the origin of those contact resistances are reported elsewhere.[50,51]

The second semi-circle at lower frequencies can then be assigned to a charge-transfer resistance (R_{CT}), which clearly differs largely for the different HE-NCM materials. First examining their impedance directly after the two activation cycles (Figure 6a), it can be seen that R_{CT} decreases with increasing Li_2MnO_3 content and thus with increasing oxygen release (Figure 3). This could be rationalized by assuming either that the oxygen vacancies in the surface layer largely increase the lithium ion mobility and/or that the surface restructuration increases the porosity at the surface of the cathode material, concomitant with an increase in interfacial surface area and thus a lowering of the apparent charge transfer resistance.

Interestingly, the above discussed trend of a decreasing charge transfer resistance with increasing Li_2MnO_3 content reverses over the course of cycling (Figure 6b). Even though the resistance represented by the second semi-circle increases for all HE-NCMs from cycle 2 to cycle 50 (Figure 6b), it increases by a much larger factor for the 0.50 Li_2MnO_3 (≈15-fold) compared to the 0.33 Li_2MnO_3 material (≈2.5-fold), so that after 50 cycles the 0.50 Li_2MnO_3 material now shows the highest impedance and therefore also the highest impedance buildup. As the thickness of the oxygen-deficient phase after the activation is expected to increase with the extent of O_2 release and thus with the extent of overlithiation, the gradual transformation of this surface layer from perhaps an initially highly conductive disordered layered structure into a more resistive ordered spinel or rocksalt structure could explain the increase in the cycling induced impedance buildup with the extent of overlithiation. This hypothesis will be examined in the following by HRTEM analysis of pristine and cycled HE-NCMs.

High-resolution TEM measurements.—Figure 7 shows representative HRTEM images of the near-surface region for the material with an intermediate extent of overlithiation (0.42 Li_2MnO_3) for the pristine material (a), after 2 cycles (b), and after 50 charge-discharge cycles (c), following the same cycling protocol as that shown/described in Figure 4. For the pristine material, a layered structure without any crystalline surface layer but with a thin amorphous surface layer can be seen, which we ascribe to carbonate and hydroxide surface impurities. The HRTEM image taken after 2 charge/discharge cycles (Figure 7b), i.e., after most of the oxygen has been released from the active material, clearly still shows a layered surface structure for which, however, a slight loss of density in the near-surface regions can be observed. This provides first hints that the release of oxygen initiates changes in the surface structure. After 50 charge/discharge cycles, Figure 7c clearly shows the presence of a pronounced surface layer with a thickness of roughly 4 nm, whereby the corresponding FFT image in Figure 7d indicates strong cation mixing within the spinel-type surface layer. These findings are consistent with the HRTEM analysis by Genevois et al.[29] on chemically delithiated HE-NCM, indicating a strong surface restructuration after several charge/discharge cycles.

Journal of The Electrochemical Society, **165** (11) A2718-A2731 (2018)

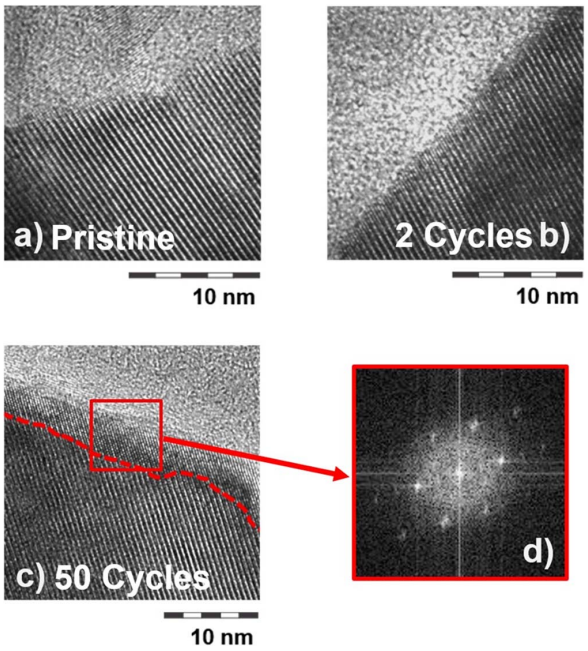

Figure 7. HRTEM analysis of the near-surface region of the 0.42 Li_2MnO_3 HE-NCM material (a) in its pristine state, (b) after 2 cycles, and (c) after 50 cycles (the cycling procedure is according to that described in Figure 4). (d) shows the corresponding FFT image for the material after 50 cycles, taken in the red marked region in (c).

Furthermore, the here presented HRTEM measurements support one of our above assumptions used to interpret the EIS measurements shown in Figure 6, namely the initial formation of surface layer with reduced density after activation and the associated O_2 release, followed by a densification[28] and spinel-type surface layer formation upon extended charge/discharge cycling.

HRTEM images for all HE-NCM compositions were also collected after 50 cycles. The 0.33 Li_2MnO_3 material is shown in Figures 8a–8c. Figure 8a shows an entire primary particle, displaying a perfectly layered bulk material as demonstrated by the FFT image (Figure 8b), with a surface-layer in the range of 1–2 nm. The latter is marked by the red dashed line and magnified in Figure 8c; unfortunately, this layer was too thin to take an FFT image. The HRTEM image of an entire primary particle of the 0.42 Li_2MnO_3 material is shown in Figure 8d, which also is a well-ordered layered bulk material, as demonstrated by the FFT image taken from the center of the particle (Figure 8f). However, the restructuration of the surface is much more pronounced for this material, showing a surface layer thickness in the range of 4 nm and even thicker in some areas (marked by the red dashed line in Figure 8d). The FFT image from the surface layer (Figure 8e) is in line with the image shown in Figure 7d, showing strong cation mixing in a spinel-type surface layer. Finally, the HRTEM images for the 0.50 Li_2MnO_3 material are shown in Figures 8g–8i. In these images it can be observed that the formation of a spinel-type structure is now not only limited to the surface, but also alters the bulk material. The FFT image in Figure 8h from one area within the particle indicates an intact layered structure, while Figure 8i from a different region within the same particle already shows cation mixing within the bulk material and changes of the layered structure. In summary, all these observations present strong evidence that the higher oxygen release during activation produced by higher degrees of overlithiation leads to an increasingly pronounced growth of surface layers, initially formed as reduced density layered structures and transformed upon cycling into spinel-type phases with strong cation mixing.

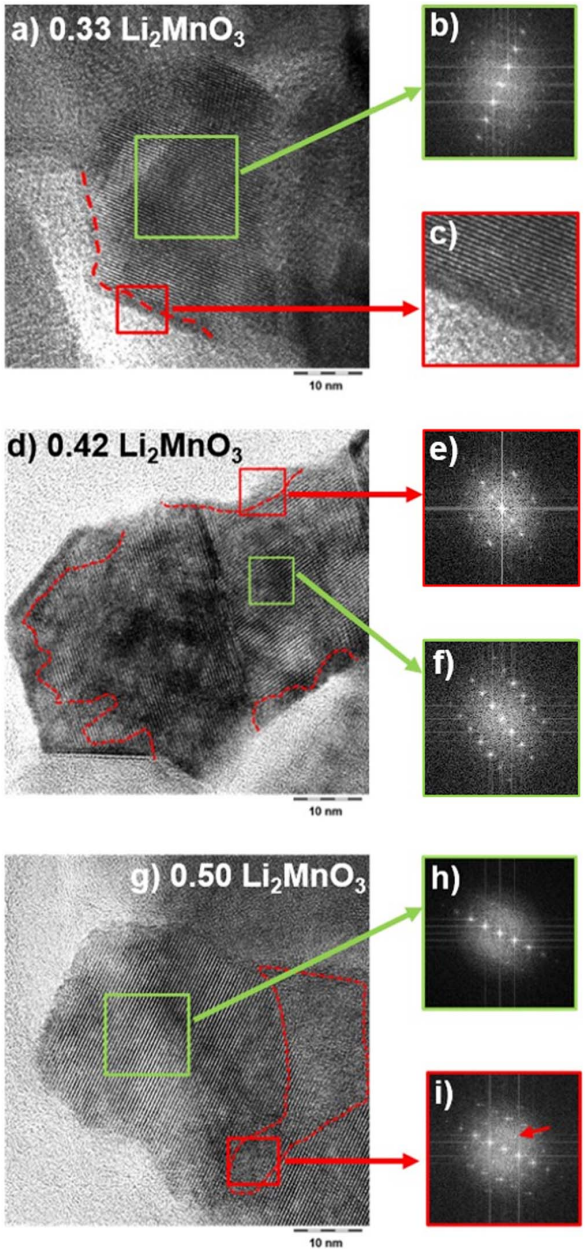

Figure 8. HRTEM images showing particle degradation for HE-NCMs with (a, c) 0.33 Li_2MnO_3, (d) 0.42 Li_2MnO_3, and (g) 0.50 Li_2MnO_3 content. Corresponding FFT images after 50 cycles from the marked regions in the HR-TEM images are shown: (b) for the bulk of the 0.33 Li_2MnO_3 material; (e) and (f) for the surface and bulk, respectively, of the 0.42 Li_2MnO_3 material; (h) and (i) for the bulk and surface, respectively, of the 0.50 Li_2MnO_3 material.

Discussion

Estimation of spinel-type surface layer thickness.—Strehle et al. have recently shown that the oxygen evolution in Li- and Mn-rich layered oxides occurs *i*) right after the activation plateau and *ii*) also continues during the OCV at 4.8 V. Based on these results it was proposed that oxygen release from the bulk material seems to be unlikely, which led to the conclusion that high voltage charging and high degrees of delithiation destabilize the material's surface and ultimately

A2726 Journal of The Electrochemical Society, **165** (11) A2718-A2731 (2018)

Table III. Li_2MnO_3 content, molar mass and theoretically required oxygen release for a 100% conversion into a spinel structure for HE-NCMs delithiated at 4.6 V ($n(O_2^{theo})$, see Equation 8),[10,25] calculated acc. to Equations 4–8.

Li_2MnO_3 content	Molar mass [g/mol]	100% O_2 conversion [µmol/g]
0.33	88.4	2941
0.42	86.8	2880
0.50	85.2	3521

result in a surface restructuration of the material.[25] Similar behavior was also shown to occur for stochiometric NCM materials, leading to a chemically driven formation of a spinel and/or rocksalt surface layer upon delithiation.[10] Such chemically driven spinel and/or rocksalt formation have been shown and intensively characterized for the thermally induced transformation of partially delithiated NCMs.[52,53] The general chemical reaction for spinel formation is given in Equation 3. Since rocksalt structures could not be observed by HRTEM measurements (see Figure 7 and Figure 8), the surface layer thickness is estimated only assuming the formation of a spinel surface layer.[10,25]

$$Li_xMe_yO_2 \rightarrow \frac{x+y}{3} Li_{3-\frac{3y}{(x+y)}} Me_{\frac{3y}{(x+y)}} O_4 + \frac{3-2(x+y)}{3} O_2 \uparrow \quad [3]$$

As starting compound for the spinel formation according to Equation 3, it is assumed that material restructuration starts at the oxygen onset potential, so the starting compound for the material restructuration is the partially delithiated phase at 4.6 V during the first charge, as already suggested by Strehle et al.[25] Thus, the amount of lithium that remains in the structure at the oxygen onset (x-value in Eq. 3) needs to be estimated using Equation 4

$$\Delta x_{Li} = \frac{QM}{F} \quad [4]$$

with Q being the capacity reached at the oxygen onset during the first charge (from Figure 3), M being the molar mass of the pristine HE-NCM, and F being the Faraday constant. With these calculations, residual lithium contents of $Li_{0.25}$ (0.33 Li_2MnO_3), $Li_{0.29}$ (0.42 Li_2MnO_3), and $Li_{0.25}$ (0.50 Li_2MnO_3) are found and can be further replaced into the general equations for spinel formation (Equations 3). The resulting transformations into the spinel phase for the different materials are shown in Equations 5 to 7.

Spinel formation for the 0.33 Li_2MnO_3 material delithiated to 4.6 V:

$$Li_{0.25}Me_{0.86}O_2 \rightarrow 0.37\ Li_{0.68}Me_{2.32}O_4 + 0.26\ O_2 \uparrow \quad [5]$$

Spinel formation for the 0.42 Li_2MnO_3 material delithiated to 4.6 V:

$$Li_{0.29}Me_{0.83}O_2 \rightarrow 0.37\ Li_{0.78}Me_{2.22}O_4 + 0.25\ O_2 \uparrow \quad [6]$$

Spinel formation for the 0.50 Li_2MnO_3 material delithiated to 4.6 V:

$$Li_{0.25}Me_{0.80}O_2 \rightarrow 0.35\ Li_{0.71}Me_{2.29}O_4 + 0.30\ O_2 \uparrow \quad [7]$$

These equations give the theoretical loss of oxygen per mole of HE-NCM for a 100% layered-to-spinel conversion (O_2^{theo}), from which the moles of oxygen released for a 100% conversion of the entire particle into the spinel ($n(O_2^{theo})$) can be easily calculated according to formula 8, using the molar mass of the different HE-NCM compositions. Table III shows the molar mass values for the different compositions, as well as the theoretical oxygen release which would be required for a 100% of spinel formation calculated from the equations above.

$$n\left(O_2^{theo}\right) = \frac{O_2^{theo}}{M} \quad [8]$$

The ratio of oxygen release expected for a 100% phase transformation ($n(O_2^{theo})$) into a spinel structure and the actual oxygen evolution measured by OEMS ($n(O_2^{meas})$) can be used to calculate the molar fraction of layered material converted into a spinel-type structure.

$$x_{surface\ layer} = \frac{n\left(O_2^{meas}\right)}{n\left(O_2^{theo}\right)} \quad [9]$$

To translate the molar fraction into a surface layer thickness, the approximate particle radius is estimated from the BET areas (A_{BET}) given in Table I according to Equations 10, with $\rho_{HE\text{-}NCM}$ being the crystallographic density of the pristine material ($\rho_{HE\text{-}NCM} = 4.2\ g/cm^3$).

$$r = \frac{3}{A_{BET}\ \rho_{HE-NCM}} \quad [10]$$

From the radius and the molar fraction of the spinel phase, the surface layer thickness can be easily assumed using Equations 11 and 12. More detailed information regarding these calculations have been reported by Strehle et al. and Jung et al.[10,25]

$$r' = r\left(1 - x_{surface\ layer}\right)^{1/3} \quad [11]$$

$$t_{surface\ layer} = r - r' \quad [12]$$

Based on the equations and assumptions discussed above, all results from the OEMS measurements and the results of the above calculations are summarized in Table IV. For the gas quantification two different models are taken into account: Model I is based on the amount of O_2 and CO_2 released above 4.6 V during the first charge, while Model II is based on the amount of O_2 and CO_2 released above 4.6 V during the first and the second charge, whereby the evolved amount of gases are taken from Figure 3 (from the gray shaded regions). As mentioned before, the assumption that the CO_2 evolved at high potentials is formed by lattice oxygen from the cathode material is still subject of ongoing discussions,[10,26,43] but recent measurements with ^{13}C labeled EC are in support of this.[44] Furthermore, the amount of evolved CO was not considered, as it is negligible with the here used FEC-based electrolytes (data not shown).

From Table IV it can be seen that the oxygen evolution strongly depends on the material composition and is nearly 100-times higher for the 0.50 Li_2MnO_3 compared to the 0.33 Li_2MnO_3 material. This is consistent with the increase of the surface (and bulk) restructuration with increasing lithium content observed in the HRTEM analysis (see Figure 8). In contrast, it is surprising that the amount of evolved CO_2 is essentially independent of the HE-NCM composition and the amount of evolved oxygen, suggesting that the reaction between electrolyte and lattice oxygen saturates at a high level of oxygen release from HE-NCM. Furthermore, since the CO_2 evolution at high potentials during the second charge is also likely due to the reaction of electrolyte with lattice oxygen (more apparent in the OEMS study by Jung et al. on NCMs),[10] Model II is assumed to be the more representative scenario.

From the total amount of CO_2 and O_2 evolved at ≥4.6 V, which we believe are reaction products of the electrolyte with lattice oxygen, the molar fraction of the resulting spinel surface layer as well as its thickness can be estimated; these are given for the different materials in Table IV. For the 0.33 Li_2MnO_3 material, a roughly 2 nm thick surface layer could be detected by HRTEM, which is consistent with the spinel layer thickness calculated for Model II (see Table IV). A similarly good quantitative agreement is found for the 0.42 Li_2MnO_3 material, with HRTEM images showing surface layers of roughly 4 nm, the same as the thickness predicted by Model II. However, for the 0.50 Li_2MnO_3 material the simple surface layer model fails, as oxygen depletion proceeds into the bulk of the material, leading to large domains of bulk degradation (see Figures 8g–8i). Nevertheless, when comparing semi-quantitatively the HRTEM images of the 0.50 Li_2MnO_3 material after 50 cycles, the molar fraction of ≈20 mol% of spinel based on the gas evolution data (Table IV) seems to be a realistic value. Please note that the results discussed above and shown in Table IV suggest the formation of a M'_3O_4 (M' = Li + Me) type spinel, as discussed in previous publications.[10,25] Another possible spinel structure formed upon oxygen release might be a $LiMn_2O_4$ type spinel layer, which would lead to a lower oxygen loss per mole

Journal of The Electrochemical Society, **165** (11) A2718-A2731 (2018)

Table IV. Amounts of O_2 and CO_2 evolved at ≥4.6 V in the 1st (Model I) as well as in the 1st + 2nd cycle (Model II) from HE-NCMs with different Li_2MnO_3 contents (from the OEMS data in Figure 3). The molar fraction of the spinel surface layer ($x_{surf.\ layer}$) is calculated from the sum of O_2 and CO_2 detected at ≥4.6 V according to the chemical reactions given in Equations 3–9 and the surface layer thickness ($t_{surf.\ layer}$) is calculated from Equations 10–12.

		Gas evolution (≥4.6 V) [μmol/g_{AM}]				
Li_2MnO_3 content	Model	Total	O_2	CO_2	$x_{surf.\ layer}$ [mol%]	$t_{surf.\ layer}$ [nm]
0.33	I	96	6	90	3.3	1.2
	II	146	6	140	5.0	1.9
0.42	I	265	180	85	9.2	3.5
	II	305	180	125	11	4.0
0.50	I	650	550	100	19	7.3
	II	695	550	145	20	7.8

of converted HE-NCM, so that for the same amount of oxygen release a thicker spinel-type surface layer would be expected, based on the following general equation:

$$Li_xMe_yO_2 \rightarrow \frac{y}{2} Li_{\frac{2x}{y}}Me_2O_4 + (1-y)\ O_2 \uparrow \quad [13]$$

Conducting the same calculations (Model II in Table IV), as shown in Equation 5–12, for the formation of a $LiMn_2O_4$ type spinel layer, the following amounts of spinel ($x_{surf.\ layer}$ in mol%) will be obtained for the different materials: 9.2 mol% (0.33 Li_2MnO_3), 16.5 mol% (0.42 Li_2MnO_3) and 29.6 mol% (0.50 Li_2MnO_3), ending up with surface layers ($t_{surf.\ layer}$ in nm) from 3.5 nm (0.33 Li_2MnO_3) to 6.4 nm (0.42 Li_2MnO_3) up to 12 nm for the 0.50 Li_2MnO_3 HE-NCM. Comparing these values to the calculations for the M'_3O_4 spinel layer, with predicted spinel fractions and thicknesses ranging from 5–20 mol.% and from 1.9–7.8 nm, respectively (see Model II, Table IV), one can see that the formation of a $LiMn_2O_4$ type spinel would result in a ~1.5 fold larger estimated for the amount and the thickness of the spinel surface layer. Therefore, one should keep in mind that the here projected surface spinel layer amounts/thicknesses do depend on the actual phase that is formed after the oxygen release and as such are just rough estimates. However, taking into regard that the spinel forms due to cation migration at room temperature, we rather expect a disordered spinel with the stoichiometry M'_3O_4 than a well ordered $LiMe_2O_4$ phase, as obtained from high temperature synthesis.

In summary, by correlating HRTEM images/analysis with the OEMS experiments we have proven that the oxygen release during the HE-NCM activation cycles is accompanied by the formation of a surface spinel-like layer and is not due to a bulk restructuration, as suggested in earlier reports.[25,27–29] However, using a material with a very high lithium content, like the 0.50 Li_2MnO_3 material in this study, a partial bulk transformation can be observed, amounting to ≈20 mol% of the material being converted into a spinel-like phase (calculated from the oxygen evolution, shown in Model II from Table IV). While the TEM data are statistically not sufficient to provide exact quantitative surface layer thickness values for averaged over the entire material, they fit well to the quantification from the OEMS results. The partial bulk conversion for highly overlithiated HE-NCMs (≈20 mol%) now also explains previous studies from which it was concluded that the activation of HE-NCMs leads to a bulk transformation to a spinel-like phase.[19,20,22,54] For example Yabuuchi et al. and Mohanty et al. have suggested bulk structural changes during the first charge due to oxygen removal from the bulk of the material based on X-ray diffraction studies, both conducted with overlithiated HE-NCM with 0.50 Li_2MnO_3 content.[22, 54] Clearly, the results of structural, non-spatially resolved measurements are strongly dependent on the extent of overlithiation and perhaps on the synthesis of HE-NCM materials, which is the reason for the different mechanistic hypotheses which can be found in the literature. However, recent approaches using spatially resolved techniques[38] lead to the same conclusions as presented in our study.

Evolution of the surface layer during cycling.—Now we want to discuss the evolution of the structural transformation during cycling, considering the OEMS measurements (Figure 3), the impedance spectroscopy analysis (Figure 6), and the HRTEM data (Figure 7 and Figure 8). The OEMS experiments show the first CO_2 onset at 4.2 V, which we believe is correlated to the oxidation of surface contaminants at potentials as low as 4.2 V,[25,44] i.e., at a potentials far below the observed onset of oxygen evolution. At a potential of ≥4.6 V, strong oxygen release occurs during the first charge cycle, accompanied by a striking increase in CO_2 evolution, whereby it was shown that oxygen from the lattice is released as molecular oxygen and, at least partially as singlet oxygen,[55] leading to CO_2 formation from the reaction of reactive oxygen (surface) species with the electrolyte.[10,26,55] While only traces of oxygen were detected by OEMS during the second charge cycle, a boost in CO_2 evolution at ≥4.6 V (where the onset of oxygen evolution is observed in the first cycle) still suggests further reaction with lattice oxygen.

In contradiction to the OEMS analysis, which shows substantial O_2 and CO_2 evolution at ≥4.6 V in the first two cycles, HRTEM investigations of the 0.42 Li_2MnO_3 material (Figure 7) do not show any structural changes at the surface of the material after 2 cycles, implying that although the main part of the oxygen is released, the layered structure is still preserved. However, a clear structural surface transformation into a spinel-like layer can be observed after 50 consecutive charge/discharge cycles for all HE-NCM compositions, the thickness of which correlates nicely with the gas evolution in the first two cycles (see above). Another key observation is that the impedance spectra in Figure 6 are consistent with the HRTEM measurements: i) after 2 cycles, the HE-NCMs with the highest oxygen release showed the lowest charge-transfer resistance (Figure 6a), which we associate with the formation of a layered surface structure with abundant vacancies caused by the high oxygen release, allowing for fast lithium diffusion; and, ii) the impedance spectra after 50 cycles showed the highest charge-transfer resistance for the material with the highest oxygen release (Figure 6b), suggesting that the initial oxygen-vacant layered surface structure underwent a structural transformation into a spinel-like phase, inhibiting lithium diffusion, particularly for the thicker layers formed at the more lithium-rich HE-NCMs. From these observations emerges the hypothesis that the release of lattice oxygen does not immediately induce a phase transformation of the formed oxygen-depleted surface layer. Instead, the above presented data suggest that only the de-lithiation/lithiation processes over the course of subsequent cycling leads to a progressive phase transformation of the layered oxygen-vacant surface region. The half-cell cycling data from Figure 4 provide strong evidence that this phase transformation process indeed takes place during the first 20 cycles, leading to the observed capacity loss due to the gradual transformation of the layered oxygen-vacant surface region into a spinel-like surface layer. This hypothesis is schematically depicted in Scheme 1.

Correlation between capacity fading and spinel surface layer formation.—In the following, the effect of the surface layer formation and its subsequent restructuration shall be examined more quantitatively and correlated to the half-cell cycling performance of the material. It was shown in Figure 4a that a higher Li_2MnO_3

A2728 Journal of The Electrochemical Society, **165** (11) A2718-A2731 (2018)

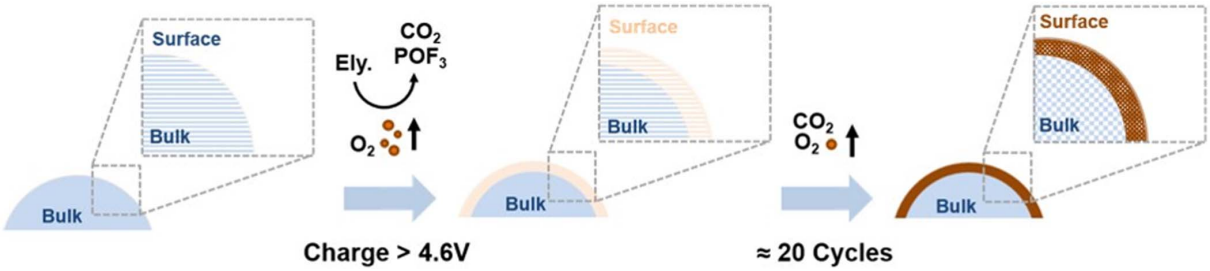

Scheme 1. Schematic presentation of the gas evolution processes and of the hypothesized mechanism of the spinel-type surface layer formation. Left panel: During the initial part of the first charge of (HE)-NCMs, surface impurities are decomposed at potentials below 4.6 V, accompanied by CO_2 evolution. Upon charging to ≥ 4.6 V, O_2 is released from the oxide lattice, also forming CO_2 by interaction of reactive oxygen (surface) species with the electrolyte. This leads to the formation of an oxygen deficient layered surface structure. Right panel: Over ≈20 subsequent charge/discharge cycles, the initially formed surface layer is converted into a resistive spinel-type surface layer. Furthermore, cation migration in the bulk material, happening independently of the O_2 release from the near-surface regions, leads to the observed voltage fading over extended cycling, evidence for which is reported in a previous study.[35]

content and thus also a higher oxygen release leads to faster capacity fading. Furthermore, the corresponding dQ/dV plots for the charging cycles show the evolution of a new phase between 2.0 V and 3.15 V (shaded areas in Figure 5), the capacitive contribution of which increases mainly during the first 20 cycles and is the larger the higher the Li_2MnO_3 content of the material and the higher the oxygen release. As it is has been shown in the literature that spinel structures delithiate at roughly the same potential,[47,48] it is conceivable that the lithiation capacity between 2.0 V and 3.15 V corresponds to the lithiation of a spinel-like surface layer formed by the structural surface transformation upon oxygen release. If this were true, part of the capacity fading should be ascribable to the lower capacity of the resulting spinel vs. the initially present layered surface phase. To examine this hypothesis, Table V compares the measured capacity losses between cycle 3 and cycle 48 ($Q_{loss}^{meas.}$) of the three HE-NCMs (data from Figure 4a) with the charge capacities between 2.0 V and 3.15 V for cycle 48 (referred to as $Q_{spinel}^{meas.}$) that correspond to the capacities under the shadowed areas in Figure 5c.

To quantitatively evaluate this hypothesis that the lower capacity of the spinel surface layer formed by oxygen release can be attributed to the observed capacity loss, we estimate the capacity contributions from the layered bulk structure of the HE-NCM ($Q_{layered}^{est.}$) and that of the surface spinel layer formed over cycling ($Q_{spinel}^{est.}$). The capacity of the former can be estimated by taking the observed capacity of the HE-NCMs after the two activation cycles (≈250 mAh/g in the third cycle, see Figure 4), at which point the spinel-layer has not yet been formed, and multiplying it with the remaining fraction of layered material, using the value of the mol% of spinel estimated by the OEMS data (taken from Table IV, Model II):

$$Q_{layered}^{est.} = (1 - x_{spinel}) \bullet 250\ mAh/g \quad [14]$$

Similarly, assuming the theoretical reversible capacity of a spinel to be roughly 140 mAh/g,[47] the estimated capacity of the surface layer after surface restructuration can be calculated by multiplying the mol% of spinel (taken from Table IV, Model II) with the theoretical capacity of a spinel:

$$Q_{spinel}^{est.} = x_{spinel} \bullet 140\ mAh/g \quad [15]$$

Thus, the capacity fade caused by the formation of a surface spinel layer ($Q_{loss}^{est.}$) would correspond to the difference between the initially observed capacity of the HE-NCMs (≈250mAh/g) and subtracting the estimated capacity contributions from the remaining layered bulk structure and the surface spinel layer:

$$Q_{loss}^{est.} = 250\ mAh/g - \left(Q_{layered}^{est.} + Q_{spinel}^{est.}\right) \quad [16]$$

In Table V, the actually measured values of $Q_{loss}^{meas.}$ (from Figure 4) and $Q_{spinel}^{meas.}$ (Figure 5) are compared with their estimated values derived from the OEMS measurements (O_2 + CO_2 from Model II, see Table IV). The striking agreement between the measured and estimated capacity losses ($Q_{loss}^{meas.}$ vs. $Q_{loss}^{est.}$) and between the measured and estimated contributions of the spinel surface layer to the capacity ($Q_{spinel}^{meas.}$ vs. $Q_{spinel}^{est.}$), provides strong evidence that the capacity fading of HE-NCMs is caused by the formation of a spinel surface layer with a lower intrinsic capacity compared to the originating layered structure.

Examination of voltage fading.—Despite the large changes in the extent of surface spinel formation and oxygen release as a function of Li_2MnO_3 content, the extent of voltage fading does seem rather independent of the Li_2MnO_3 content (see Figure 4b). Thus, we conclude that the oxygen release and the associated surface layer formation is not the main driving force for the observed voltage fading. To a smaller extent, however, it does influence the mean charge voltage, as the capacity contribution for charging the surface spinel layer at 2.0 to ≈3.15 V increases with increasing Li_2MnO_3 content (see Figure 5) and thus with increasing oxygen release (Figure 3). Nevertheless, since the capacity contribution from the surface spinel layer does not exceed 10% of the overall capacity (see Table V), it is not surprising that the charge voltage fading of the 0.50 Li_2MnO_3 material is only insignificantly larger for the 0.50 Li_2MnO_3 compared to the other materials (see Figure 4b). As oxygen release cannot be responsible for the observed voltage fading, the probable reason is that the reported

Table V. Capacity loss measured from half-cell cycling in Figure 4 ($Q_{loss}^{meas.}$) and capacity loss estimated by the amount of surface degradation ($Q_{loss}^{est.}$), as shown in Table IV. These values can be compared to the measured capacity of the spinel layer from Figure 5 ($Q_{spinel}^{meas.}$) and to the estimated capacity of the spinel layer ($Q_{spinel}^{est.}$) according to Equations 14–16.

	Capacity loss [mAh/g]		Capacity surface layer [mAh/g]	
Li_2MnO_3	Q_{loss}^{meas}	$Q_{loss}^{est.}$	Q_{spinel}^{meas}	$Q_{spinel}^{est.}$
0.33	7	6	8	7
0.42	15	12	18	15
0.50	28	22	25	28

transition metal movement within the layered bulk material leads to changes of the thermodynamic potentials, at least at low C-rates, where differences in impedance are less critical: reversible transition metal movement leading to the charge/discharge voltage hysteresis and irreversible transition metal movement to voltage-fading.[35,38,46]

At higher C-rates, the substantially larger impedance growth for more the more lithium-rich materials (see Figure 6) may lead to overall lower mean discharge voltages. Unfortunately, it is not possible to quantify this effect on the basis of the impedances shown only for 50% SOC in Figure 6, as the impedance for HE-NCMs is known to be strongly dependent on SOC.[14]

Effect of different Li_2MnO_3 contents onto full-cell performance.—So far, all data discussed in this study focused onto the half-cell performance and the structural changes of the cathode material. While the capacity and capacity fading in half-cells at low/moderate C-rate is mainly limited by the real capacity of the cathode material (impedance effects usually being small) and by cycling induced capacity changes, the performance of full-cells at faster C-rates can in addition be limited by impedance growth, cell balancing, and the loss of active lithium (also via crosstalk effects between the anode and the cathode). Therefore, in order to predict the performance of actual battery cells with a new cathode material, full-cell data are required, whereby also the amount of electrolyte added to the cells plays an important role. Wagner et al. showed that the mass ratio of electrolyte to cathode active material in large-scale commercial cells is on the order of m_{ely}:m_{CAM} ≈1:3,[56] which is typically ≈10-fold lower than what is used in coin cells (or other small-scale test cells). In the following, in order to most closely approach the value in large-scale cells, we used a ratio of m_{ely}:m_{CAM} ≈1:1, the lowest ratio with which we could still obtain reproducible coin cell data.

From Figure 9a it can be seen that the capacity fading for all the HE-NCM materials is similar over the first 50 cycles. After 50 cycles, the discharge capacity at 1C ranges from 200–220 mAh/g, only ≈20 mAh/g lower than the discharge capacity at C/5 in the half-cells (see Figure 4a). Beyond 50 cycles, the full-cell capacity of the material with 0.50 Li_2MnO_3 content (blue line in Figure 9a) actually surpasses that of the other materials, which can be explained by the larger lithium reservoir produced in the graphite anode (see Table II).

The mean discharge voltage observed in full-cells (Figure 9b) follows the same order as in half-cells (Figure 4b), being the lower the higher Li_2MnO_3 content. Over the first 50 cycles, all materials exhibit a ≈2-fold higher mean discharge voltage-fading at 1C in full-cells compared to that in half-cells at C/5, which most likely is due to the significant impact of the cathode impedance on cell voltage at the high current densities at 1C (2.1 mA/cm^2), so that an increase in the charge transfer resistance over extended cycling will have a larger effect on voltage-fading. Finally, one of the most important factors for the practical assessment of the materials is their specific discharge energy, i.e. the product of capacity and mean discharge potential, shown in Figure 9c. It demonstrates that essentially identical specific discharge energy values and fading rates are observed for all HE-NCMs, independent of their Li_2MnO_3 content. Nevertheless, regarding their practical application in large-scale cells, the 0.33 Li_2MnO_3 material is superior, as it would release the least amount of gas during the first two formation cycles, namely ≈0.25 $mmol_{O2+CO2}/g_{AM}$ (≡ 6 cm^3_{O2+CO2}/g_{AM}) for the 0.33 Li_2MnO_3 material vs. ≈0.90 $mmol_{O2+CO2}/g_{AM}$ (≡ 22 cm^3_{O2+CO2}/g_{AM}) for the 0.50 Li_2MnO_3 material (see Figure 3).

O_2 and CO_2 evolution of HE-NCM vs. NCM.—Jung et al. recently reported a similar oxygen release from stoichiometric NCM materials, also caused by a chemical spinel transformation at the particle surface.[10] The onset potential for oxygen evolution and the amount of oxygen release was shown to be strongly dependent on the nickel content of the material, whereby oxygen release was always observed at ≈80% SOC. To compare the oxygen release from HE-NCM and stoichiometric NCM, the here used base NCM material for the HE-NCMs (referred to as 0.00 Li_2MnO_3 • 1.00 $LiMeO_2$ in Table I) was also investigated by OEMS. Results for the gas evolution of the base NCM are shown in Figure 10, using the same procedure that was used for the HE-NCMs (see Figure 3). In contrast to the HE-NCMs, oxygen evolution already occurred at 4.52 V and is also mainly observed during the first cycle. Furthermore, a strong increase in the CO_2 evolution was observed at the onset of oxygen evolution in the first cycle; in the second cycle, CO_2 evolution was observed at the potential where O_2 evolution had started in the first cycle, analogous to the OEMS data with the HE-NCM materials (see Figure 3). These data strongly suggest that oxygen release and subsequent surface restructuration for HE-NCM and stochiometric NCM materials follow

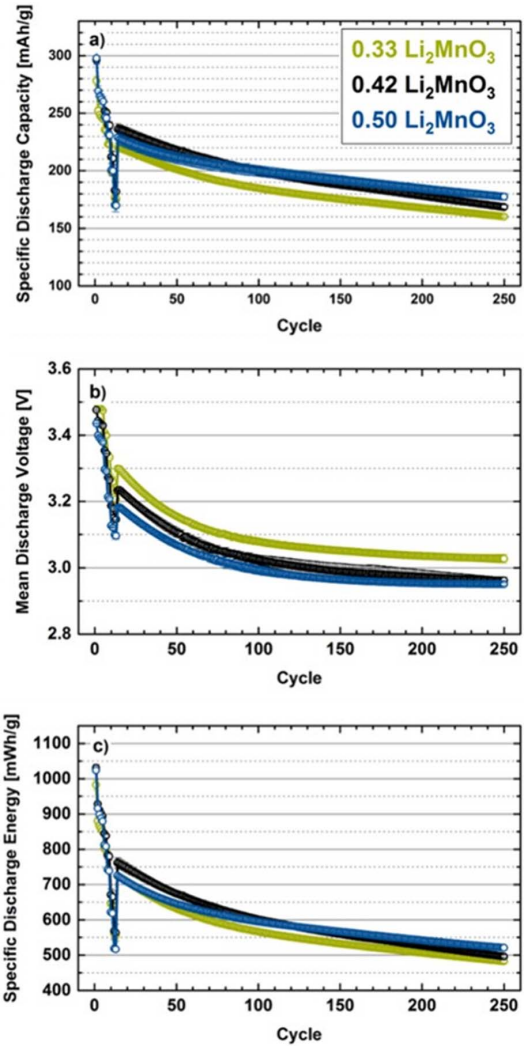

Figure 9. Electrochemical cycling of the different HE-NCM compositions in full-cells at 25°C, using a graphite anode, 14 µL of FEC:DEC (2:8 g:g) with 1 M $LiPF_6$ electrolyte with a proprietary co-solvent (m_{ely}: m_{CAM} ≈1:1) and a Celgard separator. The first activation cycles were carried out at C/15 to 4.7 V where the potential was held for 1 h and then the cell was discharged at C/15 to 2.0 V. This was followed by a rate test (up to 3C) between 2.0 V and 4.6 V, while further cycling was carried out at C/2 charge (+1h CV) rate and 1 C discharge between 2.0 V and 4.6 V. (a) Shows the specific discharge capacity as a function of the cycle number, (b) shows the mean discharge voltages, and (c) shows the specific discharge energy referenced to the cathode active material weight. All data points represent the average of at least two independent measurements and the error bars reflect the maximum and minimum of the measured values.

A2730 Journal of The Electrochemical Society, 165 (11) A2718-A2731 (2018)

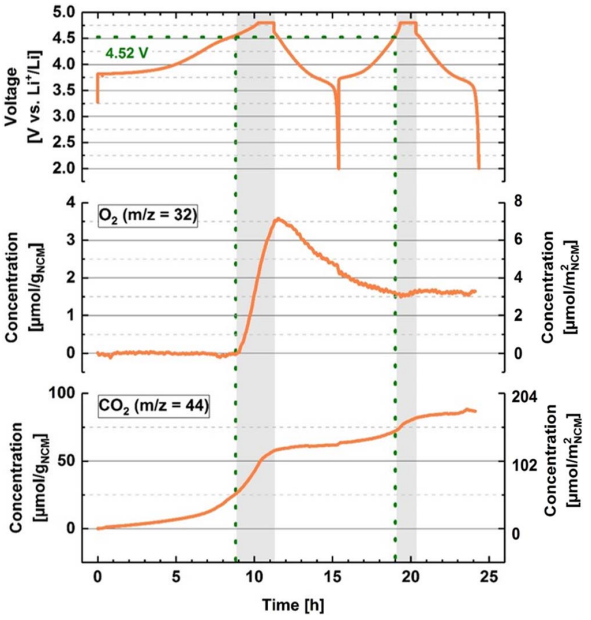

Figure 10. OEMS measurements for the stochiometric NCM (0.00 Li_2MnO_3 • 1.00 $LiMeO_2$, see Table I, using the same cell setup and procedure as in Figure 3 for the HE-NCMs. Upper panel: charge/discharge voltage vs. time; middle/lower panel: evolution of the concentrations of concomitantly evolved O_2/CO_2 given in units of either µmol/g_{AM} (left axes) or µmol/m^2_{AM} (right axes).

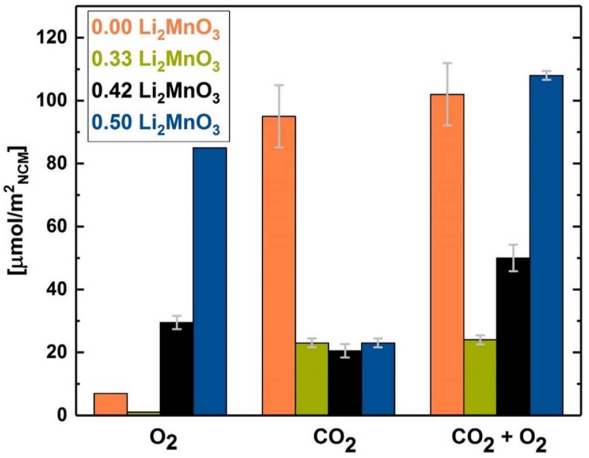

Figure 11. O_2 and CO_2 (after oxygen onset) evolution of the first two cycles are shown for the three different materials from Figure 3 (0.33, 0.42 and 0.50 Li_2MnO_3), data for 0.00 Li_2MnO_3 are from Figure 10. Total gas amounts were quantified during the first and the second cycle above the oxygen onset potential, depicted by the gray areas in Figure 3 and Figure 10. The error bars shown in this figure are derived from two separate OEMS measurements for each material.

very similar mechanisms, in both cases leading to reactions of lattice oxygen with the electrolyte via a surface reaction[57] and/or the reaction with released singlet oxygen.[55] In addition, for the stochiometric base NCM ("0.00 Li_2MnO_3") and the 0.33 Li_2MnO_3 HE-NCM, the SOC at which oxygen evolution can be observed is essentially identical (≈77%). Increasing the Li_2MnO_3 content however leads to oxygen evolution even at lower SOCs, namely at ≈72% for the 0.42 Li_2MnO_3 material and at ≈69% for the 0.50 Li_2MnO_3 material (all HE-NCM data from Figure 3). The shift of the onset of oxygen evolution to lower SOC values with increasing Li_2MnO_3 content indicates that the near-surface region of the material becomes less stable with increasing Li_2MnO_3 content, which is consistent with the observation that the thickness of the restructured surface layer increases with increasing Li_2MnO_3 content (see Figure 8), extending all the way into the bulk for the 0.50 Li_2MnO_3 material.

To compare the total amount of oxygen evolved from the different HE-NCMs and the stoichiometric NCM, all data for the gas evolution were normalized to the respective BET surface area (see Table I), as the surface area of the stoichiometric NCM was more than ten times smaller than that of the HE-NCMs. For the O_2 quantification, the O_2 evolved during the first two cycles is shown; for CO_2 quantification, the CO_2 evolved above the oxygen onset potential during the first and the second cycle is shown (gray areas in Figure 3 and Figure 10). Figure 11 shows that the 0.33 Li_2MnO_3 material evolves even less oxygen than the stoichiometric base NCM material, while a further increase of the Li_2MnO_3 content substantially increases the released amount of oxygen. Surprisingly, the surface normalized amount of evolved CO_2 for the three HE-NCM materials is essentially identical, despite the largely different oxygen release, while the base NCM releases much higher amounts of CO_2. This observation could be rationalized by either one of the following hypotheses: i) at the high absolute oxygen release rates from the high surface area HE-NCMs, the surface reaction between lattice oxygen and the electrolyte could become rate-limiting, so that a significant fraction of the oxygen is released as molecular oxygen without any further reaction with the electrolyte; or, ii) oxygen released from the surface at high rates as singlet oxygen[55] could form gas bubbles, in which reactive singlet O_2 can decay to triplet oxygen within the gas phase, while the reaction of singlet oxygen with the electrolyte to CO_2 would be limited to the gas/electrolyte interface. It is also conceivable that the latter may be influenced by particle morphology, whereby the hierarchical structure of the HE-NCM particles (consisting of primary agglomerates composed of smaller primary particles with interstitial pores) could lead to a formation/trapping of oxygen gas bubbles in contrast to NCM particles which have no internal void volume.

Despite the so far not clearly understood differences in the evolved CO_2/O_2 ratios for the different materials, the comparison of the total amount of lattice oxygen released from the materials (represented by the sum of $CO_2 + O_2$; see right-hand-side bars in Figure 11) suggests that low amounts of Li_2MnO_3 added to the base NCM can increase the active material stability at high SOCs. This stabilization may explained by the compensation of repulsive forces between the transition metal layers at low lithium content, produced by the loss of lithium from the transition metal layer, thereby creating vacancies within the transition metal layers. These repulsive forces would furthermore be reduced by the reported reversible oxygen redox,[26,32,33] whereby it is conceivable that the creation of vacancies in the transition metal layer during the first activation cycle is responsible for enabling oxygen redox processes.[38] However, increasing the Li_2MnO_3 content leads to an increased lithium occupation in the transition metal layer in the pristine material[58] that will be extracted during the first activation charge, leading to a destabilization of the surface at increasingly lower SOCs, as was discussed above.

Conclusions

In this study, we systematically compared HE-NCM materials with different amounts of Li_2MnO_3 using on-line electrochemical mass spectrometry (OEMS), high-resolution transmission electron microscopy (HRTEM) and electrochemical characterization methods, in order to understand the oxygen release as well as its influence on the active material structure and the electrochemical performance. We could show quantitatively that the half-cell capacity loss at low C-rates during the first 50 cycles can be ascribed to the formation of a surface spinel layer which can be estimated from the gas

evolution. HRTEM shows that the surface layer thickness increases with increasing Li_2MnO_3 content, hereby the thickness was in excellent agreement with the layer thickness estimated from the OEMS experiments, except the 0.50 Li_2MnO_3 material, for which spinel formation occurs all the way into the bulk of the material.

The oxygen release and the total gas release differ vastly for the different materials, even though the full-cell initial capacity, the capacity retention and the voltage fading are rather similar for all materials, which ends up in full-cell energies and energy fading that are essentially identical over 250 cycles. However, for practical applications in large-scale cells the initial gas evolution is a critical factor where the material with 0.33 Li_2MnO_3 outperforms the other materials, having a nearly 4 times lower initial gas evolution (6 cm^3/g_{CAM}) compared to the 0.50 Li_2MnO_3 material (22 cm^3/g_{CAM}). Furthermore, the increase in impedance is more critical for the 0.50 Li_2MnO_3 compared to the other materials, leading to improved rate performance for lower Li_2MnO_3 contents.

Acknowledgment

This work was supported by BASF SE within its BASF SE Battery Research Network. The authors want gratefully acknowledge A. Freiberg, K. Kleiner and R. Jung for their contribution to this work and for the very fruitful discussions.

ORCID

Tobias Teufl https://orcid.org/0000-0001-5889-5204

References

1. J. B. Goodenough and K. S. Park, *J. Am. Chem. Soc.*, **135**(4), 1167 (2013).
2. D. Andre, S.-J. Kim, P. Lamp, S. F. Lux, F. Maglia, O. Paschos, and B. Stiaszny, *J. Mater. Chem. A*, **3**(13), 6709 (2015).
3. K. Mizushima, P. Jones, P. Wiseman, and J. B. Goodenough, *Mat. Res. Bull.*, **15**(6), 783 (1980).
4. Z. Lu, D. D. MacNeil, and J. R. Dahn, *Electrochem. Solid-State Lett*, **4**(12), A200 (2001).
5. J. Choi and A. Manthiram, *J. Electrochem. Soc.*, **152**(9), A1714 (2005).
6. I. Belharouak, Y. K. Sun, J. Liu, and K. Amine, *J. Power Sources*, **123**(2), 247 (2003).
7. M.-H. Kim, H.-S. Shin, D. Shin, and Y.-K. Sun, *J. Power Sources*, **159**(2), 1328 (2006).
8. R. Jung, M. Metzger, F. Maglia, C. Stinner, and H. A. Gasteiger, *J. Phys. Chem. Lett.*, **8**(19), 4820 (2017).
9. D. Streich, C. Erk, A. Guéguen, P. Müller, F.-F. Chesneau, and E. J. Berg, *J. Phys. Chem. C*, **121**(25), 13481 (2017).
10. R. Jung, M. Metzger, F. Maglia, C. Stinner, and H. A. Gasteiger, *J. Electrochem. Soc.*, **164**(7), A1361 (2017).
11. M. M. Thackeray, S.-H. Kang, C. S. Johnson, J. T. Vaughey, R. Benedek, and S. A. Hackney, *J. Mat. Chem.*, **17**(30), 3112 (2007).
12. J. R. Croy, M. Balasubramanian, K. G. Gallagher, and A. K. Burrell, *Acc. Chem. Res.*, **48**(11), 2813 (2015).
13. S. R. Gowda, D. W. Dees, A. N. Jansen, and K. G. Gallagher, *J. Electrochem. Soc.*, **162**(7), A1374 (2015).
14. T. Teufl, D. Pritzl, S. Solchenbach, H. A. Gasteiger, and M. Mendez, *manuscript in preparation*.
15. A. R. Armstrong, M. Holzapfel, P. Novák, C. S. Johnson, S.-H. Kang, M. M. Thackeray, and P. G. Bruce, *J. Am. Chem. Soc.*, **128**(26), 8694 (2006).
16. C. S. Johnson, J. S. Kim, C. Lefief, N. Li, J. T. Vaughey, and M. M. Thackeray, *Electrochem. Commun.*, **6**(10), 1085 (2004).
17. F. La Mantia, F. Rosciano, N. Tran, and P. Novák, *J. Appl. Electrochem.*, **38**(7), 893 (2008).
18. P. Lanz, H. Sommer, M. Schulz-Dobrick, and P. Novák, *Electrochim. Acta*, **93**, 114 (2013).
19. Z. Lu, L. Y. Beaulieu, R. A. Donaberger, C. L. Thomas, and J. R. Dahn, *J. Electrochem. Soc.*, **149**(6), A778 (2002).
20. Z. Lu and J. R. Dahn, *J. Electrochem. Soc.*, **149**(7), A815 (2002).
21. D. Mohanty, J. Li, S. C. Nagpure, D. L. Wood, and C. Daniel, *MRS Energy & Sustainability*, **2**, (2015).
22. N. Yabuuchi, K. Yoshii, S. T. Myung, I. Nakai, and S. Komaba, *J. Am. Chem. Soc.*, **133**(12), 4404 (2011).
23. A. Guéguen, D. Streich, M. He, M. Mendez, F. F. Chesneau, P. Novák, and E. J. Berg, *J. Electrochem. Soc.*, **163**(6), A1095 (2016).
24. D. Streich, A. Guéguen, M. Mendez, F. Chesneau, P. Novák, and E. J. Berg, *J. Electrochem. Soc.*, **163**(6), A964 (2016).
25. B. Strehle, K. Kleiner, R. Jung, F. Chesneau, M. Mendez, H. A. Gasteiger, and M. Piana, *J. Electrochem. Soc.*, **164**(2), A400 (2017).
26. K. Luo, M. R. Roberts, R. Hao, N. Guerrini, D. M. Pickup, Y.-S. Liu, K. Edström, J. Guo, A. V. Chadwick, L. C. Duda, and P. G. Bruce, *Nat. Chem.*, **8**, 684 (2016).
27. H. Koga, L. Croguennec, M. Menetrier, K. Douhil, S. Belin, L. Bourgeois, E. Suard, F. Weill, and C. Delmas, *J. Electrochem. Soc.*, **160**(6), A786 (2013).
28. H. Koga, L. Croguennec, M. Ménétrier, P. Mannessiez, F. Weill, and C. Delmas, *J. Power Sources*, **236**, 250 (2013).
29. C. Genevois, H. Koga, L. Croguennec, M. Ménétrier, C. Delmas, and F. Weill, *J. Phys. Chem. C*, **119**(1), 75 (2014).
30. R. Petibon, L. Madec, D. W. Abarbanel, and J. R. Dahn, *J. Power Sources*, **300**, 419 (2015).
31. S. Muhammad, H. Kim, Y. Kim, D. Kim, J. H. Song, J. Yoon, J.-H. Park, S.-J. Ahn, S.-H. Kang, and M. M. Thackeray, *Nano Energy*, **21**, 172 (2016).
32. E. McCalla, A. M. Abakumov, M. Saubanère, D. Foix, E. J. Berg, G. Rousse, M.-L. Doublet, D. Gonbeau, P. Novák, G. Van Tendeloo, D. R., and J. M. Tarascon, *Science*, **350**(6267), 1516 (2015).
33. D. H. Seo, J. Lee, A. Urban, R. Malik, S. Kang, and G. Ceder, *Nat. Chem.*, **8**(7), 692 (2016).
34. H. Koga, L. Croguennec, M. Ménétrier, P. Mannessiez, F. Weill, C. Delmas, and S. Belin, *J. Phys. Chem. C*, **118**(11), 5700 (2014).
35. K. Kleiner, B. Strehle, A. R. Baker, S. J. Day, C. C. Tang, I. Buchberger, F.-F. Chesneau, H. A. Gasteiger, and M. Piana, *Chem. Mater.*, (2018), *in press*,.
36. G. Assat, C. Delacourt, D. A. D. Corte, and J.-M. Tarascon, *J. Electrochem. Soc.*, **163**(14), A2965 (2016).
37. B. Qiu, M. Zhang, Y. Xia, Z. Liu, and Y. S. Meng, *Chem. Mat.*, **29**(3), 908 (2017).
38. W. E. Gent, K. Lim, Y. Liang, Q. Li, T. Barnes, S.-J. Ahn, K. H. Stone, M. McIntire, J. Hong, J. H. Song, Y. Li, A. Mehta, S. Ermon, T. Tyliszczak, D. Kilcoyne, D. Vine, J.-H. Park, S.-K. Doo, M. F. Toney, W. Yang, D. Prendergast, and W. C. Chueh, *Nat. Commun.*, **8**(1), 2091 (2017).
39. N. Tsiouvaras, S. Meini, I. Buchberger, and H. A. Gasteiger, *J. Electrochem. Soc.*, **160**(3), A471 (2013).
40. J. R. Croy, K. G. Gallagher, M. Balasubramanian, B. R. Long, and M. M. Thackeray, *J. Electrochem. Soc.*, **161**(3), A318 (2013).
41. J. Choi and A. Manthiram, *Electrochem. Solid-State Letters*, **8**(8), C102 (2005).
42. I. Buchberger, S. Seidlmayer, A. Pokharel, M. Piana, J. Hattendorff, P. Kudejova, R. Gilles, and H. A. Gasteiger, *J. Electrochem. Soc.*, **162**(14), A2737 (2015).
43. S. E. Renfrew and B. D. McCloskey, *J. Am. Chem. Soc.*, **139**(49), 17853 (2017).
44. R. Jung, P. Strobl, F. Maglia, C. Stinner, and H. A. Gasteiger, *manuscript in preparation*.
45. J. R. Croy, K. G. Gallagher, M. Balasubramanian, Z. Chen, Y. Ren, D. Kim, S.-H. Kang, D. W. Dees, and M. M. Thackeray, *J. Phys. Chem. C*, **117**(13), 6525 (2013).
46. M. Sathiya, A. M. Abakumov, D. Foix, G. Rousse, K. Ramesha, M. Saubanere, M. L. Doublet, H. Vezin, C. P. Laisa, A. S. Prakash, D. Gonbeau, G. VanTendeloo, and J. M. Tarascon, *Nat. Mater.*, **14**(2), 230 (2015).
47. M. M. Thackeray, *Prog. Solid State Chem.*, **25**, 1 (1997).
48. P. G. Bruce, A. R. Armstrong, and L. Gitzendanner, *J. Mat. Chem.*, **9**, 193 (1998).
49. J. C. Burns, A. Kassam, N. N. Sinha, L. E. Downie, L. Solnickova, B. M. Way, and J. R. Dahn, *J. Electrochem. Soc.*, **160**(9), A1451 (2013).
50. D. Pritzl, A. Bumberger, M. Wetjen, J. Landesfeind, S. Solchenbach, and H. Gasteiger, *manuscript in preparation*.
51. J. Landesfeind, D. Pritzl, and H. A. Gasteiger, *J. Electrochem. Soc.*, **164**(7), A1773 (2017).
52. S.-M. Bak, K.-W. Nam, W. Chang, X. Yu, E. Hu, S. Hwang, E. A. Stach, K.-B. Kim, K. Y. Chung, and X.-Q. Yang, *Chem. Mat.*, **25**(3), 337 (2013).
53. S. M. Bak, E. Hu, Y. Zhou, X. Yu, S. D. Senanayake, S. J. Cho, K. B. Kim, K. Y. Chung, X. Q. Yang, and K. W. Nam, *ACS Appl. Mater. Interfaces*, **6**(24), 22594 (2014).
54. D. Mohanty, S. Kalnaus, R. A. Meisner, K. J. Rhodes, J. Li, E. A. Payzant, D. L. Wood, and C. Daniel, *J. Power Sources*, **229**, 239 (2013).
55. J. Wandt, A. T. S. Freiberg, A. Ogrodnik, and H. A. Gasteiger, *Materials Today*, 2018, *in press*,.
56. F. T. Wagner, B. Lakshmanan, and M. F. Mathias, *J. Phys. Chem. Lett.*, **1**(14), 2204 (2010).
57. T. M. Østergaard, L. Giordano, I. E. Castelli, F. Maglia, B. K. Antonopoulos, Y. Shao-Horn, and J. Rossmeisl, *J. Phys. Chem. C*, **122**(19), 10442 (2018).
58. H. Liu, Y. Chen, S. Hy, K. An, S. Venkatachalam, D. Qian, M. Zhang, and Y. S. Meng, *Adv. Energy Mat.*, **6**(7), 1502143 (2016).

3.2.3 Temperature Dependence of Oxygen Release

While the former section 3.2.2 investigated the influence of the Li_2MnO_3 content on the oxygen release, it is also interesting to have a look on its temperature dependence. In the case of stoichiometric layered oxides, Jung et al. have shown that the oxygen release from NCM-622 (in the form of O_2, CO, and CO_2) increases by a factor of ≈2.5 when going from 25°C to 50°C (under otherwise identical cycling conditions).[82] Since this leads in turn to thicker and more resistive spinel/rock-salt surface layers, the increased oxygen release adversely affects the full-cell performance during a cycle-life test. Turning again towards Li- and Mn-rich layered oxides, Erickson et al. observed the opposite effect during low-temperature electrochemical activation.[255] Performing the first two cycles at 0°C or 15°C compared to their standard temperature of 30°C increases the discharge capacity by 20-30 mAh/g in the following cycles (which were all done at 30°C, independent of the activation temperature). Furthermore, the difference in the average charge/discharge voltages gets diminished, while the capacity decay and the discharge voltage fading over 100 cycles are not affected by the activation process. In their communication, the authors could not unambiguously clarify whether the phenomenon of the low-temperature activation is a surface- or bulk-dominated process. In principle, both might be possible, as the bulk structure could be better retained at low temperatures, e.g., leading to less TM migration and faster lithium diffusion kinetics. At the surface, the reduction of the oxygen release could result in thinner and less resistive spinel layers. In order to elucidate the impact of surface effects, we performed OEMS experiments with the standard LMR-NCM containing 0.42 Li_2MnO_3 and under similar conditions as in the study by Erickson et al.[255]

Table 6 summarizes the most important cycling conditions. To stay within the OEMS measurement time of ≈30 h, the C-rates of the first three cycles were accelerated compared to Erickson et al., and the experiment was divided into two parts. After the first two cycles at the variable temperature of either 0, 15, 30, or 45°C, the cell was flushed with argon to re-establish the original base pressure for the last three cycles, which were conducted at the fixed temperature of 30°C. Furthermore, we used partially delithiated and capacitively over-sized LFP as counter-electrode, as neither O_2 nor CO_2 get reduced at the LFP potential.[155] Figure

15 shows the discharge capacities measured during the OEMS experiments. As expected from the study by Erickson et al.,[255] the low-temperature activation drastically decreases the capacity in the first two cycles, but it surpasses the higher activation temperatures by up to 25 mAh/g in the subsequent cycles at 30°C.

Table 6. Cycling conditions of the activation study, as they were originally done at Bar-Ilan University (BIU) by Erickson et al.[255] and as they were then adopted at the Technical University of Munich (TUM) for the OEMS experiments. The C-rates are based on a theoretical capacity of 250 mAh/g and the constant voltage (CV) step was conducted after reaching the upper cut-off voltage during charge. While metallic lithium was used as counter-electrode (CE) at BIU, we used partially delithiated LFP as an inert alternative (assuming voltage plateaus of 3.4 V and 3.5 V vs. Li^+/Li for the LFP counter-electrode during charge and discharge of the LMR-NCM working-electrode, respectively). The electrolyte is in both cases LP57 (1M $LiPF_6$ in EC:EMC 3:7 by weight). The cathode was coated on a steel mesh[155] and has a CAM content of 80 wt%.[255]

Cycle	Temperature [°C]	Voltage range [V vs. Li^+/Li]	C-rates [h^{-1}]		CV time [h]
			@BIU	@TUM	
1	0/15/30/45	2.0-4.7	C/15	C/7.5	3
2	0/15/30/45	2.0-4.6	C/10	C/7.5	0.5
3	30	2.0-4.6	C/10	C/7.5	0.5
4	30	2.0-4.6	C/3	C/3	0.5
5	30	2.0-4.6	C/3	C/3	0.5

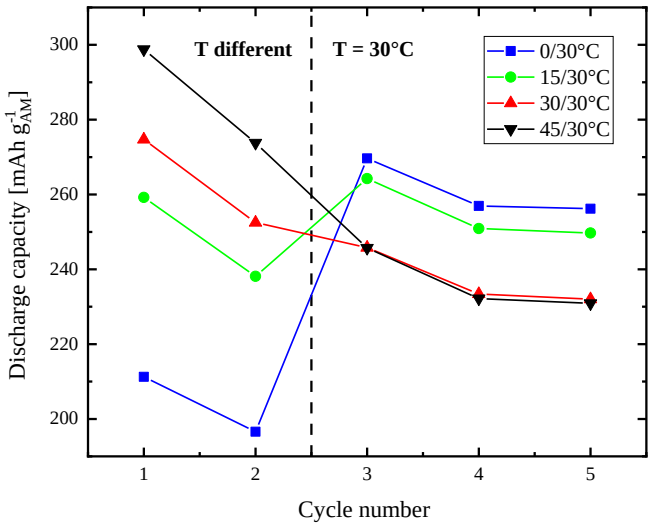

Figure 15. Discharge capacity vs. cycle number of the Li- and Mn-rich layered oxide with 0.42 Li_2MnO_3 during the four OEMS experiments described in Table 6.

Figure 16 shows the gassing results of the OEMS experiments. Focusing on the O_2 evolution in the middle panel, the released amount during the first charge ranges from only ≈5 µmol/g at 0°C until almost ≈700 µmol/g at 45°C. This is due to the largely different capacity extracted from the CAM. While the uppermost state of

charge reaches 76% at 0°C (SOC equals the charge capacity divided by the theoretical capacity of 363 mAh/g for complete lithium extraction), it increases to 93% at 45°C and is thus far beyond the ≈70-80% SOC limit, where all layered oxides start to evolve oxygen.[25,27] The voltage curves in the upper panel reveal that the initial sloping region until ≈1.0 V vs. LFP (≈4.4 V vs. Li^+/Li, originating purely from TM redox[142,143,159]) is barely affected by the temperature, but the subsequent voltage plateau extends with increasing temperature. As the plateau arises from the reversible anionic redox in the bulk (O^{2-}/O^{n-}) that is characterized by sluggish kinetics,[142,143,159] the irreversible oxygen loss at the surface also increases with temperature. Due to the increased mobility of the lattice oxide ions, the oxygen depletion penetrates deeper into the particles when increasing the temperature. Interestingly, the amount of evolved oxygen scales in a similar range as in our former study on the variation of the Li_2MnO_3 content (all measured at 25°C).[27] Consequently, the spinel transformation is restricted to a nm-thin near-surface layer during low-temperature activation, but spinel-like domains probably grow into the interior of the particles during activation at 45°C.

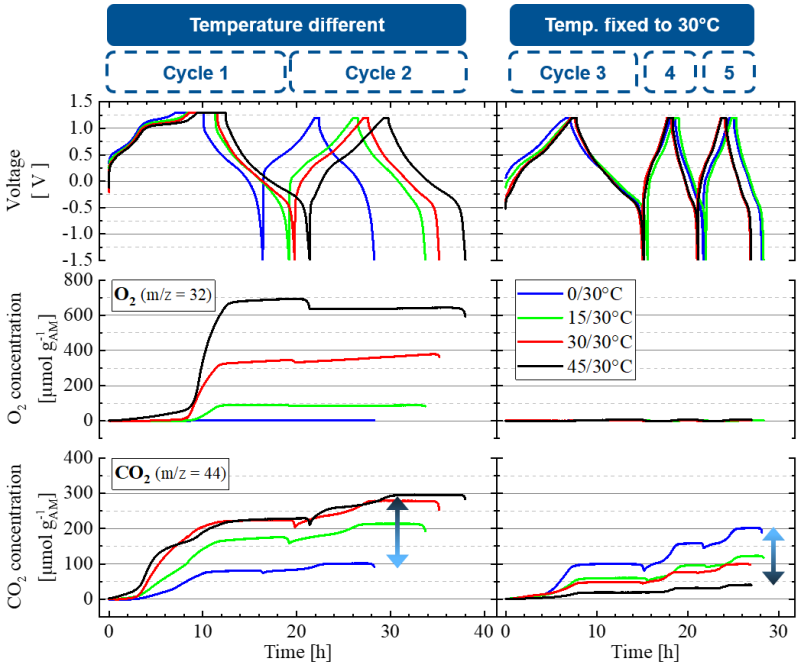

Figure 16. OEMS measurements for the different activation procedures of the over-lithiated CAM with 0.42 Li_2MnO_3 content. **Upper panel:** Charge/discharge voltage vs. the LFP counter-electrode in LP57 electrolyte. **Middle/lower panel:** Concentrations of the concomitantly evolved O_2/CO_2 given in units of µmol/g_{AM}. The first two cycles were performed at different temperatures, while the following cycles were conducted at a fixed temperature of 30°C. Since the cells were flushed with argon in between the second and third cycle to remove the already released gases, the time and concentrations are set back to 0 for the second part of the experiment. Further experimental details can be obtained from Table 6.

The release of molecular O_2 could be solely detected within the first charge, but the evolution of CO_2 also continues in the following cycles (see lower panel in Figure 16). CO_2 can be evolved from several sources. While carbonate-based electrolytes are oxidatively stable until ≈4.6 V vs. Li^+/Li (≈1.2 V vs. LFP), releasing CO_2 only beyond this onset potential by electrochemical oxidation,[46] we assign the initial CO_2 during the voltage plateau of the first charge mainly to the chemical decomposition of carbonate impurities according to: $Li_2CO_3 + 2H^+ \rightarrow 2Li^+ + H_2O + CO_2$.[256] Carbonates such as Li_2CO_3 or basic nickel carbonate, $(NiCO_3)_x \cdot (Ni(OH)_2)_y \cdot (H_2O)_z$, are well-known surface contaminants on layered oxides, which are left over from the calcination process and/or formed during ambient air storage.[165,180,199] The required protons originate from the anodic oxidation of the electrolyte solvents (at >4.6 V vs. Li^+/Li) or of trace impurities in the electrolyte, such as ethanol and ethylene glycol (EG), which get oxidized at rather low potentials of ≈3.5 V vs. Li^+/Li (−0.1 V vs. LFP).[256] This potential is slightly above the open circuit voltage of the CAM and CO_2 is indeed released directly after the start of the first charge at 45°C, where the above decomposition reactions are expected to be enhanced compared to lower temperatures due to faster kinetics. The evolved amount of ≈160 µmol/g CO_2 until the end of the voltage plateau at 45°C would correspond to a mass fraction of ≈0.1 wt% ethylene glycol in the electrolyte (releasing $2H^+$ per EG) and ≈1 wt% of carbonate impurities on the CAM surface (releasing $1CO_2$ per CO_3^{2-}). Both values represent the upper limit of contaminants that are expected either in Li-ion battery electrolytes or on cathode active materials. Regarding carbonate impurities, Pritzl et al. reported ≈0.5 wt% CO_3^{2-} on Ni-rich NCM-851005,[257] while we measured ≈0.4 wt% CO_3^{2-} on a follow-up batch of this high surface area Li- and Mn-rich CAM. Since carbonates are typically accompanied by hydroxide contaminants (e.g., LiOH and $Ni(OH)_2$ in basic nickel carbonate), a part of the (initial) CO_2 evolution might also arise from the hydroxide-driven hydrolysis of ethylene carbonate, especially at 30°C and 45°C.[82,179]

At the end of the first charge, another process is taking place that evolves CO_2 in parallel to O_2. The oxygen release from layered oxides was shown to be, at least partially, in the form of highly reactive singlet oxygen,[47] which can either transition to triplet oxygen (detected by OEMS) or react chemically with ethylene carbonate, forming in several steps CO_2.[49] In the following cycles, it is difficult to clearly

differentiate all the processes causing CO_2 evolution (viz., EC decomposition due to singlet oxygen, decomposition of carbonate impurities, chemical electrolyte oxidation, EC hydrolysis). However, the low-temperature activation, especially at 0°C, causes substantially more CO_2 evolution in the subsequent cycles. This is illustrated in Figure 17, where the total amount of CO_2 is divided into its contributions from every single cycle. While the overall amount of evolved CO_2 is in a comparable range of ≈305-380 µmol/g, lowering the activation temperature in cycle 1+2 shifts more CO_2 to the subsequent cycles. The differences in the amount of CO_2 released in cycle 3-5, all conducted at 30°C, point towards further oxygen release from the CAM surface (in the form of singlet oxygen reacting with EC) and/or from unreacted carbonate impurities to be the main origin of CO_2 evolution, because the electrolyte oxidation and EC hydrolysis are expected to depend predominantly on the applied voltage range and/or temperature, which were identical for all four experiments.

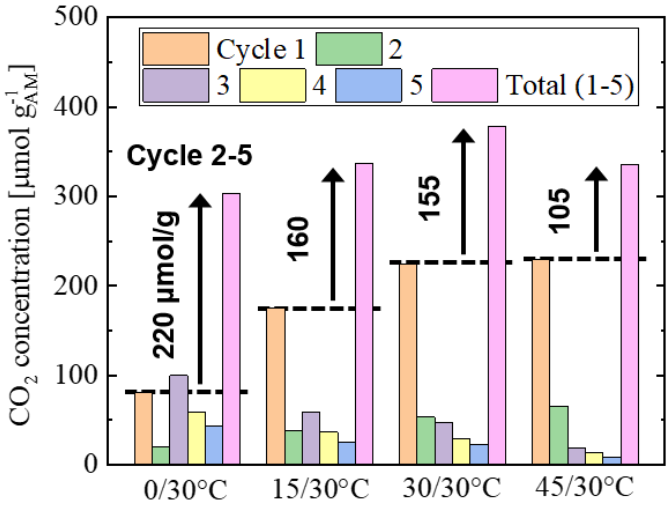

Figure 17. Bar chart of the evolved amount of CO_2 in every single cycle and during the entire OEMS experiment. Cycle 1 and 2 were performed at different temperatures, ranging from 0°C to 45°C, while the cycles 3-5 were done at a constant temperature of 30°C. The arrows and numbers indicate the CO_2 release in the cycles 2-5.

The shift of gas release between different cycles has practical implications on large-format cells. Since the degassing step is typically done within the first formation cycle, substantial gassing in the subsequent cycles represents a potential safety risk after the final sealing of the cells. Schreiner et al. addressed this issue in their study with 7 Ah LMR-NCM/graphite multi-layer pouch cells manufactured on a pilot production line.[166] Dependent on the first formation cycle, which was either done

at 25°C or 45°C, the gas release in the subsequent three cycles at 25°C amounted to ≈125 µmol/g (25°C activation) or ≈60 µmol/g (45°C activation), respectively. While the large-format pouch cells would burst open due to excessive internal gas pressure when activated at 25°C, they could be cycled for more than 250 cycles when activated at elevated temperature.[166] In the present work, the CO_2 evolution in the cycles 2-5 increases from ≈105 µmol/g upon activation at 45°C by a factor of ≈2 to ≈220 µmol/g upon activation at 0°C (see arrows and numbers in Figure 17). These amounts would probably cause the burst opening of the 7 Ah pouch cells, but the overall gassing critically depends on the Li_2MnO_3 content of the CAM[27] and the choice of electrolyte.[46] In this respect, less gassing is expected in the study by Schreiner et al., because they used a CAM with lower Li_2MnO_3 content (0.33 vs. 0.42 Li_2MnO_3) and they switched from an EC-based to an FEC-based electrolyte system, which is less vulnerable against released lattice oxygen.

Finally, let us have a closer look at the voltage curves during the OEMS experiments. After activation at different temperatures, Figure 18 shows the dQ/dV representation of cycle 3 (C/7.5) and 4 (C/3) measured at 30°C. Here, the first peak during charge (highlighted by the shaded area) corresponds to the spinel-like, electrochemically active surface layer, which is formed upon oxygen release.[27] In the 3rd cycle, this feature is absent when the LMR-NCM was activated at 0°C and 15°C, because the slowed kinetics limit the accessible SOC window at these temperatures, but the peak evolves in the 4th cycle at 30°C. The peak maximum shifts slightly from ≈3.10 V vs. Li^+/Li in cycle 3 to ≈3.15 V vs. Li^+/Li in cycle 4 due to the higher C-rate. More interestingly, the peak area and thus the spinel fraction largely depends on the activation temperature. In the previous section, we found out that the reconstruction of the oxygen-depleted surface layer into a spinel-like phase lasts over ≈20 cycles at 25°C, i.e., the dQ/dV peak at ≈3.10 V vs. Li^+/Li grew gradually upon cycling. At elevated temperature, especially at 45°C, this transformation seems to occur already in the very first cycles, as the spinel peak is very pronounced, while all the other features originating from the layered oxide are weaker compared to the low-temperature activation (extreme cases: 0°C activation in blue vs. 45°C activation in black). Since both the extent of oxygen release and the rate of the subsequent reconstruction into a spinel-like phase increase with increasing temperature, the combination of these two phenomena explains why the

low-temperature activation delivers 25 mAh/g more capacity than the high-temperature activation (see Figure 15). Considering that the spinel phase provides only 140 mAh/g,[27] while the original layered oxide provides up to 270 mAh/g (when charged at C/7.5 to 4.6 V vs. Li^+/Li plus 30 min CV; see Figure 15). The difference of 25 mAh/g between 0°C vs. 45°C activation is not expected to change notably over cycling, because the capacity loss due to spinel transformation is assumed to be less than 10 mAh/g for the 0°C activation (similarly to the 0.33 Li_2MnO_3 CAM in the former section 3.2.2). Furthermore, the surface reconstruction might not be fully completed within 5 cycles for the 45°C activation.

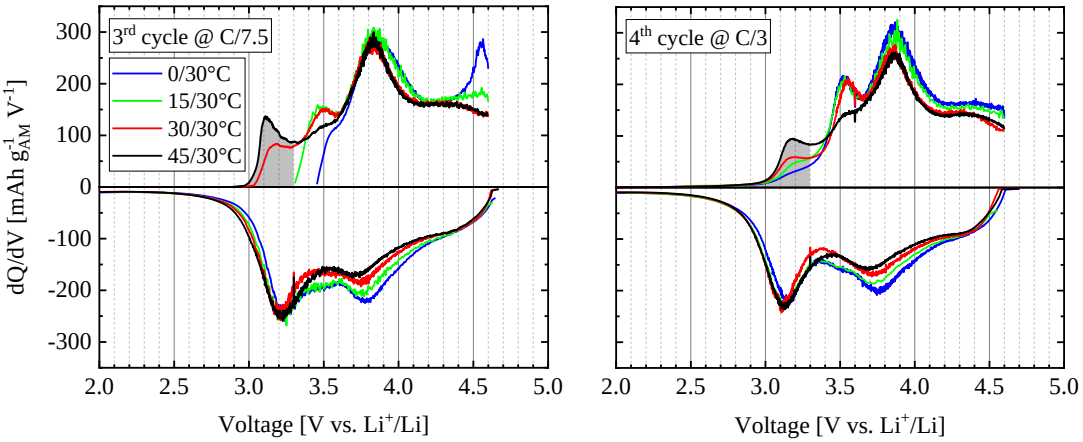

Figure 18. Differential capacity (dQ/dV) of the voltage curves in cycle 3 (conducted at C/7.5; **left**) and 4 (conducted at C/3; **right**), both measured at the fixed temperature of 30°C. The voltage scale vs. LFP was converted into Li^+/Li by adding 3.4 V during charge (LFP lithiation plateau) and 3.5 V during discharge (LFP delithiation plateau), respectively. The shaded area until 3.3 V vs. Li^+/Li during charge highlights the layered-to-spinel transformation as a guide to the eye.

In summary, the OEMS measurements proved that the capacity increase caused by the low-temperature activation is primarily a surface-dominated process, because the oxygen release and the accompanied spinel transformation critically depend on temperature. Even though the low-temperature activation would increase the energy density of battery cells using Li- and Mn-rich CAMs, the practical application in large-format cells is complicated by the more extensive gassing in the subsequent cycles, which raises safety concerns due to potential burst opening. At the expense of the energy density aspect, Li- and Mn-rich layered oxides might require a high-temperature activation to shift as much gassing as possible into the first cycle, which can be then vented before the final sealing of the cell.

3.3 *Bulk-Related Degradation of Li- and Mn-Rich Layered Oxides*

3.3.1 Correlating the Voltage Hysteresis to Reversible Structural Changes

The article entitled "Correlating the Voltage Hysteresis in Li- and Mn-Rich Layered Oxides to Reversible Structural Changes by Using X-ray and Neutron Powder Diffraction" was submitted in October 2021 to the peer-reviewed *Journal of The Electrochemical Society* and was published as "open access" article in February 2022. It is distributed under the terms of the Creative Commons Attribution 4.0 License. The main findings of this study were presented by Benjamin Strehle at the 236th Meeting of the Electrochemical Society in Atlanta, Georgia, USA (October 13-17, 2019, Abstract Number 346). The permanent weblink of this article can be found under: https://iopscience.iop.org/article/10.1149/1945-7111/ac4540.

While section 3.2 addressed degradation phenomena happening at the surface of Li- and Mn-rich layered oxides, we now turn towards processes in the bulk. After completing the first activation cycle, Li- and Mn-rich CAMs show a pronounced voltage hysteresis between the charge and discharge reaction, whose state of charge (SOC) differs by up to one third of the overall capacity at the same measured voltage.[123,124] This hysteresis is largely maintained under open circuit voltage (OCV) conditions[188,207] and further finds expression in a series of other path-dependent parameters such as the resistance,[143,145] the Li site occupation,[187] the partial molar entropy,[258] and the oxidation states of the transition-metals and oxygen.[143,207] In the literature, the origin of these hysteresis phenomena is mainly ascribed to (i) the reversible migration of transition-metals between the TM and Li layer,[150,188] (ii) the anionic redox,[143] or (iii) the combination of both processes according to $\{O^{2-} + TM\} \rightarrow \{O^{-} + TM_{mig}\} + e^{-}$.[159]

In this study, we apply *in situ* laboratory X-ray powder diffraction (L-XPD) to monitor the lattice parameter evolution of Li- and Mn-rich CAMs within the initial cycles as a function of the over-lithiation (variation of the Li_2MnO_3 content) and the cycling conditions (variation of the effective SOC window). In the rhombohedral symmetry, the lattice parameters *a* and *c* as well as the unit cell volume *V* resemble

the quasi-reversible hysteresis loop of the open circuit voltage when plotted versus the SOC. Since the lattice dimensions are governed by the redox processes, as known from stoichiometric NCMs,[24,203] their hysteresis indicates a path dependence both of the cationic and anionic redox, which is in accordance with former spectroscopic studies.[143,207] The extent of open circuit voltage and lattice hysteresis increases with increasing over-lithiation of the CAM, but it can be reduced by limiting the SOC range in window opening experiments. When correlated to the OCV (at which the XPD patterns were recorded during intermittent rest phases) instead of the SOC, the path dependence of the unit cell volume vanishes and the linear V = f(OCV) relationship of -2 Å^3/V uniquely describes all three tested CAMs on a universal curve.

To elucidate the role of TM migration on the above phenomena, we perform Rietveld refinements of *ex situ* samples. Aiming at quantifying the distribution of several elements on the Li and TM layer at the same time, we apply a co-refinement strategy of X-ray and neutron powder diffraction (NPD) data. However, our thorough analysis reveals several pitfalls in doing Rietveld refinements of Li- and Mn-rich CAMs. For example, NPD cannot differentiate between Li and Mn, because both elements have a negative neutron scattering length. Thus, their distribution is highly correlated with each other. XPD is biased by the choice of the X-ray atomic form factors, which requires to know the exact oxidation states of the elements. In summary, Rietveld refinements have to be carried out with great care and the structural models need to be simple in order to avoid misleading conclusions. Refining the Ni amount on the Li layer (Ni_{Li}) with our standard model, the maximum intra-cycle difference amounts to ΔNi_{Li} = 2.4% within the second cycle. Finally, we could not prove any direct correlation of Ni_{Li} to the lattice parameter data.

To support the main article, additional information is provided for the benefit of the reader. The Supporting Information includes all relevant details about our Rietveld refinement approach as well as the corresponding fitting results and an overview of different structural models used in the literature.

Author contributions

B.S. and T.Z. conducted all the diffraction experiments and analyzed the data. S.S. was in charge for the DFT simulations. A.K. developed the multi-layer pouch cell setup. V.B. supported the NPD experiments as beamline scientist of the SPODI instrument. The manuscript was written by B.S. and further revised by T.Z., S.S., and H.A.G. All authors discussed the data and commented on the results. B.S. and T.Z. contributed equally to this work as co-shared first authors.

Journal of The Electrochemical Society, 2022 **169** 020554

Correlating the Voltage Hysteresis in Li- and Mn-Rich Layered Oxides to Reversible Structural Changes by Using X-ray and Neutron Powder Diffraction

Benjamin Strehle,[1,=,*] Tanja Zünd,[1,=,*,z] Sabrina Sicolo,[2] Aleksandr Kiessling,[1] Volodymyr Baran,[3] and Hubert A. Gasteiger[1,]**

[1]*Chair of Technical Electrochemistry, Department of Chemistry and Catalysis Research Center, Technical University of Munich, D-85748 Garching, Germany*
[2]*BASF SE, Quantum Chemistry for Solid State Group, D-67056 Ludwigshafen, Germany*
[3]*Heinz Maier-Leibnitz Zentrum, Technical University of Munich, D-85748 Garching, Germany*

Li- and Mn-rich layered oxides (LMR-NCMs) are promising cathode active materials (CAMs) in future lithium-ion batteries (LIBs) due to their high energy density. However, the material undergoes a unique open circuit voltage (OCV) hysteresis between charge and discharge after activation, which compromises its roundtrip energy efficiency and affects the thermal management requirements for a LIB system. The hysteresis is believed to be caused by transition metal (TM) migration and/or by oxygen redox activities. Using in-situ X-ray powder diffraction (XPD), we monitor the lattice parameters of over-lithiated NCMs during the initial cycles and show that also the lattice parameters feature a distinct path dependence. When correlated to the OCV instead of the state of charge (SOC), this hysteresis vanishes for the unit cell volume and gives a linear correlation that is identical for different degrees of over-lithiation. We further aimed at elucidating the role of TM migration on the hysteresis phenomena by applying joint Rietveld refinements to a series of ex-situ XPD and neutron powder diffraction (NPD) samples. We critically discuss the limitations of this approach and compare the results with DFT simulations, showing that the quantification of TM migration in LMR-NCMs by diffraction is not as straightforward as often believed.

 [DOI: 10.1149/1945-7111/ac4540]

Manuscript submitted October 2, 2021; revised manuscript received November 23, 2021. Published February 22, 2022. *This was paper 346 presented at the Dallas, Texas, Meeting of the Society, May 26–May 30, 2019.*

Supplementary material for this article is available online

Driven by mobile applications like electric vehicles (EVs),[1–3] the demand for affordable lithium-ion batteries with a higher energy density is rising. Targets of 100 $/kWh are necessary to achieve comparable vehicle costs at acceptable driving ranges.[4,5] The only way to reach these ambitious goals is an increase of battery energy density by increasing the specific capacity of the active materials and by using abundant and inexpensive materials. On the cathode side, lithium-and manganese-rich layered oxides, often abbreviated as LMR-NCMs, provide high specific capacities of up to 250 mAh g^{-1} at low material costs that are achieved by replacing a major part of the conventionally used nickel with inexpensive manganese.[6,7] The specific capacity increase of the so-called "over-lithiated" NCMs compared to conventional NCMs originates from a slight rearrangement of the layered structure, $Li[Li_{\delta}TM_{1-\delta}]O_2$ (with TM = Mn, Ni, and Co), in the pristine cathode active materials (CAMs). Stoichiometric NCMs with δ being close to 0 offer a theoretical specific capacity of around 277 mAh g^{-1}, but due to their structural instabilities at lithium contents of $x_{Li} < 0.2$ that are caused by the release of lattice oxygen and due to their first cycle efficiency of maximum 90%, their practically usable specific capacity remains limited to approximately 200 mAh g^{-1}.[8,9] On the other hand, in LMR-NCMs, a part of the transition metals (TMs) in the TM layer is replaced by lithium,[10–12] leading to an over-lithiated structure with theoretical specific capacities of 346–377 mAh g^{-1} for δ = 0.14–0.20.[13] In contrast to stoichiometric NCMs, the over-lithiated structure can be reversibly cycled beyond the onset of oxygen release down to $x_{Li} \approx 0.1$ and delivers first charge capacities of ≈320–340 mAh g^{-1}.[13] Even though not all of the removed lithium from the first activation charge can be re-intercalated, the material delivers a reversible specific capacity of around 250 mAh g^{-1}, 25% more than stoichiometric NCMs can reach under practical cycling conditions. Despite their high specific capacity and low material costs, issues such as oxygen evolution and the associated stability problems,[13–15] the low electrode densities of the first generation of LMR-NCMs,[16] the comparably high impedances,[17] and the well-known voltage fading phenomenon[18] still hamper the commercialization of LMR-NCMs. Amongst these issues, voltage fading over cycle-life is often discussed as one of the most detrimental challenges, but Kraft et al. have shown that the voltage fading over 250 cycles in large-format LMR-NCM/graphite full-cells is in the range of ≈155 mV (compared to ≈60 mV for NCA/graphite cells), and therefore reduces the energy density by less than 5%.[19] With regards to actual applications, they further show that the well-known open circuit voltage (OCV) hysteresis LMR-NCMs does lead to lower energy efficiencies compared to stoichiometric NCAs even at low C-rates (e.g., 88% for LMR-NCM/graphite vs 98% NCA/graphite at C/10), resulting in a more pronounced temperature increase when operating large-format cells at high C-rates. One last point to consider with LMR-NCM based cells is that current battery management systems would have to be adapted, as they typically determine the state of charge (SOC) from the measured cell voltage.[20,21] For materials with a significant voltage hysteresis like LMR-NCMs and silicon, however, the SOC at a given cell voltage can differ substantially depending on the cycling history of the cell.

The voltage hysteresis of over-lithiated NCMs is well-known since their early days after invention.[22] The fact that the charge and discharge curves after activation remain separated by up to several hundreds of mV, even under OCV conditions of a few hours, shows that the voltage hysteresis is an intrinsic bulk property of LMR-NCMs.[23] It is thus not surprising that over time a variety of other properties of LMR-NCMs were also found to be path-dependent, such as its resistance (determined by the direct current internal resistance (DCIR) method)[17] and, more explicitly, the charge-transfer resistance (from EIS measurements) and the lithium diffusion coefficient (from GITT experiments).[24] On the atomic level, there are several publications about the charge/discharge hysteresis of the oxidation states, both for the transition metals[24,25]

[=]These authors contributed equally to this work.
[*]Electrochemical Society Student Member.
[**]Electrochemical Society Fellow.
[z]E-mail: tanja.zuend@tum.de

Journal of The Electrochemical Society, 2022 169 020554

and oxygen[24] as well as of the TM-O bond distances (from EXAFS analysis).[26] Even though X-ray powder diffraction (XPD) is frequently applied to analyze the structural changes of CAMs during lithiation/delithiation, Konishi et al. were the only ones who reported on the lattice parameter hysteresis (in the rhombohedral representation) of LMR-NCMs, but without diving deeply into possible reasons for their observations.[25] However, the evolution of the lattice parameters upon lithiation/delithiation, especially when measured under in-situ or operando conditions in a battery cell, can be a powerful tool to gain an understanding about the underlying mechanism(s) of the observed hysteresis phenomena. There is a lively discussion in the literature, which assigns the hysteresis in LMR-NCMs either to a path dependence of the transition metal (TM) migration,[23,27–29] the anionic redox,[24] or a combination of both.[30] TM migration typically means that transitions metals, which originally reside in the TM layer (TM_{TM}), move upon cycling (ir) reversibly into the lithium layer (TM_{Li}), whereas anionic redox refers to the O^{2-}/O^{n-} couple ($n < 2$), which occurs independently or in conjunction with the cationic redox in over-lithiated CAMs. Alternatively, a recently published study considers the anionic redox as the reversible formation of molecular O_2 trapped in voids within the particles, which is induced by the in-plane TM_{TM} disordering after the removal of Li_{TM} during the activation charge.[31]

As known from the intensively studied stoichiometric NCMs,[32–35] both the redox processes and the TM distribution are important descriptors of the lattice dimensions, because they affect the attractive and repulsive interactions of the two metal layers inside the oxide lattice. This renders diffraction methods to be very promising for elucidating the origin of the voltage hysteresis in LMR-NCMs. Beyond that, Rietveld refinements of high-quality (ex-situ) diffraction data enable the quantification of migrated TMs upon cycling.[29,30,36] Since the literature considers the distribution of typically Li, Ni, and Mn in LMR-NCMs on either octahedral and/or tetrahedral sites, it is not possible to perform the refinement solely based on XPD data, as this would result in severe correlations between all of the refined parameters. Therefore, it is beneficial to rely for such complex systems on complementary diffraction datasets, e.g., XPD and neutron powder diffraction (NPD), and to perform joint Rietveld refinements.[37–39]

In the present study, we applied in-situ XPD on our laboratory diffractometer to monitor the lattice parameter evolution of an over-lithiated CAM over the course of the initial charge/discharge cycles. The in-situ approach makes it possible to correlate the lattice dimensions to the SOC, which is equivalent to the overall lithium content in the material, but also to the OCV at which the diffractograms were recorded during intermittent rest phases. Further in-situ experiments were conducted to shed light on the lattice parameter dependence on the degree of over-lithiation and on the cycling conditions, varying the effective SOC window. Subsequently, ex-situ diffraction data were collected again on the laboratory diffractometer (L-XPD) as well as at a synchrotron (S-XPD) and a neutron source (NPD), which were analyzed by Rietveld refinements. Here, we are especially interested into the quantification of migrating TMs by applying a joint refinement approach. By evaluating different structural models and looking at several influencing factors during the refinement, we critically discuss the meaningfulness of the refinement results, and, in combination with DFT simulations, the role of TM migration on the hysteresis in Li- and Mn-rich layered oxides.

Experimental

Materials and electrode preparation.—As in our previous gassing study,[13] we used three different Li- and Mn-rich layered oxides with varying degrees of over-lithiation. Following the $Li[Li_\delta TM_{1-\delta}]O_2$ notation for the pristine CAMs, BASF SE (Germany) provided a low- ($\delta = 0.14$), mid- ($\delta = 0.17$), and high-lithium material ($\delta = 0.20$), which in an alternative notation correspond to the compositions 0.33 $Li_2MnO_3 \cdot 0.67\ LiTMO_2$, 0.42 $Li_2MnO_3 \cdot 0.58\ LiTMO_2$, and 0.50 $Li_2MnO_3 \cdot 0.50\ LiTMO_2$ that were examined by Teufl et al.[13] The high-lithium material is the same as in our previous work, whereas the other two CAMs are follow-up batches with similar composition and properties. Since the main work in the present study was done with the mid-lithium material, its precise composition was determined at the Mikroanalytisches Labor Pascher (Remagen, Germany). After dissolving the CAM by pressurized acid digestion in aqua regia, the (metal) composition was determined as $Li[Li_{0.17}Ni_{0.19}Co_{0.10}Mn_{0.54}]O_2$ by means of inductively coupled plasma atomic emission spectroscopy (ICP-AES). Here, we included surface impurities into the calculation, from which a total of ≈1 wt% could be identified mainly as carbonates. In order to assign the residual mass stoichiometrically to lattice oxygen (assuming no oxygen vacancies in the pristine material, as confirmed by Csernica et al.[40]), there has to be another total amount of ≈2 wt% of impurities. This corresponds to a theoretical specific capacity of 350 mAh g^{-1}_{CAM} for complete lithium extraction (compared to 361 mAh g^{-1}_{NCM} for the pure LMR-NCM in the absence of the ≈3 wt% of impurities). Please note that capacity values are normalized to the mass of the as-received CAM powder (i.e., 350 mAh g^{-1}_{CAM}) and that we used the $Li[Li_\delta TM_{1-\delta}]O_2$ notation throughout our work.

LMR-NCM cathode coatings were prepared by mixing 94 wt% of CAM powder, 3 wt% of Super C65 conductive carbon (Timcal, Switzerland), and 3 wt% of polyvinylidene fluoride binder (PVDF, either Kynar HSV 900, Arkema, France or Solef 5130, Solvay, Belgium) with *N*-methyl-2-pyrrolidone (NMP, anhydrous, 99.5%, Sigma-Aldrich, Germany) at a solids content of 62 wt% in a planetary orbital mixer (Thinky, USA) in several steps. The final slurry was cast onto an aluminum foil (thickness 15 μm, MTI, USA) using a 200 μm four-edge blade. The coated foil was dried overnight in a convection oven at 50 °C. This procedure results in relatively high loadings of ≈14–20 mg_{CAM} cm^{-2}, which improves the signal-to-background ratio for the in-situ L-XPD experiments. In order to obtain enough cycled CAM powder for the ex-situ NPD measurements, we also prepared double-sided cathode sheets by coating the backside of the Al foil after the first drying step. The cathode sheets were calendered (GK 300-L, Saueressig, Germany) to a porosity of around 45%. For coin cells, disk-shaped electrodes with a diameter of 14 mm were punched out from the single-sided sheets and then dried overnight in a vacuum oven (Büchi, Switzerland) at 120 °C, before transferring them inertly into an argon-filled glove box (<1 ppm O_2 and H_2O, MBraun, Germany). For single- and multi-layer pouch cells, quadratic-shaped electrodes with a coated area of 9 cm^2 were cut out and then dried overnight in the oven chamber of the glove box at 90 °C under dynamic vacuum.

X-ray powder diffraction.—X-ray powder diffraction (XPD) experiments were mainly conducted at our in-house STOE STADI P diffractometer (STOE, Germany) in Debye–Scherrer geometry, using Mo-$K_{\alpha 1}$ radiation (0.7093 Å), a Ge(111) monochromator, and a Mythen 1 K detector, and taking one data point every 0.015°/2θ. These will further on be referred to as "L-XPD" measurements, which were used (i) to monitor the evolution of lattice parameters during the first cycles from in-situ single-layer pouch cell data and (ii) to obtain structural information from ex-situ capillary data.

The in-situ L-XPD data were recorded in a similar fashion as in our previous publication.[41] The 9 cm^2 single-sided cathode was assembled with an over-sized lithium counter-electrode (10.9 cm^2, thickness 450 μm, Albemarle, USA), a glass-fiber separator (14.4 cm^2, glass microfiber filter 691, VWR, Germany), and 400 μl of LP57 electrolyte (1 M $LiPF_6$ in EC:EMC = 3:7 by weight, BASF SE) in a relatively thin pouch foil (12 μm-thick Al layer, Gruber-Folien, Germany). The pouch cell was fixed without external compression between two metal plates (with a 15 mm hole in the center of the battery stack) and then connected to the diffractometer as well as a potentiostat (SP200, Biologic, France), as shown in Fig. S1 (available online in the Supporting Information at stacks.iop.org/JES/169/020554/mmedia). The cell was aligned in the direction of the X-ray beam on the basis of the most intense (003) reflection of the pristine CAM. Electrochemical cycling was done at a C-rate of

C/10 (based on a nominal specific capacity of 300 mAh g^{-1} used throughout this study) in the cell voltage window between 2.0 and 4.8 V. The room temperature remained within 24 ± 2 °C. Diffractograms were recorded every 25 mAh g^{-1} (15 mAh g^{-1} when studying smaller voltage windows) during intermittent OCV periods of 50 min in the 2θ range of 6°–48° (Q range 0.9–7.2 $Å^{-1}$, acquisition time ≈40 min, start after the first ≈5 min of the OCV break). The XPD patterns were collected at fixed SOCs of 0, 25, 50 mAh g^{-1}, etc. for all succeeding cycles (plus additional diffractograms after running into the cut-off voltages).

Ex-situ L-XPD measurements of cycled cathode electrodes were conducted in 0.3 mm Lindemann glass or borosilicate glass capillaries (both from Hilgenberg, Germany) in the 2θ range of 3°–60° (Q range 0.5–8.9 $Å^{-1}$, acquisition time ≈14 h). For this, 2325-type coin cells with a cathode electrode (14 mm diameter), a lithium metal anode (15 mm diameter), two glass-fiber separators (16 mm diameter), and 80 μl of LP57 electrolyte were cycled at C/10 and 25 °C in the cell voltage window of 2.0–4.8 V to the desired SOC either during charge or discharge of the second cycle (Series 4000 battery cycler, Maccor, USA). The coin cells were opened in the glove box to harvest the cathode electrodes, and the scratched-off cathode electrode material, without any prior washing, was loaded and air-tightly sealed into the capillaries.

Some additional capillaries were sent to the Material Science beamline MS-X04SA of the Swiss Light Source (Paul Scherrer Institute, Villigen, Switzerland), where they were stored for ≈5 months prior to the measurements.[42] X-ray diffractograms were measured at ambient temperature in Debye–Scherrer geometry using synchrotron radiation at 22 keV (0.5646 Å; equipped with a Si(111) double-crystal monochromator and Mythen II microstrip detector) in the 2θ range of 1°–90° (Q range 0.2–15.7 $Å^{-1}$, exposure time 4 min sample, one data point every 0.0036°/2θ), which will further on be abbreviated as ex-situ "S-XPD" measurements.

Neutron powder diffraction.—Since the ex-situ NPD measurements require (cycled) CAM in the gram scale, we assembled hand-made multi-layer pouch cells in our laboratory, which consisted of two single-sided and two double-sided cathode sheets (i.e., in total six cathode layers at 9 cm^2 each). Their loading deviation was set to be less than 0.5 mg_{CAM} cm^{-2} per layer and the absolute capacity of the pouch cells amounted to ≈260 ± 50 mAh (based on a nominal specific capacity of 300 mAh g^{-1}). Three over-sized lithium metal anodes (10.9 cm^2) were placed between the cathode sheets, alternating within total six glass-fiber separators (14.4 cm^2) and packed in a battery pouch foil (40 μm-thick Al layer, DNP, Japan) with 2.4 ml of LP57 electrolyte. As done above for the coin cells, the pouch cells were cycled at C/10 and 25 °C in the voltage window of 2.0–4.8 V (and fixed in a cell holder with a homogeneous compression of ≈2 bar). After reaching the desired SOC in either charge or discharge direction within the first two cycles, the cells were opened in the glove box to harvest the cathode electrodes. For this, the cathode electrodes were scratched off the Al foil with a scalpel, hand-mixed in a mortar using the material from three nominally identical cells, and dried overnight in a vacuum oven at room temperature. The samples were loaded in thin-walled 6 mm vanadium cans (thickness 0.15 mm), which were metal-sealed using an indium wire (loading ≈1.7 ± 0.1 g_{CAM}; for the pristine CAM powder, a 10 mm vanadium can was used). A tiny fraction of the cathode electrode material was filled in X-ray capillaries for ex-situ L-XPD measurements.

The samples were prepared within two weeks prior to the high-resolution neutron powder diffraction (NPD) measurements at the SPODI beamline of the research reactor FRM II (Garching, Germany), which operates in Debye–Scherrer geometry with thermal neutrons at a constant wavelength of 1.5481 Å by using a Ge(551) monochromator and a ^{3}He multidetector system.[43] The NPD patterns were collected at ambient temperature for constantly rotating samples in the 2θ range of 1°–152° (Q range 0.1–7.9 $Å^{-1}$, acquisition time ≈5 h sample, one data point every 0.05°/2θ) and afterwards corrected for geometrical aberrations and detector non-linearities, as described by Hoelzel et al.[43] To perform a joint refinement of L-XPD and NPD data, X-ray diffractograms of the same samples were recorded in parallel at our in-house instrument.

Analysis of diffraction data.—The structural complexity of Li- and Mn-rich layered oxides first raises the question about the proper structural model if it comes to the analysis of diffraction data.[10,12] The incorporation of additional lithium in the TM layer causes an in-plane Li/TM ordering of the pristine LMR-NCM materials, which becomes visible as small, typically very broad superstructure peaks in the powder diffraction patterns.[10,44] In the literature, the authors choose most commonly between three different models: (i) the rhombohedral model ($R-3m$) known from conventional layered oxides, which neglects the in-plane ordering and distributes all ions randomly in the TM layer;[22,36,40] (ii) the monoclinic model ($C2/m$), which takes the ordering into account by dividing each layer into two crystallographic sites at a ratio of 1/2;[30,44] and, (iii) a composite model comprising a rhombohedral and monoclinic phase, which are typically assigned to the $LiTMO_2$ and Li_2MnO_3 composition, respectively.[25,44] As none of our diffractograms show a clear splitting of the main reflections (e.g., of the (003) peak, as was observed by Konishi et al.[25]), not even a shoulder, which would justify the application of the composite model, we do not use it in this work. Furthermore, it is well-known that the superstructure peaks gradually vanish within the first battery cycle(s),[45,46] which puts the monoclinic model in question. The monoclinic model also has more than double the amount of refinement parameters than the rhombohedral model, which involves the danger of severe correlations between interdependent (structural) parameters. All these considerations make the rhombohedral model the main approach to analyze diffraction data in the course of this work, as was done previously by Kleiner et al.[36]

Standard reference materials (i.e., silicon and at the synchrotron also NAC ($Na_2Ca_3Al_2F_{14}$)) were measured before each set of samples. Silicon was used to perform an angle correction of the L-XPD raw data with the WinXPOW software[47] and to determine the accurate wavelength of the X-ray and neutron beamline. In addition, silicon and NAC were used to determine the instrumental peak broadening with the Thompson-Cox-Hastings pseudo-Voigt function, whose parameters were fixed during the subsequent refinement of the samples. The diffraction data were all refined with the software package TOPAS.[48]

The in-situ L-XPD data are used to monitor the lattice parameters during the initial cycles. Here, the rhombohedral model is the common approach in the literature.[23,49,50] To extract the lattice parameters a and c as well as the unit cell volume V, the LMR-NCM phase was refined with a structure-independent Pawley fit. The multi-pattern datasets were analyzed by means of sequential refinements, which also include the Al reflections in the diffractograms. The error of the extracted lattice parameters is on the order of ≈0.01%–0.05% (based on their estimated standard deviations relative to the refined values), which is deemed to be sufficiently precise, as the lattice parameters change by a few percent during a charge/discharge cycle. For the mid-lithium material ($\delta = 0.17$), the state of charge of each diffraction pattern was converted into the overall lithium content, x_{Li}, by considering its theoretical specific capacity (350 mAh g^{-1}, using the above described results from elemental analysis) and its total lithium content (i.e., $1 + \delta = 1.17$ based on the $Li[Li_\delta TM_{1-\delta}]O_2$ notation):

$$x_{Li} = \frac{350\ \text{mAh g}^{-1} - \text{SOC [mAh g}^{-1}]}{350\ \text{mAh g}^{-1}} \cdot 1.17 \qquad [1]$$

Here, it is assumed that the electrochemically measured capacity solely originates from lithium insertion/extraction into the LMR-NCM material and that the extent of parasitic reactions is negligible. The OCV value of each diffractogram was averaged from the last minute of the 50 min OCV step used for data collection, where the

Journal of The Electrochemical Society, 2022 **169** 020554

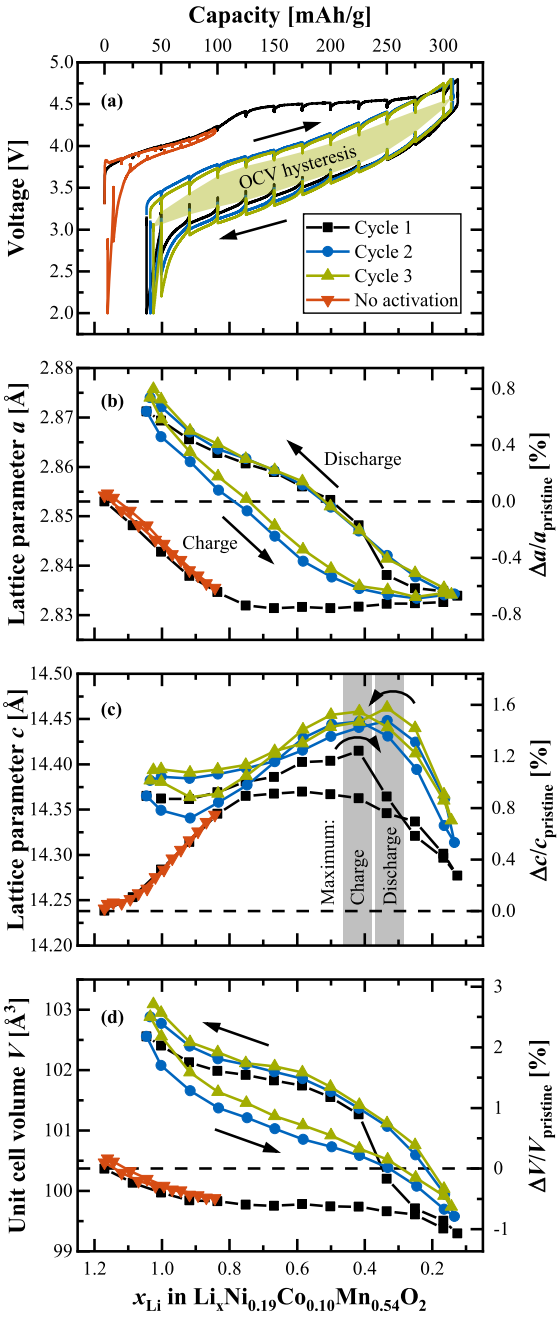

Figure 1. Lattice parameter evolution of the mid-lithium LMR-NCM (δ = 0.17) during the initial cycles, as obtained from two independent in-situ L-XPD experiments in a half-cell configuration (i.e., with a lithium metal anode). "Cycle 1–3" were measured at C/10 in the full voltage window of 2.0–4.8 V, whereas the curve labeled "no activation" shows the first cycle in the smaller window of 2.0–4.2 V. The diffractograms were collected during OCV breaks every 25 and 15 mAh g^{-1}, respectively. The panels show from top to bottom (a) the voltage curves, (b) the lattice parameter a, (c) the lattice parameter c, and (d) the unit cell volume V as a function of the overall lithium content, x_{Li} (lower x-axis), which was calculated according to the respective SOC (upper x-axis, see Eq. 1). In panel (a), the OCV share of the total voltage hysteresis is shown for cycle 3 by the green shaded area. The right y-axes illustrate the lattice parameter changes in percentage terms relative to the pristine state.

remaining voltage relaxation, dV/dt, was in the range of ≈5–25 mV h^{-1} (depending on SOC and charge/discharge; for OCV holds of 10 h, it was <1 mV h^{-1}). According to Croy et al., this approach closely represents the OCV function of the CAM at the time scales of interest.[23]

All ex-situ data of the mid-lithium material were processed by Rietveld refinements. Here, the site occupancy factors are of particular interest, since they might provide insights into the lithium de-/intercalation mechanism and the migration of transition metals into the lithium layer. Important refinement details are given in paragraph S3 of the Supporting Information. Regarding the joint refinement of L-XPD and NPD data, some parameters (viz., background, zero shift, absorption, peak broadening, and scale factor) were refined on a local level independent for each dataset, whereas the lattice parameters and structural parameters (viz., fractional coordinates, atomic displacement parameters, and site occupancy factors) were optimized on a global level together for both datasets. We used three different structural models, which will be introduced as the extended rhombohedral *model* 1, the simplified rhombohedral *model* 2, and the monoclinic *model* 3 in the Results and Discussion section (together with the corresponding refinement results).

Beyond the Supporting Information, we also attached the diffraction raw data of the ex-situ L-XPD and NPD samples (.xy and .xye file types) as well as the input files for the TOPAS refinement program (.inp file type) as supplementary data to this work (see attached .zip folder which comprises all above files). With the *LMR-NCM_Pawley_Refinement.inp* input file, the lattice parameters and the sample broadening can be optimized in a first step by means of an independent Pawley fit for each dataset, while *LMR-NCM_Rombohedral_Refinement.inp* and *LMR-NCM_Monoclinic_Refinement.inp* allow for testing the (joint) Rietveld refinement of the here presented structural models (and beyond).

DFT simulation.—Spin-polarized calculations in the framework of DFT have been performed using the Vienna Ab-initio Simulation Package (VASP)[51–54] with projector augmented wave pseudopotentials.[55,56] The exchange-correlation functional of choice is the strongly constrained and appropriately normed (SCAN) meta-generalized gradient approximation supplemented with the long-range van der Waals interaction from rVV10, the revised Vydrov-Van Voorhis nonlocal correlation functional, which performs very well on layered compounds.[57] Within a 4 × 5 × 1 supercell of the conventional rhombohedral cell, all structures have been fully relaxed until the forces were lower than 10^{-2} eV·Å^{-1} with a cut-off energy of 600 eV at the Γ-point only, which is justified by the large dimensions of the supercell. In selected cases, a pre-relaxation by means of short molecular dynamics at 300 K helped to find a better local minimum. Because VASP cannot handle partial occupancies, structures with integer occupancies compatible with the experimental site occupancy factors have been generated with the combinatorial approach implemented in the supercell software.[58]

The material with the mid-lithium composition, $Li[Li_{0.17}Ni_{0.19}Co_{0.10}Mn_{0.54}]O_2$, has been simulated with a 4 × 5 × 1 supercell of the conventional rhombohedral cell and thus contains 60 formula units. The supercell contains 72 Li (60 in the Li layer and 12 in the TM layer), 12 Ni, 6 Co, 30 Mn and 120 O that corresponds to the formula unit (f.u.) $Li_{1.2}Ni_{0.2}Co_{0.1}Mn_{0.5}O_2$ of the model composition (which represents the over-lithiation degree of the high-lithium material, since simulating the precise lithium content of the mid-lithium material would have required an excessively large supercell). With a supercell of this size, the sheer number of possible ways to distribute the cations into the Li and TM sub-lattices is astronomical. A good structural candidate has been determined by letting the combinatorial calculator supercell find the cation distribution with the lowest electrostatic energy within a point-charge approximation based on given oxidation states (viz., Li^+, Ni^{2+}, Co^{3+}, Mn^{4+}, and O^{2-}). The key features associated with the progressive delithiation of the material are analyzed by investigating structural models at different Li contents and comparing their

Journal of The Electrochemical Society, 2022 169 020554

thermodynamic stability at each composition. Already at this point, it is important to reiterate that the extremely large configurational space renders it virtually impossible to determine with certainty the true ground state for a given composition (bar the construction of an exhaustive compositional phase diagram, which falls beyond the scope of this work). Calculation of the voltage profile also requires the knowledge of the compositional convex hull. Therefore, we will not report on voltages but rather compare the total energies of structures with the same composition.

Results and Discussion

SOC dependence of lattice parameters.—Most of our previous work on Li- and Mn-rich layered oxides, including studies about their gassing behavior,[59] resistance build-up,[17] and the irreversible TM migration during long-term cycling,[36] used exclusively materials with a medium degree of over-lithiation ($\delta = 0.17$). Here, the work of Teufl et al. revealed a path-dependent resistance hysteresis of this particular LMR-NCM within a charge/discharge cycle.[17] It is thus reasonable to focus first on a very similar CAM to monitor its lattice parameters during the first battery cycles and to look for any structural hysteresis behavior. Figure 1 shows the results from two in-situ L-XPD measurements of the mid-lithium material, whose pristine composition was determined to be $Li[Li_{0.17}Ni_{0.19}Co_{0.10}Mn_{0.54}]O_2$ by elemental analysis. The voltage curves obtained in a half-cell (i.e., with a lithium metal anode) and the lattice parameters (i.e., a, c, and the unit cell volume V; as based on the rhombohedral model) are plotted vs the exchanged capacity (upper x-axis) and the lithium content, x_{Li} (lower x-axis), of the CAM, which are equivalent measures of the state of charge (see Eq. 1). Three consecutive cycles (the first cycle in black and the 2nd and 3rd cycle in blue and green, respectively) of one cell operated at C/10 in the full voltage window of 2.0–4.8 V are compared to the first cycle (in red) of another cell, that was reversed at 4.2 V, just before reaching the activation plateau. The electrochemistry matches our previous work and is not affected by the simplified pouch cell setup or X-radiation, with the expected capacities of ≈313 mAh g^{-1} for the first activation charge and ≈276–264 mAh g^{-1} for the following discharge cycles. The vertical spikes in the voltage curves indicate the intermittent OCV periods used for XPD data collection. Connecting the final OCV values at each SOC, as exemplarily done for cycle 3 in Fig. 1a, makes it obvious that the main part of the voltage hysteresis, especially in the mid-SOC regime, is maintained during OCV and reaches almost up to ≈400 mV.

Let us now turn towards the lattice parameters. We directly discuss the refinement results, because the raw data do not contribute any additional information. For the sake of completeness, paragraph S1 of the Supporting Information (SI) shows a contour plot of the in-situ L-XPD patterns of "Cycle 1–3" and two Pawley fits in the discharged and charged state, respectively (see Figs. S2 and S3). At a first glance, the lattice parameters a and c in Fig. 1 seem to resemble the voltage characteristics: the first-cycle charge curve that differs from the subsequent charge curves (Fig. 1a) is reflected in the behavior of a (Fig. 1b) and c (Fig. 1c) that also show different functionalities in the first compared to the subsequent cycles. The first-cycle activation charge (upper black line in Fig. 1a) can be divided into a sloping region until ≈4.4 V (corresponding to $1.17 > x_{Li} > 0.76$) and an extended voltage plateau at ≈4.5 V ($0.76 > x_{Li} > 0.23$). In a similar manner, the lattice parameters change monotonically in the sloping region (lower black lines in Figs. 1b and 1c), then remain approximately constant during the voltage plateau, and move (slightly) back at the end of the first charge. Following the activation, there is a drastic change of the lattice parameters, which also feature a pronounced hysteretic behavior during charge and discharge. Former in-situ XPD studies have seen similar lattice parameter trends within the initial cycles, e.g., for $Li[Li_{0.20}Ni_{0.15}Co_{0.10}Mn_{0.55}]O_2$ by Mohanty et al.[50] and for $Li[Li_{0.20}Ni_{0.20}Mn_{0.60}]O_2$ by Croy et al.,[23] but the hysteresis in the evolution of the lattice parameters over a charge/discharge cycle was not so obvious there, as in the former study the lattice parameters were only plotted vs time while in the latter study there were too few data points over a charge/discharge cycle. To the best of our knowledge, only Konishi et al. reported a clear lattice parameter hysteresis for $Li[Li_{0.20}Ni_{0.13}Co_{0.13}Mn_{0.54}]O_2$, whereby the hysteresis was assigned to the $LiTMO_2$-like phase in their 2-phase refinement with a composite model comprising a rhombohedral ($LiTMO_2$-like) and monoclinic (Li_2MnO_3-like) phase.[25]

Since Li- and Mn-rich layered oxides are closely related to conventional NCM materials, most authors apply the same structural and electronic considerations to explain the change of the lattice parameters. The lattice parameter a reflects the intra-layer nearest-neighbor distances, which are all the same for Li-Li in the Li layer, TM-TM in the TM layer, and O-O in the O layer, respectively. As the transition metals decrease their ionic radii upon oxidation, the contraction of the lattice parameter a during charging is however dominated by the TM-TM distance.[32,60] As shown in Fig. 1b (lower black line), the lattice parameter a decreases by ≈0.8% from ≈2.854 to ≈2.831 Å during the sloping region of the first charge and remains almost constant afterwards. This result fits to several spectroscopic studies,[24,30,61] which have shown that the TM oxidation only occurs during the first part of the activation. Assuming that all TMs get oxidized to their 4+ state, starting from Ni^{2+}, Co^{3+}, and Mn^{4+} in the pristine material, the TM redox can theoretically compensate for 144 mAh g^{-1} ($\Delta x_{Li} = 0.48$), what is reasonably close the exchanged capacity of ≈123 mAh g^{-1} ($\Delta x_{Li} \approx 0.41$) until the end of the sloping voltage region at 4.4 V. If the cycling is restricted to this region, i.e., if the charge is stopped prior to reaching the subsequent voltage plateau at ≈4.5 V, the lattice parameters move reversibly back (see red lines labeled "no activation" in Fig. 1). Such a "non-activated" LMR-NCM shows no voltage fade over extended cycling and thus may be considered as a conventional layered oxide.[17] On the other hand, after a full activation charge to 4.8 V, the lattice parameter a changes afterwards between ≈2.874 and ≈2.834 Å ($\Delta a/a_{pristine} \approx 1.4\%$) in a hysteresis loop (see upper black as well as green and blue lines in Fig. 1b). It thus exceeds its value in the pristine material by ≈0.02 Å (≈0.7%) at the end of discharge. This could be explained by the additional activation of the Mn^{3+}/Mn^{4+} redox couple, as was evidenced through HAXPES measurements by Assat et al. (≈10% Mn^{3+} in the discharged state).[24,62]

The lattice parameter c is a measure of the inter-layer distances. Due to the alternating stacking of O-Li-O and O–TM–O layers, c can be separated into a lithium, h_{Li}, and TM layer height, h_{TM}, respectively.[33] De Biasi et al. have investigated many regular NCM materials, ranging from NCM-111 to NCM-851005, by operando XPD.[32] In their study, the lattice parameter c increases by ≈1.5% until the delithiation reaches x_{Li} values of ≈0.4–0.5, what is explained by the increasing Coulomb repulsion of O^{2-} anions facing each other in the depleting Li layers (and thus referring to the h_{Li} component). Upon further delithiation, c falls back and even below the value in the discharged (lithiated) state, reaching up to minus 4.7% for NCM-851005 (at $x_{Li} \approx 0.1$). The repulsive interactions get diminished through an increasing covalent bond character between the transition metals (especially Ni) and oxygen, which in turn reduces the effective negative charge of the O atoms.[32,34,63] Thus, oxygen is involved into the charge compensation of regular layered oxides, but its participation is confined to the standard TM-O hybridization model. This model is not sufficient for Li- and Mn-rich layered oxides, which experience a TM-independent anionic redox during cycling (typically expressed as O^{2-}/O^{n-} redox, $n < 2$).[24,30,61] According to these spectroscopic studies, the anionic redox gets activated during the voltage plateau at ≈4.5 V in the first charge and stays present in the following cycles. In general, the lattice parameter c of the mid-lithium LMR-NCM resembles the trends known from regular NCMs, with c increasing until a delithiation level of $x_{Li} \approx 0.4$ and then decreasing again (see Fig. 1c). The magnitude of this change in c is however significantly smaller. The maximum difference $\Delta c/c_{pristine}$ amounts to less than 1% within one cycle. This damping effect could be rationalized by the O^{2-}/O^{n-} redox, which distributes over the entire SOC range

Journal of The Electrochemical Society, 2022 **169** 020554

after activation.[24,62] Assuming that the anionic redox scales approximately linearly with the extent of delithiation, it reduces the Coulomb repulsion at high x_{Li} values (i.e., low SOCs), what in turn diminishes the c increase at $x_{Li} > 0.4$. For $x_{Li} < 0.4$ (i.e., high SOCs), the anionic redox might compete with the TM–O hybridization,[64] thus damping the subsequent decrease of c. Please note that the Ni–O bonding (important for Ni-rich stoichiometric oxides) tends towards stronger covalency than the Mn–O bonding (important for Mn-rich over-lithiated oxides), which has a more ionic nature.[65] Assat et al. report that the O^{2-}/O^{n-} redox is not evenly distributed during charge and discharge.[24] This could explain the hysteretic behavior of c, which does not manifest as a simple hysteresis loop. In contrast to the lattice parameter a, the charge and discharge curves of c intersect at ≈0.67 and ≈0.40. Furthermore, their maxima are shifted on the x_{Li} axis (viz., at ≈0.42 during charge and at ≈0.33 during discharge; as highlighted by the grey bars in Fig. 1c). At this point, we have to call to mind that the lattice parameter c consists of two individual layer heights, h_{Li} and h_{TM}, which might evolve quite differently compared to their summed-up value of c. Their calculation however requires the z-coordinate of oxygen from Rietveld refinements, what will be done later.

Let us examine once again the first activation charge. As discussed above, the Li- and Mn-rich layered oxide can be regarded as a regular NCM material in the sloping region, i.e., a decreases due to TM oxidation and c increases due to Coulomb repulsion of the O^{2-} anions. During the voltage plateau, where the lattice parameters remain almost constant, the anionic redox comes into play. Another not yet considered aspect is the lithium extraction, which includes both the lithium ions from the Li layer (Li_{Li}) and from the TM layer (Li_{TM}). Liu et al. investigated the delithiation process of $Li[Li_{0.20}Ni_{0.15}Co_{0.10}Mn_{0.55}]O_2$ by operando NPD.[66] They determined the Li_{Li}/Li_{TM} extraction ratio to be ≈24/1 in the sloping region and ≈2.6/1 in the plateau region at ≈4.5 V, and also found out that Li_{TM} cannot be re-intercalated during the subsequent discharge. Hence, the lithium ions in the TM layer get predominantly and permanently removed in the voltage plateau region during the first charge. It is however difficult to estimate the consequences for the lattice parameters, because the Li_{TM} removal goes along with the depopulation of Li_{Li}-O-Li_{TM} configurations[64] and the loss of in-plane ordering in the TM layer.[31,46] Both processes connect the Li_{TM} removal to the anionic redox, as they make it energetically favorable. Even though most lithium ions in the TM layer are extracted during the activation charge, NMR measurements by Jiang et al. have shown that their complete removal might require up to ≈10 cycles.[46] This possibly explains why the lattice parameters increase irreversibly from cycle to cycle in Fig. 1 (e.g., when comparing the discharge curves of the lattice parameters). Here, the difference of the discharge curves between cycle 2 and 3 is smaller than between cycle 1 and 2. We also want to mention that the first three lattice parameter values of the first discharge ($0.33 < x_{Li} < 0.17$) are shifted towards lower values compared to the preceding charge, probably due to a temporary misalignment of the pouch cell resulting from CAM gassing at the end of the activation charge (which also continues during OCV).[59] The comparison with a second in-situ L-XPD measurement (cell #2 in Fig. S4 of the SI) however shows that this artefact does not affect the progression of the lattice parameters.

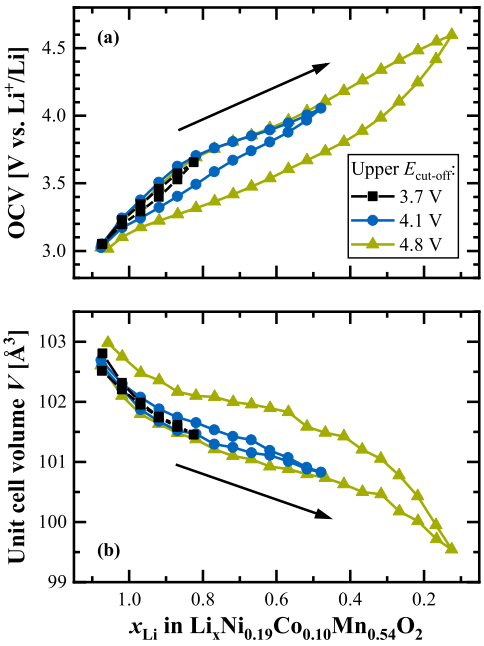

Figure 2. Charge window opening experiment at C/10 with the fully activated mid-lithium LMR-NCM (after 2 activation cycles between 2.0–-4.8 V), where the upper cut-off voltage is stepwise increased from 3.7 to 4.1 to 4.8 V (lower cut-off voltage fixed to 2.0 V, what is also the starting point). As a function of the lithium content, panel (a) shows the open circuit voltage, at which the diffractograms were measured every 15 mAh g^{-1}, and panel (b) depicts the unit cell volume from the corresponding Pawley fits.

The unit cell volume V (see Fig. 1d) represents the net response of the crystal lattice upon lithium insertion/extraction. Its behavior is similar to that of the lattice parameter a, also showing a hysteresis loop after the first activation cycle. This resemblance is reasonable because a affects the unit cell volume to the second power (according to $V = \sqrt{3/2 \cdot a^2 \cdot c}$) and the relative changes of a are larger than for c. The unit cell volume is an important measure for the tendency of a CAM particle to crack during cycling. The larger the volume change, the larger the mechanical stress of the particles due to (i) the anisotropic change of the lattice parameters a and c and (ii) the different orientation of the primary particles inside the

Table I. Comparison of lattice parameter changes in regular NCMs and in the mid-lithium LMR-NCM. The NCM data were taken from the operando XPD study of de Biasi et al. and present the therein investigated NCM materials with the lowest (NCM-111, 33%$_{Ni}$ on TM basis) and highest Ni content (NCM-851005, 85%$_{Ni}$), respectively.[32] As in our work, the CAMs were cycled in half-cells at C/10, but in the voltage window of 3.0–4.6 V. The lattice parameter changes are given as the difference between the completely discharged (lithiated, $x_{Li,dis}$) and charged (delithiated, $x_{Li,cha}$) state of the respective charge cycle and are normalized to the starting value (in a given particular cycle). For the unit cell volume V, this procedure always yields the maximum difference within a cycle, whereas a and c might run through minima and maxima, respectively. The Δx_{Li} range is calculated according to $\Delta x_{Li} = x_{Li,dis} - x_{Li,cha}$.

Material	Cycle	$x_{Li,dis}$ [−]	$x_{Li,cha}$ [−]	Δx_{Li} [−]	$\Delta a/a_0$ [%]	$\Delta c/c_0$ [%]	$\Delta V/V_0$ [%]
Regular NCMs[32]							
NCM-111	4 (reversible)	0.94	0.21	0.73	–1.2	±0.0	–2.3
NCM-851005	4 (reversible)	0.89	0.09	0.80	–1.7	–4.7	–8.0
Over-lithiated NCMs							
Mid-lithium LMR-NCM	1 (activation)	1.17	0.13	1.04	–0.7	+0.3	–1.1
Mid-lithium LMR-NCM	2 + 3 (reversible)	1.04	0.13	0.91	–1.3	–0.3	–3.0

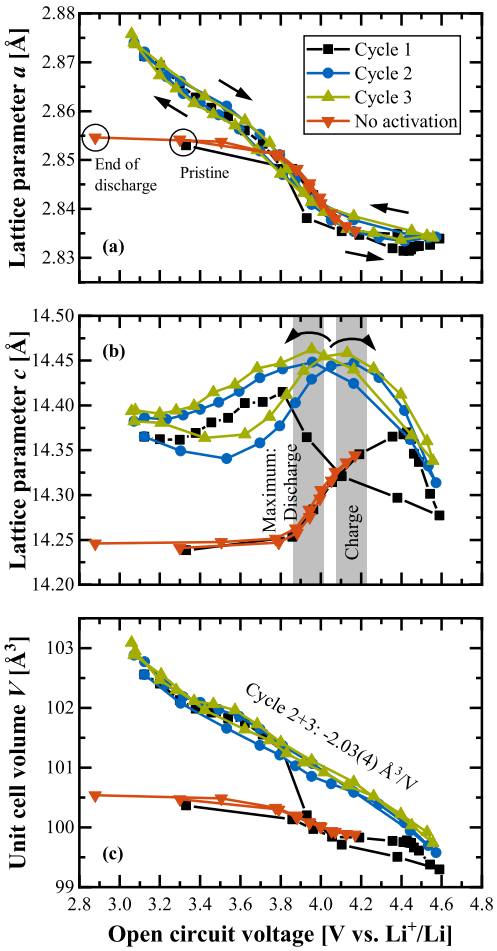

Figure 3. Lattice parameter data (taken from Fig. 1) for the mid-lithium LMR-NCM shown as a function of OCV at which the diffractograms were collected during the in-situ L-XPD experiments. (a), (b) Evolution of the lattice parameters a and b during the first three cycles at C/10. (c) Evolution of the corresponding unit cell volume, whereby the linear regression of the "cycle 2+3" data results in V = 109.0(1) Å^3 – 2.03(4) Å^3/V · OCV, with R^2 = 0.985.

secondary agglomerates of a typical polycrystalline CAM.[63,67] In Table I, we compare the relative lattice parameter changes of the over-lithiated NCM in Fig. 1 with two regular NCMs from the study of de Biasi et al.[32] In their work, NCM-111 and NCM-851005 are the end members with respect to the range of Ni content (33%$_{Ni}$ vs 85%$_{Ni}$ on TM basis). It is well-known in the literature that the degree of cracking increases with the Ni content[63,67] and with the upper cut-off potential.[68,69] Since increasing both parameters yields higher delithiation levels (i.e., lower $x_{Li,cha}$ values), this trend can be explained in good approximation by the steep volume contraction at x_{Li} values smaller than ≈0.3.[32,70] The overall volume contraction of the mid-lithium LMR-NCM (amounting to –1.1% during activation and –3.0% reversibly in the following cycles) is much closer to NCM-111 (–2.3%) than to NCM-851005 (–8.0%), even though its delithiation level ($x_{Li,cha}$ = 0.13) resembles the latter one (0.09). This discrepancy is largely driven by the smaller change of the lattice parameter *c*, whereas the reversible change of *a* is rather similar among the different CAMs. Despite the broader SOC range of Li- and Mn-rich layered oxides, we thus hypothesize that they are less prone to particle cracking and its detrimental consequences (such as CAM loss, TM dissolution, and surface reconstruction) than their Ni-rich (polycrystalline) competitors.

The "no activation" dataset in Fig. 1 revealed that the structural hysteresis observed in cycle 2 and onwards is directly connected to the activation plateau at ≈4.5 V. This raises the question if there is any chance to re-establish the pre-activated state without hysteresis even after passing this plateau. Therefore, we performed a charge window opening experiment.[24,25] After two cycles in the full voltage window of 2.0–4.8 V to activate the mid-lithium LMR-NCM material, Fig. 2 shows three consecutive cycles, where the upper cut-off voltage during charge was stepwise increased from 3.7 to 4.1 to 4.8 V, while always going back to 2.0 V during discharge. The extent of OCV hysteresis (see Fig. 2a) and lattice parameter hysteresis (exemplary shown for the unit cell volume in Fig. 2b) depends on the SOC range (equivalent to Δx_{Li}) that the CAM has passed through in every single cycle. Konishi et al. made the same observation for the OCV as well as the lattice parameters *a* and *c* of the $LiTMO_2$-like phase in their 2-phase refinement.[25] For the smallest SOC window of ≈74 mAh g^{-1} (Δx_{Li} ≈ 0.25) measured until 3.7 V (black lines in Fig. 2), the charge/discharge values of the unit cell volume agree within the error of measurement, while the OCV differs by a maximum of ≈60 mV (at x_{Li} ≈ 0.92). Since the voltage relaxation is not completed after 50 min resting (d*V*/d*t* ≈ 5 mV h^{-1}), this difference would get even smaller during a prolonged OCV step. Hence, the fully activated LMR-NCM exhibits almost no path dependence when cycled under this condition, but the hysteresis grows strongly when charged further (blue and green lines). As already described for the voltage by Assat et al.,[24] the in-situ L-XPD data also show on a structural level that the hysteresis raises mainly at the end of charge and stays open until the end of the discharge. Furthermore, the voltage and lattice parameter hysteresis must have the same driving force. In Fig. S5 in paragraph S2 of the SI, this measurement is contrasted with a discharge window opening experiment.

OCV dependence of lattice parameters.—Since the diffractograms were measured under open circuit voltage conditions, the lattice parameters of the mid-lithium material in Fig. 1 are re-plotted in Fig. 3 vs the OCV value averaged over the last minute of the 50 min rest phase. Here, we directly see a completely different dependency than when plotted vs the state of charge as was done in Fig. 1: When plotted vs OCV, the lattice parameter *a* exhibits almost no hysteresis between charge and discharge after the first activation charge (see Fig. 3a). Only upon closer inspection, it can be noticed that the *a* values during charge are slightly higher than during discharge (directions marked by arrows) for OCVs smaller than ≈4.0 V, where both curves intersect (this subtle difference was not be resolved in the study by Konishi et al.[25]). Interestingly, the "no activation" data (red lines) coincide perfectly with the charge curve. In the previous paragraph, we assigned any changes of *a* as to mainly originating from TM redox activities, which are initially restricted to the potential range of ≈3.6–4.2 V, but expand to lower potentials after activation (probably due to Mn^{3+}/Mn^{4+} redox). As the hysteresis of *a* when plotted vs OCV is negligibly small (Fig. 3a) compared to when it is plotted vs SOC (Fig. 1b), the TM redox seems to be uniquely associated with the thermodynamic state of the CAM that is marked by the OCV, whereas there seems to be no causal relationship to the lithium content. In contrast, the lattice parameter *c* still shows a hysteretic behavior even when plotted vs OCV (as shown in Fig. 3b). Due to the large voltage drop after current reversal at the upper cut-off, the maximum of the charge curve, that was at a lower SOC than during discharge (see Fig. 1c), is now at a higher OCV than the discharge curve (viz., at ≈4.15 V_{charge} vs ≈3.95 $V_{discharge}$, as highlighted by the grey bars).

The most interesting observation is the behavior of the unit cell volume *V* (see Fig. 3c) which, within the accuracy of the in-situ L-XPD measurements, exhibits no hysteresis after the first activation charge, with *V* changing linearly with OCV by about –2 Å^3 V^{-1}. As

Journal of The Electrochemical Society, 2022 **169** 020554

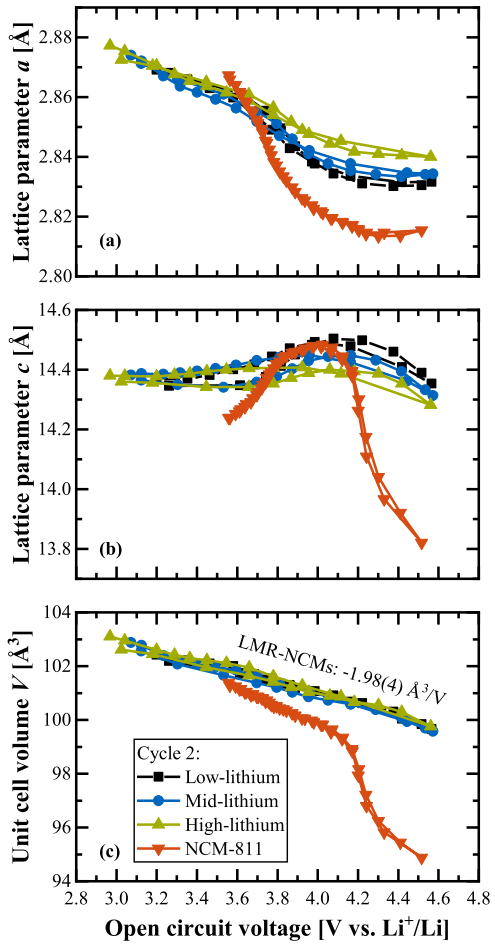

Figure 4. Evolution of the lattice parameters of three different LMR-NCMs during the second cycle (i.e., after activation) vs OCV, as determined from in-situ L-XPD experiments at C/10 in the voltage window of 2.0–4.8 V. The CAMs differ with respect to the degree of over-lithiation, ranging from a low-lithium ($\delta = 0.14$) over a mid-lithium ($\delta = 0.17$, same data as in Fig. 3) to a high-lithium material ($\delta = 0.20$). They are additionally contrasted with stoichiometric NCM-811 ($\delta = 0.01$), which was investigated at C/7.5 between 3.0–4.6 V (data taken from Fig. S6 in the SI of Friedrich et al.,[41] published by ECS, licensed as CC BY 4.0). In panel (c), the linear regression of all three LMR-NCMs results in V = 108.9(1) Å^3 – 1.98(4) Å^3/V · OCV, with $R^2 = 0.977$.

for any given OCV, the lithium content (x_{Li}) is different between the charge and the discharge reaction by up to $\Delta x_{Li} \approx 0.33$ (see blue/green lines in Fig. 1a). The linear and direction-independent relationship between V and OCV in turn means that very different lithium contents can yield the same unit cell volume: for example, $[Li_{0.75}TM_{0.83}O_2]_{charge}$ and $[Li_{0.42}TM_{0.83}O_2]_{discharge}$ both have an OCV of ≈3.80 V and a unit cell volume of ≈101.3 Å^3 within the second cycle. Such a behavior is quite remarkable and completely unknown for regular NCMs that exhibit no charge/discharge hysteresis and for which the lattice parameters uniquely scale both with the SOC and OCV.[41] The red lines in Figs. 1 and 3 show that the same is true for LMR-NCMs if they are not cycled into their activation plateau (labeled as "no activation"), contrary to the irreversible changes induced by cycling into the activation plateau.

So far, we only discussed the mid-lithium material, but it is also interesting to examine the lattice parameter changes for different degrees of over-lithiation. Figure 4 compares their OCV dependence during the second cycle for the already introduced mid-lithium material ($\delta = 0.17$ in $Li[Li_\delta TM_{1-\delta}]O_2$, same data as in Fig. 3) as well as for a low- ($\delta = 0.14$) and high-lithium material ($\delta = 0.20$). Beyond that, the Mn-rich over-lithiated CAMs are contrasted with the Ni-rich stoichiometric NCM-811. A zoomed-in view of the data for only the LMR-NCMs is given in Fig. S6 in paragraph S2 of the SI.

Starting again with the lattice parameter a, Fig. 4a shows that a decreases as the OCV increases from ≈3.6 to 4.2 V (i.e., in the region that is ascribed to the $Ni^{2+}/Ni^{3+}/Ni^{4+}$ and Co^{3+}/Co^{4+} redox). The decrease is the higher the lower the degree of over-lithiation, with a decreasing to only ≈2.840 Å for the high-lithium material while decreasing to ≈2.833 and ≈2.830 Å for the mid- and low-lithium material, respectively. The lower the degree of over-lithiation, the more transition metals are present in the transition metal layer and the lower is their average oxidation state (i.e., 3.33+, 3.41+, and 3.50+ in the pristine LMR-NCMs with low-, mid-, and high-lithium content, respectively; according to $(3-\delta)/(1-\delta)$). Consequently, for lower over-lithiation, more charge can be compensated by the classical TM redox until their formal 4+ state, apparently resulting in the observed larger a parameter changes. The lattice parameter a of NCM-811 varies exactly in the same voltage window, but its change is ≈2–3 times stronger (note that the average TM oxidation state is 3+ in pristine stoichiometric NCMs, because δ is essentially 0). The rise of a at potentials below ≈3.6 V (better visible in Fig. S6), which only occurs after activation and is not present in NCM-811, increases with increasing over-lithiation. It is reaching both lower OCV values (viz., from ≈3.20 V_{low} to ≈2.97 V_{high} at the end of the second discharge) and higher a values (viz., from ≈2.869 $Å_{low}$ to ≈2.877 $Å_{high}$; same data points). This trend could be explained by an increasing Mn^{3+}/Mn^{4+} redox fraction,[24,62] which is a concomitant feature of the anionic redox. To the best of our knowledge, there is no spectroscopic comparison of several Li- and Mn-rich layered oxides in one single publication, but the strong increase of irreversible O_2 loss (at the end of the activation charge; as was studied by Teufl et al.[13]) suggests that its reversible O^{2-}/O^{n-} redox counterpart also grows with increasing over-lithiation. This argument is in line with the increasing damping effect of the lattice parameter c (as shown in Fig. 4b). Both the initial rise (due to Coulomb repulsion) and the following drop (due to TM-O hybridization) get reduced with increasing over-lithiation and are much smaller compared to NCM-811, because the anionic redox most likely competes with the afore-mentioned electrostatic effects.

Despite the shifting ratio of cationic and anionic redox, which becomes visible in the individual lattice parameters a and c, the unit cell volume V vs OCV is essentially identical among the investigated LMR-NCMs, with a uniform slope of about –2 Å^3 V^{-1} (see Fig. 4). This indicates that the $V = f(OCV)$ representation is some kind of universal curve, as it uniquely describes all three LMR-NCMs independent of their degree of over-lithiation. There is obviously a close relationship between the crystal lattice dimensions and the open circuit voltage, but we do not yet know which structural and/or electronic parameter(s) command them.

As already noted above, the overall relative volume change of $\Delta V/V_0 \approx 2.5\%–3.0\%$ in the second cycle over an SOC range of ΔSOC ≈ 240–270 mAh g$^{-1}_{CAM}$ for all of the here examined LMR-NCMs, almost independent of their degree of over-lithiation (δ = 0.14–0.20), is much smaller than that of NCM-811 that exhibits $\Delta V/V_0 \approx 6.3\%$ for ΔSOC ≈ 220 mAh g$^{-1}_{CAM}$. Based on this, one would expect that the tendency for CAM particle cracking should be reduced for LMR-NCMs compared to Ni-rich NCMs.

Determination of the lithium and transition metal layer heights.—Before discussing possible reasons of the observed hysteresis phenomena, let us first deconvolute the lattice parameter c. This requires a determination of the z-coordinate of oxygen, $z_{6c,O}$, in order to calculate the lithium, h_{Li}, and TM layer heights, h_{TM}, according to[60]

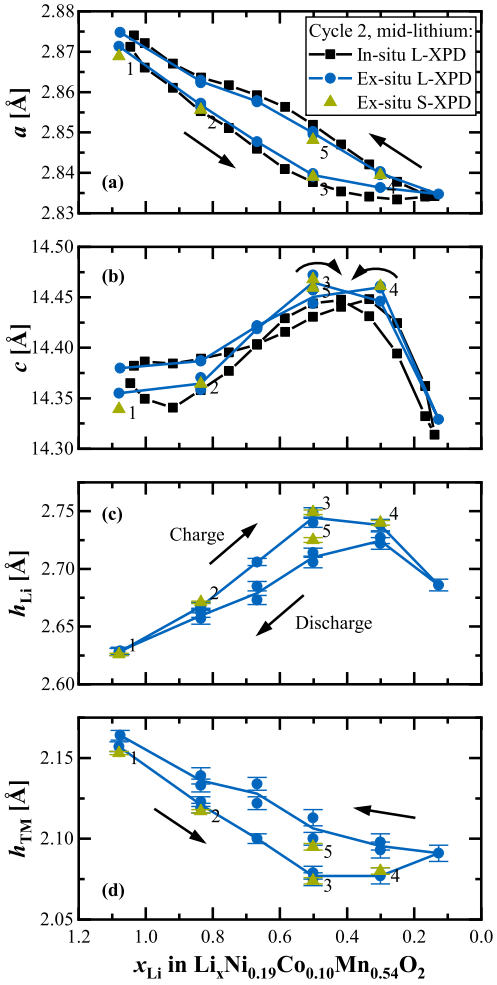

Figure 5. Determination of structural parameters over the course of the second charge/discharge cycle of the mid-lithium LMR-NCM material based on ex-situ XPD data from harvested electrodes, either acquired at the laboratory diffractometer (L-XPD; blue circles, with blue lines connecting their average values) or at the synchrotron (S-XPD; green triangles, labeled with numbers: 1/2/3 on the charge branch and 4/5 on the discharge branch). (a), (b) Lattice parameters a and c derived from ex-situ L-XPD and S-XPD data, including a comparison with the in-situ L-XPD derived data shown in Fig. 1. (c), (d) Determination of the lithium layer height, h_{Li}, and of the transition metal layer height, h_{TM}, via Rietveld refinements using the following rhombohedral model: $[Li_{x-u}Ni_v]_{3a}[Li_uTM_{0.83-v}]_{3b}[O_w]_{6c}$ with $u_{Li} = 0$ (except for the completely discharged samples with $x_{Li} > 1$, so that the occupation of the Li layer would be mistakenly greater than 1) and $w_O = 1$. The error bars correspond to the estimated standard deviation (e.s.d.) of each sample, as given out by the refinement program. Please note that some points of the ex-situ L-XPD dataset were measured twice with two independent samples.

$$\text{3a site: } h_{Li} = 2 \cdot (1/3 - z_{6c,O}) \cdot c \quad [2]$$

$$\text{3b site: } h_{TM} = 2 \cdot (z_{6c,O} - 1/6) \cdot c = 1/3 \cdot c - h_{Li} \quad [3]$$

Please note that the definition of the 3a/3b sites as Li/TM layers might also be opposite to that which is used in some instances in the literature.

The layer heights are a good starting point for Rietveld refinements. Liu et al. have shown in a detailed study about the sensitivity of the analysis of diffraction data (with stoichiometric NCA as a test case) that $z_{6c,O}$ is barely correlated to any other structural parameter.[39] It is thus the structural parameter that can be determined most accurately from X-ray powder diffraction data. Since in-situ data are usually biased due to overlapping reflections from other cell components (e.g., Al)[41] and have low counting statistics (in particular at laboratory diffractometers), which makes the detailed evaluation of structural parameters (other than lattice parameters) really challenging, we decided to rely just on ex-situ data for Rietveld refinements. Here, the cathode was cycled to the desired SOC, then the CAM powder was scratched off and air-tightly sealed in capillaries (see Experimental section for more details). Focusing on the quasi-reversible hysteresis after activation, Fig. 5 shows the Rietveld refinement results of the mid-lithium material within the second cycle, where ex-situ L-XPD measurements were conducted every ≈50 mAh g^{-1} during charge/discharge (blue circles/lines). Additionally, we sent some samples to the Swiss Light Source to obtain high-quality ex-situ S-XPD data (green triangles). The two upper panels of Fig. 5 compare the lattice parameters to the in-situ L-XPD data from V 1 (black squares/lines), while the layer heights, h_{Li} and h_{TM}, derived from the ex-situ XPD data are depicted in the two lower panels.

The lattice parameters a and c derived from ex-situ L-XPD data are in good agreement with those derived from in-situ L-XPD data and show the same characteristic hysteresis features. For the lattice parameter a in Fig. 5a, the ex-situ determined hysteresis loop (blue circles/line) is however slightly smaller, as the data points lie consistently in between the in-situ determined values (black squares/line). This might be due to a continued relaxation of the material within the first hours and days after transitioning into the OCV condition. In contrast, the lattice parameter c (see Fig. 5b) is shifted upwards for most of the ex-situ derived data, especially at x_{Li} values smaller than ≈0.8. Even though the shifts of a and c are not all in the same direction, the observed differences could be at least partially explained by a small misalignment of the in-situ pouch cell (see also Fig. S4 of the SI). Whatever the reason for these relatively small differences might be, a comparison of the ex-situ L-XPD derived lattice parameters that were measured within a few days after cell disassembly (blue circles) and those obtained by ex-situ S-XPD that were measured only after ≈5 months (green triangles) are in excellent agreement. This proves that the extended storage in the glass capillaries does not affect the harvested electrode samples (in call cases, the samples were sealed into the glass capillaries immediately after harvesting the electrodes), which is an important prerequisite for the much more time-consuming NPD experiments presented later. Furthermore, we can conclude here that the ex-situ approach is suitable for the quantification of detailed structural parameters under defined state of charge conditions.

The individual components h_{Li} and h_{TM} of the lattice parameter c are derived from ex-situ XPD data and presented in Figs. 5c and 5d, respectively. Surprisingly, their hysteresis behavior is much simpler than that of c (see Fig. 5b), because the charge branch is permanently higher than the discharge branch for h_{Li} or vice versa for h_{TM}. The general evolution of c over the charge/discharge cycle is dominated by the h_{Li} component (since its changes are typically higher than the changes of h_{TM}),[33,63] which is why any changes of c are typically explained with respect to this component (as we also did in the previous paragraphs). On the other hand, the evolution of the h_{TM} component resembles that of the lattice parameter a (see Fig. 5a). This means that the contraction/expansion of the TM-O_6 octahedra in the TM layer is fairly isotropic, as they respond uniformly in the ab plane (seen in a) and along the c direction (seen in h_{TM}) to the actual oxidation state (and ionic radius) of the TMs.[63]

Let us shortly comment on the accuracy of the quantification of the layer heights. Their relative error of 0.10%–0.25% (based on the estimated standard deviation given by the refinement program and

Journal of The Electrochemical Society, 2022 **169** 020554

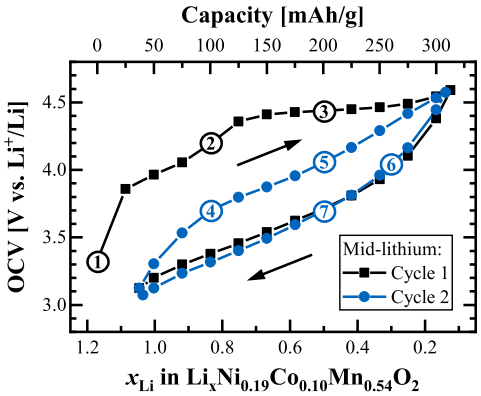

Figure 6. Selection of data points for the joint Rietveld refinement of ex-situ L-XPD and NPD data from the mid-lithium LMR-NCM, illustrated via the OCV vs SOC curves for the first (in black) and second charge/discharge cycle (in blue). The curves were extracted from the data shown in Fig. 1, which were recorded at C/10 with intermittent OCV periods. Using a nomenclature that specifies the cycle number (#), whether it is a charge or discharge step (CHA or DIS), and the measured SOC (in mAh g^{-1}), the points marked in the figure, given in chronological order, correspond to: ① pristine, ② #1-CHA-100, ③ #1-CHA-200, ④ #2-CHA-100, ⑤ #2-CHA-200, ⑥ #2-DIS-260, and ⑦ #2-DIS-200.

marked by the error bars in Figs. 5c, 5d) is roughly one order of magnitude higher than that of the lattice parameter *c*. The reproducibility among two nominally identical data points is fairly good, even though some other structural parameters might differ strongly (especially v_{Ni}/Ni_{Li} and $b_{3a,Li}$). This underlines the weak interdependence of $z_{6c,O}$ with other structural parameters.[39] Comparing the L-XPD to the S-XPD data, they coincide nicely on the charge branch (S-XPD data points 1, 2 and 3), but there are deviations on the discharge branch (points 4 and 5; note that the high-SOC point 4 appears to be on the charge branch). Taking all this into consideration, we believe that the ex-situ XPD data correctly describe the separation of the charge/discharge curves, but that the actual values of the layer heights and thus the extent of hysteresis have some uncertainty.

Origin of the reversible structural changes.—In the literature, hysteresis phenomena in Li- and Mn-rich layered oxides are usually ascribed to a path dependence of TM migration,[28,29,36,71] which was first proposed by the Argonne National Laboratory.[18,23,27] This migration process might involve both Ni and/or Mn moving from their native spot in the TM layer into tetrahedral and/or octahedral sites in the Li layer. As long as this process is reversible, it is believed that it causes the voltage hysteresis during charge/discharge cycling, whereas the irreversible capture of TMs in the Li layer would lead to voltage fade during long-term cycling. Assat et al. reported instead that the anionic redox is the real cause for hysteresis phenomena and that any structural rearrangements are just a consequence of that.[24] On the other hand, Gent et al. proposed a coupled $\{O^{2-} + TM\} \rightarrow \{O^{-} + TM_{mig}\} + e^{-}$ process, where TM_{mig} indicates a migrated TM into the Li layer, thus combining both afore-mentioned theories.[30] House et al. showed a link between the superstructure ordering and the anionic redox. Both in alkali-rich $Na_x[Li_\delta Mn_{1-\delta}]O_2$ compounds[72] and in $Li_{1.20}Ni_{0.13}Co_{0.13}Mn_{0.54}O_2$,[31] they showed that molecular O_2 is reversibly formed and trapped in the bulk, which would connect the voltage hysteresis to the in-plane TM migration in the TM layer (after Li_{TM} removal).[72] Recently, Csernica et al. proposed an oxygen vacancy model, where the oxygen deficiency penetrates into the bulk of the material by a diffusion process, while maintaining the native layered phase.[40] An oxygen vacancy leads to an undercoordinated transition metal, which promotes its migration into the Li layer. Csernica's model provides an atomistic link between cation disordering and oxygen release, both of which occur progressively upon cycling and could thus explain together the voltage fade.[40]

Assat et al. and Gent et al. are one of the few publications who quantified the extent of anionic redox and/or TM migration within one cycle and visualized their path dependence as a function of SOC (as we have done for the lattice dimensions in Figs. 1 and 5). Their results are however not identical. Assat et al. have shown by HAXPES measurements for $Li_{1.20}Ni_{0.13}Co_{0.13}Mn_{0.54}O_2$ within the first two cycles that the fraction of oxidized lattice oxygen, % O^{n-}, is consistently higher during charge than during discharge (see Fig. 2 in their paper).[24] In contrast, Gent et al. reported for $Li_{1.17}Ni_{0.21}Co_{0.08}Mn_{0.54}O_2$ within the first activation cycle that % O^{n-} (measured by STXM-XAS) and % TM_{Li} (measured by S-XPD) are smaller during charge than during discharge (see Fig. 6 in their paper).[30] Even though Assat et al. mention that their result conflicts with the hysteresis loop of the Ni oxidation state (which shows the same trend, but should be opposite for charge balancing), there is obviously not a general consensus yet in the literature—at least when attempting to quantify these sensitive parameters which are apparently difficult to determine.

The structural parameters determined in the present study might help to qualitatively track the path dependence during charge/discharge. Assuming a significant fraction of % O^{n-} and/or % TM_{Li}, the O-O repulsion in the Li layer gets reduced compared to 0% O^{n-} and/or TM_{Li}, what leads to smaller h_{Li} values. On the other hand, the TM-O attraction in the TM layer might get reduced as well, what in turn increases *a* and h_{TM}. According to the observed trends in Fig. 5 (h_{Li}: charge > discharge; *a* and h_{TM}: charge < discharge), these considerations support the findings by Gent et al.[30] In a simplified picture, the anionic redox and/or TM migration mainly occur at high SOCs during charge, but revert at low SOCs during discharge, i.e., the hysteresis is maximized in the mid-SOC regime (what is actually true for the OCV and lattice dimensions; see Figs. 1 and 5). It is however not really clear where the (energetic) penalty for such a huge delay comes from Refs. 23, 27, 73. An alternative explanation for the analogous hysteresis of *a* and h_{TM} is the path dependence of the cationic redox, which is spectroscopically easier to access than the anionic redox and which basically follows the OCV hysteresis.[24,25] The large number of (potentially) hysteretic parameters, including the open circuit voltage, lattice parameters, TM migration, cationic and anionic redox, raises the fundamental question about their "true" causal chain, which is lively discussed in the literature. Since there are so many different perspectives at the moment, it is difficult, if not impossible, to unequivocally assign the lattice parameter hysteresis to one particular parameter.

To break complexity down, we want to focus on TM migration in the following. The distribution of transition metals in Li- and Mn-rich layered oxides is usually investigated by (i) diffraction, using either XPD[30,45,74–76] or NPD data,[29,44] and (ii) a combination of microscopy techniques such as HAADF-STEM, EELS, and electron diffraction.[77–79] While microscopy is a local probe, which often resolves changes of the TM arrangement close to the particle surface, diffraction is a bulk method, which allows quantifying the TM distribution by the use of proper structural models to obtain average information for the entire CAM particle. There are single examples of other techniques such as X-ray diffraction spectroscopy (XDS),[71,80] atomic resolution STEM-EDS mapping,[81] and ^{6}Li MAS NMR spectroscopy,[28] but they are not used on a routine basis. Despite being the main technique, diffraction is full of pitfalls, especially due to the possible correlation of interdependent (structural) parameters, which hampers their precise quantification.[39] This problem can be minimized by the joint Rietveld refinement of complementary diffraction datasets, typically XPD and NPD,[82–84] but there are also a few examples in the battery field about the additional use of resonant X-ray diffraction (at energies close to the K edge of the transition metals).[37,38,85] As the scattering power of the elements varies among these different datasets, the joint

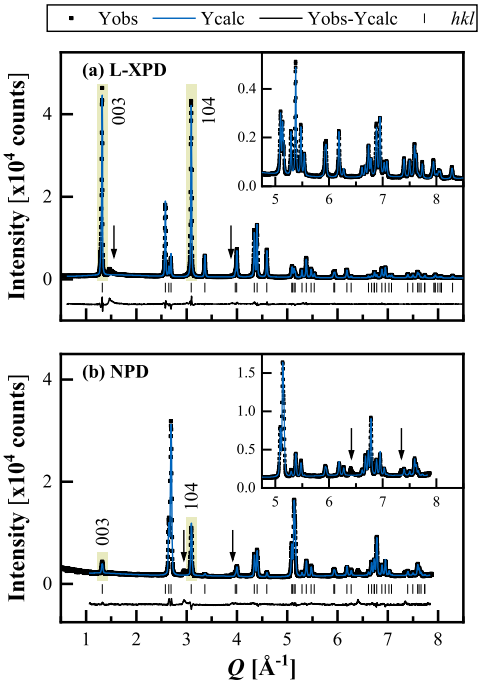

Figure 7. Joint Rietveld refinement of the pristine mid-lithium LMR-NCM powder, using (a) the L-XPD and (b) the NPD dataset with the rhombohedral *model 2* (described later in detail). The observed (black points), calculated (blue lines), and difference diffraction profiles (black lines) are shown together with the position of the Bragg peaks (black ticks) as a function of Q (in order to compensate for different wavelengths; $Q = 4\pi/\lambda \cdot \sin\theta = 2\pi/d$). The insets show a magnification of the high-Q range. The arrows indicate superstructure peaks due to in-plane ordering in the TM layer, which are not described by the rhombohedral model. The green highlighted regions mark the (003) and (104) reflections.

Table II. Fractional contribution of the scattering power from each crystallographic site relative to the total scattering power of the compound at $2\theta = 0$, f_i^*, as described by Yin et al.[89] The calculation is done for the ideal composition of the pristine mid-lithium LMR-NCM, $[Li]_{3a}[Li_{0.17}Ni_{0.19}Co_{0.10}Mn_{0.54}]_{3b}[O]_{6c}$, using X-ray form factors of neutral atoms ($f_{Li} = 3$, $f_{Ni} = 28$, $f_{Co} = 27$, $f_{Mn} = 25$, and $f_O = 8$; all in number of electrons) and neutron scattering lengths as implemented in Topas ($f_{Li} = -1.9$, $f_{Ni} = 10.3$, $f_{Co} = 2.49$, $f_{Mn} = -3.73$, $f_O = 5.803$; all in fm).[48]

Crystallographic site		Fractional scattering power	
		XPD	NPD
3a (Li layer)	$f^*_{3a,Li}$	0.073	0.139
3b (TM layer)	$f^*_{3b,TM}$	0.537	0.010
6c (O layer)	$f^*_{6c,O}$	0.390	0.851

refinement approach allows refining more elements on a single crystallographic site than only one dataset could do. This is in particular advantageous for Li- and Mn-rich layered oxides, because (i) Li can be extracted from two layers (Li_{Li} vs Li_{TM}), and (ii) both Ni and Mn are considered to migrate into the Li layer (Ni_{Li} vs Mn_{Li}). In contrast to XPD, where the X-ray atomic form factor scales with the number of electrons in the atom, NPD is sensitive to light elements (such as Li and O) and to elements with similar atomic numbers (such as Ni and Mn), as the neutron scattering length varies irregularly with atomic number and isotope.[39]

Figure 6 shows the OCV curve of the mid-lithium LMR-NCM plotted vs the lithium content for the first and second cycle, marking the selected samples of harvested cathodes for the combined refinement of ex-situ L-XPD and NPD data. Here, NPD needs CAM powder in the gram scale, which was prepared in multi-layer pouch cells (see Experimental section for more details). Apart from the pristine LMR-NCM (sample ①), we chose two samples from the first charge (②+③), two from the second charge (④+⑤), and two from the second discharge (⑥+⑦). During the first activation charge (in black), sample ② is at the end of the sloping region, whereas ③ resides in the middle of the voltage plateau. Their comparison might allow discerning the lithium extraction mechanism (Li_{Li} vs Li_{TM}). For the quasi-reversible hysteresis of the second cycle (in blue), we selected charge/discharge samples with either the same SOC or lithium content (i.e., ⑤↔⑦ in Fig. 6) or with the same OCV (and thus the same unit cell volume, i.e., ④↔⑦ and ⑤↔⑥), analogous to what was done by Mohanty et al.[29] Even though the number of data points is too little to resolve any hypothetical hysteresis loop of TM migration, their comparison might help to answer the question whether the amount of migrated TMs is similar at a given SOC or at a given OCV and hence whether there is any correlation to the lattice dimensions.

L-XPD and NPD diffractograms.—Before moving on to the Rietveld refinement results, it is worth to have a look on the diffractograms. Figure 7 shows the L-XPD and NPD diffractograms of the pristine mid-lithium LMR-NCM, which was measured as pure powder. We used a rhombohedral model for the combined refinement, as will be discussed later in detail. Both datasets cover a similar Q range and have comparable intensities, thus contributing equally to the refinement.

The in-plane Li/TM ordering in the TM layer is typically discussed on the basis of the small superstructure reflections following the intense (003) peak in the L-XPD pattern (at ≈1.4–2.0 $Å^{-1}$, marked by the left arrow in Fig. 7a). Interestingly, there are several peaks at ≈2.9,[44,86] ≈ 3.9, ≈6.4,[86] and ≈7.3 $Å^{-1}$ in the NPD pattern (as highlighted by the arrows in Fig. 7b), which are also not included in the rhombohedral model. They are only described by the monoclinic model and are thus another indicator for Li/TM ordering (see monoclinic refinement in Fig. S7 in paragraph S3 of the SI). As the ordering is not perfect, both in c direction (due to the presence of stacking faults) and in the ab plane (due to the off-stoichiometric Li/TM ratio), the superstructure peaks are quite broad and have a low intensity.[82,86,87] The peak at ≈3.9 $Å^{-1}$ in the NPD profile also appears in the L-XPD pattern (better visible on a logarithmic intensity scale).

To qualitatively estimate the cation mixing in pristine layered oxides, it is common to compute the integrated intensity ratio of the (003) and (104) reflections from XPD data (higher ratios point towards less migrated TMs).[60,88] While these two reflections are the most intense peaks in the L-XPD pattern, they are relatively weak in the NPD pattern (see yellow highlighted regions in Fig. 7). This discrepancy raises the question about the sensitivity of the NPD dataset with regard to the quantification of TM migration. Here, it is useful to apply the "diffraction parameter space" concept introduced by Yin et al.,[89] which allows calculating the zero-angle scattering power, f_i^*, of each crystallographic site i according to

$$f_i^* = \frac{m_i \cdot \left| \sum_{\text{all atoms j on site i}} c_j \cdot f_j \right|}{\sum_{\text{all sites i}} m_i \cdot \left| \sum_{\text{all atoms j on site i}} c_j \cdot f_j \right|} \quad [4]$$

where m_i is the multiplicity, c_j the fractional occupancy, and f_j the scattering power of each atom j residing at the site i. This term is normalized by the sum over all sites. Consequently, f_i^* is the fractional contribution of the scattering power from each crystallographic site i relative to the total scattering power of the compound at $2\theta = 0$, with $F_{000} = \sum_{\text{all sites i}} f_i^* = 1$. As described in more detail

Journal of The Electrochemical Society, 2022 **169** 020554

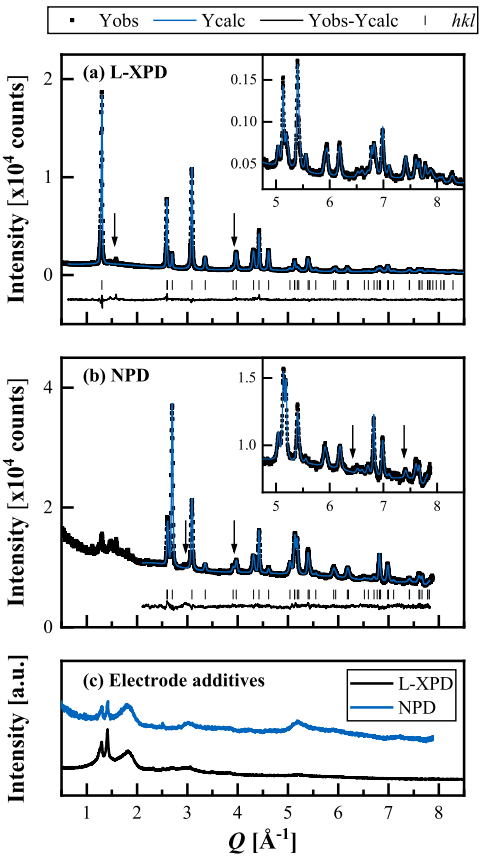

Figure 8. Joint Rietveld refinement of the harvested electrode sample ⑤ #2-CHA-200 (specified in Fig. 6), using (a) the L-XPD and (b) the NPD dataset with the rhombohedral *model 2*. As for all harvested electrode samples (②–⑥), the minimum Q value for fitting the NPD pattern, Q_{min}^{NPD}, was set to 2.1 Å^{-1}. The arrows indicate the expected positions of the superstructure peaks. Panel (c) shows the diffractograms of a 1/1 g/g mixture of conductive carbon (Super C65) and PVDF binder (Solef 5130) on an arbitrary intensity scale.

in the original publication by Yin et al.,[89] this concept is based on the simplified scenario for the hypothetical F_{000} reflection, where the phase factor ω_i of the site i is 1, and therefore the net scattering power of the m atoms comprising on this site is equal to m times the scattering power of a single one of these atoms. The individual scattering power of each atom, f_j, either corresponds to the X-ray atomic form factor or the neutron coherent scattering length.

In the rhombohedral model, there are three octahedral sites: 3a (Li layer), 3b (TM layer), and 6c (O layer). Table II summarizes their fractional scattering power, f_i^*, for the "ideal" pristine mid-lithium LMR-NCM (without any cation mixing) in both datasets. In the XPD pattern, the TM layer has the strongest scattering power amounting to ≈54% due to the high number of electrons, whereas the O and Li layer amount to ≈39% and ≈7%, respectively. Thus, all sites have a measurable contribution to the diffractogram. This is in stark contrast with the NPD pattern, which is dominated by the O layer with a share of ≈85%, whereas the TM layer contributes only with ≈1% to the total scattering power. The unfavorable combination of Ni (medium abundance and high positive scattering length, see caption of Table II) and Mn (high abundance and negative scattering length, see caption of Table II) effectively cancels out the scattering power of this site. The domination of the O layer is not altered by lithium extraction (in cycled samples) or by the incorporation of occupancy defects such as TM migration (e.g., Ni_{Li} and Mn_{Li}) and oxygen vacancies (considering that the expected extent of these defects is less than 10%). We conclude that the sensitivity of the recorded NPD patterns for the quantification of site occupancy factors in this particular compound is not as high as typically believed in the literature.

Figure 8 illustrates the diffractograms of the cycled sample ⑤ #2-CHA-200 (see also Fig. 6). All harvested electrode samples have in common that the NPD background is substantially increased compared to the pristine LMR-NCM powder (compare Figs. 8b with 7b), probably due to the presence of hydrogen in the PVDF binder and electrolyte residuals (hydrogen has a large incoherent neutron scattering cross-section).[29,90] Furthermore, there are several foreign reflections in the Q range of 1–2 Å^{-1}. According to the simple mixture of conductive carbon and PVDF binder (at a mass ratio of 1/1) in Fig. 8c, these reflections could be mainly assigned to the two electrode additives. As hydrogen and carbon are relatively strong neutron scatterers, the electrode additives are much more visible in the NPD profile than in the L-XPD pattern. Consequently, the weak (003) reflection in the NPD pattern had to be omitted from the joint refinement of harvested electrode samples ($Q_{min}^{NPD} = 2.1$ Å^{-1} for the samples ②–⑦ in Fig. 6). On the other hand, the superstructure peaks (expected positions indicated by the arrows in Fig. 8) are either superimposed by stronger reflections of the LMR-NCM phase and the electrode additives or they are difficult to distinguish from the background. This applies to all other harvested electrode samples as well, which is why we decided to additionally exclude the first superstructure region in the L-XPD pattern from any monoclinic refinement ($1.4 < Q_{excluded}^{L\text{-}XPD} < 2.3$ Å^{-1}), because the electrode additives' peaks might falsify the refinement results. For the sake of comparability and due to their poor description without any extra broadening, these peaks were also excluded from the monoclinic refinement of the pristine LMR-NCM powder sample.

Results of the joint Rietveld refinement.—In the literature, there are numerous structural models used for the Rietveld refinement of diffraction data from Li- and Mn-rich layered oxides, which reach from rhombohedral to monoclinic all the way to composite models with increasing complexity. In Table SV in paragraph S4 of the SI, we tried to give an overview of structural models by comparing 15 publications from different research groups (i.e., with respect to the investigated CAM, the type of diffraction data, and the number of refined structural parameters). Here, we made the following observations: (i) In some publications, it is not clear how all of the structural parameters are actually treated during the refinement (especially atomic displacement parameters, ADPs). This makes it difficult for the reader to evaluate the quality of the applied model. (ii) Even for the same base model, the amount of refined (or constrained) structural parameters might differ significantly (especially site occupancy factors, SOFs). A high number of refined parameters potentially causes severe correlations and thus restricts their validity. (iii) Finally, the application of composite models is in our opinion mostly not well justified on the basis of the raw data, e.g., by the occurrence of peak splitting. It is further not always clear how the overall composition is maintained when the phase fractions are freely refined (without adapting, e.g., the TM distribution among the two phases).

Since the literature reports are largely different, we want to start the joint Rietveld refinement with a simple rhombohedral model for the X-ray and neutron diffraction data of the mid-lithium LMR-NCM material (with the sample specifications given in Fig. 6). This model referred to as *model 1* looks as follows in the crystallographic notation: $[Li_{x-u}Ni_v]_{3a}[Li_uTM_{0.83-v}]_{3b}[O_w]_{6c}$ (corresponding to $Li_{x-u}Ni_v[Li_uTM_{0.83-v}]O_{2w}$ in the formula unit notation). Here, the three most common fractional occupancies are freely refined: (i) the Li distribution in the Li/TM layers, which finds expression in the parameter u_{Li} (equivalent to Li_{TM}), (ii) the migrated Ni into the Li layer (v_{Ni}, equivalent to Ni_{Li}), and (iii) the oxygen vacancies (w_O, equivalent to O). The overall lithium content, x_{Li}, is determined by the SOC of the cycled samples according to Eq. 1. Since the 3a/

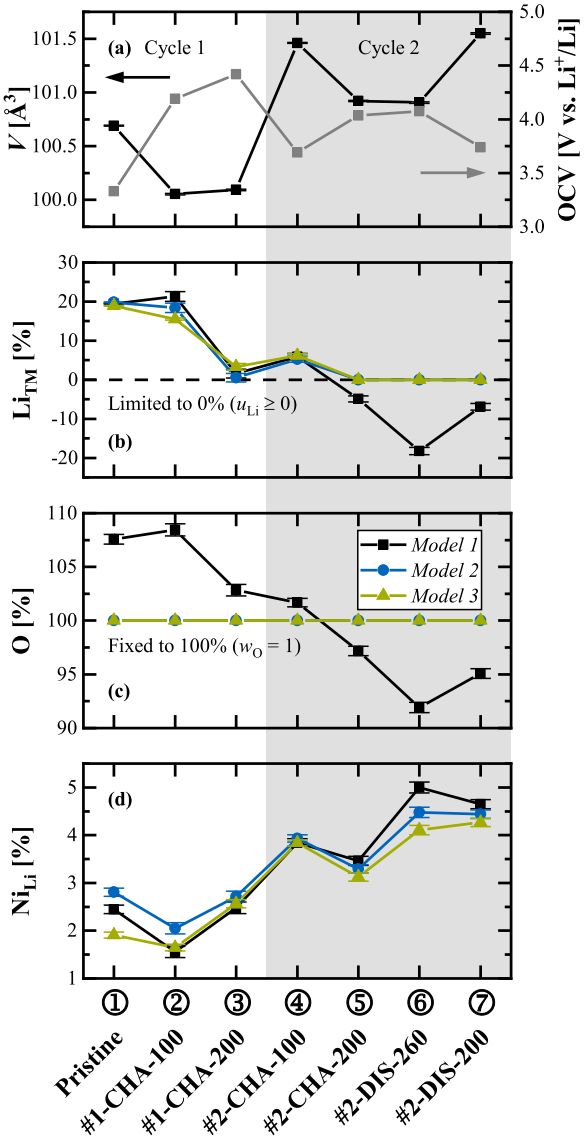

Figure 9. Summary of the combined L-XPD and NPD Rietveld refinement for the seven mid-level LMR-NCM samples described in Fig. 6. (a) Refined unit cell volume (in the rhombohedral representation; left y-axis) and open circuit voltage after 2 h (right y-axis). The following panels show the refined (or fixed) amount of (b) lithium in the TM layer ($Li_{TM} = u_{Li} \cdot 100\%$), (c) oxygen in the O layer ($O = w_O \cdot 100\%$), and (d) nickel in the Li layer ($Ni_{Li} = v_{Ni} \cdot 100\%$) according to three different structural models: (i) the extended rhombohedral *model 1* with $[Li_{x-u}Ni_v]_{3a}[Li_uTM_{0.83-v}]_{3b}[O_w]_{6c}$, (ii) the simplified rhombohedral *model 2* ($u_{Li} \geqslant 0$, $w_O = 1$), and (iii) its monoclinic counterpart, *model 3*, which also accounts for the in-plane Li/TM ordering in the TM layer. The overall lithium content, x_{Li}, is determined by the state of charge (see Eq. 1). For further refinement results see Tables SII-SIV in paragraph S3 of the SI. The gray highlighted area marks the refinement results for the electrode samples harvested in the second cycle.

3b metal sites are fully occupied in the pristine state, u_{Li} and v_{Ni} are constrained with respect to each other ($u_{Li} = 0.17 + v_{Ni}$ at $x_{Li} = 1.17$). This reduces the number of freely refined site occupancy factors (SOFs) to two. The calculated values of Li_{TM}, Ni_{Li}, and O, which represent the afore-mentioned SOFs in percentage terms, are summarized in Fig. 9 for all seven samples (together with their unit cell volume and OCV).

Starting with Li_{TM} (see black data points for *model 1* in Fig. 9b), the lithium occupation in the transition metal layer stays at its pristine value of ≈20% until the end of the sloping region (sample ②), but drops to ≈2% in the middle of the first charge plateau (③) and reaches even negative values in the second cycle (⑤–⑦), which are physically meaningless, but mathematically possible in the least squares refinement (without applying any constraints with respect to the SOFs). This result is qualitatively in line with the operando NPD study of Liu et al.,[66] who reported that the delithiation mechanism operates solely through the extraction of lithium from the lithium layer (Li_{Li}) in the sloping region, but involves the extraction of lithium from the transition metal layer (Li_{TM}) during the activation plateau, whereby the latter cannot be re-intercalated within the first discharge (constant level of ≈6%–7% in their study). We observe ≈6% Li_{TM} for sample ④ at the beginning of the second charge (#2-CHA-100). Since the SOC provides a lower limit of the actual lithium content due to the possibility of parasitic reactions at high voltages,[39,84] x_{Li} is definitely greater than 1 in the discharged state ($x_{Li} \approx 1.05$ at the end of the first discharge, see lower x-axis in Fig. 6), what in turn imposes the partial occupation of Li_{TM} after activation.

Approaching the delithiation process by DFT simulation of the model material, $Li_{60}[Li_{12}Ni_{12}Co_6Mn_{30}]O_{120}$, Table SVI in paragraph S5 of the SI shows that the potential energy surface for these systems exhibits a multitude of nearly degenerate local minima for each delithiation step. We start the analysis considering the removal of 13 Li ($x_{Li} = 0.98$). Among the calculated structures, it is energetically more favorable to remove Li from the Li layer only, leaving the 12 Li in the TM layer intact. The layered structure is retained; of the 47 Li in the Li layer, only one in the central layer seems to have changed its coordination to tetrahedral. Further delithiation of in total 42 Li ($x_{Li} = 0.50$) brings us experimentally to the middle of the voltage plateau in the first charge. By DFT, we found that the most stable structure was achieved by removing all Li from the TM layer, while maintaining the layered structure. An alternative model where 6 Li still reside in the TM layer has been found to be 18 meV/atom higher in energy. To sum up, the DFT results qualitatively agree with the experimental data of the first activation charge. Hence, we are confident that the CAM activation follows the energetically favorable delithiation pathway.

The oxygen content of *model 1* in Fig. 9c changes from almost +10% to –10% upon progressive cycling. Former gassing studies of the mid-lithium material suggest the oxygen release to be on the order of ≈3% within the first two cycles, originating from the near-surface region of the primary particles.[13,59] Despite the presence of intragranular nanopores in pristine CAMs and further intragranular cracking upon cycling, which inject oxygen vacancies also into the bulk lattice,[68,91,92] the refined level seems to be unlikely. Recently, Csernica et al. estimated the oxygen release, including bulk oxygen vacancies, for a similar LMR-NCM material ($\delta = 0.18$) on the basis of XAS data.[40] They reported ≈3.3% lost oxygen after the first cycle, which is consistent with the gassing studies.[13,59] After 500 cycles, the oxygen release amounted to ≈6.5% and is thus far below the here refined changes of almost 20% within the first two cycles. This variation also exceeds the maximum of ≈10% of reversibly trapped lattice oxygen in the form of molecular O_2, as was reported by House et al.[31] Beyond that, O values greater than 100% are again physically meaningless and the parameter w_O is strongly correlated to the NPD scale factor (≈70%–80%), which can be explained by the overwhelming scattering power from the O layer in the NPD pattern (see Table II). This makes the neutron data insensitive to the oxygen occupancy, as was also observed by Csernica et al.[40] In view of these findings, it seems to be reasonable to neglect oxygen vacancies from refinements of LMR-NCM samples within the initial cycles.

The refined amount of Ni migrated into the lithium layer, Ni_{Li}, lies in the range of ≈1.6% to ≈5.0% for all of the examined samples (see Fig. 9d). Gent et al. determined comparable TM_{Li} values from ≈2.6% in their pristine LMR-NCM until ≈7.5% at the end of the

Journal of The Electrochemical Society, 2022 **169** 020554

first charge. Please note that their reported % TM_{Li} values are divided by the total TM stoichiometry, % TM_{Li} (as used by Gent et al.) = TM_{Li} (as used in this work)/(1−δ) with $\delta = 0.17$.[30] Since NPD could help to differentiate the migrating TM species due the sign of their neutron scattering length (Ni and Co positive, Mn negative), we also tried joint Rietveld fits with Mn_{Li} instead of Ni_{Li}. However, the refinements gave unreliable Li_{TM} values of up to ≈40% for the cycled samples. As Li and Mn have both negative neutron scattering lengths, they are highly correlated (≈80%) and it is thus not viable to refine their distribution in the metal layers simultaneously (analogous to the difficulty to differentiate the transition metals from XPD data). Refining simultaneously Li, Ni, and Mn would lead to a 100% correlation among the three parameters. In this context, we should recall that diffraction probes the scattering power of crystallographic sites, but not of their individual constituents. This restricts the number of simultaneously refined SOFs on a single site to the available number of complementary diffraction datasets. The combination of L-XPD and NPD, as used in this work, enables a maximum of two SOFs on the same site(s). If the scattering power of two elements is however unfavorably close in one of the datasets (e.g., Li and Mn in NPD, Ni and Mn in regular XPD), their simultaneous refinement might lead to severe correlations and hence to erroneous results.

Since *model 1* led, in part, to physically meaningless results, we explored another rhombohedral model, referred to as *model 2*, in which the lower limit for Li_{TM} is set to 0% ($u_{Li} \geqslant 0$) and which assumes that there are no oxygen vacancies ($w_O = 1$; see blue data points in Fig. 9). These constraints change the refined Ni_{Li} values by a maximum of 0.5% (absolute) for the samples ② and ⑥ compared to *model 1*, which is mainly driven by excluding oxygen vacancies (v_{Ni} and w_O are inversely proportional). In a former publication, we also refined the migrated Ni amount into the tetrahedral sites of the Li layer, Ni_{Li}^{tet}, for the completely charged state (at 4.6 V).[36] Including Ni_{Li}^{tet} to the mid/high-SOC samples ⑥ and ⑦ however leads to small values of ≈1%, in contrast to a constantly high level of ≈8%–9% over 100 cycles in the previous study (since Ni_{Li}^{tet} resides on a 6c site, its amount is calculated according to $Ni_{Li}^{tet} = 2 \cdot SOF(6c) \cdot 100\%$ to enable direct comparability with the 3a/3b metal sites). We therefore did not include tetrahedral sites in any of the refinements. Replacing Ni_{Li} again by Mn_{Li}, while constraining Li_{TM} to remain constant, shows the same trend for the migrating TM. Mn_{Li} (≈2.1%–6.0%) is up to ≈0.6% higher than Ni_{Li} (≈2.0%–4.5%); only for sample ⑥ Mn_{Li} is higher by ≈1.5% (see full comparison in Fig. S8 of the SI). Even though it is difficult to identify the migrating TM species by this comparison, Ni_{Li} is the preferred choice for the further analysis, because Ni can be simultaneously refined with Li, but Mn cannot.

Lastly, we also tested a monoclinic model, referred to as *model 3* (see green data points in Fig. 9), where the superstructure region in the L-XPD pattern was excluded from the refinement ($1.4 < Q_{excluded}^{L\text{-}XPD} < 2.3$ Å^{-1}, as discussed in the context of Fig. 8). This approach does not only consider the inter-layer Li/TM arrangement, but it also accounts for their in-plane ordering by dividing each layer into two crystallographic sites (Li layer: 2c/4h, TM layer: 2b/4g, O layer: 4i/8j). Due to the different multiplicities, special care must be taken to maintain the overall stoichiometry. The monoclinic *model 3* has the following crystallographic notation: $[Li_{x-u}Ni_v]_{2c,4h}[Li_{3u}Ni_oMn_p]_{2b}[Ni_{0.285-o/2-3v/2}Co_{0.15}Mn_{0.81-p/2}]_{4g}[O_w]_{4i,8j}$, which translates into the formula unit $Li_{x-u}Ni_v[(Li_uNi_{o/3}Mn_{p/3})^{2b}(Ni_{0.19-o/3-v}Co_{0.10}Mn_{0.54-p/3})^{4g}]O_{2w}$. Since the in-plane Li/TM ordering matters mainly for the TM layer, the Li and O layer were not split into two parts (i.e., the distribution in these layers is homogenous). Beyond the known parameters u_{Li}, v_{Ni} and w_O from the rhombohedral models, o_{Ni} and p_{Mn} describe the distribution of Ni and Mn in the TM layer, respectively. Please note that Li_{TM} was only put on the 2b site, as it is also the case in the archetypal Li_2MnO_3 (= $Li[(Li_{1/3})^{2b}(Mn_{2/3})^{4g}]O_2$).[93] Limiting Li_{TM} again to greater or equal than 0% ($u_{Li} \geqslant 0$) and also neglecting oxygen vacancies ($w_O = 1$), there is a maximum amount of four refined SOFs (viz., u_{Li}, v_{Ni}, o_{Ni}, and p_{Mn}). This number reduces to three for most of the cycled samples due to constraints ($3u_{Li} + o_{Ni} + p_{Mn} \leqslant 1$ at the 2b site for the samples ② and ④, $u_{Li} \geqslant 0$ for ⑤–⑦) and further to two for the pristine sample ① due to full occupation ($u_{Li} = 0.17 + v_{Ni}$ and $p_{Mn} = 0.49 - 3v_{Ni} - o_{Ni}$). The results are pretty close to the rhombohedral counterpart, *model 2*. Li_{TM} agrees within ±3% and Ni_{Li} differs at the maximum by ≈0.4% (for the samples ② and ⑥) and ≈0.9% (for the pristine sample ①). Furthermore, o_{Ni} and p_{Mn} confirm the expected TM distribution in the TM layer (see Table SIV in the SI). Due to the similar ionic radii of Li^+ and Ni^{2+}, Ni resides mainly on the 2b site (2b/4 g ratio ≈2/1 in the f.u. notation),[44] but Mn accumulates on the 4g site (2b/4g ratio not greater than ≈1/3).

Comparison of the migrated Ni_{Li} amount.—Overall, the refined amount of Ni migrated into the Li layer follows the same trends among the three tested structural models (see Fig. 9d). The quality factors of the Rietveld fit (viz., R_{wp}, R_{bragg}, and χ^2) typically improve from *model 2* to *model 1* to *model 3* (see Tables SII–SIV of the SI), which can be explained by the increasing amount of freely refined parameters (see comparison in Table SV of the SI). Since the results from *model 1* were in some cases not physically sound and since the monoclinic extension of *model 3* aims primarily at the in-plane Li/TM ordering (which further might get lost within the first cycles[45,46]), we think that the rhombohedral *model 2* (with the constraints $u_{Li} \geqslant 0$ and $w_O = 1$) is the simplest and most robust approach to determine Ni_{Li} in this study. In the following, we want to systematically compare the amount of migrated Ni_{Li} from *model 2* in the second cycle (highlighted in gray in Fig. 9). After activation, this cycle is characterized by a quasi-reversible hysteresis of the OCV and the lattice parameters as a function of SOC. Table III contrasts the results from the harvested electrodes of the second cycle according to their SOC, OCV, unit cell volume V, and migrated Ni_{Li} amount. As discussed in Fig. 6, the charge/discharge pairs have either the same SOC (⑤↔⑦), essentially the same OCV and unit cell volume V (④↔⑦ and ⑤↔⑥), or they differ for all of the three parameters (④↔⑥). On the other hand, the Ni_{Li} amount deviates by ≈0.5%–1.2% (absolute) for each pair (see last column in Table III), which is quite a lot with regards to the maximally observed difference of ≈2.4% (between the samples ② and ⑥; see Fig. 9d). Consequently, we could not prove a causal relationship between the extent of TM migration, in particular Ni_{Li}, to the electrochemical (SOC, OCV) and lattice parameter data (for none of the tested models), as we would have intuitively expected based on the TM_{Li} hysteresis reported by Mohanty et al.[29] and Gent et al.[30] in comparison to the here examined hysteresis of the OCV and lattice dimensions. Comparing all samples, we see an increase of the average Ni_{Li} level in *model 2* from the low/mid-SOC range of the first charge (≈2.1%–2.8% for the samples ①–③) to the low/mid-SOC range of the second charge (≈3.3%-3.9% for ④+⑤) to the mid/high-SOC range of the second discharge (≈4.4%–4.5% for ⑥+⑦). This trend is in line with the irreversible increase of TM_{Li}, which is frequently reported in other studies and amounts there to $\Delta TM_{Li}^{irrev} \approx$ 1.3%–1.9% after the first activation cycle and to ≈2.8%–2.9% after 15-25 cycles (ΔTM_{Li}^{irrev} analyzed as the difference of the discharged state relative to the pristine material).[30,36,40] On the other hand, our data do not entirely contradict a partially reversible intra-cycle TM migration within the second cycle; however, this hysteresis would be significantly smaller than the $\Delta TM_{Li}^{rev} \approx 3.6\%$ reported by Gent et al. for the first activation cycle (ΔTM_{Li}^{rev} analyzed as the difference between the charged and discharged state).[30] To prove such a small tendency (probably smaller than the overall increase of 2.4% in this study), one certainly needs more data points (including samples in the completely discharged and charged state, which should represent the limit values of Ni_{Li} within a cycle, and low-SOC samples during the second discharge, where Ni_{Li} would have to go down again).

DFT simulations of the fully charged structure raise further doubts on a correlation between the TM migration and the voltage hysteresis. Although x_{Li} in reality does not fall below 0.1 at the end

Journal of The Electrochemical Society, 2022 169 020554

Table III. Comparison of mid-lithium LMR-NCM electrode samples harvested in the second cycle (shown in blue in Fig. 6) with respect to their SOC, OCV, unit cell volume V, and migrated Ni_{Li} amount (according to the rhombohedral *model 2*). The relation of the charge/discharge pairs is either classified as identical (=), similar (≈), or different (≠). The respective difference is given as Δ = DIS—CHA. The maximum differences from the completely discharged (2.0 V) to charged state (4.8 V) in the second cycle are: ΔSOC ≈ 270 mAh g^{-1}, ΔOCV ≈ 1.5 V, and ΔV ≈ 3.1 $Å^3$.

Samples		SOC [mAh/g]		OCV [V vs. Li^+/Li]		V [$Å^3$]		Ni_{Li} [%]			
CHA	DIS	Relation	Δ	Relation	Δ	Relation	Δ	Relation	CHA	DIS	Δ
⑤	⑦	=	0	≠	–0.30	≠	+0.63	≠	3.29(9)	4.44(9)	+1.15
④	⑦	≠	+100	≈	+0.05	≈	+0.09	≠	3.93(8)	4.44(9)	+0.51
⑤	⑥	≠	+60	≈	+0.04	≈	–0.02	≠	3.29(9)	4.48(11)	+1.19
④	⑥	≠	+160	≠	+0.39	≠	–0.55	≠	3.93(8)	4.48(11)	+0.55

of charge (see Fig. 6), we assume $x_{Li} = 0$ for the DFT calculation (i.e., $Li_0Ni_{12}Co_6Mn_{30}O_{120}$), thereby removing the combinatorial complexity due to the Li distribution and greatly reducing the computational effort. A structure where 10 Mn moved to tetrahedral positions in the TM layer (see 4th row from the bottom of Table SVI in the SI) is 50 meV $atom^{-1}$ more stable than a perfectly layered model with every TM in octahedral sites (bottom row of Table SVI). We found several structural candidates where the diffusion of Ni into octahedral sites of the Li layer further lowered the total energy of the system. In many instances we also observed the concomitant formation of $O\text{-}O^{\delta-}$ dimers in the TM layer from which the diffusing atom(s) originated (see second to last column in Table SVI).[30] All these structures for $Li_0Ni_{12}Co_6Mn_{30}O_{120}$ are within 13 meV $atom^{-1}$ (see last 9 rows in Table SVI), which is well below the value of k_BT at 300 K (25 meV $atom^{-1}$), and at least 43 meV $atom^{-1}$ lower in energy than the perfectly layered structure without migrated TMs. This result highlights the complexity of the potential energy surface, where many local minima, even with very different structural features, coexist within an energy range comparable with the thermal energy at room temperature. Therefore, the completely delithiated structure appears to be a very "fluxional" system where many processes can happen at virtually no energetical cost.

We now raise the question of what happens when we reinsert Li into the structure with migrated Ni. The expectation is that, after the first charge, we should generally end up at lower voltages (i.e., energies) than before. Instead, every calculated structure containing 1–2 Ni in the lithium layer at $x_{Li} = 0.5$ (i.e., for $Li_{30}Ni_{12}Co_6Mn_{30}O_{120}$) is consistently higher in energy (by 9–27 meV $atom^{-1}$; see Table SVI) than the counterpart where the TMs reside solely in the TM layer. This contradicts our expectation based on the lattice parameter results, where we learned that the structural changes (e.g., TM migration) occur mainly at the end of the charge process. Therefore, we would have expected that the lower voltages/energies of the partially lithiated structure with a lithium content of $x_{Li} = 0.5$ that lies in the voltage plateau region would correlate with a significant number of TMs migrated into the lithium layer.

Based on our calculations, which however do not comprise an exhaustive screening, we can say that TM migration is only at the fully charged state energetically degenerated. The data do not provide any hint for the lower voltages/energies between the charge and discharge process caused by nickel migration because the TM movements stays unfavorable with increasing lithium content. This means that there is no driving force to energetically maintain a possibly moved TM in the lithium layer after charging the material.

Finally, let us comment on the accuracy of the Ni_{Li} amount from our joint Rietveld refinements. Using the example of *model 2*, all correlations of Ni_{Li} are below ≈55% and thus minor for most of the samples (①–④). The level of correlations rises with increasing SOC, reaching up to ≈70% to the L-XPD scale factor and ≈60% to the atomic displacement parameter of the Li layer, $b_{3a,Li}$, for the high-SOC sample ⑥. In general, the ADPs are in a reasonable range for layered oxides ($0.5 < b_{3a,Li} < 2.1$, $0.1 < b_{3b,TM} < 0.3$, $0.8 < b_{6c,O} < 1.2$, all in $Å^2$; see Table SIII in the SI),[39,89] but $b_{3a,Li}$ and $b_{3b,TM}$ run into the lower limit of 0 for sample ⑥. Fixing them intentionally to 1.0 and 0.25 $Å^2$, respectively, changes the Ni_{Li} amount in *model 2* from 4.48(11)% to 4.90(9)%. This difference is undesirably large and thus emphasizes the strong dependence of SOFs on ADPs. The accurate determination of ADP values needs high-Q diffraction data in the range of ≈10–20 $Å^{-1}$, as they could be obtained from S-XPD and time-of-flight NPD (TOF-NPD would be most qualified, because the neutron scattering length does not fall off with increasing Q).[39,89]

By applying high-quality S-XPD and TOF-NPD data separately to a series of twelve pristine NCM materials, Yin et al. achieved an absolute agreement of 0.1% for the paired anti-site Ni_{Li}/Li_{TM} defect between both Rietveld fits (with partially constrained ADP values).[89] In a similar manner, we also tested *model 2* individually against every L-XPD, S-XPD, and NPD pattern of the seven co-refined samples (by combining all available data from Figs. 5 and 9). The comparison of the structural parameters in Fig. S9 of the SI shows that $z_{6c,O}$ is fairly invariant among the different datasets,[39] while Ni_{Li} and $b_{3a,Li}$ have a significant scatter. The steady increase of Ni_{Li} over the course of the two charge/discharge cycles is reflected, on average, in all datasets, but the variation of the Ni_{Li} amount for a given sample ranges from 0.2% to 3.8%. We thus think that an accuracy of 0.1% is extremely difficult, if not impossible, to accomplish in our work and related studies about Li- and Mn-rich layered oxides. This type of CAMs is crystallographically more challenging than regular NCMs without over-lithiation, because lithium also resides in the TM layer, where it causes an (imperfect) Li/TM ordering. Both the lithium occupation and the in-plane ordering change upon electrochemical cycling. Furthermore, the atoms of the layered oxides go through different oxidation states during cycling, involving both cationic and anionic redox activities in LMR-NCMs.

This electronic aspect raises the question about the proper choice of X-ray atomic form factors. We applied neutral atoms because they ensure charge neutrality for any (cycled) sample. Using ions, namely Li^+, Ni^{2+}, Co^{3+}, Mn^{4+}, and O^{2-}, would yield consistently lower Ni_{Li} values by 0.5%–0.9% (see Fig. S10 of the SI). Yin et al. proposed alternatively the combination of neutral metal species with ionic O^{2-}.[89] As the oxidation states are different, but not exactly known at any given SOC, they add an unavoidable bias to the refined Ni_{Li} amount of cycled samples. For this reason, Liu et al. proposed to exclude low-Q values from XPD refinements, because different oxidation states have the biggest impact there.[39] Following their suggestion, we tested *model 2* again with $Q_{min}^{L\text{-}XPD} = 2.9$ $Å^{-1}$, which ignores the rhombohedral reflections (003), (101), (006), and (102). The comparison of the refinements using atomic form factors with either full or limited Q^{L-XPD} range is also provided in Fig. S10 of the SI, yielding by 0.2%–1.1% smaller Ni_{Li} values for the latter.

Journal of The Electrochemical Society, 2022 **169** 020554

Since these variations are within the magnitude which is often discussed in the literature as a meaningful difference when analyzing different CAMs, it is essential to report all these refinement details to enable a minimum of comparability between different publications.

Even though the purpose of Rietveld refinements of diffraction data from Li- and Mn-rich layered oxides is to determine Ni_{Li} and site occupancy factors, their quantification is clearly subject to much uncertainty. As there is no generally accepted agreement yet in the literature about the proper choice of instrumentation (e.g., synchrotron vs laboratory diffractometer), X-ray atomic form factors, and structural models, all these uncertainties clamor in our opinion for a systematic study, as it was done for regular layered oxides by Liu et al.[39] and Yin et al.[89] Comparing high-quality diffraction data, preferably S-XPD and TOF-NPD, of over-lithiated CAMs at different SOCs might show a path towards the precise quantification of TM migration. The current efforts to synthesize Co-free LMR-NCM[6,94] would additionally reduce the compositional complexity in diffraction experiments. We hope that this work can serve as a starting point in this respect.

Conclusions

In this work, we investigated the well-known open circuit voltage (OCV) hysteresis in Li- and Mn-rich layered oxides (LMR-NCMs, i.e., $Li[Li_\delta TM_{1-\delta}]O_2$ with $0.1 < \delta < 0.2$ and TM = Ni, Co, Mn) on a structural level, using a combination of diffraction techniques and DFT simulations. In the first part, the lattice parameter evolution of a mid-lithium LMR-NCM with $\delta = 0.17$ was monitored within the initial cycles by in-situ X-ray powder diffraction on a laboratory instrument (L-XPD). After passing the activation voltage plateau during the first charge, the lattice parameters a and c as well as the unit cell volume V, from which c can be further divided into the layer heights h_{Li} and h_{TM}, resemble the quasi-reversible hysteresis of the OCV. Here, changes of a and h_{TM} are determined by the cationic redox of the transition metals, while h_{Li} and the overall shape of c are a measure of the anionic redox, O^{2-}/O^{n-} with $n < 2$. These assignments are derived from the literature about stoichiometric NCMs with δ being close to 0, and could be further verified by the comparison of three LMR-NCM with different extents of over-lithiation (ranging from $\delta = 0.14$ to 0.20) with a regular NCM-811. The hysteresis does not occur when LMR-NCMs are cycled in their pre-activated state before the first charge plateau at ≈4.5 V, but it can also be diminished afterwards by narrowing the effective SOC window, as was shown by window opening experiments. When correlated to the OCV instead of the SOC, the path dependence of the lattice parameters c remains for the activated LMR-NCMs, but gets really small for the lattice parameter a. On the other hand, the path dependence of the unit cell volume vanishes completely and gives a linear correlation with OCV with a slope of ca. $-2\ Å^3\ V^{-1}$, independent of the extent of over-lithiation. Therefore, the V-OCV relationship can be seen as universal property, which applies to all here investigated LMR-NCMs.

In the second part, we aimed at quantifying the amount of migrating transition metals (TMs) in the bulk by a joint Rietveld refinement approach of ex-situ L-XPD and neutron powder diffraction (NPD) data of the mid-lithium material. It is often believed in the literature that the reversible TM migration between their native TM layer, TM_{TM}, and the Li layer, TM_{Li}, causes the reversible hysteresis phenomena in LMR-NCMs, whereas the irreversible capture of TMs in the Li layer is attributed to the voltage fade during long-term cycling.[27,30] Due to limitations with regards to the measurement time and the large amount of sample that is required for NDP, we could only look at a few samples within the first two cycles and could hence not resolve an intra-cycle hysteresis loop of TM_{Li}. Furthermore, with the four samples of the second cycle, we could not observe any correlation of the refined Ni_{Li} amount to the electrochemical and lattice parameter data. Using a simplified rhombohedral model for which the amount of lithium in the TM layer, Li_{TM}, was constrained and that did not allow for oxygen vacancies (referred to as *model 2*), the maximum difference of Ni_{Li} was 2.4% (absolute) among the investigated samples. In view of all the assumptions and uncertainties associated with the Rietveld refinement of LMR-NCMs, it is in our opinion difficult and speculative to discuss even smaller differences within a subgroup of samples.

A huge variety of structural models is used in the literature, spanning from rhombohedral to monoclinic to composite models, from which we tested the first two under various assumptions. For none of them we observed the hoped-for correlation between voltage hysteresis and TM migration. The error of the refined Ni_{Li} values is estimated to be on the order of ±0.5%. Since the maximum difference between the four samples of the second cycle is less than 2% for any of the tested models (using the joint Rietveld refinement approach), we thus assume the reversible intra-cycle ΔN_{Li} to be smaller than 3%. Even though our DFT simulations did also not find any hint that TM migration causes the observed OCV hysteresis, it is actually not known in the literature how much migrated Ni_{Li} would be needed to explain the separation of the charge/discharge curves by hundreds of mV. If ⩽3% are indeed sufficient, Rietveld refinements are in our opinion not fully established yet to resolve TM migration in LMR-NCMs, but further in-depth work might bring us to the point.

Acknowledgments

We want to acknowledge BASF SE for the support through its Scientific Network on Electrochemistry and Batteries and the BMBF (Federal Ministry of Education and Research, Germany) for its financial support within the ExZellTUM II project (grant no. 03XP0081). We also thank the Heinz Maier-Leibnitz Zentrum (MLZ) for granting beamtime at FRM II (proposal no. 14350 and 14839). Beyond that, we wish to acknowledge the beamline scientist Nicola Casati (Material Science beamline MS-X04SA, Swiss Light Source) for his support during sample preparation, data collection, and data analysis of the ex-situ S-XPD data. Further gratitude is expressed to Franziska Friedrich and Rebecca Wilhelm for their help with the in-situ L-XPD measurements and during the NPD beamtime preparation, respectively.

ORCID

Benjamin Strehle https://orcid.org/0000-0001-8878-1160
Tanja Zünd https://orcid.org/0000-0002-1650-3636
Hubert A. Gasteiger https://orcid.org/0000-0001-8199-8703

References

1. D. Andre, S.-J. Kim, P. Lamp, S. F. Lux, F. Maglia, O. Paschos, and B. Stiaszny, *J. Mater. Chem. A*, **3**, 6709 (2015).
2. O. Gröger, H. A. Gasteiger, and J.-P. Suchsland, *J. Electrochem. Soc.*, **162**, A2605 (2015).
3. Y. Ding, Z. P. Cano, A. Yu, J. Lu, and Z. Chen, *Electrochem. Energy Rev.*, **2**, 1 (2019).
4. P. Liu, R. Ross, and A. Newman, *MRS Energy Sustain.*, **2**, E12 (2015).
5. USCAR (2020), USABC Goals for Advanced High-Performance Batteries for Electric Vehicle (EV) Applications, http//uscar.org/usabc.
6. J. Helbig, T. Beuse, V. Siozios, T. Placke, M. Winter, and R. Schmuch, *J. Electrochem. Soc.*, **167**, 060519 (2020).
7. N. Leifer, T. Penki, R. Nanda, J. Grinblat, S. Luski, D. Aurbach, and G. Goobes, *Phys. Chem. Chem. Phys.*, **22**, 9098 (2020).
8. R. Jung, M. Metzger, F. Maglia, C. Stinner, and H. A. Gasteiger, *J. Electrochem. Soc.*, **164**, A1361 (2017).
9. S.-K. Jung, H. Gwon, J. Hong, K.-Y. Park, D.-H. Seo, H. Kim, J. Hyun, W. Yang, and K. Kang, *Adv. Energy Mater.*, **4**, 1300787 (2014).
10. M. M. Thackeray, S.-H. Kang, C. S. Johnson, J. T. Vaughey, R. Benedek, and S. A. Hackney, *J. Mater. Chem.*, **17**, 3112 (2007).
11. P. Rozier and J. M. Tarascon, *J. Electrochem. Soc.*, **162**, A2490 (2015).
12. J. Hong, H. Gwon, S.-K. Jung, K. Ku, and K. Kang, *J. Electrochem. Soc.*, **162**, A2447 (2015).
13. T. Teufl, B. Strehle, P. Müller, H. A. Gasteiger, and M. A. Mendez, *J. Electrochem. Soc.*, **165**, A2718 (2018).
14. A. T. S. Freiberg, M. K. Roos, J. Wandt, R. de Vivie-Riedle, and H. A. Gasteiger, *J. Phys. Chem. A*, **122**, 8828 (2018).
15. T. Teufl, D. Pritzl, P. Krieg, B. Strehle, M. A. Mendez, and H. A. Gasteiger, *J. Electrochem. Soc.*, **167**, 110505 (2020).

16. D. Schreiner et al., *J. Electrochem. Soc.*, **168**, 030507 (2021).
17. T. Teufl, D. Pritzl, S. Solchenbach, H. A. Gasteiger, and M. A. Mendez, *J. Electrochem. Soc.*, **166**, A1275 (2019).
18. J. R. Croy, M. Balasubramanian, K. G. Gallagher, and A. K. Burrell, *Acc. Chem. Res.*, **48**, 2813 (2015).
19. L. Kraft, T. Zünd, D. Schreiner, R. Wilhelm, F. J. Günter, G. Reinhart, H. A. Gasteiger, and A. Jossen, *J. Electrochem. Soc.*, **168**, 020537 (2021).
20. S. Susanna, B. R. Dewangga, O. Wahyungoro, and A. I. Cahyadi, *2019 International Conference on Information and Communications Technology (ICOIACT)*, Piscataway, NJ (IEEE) p. 738 (2019).
21. L. Wang, D. Lu, Q. Liu, L. Liu, and X. Zhao, *Electrochim. Acta*, **296**, 1009 (2019).
22. Z. Lu, L. Y. Beaulieu, R. A. Donaberger, C. L. Thomas, and J. R. Dahn, *J. Electrochem. Soc.*, **149**, A778 (2002).
23. J. R. Croy, K. G. Gallagher, M. Balasubramanian, Z. Chen, Y. Ren, D. Kim, S.-H. Kang, D. W. Dees, and M. M. Thackeray, *J. Phys. Chem. C*, **117**, 6525 (2013).
24. G. Assat, D. Foix, C. Delacourt, A. Iadecola, R. Dedryvère, and J.-M. Tarascon, *Nat. Commun.*, **8**, 2219 (2017).
25. H. Konishi, T. Hirano, D. Takamatsu, A. Gunji, X. Feng, S. Furutsuki, T. Okumura, S. Terada, and K. Tamura, *J. Solid State Chem.*, **262**, 294 (2018).
26. H. Koga, L. Croguennec, M. Ménétrier, P. Mannessiez, F. Weill, C. Delmas, and S. Belin, *J. Phys. Chem. C*, **118**, 5700 (2014).
27. K. G. Gallagher, J. R. Croy, M. Balasubramanian, M. Bettge, D. P. Abraham, A. K. Burrell, and M. M. Thackeray, *Electrochem. Commun.*, **33**, 96 (2013).
28. F. Dogan, B. R. Long, J. R. Croy, K. G. Gallagher, H. Iddir, J. T. Russell, M. Balasubramanian, and B. Key, *J. Am. Chem. Soc.*, **137**, 2328 (2015).
29. D. Mohanty, J. Li, D. P. Abraham, A. Huq, E. A. Payzant, D. L. Wood, and C. Daniel, *Chem. Mater.*, **26**, 6272 (2014).
30. W. E. Gent et al., *Nat. Commun.*, **8**, 2091 (2017).
31. R. A. House, G. J. Rees, M. A. Pérez-Osorio, J.-J. Marie, E. Boivin, A. W. Robertson, A. Nag, M. Garcia-Fernandez, K.-J. Zhou, and P. G. Bruce, *Nat. Energy*, **5**, 777 (2020).
32. L. de Biasi, A. O. Kondrakov, H. Geßwein, T. Brezesinski, P. Hartmann, and J. Janek, *J. Phys. Chem. C*, **121**, 26163 (2017).
33. A. O. Kondrakov et al., *J. Phys. Chem. C*, **121**, 24381 (2017).
34. Z. W. Lebens-Higgins et al., *Mater. Horizons*, **6**, 2112 (2019).
35. L. Yin et al., *Chem. Mater.*, **32**, 1002 (2020).
36. K. Kleiner, B. Strehle, A. R. Baker, S. J. Day, C. C. Tang, I. Buchberger, F.-F. Chesneau, H. A. Gasteiger, and M. Piana, *Chem. Mater.*, **30**, 3656 (2018).
37. P. S. Whitfield, I. J. Davidson, L. M. D. Cranswick, I. P. Swainson, and P. W. Stephens, *Solid State Ionics*, **176**, 463 (2005).
38. P. S. Whitfield, I. J. Davidson, P. H. J. Mercier, Y. Le Page, L. D. Mitchell, P. W. Stephens, L. M. D. Cranswick, and I. P. Swainson, *Powder Diffr.*, **21**, 172 (2006).
39. H. Liu, H. Liu, S. H. Lapidus, Y. S. Meng, P. J. Chupas, and K. W. Chapman, *J. Electrochem. Soc.*, **164**, A1802 (2017).
40. P. M. Csernica et al., *Nat. Energy*, **6**, 642 (2021).
41. F. Friedrich, B. Strehle, A. T. S. Freiberg, K. Kleiner, S. J. Day, C. Erk, M. Piana, and H. A. Gasteiger, *J. Electrochem. Soc.*, **166**, A3760 (2019).
42. P. R. Willmott et al., *J. Synchrotron Radiat.*, **20**, 667 (2013).
43. M. Hoelzel, A. Senyshyn, N. Juenke, H. Boysen, W. Schmahl, and H. Fuess, *Nucl. Instruments Methods Phys. Res. Sect. A Accel. Spectrometers, Detect. Assoc. Equip.*, **667**, 32 (2012).
44. D. Mohanty, A. Huq, E. A. Payzant, A. S. Sefat, J. Li, D. P. Abraham, D. L. Wood, and C. Daniel, *Chem. Mater.*, **25**, 4064 (2013).
45. H. Yu et al., *J. Am. Chem. Soc.*, **140**, 15279 (2018).
46. M. Jiang, B. Key, Y. S. Meng, and C. P. Grey, *Chem. Mater.*, **21**, 2733 (2009).
47. 2011 WinXPOW V3.0.2.1, STOE & Cie GmbH, Darmstadt, Germany.
48. 2016 TOPAS-Academic V6, Coelho Software, Brisbane, Australia.
49. Z. Lu and J. R. Dahn, *J. Electrochem. Soc.*, **149**, A815 (2002).
50. D. Mohanty, S. Kalnaus, R. A. Meisner, K. J. Rhodes, J. Li, E. A. Payzant, D. L. Wood, and C. Daniel, *J. Power Sources*, **229**, 239 (2013).
51. G. Kresse and J. Hafner, *Phys. Rev. B*, **47**, 558 (1993).
52. G. Kresse and J. Hafner, *Phys. Rev. B*, **49**, 14251 (1994).
53. G. Kresse and J. Furthmüller, *Comput. Mater. Sci.*, **6**, 15 (1996).
54. G. Kresse and J. Furthmüller, *Phys. Rev. B*, **54**, 11169 (1996).
55. P. E. Blöchl, *Phys. Rev. B*, **50**, 17953 (1994).
56. G. Kresse and D. Joubert, *Phys. Rev. B*, **59**, 1758 (1999).
57. H. Peng, Z.-H. Yang, J. P. Perdew, and J. Sun, *Phys. Rev. X*, **6**, 041005 (2016).
58. K. Okhotnikov, T. Charpentier, and S. Cadars, *J. Cheminform.*, **8**, 17 (2016).
59. B. Strehle, K. Kleiner, R. Jung, F. Chesneau, M. Mendez, H. A. Gasteiger, and M. Piana, *J. Electrochem. Soc.*, **164**, A400 (2017).
60. X. Zhang, A. Mauger, Q. Lu, H. Groult, L. Perrigaud, F. Gendron, and C. M. Julien, *Electrochim. Acta*, **55**, 6440 (2010).
61. K. Luo et al., *Nat. Chem.*, **8**, 684 (2016).
62. G. Assat, A. Iadecola, D. Foix, R. Dedryvère, and J.-M. Tarascon, *ACS Energy Lett.*, **3**, 2721 (2018).
63. A. O. Kondrakov, A. Schmidt, J. Xu, H. Geßwein, R. Mönig, P. Hartmann, H. Sommer, T. Brezesinski, and J. Janek, *J. Phys. Chem. C*, **121**, 3286 (2017).
64. D.-H. Seo, J. Lee, A. Urban, R. Malik, S. Kang, and G. Ceder, *Nat. Chem.*, **8**, 692 (2016).
65. D.-H. Seo, A. Urban, and G. Ceder, *Phys. Rev. B*, **92**, 115118 (2015).
66. H. Liu, Y. Chen, S. Hy, K. An, S. Venkatachalam, D. Qian, M. Zhang, and Y. S. Meng, *Adv. Energy Mater.*, **6**, 1502143 (2016).
67. H.-H. Ryu, K.-J. Park, C. S. Yoon, and Y.-K. Sun, *Chem. Mater.*, **30**, 1155 (2018).
68. P. Yan, J. Zheng, M. Gu, J. Xiao, J.-G. Zhang, and C.-M. Wang, *Nat. Commun.*, **8**, 14101 (2017).
69. S. Oswald, D. Pritzl, M. Wetjen, and H. A. Gasteiger, *J. Electrochem. Soc.*, **167**, 100511 (2020).
70. H. Li, A. Liu, N. Zhang, Y. Wang, S. Yin, H. Wu, and J. R. Dahn, *Chem. Mater.*, **31**, 7574 (2019).
71. H. Komatsu et al., *J. Phys. Chem. C*, **122**, 20099 (2018).
72. R. A. House et al., *Nature*, **577**, 502 (2020).
73. G. Assat, S. L. Glazier, C. Delacourt, and J.-M. Tarascon, *Nat. Energy*, **4**, 647 (2019).
74. N. Yabuuchi, K. Yoshii, S.-T. Myung, I. Nakai, and S. Komaba, *J. Am. Chem. Soc.*, **133**, 4404 (2011).
75. C. R. Fell, D. Qian, K. J. Carroll, M. Chi, J. L. Jones, and Y. S. Meng, *Chem. Mater.*, **25**, 1621 (2013).
76. N. Ishida, N. Tamura, N. Kitamura, and Y. Idemoto, *J. Power Sources*, **319**, 255 (2016).
77. C. Genevois, H. Koga, L. Croguennec, M. Ménétrier, C. Delmas, and F. Weill, *J. Phys. Chem. C*, **119**, 75 (2015).
78. A. Boulineau, L. Simonin, J.-F. Colin, C. Bourbon, and S. Patoux, *Nano Lett.*, **13**, 3857 (2013).
79. P. Yan et al., *Nano Lett.*, **15**, 514 (2015).
80. I. Takahashi et al., *J. Phys. Chem. C*, **120**, 27109 (2016).
81. P. Yan et al., *Chem. Mater.*, **27**, 5393 (2015).
82. J. Ma, S.-H. Bo, L. Wu, Y. Zhu, C. P. Grey, and P. G. Khalifah, *Chem. Mater.*, **27**, 2387 (2015).
83. C.-J. Chen et al., *J. Am. Chem. Soc.*, **138**, 8824 (2016).
84. H. Liu et al., *J. Mater. Chem. A*, **6**, 4189 (2018).
85. J. M. Joubert, R. Cerný, M. Latroche, A. Percheron-Guégan, and K. Yvon, *J. Appl. Crystallogr.*, **31**, 327 (1998).
86. H. Koga, L. Croguennec, P. Mannessiez, M. Ménétrier, F. Weill, L. Bourgeois, M. Duttine, E. Suard, and C. Delmas, *J. Phys. Chem. C*, **116**, 13497 (2012).
87. J. Liu, L. Yin, L. Wu, J. Bai, S.-M. Bak, X. Yu, Y. Zhu, X.-Q. Yang, and P. G. Khalifah, *Inorg. Chem.*, **55**, 8478 (2016).
88. T. Ohzuku, *J. Electrochem. Soc.*, **140**, 1862 (1993).
89. L. Yin et al., *Rev. Sci. Instrum.*, **89**, 093002 (2018).
90. G. Liang, C. Didier, Z. Guo, W. K. Pang, and V. K. Peterson, *Adv. Mater.*, **1904528**, 1 (2019).
91. P. Yan, J. Zheng, Z.-K. Tang, A. Devaraj, G. Chen, K. Amine, J.-G. Zhang, L.-M. Liu, and C. Wang, *Nat. Nanotechnol.*, **14**, 602 (2019).
92. S. Ahmed et al., *ACS Nano*, **13**, 10694 (2019).
93. J. Bréger, M. Jiang, N. Dupré, Y. S. Meng, Y. Shao-Horn, G. Ceder, and C. P. Grey, *J. Solid State Chem.*, **178**, 2575 (2005).
94. W.-C. Chen, Y.-F. Song, C.-C. Wang, Y. Liu, D. T. Morris, P. A. Pianetta, J. C. Andrews, H.-C. Wu, and N.-L. Wu, *J. Mater. Chem. A*, **1**, 10847 (2013).

Supporting Information

Correlating the Voltage Hysteresis in Li- and Mn-Rich Layered Oxides to Reversible Structural Changes by Using X-Ray and Neutron Powder Diffraction

Benjamin Strehle,[1,=,*] Tanja Zünd,[1,=,*,z] Sabrina Sicolo,[2] Aleksandr Kiessling,[1] Volodymyr Baran,[3] and Hubert A. Gasteiger[1,**]

[1] *Chair of Technical Electrochemistry, Department of Chemistry and Catalysis Research Center, Technical University of Munich, D-85748 Garching, Germany*

[2] *BASF SE, Quantum Chemistry for Solid State Group, D-67056 Ludwigshafen, Germany*

[3] *Heinz Maier-Leibnitz Zentrum, Technical University of Munich, D-85748 Garching, Germany*

[=]These authors contributed equally to this work.

*Electrochemical Society Student Member.

**Electrochemical Society Fellow.

[z]E-mail: tanja.zuend@tum.de

Table of Contents

S1: In-Situ L-XPD Pouch Cell Setup and Data Analysis

Figure S1 shows the pouch cell setup for the in-situ L-XPD measurements. The alignment of the pouch cell along the direction of the X-ray beam works with the micrometer screw of the holder. In the pristine state, the pouch cell is moved according to the (003) reflection of the CAM phase, until its position matches by eye the (003) reflection of an ex-situ capillary, which was loaded with the pristine CAM powder and measured right before the pouch cell.

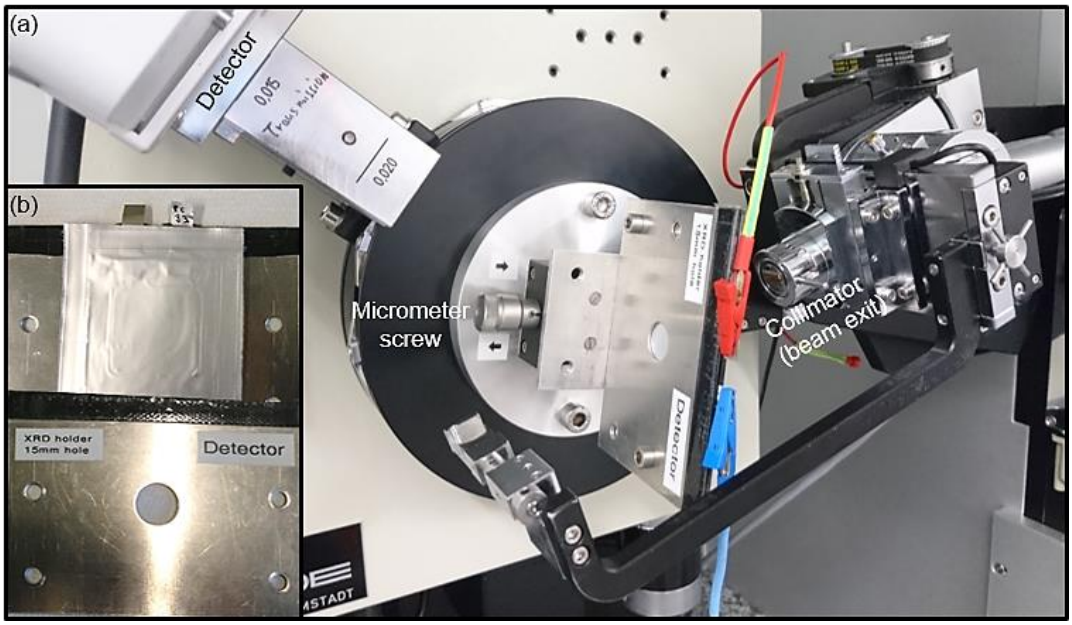

Figure S1. Setup for the in-situ L-XPD measurements, highlighting (a) the connection of the pouch cell to the diffractometer and the potentiostat (red and blue crocodile clips) and (b) the two metal plates used for fixation.

Figure S2 shows a contour plot of the in-situ L-XPD patterns, which were used to calculate the "Cycle 1-3" lattice parameters in **Figure 1** of the main text. Despite the rather low intensity and the presence of several Al reflections from the current collector and pouch foil (see vertical lines corresponding to the Al(111), Al(200), and Al(220) reflections at 2Theta values of ≈17.5°, ≈20.2°, and ≈28.7°, respectively), the strongest CAM reflections are clearly visible and they can be monitored during battery operation (see *hkl* assignment of the CAM phase and Al side phases above the plot). The evolution of the lattice parameters can be best read from the (003) and (110) reflections, which represent solely the lattice parameter *c* and *a*, respectively. When the peak moves to the left to lower 2Theta angles, the corresponding lattice parameter increases and vice versa. **Figure S3** shows exemplary Pawley fits of "pattern 1" for the pristine (discharged) mid-lithium LMR-NCM and of "pattern 14" for the completely charged material at the end of the first cycle (at 4.8 V). The two polymer peaks from the pouch foil at ≈10° and ≈11° 2Theta overlap the superstructure peaks of the CAM. Since these peaks were not included into the refinement and since we only used four Chebyshev background parameters, the R_{wp} values are relatively high, but the accuracy of the lattice parameters is not affected (as indicated by the low R_{bragg} values). In summary, in-situ L-XPD is a facile tool to study the evolution of lattice parameters from battery materials. If it however comes to the analysis of structural parameters by Rietveld refinement, ex-situ data from powder samples are the preferred choice due to better counting statistics, larger *Q* ranges, and less side phases.

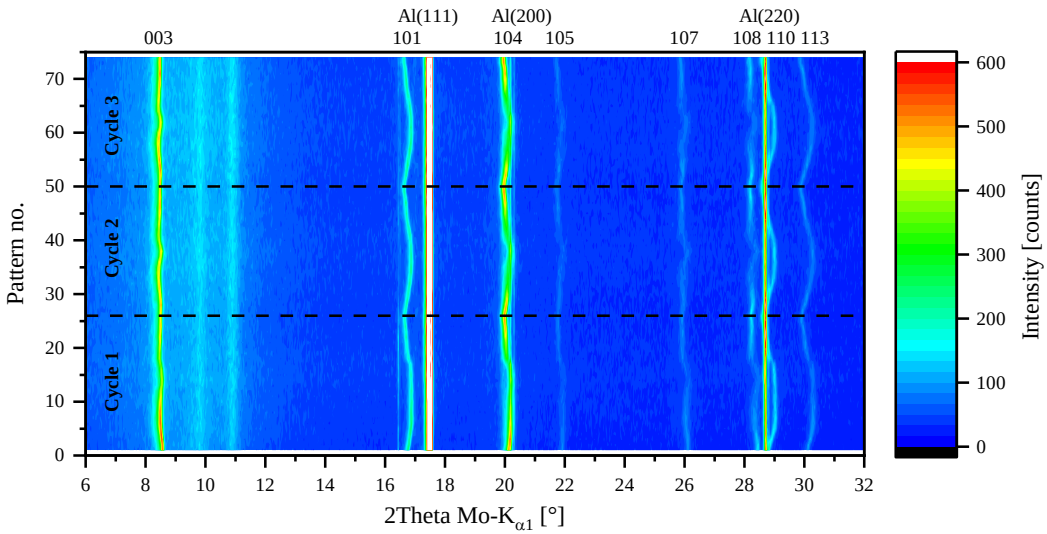

Figure S2. Contour plot of the in-situ L-XPD patterns collected from the mid-lithium LMR-NCM material (δ = 0.17 in Li[Li$_\delta$TM$_{1-\delta}$]O$_2$) within the first three battery cycles. The 2Theta range is limited to 6-32°. The strongest *hkl* reflections of the CAM and of the Al phases are marked above the plot. The lattice parameters from the sequential refinement are presented in **Figure 1** of the main text.

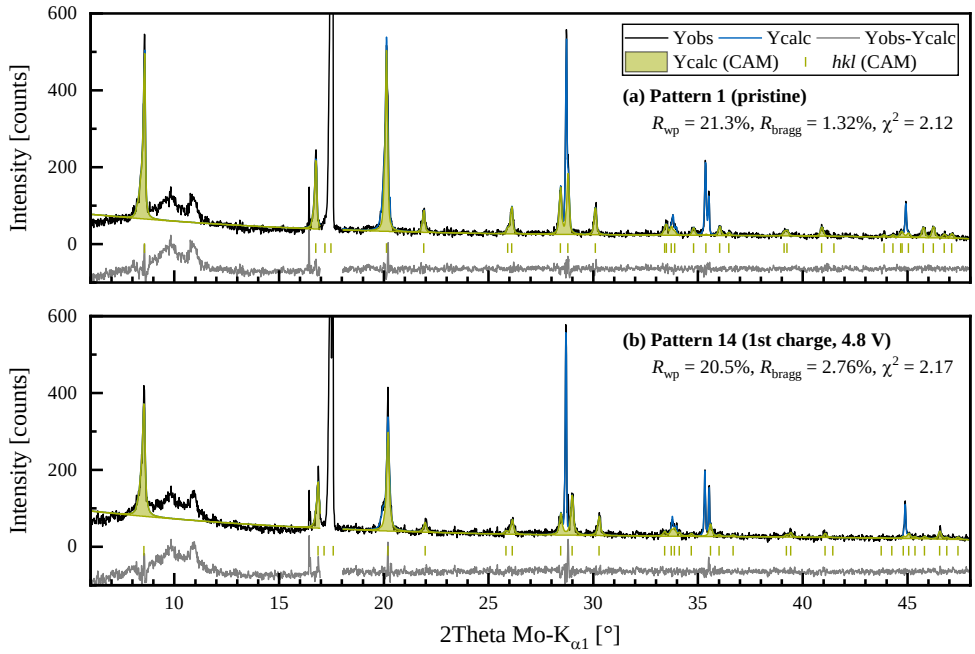

Figure S3. Exemplary Pawley refinements of two in-situ L-XPD patterns in **Figure S2**: (a) pattern 1 of the pristine CAM in the pouch cell and (b) pattern 14 in the completely charged state at the end of the first half-cycle to 4.8 V. The calculated intensity of the CAM phase is highlighted by the green area. The 2Theta region of 17-18° is omitted from the refinement due to the strong Al(111) reflections from the current collector and the pouch foil.

Due to the discontinuity of the lattice parameters of the mid-lithium material at the beginning of the first discharge that was observed in **Figure 1** of the main text, we compare this experimental dataset of "cell #1" with another dataset obtained from a different cell (referred to as "cell #2") in **Figure S4**. Apart from a slightly different alignment of the pouch cells prior to the in-situ experiments (as also compared to an ex-situ measurement of the pristine CAM powder) and the three anomalous data points from "cell #1" at the beginning of the discharge (black symbols in the gray highlighted area), both datasets agree pretty well in a qualitative and quantitative manner. We think that the deviating data points originate from O_2 and CO_2 gassing induced by the CAM at the end of the activation charge (at 4.8 V),[1] which continues during the OCV hold for XPD data collection and thereby disturbs the cell alignment in the diffractometer. As the evolved gases seem then to be re-distributed in the pouch cell, both curves coincide again in the second part of the discharge. We discuss exclusively the data obtained from "cell #1" in the main text, because cycling of "cell #2" was not continued for a second and third cycle.

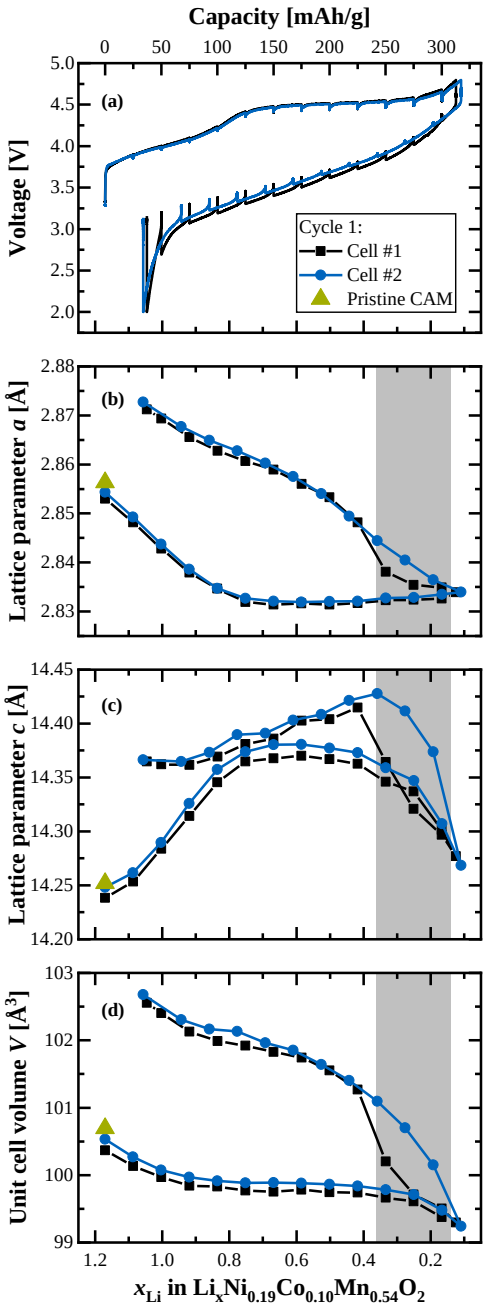

Figure S4. Comparison of two nominally identical in-situ L-XPD measurements of the first cycle of the mid-lithium material (δ = 0.17), where "cell #1" represents the same dataset that was shown in **Figure 1** of the main text. Here, the first three lattice parameter values of the discharge are shifted likely due to an artefact caused by gassing at the end of the first charge. This artefact is absent in the repeat experiment with "cell #2" (as higlighted by the gray bars). Additionally, the lattice parameters of the pristine CAM powder are shown from an ex-situ L-XPD measurement in a capillary.

S2: Additional In-Situ L-XPD Lattice Parameter Results

Figure S5 shows the results from two independent window opening experiments with the mid-lithium LMR-NCM, where either the charge or discharge window are gradually opened from 2.0 to 4.8 V or in the reverse direction from ≈4.7 V to 2.0 V, respectively. The charge window opening dataset is the same as that presented in **Figure 2** of the main text. We see that the enclosed area of the hysteresis loops largely depends on the cut-off voltages and thus on the accessed Δx_{Li} windows. It shows that the hysteresis gets just fully developed when the CAM runs through the last third of the charge (at potentials greater than 4.1 V, $x_{Li} < 0.48$) and it only forms completely back in the last third of the discharge (at potentials smaller than 3.3 V, $x_{Li} > 0.66$). This applies to both the open circuit voltage and the unit cell volume (which is calculated according to $V = \sqrt{3}/2 \cdot a^2 \cdot c$ from the individual lattice parameters).

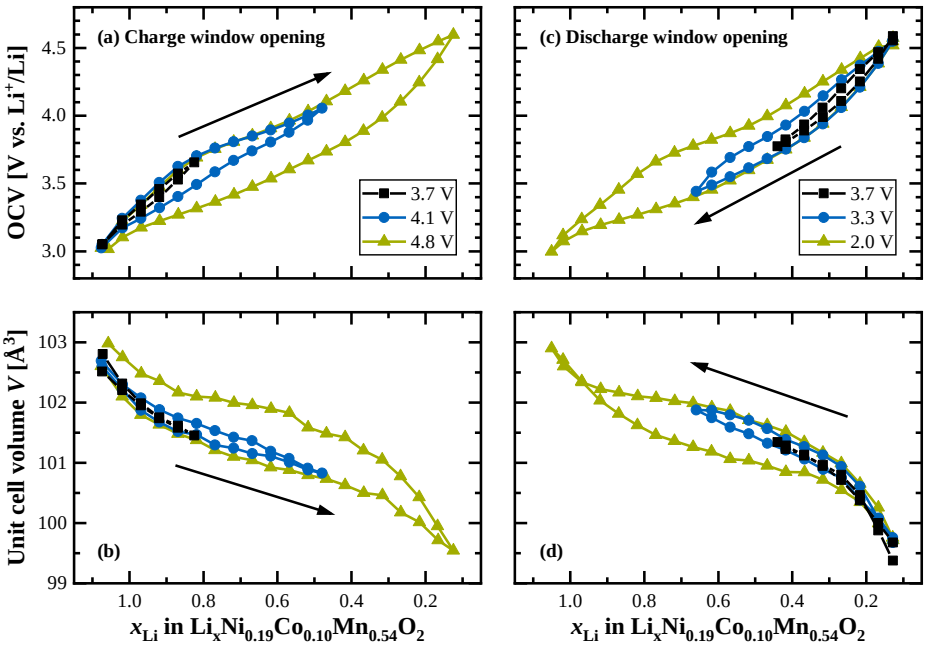

Figure S5. Window opening experiments at C/10 with the fully activated mid-lithium LMR-NCM material after two complete cycles between 2.0-4.8 V. (a,b) Charge window opening, where the upper cut-off voltage is stepwise increased from 3.7 to 4.1 to 4.8 V (lower cut-off voltage fixed to 2.0 V, what is also the starting point. (c,d) Discharge window opening, where the lower cut-off voltage is stepwise decreased from 3.7 to 3.3 to 2.0 V (upper SOC limit of 312 mAh g^{-1}, corresponding to ≈4.7 V). As a function of the lithium content, the panels (a,c) show the open circuit voltage, at which the diffractograms were measured every 15 mAh g^{-1}, and the panels (b,d) depict the unit cell volume from the corresponding Pawley fits.

Figure S6 gives a detailed view of the lattice parameter changes of the three tested LMR-NCMs with different degrees of over-lithiation within the second cycle as a function of their open circuit voltage. The additional comparison with the stoichiometric NCM-811 is shown in **Figure 4** of the main text.

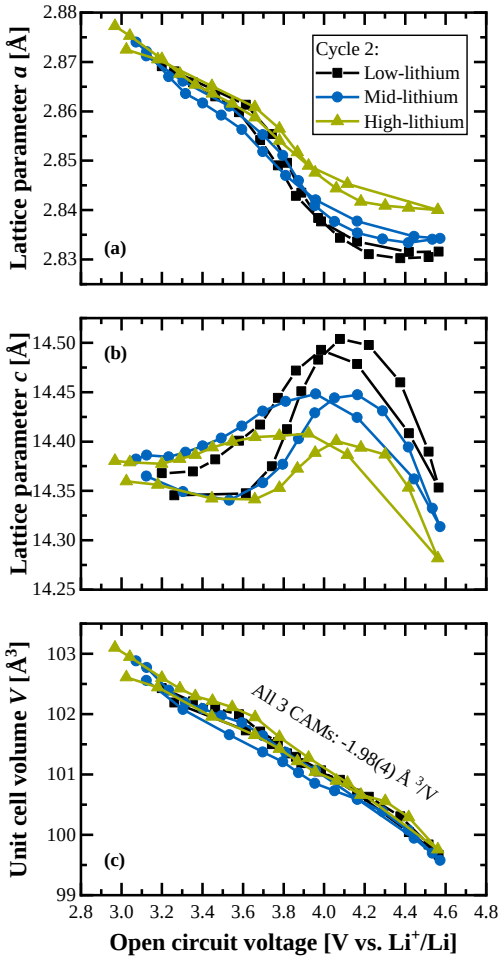

Figure S6. Same representation of the lattice parameters vs. OCV during the second cycle as in **Figure 4** of the main text, but showing only the three over-lithiated CAMs to better resolve the small changes among them. In panel (c), the linear regression results in V = 108.9(1) Å^3 – 1.98(4) Å^3/V · OCV, with R^2 = 0.977.

S3: Ex-Situ Diffraction and Rietveld Refinement Results

The following list gives an overview of the non-structural refinement parameters for the different types of ex-situ diffraction data:

- Background: Chebyshev polynomial with 10 (L-XPD and NPD) or 15 parameters (S-XPD).
- Instrument: Zero shift (all) and axial divergence asymmetry (L-XPD).
- Absorption: Cylindrical absorption correction. The volume fraction of the cycled and harvested LMR-NCM electrode powder in the vanadium cans used for the neutron experiments amounts to ≈34% (≈43% for the pristine sample, which was loaded as pure CAM powder), whereas we estimate it to be ≈25% in the X-ray capillaries. Neglecting other components (such as electrode conductive additives, binder, and electrolyte residuals), the absorption is reasonably low, since the μR values amount to ≤0.20 for the cycled NPD samples, ≈0.54 for the pristine NPD sample, and ≈0.34 for the XPD samples, respectively.

The LMR-NCM was refined either in the rhombohedral or monoclinic model. We could not identify any crystalline side phase in the X-ray and neutron diffractograms. As the samples cover a broad SOC range and as the charge compensation involves both the transition metals and oxygen, we decided to use the X-ray form factors of neutral atoms, which always ensure charge neutrality. Furthermore, we only consider octahedral sites for all of the metals, because the occupation of tetrahedral sites in the lithium layer did not improve the fits significantly, but unnecessarily increases the number of refinement parameters. **Table SI** summarizes all sample- and structure-related refinement parameters.

Table SI. General overview about the handling of sample broadening, lattice parameters and structural refinement parameters for both applied base models used for fitting the diffraction data.

Parameter	**Rhombohedral model (*R*-3*m*)**	**Monoclinic model (*C*2/*m*)**
Sample broadening	- Isotropic contribution from crystallite size - Anisotropic contribution from microstrain with Stephens model[2] (anisotropic strain parameters only used when e.s.d. less than ≈10% of actual value)	
	Hexagonal Stephens model: - up to 5 parameters - mixing parameter, S_{400}, S_{004}, and S_{202} used	Monoclinic Stephens model: - up to 10 parameters - mixing parameter, typically S_{004}, S_{220}, S_{202}, and S_{022} used
Lattice parameters	*a*, *c*	*a*, *b*, *c*, *β*
Fractional coordinates	*z*-coordinate of oxygen ($z_{6c,O}$)	7 parameters: - $y_{4g,Li}$, $y_{4h,TM}$, $x_{4i,O}$, $z_{4i,O}$, $x_{8j,O}$, $y_{8j,O}$, and $z_{8j,O}$ - $z_{4i,O}$ and $z_{8j,O}$ constrained to be identical due to high correlation
Atomic displacement parameters	- Isotropic and layer-specific (3 parameters for Li, TM, and O layer) - Lower limit set to 0 (i.e., only positive values accepted)	
Site occupancy factors	- Sum of lithium fixed to SOC - Sum of transition metals fixed to elemental analysis of pristine sample - Total occupancy of each site constrained between 0 and 1 - Distribution explained in the main text	

Figure S7 shows the Rietveld refinement fits of the pristine mid-lithium LMR-NCM based on the monoclinic *model 3*, $[Li_{x-u}Ni_v]_{2c,4h}[Li_{3u}Ni_oMn_p]_{2b}[Ni_{0.285-o/2-3v/2}Co_{0.15}Mn_{0.81-p/2}]_{4g}[O_w]_{4i,8j}$ with $u_{Li} \geq 0$ and $w_O = 1$ (see main text for more information). This model describes the superstructure peaks indicated by the vertical arrows in the figure. Please note that the first set of superstructure peaks in the L-XPD pattern ($1.4 < Q < 2.3$ Å^{-1}) was intentionally excluded from this monoclinic refinement (also for the cycled and harvested samples), but the green line shows the calculated peaks according to the model's prediction in this region. In general, the description of all of the superstructure peaks is poor compared to that of the main peaks, because the model does not include any extra broadening due to the presence of stacking faults.

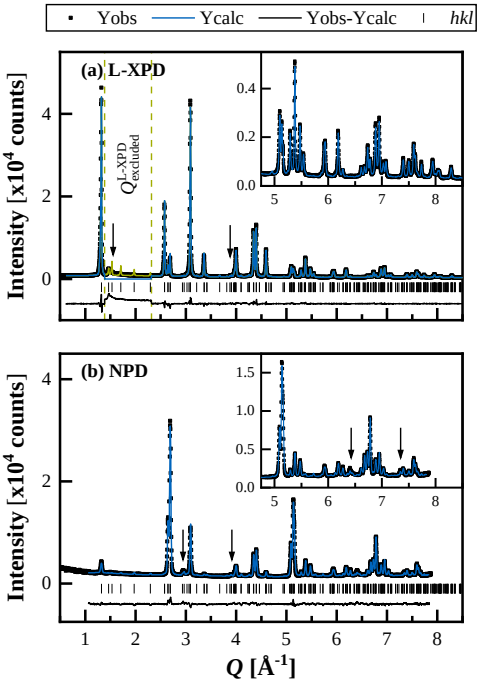

Figure S7. Joint Rietveld refinement of the pristine mid-lithium LMR-NCM with the monoclinic *model 3*. The arrows indicate the superstructure peaks due to in-plane Li/TM ordering in the TM layer; however, the Q range of $1.4 < Q < 2.3$ Å^{-1} was excluded from the fit of the L-XPD pattern (the green line shows the calculated peaks according to this model).

Figure S8 compares the co-refinement results of the generalized rhombohedral *model 2*, $[Li_{x-u}X_v]_{3a}[Li_uTM_{0.83-v}]_{3b}[O_w]_{6c}$ with $u_{Li} \geq 0$ and $w_O = 1$, where the migrating TM species, X, is either Ni or Mn. To enable the unbiased refinement of Mn_{Li}, Li_{TM} has to be fixed to the results of the Ni_{Li} refinement for all cycled samples. The variation of Ni_{Li} and Mn_{Li} ranges between 0% and 1.5% (absolute) for a given sample.

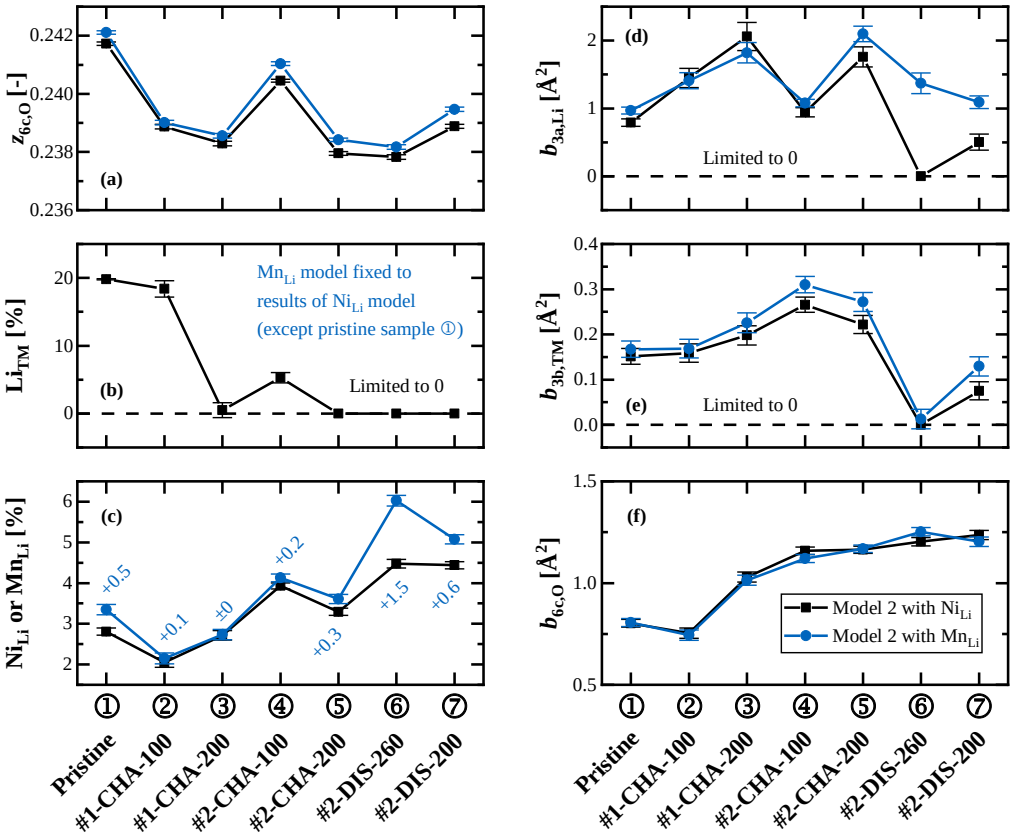

Figure S8. Variation of the migrating TM species, Ni_{Li} or Mn_{Li}, for the mid-lithium LMR-NCM samples (see **Figure 6** of the main text) in the generalized rhombohedral *model 2*, $[Li_{x-u}X_v]_{3a}[Li_uTM_{0.83-v}]_{3b}[O_w]_{6c}$ with X being either Ni or Mn ($u_{Li} \geq 0$ and $w_O = 1$). The six panels compare the structural parameters, which are the *z*-coordinate of oxygen (a), the site occupancy factors u_{Li}/Li_{TM} and v_X/X_{Li} (b,c), and the three atomic displacement parameters (d-f). Since Li_{TM} and Mn_{Li} cannot be refined simultaneously, Li_{TM} is constrained to its value from the Ni_{Li} refinement (except for the pristine sample, where $u_{Li} = 0.17 + v_X$). The numbers in panel (c) give the absolute deviation of Mn_{Li} relative to Ni_{Li} for each sample.

Figure S9 compares the co-refinement results of the rhombohedral *model 2*, $[Li_{x-u}Ni_v]_{3a}[Li_uTM_{0.83-v}]_{3b}[O_w]_{6c}$ with $u_{Li} \geq 0$ and $w_O = 1$, to Rietveld fits which were applied to each diffractogram individually. Combining the data of **Figure 5** and **Figure 9** in the main text, there are two independent datasets which comprises ex-situ L-XPD, S-XPD, and NPD data, respectively. Please note that the second cycle samples ④-⑦ appear in both datasets, providing two L-XPD data points from two separate cells. This comparison gives an impression about the accuracy of the derived structural parameters and about their dependence on different diffraction data types. The results are from panel (a) to (f) as follows:

(a) The *z*-coordinate of oxygen, $z_{6c,O}$, is barely influenced by the type of diffraction data and thus the most accurate structural parameter. Only for the high-SOC sample ⑥, where all parameters scatter strongly, there is a notable difference between the XPD and NPD data. The latter dominates the co-refinement result of sample ⑥.

(b) Since u_{Li}/Li_{TM} and v_{Ni}/Ni_{Li} cannot be refined simultaneously using only one diffractogram, the Li amount in the TM layer, Li_{TM}, was fixed to the co-refinement results for the cycled and harvested samples ②-⑦. For the pristine sample ①, u_{Li} and v_{Ni} are instead correlated with each other due to full occupation ($u_{Li} = 0.17 + v_{Ni}$).

(c) The increasing level of migrating Ni into the Li layer, Ni_{Li}, as determined from the joint refinement of L-XPD & NPD data, is also present in most of the individual Rietveld fits. There is an exception from this trend for the high-SOC samples ⑥ and ⑦ in the case of the NPD-only refinement. Even if neglecting these two Ni_{Li} values, the scatter among the different types of diffraction data is on the order of 0.2-1.6% and thus unfavorably high with respect to the changes we aim at resolving due to battery cycling. The co-refinement results are not consistently dominated by either L-XPD or NPD, but L-XPD and S-XPD agree reasonably in most cases.

(d) The atomic displacement parameter of the Li layer, $b_{3a,Li}$, has the highest uncertainty among the investigated structural parameters, which is why it is often fixed in the literature (e.g., to 1 Å^2).[3,4] In the study by Yin et al., S-XPD and TOF-NPD data of twelve pristine stoichiometric NCMs gave $b_{3a,Li}$ values in the range of 0.4-1.3 Å^2 (average of ≈0.9 Å^2 from global fits).[5] In our work, this range is best met by the S-XPD and NPD data, while L-XPD is not reliable.

(e) The atomic displacement parameter of the TM layer, $b_{3b,TM}$, can only be determined from XPD data. As the TM layer barely contributes to the scattering power of the compound in the NPD pattern (≈1%, see **Table 2** in the main text), its $b_{3b,TM}$ values were completely off, often negative, and had to be intentionally fixed to the co-refinement results. The latter are thus dictated by the L-XPD counterpart. Yin et al. measured $b_{3b,TM}$ to be mainly in the range of 0.22-0.33 Å^2 (average of ≈0.28 and ≈0.30 Å^2 from global fits),[5] which was confirmed for NCA by Liu at al. (using anisotropic *b* values, $b^{11}_{3b,TM}$ and $b^{33}_{3b,TM}$) and which is nicely satisfied by the S-XPD data in our work. There is some evidence in the literature that the $b^{33}_{3b,TM}$ component from an anisotropic

treatment might rise until ≈1.5 Å^2 upon charging (due to a static displacement of transition metals along the *c* direction).[3,6]

(f) The atomic displacement parameter of the O layer, $b_{6c,O}$, is the most reliable ADP, because it can be quantified within a deviation of ≈0.5 Å^2 from every type of diffraction data. This is why $b_{6c,O}$ is often refined anisotropically in the literature, where in the work by Yin et al. $b^{11}_{6c,O}$ is greater than $b^{33}_{6c,O}$, ranging between ≈0.7-0.9 Å^2 and ≈0.5-0.7 Å^2, respectively.[5] In the co-refinement, the NPD pattern dominates the $b_{6c,O}$ values, probably due to the ≈85% share of the O layer to the scattering power (vs. ≈39% in the XPD pattern, see **Table 2** in the main text).

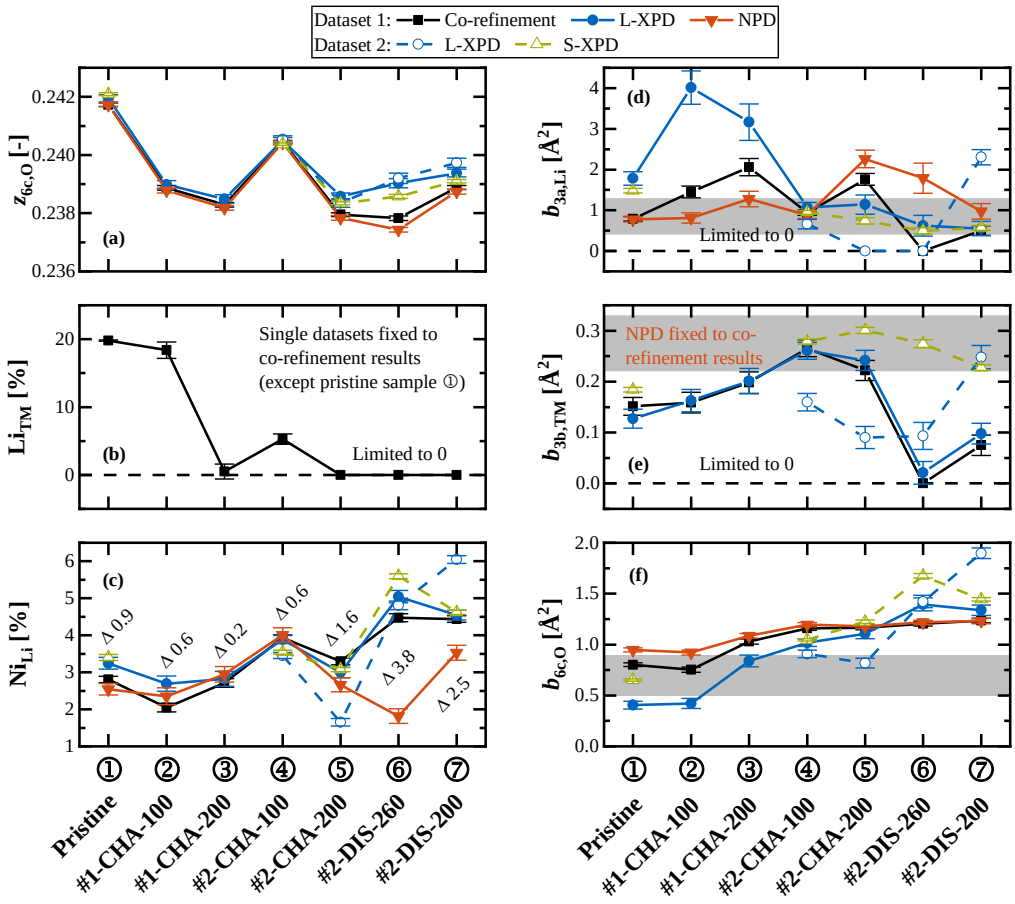

Figure S9. Comparison of the co-refinement results in the rhombohedral *model 2*, $[Li_{x-u}Ni_v]_{3a}[Li_uTM_{0.83-v}]_{3b}[O_w]_{6c}$ ($u_{Li} \geq 0$, $w_O = 1$), to all available individual datasets using the same model. Merging the data presented in **Figure 5** and **Figure 9** of the main text, this comparison includes ex-situ L-XPD, S-XPD, and NPD data, respectively. Here, the cycled samples of "dataset 1" were prepared in multi-layer pouch cells, while "dataset 2" was simply obtained from coin cells. Since only one site occupancy factor can be refined using one diffractogram, Li_{TM} is fixed to its co-refinement results for the single fits (except for the pristine sample, where $u_{Li} = 0.17 + v_{Ni}$). In the NPD-only refinement, $b_{3b,TM}$ has also to be constrained to its co-refinement results. The numbers in panel (c) give the absolute range of Ni_{Li} among all available datasets. The gray bars in the panels (d-f) indicate the main ADP ranges reported by Yin et al. for twelve pristine stoichiometric NCMs.[5] The ADP values were extracted from independent S-XPD and TOF-NPD refinements using also X-ray form factors of neutral atoms and a single defect model of paired anti-site Ni_{Li}/Li_{TM} (see Table S4 in their Supporting Information).

Figure S10 shows the influence of the X-ray atomic form factors (atoms vs. ions) and of the *Q* range of the L-XPD pattern (full vs. limited *Q* range) on the co-refinement results of the rhombohedral *model 2*, $[Li_{x-u}Ni_v]_{3a}[Li_uTM_{0.83-v}]_{3b}[O_w]_{6c}$ with $u_{Li} \geq 0$ and $w_O = 1$. Beyond the comparison of the Ni_{Li} values, it is an interesting observation that Li_{TM} is slightly above the lower limit of 0% for the samples ⑤ and ⑦ when refining ions with full $Q^{L\text{-}XPD}$, whereas the other two refinements would give negative values without constraining them (sample ⑥ has negative Li_{TM} values for any of the tested models). On the other hand, the atoms & limited $Q^{L\text{-}XPD}$ refinement stabilizes the $b_{3b,TM}$ values in the plausible range of 0.17-0.31 Å^2. This might be due to the fact that the transition metals experience the biggest change of their oxidation state upon cycling (possible variation between 2+ and 4+) and excluding low-*Q* values cancels this variation effectively out.

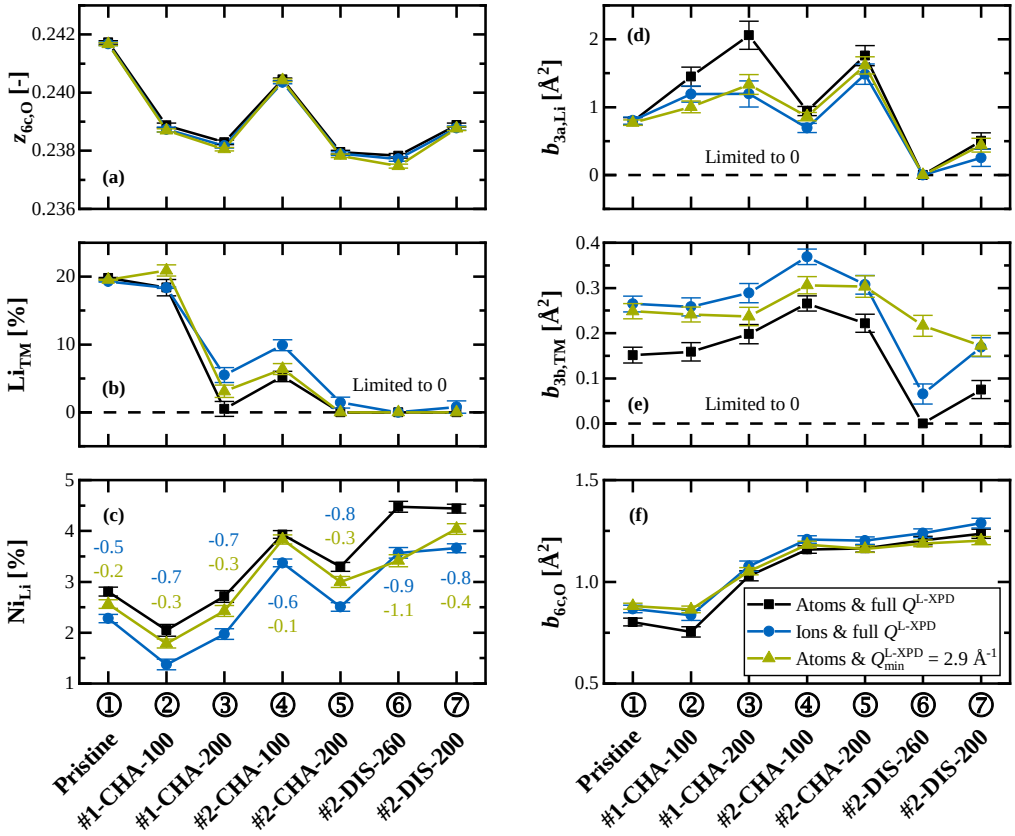

Figure S10. Dependence of the co-refinement results with the rhombohedral *model 2*, $[Li_{x-u}Ni_v]_{3a}[Li_uTM_{0.83-v}]_{3b}[O_w]_{6c}$ ($u_{Li} \geq 0$, $w_O = 1$), on the choice of X-ray form factors (neutral atoms vs. ions, viz., Li^+, Ni^{2+}, Co^{3+}, Mn^{4+}, and O^{2-}) and on the analyzed *Q* range of the L-XPD pattern (full vs. limited range with $Q^{L\text{-}XPD}_{min}$ = 2.9 Å^{-1}). The standard approach in this work uses atoms and the full *Q* range (black data points). The numbers in panel (c) give the absolute deviation of Ni_{Li} relative to the standard approach.

The following **Tables SII-SIV** summarize the co-refinement results of the three structural models presented in **Figure 9** of the main text. From top to bottom, the tables show the quality factors, lattice parameters, fractional coordinate(s), atomic displacement parameters, and site occupancy factors. Errors are given in parentheses following the recommendations by Schwarzenbach et al.[7] Parameters provided with "=" are not independently refined, but fixed due to constraints. The overall lithium content, x_{Li}, is calculated according to the SOC of each sample.

Table SII. Results of the joint L-XPD and NPD Rietveld refinement according to the rhombohedral *model 1*, $[Li_{x-u}Ni_v]_{3a}[Li_uTM_{0.83-v}]_{3b}[O_w]_{6c}$ without any constraints for the site occupancy factors u_{Li}, v_{Ni}, and w_O (except for the pristine sample, where $u_{Li} = 0.17 + v_{Ni}$).

Sample	①	②	③	④	⑤	⑥	⑦
	Pristine	#1-CHA-100	#1-CHA-200	#2-CHA-100	#2-CHA-200	#2-DIS-260	#2-DIS-200
Overall:							
R_{wp} [%]	7.95	4.46	3.68	2.83	2.52	2.62	2.59
χ^2 [-]	9.22	5.16	3.57	2.93	2.41	2.77	2.68
L-XPD:							
R_{wp} [%]	9.19	7.71	6.90	5.50	5.14	5.69	5.35
R_{bragg} [%]	1.90	1.65	2.21	1.13	2.42	3.18	2.56
χ^2 [-]	9.74	5.61	4.36	2.71	2.17	2.90	2.57
NPD:							
R_{wp} [%]	6.72	2.18	2.10	2.02	1.82	1.69	1.79
R_{bragg} [%]	2.10	0.962	1.10	1.08	0.878	0.747	0.943
χ^2 [-]	8.53	3.76	2.34	3.30	2.81	2.56	2.86
a [Å]	2.85629(5)	2.85629(5)	2.85629(5)	2.85629(5)	2.85629(5)	2.85629(5)	2.85629(5)
c [Å]	14.2512(4)	14.3487(7)	14.3803(8)	14.3582(4)	14.4572(7)	14.4549(9)	14.4431(7)
V [Å^3]	100.689(4)	100.055(6)	100.094(7)	101.460(4)	100.921(7)	100.912(8)	101.549(7)
$z_{6c,O}$ [-]	0.24178(6)	0.23890(8)	0.23830(8)	0.24046(5)	0.23796(6)	0.23767(8)	0.23886(7)
$b_{3a,Li}$ [Å^2]	0.57(6)	0.85(14)	1.7(3)	0.85(8)	2.28(16)	2.0(3)	1.18(14)
$b_{3b,TM}$ [Å^2]	0.059(18)	0.04(3)	0.15(3)	0.239(18)	0.28(3)	0.10(3)	0.130(16)
$b_{6c,O}$ [Å^2]	0.94(3)	0.92(3)	1.07(3)	1.19(2)	1.148(19)	1.17(3)	1.18(3)
x_{Li} [-]	= 1.17	= 0.835	= 0.501	= 0.835	= 0.501	= 0.301	= 0.501
u_{Li} [-]	= 0.1945(9)	0.213(13)	0.016(12)	0.059(8)	-0.049(8)	-0.183(10)	-0.070(9)
v_{Ni} [-]	0.0245(9)	0.0156(12)	0.0248(13)	0.0385(8)	0.0347(10)	0.0500(12)	0.0465(10)
w_O [-]	1.076(5)	1.084(6)	1.028(6)	1.017(4)	0.972(5)	0.919(5)	0.951(5)

Table SIII. Results of the joint L-XPD and NPD Rietveld refinement according to the rhombohedral *model 2*, $[Li_{x-u}Ni_v]_{3a}[Li_uTM_{0.83-v}]_{3b}[O_w]_{6c}$ with $u_{Li} \geq 0$ and $w_O = 1$.

Sample	①	②	③	④	⑤	⑥	⑦
	Pristine	#1-CHA-100	#1-CHA-200	#2-CHA-100	#2-CHA-200	#2-DIS-260	#2-DIS-200
Overall:							
R_{wp} [%]	8.14	4.58	3.69	2.83	2.53	2.72	2.62
χ^2 [-]	9.68	5.44	3.58	2.94	2.44	2.98	2.74
L-XPD:							
R_{wp} [%]	9.56	7.93	6.91	5.53	5.17	5.89	5.43
R_{bragg} [%]	2.68	1.98	2.16	1.14	2.54	3.57	2.86
χ^2 [-]	10.5	5.94	4.37	2.73	2.19	3.11	2.64
NPD:							
R_{wp} [%]	6.71	2.23	2.10	2.02	1.83	1.77	1.81
R_{bragg} [%]	2.12	0.962	1.10	1.08	0.889	0.861	0.960
χ^2 [-]	8.51	3.90	2.36	3.29	2.83	2.79	2.90
a [Å]	2.85628(5)	2.83758(6)	2.83501(6)	2.85650(4)	2.83913(5)	2.83922(7)	2.84932(6)
c [Å]	14.2512(4)	14.3487(7)	14.3803(8)	14.3582(4)	14.4572(7)	14.4549(9)	14.4431(7)
V [Å^3]	100.689(5)	100.055(6)	100.094(7)	101.460(4)	100.921(7)	100.912(8)	101.549(7)
$z_{6c,O}$ [-]	0.24173(6)	0.23887(8)	0.23829(8)	0.24045(5)	0.23795(6)	0.23783(8)	0.23888(7)
$b_{3a,Li}$ [Å^2]	0.79(6)	1.45(15)	2.1(3)	0.94(7)	1.76(15)	= 0	0.50(12)
$b_{3b,TM}$ [Å^2]	0.151(18)	0.16(3)	0.20(3)	0.266(17)	0.22(2)	= 0	0.08(3)
$b_{6c,O}$ [Å^2]	0.802(19)	0.75(3)	1.03(3)	1.159(19)	1.164(18)	1.20(3)	1.24(3)
x_{Li} [-]	= 1.17	= 0.835	= 0.501	= 0.835	= 0.501	= 0.301	= 0.501
u_{Li} [-]	= 0.1981(9)	0.184(13)	0.005(11)	0.053(8)	= 0	= 0	= 0
v_{Ni} [-]	0.0281(9)	0.0205(12)	0.0271(12)	0.0393(8)	0.0329(9)	0.0448(11)	0.0444(9)
w_O [-]	= 1	= 1	= 1	= 1	= 1	= 1	= 1

Table SIV. Results of the joint L-XPD and NPD Rietveld refinement according to the monoclinic *model 3*, $[Li_{x-u}Ni_v]_{2c,4h}[Li_{3u}Ni_oMn_p]_{2b}[Ni_{0.285-o/2-3v/2}Co_{0.15}Mn_{0.81-p/2}]_{4g}[O_w]_{4i,8j}$ with $u_{Li} \geq 0$ and $w_O = 1$.

Sample	①	②	③	④	⑤	⑥	⑦
	Pristine	#1-CHA-100	#1-CHA-200	#2-CHA-100	#2-CHA-200	#2-DIS-260	#2-DIS-200
Overall:							
R_{wp} [%]	6.16	2.93	2.70	2.31	2.36	2.47	2.52
χ^2 [-]	5.63	2.35	1.99	2.06	2.23	2.58	2.67
L-XPD:							
R_{wp} [%]	7.17	4.85	4.58	4.27	4.66	5.39	4.87
R_{bragg} [%]	7.20	4.15	3.95	1.48	2.98	4.58	3.32
χ^2 [-]	5.99	2.16	1.85	1.59	1.73	2.51	2.06
NPD:							
R_{wp} [%]	5.26	1.92	2.03	1.84	1.86	1.73	2.00
R_{bragg} [%]	2.22	0.917	1.03	0.956	1.11	0.887	1.18
χ^2 [-]	5.23	2.93	2.20	2.73	2.94	2.70	3.55
a [Å]	4.94899(18)	4.91582(19)	4.9113(2)	4.9489(2)	4.91804(19)	4.9188(3)	4.9369(3)
b [Å]	8.5675(3)	8.5117(3)	8.5039(3)	8.5682(3)	8.5160(4)	8.5163(4)	8.5453(3)
c [Å]	5.03300(12)	5.0566(3)	5.0657(4)	5.0638(3)	5.0897(4)	5.0899(5)	5.0870(4)
β [°]	109.270(3)	108.932(6)	108.870(6)	109.055(6)	108.795(6)	108.804(9)	108.864(7)
V [Å^3]	201.444(12)	200.133(16)	200.198(18)	202.956(17)	201.80(2)	201.83(3)	203.08(3)
$y_{4h,Li}$ [-]	0.6581(12)	0.649(3)	0.641(4)	0.652(2)	0.685(5)	0.6732(12)	0.684(4)
$y_{4g,TM}$ [-]	0.1667(3)	0.1672(4)	0.1668(7)	0.1639(8)	0.1648(11)	0.1671(15)	0.1655(13)
$x_{4i,O}$ [-]	0.2230(8)	0.2255(15)	0.2274(15)	0.2325(17)	0.2450(16)	0.237(3)	0.241(3)
$z_{4i,O}$ [-]	0.22539(13)	0.21618(17)	0.21505(19)	0.22117(14)	0.21494(19)	0.2140(3)	0.2175(3)
$x_{8j,O}$ [-]	0.2489(6)	0.2467(11)	0.2383(10)	0.2461(13)	0.2289(9)	0.2341(13)	0.2349(14)
$y_{8j,O}$ [-]	0.3261(3)	0.3263(5)	0.3273(7)	0.3268(5)	0.3272(7)	0.3286(10)	0.3283(9)
$z_{8j,O}$ [-]	= $z_{4i,O}$	= $z_{4i,O}$	= $z_{4i,O}$	= $z_{4i,O}$	= $z_{4i,O}$	= $z_{4i,O}$	= $z_{4i,O}$
$b_{2c,Li}$ [Å^2]	0.52(5)	0.79(15)	0.7(3)	0.58(10)	1.4(3)	= 0	0.2(3)
$b_{4h,Li}$ [Å^2]	= $b_{2c,Li}$	= $b_{2c,Li}$	= $b_{2c,Li}$	= $b_{2c,Li}$	= $b_{2c,Li}$	= $b_{2c,Li}$	= $b_{2c,Li}$
$b_{2b,TM}$ [Å^2]	0.167(14)	0.230(14)	0.240(17)	0.281(16)	0.27(2)	0.12(3)	0.17(3)
$b_{2b,TM}$ [Å^2]	= $b_{2b,TM}$	= $b_{2b,TM}$	= $b_{2b,TM}$	= $b_{2b,TM}$	= $b_{2b,TM}$	= $b_{2b,TM}$	= $b_{2b,TM}$
$b_{4i,O}$ [Å^2]	0.484(18)	0.57(3)	0.93(3)	1.02(3)	1.13(3)	1.17(3)	1.26(3)
$b_{8j,O}$ [Å^2]	= $b_{4i,O}$	= $b_{4i,O}$	= $b_{4i,O}$	= $b_{4i,O}$	= $b_{4i,O}$	= $b_{4i,O}$	= $b_{4i,O}$
x_{Li} [-]	= 1.17	= 0.835	= 0.501	= 0.835	= 0.501	= 0.301	= 0.501
u_{Li} [-]	= 0.1891(6)	= 0.155(3)	0.033(9)	= 0.062(5)	= 0	= 0	= 0
v_{Ni} [-]	0.0191(7)	0.0165(7)	0.0257(9)	0.0384(7)	0.0313(9)	0.041(1)	0.0427(9)
o_{Ni} [-]	0.336(6)	0.334(17)	0.316(13)	0.37(2)	0.312(16)	0.303(16)	0.316(16)
p_{Mn} [-]	= 0.097(6)	0.200(15)	0.285(17)	0.445(15)	0.43(3)	0.36(3)	0.39(4)
w_O [-]	= 1	= 1	= 1	= 1	= 1	= 1	= 1

S4: Overview of Structural Models Used in the Literature

To the best of our knowledge and understanding, we tried to summarize different refinement models for Li- and Mn-rich layered oxides in **Table SV**, as they were reported in the literature. Here, we want to focus on the amount of refined structural parameters, including fractional coordinates (FCs), atomic displacement parameters (ADPs), and especially site occupancy factors (SOFs). The latter comprise the occupation of octahedral sites in the Li/TM layer (abbreviated as X_{Li}/X_{TM} with X being the refined element), of tetrahedral sites in the lithium layer (X_{Li}^{tet}), and oxygen vacancies (O). Since the refinement details are incomplete in some publications (highlighted by a question mark), we assumed that each structural parameter without estimated standard deviation (e.s.d.; typically given in parentheses, as defined by Schwarzenbach et al.[7]) is fixed. Furthermore, we assumed that parameters with the same value (and e.s.d.) are constrained to be identical. In XPD datasets, Ni is often selected to migrate into the Li layer, but it is representative for any of the three transition metals Ni, Co, and Mn due to their similar X-ray atomic form factors.

Table SV. Comparison of the structural models used in this work with several models applied for Li- and Mn-rich layered oxides in the literature. The table summarizes the investigated CAM, the number and type of samples, the number and type of diffraction datasets, and the number of simultaneously refined structural parameters in each model, including fractional coordinates (FCs), atomic displacement parameters (ADPs), and site occupancy factors (SOFs). The latter are specified by the type of element/site. If refinement details are not clearly described (or absent) in the publication, this is highlighted by a question mark. Further experimental and refinement details are presented below the table.

Reference	Material	# samples	# datasets	Refinement approach	# refined structural parameters			
					FCs	ADPs	SOFs	Selected SOFs
This work	$Li_{1.17}Ni_{0.19}Co_{0.10}Mn_{0.54}O_2$	7 (pristine/cycle 1+2)	2 (L-XPD/NPD)	*Model 1: R*-3*m*	1	3	2-3	Ni_{Li}, Li_{TM}, O
				Model 2: R-3*m*	1	3	1-2	Ni_{Li}, Li_{TM}
				*Model 3: C*2/*m*	6	3	2-4	Ni_{Li}, Li_{TM}, Ni_{TM}, Mn_{TM}
Lu[8]	$Li_{(4-2x)/3}Ni_xMn_{(2-x)/3}O_2$	2+3 (pristine)	1+1 (L-XPD/NPD)	*R*-3*m*	1	?	1	Ni_{Li} or Mn_{Li}
Lu[9]	$Li_{(4-2x)/3}Ni_xMn_{(2-x)/3}O_2$	3 (charged)	1 (L-XPD)	*R*-3*m*	1	?	1	O
Yabuuchi[10]	$Li_{1.20}Ni_{0.13}Co_{0.13}Mn_{0.54}O_2$	3 (pristine/discharged)	1 (S-XPD)	*R*-3*m*	1	0	1-2	TM_{Li}, O
Kleiner[11]	$Li_{1.17}Ni_{0.19}Co_{0.10}Mn_{0.54}O_2$	In-situ (100 cycles, discharged/charged)	1 (S-XPD)	*R*-3*m*	1-2	1	1	Discharged: Ni_{Li} Charged: Ni_{Li}^{tet}
Liu[12]	$Li_{1.20}Ni_{0.15}Co_{0.10}Mn_{0.55}O_2$	Operando (cycle 1)	1 (NPD)	*R*-3*m*	1	?	1(?)	Li_{Li}, Li_{TM}

Fell[13]	$Li_{1.20}Ni_{0.20}Mn_{0.60}O_2$	7 (pristine/cycle 1)	1 (S-XPD)	*R*-3*m* + *R*-3*m*	1 2(?)	? ?	1(+1) 2(+1)	Ni_{Li}, O Ni_{Li}, Li_{Li}^{tet}, O
Koga[14]	$Li_{1.20}Ni_{0.13}Co_{0.13}Mn_{0.54}O_2$	1+2 (pristine)	1+1 (L-XPD/NPD)	*Model 1: R*-3*m* *Model 2: C*2/*m*	1 7	3 6	1 3(?)	Ni_{Li} Ni_{Li}, Li_{TM}, Mn_{TM}
Csernica[15]	$Li_{0.18}Ni_{0.21}Co_{0.08}Mn_{0.53}O_2$	1+6+1 (pristine/ discharged/annealed)	1 (S-XPD)	*Model 1: R*-3*m* *Model 2: C*2/*m*	1 6	0 0	2 2	TM_{Li}, O TM_{Li}, O
Whitfield[16]	$Li_{1.20}Ni_{0.30}Co_{0.10}Mn_{0.40}O_2$	1 (pristine)	4 (S-XPD/NPD)	*C*2/*m*	7	6	10	Ni_{Li}, Co_{Li}, Mn_{Li}, Li_{TM}, TM_{TM}
Gent[17]	$Li_{1.17}Ni_{0.21}Co_{0.08}Mn_{0.54}O_2$	8 (pristine/cycle 1)	1 (S-XPD)	*C*2/*m*	4(?)	?	1(+1)	TM_{Li}, O
Ishida[18]	$Li_{1.20}Ni_{0.13}Co_{0.13}Mn_{0.54}O_2$	7 (pristine/cycle 1/ chem. delithiated)	1 (S-XPD)	*C*2/*m*	7	≤5	≤10(?)	Ni_{Li}, Li_{TM}, TM_{TM}, O
Mohanty[19]	$Li_{1.20}Ni_{0.15}Co_{0.10}Mn_{0.55}O_2$	1 (pristine)	1 (NPD)	*Model 1: C*2/*m* *Model 2: R*-3*m* (NCM) + *C*2/*m* (Li_2MnO_3)	5 1 5	6 3 4(?)	4 1 0	Ni_{Li}, Li_{TM} Ni_{Li}
Mohanty[20]	$Li_{1.20}Ni_{0.15}Co_{0.10}Mn_{0.55}O_2$	11 (cycle 2+26)	1 (NPD)	*R*-3*m* (NCM) + *C*2/*m* (Li_2MnO_3) + *Fd*-3*m* ($LiMn_2O_4$)	1 5 0	4(?) 4(?) 3	6 2 0	Ni_{Li}, Mn_{Li}, Mn_{Li}^{tet}, Li_{Li}^{tet}, O O
Yu[21]	$Li_{1.20}Ni_{0.167}Co_{0.067}Mn_{0.567}O_2$	3 (pristine/discharged)	1 (S-XPD)	*Model 1: R*-3*m* *Model 2: R*-3*m* (NCM) + *C*2/*m* (Li_2MnO_3)	1 1 5	0 ? ?	2 0(?) 2	TM_{Li}, O O
Chen[22]	$Li_{1.24}Ni_{0.18}Co_{0.08}Mn_{0.50}O_2$	1 (pristine)	2 (L-XPD/NPD)	*R*-3*m* (Li-rich NCM) + *C*2/*m* (Li_2MnO_3)	1 7	2 3	1 0	Ni_{Li}

Lu:[8] All five samples (heated to 900°C) investigated by L-XPD and two of them additionally by NPD. Validation of migrating TM species by separate refinements.
Lu:[9] Li_{Li} vacant, Ni_{Li} and Li_{TM} fixed to the values of the pristine samples.
Yabuuchi:[10] Imaginary TM species used (16% Ni, 16% Co, and 68% Mn). Li/TM ratio additionally refined for the pristine sample. Li_{Li}/Li_{TM} vacancies equally created in the discharged samples.
Kleiner:[11] Single-layer pouch cells with metallic lithium anode. Ni_{Li} in the charged state fixed to the same value as in the discharged state (of the same cycle). Li content measured by ICP-OES for selected discharged/charged samples. Ni_{Li} created as paired anti-site defect ($Ni_{Li} = Li_{TM}$).
Liu:[12] Multi-layer pouch cells with amorphous silicon anode. Focus on lithium insertion/extraction mechanism. Ni_{Li} refined in pristine state before cycling (afterwards not described). Li content probably fixed to exchanged capacity. $Li_{1.08}Ni_{0.25}Co_{0.25}Mn_{0.42}O_2$ with low degree of over-lithiation also studied.

Fell:[13] Second *R*-3*m* phase introduced during activation plateau and onwards (phase compositions not disclosed). Oxygen vacancies optional.
Koga:[14] All three samples (synthesized at different calcination temperatures) investigated by L-XPD (using *model 1*) and one of them additionally by NPD (using *model 1/2*).
Csernica:[15] Discharged samples range from the first to the 500th cycle. X-ray atomic form factors treated as neutral atoms. ADPs fixed to the values reported by Yin et al.[5] Pristine sample also refined in the *C*2/*m* space group, but *R*-3*m* is preferred due to the lack of in-plane Li/TM ordering peaks in the cycled samples.
Whitfield:[16] Joint refinement of S-XPD (3 datasets including conventional and resonant XPD: off-edge, Co-edge, and Mn-edge) and NPD data. Both crystallographic sites in metal layers treated individually (SOFs in Li layer: 2c ≠ 4h; TM layer: 2b ≠ 4g; including all 4 metals on every site). Overall Li/TM ratio refined, but TM ratio kept constant.
Gent:[17] In-plane ordering effects neglected (SOFs in Li layer: 2c = 4h; TM layer: 2b = 4g). Li_{Li}/Li_{TM} values (of cycled samples) fixed according to previous operando NPD study by Liu et al.[12] Oxygen vacancies optional.
Ishida:[18] Both crystallographic sites in each layer treated individually (SOFs in Li layer: 2c ≠ 4h, including Li/Ni; TM layer: 2b ≠ 4g, including Li/Ni/Co/Mn; O layer: 4i ≠ 8j). Choice and number of refined parameters not identical among all samples. Metal composition of all samples measured by ICP-OES.
Mohanty:[19] *Model 1*: Both crystallographic sites in the metal layers treated individually (SOFs in Li layer: 2c ≠ 4h, including Li/Ni; TM layer: 2b ≠ 4g, including Li/Ni/Mn, Co only on 4g site). *Model 2*: Ni_{Li} in *R*-3*m* phase created as paired anti-site defect ($Ni_{Li} = Li_{TM}$).
Mohanty:[20] Li content in *R*-3*m* phase first refined as pure Li_{TM} and then freely distributed among three sites (Li_{Li}, Li_{TM}, and Li_{tet}) with constrained total occupancy (from first step). Cubic spinel phase (*Fd*-3*m*) only added in 26th cycle.
Yu:[21] *Model 1*: Focus on TM migration. Li_{Li}/Li_{TM} vacancies equally created in the discharged samples. *Model 2*: Focus on phase fractions. Individual phase compositions not disclosed. Oxygen vacancies of the *C*2/*m* phase only allowed for the discharged samples.
Chen:[22] Joint refinement of L-XPD and NPD data.

S5: DFT Simulation Results

To simulate the experimentally investigated material with the following composition, $Li[Li_{0.17}Ni_{0.19}Co_{0.10}Mn_{0.54}]O_2$, a model material with the formula unit (f.u.) of $Li[Li_{0.2}Ni_{0.2}Co_{0.1}Mn_{0.5}]O_2$ is chosen. This allows a model system with an integer atom numbers for a supercell with the size of 60 f.u. **Table SVI** summarizes the calculated structural energies for a supercell containing 72 Li (60 in the Li layer and 12 in the TM layer), 12 Ni, 6 Co, 30 Mn, and 120 O atoms. The obtained occupancies of the different layers (either Li, TM, or O layer) and atomic positions (octahedral or if specified tetrahedral (tet) voids) are summarized in the right part of **Table SVI**. The migration of one atom to the Li layer corresponds to 1.67% movement with respect to the f.u. used for the experimental data. Oxygen dimers are listed as $O\text{-}O^{\delta-}$ in the table but not further discussed with respect to the TM movement within this work.

Table SVI. Comparison of DFT energies for different delithiation states of the model composition $Li[Li_{0.2}Ni_{0.2}Co_{0.1}Mn_{0.5}]O_2$ within a 4×5×1 supercell (60 formula units). For every Li content, structures are ordered according to ascending energy. The structures with the lowest energies are taken as the energy references although no guarantee exists that they actually are the ground states for their respective compositions. In the right part of the table, the calculated atomic occupancies for the different sites within the lattice are given for the obtained local energy minima of the supercell.

Supercell (= 60 f.u.)	x_{Li} per f.u.	ΔE to reference [meV/atom]	Li layer						TM layer								O layer
			Li	Li^{tet}	Ni	Ni^{tet}	Mn	Mn^{tet}	Li	Li^{tet}	Ni	Ni^{tet}	Mn	Mn^{tet}	Co	$O\text{-}O^{\delta-}$	O
$Li_{72}Ni_{12}Co_6Mn_{30}O_{120}$	1.20		60	0	0	0	0	0	12	0	12	0	30	0	6	0	120
$Li_{59}Ni_{12}Co_6Mn_{30}O_{120}$	0.98	0	46	1	0	0	0	0	12	0	12	0	30	0	6	0	120
		20	59	0	0	0	0	0	0	0	12	0	30	0	6	0	120
		31	59	0	1	0	0	0	0	0	11	0	30	0	6	1	118
		37	59	0	0	0	1	0	0	0	12	0	29	0	6	0	120
		42	59	0	1	0	0	0	0	0	11	0	30	0	6	0	120
$Li_{30}Ni_{12}Co_6Mn_{30}O_{120}$	0.50	0	19	11	0	0	0	0	0	0	12	0	30	0	6	0	120
		9	19	11	1	0	0	0	0	0	11	0	30	0	6	1	118
		11	19	11	1	0	0	0	0	0	11	0	30	0	6	0	120
		11	17	13	1	0	0	0	0	0	11	0	30	0	6	0	120
		17	17	13	1	0	0	0	0	0	11	0	30	0	6	2	116
		18	19	5	0	0	0	0	6	0	12	0	30	0	6	0	120

		27	20	10	2	0	0	0	0	0	10	0	30	0	6	2	116
$Li_0Ni_{12}Co_6Mn_{30}O_{120}$	0	0	0	0	1	0	0	0	0	0	11	0	23	7	6	2	116
		2	0	0	0	0	0	0	0	0	12	0	24	6	6	0	120
		2	0	0	2	0	0	0	0	0	10	0	24	6	6	2	116
		2	0	0	1	0	0	1	0	0	11	0	22	8	6	2	116
		5	0	0	1	0	0	0	0	0	11	0	24	6	6	1	118
		6	0	0	0	0	0	0	0	0	12	0	20	10	6	0	120
		6	0	0	1	0	0	0	0	0	11	0	24	6	6	2	116
		13	0	0	1	0	0	0	0	0	11	0	24	6	6	0	120
		56	0	0	0	0	0	0	0	0	12	0	30	0	6	0	120

S21

S6: Literature

1. B. Strehle, K. Kleiner, R. Jung, F. Chesneau, M. Mendez, H. A. Gasteiger, and M. Piana, *J. Electrochem. Soc.*, **164**, A400–A406 (2017).
2. P. W. Stephens, *J. Appl. Crystallogr.*, **32**, 281–289 (1999).
3. H. Liu, H. Liu, S. H. Lapidus, Y. S. Meng, P. J. Chupas, and K. W. Chapman, *J. Electrochem. Soc.*, **164**, A1802–A1811 (2017).
4. A. Grenier, H. Liu, K. M. Wiaderek, Z. W. Lebens-Higgins, O. J. Borkiewicz, L. F. J. Piper, P. J. Chupas, and K. W. Chapman, *Chem. Mater.*, **29**, 7345–7352 (2017).
5. L. Yin, G. S. Mattei, Z. Li, J. Zheng, W. Zhao, F. Omenya, C. Fang, W. Li, J. Li, Q. Xie, J.-G. Zhang, M. S. Whittingham, Y. S. Meng, A. Manthiram, and P. G. Khalifah, *Rev. Sci. Instrum.*, **89**, 093002 (2018).
6. H. Liu, H. Liu, I. D. Seymour, N. Chernova, K. M. Wiaderek, N. M. Trease, S. Hy, Y. Chen, K. An, M. Zhang, O. J. Borkiewicz, S. H. Lapidus, B. Qiu, Y. Xia, Z. Liu, P. J. Chupas, K. W. Chapman, M. S. Whittingham, C. P. Grey, and Y. S. Meng, *J. Mater. Chem. A*, **6**, 4189–4198 (2018).
7. D. Schwarzenbach, S. C. Abrahams, H. D. Flack, E. Prince, and A. J. C. Wilson, *Acta Crystallogr. Sect. A Found. Crystallogr.*, **51**, 565–569 (1995).
8. Z. Lu, L. Y. Beaulieu, R. A. Donaberger, C. L. Thomas, and J. R. Dahn, *J. Electrochem. Soc.*, **149**, A778 (2002).
9. Z. Lu and J. R. Dahn, *J. Electrochem. Soc.*, **149**, A815 (2002).
10. N. Yabuuchi, K. Yoshii, S.-T. Myung, I. Nakai, and S. Komaba, *J. Am. Chem. Soc.*, **133**, 4404–4419 (2011).
11. K. Kleiner, B. Strehle, A. R. Baker, S. J. Day, C. C. Tang, I. Buchberger, F.-F. Chesneau, H. A. Gasteiger, and M. Piana, *Chem. Mater.*, **30**, 3656–3667 (2018).
12. H. Liu, Y. Chen, S. Hy, K. An, S. Venkatachalam, D. Qian, M. Zhang, and Y. S. Meng, *Adv. Energy Mater.*, **6**, 1502143 (2016).
13. C. R. Fell, D. Qian, K. J. Carroll, M. Chi, J. L. Jones, and Y. S. Meng, *Chem. Mater.*, **25**, 1621–1629 (2013).
14. H. Koga, L. Croguennec, P. Mannessiez, M. Ménétrier, F. Weill, L. Bourgeois, M. Duttine, E. Suard, and C. Delmas, *J. Phys. Chem. C*, **116**, 13497–13506 (2012).
15. P. M. Csernica, S. S. Kalirai, W. E. Gent, K. Lim, Y.-S. Yu, Y. Liu, S.-J. Ahn, E. Kaeli, X. Xu, K. H. Stone, A. F. Marshall, R. Sinclair, D. A. Shapiro, M. F. Toney, and W. C. Chueh, *Nat. Energy*, **6**, 642–652 (2021).
16. P. S. Whitfield, I. J. Davidson, P. H. J. Mercier, Y. Le Page, L. D. Mitchell, P. W. Stephens, L. M. D. Cranswick, and I. P. Swainson, *Powder Diffr.*, **21**, 172–172 (2006).
17. W. E. Gent, K. Lim, Y. Liang, Q. Li, T. Barnes, S.-J. Ahn, K. H. Stone, M. McIntire, J. Hong, J. H. Song, Y. Li, A. Mehta, S. Ermon, T. Tyliszczak, D. Kilcoyne, D. Vine, J.-H. Park, S.-K. Doo, M. F. Toney, W. Yang, D. Prendergast, and W. C. Chueh, *Nat. Commun.*, **8**, 2091 (2017).
18. N. Ishida, N. Tamura, N. Kitamura, and Y. Idemoto, *J. Power Sources*, **319**, 255–261 (2016).
19. D. Mohanty, A. Huq, E. A. Payzant, A. S. Sefat, J. Li, D. P. Abraham, D. L. Wood, and C. Daniel, *Chem. Mater.*, **25**, 4064–4070 (2013).
20. D. Mohanty, J. Li, D. P. Abraham, A. Huq, E. A. Payzant, D. L. Wood, and C. Daniel, *Chem. Mater.*, **26**, 6272–6280 (2014).
21. H. Yu, Y.-G. So, Y. Ren, T. Wu, G. Guo, R. Xiao, J. Lu, H. Li, Y. Yang, H. Zhou, R. Wang, K. Amine, and Y. Ikuhara, *J. Am. Chem. Soc.*, **140**, 15279–15289 (2018).
22. C.-J. Chen, W. K. Pang, T. Mori, V. K. Peterson, N. Sharma, P.-H. Lee, S. Wu, C.-C. Wang, Y.-

F. Song, and R.-S. Liu, *J. Am. Chem. Soc.*, **138**, 8824–8833 (2016).

3.3.2 Correlating the Voltage Fading to Irreversible Transition-Metal Migration

The article "Origin of High Capacity and Poor Cycling Stability of Li-Rich Layered Oxides: A Long-Duration in Situ Synchrotron Powder Diffraction Study" was submitted in January 2018 to the peer-reviewed journal *Chemistry of Materials* and published in May 2018.[192] It is reprinted with permission from the American Chemical Society (Copyright 2018). The study was presented by Michele Piana as Paper 376 at the 233rd Meeting of the Electrochemical Society in Seattle, Washington, USA (May 13-17, 2018). The permanent weblink of this article can be found under: https://pubs.acs.org/doi/10.1021/acs.chemmater.8b00163.

Li- and Mn-rich layered oxides suffer from poor capacity retention and voltage fading upon cycling, especially during discharge.[189,195] As section 3.2.2 showed that the surface reconstruction is completed within the initial ≈20 cycles, the voltage fading has to be caused by bulk changes in the CAM. The most widely accepted explanation was introduced by researchers at the Argonne National Laboratory, which attributed both voltage hysteresis and fading to inter-layer TM migration.[144,188,189] It suggests that the reversible migration of transition-metals into tetrahedral sites of the Li layer leads to voltage hysteresis between charge and discharge. As some of the TMs might not move back into the TM layer but are irreversibly captured in the octahedral sites of the Li layer, their accumulation causes the voltage fading upon cycling.

In this study, we aim at monitoring the extent of TM migration in $Li[Li_{0.17}Ni_{0.19}Co_{0.10}Mn_{0.54}]O_2$ by *in situ* synchrotron XPD (S-XPD) and difference Fourier analysis. The long-duration experiment facility of the beamline I11 at the Diamond Light Source[232] allows for recording XPD patterns in a custom-made pouch cell setup every ≈15 cycles in the completely discharged state (after running into the lower voltage cut-off of 2.0 V vs. Li^+/Li) and in the charged state (4.6 V vs. Li^+/Li) over the duration of ≈100 cycles. Starting with the discharged state, the structural model for the Rietveld refinement includes only octahedral sites and looks as follows: $[Li_{1-x}TM_x]^{oct}_{Li}[Li_xTM_{0.83-x}]^{oct}_{TM}O_2$. As XPD cannot differentiate between the three transition-metals due to their similar electron density, we select exemplarily Ni to be the migrating ion. The TM disorder (equivalent to x) rises from

≈2% after the first cycle to almost ≈5% after 100 cycles. In the charged state, the difference Fourier maps suggest the additional occupation of tetrahedral Li-sites, as it was also observed experimentally by others[125,150] and further predicted at high SOCs based on computational studies.[259,260] Fixing the TM disorder in the octahedral Li-site (x value obtained from the prior discharged state), the charged state was refined as follows: $[Li_0TM_x]^{oct}_{Li}[TM_y]^{tet}_{Li}[Li_0TM_{0.83-x-y}]^{oct}_{TM}O_2$. The TM disorder in the tetrahedral site (equivalent to y) stays unaltered at a high level of 8-9% throughout cycling.

We correlate the structural information to the electrochemical data and hypothesize a causal relationship among them, as already proposed in the literature.[188] The irreversible delithiation of the TM layer during the activation charge[178,240] lowers the energy barrier for the reversible occupation of tetrahedral Li-sites in the charged state. This TM disorder stabilizes high delithiation levels due to reduced repulsive interactions between adjacent oxygen layers and could thus explain the high capacity of Li- and Mn-rich layered oxides compared to stoichiometric NCM variants. The gradual and irreversible migration of transition-metals from tetrahedral to octahedral Li-sites, as determined in the discharged state, is connected to the observed voltage fading.

To support the main article, additional information is supplied for the benefit of the reader. The Supporting Information includes details about our Rietveld refinement strategy as well as the corresponding fitting results for both the discharged state and the charged state.

Author contributions

B.S. built the pouch cells for the synchrotron experiments, while K.K. and I.B. designed the corresponding pouch cell holder. The synchrotron experiments were set up by K.K. and B.S. The beamline scientists A.R.B., S.J.D., and C.C.T. measured the diffraction data over the course of several months. K.K. analyzed the diffraction data and wrote the manuscript. All authors discussed the data and edited the manuscript.

CHEMISTRY OF MATERIALS
Cite This: Chem. Mater. 2018, 30, 3656−3667
Article
pubs.acs.org/cm

Origin of High Capacity and Poor Cycling Stability of Li-Rich Layered Oxides: A Long-Duration in Situ Synchrotron Powder Diffraction Study

Karin Kleiner,*[,†,‡] Benjamin Strehle,[†] Annabelle R. Baker,[‡] Sarah J. Day,[‡] Chiu C. Tang,[‡] Irmgard Buchberger,[†] Frederick-Francois Chesneau,[§] Hubert A. Gasteiger,[†] and Michele Piana[†]

[†]Chair of Technical Electrochemistry, Department of Chemistry and Catalysis Research Center, Technical University of Munich, D-85748 Garching, Germany

[‡]Harwell Science and Innovation Campus, Diamond Light Source, Didcot, Oxfordshire OX11 0DE, U.K.

[§]Badische Anilin- & Soda-Fabrik Societas Europaea (BASF SE, GCN/EE - M311), D-67056 Ludwigshafen, Germany

Supporting Information

ABSTRACT: High-energy $Li_{1.17}Ni_{0.19}Co_{0.10}Mn_{0.54}O_2$ (HE-NCM) is a lithium-rich layered oxide with alternating Li- and transition-metal (TM) layers in which excess lithium ions replace transition metals in the host structure. HE-NCM offers a capacity roughly 50 mAh g^{-1} higher compared to that of conventional layered oxides but suffers from capacity loss and voltage fade upon cycling. Differential capacity plots (taken over 100 cycles) show that the origin of the fading phenomenon is a bulk issue rather than a surface degradation. Although previous studies indicate only minor changes in the bulk material, long duration in situ synchrotron X-ray powder diffraction measurements, in combination with difference Fourier analysis of the data, revealed an irreversible transition-metal motion within the host structure. The extensive work provides new insights into the fading mechanism of the material.

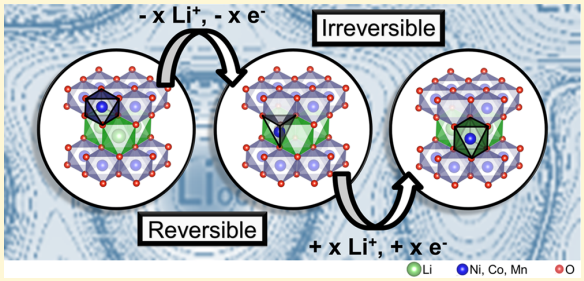

INTRODUCTION

Since the introduction of lithium-ion batteries in 1991 by Sony, their global market reached several billion US dollars and is still increasing. The main driving force of this trend is the renaissance of electromobility. Climatic changes (caused by the combustion of fossil fuels), the limited availability of nonrenewable energy sources, and a growing environmental awareness are arguments leading to this trend. However, these arguments will not lead to a large-scale commercialization of battery electric vehicles (BEVs) as long as their price is higher and their range is shorter in comparison to the current fossil-fuel-powered vehicles.[1,2] Both factors are related to the energy density of lithium-ion batteries, which is limited up to now by the cathode active materials.[2,3]

Lithium-rich layered oxides offer a reversible discharge capacity of 250 mAh g^{-1} at a relatively high mean discharge voltage of 3.5 V (vs graphite) and would therefore fulfill the energy density requirements of the automotive industry.[1,2] However, the material suffers from a poor capacity retention and voltage fade upon cycling, which currently hinders its market penetration.[4,5] Many efforts seeking to improve these issues have been put into doping and/or surface modifications.[6,7] In many cases, this led to better cycling stabilities, with the drawback of a lower capacity, but the capacity retention was still not satisfying, or apparently successful modifications were only compared to poor reference samples.[6,7]

Less attention has been paid to understanding the fading mechanism of the material, which could help to find a way for improving its cycling stability. Until now, the common understanding is that oxygen release from the host structure is the main reason for capacity drop and voltage fade.[8−10] However, more recent online electrochemical mass spectrometry and transmission electron microscopy (TEM) studies suggest that an irreversible lattice-oxygen oxidation is limited to near-surface parts of the particles and is associated with the formation of a spinel or rock-salt structure, causing high overpotentials (in charge and discharge).[11−15] Irreversible changes observed over extended cycling data show an overpotential increase only for the discharge. Furthermore, according to differential capacity plots, redox processes appear, change, and shift with an increasing number of cycles. Both of these observations cannot be explained by surface effects because such processes would change the overpotentials of the charge and discharge to the same extent and would not lead to new peaks in the differential capacity plots.[4,6,16] Therefore, the

Received: January 12, 2018
Revised: May 3, 2018
Published: May 3, 2018

DOI: 10.1021/acs.chemmater.8b00163
Chem. Mater. 2018, 30, 3656−3667

electrochemical performance suggests structural changes (e.g., disorder) as the origin of the observed drop in the cycling performance, which are more suitably studied by methods sensitive to the bulk structure (e.g., powder diffraction).[17] Although very pronounced structural changes have been observed, e.g. with TEM[13,18] in surface near parts of the particles, these changes are not observed when investigating the bulk structure and are therefore not relevant to the conclusions made in the work. Nevertheless, the incidence of transition-metal migration during cycling is supported by theoretical calculations.[19] At best, the idea of the fading mechanism is currently too simplified, and a deeper understanding is necessary. Furthermore, the question of why lithium-rich materials offer a capacity 50 mAh g^{-1} higher compared to that of structurally related layered oxides still remains unanswered.

In the present study, new insights into the origin of the poor cycling stability and the high capacity of lithium-rich layered oxides are obtained from long-duration synchrotron X-ray powder diffraction (SXPD) measurements. Using pouch cells suitable for in situ SXPD, the electrochemistry and structural behavior of HE-NCM was studied over long-term cycling, performed for the first time at the long duration experiment facility I11 at the Diamond Light Source, United Kingdom. Although there is no evidence for changes in the bulk structure geometry of the unit cell, it is possible to determine and quantify transition-metal (TM) migration upon cycling by detailed reflection profile analysis and difference-Fourier mapping. The relationship of reversible and irreversible transition-metal disorder with the strain in the material can provide guidance to improve the cycling stability of lithium-rich cathodes or to synthesize application-oriented materials in the future.

■ MATERIALS AND METHODS

High-energy $Li_{1.17}Ni_{0.19}Co_{0.10}Mn_{0.54}O_2$ (HE-NCM) electrodes (92.5 wt % BASF SE HE-NCM, 2% Timcal SFG6L graphite, 2% Timcal Super C65, 3.5% Solef PVDF, ≈6.3 $mg_{HE\text{-}NCM}$ cm^{-2}) were cycled in pouch cells (cathode: 30 × 30 mm^2) versus lithium (33 × 33 mm^2, 0.45 mm thick, 99.9% Rockwood Lithium, United States). To avoid short circuits due to lithium dendrite formation upon cycling, four glass-fiber separators (36 × 36 mm^2, glass microfiber filter 691, VWR, Germany) were used, and 1.5 mL LP57 (1 M $LiPF_6$ in EC:EMC 3:7 by weight, <20 ppm of H_2O, BASF SE, Germany) was added. Furthermore, a homemade pouch cell holder (Section S1) was used for a homogeneous compression of the cells (2 bar) during operation, ensuring reproducible and stable electrochemical measurements. The first cycle was performed with a C-rate of C/20 (constant current, corresponding to ≈12.5 mA/$g_{HE\text{-}NCM}$ using a nominal capacity of 250 mAh/$g_{HE\text{-}NCM}$), and the HE-NCM was charged to 4.8 V vs Li^+/Li to activate the material.[12] During the subsequent cycles, two cells (referred to as Cell1 and Cell2) were cycled simultaneously at a rate of C/5 (constant current, corresponding to ≈50 mA/$g_{HE\text{-}NCM}$ using a nominal capacity of 250 mAh/$g_{HE\text{-}NCM}$) between 2.0 and 4.6 V, completing 14.5 cycles each week, until 105 cycles were reached. Due to synchrotron shutdowns within the provided beamtime of 6 months, the measurements were performed in two runs. Cell1 and Cell2 were cycled up to 49 cycles (at 22 °C, Arbin cycler, United States) at the synchrotron beamline I11 (Diamond Light Source, UK). Cell3 and Cell4 (nominally identical cells) were then first cycled up to 49 cycles in a climatic chamber (at 25 °C, Maccor cycler, UK) at the Chair of Technical Electrochemistry (Technical University of Munich, Germany) and were then stopped/restarted at the beamline (cycle 50−105, at 22 °C).

Time-resolved synchrotron X-ray powder diffraction (SXPD) data were collected at beamline I11. The evolution of the lattice parameters during the first charge was studied using a fast position-sensitive detector (PSD) at the beamline.[20] The energy of the X-ray beam was tuned to ∼15 keV, and the calibrated wavelength was λ= 0.826117(10) Å. A battery cell was mounted onto an *xyz*-stage that was adjusted to the center of the diffraction instrument.

In situ long-term studies (105 cycles) from two identical battery cells were performed using SXPD on the recently commissioned long duration experiment (LDE) facility at the beamline. The detailed technical description of the LDE instrument is given by Murray et al.[21] Using a higher energy beam of ∼25 keV ($\lambda \approx 0.496$ Å), SXPD patterns were taken every week upon long-term cycling. Data were collected with a 2D Pixium area detector at a detector distance of ∼0.49 m. CeO_2 (NIST Standard Reference Material 674b, United States) was measured before every HE-NCM pattern to refine the wavelength and the detector distance each time and evaluate the instrumental reflection broadening.

During data collection, both cells were held at open circuit voltage (OCV), one in the charged and one in the discharged state. The charge/discharge during OCV alternated every week to assess the reproducibility of the experiment and have powder diffraction patterns in both the charged and the discharged state at the same cycle. The exposure time during the powder diffraction measurements was 5 min. The data were reduced with the software package DAWN[22,23] and refined with the software package Fullprof (2θ range: 0−40°).[24] Due to preferential orientations of aluminum (pouch foil, current collector) and lithium (counter electrode), these phases were included in the refinements using the Le Bail method (only profile fitting). When these reflections are excluded, partially overlapping HE-NCM reflections would also be excluded, which means a loss of information. As the HE-NCM reflections exhibited a mismatch in intensities and an unusual broadening (especially observed for the charged states), difference Fourier (DF) analysis with the software packages WinGX and VESTA was used to evaluate and confirm disorder within the crystallographic structure.[25,26] Reflection broadening due to increased microstrain during charge of HE-NCM was further analyzed with Rietveld refinement to enable the determination of Li/transition-metal (TM) disorder parameters in the charged material. A detailed description of the refinement can be found in the Supporting Information, Sections S4 and S5.

Inductively coupled plasma optical emission spectroscopy (ICP-OES) was performed at Mikroanalytisches Labor Pascher (Remagen, Germany). Prior to the measurements, the materials were cycled in pouch cells (2 and 30 cycles, respectively). The pouch cells were disassembled in an argon-filled glovebox and the cathode materials were washed with dimethyl carbonate. In addition, pristine HE-NCM, also coated on an aluminum current collector, was analyzed. The materials were removed from the current collector and the obtained powder was dissolved with an acid digestion. ICP-OES was performed using a Thermo Scientific iCAP 6500 duo instrument. For each measurement, 5−10 mg of the powder was taken and for every sample, 2 measurements were performed.

■ RESULTS

4.1. Electrochemistry. Figure 1A shows the averaged specific capacity of Cell1 and Cell2 (first run) as well as Cell3 and Cell4 (second run) upon cycling. Cell1 and Cell2 were cycled for 49 cycles at 22 °C at the I11 beamline while Cell3 and Cell4 were started first in a climatic chamber at the Technical University of Munich at 25 °C and were stopped/restarted at the beamline after 49 cycles. Due to the strong temperature dependence of the cycling performance of HE-NCM, Cell3 and Cell4 show a 7 mAh g^{-1} higher capacity after 49 cycles (see Section S2 for further details). The highest capacity drop (ca. 50 mAh g^{-1}) is observed between the first and the second discharge due to activation and the difference in C-rates. The mean capacity drop in the subsequent cycles is 0.4 mAh g^{-1} per cycle.

DOI: 10.1021/acs.chemmater.8b00163
Chem. Mater. 2018, 30, 3656−3667

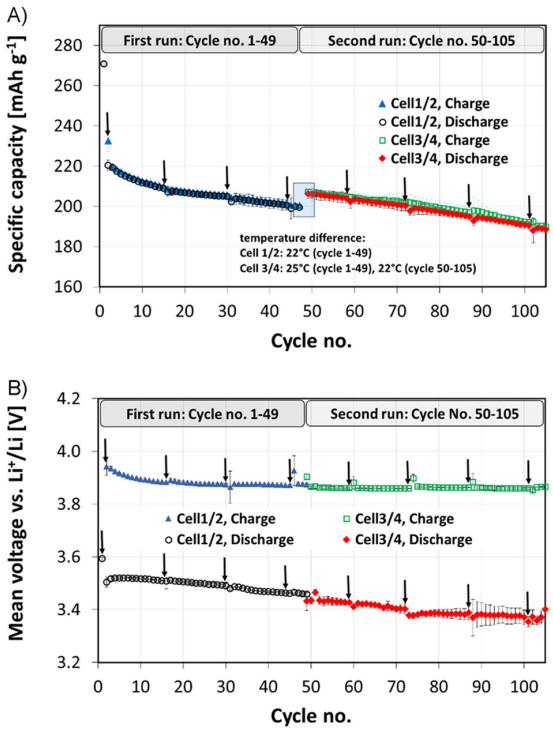

Figure 1. Mean specific capacity (A) and mean dis-/charge voltage (B), measured with Pouch cells at beamline I11 (Diamond Light Source, UK). The values shown are an average of the two cells cycled simultaneously (Cell1/2: cycles 1−49, Cell3/4: cycles 49−105), and the error bars represent the standard deviation between the two cells. During data collection (indicated by the arrows), both cells were held at open circuit voltage (OCV), one in the charged and one in the discharged state, alternating upon cycling. This results in SXPD data collection for the same cell occurring after 14.5 cycles. Slight deviations of the measured data points from the characteristic curve (and a higher error bar) are observed for the points at which SXPD data were collected, most probably due to the longer OCV period (relaxation of polarization effects).

Figure 1B shows the mean voltage integrated over the amount of exchanged charges from Cell1 and Cell2 and from Cell3 and Cell4 upon cycling. Although the capacity is highly affected by the temperature, the mean voltage is not. It is noteworthy that the mean charge voltage stays relatively constant after the first ~30 cycles, while the discharge voltage decreases about 1 mV per cycle, indicating an asymmetric evolution of the overpotentials during charge and discharge. Therefore, a simple surface-related degradation mechanism (e.g., an impedance increase due to surface film formation), which would block both lithiation and delithiation of HE-NCM to the same extent, can be excluded as the only reason for the observed capacity and voltage fade. For a better understanding and identification of the origin of this asymmetric increase of the charge/discharge overpotentials, Figure 2 shows the differential capacity vs electrode potential (dq/dV) upon cycling. The main process leading to voltage and capacity fade in the discharge is the reduction peak at ca. 3.8 V (negative dq/dV values), shifted toward lower potentials and decreasing in intensity upon cycling. Additionally to this prominent change, new peaks appear, change their shape or shift to lower voltages in the discharge and charge.

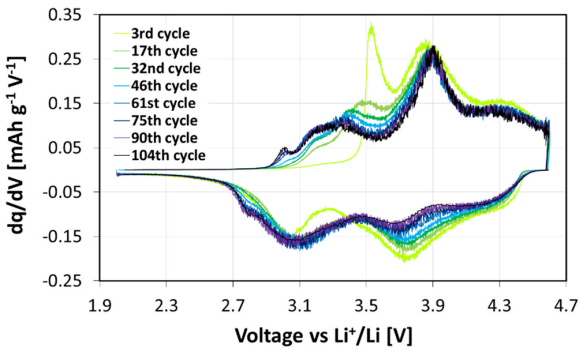

Figure 2. Evolution of the differential capacity as a function of the voltage (HE-NCM vs Li^+/Li) over the course of 104 cycles at C/5. The data were taken from Cell1 (cycles 1−49) and Cell3 (cycles 50−105) always at the second cycle after the SXPD data collection. The cycling data of Cell2 and Cell4 are analogous. The second cycle after each measurement is shown due to larger deviations of the cells in the cycle in which powder diffraction data were taken.

Although some literature studies claim that the individual dq/dV peaks can be assigned to transition-metal (TM) oxidation/reduction, there are some contradicting arguments. With TM near edge absorption spectroscopy (NEXAFS, TM L-edge) it was shown, for example, that the only redox active TM in layered oxides (structurally related to HE-NCM) is nickel, although the dq/dV plot shows two or even more peaks.[27,28] In the same literature, collecting NEXAFS data also on the oxygen K-edge, it was deduced that the redox process occurs via the oxidation of nickel and oxygen at the same time (electrons are taken out of or put into TM-oxygen hybrid orbitals) instead of considering independent redox couples.[27] Without a first activation cycle (end of charge voltage <4.5 V), the electrochemical performance of HE-NCM is comparable (in terms of cycling stability, voltage vs capacity plots, dq/dV-plots, etc.) to that of conventional layered oxides.[4] In this case, the dq/dV-peaks at 3.8 V (discharge) and 3.9 V (charge) shown in Figure 2 are still observed, while the peaks at lower voltages are missing. Therefore, it can be inferred that the process related to the peaks at high voltages belongs to the oxidation/reduction of nickel−oxygen hybrid orbitals (like it is the case in conventional layered oxides), which will be investigated in further NEXAFS studies.

Synchrotron Powder Diffraction Measurements. Background. The present SXPD study aims to understand how the transition-metal (TM) migration progresses in HE-NCM and how it is related to capacity and voltage decay of the cathode material in lithium-ion batteries. Although this relationship is poorly understood up to now, the tendency of some layered oxides to form disordered structures is well-known in literature.[29−31] In highly delithiated (charged) states (Figure 3A), TMs tend to occupy tetrahedral sites in the lithium layer (Figure 3B). The energy barrier for this migration is lower in the charged compared to the discharged state because the neighboring octahedral lithium sites are empty.[19,32] The occupation of tetrahedral sites in the TM layer is less favorable because all neighboring octahedral sites are occupied by cationic species. A TM in tetrahedral sites of the Li-layer can either move back or move to and occupy octahedral lithium sites (Figure 3C). A delithiated, disordered structure as in Figure 3C is thermodynamically more stable; thus, such a migration is energetically favorable.[33] Moreover, such a

DOI: 10.1021/acs.chemmater.8b00163
Chem. Mater. 2018, 30, 3656−3667

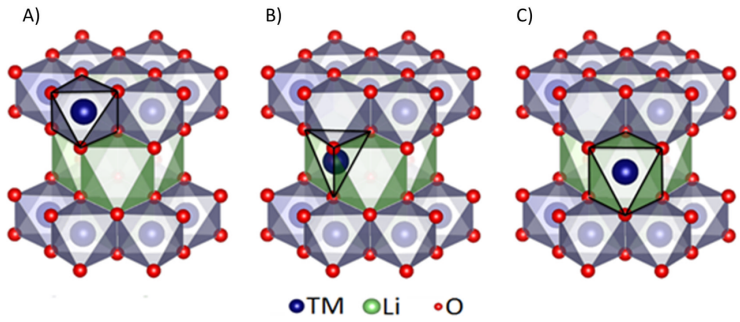

Figure 3. Schematic illustration of transition-metal migration in layered oxides. The transition metals can move from octahedral sites in the transition-metal layer (A) via tetrahedral sites in the lithium layer (B) into octahedral sites in the lithium layer (C).

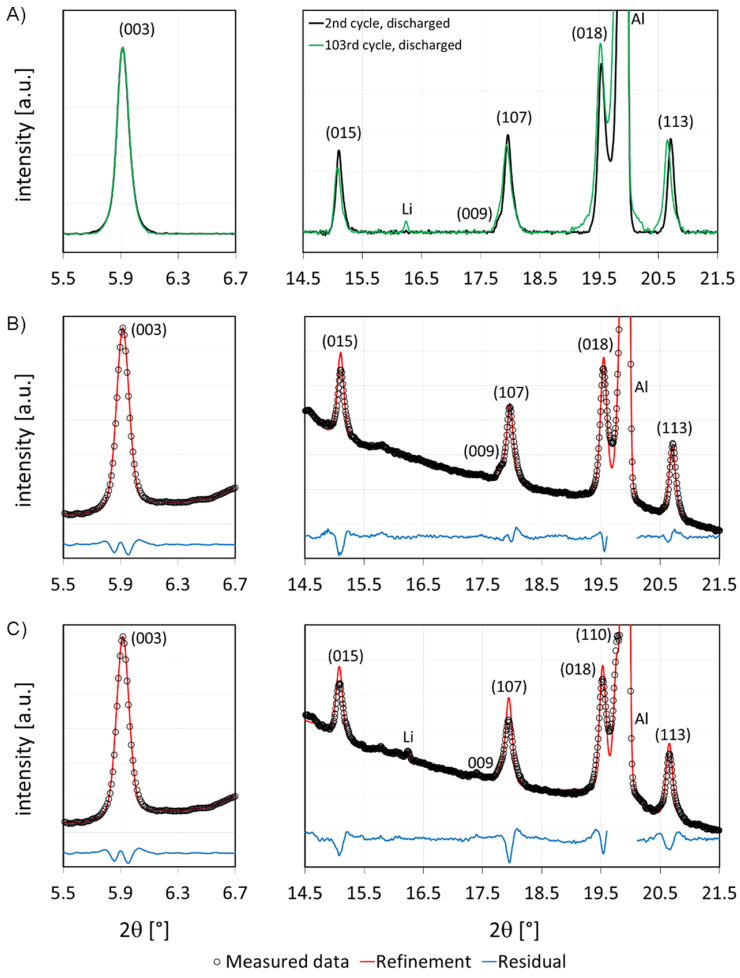

Figure 4. (A) Background corrected and (003)-reflection normalized SXPD patterns (λ = 0.496 Å), measured after the 1st (black line) and 103rd (green line) cycle. (B and C) Corresponding refinements of the patterns after the 1st and the 103rd cycle, performed with a $R\bar{3}m$ structure.

disordered structure may tend to release oxygen, especially in the case of nickel-rich layered oxides.[12]

According to theoretical calculations, lithium-rich layered oxides tend also to form disordered structures upon cycling, like it was first shown by Van der Ven et al. for $Li(Ni_{0.5}Mn_{0.5})O_2$.[19,32] In contrast to conventional layered oxides, almost all lithium ions (≈90%) are deintercalated during the first charge without losing structural integrity of the material.[34] The 60 mAh g^{-1} lower capacity of the following discharge and the subsequent cycles as well as NMR studies suggest that the lithium positions in the transition-metal plane are almost not occupied anymore.[34] The vacancies left by the lithium-ions in the transition-metal plane may lower the energy

DOI: 10.1021/acs.chemmater.8b00163
Chem. Mater. 2018, 30, 3656−3667

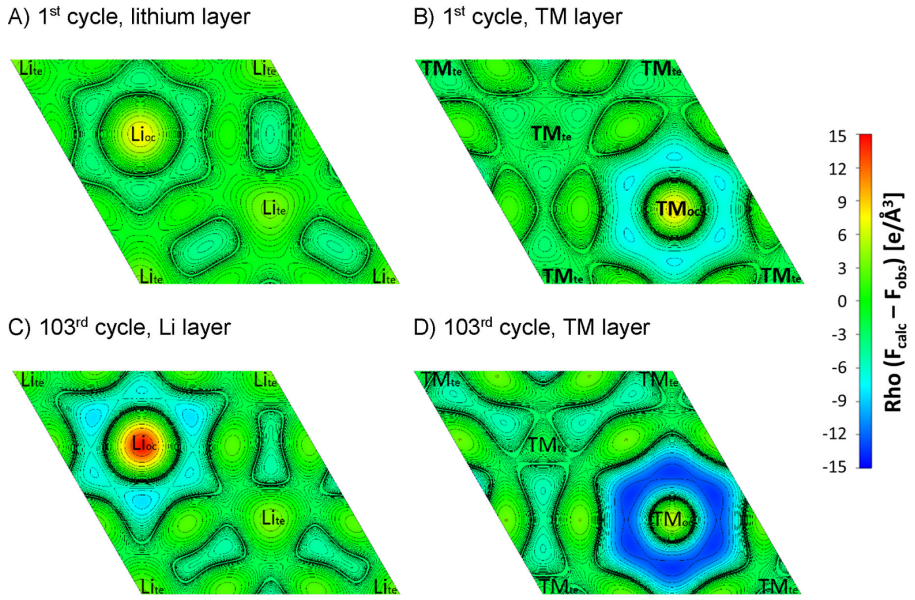

Figure 5. Difference Fourier maps of the *ab* plane of discharged HE-NCM after the 1st cycle (A and B, with *a* and *b* = 2.8791(1) Å, *c* = 14.378(2) Å) and after 103 cycles (C and D, with *a* and *b* = 2.8801(1) Å, *c* = 14.375(2) Å). The A, C and B, D projections are the Li and TM planes which are 1/6 and 1/3 of the *c*-direction in the unit cell from the origin, respectively. The positions at which the maps are taken are shown in Section S3.

barrier of the transition-metal motion[32] and therefore accelerate the formation of a more disordered structure.[19]

As HE-NCM is a layered oxide, though lithium-rich, lithium ions and transition metals occupy octahedral sites in alternating layers (rhombohedral $R\bar{3}m$ structure). Nevertheless, in HE-NCM there are lithium ions in excess which replace transition metals and break the rhombohedral symmetry, leading to a monoclinic $C2/m$ structure characterized by weak reflections at low diffraction angles. Therefore, HE-NCM is commonly refined as a composite of an overlithiated $C2/m$ and a rhombohedral $R\bar{3}m$ phase.[35] The refinement parameters of powder diffraction patterns and the obtained results for the pristine HE-NCM powder are given in Section S4. Due to a large background at low diffraction angles, introduced by the pouch foil and the electrolyte, the weak monoclinic reflections of the excess Li-ions were obscured in the case of in situ experiments (Section S4). Therefore, the HE-NCM phase was refined as a conventional layered oxide ($R\bar{3}m$ rhombohedral structure) with the Rietveld method. As described by Jiang et al., for the calculation of the occupancy of the individual sites, it was assumed that the lithium ions in the transition-metal layer were removed during the first charge, leaving vacancies which remain upon the subsequent cycling.[34] The compositions implemented in the refinement for the discharged and the charged state of HE-NCM were $Li[Ni_{0.18}Co_{0.10}Mn_{0.55}\square_{0.17}]O_2$ and $[Ni_{0.18}Co_{0.10}Mn_{0.55}\square_{0.17}]O_2$, respectively. The detailed structural parameters implemented in the refinement are given in Sections S4 and S5.

Discharged State. The main changes between the patterns measured in the discharged state are observed in the reflection intensities rather than in the reflection positions and/or in the presence/absence of reflections. Figure 4 shows background corrected and normalized SXPD data of the first and the 103rd cycle as well as the corresponding refinements B and C with an ideal rhombohedral $R\bar{3}m$ structure (for details about the refinement, see Section S5). Two 2θ ranges (5.5−6.7° and 14.5−21.5°) are shown to depict the most important information. While a minor mismatch in the refined reflection intensities of the first cycle was observed (Figure 4B), the mismatch became more significant for the 103rd cycle (Figure 4C), as can be seen for example in the reflections (015) and (107).

The discrepancy in the measured and refined reflection intensities can provide useful information if further analyzed, as it originates from the difference of the measured and calculated electron density in the crystallographic structure. The only elements in the HE-NCM structure that can cause such an effect are the TMs due to their relatively high number of electrons and thus their high contribution to the X-ray diffraction profiles. Therefore, as will be demonstrated with further refinements, the poor initial fit is caused by TMs migrating to other locations within the lattice, leading to a disordered structure. To investigate which sites are occupied to which extent by TMs in HE-NCM upon cycling, DF analysis of the diffraction data was performed because it is an established method to locate missing atoms in a crystal structure.[36] In a DF map, the electron density calculated from the structure factors of the fitting model (F_{cal}) is subtracted from the experimental structure factors (F_{obs}), and any abnormal difference corresponds to atoms missing or exceeding in the calculated model structure. The maximum resolution of the obtained difference Fourier maps can be approximated with the minimum distance of the diffracting lattice planes from Bragg's law $d_{min} = \lambda/(2 \sin \theta_{max})$ that, in our case, is $d_{min} \approx 0.7$ Å. Although this *d*-space is low compared to high-Q total scattering data, it allows to distinguish between different atoms. Furthermore, the deficient or enhanced electron density from TM disorder can be identified due to the high electronic contrast between Li and TMs. In addition, the oxygen host structure allows only four different positions for transition metals and lithium ions: the tetrahedral and octahedral sites in the lithium layer (Li_{te} and Li_{oc}) as well as in the transition-metal layer (TM_{te}, TM_{oc}).

DOI: 10.1021/acs.chemmater.8b00163
Chem. Mater. 2018, 30, 3656−3667

The DF maps of the first discharged state (Figures 5A and B) show that the electron density of octahedral sites (Li_{oc} and TM_{oc}) is apparently poorly described by the ideal rhombohedral structure. The electron density of Li_{oc} and TM_{oc} sites at a small radius around the ions position is underestimated ($F_{obs} > F_{cal}$). By increasing the radius around the TM position, the electron density becomes overestimated ($F_{obs} < F_{cal}$). The differences become even more significant for the 103rd cycle (Figures 5C and D). The changes from under- to overestimated electron densities around the octahedral sites appear to derive from the poor description of the reflection intensities. In other words, if the measured and refined intensities of the individual reflections do not match (some reflections are too high while others are too low in intensity), the scale factor of the phase is adjusted so that the deviation of the refinement and the measured data reaches a minimum. However, if the reflection intensities are not described properly, the full-width at half-maximum (FWHM) is also a compromise (to minimize the mismatch), and the observed change from over- to underestimated electron densities around the atomic positions is the consequence.

The reflection intensity mismatch (electron densities around the distinct positions) can only be ascribed to TMs which also occupy octahedral lithium sites, as discussed earlier. Therefore, any vacancy in the Li-layer generated from battery discharge can be occupied by TMs, as will be demonstrated with further refinements.

To account for the Li/TM-disorder during the Rietveld refinement of the SXPD patterns of the discharged states, the amount of nickel in octahedral TM-sites was reduced, while at the same time and to the same extent, the amount of nickel in octahedral Li-sites was increased. Although only Ni/Li disorder was considered in the refinements, it is not possible to distinguish which TM is actually migrating due to the similar number of electrons of nickel, cobalt, and manganese (the differences in the form factors are too low). Figure 6 shows the evolution of the occupation of Li_{oc} sites by TMs upon cycling. The fraction of nickel in octahedral lithium sites was calculated by dividing the amount of nickel in octahedral lithium sites by the total amount of TMs in the HE-NCM structure. The improved refinements can be observed by comparing Figure 7 and Figure 4, while the refinement results, including the R_{Bragg} values, are given in Section S6.

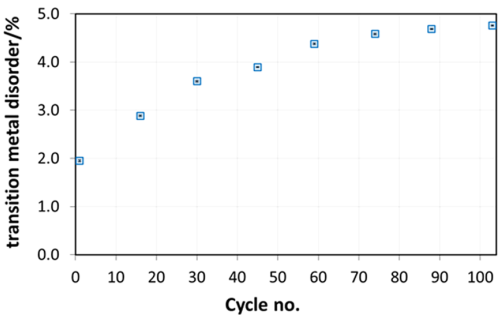

Figure 6. Fraction of the transition metals in octahedral lithium sites over the course of 104 cycles, determined from refinements of SXPD patterns in the discharged state. Cycle zero represents pristine HE-NCM.

According to the results, ≈2% of the transition metals move into the lithium layer during the first cycle. Such an increase of Li/TM disorder within the first cycle is not known for conventional layered oxides and therefore it supports the assumption that lithium vacancies in the TM layer (created during the first charge, the so-called activation) accelerate the transition-metal migration. During the subsequent cycles, the disorder increases more gradually, reaching a value of roughly 5% of the transition metals in Li_{oc} sites after 100 cycles. This observed increase of disorder leads to the conclusion that this kind of cationic migration is to some extent irreversible.

Considering the tetrahedral sites in the difference Fourier analysis applied to the discharged state, no mismatch in the measured and ideal electron density was found (Figure 5, tetrahedral sites Li_{te} and TM_{te}). Even if the migration of transition metals via an intermediate site is very fast (in the order of picoseconds), the difference Fourier maps should show a mismatch because they are a measure of the statistical occupation of these sites. Therefore, it can be excluded that the transition-metal motion described in Figure 3 occurs with a significant amount in the discharged state.

Charged State. The DF maps of the 1.5 and 102.5 charged states (Figure 8A and B, lithium layer) show, beside a mismatch of the measured and calculated electron density of the Li_{oc} sites (discussed in the previous sections), underestimated electron densities in Li_{te} sites (tetrahedral sites in the lithium layer). This confirms the migration of TMs via these sites in the charged state. However, areas with overestimated and underestimated electron densities in the maps are smeared out in comparison to the discharged state (Figure 5); this can be attributed to higher microstrain in the material, which leads to more severe reflection broadening in comparison to the discharged state. Such broadening is, in this case, anisotropic, as can be seen by the mismatch of the FWHM of the reflections exemplarily shown in Figure 9A (pattern of charged HE-NCM, 1.5 cycle). While the reflections (015) and (018) are described as too narrow, the refinement of other reflections such as (113) appear too broad.

To overcome the mismatch of the measured and refined patterns, the origin of reflection broadening has to be considered. The reflection broadening is a function of the crystallite size ($FWHM_{size}$) and the microstrain ($FWHM_{strain}$) within the investigated material (eq 1).[37] The particle size broadening scales with cos θ, while the microstrain scales with tan θ, as described by eq 2, where ε is the microstrain, θ the diffraction angle, K the Scherrer constant, λ the wavelength of the X-ray beam, and L the crystallite size. According to eq 3 (a variation of eq 2), the FWHM of the individual reflections times cos θ versus sin θ (the so-called Williamson–Hall plot) should give a line with a slope which describes the microstrain broadening. The intercept on the y-axis is then a measure of the apparent particle size.

$$FWHM_{tot} = FWHM_{strain} + FWHM_{size} \quad (1)$$

$$FWHM_{tot} = \varepsilon \tan\theta + \frac{K\lambda}{L\cos\theta} \quad (2)$$

$$FWHM_{tot}\cos\theta = \varepsilon \sin\theta + \frac{K\lambda}{L} \quad (3)$$

Figure 10 shows the Williamson–Hall plot of the discharged (blue circles) and charged (red squares) cells, measured after the 1st cycle and after 1.5 cycles, respectively. To have a comparison with an ideal material with isotropic broadening, the reflection profile analysis was also performed for CeO_2

DOI: 10.1021/acs.chemmater.8b00163
Chem. Mater. 2018, 30, 3656–3667

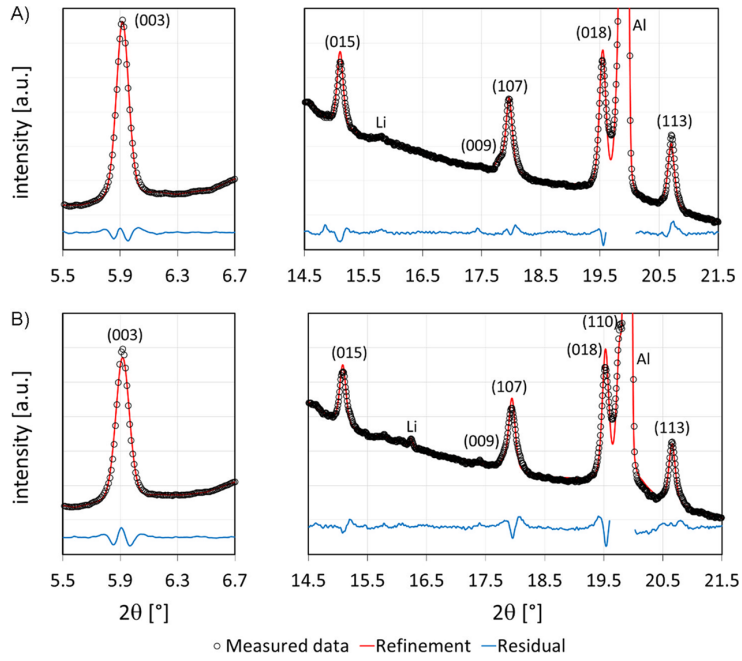

Figure 7. SXPD patterns (λ = 0.496 Å) and corresponding refinement of HE-NCM, performed with a $R\bar{3}m$ structure and the consideration of TM/Li-disorder. The diffraction patterns were measured in the discharged state of HE-NCM after the 1st (A) and 103rd cycle (B).

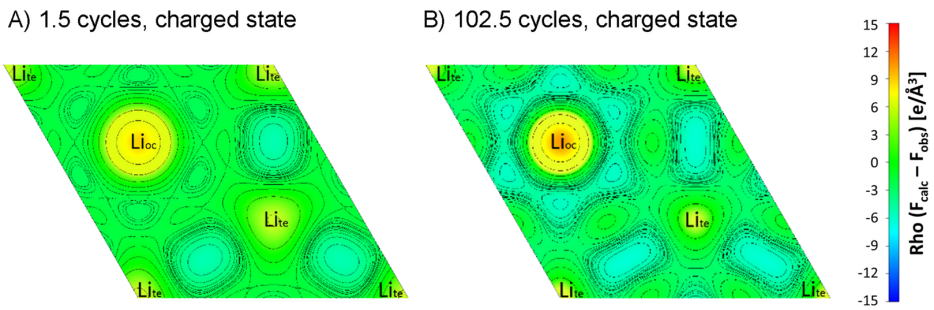

Figure 8. Difference Fourier maps of charged HE-NCM after 1.5 (A, with a and b = 2.8539(2) Å, c = 14.283(2) Å) and 102.5 cycles (B, with a and b = 2.8142(2) Å, c = 14.283(2) Å). The selected ab planes show the lithium layer with octahedral and tetrahedral lithium sites, Li_{oc} and Li_{te}. The A and B projections lie 1/3 of the c-distance above the origin of the unit cell. The positions at which the maps are taken are shown in Section S3.

(gray triangles), a high quality powder standard (NIST SRM674b). The CeO_2 data lie on a straight line (the standard deviation of one data point from the regression line is 0.00009 $Å^{-1}$, the measurement was repeated three times) with an almost zero slope (no microstrain). The data points of the discharged HE-NCM (blue symbols) show a standard deviation of 0.001 $Å^{-1}$. This reasonably low standard deviation, however, increases by almost 1 order of magnitude (0.009 $Å^{-1}$) in the case of the charged HE-NCM (red symbols), which does not follow a Williamson−Hall behavior. Therefore, the assumption of isotropic strain cannot be made in the case of the charged material, as discussed for example by Nikolowski et al. and Kondrakov et al.[38,39] In the present case, a line between the (003) and the (009) reflection (Figure 10, red squares) would be a line with the highest slope (largest microstrain in the c or (00l)-direction). This fits in the picture that the calculated profile of reflections with large Miller indices ((015), (009), (107), (018)) appears too narrow in the refinement, while for other reflections (e.g., (113)) it appears too broad (Figure 9). Because of that, it is concluded that the microstrain in the c-direction is larger compared to the a- or b-direction. This also makes sense if structural changes upon charge (delithiation) are considered, as the stress in c-direction increases with reduced lithium content due to increasing repulsive interactions between adjacent oxygen layers.

There are several reasons which can cause anisotropic reflection broadening such as an inhomogeneous Li de/intercalation, oxygen deficient regions in the particles, or distortions. All of these effects lead to a variation in one or more structural parameters. To overcome these issues while refining the structure, it is necessary to describe the affected parameters with a distribution function rather than with a distinct value. A general anisotropic strain model implemented in FullProf was used which mathematically describes anisotropic strain broadening by using a Gaussian distribution function (see also Section S5).[40] An additional anisotropy parameter Str2 (pointing in the c-direction of the hexagonal unit cell) was refined in the present work to obtain direction-

DOI: 10.1021/acs.chemmater.8b00163
Chem. Mater. 2018, 30, 3656−3667

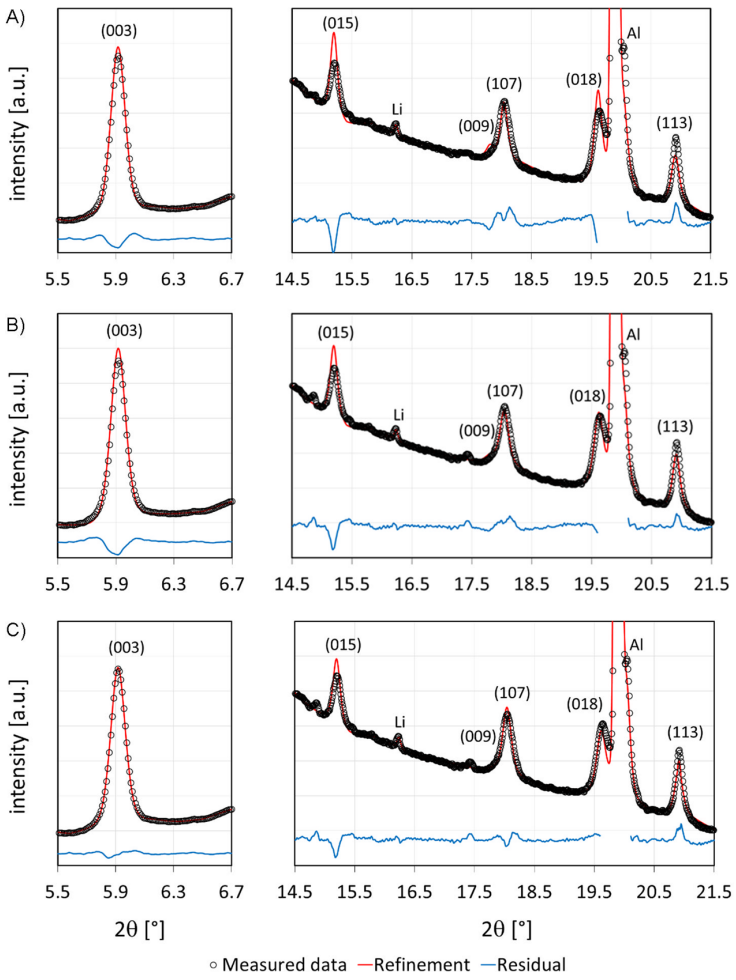

Figure 9. SXPD patterns (λ = 0.496 Å) of charged HE-NCM after 1.5 cycles, refined with an ideal rhombohedral structure (A), with a variation in the *c*-lattice parameter to account for anisotropic microstrain in the structure (B), and with partial occupancy of tetrahedral sites in the lithium layer by transition metals (C).

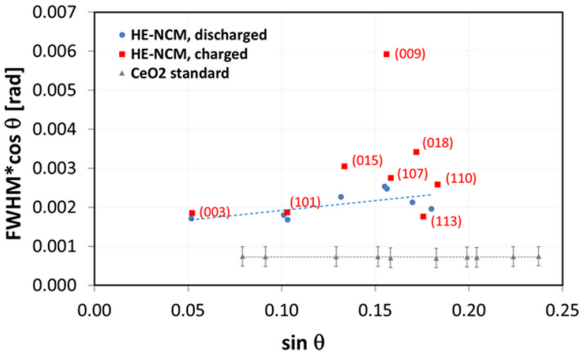

Figure 10. Williamson–Hall plot of discharged HE-NCM after the 1st cycle (blue dots) and of charged HE-NCM after 1.5 cycles (red squares). The data of CeO_2 (gray triangles) are shown for comparison.

specific reflection broadening. The improved fit (1.5 cycles, charged HE-NCM) is shown in Figure 9B. As it was deduced earlier that the migration of transition metals into octahedral lithium sites is irreversible, the occupancy obtained from the discharged state was therefore held constant while refining the anisotropic strain broadening of the reflections. For refining the occupancy of tetrahedral sites in the lithium layer, all parameters refined in the previous steps (due to anisotropic reflection broadening) were kept constant, while the occupancy and the position in the *c*-direction of the tetrahedral sites in the lithium layer were set variable. After reasonable values were obtained from this refinement (e.g., the occupancy of any crystallographic site in the lattice cannot be negative or the overall occupancy of one site cannot be higher than the overall amount of transition metals in the structure), all other parameters (excluding the ones which describe the anisotropic reflection broadening) were set variable again and refined in various steps. With these assumptions and corrections, it was possible to refine the occupancy of tetrahedral sites in the lithium plane (Figure 9C and Section S6). The amount of TMs in tetrahedral sites of the lithium layer in the charged state is shown in Figure 11. It should be emphasized that the refinement of this kind of disorder is strongly influenced by the corrections and assumptions done before (i.e., the preconditions of the refinements). Therefore, the overall uncertainty for the occupancy of tetrahedral sites in the lithium

DOI: 10.1021/acs.chemmater.8b00163
Chem. Mater. 2018, 30, 3656–3667

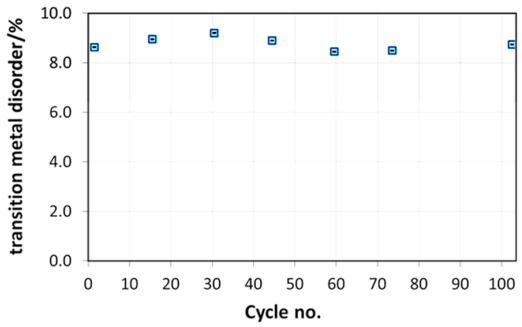

Figure 11. Occupancy of tetrahedral sites in the lithium layer by transition metals in charged HE-NCM over the course of 104 cycles. The error bars determined with Rietveld refinement are smaller than the plotted points. However, the accuracy of these data points should be poor due to the preconditions of the refinements (see main text).

layer for the charged HE-NCM is much higher than the value deduced by the refinement software. The maximum entropy method (MEM) may help to overcome these issues in future work.[41] Nevertheless, these results support the migration pathway shown in Figure 3 and suggest that transition-metal motion takes place at high states of charge (in the delithiated or charged state of HE-NCM). Because no occupation of tetrahedral sites was observed in the discharged state throughout the 100 charge/discharge cycles, the migration of TMs into tetrahedral sites has to be largely reversible. Ca. 8% of the TMs occupy tetrahedral sites in the charged state. At the end of discharge, 2−5% of the TMs are refined to be in octahedral Li-sites, while the tetrahedral sites are unoccupied. This strongly suggests that 3−6% of the TMs migrate reversibly back from tetrahedral sites into octahedral TM sites upon delithiation.

DISCUSSION

Several TEM studies revealed severe structural changes upon cycling (especially upon the first charge)[14,34,42] which are hardly visible with powder diffraction. Inhomogeneities in the structure observed with TEM are localized in a 6 nm thick surface film around the particles[12] and the overall volume of the surface shell is too small to lead to a significant contribution to the powder diffraction patterns (bulk technique). Nevertheless, increasing anisotropic microstrain observed upon cycling confirms the presence of inhomogeneities on an atomistic scale, although the origin cannot be localized with powder diffraction. However, as mentioned in the introduction, the performance drop of the material upon cycling cannot be explained by surface effects, as such processes are mainly limited to the first cycle,[42] they cannot explain the disparate increase of charge and discharge overpotentials and would not lead to new peaks in the differential capacity plots (changes in the redox process) upon long-term cycling. To investigate the true origin of the fading mechanism it is therefore mandatory to have a closer look into the changes of the bulk structure.

In this study, the main structural change occurring in HE-NCM upon cycling is an increase of the TM/Li disorder in the discharged state, i.e. an increased occupancy of TM in octahedral sites normally occupied by Li (Figure 6). During the first activation cycle, this TM/Li disorder develops very rapidly and then increases gradually over the first 50 cycles; a less pronounced increase is observed between 50 and 100 cycles. It is also remarkable that the *c*-lattice parameter increases during the first charge only by a maximum of ∼0.11 Å at ca. 50% state of charge (SOC), after which it gradually decreases until at ca. 100% SOC it reaches a value which is ∼0.07 Å above its initial value (see Figure 12A). This is in

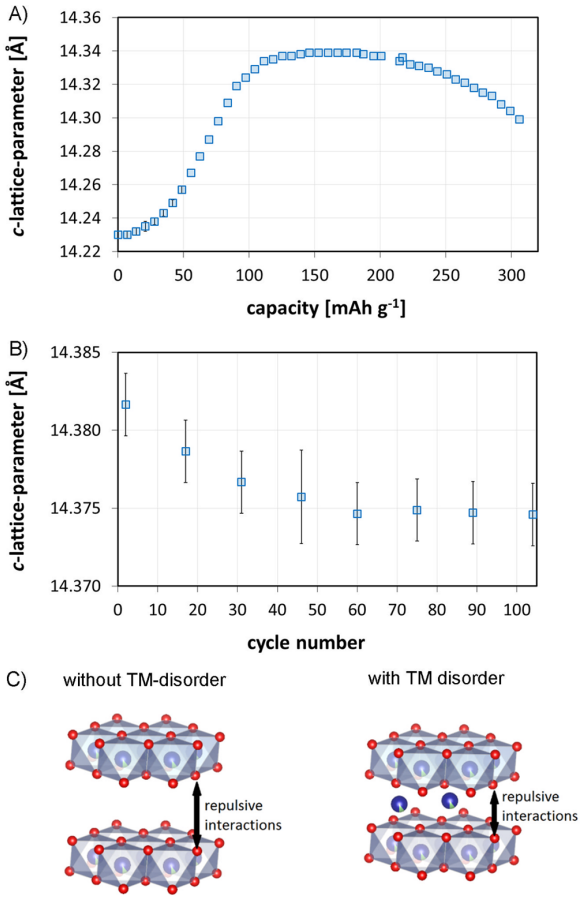

Figure 12. (A) Evolution of the *c*-lattice parameter upon the 1st charge and (B) of discharged HE-NCM during subsequent cycling from the 1st to the 104th cycle. Data in panel A were measured with the PSD (data collection was interrupted leading to the gap at 210 mAh g^{-1} due to apparatus and circuitry checks) while those in panel B were obtained from the LDE 2D detector. A schematic illustration of repulsive interactions without and with TM-disorder is presented in panel C. The lattice expands in *c*-direction during delithiation due to repulsive interactions of oxygen atoms from opposite TM layers. In the case of TMs in Li sites, these repulsive interactions are reduced.

strong contrast to what has been observed for the so-called NCM111 ($Li[Ni_{1/3}Co_{1/3}Mn_{1/3}]O_2$), where the *c*-lattice parameter starts at the same value and reaches a ca. 0.3 Å higher value at its maximum at ca. 55% SOC, thus experiencing a roughly three times higher expansion.[43] Because the *c*-axis is perpendicular to both Li and TM layers, the milder variation of the *c*-lattice parameter can be likely correlated with the migration of TMs to the Li octahedral and tetrahedral sites during the charging process, which decreases the repulsive interaction between the TM−oxygen layers (see Figure 12C) at high levels of Li^+ deintercalation (high SOC). This correlation is confirmed by the trend of the *c*-lattice parameter upon

DOI: 10.1021/acs.chemmater.8b00163
Chem. Mater. 2018, 30, 3656−3667

cycling (Figure 12B) that replicates the trend of the TM/Li disorder (Figure 6). The lithium content in the discharged state decreases upon cycling from $x = 1.210 \pm 0.005$ (pristine) over $x = 1.107 \pm 0.001$ (1st cycle) to $x = 1.022 \pm 0.007$ (30th cycle) in Li_xMeO_2, determined with inductively coupled plasma optical emission spectroscopy. Although this should lead to an increase in the *c*-lattice parameter of the discharged material upon cycling, the lattice shrinks in *c*-direction with an increasing number of cycles (Figure 12B), which we believe is a manifestation of the reduced repulsion between the Li and the TM layers due to the increased number of TMs in octahedral Li sites. Note the difference between the two sets of lattice parameters in Figures 12A and B is due to the differences in the occupation of TM-octahedral sites by Li before and after the first cycle.

What behaves differently between charge and discharge upon cycling is the occupancy of tetrahedral sites by TMs, which occurs only in the charged state. It is refined to be at a constant value of ≈8% in the charged state over the course of 100 cycles, whereby we assumed that the TM occupancy of the octahedral sites in the Li layer remains exactly the same as in the corresponding discharged state. The thus deduced absence of TMs in tetrahedral sites of the lithium layer in the discharged state suggests that TM migration into tetrahedral sites occurs at high states of charge of the HE-NCM material. A different trend between charge and discharge is also evident in the voltage decay upon cycling (Figure 1B), which is nearly absent after the first 15 cycles for the averaged charge voltage, while the averaged discharge voltage decreases continuously over cycling. To show a possible correlation between mean charge and discharge voltage and TM/Li disorder (i.e., the TM occupation of octahedral Li-layer sites), the mean discharge voltages versus the TM/Li disorder are plotted in Figure 13.

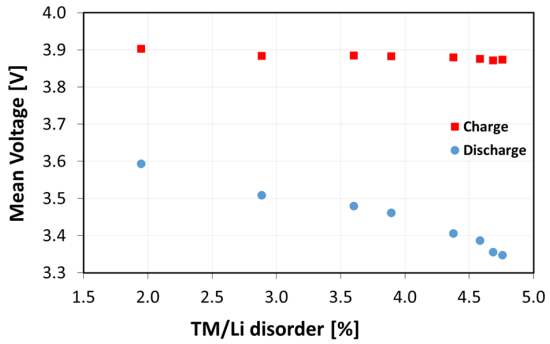

Figure 13. Mean charge (red squares) and discharge voltage (blue circles), integrated over the exchanged amount of charges, versus TM/Li-disorder (TM occupation in octahedral sites of the Li-layer), as determined with Rietveld refinement of SXPD patterns in discharged state of HE-NCM.

Except for the first cycle, the mean charge voltage (Figure 13, red squares) decreases very mildly with the degree of TM/Li disorder and can therefore be considered only weakly correlated with TM/Li disorder. In contrast, the mean discharge voltage (Figure 13, blue circles) seems to be more strongly correlated to the TM/Li disorder and decreases with increasing disorder. As a note of caution, we need to state that this correlation does not necessarily imply a causation, even though we believe that a causal relationship between these two observables is likely and has already been postulated in the literature.[4]

Understanding whether the origin of the mean voltage decay is due to a change of kinetic or thermodynamic properties of the material (or a combination of the two) goes beyond the purpose of this study. Nevertheless, a discussion of the possible effects can be provided. The presence of TMs in the octahedral Li sites surely could cause a kinetic hindrance in Li-ion (de)intercalation (as evident from the Li-ion path).[44] However, this should happen in both charge and discharge, and one would expect an increase of the mean charge voltage and a decrease of the mean discharge voltage over the course of extended cycling, which is not observed. Thus, if a pure kinetic effect were to be postulated, an inhomogeneous intercalation/deintercalation process would have to be invoked: for example, in the charged state, lithium deintercalation would have to be facile, while intercalation into lithium enriched regions would have to be retarded in the discharge process. On the other hand, the migration of TMs into lithium octahedral sites could also change the redox potential of Li intercalation/deintercalation, but this effect should similarly affect both charge and discharge. Thus, if a pure thermodynamic effect were to be postulated, some different and reversible TM migration must be invoked in charge and discharge. Because TM occupancy is detected in the tetrahedral sites in the charged state and not in the discharged state, a possible explanation would be the reversible migration of TMs to the tetrahedral sites upon charging, keeping the thermodynamic potential similar to the pristine material, while the growing TM occupation in the octahedral Li sites (see Figure 6) might result in a lowering of the thermodynamic discharge potential upon cycling. A mechanism similar to this is described by Croy et al.,[4] where they relate the reversible migration of disordered Ni between alternating layers during charge and discharge, varying the energy and position of the sites available for Li during cycling, evidenced by EXAFS results on Ni K-edge. This is in agreement with the assumption that the main process leading to voltage and capacity fade is probably related to a partially irreversible nickel reduction (Figure 2 and following discussion). The same mechanism could also be the origin of different (de)-intercalation kinetics of the material during charge and discharge. A combination of kinetic (higher hysteresis, i.e. lower discharge/higher charge voltage) and thermodynamic effects (lower potential in both charge and discharge) can also be an explanation of a decreased mean discharge voltage and a rough stability of the mean charge voltage upon cycling.

Besides this, cationic disorder may explain the outstanding capacity of HE-NCM. It is likely that the increasing Li/TM disorder is accompanied by a decrease of the repulsive interactions between adjacent oxygen layers (Figure 12C), leading to a lower expansion of the material in *c*-direction (Figure 12A) and a stabilization of the material upon deintercalation. Therefore, it is reasonable to assume that more Li ions can be extracted compared to conventional layered oxides before the host structure starts to decompose irreversibly.

■ CONCLUSIONS

In this contribution, we experimentally demonstrated for the first time that the transition-metal migration in lithium-rich layered oxides proceeds upon cycling from the octahedral transition-metal sites via tetrahedral sites in the lithium layer into octahedral lithium sites. These results were up to now

DOI: 10.1021/acs.chemmater.8b00163
Chem. Mater. 2018, 30, 3656−3667

claimed only by theoretical investigations. TMs move nearly reversibly between its octahedral sites and the tetrahedral sites in the Li-layer, reaching an occupancy of ca. 8% at 100% SOC and 0% at 0% SOC, which remains unchanged over the course of cycling. Furthermore, TMs move gradually and irreversibly from tetrahedral to octahedral Li-sites because a continuous increase of TMs in octahedral Li-sites (from 2% in the first cycle to ≈5% after 100 cycles) was observed. TM/Li disorder may reduce microstrain in the charged state of HE-NCM and therefore allows a higher degree of delithiation (higher reversible capacity) but it probably leads to a poor cycling stability. Further investigations are necessary to show whether the origin of the poor cycling stability has kinetic or thermodynamic reasons, which will also point out the correlation of TM/Li disorder and the performance drop more clearly. Because both the reversible capacity and the cycling stability seem to be affected by TM/Li disorder, future investigations have to focus on how transition-metal motion can become completely reversible to ensure a high capacity retention during cycling rather than keeping the ideal rhombohedral structure and suppress disorder.

■ ASSOCIATED CONTENT

Supporting Information

The Supporting Information is available free of charge on the ACS Publications website at DOI: 10.1021/acs.chemmater.8b00163.

Outline of pouch cell holder, additional cycling data, additional information about the Fourier transform maps, Refinement of Li-rich layered oxides, quality and reliability of the refinements, and further results of Rietveld refinements (PDF)

■ AUTHOR INFORMATION

Corresponding Author

*E-mail: karin.kleiner@diamond.ac.uk.

ORCID

Karin Kleiner: 0000-0003-0203-440X

Hubert A. Gasteiger: 0000-0001-8199-8703

Notes

The authors declare no competing financial interest.

■ ACKNOWLEDGMENTS

Financial support by the BASF SE through its Network on Electrochemistry and Batteries is gratefully acknowledged. We thank Diamond Light Source for the provision of beamtime (EE14552, EE15348) and financial support. Our thanks are extended to Jonathan Potter and Stuart Gurney for their technical support.

■ REFERENCES

(1) Thackeray, M. M.; Wolverton, C.; Isaacs, E. D. Electrical Energy Storage for Transportation—approaching the Limits Of, and Going Beyond, Lithium-Ion Batteries. *Energy Environ. Sci.* **2012**, *5*, 7854–7863.

(2) Andre, D.; Kim, S.-J.; Lamp, P.; Lux, S. F.; Maglia, F.; Paschos, O.; Stiaszny, B. Future Generations of Cathode Materials: An Automotive Industry Perspective. *J. Mater. Chem. A* **2015**, *3*, 6709–6732.

(3) Myung, S.-T.; Maglia, F.; Park, K.-J.; Yoon, C. S.; Lamp, P.; Kim, S.-J.; Sun, Y.-K. Nickel-Rich Layered Cathode Materials for Automotive Lithium-Ion Batteries: Achievements and Perspectives. *ACS Energy Lett.* **2017**, *2*, 196–223.

(4) Croy, J. R.; Gallagher, K. G.; Balasubramanian, M.; Chen, Z.; Ren, Y.; Kim, D.; Kang, S.-H.; Dees, D. W.; Thackeray, M. M. Examining Hysteresis in Composite $xLi_2MnO_3\cdot(1-x)LiMO_2$ Cathode Structures. *J. Phys. Chem. C* **2013**, *117*, 6525–6536.

(5) Xiang, X.; Li, W. Significant Influence of Insufficient Lithium on Electrochemical Performance of Lithium-Rich Layered Oxide Cathodes for Lithium Ion Batteries. *Electrochim. Acta* **2014**, *133*, 422–427.

(6) Rozier, P.; Tarascon, J. M. Review—Li-Rich Layered Oxide Cathodes for Next-Generation Li-Ion Batteries: Chances and Challenges. *J. Electrochem. Soc.* **2015**, *162*, A2490–A2499.

(7) Deng, Z. Q.; Manthiram, A. Influence of Cationic Substitutions on the Oxygen Loss and Reversible Capacity of Lithium-Rich Layered Oxide Cathodes. *J. Phys. Chem. C* **2011**, *115*, 7097–7103.

(8) Lu, Z.; Dahn, J. R. Structure and Electrochemistry of Layered $Li[Cr_xLi_{(1/3-x/3)}Mn_{(2/3-2x/3)}]O_2$. *J. Electrochem. Soc.* **2002**, *149*, A1454–A1459.

(9) La Mantia, F.; Rosciano, F.; Tran, N.; Novák, P. Direct Evidence of Oxygen Evolution from $Li_{1+x}(Ni_{1/3}Mn_{1/3}Co_{1/3})_{1-X}O_2$ at High Potentials. *J. Appl. Electrochem.* **2008**, *38*, 893–896.

(10) Armstrong, A. R.; Holzapfel, M.; Novak, P.; Kang, S.; Thackeray, M. M.; Bruce, P. G.; Johnson, C. S. Demonstrating Oxygen Loss and Associated Structural Reorganization in the Lithium Battery Cathode $Li[Ni_{0.2}Li_{0.2}Mn_{0.6}]O_2$. *J. Am. Chem. Soc.* **2006**, *128*, 8694–8698.

(11) Yan, P.; Xiao, L.; Zheng, J.; Zhou, Y.; He, Y.; Zu, X.; Mao, S. X.; Xiao, J.; Gao, F.; Zhang, J.-G.; Wang, C.-M. Probing the Degradation Mechanism of Li_2MnO_3 Cathode for Li-Ion Batteries. *Chem. Mater.* **2015**, *27*, 975–982.

(12) Strehle, B.; Kleiner, K.; Jung, R.; Chesneau, F.; Mendez, M.; Gasteiger, H. A.; Piana, M. The Role of Oxygen Release from Li- and Mn-Rich Layered Oxides during the First Cycles Investigated by On-Line Electrochemical Mass Spectrometry. *J. Electrochem. Soc.* **2017**, *164*, A400–A406.

(13) Genevois, C.; Koga, H.; Croguennec, L.; Ménétrier, M.; Delmas, C.; Weill, F. Insight into the Atomic Structure of Cycled Lithium-Rich Layered Oxide $Li_{1.20}Mn_{0.54}Co_{0.13}Ni_{0.13}O_2$ Using HAADF STEM and Electron Nanodiffraction. *J. Phys. Chem. C* **2015**, *119*, 75–83.

(14) Xu, B.; Fell, C. R.; Chi, M.; Meng, Y. S. Identifying Surface Structural Changes in Layered Li-Excess Nickel Manganese Oxides in High Voltage Lithium Ion Batteries: A Joint Experimental and Theoretical Study. *Energy Environ. Sci.* **2011**, *4*, 2223–2233.

(15) Jiang, M.; Key, B.; Meng, Y. S.; Grey, C. P. Electrochemical and Structural Study of the Layered, "Li-Excess" Lithium-Ion Battery Electrode Material $Li[Li_{1/9}Ni_{1/3}Mn_{5/9}]O_2$. *Chem. Mater.* **2009**, *21*, 2733–2745.

(16) Manthiram, A.; Knight, J. C.; Myung, S.-T.; Oh, S.-M.; Sun, Y.-K. Nickel-Rich and Lithium-Rich Layered Oxide Cathodes: Progress and Perspectives. *Adv. Energy Mater.* **2016**, *6*, 1501010.

(17) Liu, H.; Fell, C. R.; An, K.; Cai, L.; Meng, Y. S. In-Situ Neutron Diffraction Study of the $xLi_2MnO_3\cdot(1 - X)LiMO_2$ (x = 0, 0.5; M = Ni, Mn, Co) Layered Oxide Compounds during Electrochemical Cycling. *J. Power Sources* **2013**, *240*, 772–778.

(18) Koga, H.; Croguennec, L.; Ménétrier, M.; Mannessiez, P.; Weill, F.; Delmas, C.; Belin, S. Operando X-Ray Absorption Study of the Redox Processes Involved upon Cycling of the Li-Rich Layered Oxide $Li_{1.20}Mn_{0.54}Co_{0.13}Ni_{0.13}O_2$ in Li Ion Batteries. *J. Phys. Chem. C* **2014**, *118*, 5700–5709.

(19) Bréger, J.; Jiang, M.; Dupré, N.; Meng, Y. S.; Shao-Horn, Y.; Ceder, G.; Grey, C. P. High-Resolution X-Ray Diffraction, DIFFaX, NMR and First Principles Study of Disorder in the Li_2MnO_3-$Li[Ni_{1/2}Mn_{1/2}]O_2$ Solid Solution. *J. Solid State Chem.* **2005**, *178*, 2575–2585.

(20) Thompson, S. P.; Parker, J. E.; Marchal, J.; Potter, J.; Birt, A.; Yuan, F.; Fearn, R. D.; Lennie, A. R.; Street, S. R.; Tang, C. C. Fast X-Ray Powder Diffraction on I11 at Diamond. *J. Synchrotron Radiat.* **2011**, *18*, 637–648.

DOI: 10.1021/acs.chemmater.8b00163
Chem. Mater. 2018, 30, 3656–3667

(21) Murray, C. A.; Potter, J.; Day, S. J.; Baker, A. R.; Thompson, S. P.; Kelly, J.; Morris, C. G.; Yang, S.; Tang, C. C. New Synchrotron Powder Diffraction Facility for Long-Duration Experiments. *J. Appl. Crystallogr.* **2017**, *50*, 172−183.
(22) Basham, M.; Filik, J.; Wharmby, M. T.; Chang, P. C. Y.; El Kassaby, B.; Gerring, M.; Aishima, J.; Levik, K.; Pulford, B. C. A.; Sikharulidze, I.; Sneddon, D.; Webber, M.; Dhesi, S. S.; Maccherozzi, F.; Svensson, O.; Brockhauser, S.; Náray, G.; Ashton, A. W. Data Analysis WorkbeNch (DAWN). *J. Synchrotron Radiat.* **2015**, *22*, 853−858.
(23) Filik, J.; Ashton, A. W.; Chang, P. C. Y.; Chater, P. A.; Day, S. J.; Drakopoulos, M.; Gerring, M. W.; Hart, M. L.; Magdysyuk, O. V.; Michalik, S.; Smith, A.; Tang, C. C.; Terrill, N. J.; Wharmby, M. T.; Wilhelm, H. Processing Two-Dimensional X-Ray Diffraction and Small-Angle Scattering Data in DAWN 2. *J. Appl. Crystallogr.* **2017**, *50*, 959−966.
(24) Rodríguez-Carvajal, J. Recent Developments of the Program FULLPROF. *Commission on Powder Diffraction (IUCr) Newsletter* **2001**, *26*, 12−19.
(25) Farrugia, L. J. WinGX Suite for Small-Molecule Single-Crystal Crystallography. *J. Appl. Crystallogr.* **1999**, *32*, 837−838.
(26) Momma, K.; Izumi, F. VESTA: A Three-Dimensional Visualization System for Electronic and Structural Analysis. *J. Appl. Crystallogr.* **2008**, *41*, 653−658.
(27) Kleiner, K.; Melke, J.; Merz, M.; Jakes, P.; Nagel, P.; Schuppler, S.; Liebau, V.; Ehrenberg, H. Unraveling the Degradation Process of $LiNi_{0.8}Co_{0.15}Al_{0.05}O_2$ Electrodes in Commercial Lithium Ion Batteries by Electronic Structure Investigations. *ACS Appl. Mater. Interfaces* **2015**, *7*, 19589−19600.
(28) Montoro, L. A.; Abbate, M.; Almeida, E. C.; Rosolen, J. M. Electronic Structure of the Transition Metal Ions in $LiCoO_2$, $LiNiO_2$ and $LiCo_{0.5}Ni_{0.5}O_2$. *Chem. Phys. Lett.* **1999**, *309*, 14−18.
(29) Cai, L.; Liu, Z.; An, K.; Liang, C. Probing Li-Ni Cation Disorder in $Li_{1-x}Ni_{1+x-y}Al_yO_2$ Cathode Materials by Neutron Diffraction. *J. Electrochem. Soc.* **2012**, *159*, A924−A928.
(30) Meng, Y. S.; Ceder, G.; Grey, C. P.; Yoon, W.-S.; Jiang, M.; Bréger, J.; Shao-Horn, Y. Cation Ordering in Layered O3 Li-$[Ni_XLi_{1/3-2X/3}Mn_{2/3-X/3}]O_2$ ($0 \leq X \leq 1/2$) Compounds. *Chem. Mater.* **2005**, *17*, 2386−2394.
(31) Choi, S.; Manthiram, A. Factors Influencing the Layered to Spinel-like Phase Transition in Layered Oxide Cathodes. *J. Electrochem. Soc.* **2002**, *149*, A1157−A1163.
(32) Van der Ven, A.; Ceder, G. Ordering in $Li_x(Ni_{0.5}Mn_{0.5})O_2$ and Its Relation to Charge Capacity and Electrochemical Behavior in Rechargeable Lithium Batteries. *Electrochem. Commun.* **2004**, *6*, 1045−1050.
(33) Chang, K.; Hallstedt, B.; Music, D. Thermodynamic Description of the $LiNiO_2$−NiO_2 Pseudo-Binary System and Extrapolation to the Li(Co,Ni)O_2−(Co,Ni)O_2 System. *CALPHAD: Comput. Coupling Phase Diagrams Thermochem.* **2012**, *37*, 100−107.
(34) Jiang, M.; Key, B.; Meng, Y. S.; Grey, C. P. Electrochemical and Structural Study of the Layered, "Li-Excess" Lithium-Ion Battery Electrode Material $Li[Li_{1/9}Ni_{1/3}Mn_{5/9}]O_2$. *Chem. Mater.* **2009**, *21*, 2733−2745.
(35) Amalraj, F.; Talianker, M.; Markovsky, B.; Sharon, D.; Burlaka, L.; Shafir, G.; Zinigrad, E.; Haik, O.; Aurbach, D.; Lampert, J.; Schulz-Dobrick, M.; Garsuch, A. Study of the Lithium-Rich Integrated Compound xLi_2MnO_3 (1-x)$LiMO_2$ (X around 0.5; M = Mn, Ni, Co; 2:2:1) and Its Electrochemical Activity as Positive Electrode in Lithium Cells. *J. Electrochem. Soc.* **2013**, *160*, A324−A337.
(36) McCusker, L. B.; Von Dreele, R. B.; Cox, D. E.; Louër, D.; Scardi, P. Rietveld Refinement Guidelines. *J. Appl. Crystallogr.* **1999**, *32* (1), 36−50.
(37) Williamson, G. K.; Hall, W. H. X-Ray Line Broadening from Filed Aluminium and Wolfram. *Acta Metall.* **1953**, *1*, 22−31.
(38) Nikolowski, K. *Situ Strukturuntersuchungen an Li(Ni, Co)O_2 als Kathodenmaterial für Lithiumionenbatterien*, Ph.D Thesis, Technische Universität Darmstadt, Germany, August 2007.
(39) Kondrakov, A. O.; Schmidt, A.; Xu, J.; Geßwein, H.; Mönig, R.; Hartmann, P.; Sommer, H.; Brezesinski, T.; Janek, J. Anisotropic Lattice Strain and Mechanical Degradation of High- and Low-Nickel NCM Cathode Materials for Li-Ion Batteries. *J. Phys. Chem. C* **2017**, *121*, 3286−3294.
(40) Rodríguez-Carvajal, J.; Fernandez-Diaz, M. T.; Martinez, J. L. Neutron Diffraction Study on Structural and Magnetic Properties of La_2NiO_4. *J. Phys.: Condens. Matter* **1991**, *3*, 3215−3234.
(41) Sakata, M.; Mori, R.; Kumazawza, S.; Takata, M.; Toraya, H. Electron-Density Distribution from X-Ray Powder Data by Use of Profile Fits and the Maximum-Entropy Method. *J. Appl. Crystallogr.* **1990**, *23*, 526−534.
(42) Boulineau, A.; Simonin, L.; Colin, J.-F.; Bourbon, C.; Patoux, S. First Evidence of Manganese − Nickel Segregation and Densi Fi Cation upon Cycling in Li-Rich Layered Oxides for Lithium Batteries. *Nano Lett.* **2013**, *13*, 3857−3863.
(43) Buchberger, I.; Seidlmayer, S.; Pokharel, A.; Piana, M.; Hattendorff, J.; Kudejova, P.; Gilles, R.; Gasteiger, H. A. Aging Analysis of Graphite/$LiNi_{1/3}Mn_{1/3}Co_{1/3}O_2$ Cells Using XRD, PGAA, and AC Impedance. *J. Electrochem. Soc.* **2015**, *162*, A2737−A2746.
(44) Van der Ven, A.; Ceder, G. Lithium Diffusion Mechanisms in Layered Intercalation Compounds. *J. Power Sources* **2001**, *97*−*98*, 529−531.

DOI: 10.1021/acs.chemmater.8b00163
Chem. Mater. 2018, 30, 3656−3667

SUPPORTING INFORMTION

Origin of high capacity and poor cycling stability of Li-rich layered oxides - A long-duration *in situ* synchrotron powder diffraction study

Karin Kleiner[a,b,*], Benjamin Strehle[a], Annabelle R. Baker[b], Sarah J. Day[b], Chiu C. Tang[b], Irmgard Buchberger[a], Frederick-Francois Chesneau[c], Hubert A. Gasteiger[a], Michele Piana[a]

a) Chair of Technical Electrochemistry, Department of Chemistry and Catalysis Research Center, Technical University of Munich, D-85748 Garching, Germany; b) Diamond Light Source, Harwell Science and Innovation Campus, Didcot, Oxfordshire OX11 0DE, UK; c) BASF SE, GCN/EE - M311, D-67056 Ludwigshafen, Germany.

1

S1. Pouch cell holder

Due to gassing of HE-NCM upon cycling, the use of an uncompressed pouch cell was not possible; therefore a compression tool (Supporting Figure 1) was built to ensure the reproducibility and stability of the cycling performance. A schematic drawing of the basic elements (the compression plates) is given in Supporting Figure 2.

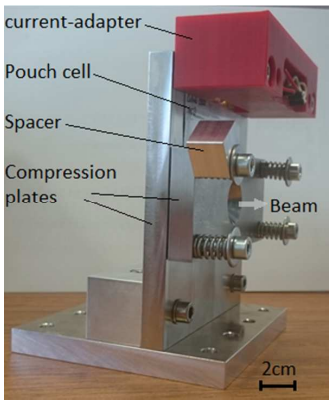

Supporting Figure 1: Pouch cell holder which ensures a homogeneous compression upon cycling.

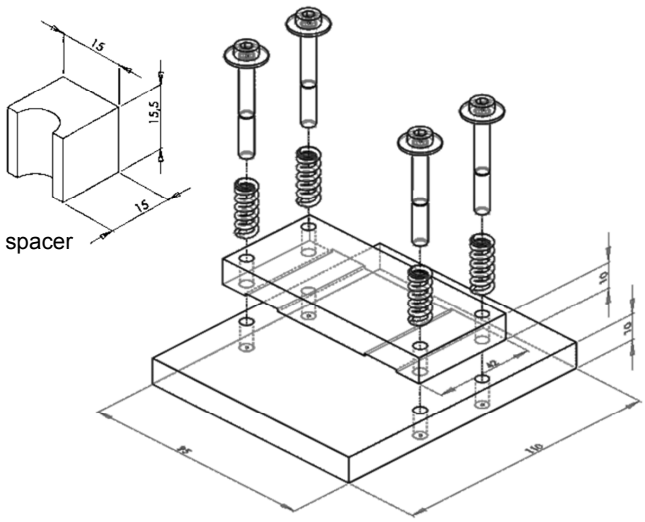

Supporting Figure 2: Drawing of steel-plates ensuring homogenous compression of the pouch cell. In the left upper corner, a spacer is shown with which the compression of the plates is adjusted.

A spacer (upper left corner, Supporting Figure 2) is used to tighten the screws and to ensure a reproducible compression of the pouch cells of 2 bar. A hole (1.5 mm in diameter)

2

through the plates and a cone shaped opening towards the synchrotron X-ray-detector (in the direction of the beam, Supporting Figure 1) allows the X-ray beam to be diffracted by the cell and the SXPD measurements to be collected.

S2. Cycling data

Supporting Figure 3 shows the cycling data of the tested pouch cells. Cell1 and Cell2 were started at the I11 beamline (Diamond Light Source, UK) where the temperature was 22 °C. Due to synchrotron maintenance, Cell1 and Cell2 were then stopped and replaced after maintenance with Cell3 and Cell4, cycled for the first 49 cycles in a climatic chamber (25 °C) at the Chair of Technical Electrochemistry (TEC) at the Technical University of Munich and then brought to the I11 beamline to be restarted.

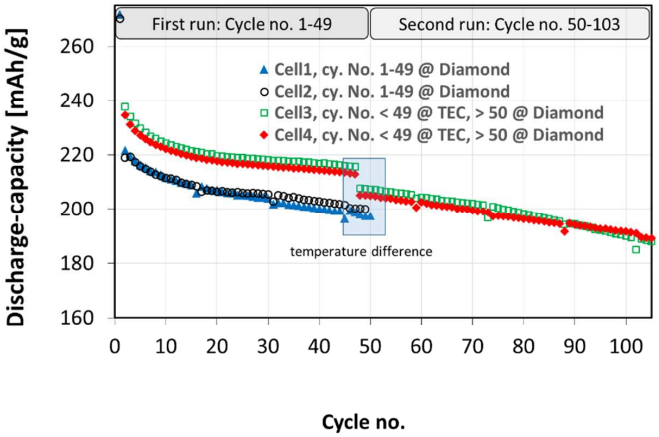

Supporting Figure 3: Variation upon cycling of the specific discharge capacity of the tested cells. Cell1 and Cell2 were cycled at the I11 beamline (Diamond Light Source) at ≈22 °C from the first up to the 49th cycle. Cell3 and Cell4 were cycled at the Chair of Technical Electrochemistry (TEC) at 25 °C for the first 49 cycles and then were stopped and restarted at the I11 beamline.

Cell 5 (Supporting Figure 4, blue triangles) was cycled at 25 °C with C/5 for 15 cycles and then the temperature was decreased to 22°C. After this, Cell5 showed a similar drop in the capacity (about 5 mAh g^{-1}) as observed for Cell3/4 at the point, at which they were stopped at TEC and restarted at I11 (Supporting Figure 3, red diamonds and green squares). Since

the temperature at TEC is 25°C and at I11 it is 22°C, the capacity drop of Cell3/4 can be attributed to the difference in temperature, which seems to remarkably influence the kinetics. Cell1/2 (Supporting Figure 3, black circles and blue triangles) show an even lower capacity from the first cycle on, most probably due to the lower temperature at I11 (kinetic of the material).

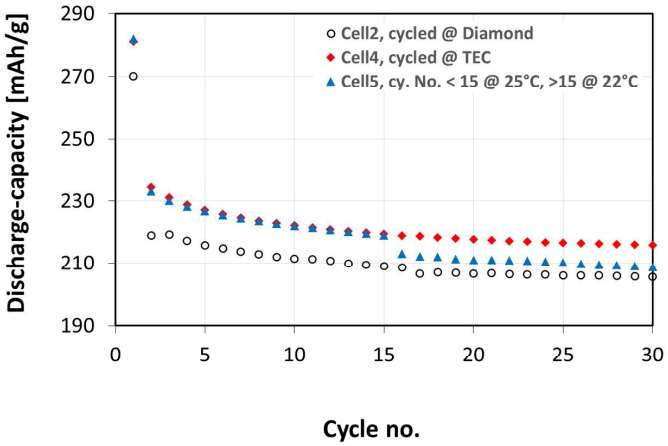

Supporting Figure 4: Comparison of the discharge capacity of a pouch cell cycled for the first 15 cycles at 25°C and then for an additional 15 cycles at 22°C (blue triangles) with a cell cycled at 25°C at TEC (red diamonds) and at 22 °C at I11 (Diamond Light Source, UK).

S3. Position of Fourier Transform maps

Supporting Figure 5 shows the planes in the rhombohedral unit cell of HE-NCM, where Fourier transform maps are taken from. For the calculation of the DF-maps all tetrahedral and octahedral sites in the structure were included. Thereby, the occupancy of the tetrahedral sites, which are not occupied in the model structure, was set to zero.

4

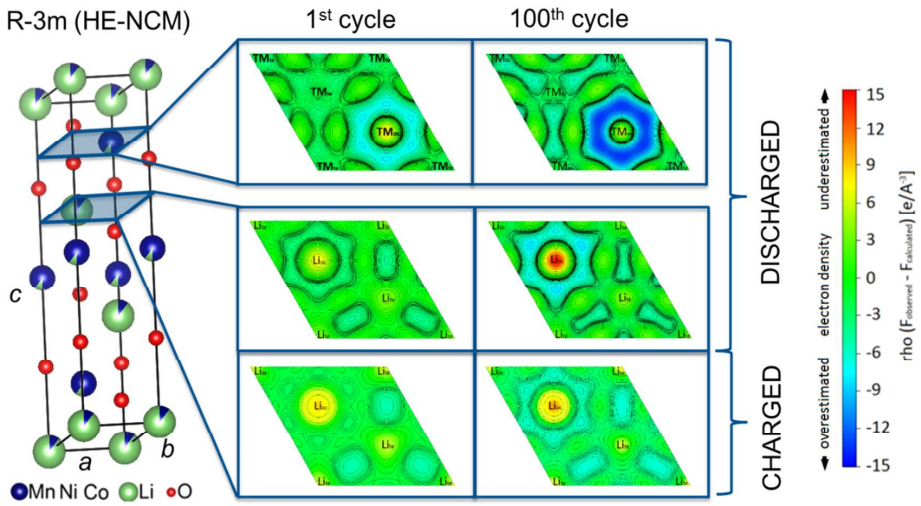

Supporting Figure 5: Rhombohedral unit cell of HE-NCM and a sketch describing the planes for which the Fourier-transform maps discussed in the main text were determined.

S4. Refinement of Li-rich layered oxides

HE-NCM is structurally related to the $R\bar{3}m$ layered oxides (Supporting Figure 6A and D), in which lithium ions and transition metals occupy oxygen octahedra in alternating layers. However, in HE-NCM excess Li ions replace transition metals forming a honey comb ordering in the transition metal planes, breaking the rhombohedral symmetry down to a monoclinic $C2/m$ structure (Supporting Figure 6B, E and F). Supporting Figure 7 shows powder diffraction patterns of pristine HE-NCM (0.5 mm capillary), measured with a Mo $K\alpha_1$ STOE diffractometer (λ=0.709300 Å, 0.015°-steps, 35 s/step) in Debye-Scherrer geometry. The less-ordered structure causes additional weak reflections at around 7° (2θ) in the powder diffraction pattern, Supporting Figure 7A. Therefore the pattern cannot be completely refined with an ideal rhombohedral $R\bar{3}m$-structure.

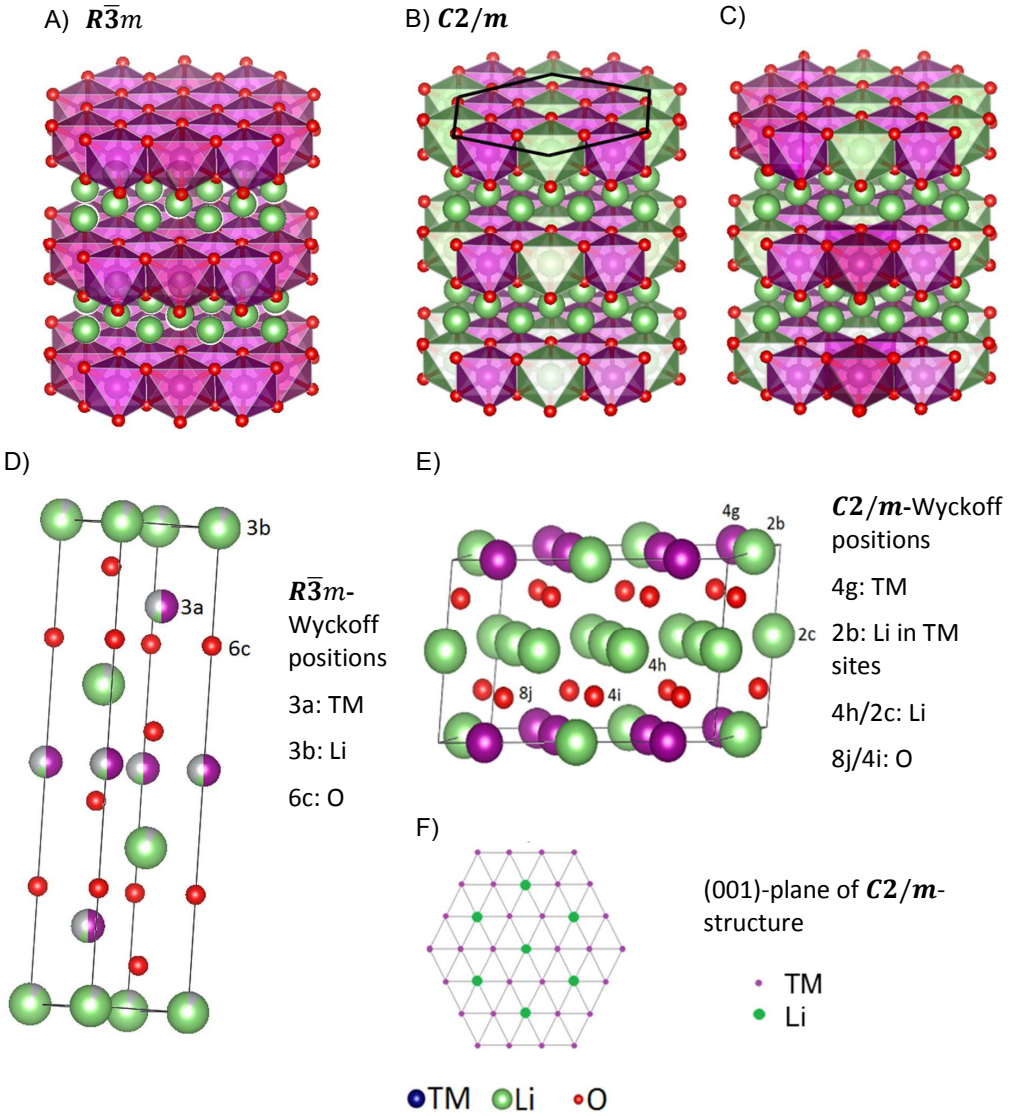

Supporting Figure 6: $R\bar{3}m$ (A), $C2/m$ (B) and disordered structure (C), depicting the difference between conventional layered oxides and lithium rich materials (HE-NCM). (D) and (E) shows the rhombohedral $R\bar{3}m$ and the monoclinic $C2/m$ unit cell while (F) depicts the Li-ordering in the transition metal plane of the monoclinic structure. Thereby, TM means transition metal (Ni, Co or Mn).

The refinement with an ideal monoclinic structure $C2/m$ is shown in Supporting Figure 7B. Because not every third transition metal is replaced by lithium as indicated in Supporting Figure 6C, the reflection intensities are poorly described. Either it has to be assumed that some Li-sites in the transition metal plane (2b sites, monoclinic structure) are occupied by TM (in this case we used Mn) as well (see Supporting Figure 7C) or the pattern has to be

refined as a composite of a conventional layered oxide ($R\bar{3}m$ structure) and a lithium-rich material ($C2/m$ structure), see Supporting Figure 7D. Both refinements lead to similar results since powder diffraction is a bulk sensitive method and the averaged structure of the composite and the Mn-excess monoclinic structure appear to be equal in this case. In other words, it cannot be deduced from powder diffraction data of pristine HE-NCM whether the material is a composite of Li_2MnO_3 (=$Li[Li_{1/3}Mn_{2/3}]O_2$), the Li-rich component, and $LiTMO_2$ the rhombohedral component, or a disordered monoclinic single-phase material.

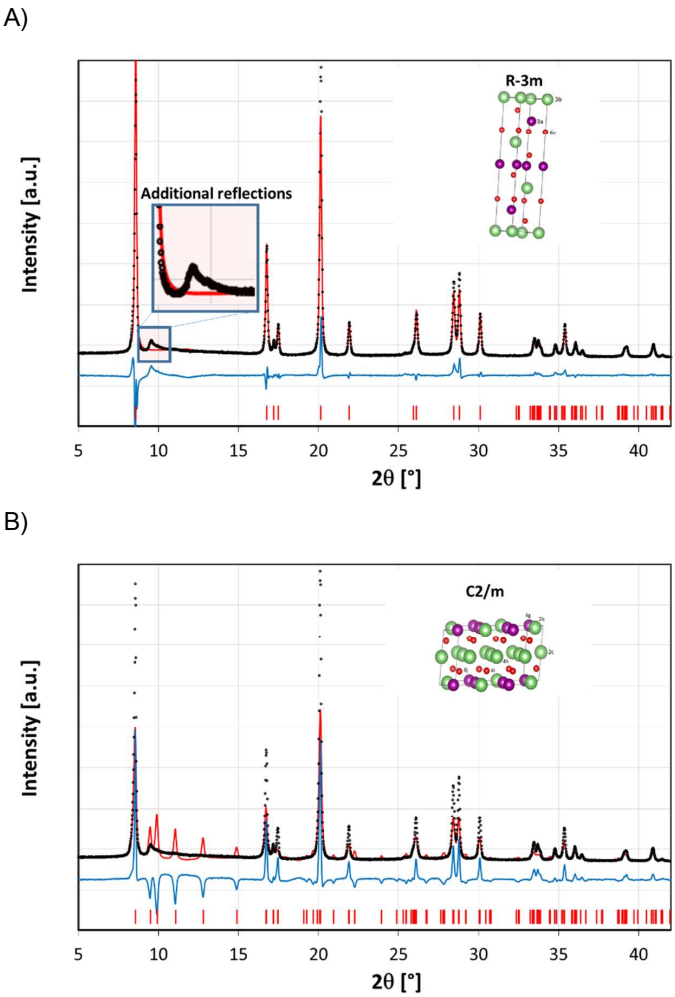

7

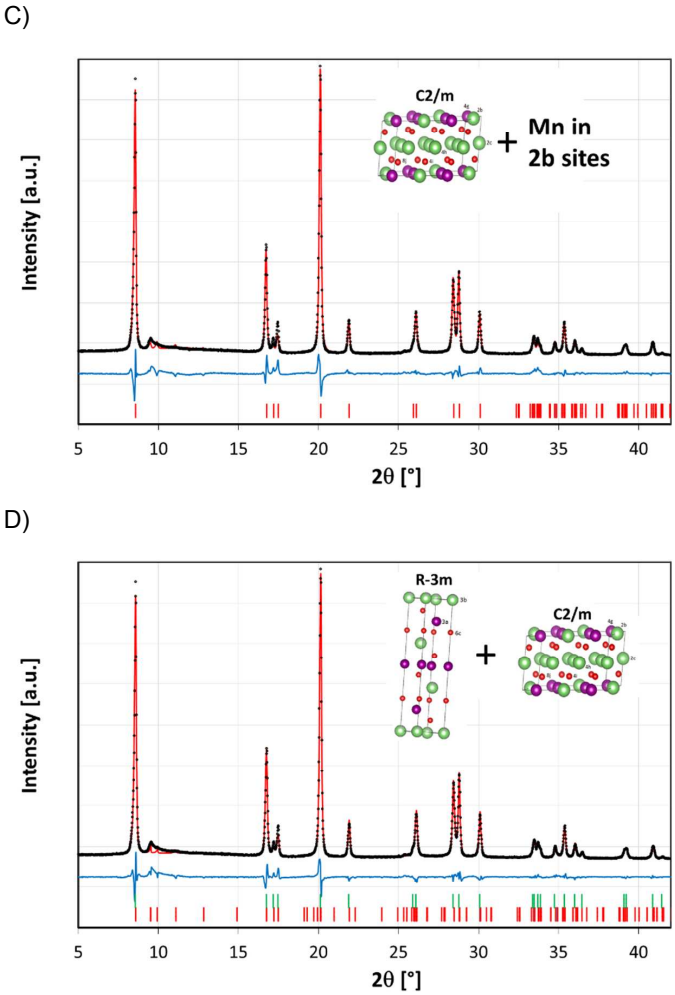

Supporting Figure 7: Measurement (black dots) and refinement (red line) of a HE-NCM powder diffraction pattern (Mo K-α_1 radiation, λ=0.70930), the residual of the calculated minus the measured data (blue line) as well as the reflection positions indicated by the red, vertical bars. (A) shows the refinement of the pattern with an ideal rhombohedral structure, (B) the refinement with an ideal monoclinic structure, (C) with a disordered monoclinic structure and (D) with a composite of a rhombohedral and a monoclinic structure.

The structural parameters used for the refinement of pristine HE-NCM are given in Table S1 (shown are the refinements as a single-phase material A and a composite B, C). The occupancy was determined by multiplying the product of the multiplicity of the Wyckoff position by the stoichiometric occupation of these sites, divided by the overall multiplicity of the structure. The stoichiometry of lithium, nickel, cobalt and manganese in the pristine and

charged material was determined with ICP-OES as described in the "Materials and methods" section of the main text. Thereby, the notations $LiMeO_2$ and $Li[Li_{1/3}Mn_{2/3}]O_2$ were used, respectively. The oxygen stoichiometry was fixed to 2 in both cases to balance the Li- and TM charges. Constraints are set in the case of the refinement of the disordered monoclinic structure between the occupancy of 2b Li sites and 2b TM (in this case, Mn) sites. For each Mn occupying Li-sites one Li was removed from the structure. Thereby the overall manganese content was varied and not taken from the ICP-OES results.

Table S1: Structural starting parameters used for the refinement of pristine HE-NCM. (A) shows the parameters for the refinement as the monoclinic structure with additional Mn in 2b sites (x denotes the amount of Mn substituting nickel). (B) and (C) lists the parameters for $\boldsymbol{R\bar{3}m}$ and $\boldsymbol{C2/m}$ respectively when refined as a composite material.

A)

sites	element	x	y	z	Occupancy
4h	Li	0.00000	0.68100	0.50000	0.50000
2c	Li	0.00000	0.00000	0.50000	0.25000
2b	Li	0.00000	0.50000	0.00000	0.25000-x
2b	Mn	0.00000	0.50000	0.00000	0.00000+x
4g	Mn	0.00000	0. 16708	0.00000	0.50000
8j	O	0.25300	0.32300	0.22750	1.00000
4i	O	0.22400	0.00000	0.22500	0.50000

9

B)

sites	element	x	y	z	Occupancy
3a	Li	0.00000	0.00000	0.50000	0.08333
3b	Ni	0.00000	0.00000	0.00000	0.03333
3b	Co	0.00000	0.00000	0.00000	0.01667
3b	Mn	0.00000	0.00000	0.00000	0.03333
6c	O	0.00000	0.00000	0.25630	0.16667

C)

sites	element	x	y	z	Occupancy
4h	Li	0.00000	0.68100	0.50000	0.50000
2c	Li	0.00000	0.00000	0.50000	0.25000
2b	Li	0.00000	0.50000	0.00000	0.25000
4g	Mn	0.00000	0. 16708	0.00000	0.50000
8j	O	0.25300	0.32300	0.22750	1.00000
4i	O	0.22400	0.00000	0.22500	0.50000

The results of both refinements are listed in Table S2 (A, refinement as a one-phase material and B, C, refinement as a composite).

10

Table S2: Summary of Rietveld refinement results for the monoclinic one-phase structure (A) and the composite of the rhombohedral (B) and monoclinic (C) phase.

A)

Monoclinic $C2/m$	Refinement results
Lattice parameter *a*	4.9485(2) Å
Lattice parameter *b*	8.5651(3) Å
Lattice parameter *c*	5.0318(1) Å
β angle	109.313(2)
Mn in 2b sites	0.167(2)
Density	7.133(2) g cm^{-3}
R_{Bragg}	3.865

B)

Rhombohedral $R\bar{3}m$	Refinement results
Lattice parameter *a, b*	2.8525(2) Å
Lattice parameter *c*	14.228(1) Å
Phase content	95(1)%
Density	4.349(1) g cm^{-3}
R_{Bragg}	4.01

C)

Monoclinic $C2/m$	Refinement results
Lattice parameter *a*	4.9488(2) Å
Lattice parameter *b*	8.5637(3) Å
Lattice parameter *c*	5.0328(2) Å
β angle	109.379(2)
Phase content	4(2)%
Density	4.762(5) g cm^{-3}
R_{Bragg}	7.43

Although it is not possible to deduce from the refinement of the pristine material whether it is a single-phase material or a composite, we can analyze in further detail the behavior of the reflections upon lithium extraction (charge). Supporting Figure 8 shows, therefore, the evolution of the (003) and (101) reflection upon the first charge. All other reflections have a similar behavior. No splitting was observed upon the entire half cycle and thus the assumption of a homogenous phase (on a macroscopic scale) is valid. Based on these findings (and the fact that the additional reflections of the lower ordered structure are not visible in the *in situ* experiments, see discussion below) the higher ordered rhombohedral structure was used for all refinements to minimize the amount of variables.

12

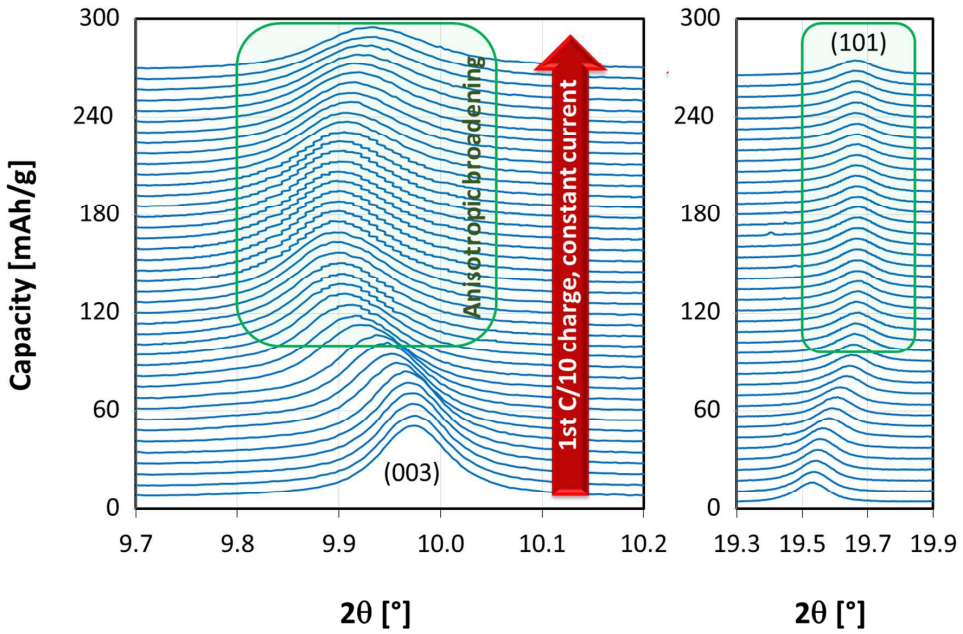

Supporting Figure 8: The (003) and (101) reflection upon the first charge, performed with a constant current at room temperature and with a charging rate of C/10. Powder diffraction patterns were measured every 300 s (for a better overview only every 5th pattern is shown) with the PSD (λ = 0.82612(1) Å). For a detailed description of the measurement conditions see Section 3 (Materials and method) in the main text.

However, at ca. 4.45 V the (003) reflection starts to get broader since anisotropic reflection broadening sets in. Indeed, by implementing this into the refinement the R_{Bragg} values of the refinements improve significantly at voltages higher than 4.45 V, see Supporting Figure 9. As already mentioned in the main text, this means that the *c*-lattice parameter cannot be described any longer with a distinct value. In fact, the *c*-lattice parameter is described with a Gaussian distribution function which means that the material is not homogenous anymore (on an atomistic scale). This is not a proof of coexisting phases since there is still no defined phase boundary. The deviations vary in a continuous way instead of showing two distinct values for one or the other phase. The inhomogeneity might arise from an inhomogeneous de-/intercalation, from distortions of octahedra or from oxygen deficient near-surface regions. It should be noted that it is not possible with powder

diffraction to locate such inhomogeneity effects since this is a bulk sensitive method. The amount of TM/Li disorder is within the accuracy of the measurements and therefore the refinement is not meaningful. However, it is very likely that transition metal migration sets in at the point at which anisotropic microstrain starts to increase.

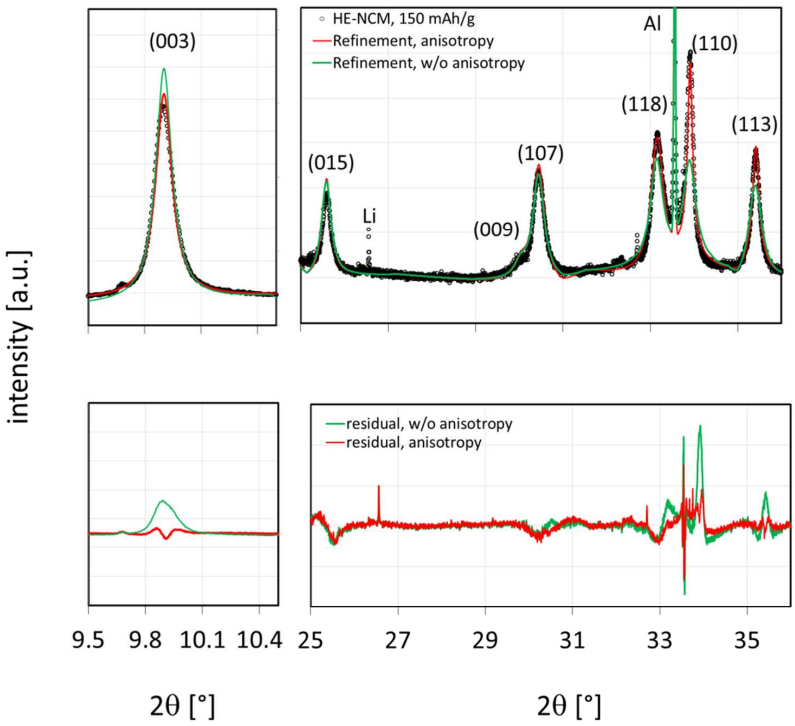

Supporting Figure 9: Refinements of HE-NCM, charged with C/10 to 150 mAh/g in the first cycle (PSD data, λ=0.82612 Å). The green lines show the refinement and the residual without considering anisotropy while in the refinement depicted with the red line anisotropy was implemented.

The additional reflections of the lower ordered $C2/m$ structure (Supporting Figure 7A) are not visible in the case of the *in situ* experiment (Supporting Figure 10, black pattern). Thus the data obtained from the pouch cells have to be refined with the higher-ordered rhombohedral structure $R\bar{3}m$. The background of the *in situ* pouch cell components (electrolyte in combination with the pouch foil) cover the additional $C2/m$ reflections, as can be seen in the red and blue patterns of Supporting Figure 10. The separator (Supporting Figure 10B, green pattern) does not contribute to the background-intensity in this region. It should be noted that the dominant reflections of the $C2/m$ structure are the same reflections

present in a $R\bar{3}m$ structure and the reflections do not show any splitting (even upon charge). Hence reflection broadening observed upon delithiation is present no matter which phase(s) is (are) chosen for refinement.

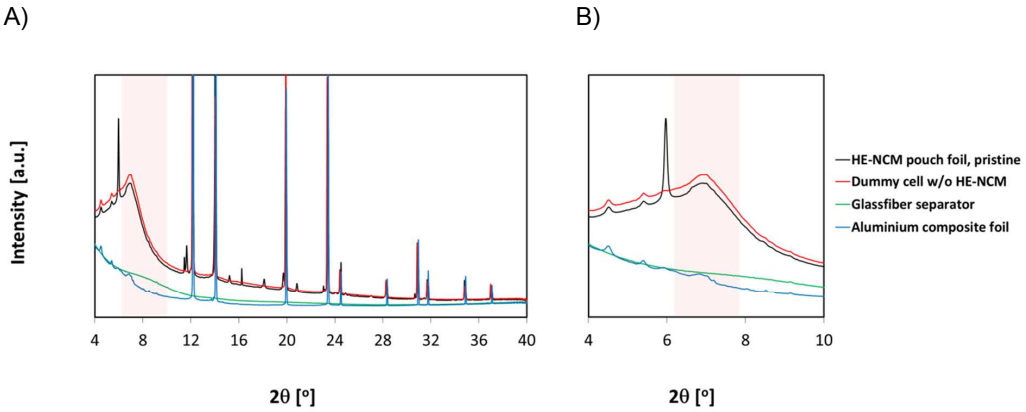

Supporting Figure 10: SXPD pattern of pristine HE-NCM, coated on aluminum foil and mounted in a pouch cell (black curve), a dummy cell without HE-NCM (red curve), a glass-fiber separator (green curve), and aluminum composite foil (blue curve) are shown in (A) (Pixium data, λ=0.496 Å). A zoom into the 4-10° 2θ region of the pattern is given in (B).

lists the structural parameters used for the refinement of discharged (A) and charged HE-NCM (B). Lithium and aluminum (from the counter electrode, the pouch foil, and the current collector) show also reflections in the measured patterns. Since both crystal structures have preferred orientations they were refined with the Le Bail method (profile fitting only) while the HE-NCM phase was treated using the Rietveld (structure) method. In the refinements it was assumed that all lithium ions in the transition-metal planes were removed during the first charge, leaving lithium vacancies in the subsequent cycles.

Table S3: Structural starting parameters used for the refinement of discharged (A) and charged HE-NCM (B).

A) $R\bar{3}m$, discharged HE-NCM, $Li_{1.42}[Ni_{0.18}Co_{0.10}Mn_{0.55}]O_2$

sites	element	x	y	z	Occupancy
3a	Li	0.00000	0.00000	0.50000	0.08333
3b	Ni	0.00000	0.00000	0.00000	0.01500
3b	Co	0.00000	0.00000	0.00000	0.00833
3b	Mn	0.00000	0.00000	0.00000	0.04500
6c	O	0.00000	0.00000	0.25642	0.16667

B) $R\bar{3}m$, charged HE-NCM, $Li_{0.004}[Ni_{0.18}Co_{0.10}Mn_{0.55}]O_2$

sites	element	x	y	z	Occupancy
3a	Li	0.00000	0.00000	0.50000	0.00030
3b	Ni	0.00000	0.00000	0.00000	0.01500
3b	Co	0.00000	0.00000	0.00000	0.00833
3b	Mn	0.00000	0.00000	0.00000	0.04500
6c	O	0.00000	0.00000	0.25642	0.16667

The HE-NCM reflections (and the observed reflection broadening) are symmetric in the case of the *in situ* Pixium (see Figure 4, 7 and 9) and PSD data (see Supporting Figure 8). Therefore possible stacking faults, as described e.g. by Jarvis et al. (Chem. Mater. 2011, **23(16)**, 3614), which generally cause a significant asymmetry in reflections (see T. K. Wallace et al., Phys. Chem. Chem. Phys. 2013, **15**, 8672; E. Estevez-Rams et al., Philos. Mag. 2003, **83(36)**, 4045; S. Bette et al., J. Appl. Cryst. 2015, **48**, 1) are not considered in the

refinements. Nevertheless, if stacking faults are present, the average bulk structure is still a $R\bar{3}m$ structure (or the lower ordered $C2/m$) and the conclusions made in the present work would still be valid.

S5. Quality and Reliability of the refinements

An intense synchrotron X-ray beam tuned at a penetration energy of 25 keV was used. With an incident flux of ~10^{11}-10^{12} photons s^{-1} mm^{-2} $(0.01\%bw)^{-1}$ the intention was to probe deep into the structure. The good resolution of $\Delta 2\theta \leq 0.05°$ ($\Delta d/d \geq 10^{-3}$) and the high signal-to-noise contrast (see below) of the I11 SXPD instrument was used to study transition metal migration in HE-NCM. The much better quality diffraction data (3 min per pattern) allows to reveal detailed structural information when analyzed which would not be possible using a laboratory or conventional X-ray machine. In Supporting Figure 11 *in situ* synchrotron measurement of charged HE-NCM (1.5 cycles) is compared to a pristine HE-NCM powder diffraction pattern, measured with a Mo-$K\alpha_1$ laboratory X-ray source in transmission mode (for details of the measurement see section S4). The charged material was chosen for this comparison since anisotropy and disorder are much more pronounced (the reflection profiles are more smeared out) and therefore the patterns are in the worst scenario one can get considering the signal-to-noise contrast.

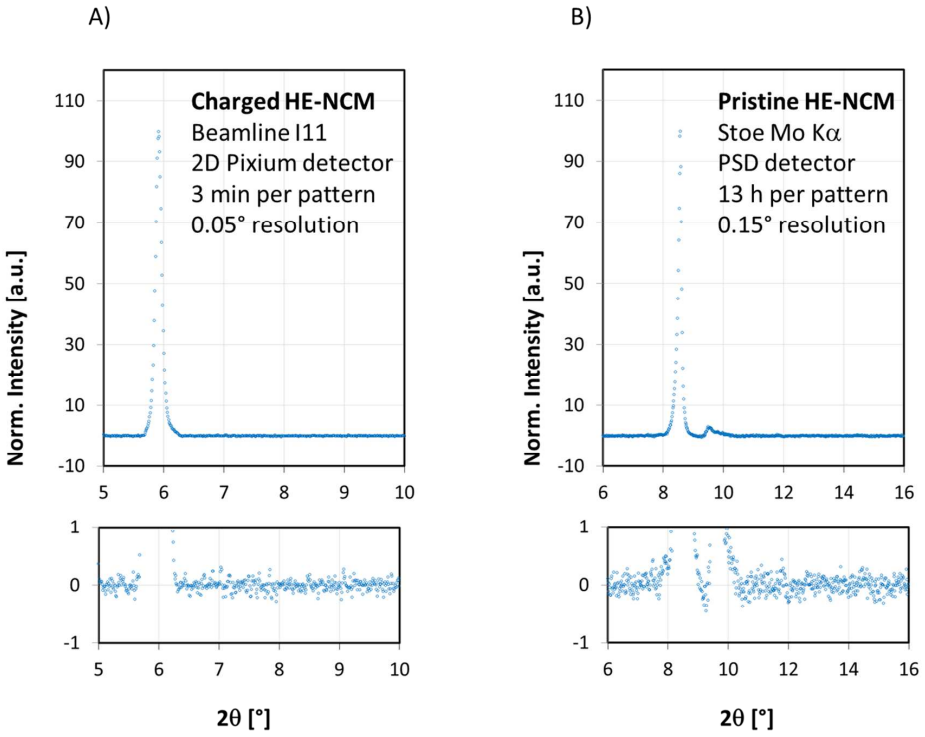

Supporting Figure 11: Comparison of the (003) reflection of HE-NCM measured at the Beamline I11 in the charged state after 1.5 cycles in the pouch cell with a beam of 25 keV (λ~0.496 Å) (A) and with a Mo-Kα_1 (λ~0.709 Å) Stoe laboratory X-ray diffractometer (B) after background subtraction and normalization to the (003) reflection. A zoom into the backgrounds shows the difference in the signal-to-noise, where the SXPD noise is much quieter.

In the case of the SXPD data the noise is about ±0.25 a.u. while it is about ±0.35 a.u. in the case of the data collected with the laboratory X-ray diffractometer (both patterns are background corrected and normalized to the (003) reflection, which has an intensity of 100 a.u.). The signal-to-noise ratio is 400 for the SXPD data and 286 for the laboratory data. In the case of the charged material the signal-to-noise ratio of the Mo Kα_1 data goes down to ≈50. By measuring HE-NCM in the *in situ* pouch cell with the laboratory X-ray diffractometer, the collection time has to be increased to 40 h and the signal-to-noise ratio goes further down to ≈10. Due to the improved signal-to-noise ratio in the synchrotron data, structural disorder and variations can be evidenced more clearly in the refinements.

18

Data were collected in in Debye-Scherrer geometry using a 2D Pixium detector. The distance between the sample and the detector as well as the wavelength, were calibrated using a CeO_2 NIST standard measured prior to every data collection. Instrumental broadening was also obtained using the standard (mainly W parameter, U and V were always close to zero) and was added as an instrumental resolution file for the refinements. The size of the HE-NCM particles is 300-500 nm and no preferred orientations are present (uniform diffraction rings). The HE-NCM coatings are 40 μm thick and therefore the beam (0.4 μm diameter) passes through a sufficient amount of crystallites producing uniform powder diffraction (Debye-Scherrer) rings projected on to the area detector. These diffraction rings were geometrically corrected and integrated radially on-the-fly using an in-house developed software package DAWN 2 (J. Filik et. al, J. Appl. Crystallog. 2017, **50**, 959–966).

- **Absorption**

Data collection of the 40 μm thick HE-NCM electrodes was performed at 25 keV. The high energy as well as the thin film (40 μm) ensured a negligible absorption. Supporting Figure 12 shows a depiction of the cross section of a pouch cell through which the X-rays have to pass. Table S4 gives the calculated absorption cross sections $\mu \cdot R$ (μ=absorption coefficient, R=material thickness) of the materials contributing to the absorption (neglecting carbon, binder, electrolyte in the porosities of the coating, separator, 6-Nylon and polypropylene since the absorption cross section of these materials is < 0.001). With $\mu \cdot R_{total} \approx 0.13$ the absorption cross section is relatively small. Although the refinement with and without considering the absorption does not show any difference, the $\mu \cdot R$ was added to the refinements.

19

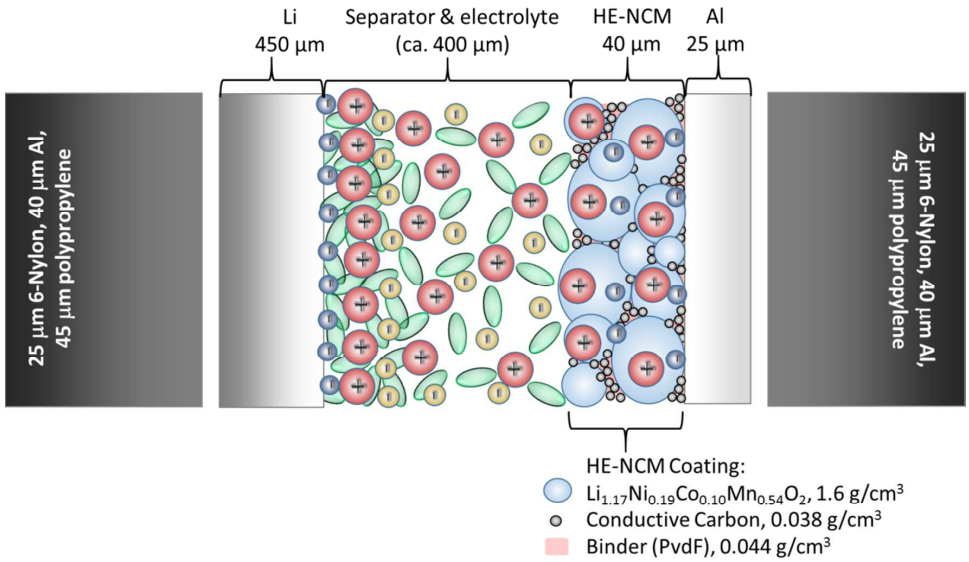

Supporting Figure 12: Schematic illustration of a cross section of a pouch cell used to cycle HE-NCM. The thickness of the individual cell components along the beam direction was used to calculate the individual absorption.

Table S4: Thickness (in total), density, attenuation coefficient μ at 25 keV and cross section of the absorbing components along the X-ray beam.

Material	Thickness (mm)	Attenuation coefficient (cm^{-1})	Volume fraction	μ·R
Lithium	0.45	0.09	1	0.002
Aluminum	0.105	6.79	1	0.07
$Li_{1.17}Ni_{0.19}Co_{0.10}Mn_{0.54}O_2$	0.04	11.28	0.44	0.06

- **Background**

The background was measured without HE-NCM (dummy pouch cell) before starting the experiment (section S4). Due to the contributions of the pouch foil, the current collector, the separator and the electrolyte, the background cannot be described with a polynomial function. Instead, background interpolation and subtraction was used for the refinements. Therefore we have chosen 60 points on the background which represent the progression,

added the points to the refinement, interpolated and subtracted the obtained background as schematically shown in Supporting Figure 13. Again, the high resolution of synchrotron data allows the background intensities between peaks to be estimated more reliably as shown by L. B. McCusker (J. Appl. Crystallogr. 1999, **32**, 36-50). During the refinements the 2θ values of the selected points were kept constant (always the same for all patterns) while the intensity of the background at the selected 2θ values (initially obtained from the background measurement) were refined after refining the Al and Li phases as well as the lattice parameters, the scale factor, B_{iso} and the reflection half-width of the HE-NCM phase. The variations in the background intensity of the different patterns were very small so that the changes due to the refinement of the background were negligible.

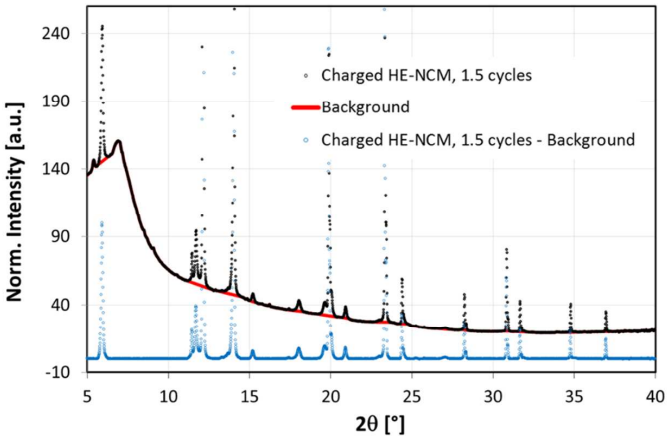

Supporting Figure 13: Charged HE-NCM (after 1.5 cycles) and background as well as the background corrected data (λ = 0.496 Å).

➢ **Refinement strategy**

Rietveld refinement was used with the minimum number of variables to ensure the data were not over-refined. In this section the sequence of parameter refinement will be briefly described. Aluminum is the dominant phase in the present patterns due to the contribution of the pouch foil and the current collector in the beam (Supporting Figure 14). Therefore it has to be refined first. The refinement of these reflections had to be performed for each pattern

individually, because the volume of the pouch cell changed slightly upon charge and discharge, introducing a slight variation of the Al foil positions (and thus of the Al reflection positions). For completeness, the lithium phase (used as counter electrode) was added and refined. All the refined parameters of the Al and Li phases were then fixed for the refinements of cathode material.

Although HE-NCM is not the dominant phase in the patterns and some of its reflections are overlapping with Al reflections, it still could be refined in a reliable way since more than 15 reflections (Debye-Scherrer rings) could be assigned to the HE-NCM phase, showing no or only a tiny overlap with other reflections (Supporting Figure 15). The lattice parameters and the scale factor of HE-NCM ($R\bar{3}m$ structure) were refined first. After that, the scale factor, the B_{ov} (overall displacement factor, see also “Isotropic displacement parameters" below), the particle size broadening (Y) and the isotropic strain broadening (X) were refined before detailed reflection profile analysis considering anisotropy and disorder were performed.

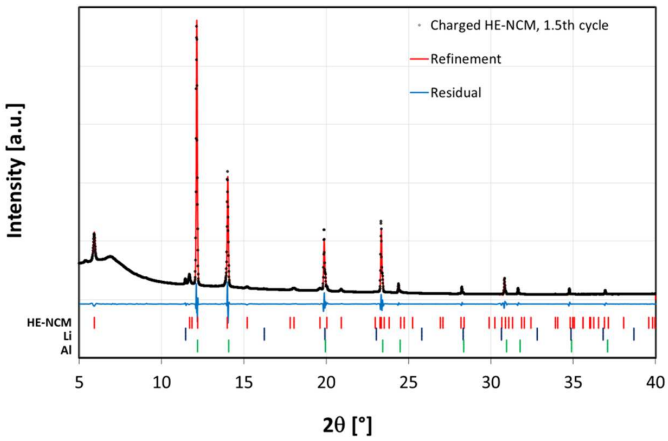

Supporting Figure 14: Whole pattern refinement of charged HE-NCM after 1.5 cycles (λ = 0.496 Å).

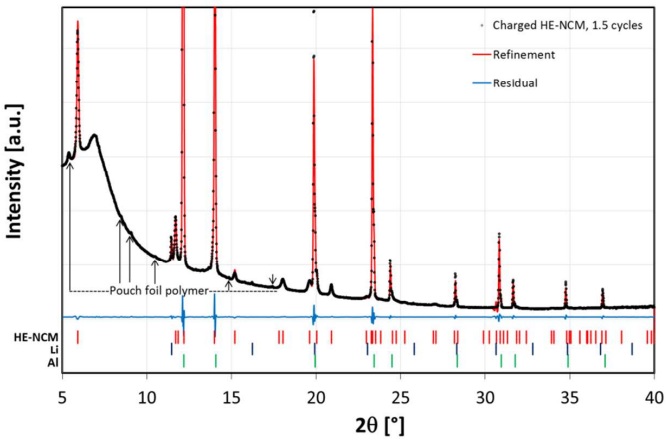

Supporting Figure 15: Whole pattern refinement of charged HE-NCM (λ = 0.496 Å) after 1.5 cycles. The figure shows a zoom into the y-axis in order to depict better the HE-NCM reflections.

➢ **Isotropic displacement parameters**

Refining the isotropic displacement factor of the individual sites (B_{iso} parameters) is very sensitive because a displacement of the effective scattering center of atoms can introduce distortions larger than the precision of the lattice parameters (L. B. McCusker, J.Appl.Cryst. 1999, **32**, 36-50). Therefore the B_{iso} values were set to zero in the first step and the overall displacement parameter B_{ov} was refined, instead. When a minimization of the difference between the structural model and the measured data was obtained with the underlying fitting parameters, transition metal disorder and/or anisotropy were refined. After this the individual B_{iso} values were fixed to known values (L. Croguennec et. al, J. Mater. Chem. 2001, **11**, 131-141, B_{iso}(Li)=1.2 Å^2, B_{iso}(transition metals)=0.5 Å^2, B_{iso}(O)=0.8 Å^2) while B_{ov} was set to zero, which did not lead to any changes in the site occupancy. The B_{iso} values of the transition metals in 3b sites were refined next to vary from 0.6 to 1.1 Å^2 without any significant changes in the site occupancy. However, in order to refine B_{iso} of Li or of transition metals in Li or tetrahedral sites, constraints have to be set. Otherwise the refinement leads to negative site occupancies. Therefore, the B_{iso}(Li) was fixed to two times the values of B_{iso}(transition metals in 3b sites) and all other B_{iso} values of transition metals to B_{iso}(transition metals in 3b sites). Again, this did not change the site occupancies. No improvement or changes were obtained by refining the isotropic displacement parameters for each individual site. To minimize the

number of variables only the refinements using B_{ov} are shown and discussed in the main text (see Table S6, Table S7 and Table S9), which vary from 1.2 $Å^2$ to 2.8 $Å^2$.

- **Reflection profile analysis**

The Thompson Cox Hastings peak function was used to model the reflection profiles. It is a modified pseudo-Voigt function generally used for synchrotron powder diffraction. The reflection profiles from the area detector are highly symmetric and no asymmetry parameters had to be refined. However, a mismatch in the intensities (in the case of the discharged and charged materials) and in the reflection broadening (in the case of the charged material) were observed which could not sufficiently be described by the initial pseudo-Voigt function (see "Refinement of disorder" and "Refinement of Anisotropic reflection broadening" below).

- **Refinement of disorder**

To overcome the issues in the mismatch of the observed and calculated reflection intensities, lithium-transition-metal disorder was introduced (section 4.2.2 of the main text). Aiming at simplicity, only nickel to represent TM was assumed to migrate. However, it is not possible to determine which transition metal is actually migrating due to the similar electron density of nickel, cobalt and manganese. The nickel and lithium contents were measured before the experiment with ICP-OES (inductively coupled plasma - optical emission spectroscopy) for charged and discharged HE-NCM samples (section 3, main text) and the obtained values were used to calculate the initial occupancy of sites in the structure (assumption of no disorder). Disorder was introduced by increasing (or decreasing) the amount of nickel in lithium sites (3a) while at the same time the same amount of nickel in nickel sites (3b) was decreased (or increased). Constraints were also set to refine lithium motion. Whenever one nickel was moving into a lithium site, one lithium was moving into a nickel site. Therefore, the overall amount of nickel and lithium in the structure was kept constant. However, the refinement of lithium disorder does not affect the results due to its small scattering factor and was only introduced in order to keep the mass balance in the system correct. Migration of

transition metals into tetrahedral sites was treated similarly. The TM/Li disorder was kept as it was refined in the discharged state. The amount of nickel (in 3b sites) was decreased (or increased) while the occupancy of tetrahedral sites (6c) by nickel was increased (or decreased) by the same amount.

- **Refinement of Anisotropic reflection broadening**

The general anisotropic strain model of hexagonal symmetry described by J Rodriguez-Carvajal et. al. (J. Phys. Condens. Matter. 3, 1991, 3215) was used to refine anisotropic reflection broadening of charged HE-NCM (*Strain model 8* in the FullProf software). Thereby the anisotropy parameter *Str2*, which points in the c-direction of the hexagonal unit cell, was refined in addition to the normal refinement.

S6. Results of Rietveld Refinements

In order to give the reader a better understanding of how the refinement of the data was performed, the following section gives parameters used and obtained upon data processing. Although it is of fundamental importance to look into the difference profile obtained from a refinement rather than looking into numerical parameters describing the quality of the fit, R_{Bragg} values of the HE-NCM phase are given for the most important refinements. These values reflect the difference between the observed and calculated structure factors normalized to the observed values, multiplied with their multiplicity. It should be noted, that R_{Bragg} values are not actively included to minimize mismatches in the refinement.

Other parameters are the R_{wp}, the weighted profile error or difference between observed and calculated intensities normalized to the observed intensities, and χ^2, i.e., R_{wp}/R_{exp}, where R_{exp} is the statistically expected R-value defined by the number of observables or number of reflections and P, the number of refined parameters. These parameters are not provided since they are mainly dominated by the aluminum reflections of the pouch cell and the current collector in the patterns. Furthermore, it is problematic to look into these values in the

case of synchrotron data, since for such patterns the signal-to-noise ratio is very high - the normalization to the observed intensities (including the background) means that the R_{wp} value increases with decreasing background, leading to a worse R_{wp} in the case of SXPD data compared to standard data (B. H. Toby et al., Powder Diff. 2006, 21, 67-70).

a) Discharged State

To account for Li/TM-disorder, the amount of nickel in 3a sites was increased by the same amount (and at the same time) as the amount of nickel in 3b sites was decreased during the refinement. Although only Ni/Li-disorder was refined in this work, it is not possible to distinguish which TM is actually migrating due to the similar number of electrons of these elements. The structural parameters of the Li/TM-disorder refinement (input file) is given in Table S5. The results of the refinements are shown in Table S6.

Table S5: Structural starting parameters for the refinement of TM/Li-disorder in HE-NCM.

sites	element	x	y	z	Occupancy
3a	Li	0.00000	0.00000	0.50000	0.08332
3a	Ni	0.00000	0.00000	0.50000	0.00001
3b	Ni	0.00000	0.00000	0.00000	0.01499
3b	Li	0.00000	0.00000	0.00000	0.00001
3b	Co	0.00000	0.00000	0.00000	0.00833
3b	Mn	0.00000	0.00000	0.00000	0.04500
6c	O	0.00000	0.00000	0.25642	0.16667

Table S6: The lithium/transition-metal disorder versus cycle number obtained by Rietveld refinement of HE-NCM SXPD patterns, measured every 15th cycle in the discharged state. The 5th and 6th column show the corresponding R_{Bragg} values of the refined HE-NCM phase with and without disorder. In the last column the B_{ov} values of the disordered refinements are listed.

Number of cycles	Disorder [%]	Lattice parameter *c* [Å]	Lattice parameter *a/b* [Å]	R_{Bragg} (without disorder)	R_{Bragg} (with disorder)	B_{ov} [Å^2] (with disorder)
0	-	14.232(2)	2.8549(1)	4.73	4.70	1.8(1)
1	1.94(2)	14.379(2)	2.8791(1)	4.85	3.51	1.2(1)
16	2.88(1)	14.377(2)	2.8789(1)	4.55	3.63	1.9(2)
30	3.60(1)	14.376(2)	2.8798(1)	3.83	3.09	1.9(1)
45	3.89(1)	14.375(2)	2.8800(1)	4.60	3.27	1.8(1)
59	4.37(1)	14.375(2)	2.8801(1)	4.62	3.62	1.8(1)
74	4.58(2)	14.375(2)	2.8802(1)	5.76	3.46	1.9(1)
88	4.68(1)	14.375(2)	2.8800(1)	4.44	3.71	1.9(1)
103	4.76(1)	14.375(2)	2.8801(1)	4.86	3.95	1.8(1)

b) Charged State

Due to a significant mismatch in the reflection profiles, the refinement of the charged states leads to R_{Bragg} values of the HE-NCM phase larger than 20 (Table S7, 2nd column). Introducing a variance in the *c*-lattice parameter leads to a significant improvement of the refinement (Table S7, 4th column). Due to an experimental issue with the cycling procedure, both cells were incidentally measured in the discharged state of the 89th cycle. Therefore, this data point is missing for the evaluation of the charged states. Allowing migration of transition

metals into tetrahedral lithium sites leads additionally to an improvement of the refinement (Table S7, 5th column). The structural input parameters are given in Table S8.

Table S7: Results of the refinement of the charged HE-NCM patterns upon cycling. The TM/Li-disorder refined in the corresponding discharged state was always kept constant while refining charged HE-NCM patterns. The second column shows the R_{Bragg} refinement values, with an ideal rhombohedral structure (not including TMs in tetrahedral sites of the Li-layer and the variance of the *c* lattice parameter). The 3rd and 4th column give σ and the obtained R_{Bragg} values by introducing a variation in the *c* lattice parameter. The 5th column gives the R_{Bragg} values also taking into account that TMs can move into tetrahedral sites of the Li layer and the last column lists the B_{ov} values of the refinements.

Number of cycles	R_{Bragg} (without *c* variance)	Strain parameter *σ*	R_{Bragg} (without disorder)	R_{Bragg} (with disorder)	B_{ov} [Å^2] (with disorder)
0	25.37	0.3(1)	8.73	-	1.8(1)
1.5	20.55	0.3(1)	5.85	3.47	1.9(1)
15.5	29.84	0.3(1)	6.48	3.33	1.9(1)
30.5	32.32	0.3(1)	7.21	4.27	1.9(1)
44.5	28.93	0.3(1)	6.53	3.23	1.8(1)
59.5	27.34	0.3(1)	6.98	3.46	2.0(1)
73.5	30.23	0.3(1)	6.67	3.14	1.9(1)
88.5	-	0.3(1)	-	-	1.9(1)
102.5	28.83	0.3(1)	6.32	2.97	1.8(1)

Table S8: Structural parameters (starting values) for the refinement of the occupation of tetrahedral sites in the Li-layer by TMs.

sites	element	x	y	z	Occupancy
3a	Li	0.00000	0.00000	0.50000	0.08332-x
3a	Ni	0.00000	0.00000	0.50000	x, see discharged state
3b	Ni	0.00000	0.00000	0.00000	0.01499-x
6c	Ni	0.00000	0.00000	z (start: 0.2)	0.00001
3b	Li	0.00000	0.00000	0.00000	x, see discharged state
3b	Co	0.00000	0.00000	0.00000	0.00833
3b	Mn	0.00000	0.00000	0.00000	0.04500
6c	O	0.00000	0.00000	0.25642	0.16667

In order to investigate whether there are deviations upon charge in the patterns (besides the increasing TM/Li-disorder), the refinement of the 103rd cycle of charged HE-NCM is shown for comparison with Figure 9 (main text). However, the refinement of the charged pattern after 102.5 cycles (Supporting Figure 16), as well as all other patterns obtained in the charged state of HE-NCM upon cycling, showed the same difficulties as discussed for the 2nd cycle (see discussion in the main text). Table S9 lists the results of the refinement of the charged HE-NCM patterns.

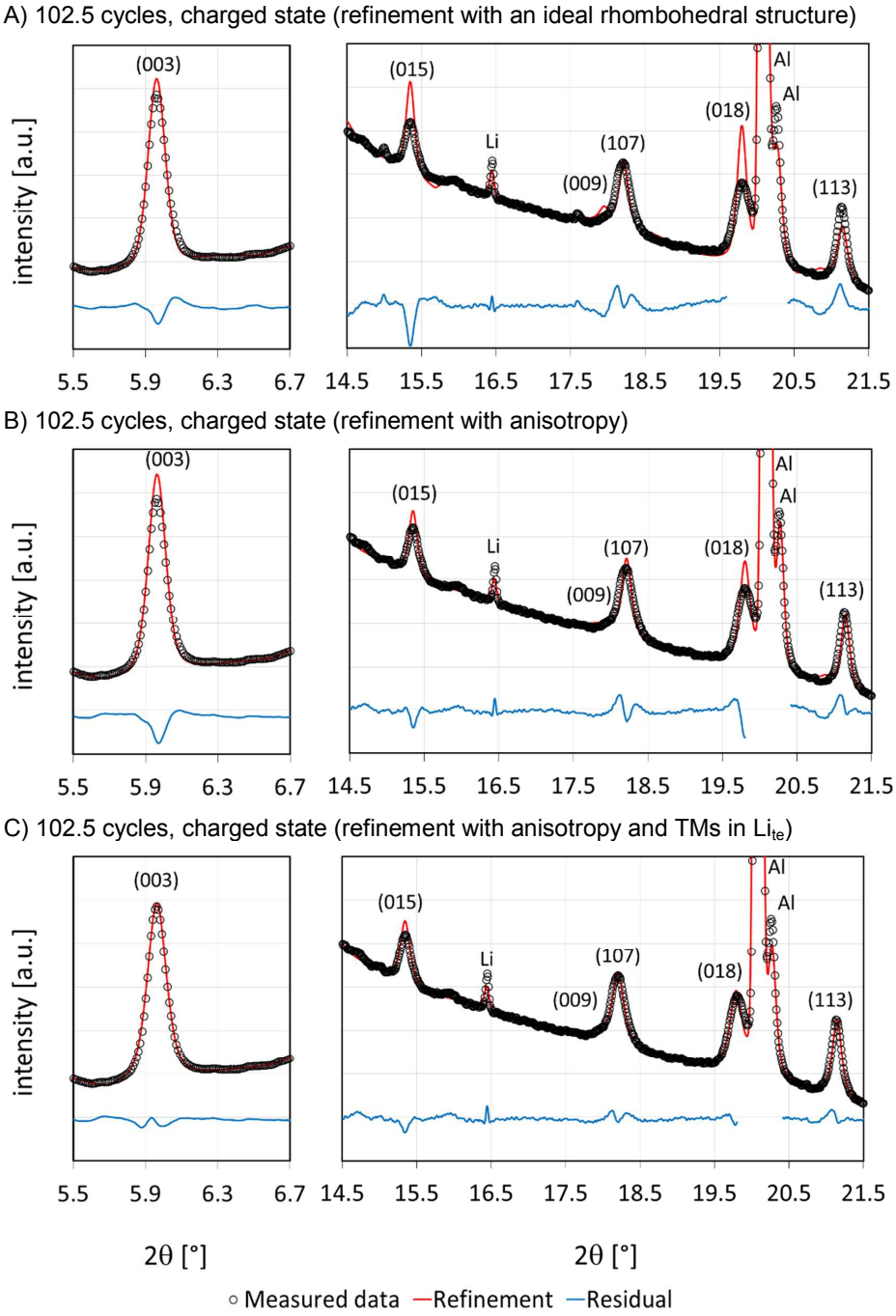

Supporting Figure 16: SXPD patterns of charged HE-NCM (after 102.5 cycles), refined with an ideal rhombohedral structure (A), with a variation in the *c*-lattice parameter (B), and with the occupancy of tetrahedral sites in the lithium layer by transition metals (C).

Table S9: Disorder of tetrahedral sites in the lithium layer by transition metals (2nd column) and lattice parameters in charged state.

Number of cycles	Disorder [%]	Lattice parameter *c* [Å]	Lattice parameter *a/b* [Å]	B_{ov} [Å^2] (with disorder)
0	-	14.283(2)	2.8539(2)	1.9(1)
1.5	8.63(2)	14.282(2)	2.8150(2)	1.9(1)
15.5	8.95(2)	14.283(2)	2.8140(2)	1.8(1) 1.9(1)
30.5	9.20(2	14.283(2)	2.8139(2)	1.8(1)
44.5	8.90(2)	14.283(2)	2.8142(2)	2.0(1)
59.5	8.45(2)	14.283(2)	2.8141(2)	1.9(1)
73.5	8.49(3)	14.283(2)	2.8142(2)	1.9(1)
88.5	-	-	-	-
102.5	8.74(2)	14.283(2)	2.8142(2)	2.8(1)

3.4 *Degradation Mechanisms of Ni-Rich Layered Oxides during Long-Term Cycling*

3.4.1 *In Situ* Synchrotron Study Performed at Ambient Temperature

This section presents the article "Capacity Fading Mechanisms of NCM-811 Cathodes in Lithium-Ion Batteries Studied by X-ray Diffraction and Other Diagnostics".[208] The manuscript was submitted in September 2019 and published in November 2019 as peer-reviewed publication in the *Journal of The Electrochemical Society*. It is available as an "open access" article and distributed under the terms of the Creative Commons Attribution Non-Commercial No Derivatives 4.0 License. Benjamin Strehle presented the main findings of this work as Paper 559 at the 235th Meeting of the Electrochemical Society in Dallas, Texas, USA (May 26-30, 2019). The permanent weblink of this article can be found under: https://iopscience.iop.org/article/10.1149/2.0821915jes.

The sections 3.1, 3.2, and 3.3 revealed several challenges of Li- and Mn-rich layered oxides, which hinder their large-scale commercialization.[29] Therefore, stoichiometric layered oxides such as NCMs and NCAs are primarily used in applications, especially in the automotive sector.[16,80] In order to improve the energy density and to reduce the cost of Li-ion batteries, there is a continuous trend to increase the lithium utilization from these CAMs—either by going to higher nickel contents and/or by operating at higher voltages.[18] However, this development goes along with an enhanced capacity fading, whereby numerous degradation mechanisms are reported in the literature, e.g., surface reconstruction caused by oxygen release,[25,261] resistance build-up,[25,261] particle cracking,[87–89] and Li-Ni mixing.[93] The degradation modes are typically quantified in terms of different properties (e.g., impedance build-up, thickness of the surface layer, and amount of Li-Ni mixing),[93,262] which makes it difficult to evaluate their actual contribution to the observed capacity loss upon long-term cycling and thus to design proper mitigation strategies.

In this study, we investigate the capacity fading of NCM-811/graphite full-cells over the duration of 1000 cycles at ≈22°C. To focus on the CAM degradation, we provide

a sufficiently large Li reservoir by partially pre-lithiating the graphite anode, such that the NCM-811 cathode can be cycled at C/2 between 2.0 and 4.5 V against the Li-RE. Using *in situ* synchrotron XPD, we establish a quantitative correlation between the evolution of the NCM-811 lattice parameters and the capacity fading. While the bulk structure turns out to be stable with a constant Li-Ni mixing, the growth of a resistive surface layer leads to two capacity loss terms: (i) an irreversible contribution due to the CAM fraction lost for its formation and (ii) a reversible contribution due to the increasing charge-transfer resistance (which can be overcome at low C-rates). From the XPD analysis, the fraction of lost CAM due to the formation of the oxygen-depleted surface layer is quantified to be ≈8.5% after 1000 cycles, which agrees perfectly with a rate test of the harvested cathode electrodes. Further techniques such as electrochemical impedance spectroscopy (EIS) and XPS verify the resistive and spinel/rock-salt-like nature of the surface layer, while a relaxation test of the (003) reflection provides evidence that the surface layer is formed around the primary NCM-811 particles.

To support the main article, additional information is provided for the benefit of the reader. The Supporting Information includes details about our various diffraction experiments and the impedance measurements as well as microscopy images (cross-sectional SEM, STEM) of pristine and cycled NCM-811 electrodes.

Author contributions

F.F. and B.S. designed and carried out the electrochemical measurements as well as the in-house diffraction experiments at the laboratory diffractometer. The beamline scientists K.K. and S.J.D. measured the synchrotron diffraction data. F.F. and B.S. evaluated all the diffraction data. A.T.S.F. conducted the XPS measurements. C.E. provided the cathode electrode sheets and initiated the STEM measurements. The manuscript was written by F.F. and edited by B.S. and H.A.G. All authors discussed the data. F.F. and B.S. are co-shared first authors of this publication.

A3760 *Journal of The Electrochemical Society*, **166** (15) A3760-A3774 (2019)

EDITORS' CHOICE

Capacity Fading Mechanisms of NCM-811 Cathodes in Lithium-Ion Batteries Studied by X-ray Diffraction and Other Diagnostics

Franziska Friedrich,[1,=,*,z] Benjamin Strehle,[1,=,*] Anna T. S. Freiberg,[1,*] Karin Kleiner,[1,2] Sarah J. Day,[2] Christoph Erk,[3] Michele Piana,[1,] and Hubert A. Gasteiger[1,***]**

[1] *Chair of Technical Electrochemistry, Department of Chemistry and Catalysis Research Center, Technical University of Munich, D-85748 Garching, Germany*
[2] *Harwell Science and Innovation Campus, Diamond Light Source, Didcot, Oxfordshire OX11 0DE, UK*
[3] *BASF SE Ludwigshafen, Lithium-Ion Battery Research, D-67056 Ludwigshafen, Germany*

Ni-rich layered oxides, like NCM-811, are promising lithium-ion battery cathode materials for applications such as electric vehicles. However, pronounced capacity fading, especially at high voltages, still lead to a limited cycle life, whereby the underlying degradation mechanisms, e.g. whether they are detrimental reactions in the bulk or at the surface, are still controversially discussed. Here, we investigate the capacity fading of NCM-811/graphite full-cells over 1000 cycles by a combination of in situ synchrotron X-ray powder diffraction, impedance spectroscopy, and X-ray photoelectron spectroscopy. In order to focus on the NCM-811 material, we excluded Li loss at the anode by pre-lithiating the graphite. We were able to find a quantitative correlation between NCM-811 lattice parameters and capacity fading. Our results prove that there are no considerable changes in the bulk structure, which could be responsible for the observed ≈20% capacity loss over the 1000 cycles. However, we identified the formation of a resistive surface layer, which is responsible for (i) an irreversible loss of capacity due to the material lost for its formation, and (ii) for a considerable impedance growth. Further evidence is provided that the surface layer is gradually formed around the primary NCM-811 particles.

Manuscript submitted September 3, 2019; revised manuscript received October 23, 2019. Published November 14, 2019. This was Paper 559 presented at the Dallas, Texas, Meeting of the Society, May 26–May 30, 2019.

Introduced by Sony in 1991, lithium-ion batteries (LIB) now dominate the battery market. However, a large-scale commercialization of battery electric vehicles (BEVs) and storage systems for renewable energy sources requires higher energy density, lower price, and longer cycle life, all of which critically depend on the cathode active material (CAM). Layered transition-metal oxides ($LiTMO_2$, where TM refers to one or a combination of the transition-metals (TMs) Ni, Co, and/or Mn, so-called NCMs) have been successfully used as CAMs in LIBs owing to their high specific capacity and high thermal stability. For example, the currently sold BMW i3 BEV uses NCM-111, which is expected to be replaced by NCM-622 in the near future in order to increase energy density and to reduce the cobalt content,[1] as the latter is problematic from a sustainability and geopolitical point of view.[2–4] For these reasons, the more Ni-rich NCM variants (e.g., NCM-811) are the most promising candidates for future BEV applications, particularly as a higher Ni content leads to an increase in specific capacity at a given cut-off voltage compared to the less Ni-rich NCMs. However, large amounts of Ni in the CAM result in reduced structural, cycling and thermal stability.[5–7] Especially at high potentials (>4 V vs. Li^+/Li), structural instabilities such as bulk structural transformations[6,8–10] and cation disorder (anti-site disorder between lithium and a transition-metal)[11] are reported to deteriorate the electrochemical performance of layered oxides. Some authors identified micro-strain and intergranular cracking as major causes for capacity fading in Ni-rich NCMs.[12–14]

Other research activities focus on the structural evolution of the CAM surface, because it happens simultaneously with electrochemical cycling and determines the interaction between active material and the other components of the battery. Recent on-line electrochemical mass spectrometry (OEMS) and transmission electron microscopy (TEM) studies on NCMs and their over-lithiated variants (referred to as HE-NCMs) report oxygen release at the particle surface[15–18] accompanied by the formation of rock-salt and spinel-type surface layers.[17–20] The low conductivity of these reconstructed phases is believed to cause an increased impedance on the cathode side and therefore contribute considerably to the capacity loss.[18,20] Furthermore, the literature reports that transition-metal dissolution from the CAM deteriorates cycling performance in NCM/graphite full-cells. While on the cathode side active material is lost and the particle surface is reconstructed, the deposition of dissolved transition-metals on the anode side leads to enhanced electrolyte decomposition and an impedance rise.[21–23]

In view of the required lifetime of 15 years and a cycle life over 1000 cycles for large-scale commercialization of LIBs for applications such as electric vehicles,[24,25] it is essential to gain a fundamental understanding of the underlying mechanisms and their interrelations contributing to battery failure. As ex situ techniques may lead to deviations from the original state of the CAMs during electrode harvesting (e.g., changes in the state-of-charge (SOC) of the CAMs), much more authoritative information can be achieved by in situ and operando techniques, which allow for the characterization of electrode materials under real operating conditions. In situ X-ray powder diffraction (XPD) is a powerful analytical tool, which provides insights about bulk structural changes in cathode and anode over the course of cycling.

In the present study, detailed information on the fading mechanisms of NCM-811/graphite full-cells is obtained from the combination of X-ray powder diffraction, electrochemical impedance spectroscopy (EIS), rate tests, X-ray photoelectron spectroscopy (XPS) and scanning electron microscopy (SEM). To get unambiguous insights about the cathode active material fading mechanisms, the graphite counter-electrode was pre-lithiated to eliminate capacity fading from active lithium loss at the anode, while allowing for long-term cycling which is more problematic with a metallic lithium anode. In situ synchrotron X-ray powder diffraction experiments were conducted with pouch cells cycled over 1000 times at the long duration experiment (LDE) facility of beamline I11 at the Diamond Light Source, UK. The results from the LDE synchrotron XPD study were combined with operando XPD measurements using a lab diffractometer with a molybdenum

[=] These authors contributed equally to this work.
[*] Electrochemical Society Student Member.
[**] Electrochemical Society Member.
[***] Electrochemical Society Fellow.
[z] E-mail: franziska.friedrich@tum.de

Journal of The Electrochemical Society, **166** (15) A3760-A3774 (2019)

source to allow for a quantitative correlation between lattice parameter changes in the CAM and capacity losses, seeking to clarify whether bulk or surface related phenomena are responsible for capacity fading in NCM-811 CAMs.

Experimental

Battery assembly and cycling.—NCM-811 cathode electrode sheets (94 wt% BASF SE NCM-811, 2 wt% Timcal SFG6L graphite, 1 wt% Timcal C65 conductive carbon, 3 wt% Kynar PVDF binder HSV900) with a loading of ≈7.4 mg_{CAM}/cm^2 (corresponding to ≈1.5 mAh/cm^2 based on 200 mAh/g) and with a precise composition of $Li_{1.01}Ni_{0.79}Co_{0.1}Mn_{0.1}O_2$ (Mikroanalytisches Labor Pascher, Germany; see below) were provided by BASF SE (Germany). The pristine NCM-811 has a BET surface of ≈0.27 m^2/g (determined by N_2 and Kr physisorption; see below). Cathodes with a geometric area of 9 cm^2 (30 × 30 mm^2) were assembled in single layer pouch cells (with a 40 μm-thick Al layer) versus graphite counter-electrodes (CE, geometrically oversized, 33 × 33 mm^2) in an argon-filled glove box (<0.1 ppm O_2 and H_2O, MBraun, Germany). These capacitively oversized graphite sheets (96 wt% active material, ≈7.1 $mg_{Graphite}/cm^2$, reversible capacity of ≈2.3 mAh/cm^2) were also provided by BASF SE. To avoid capacity fading due to the loss of cyclable lithium caused by the formation of the solid electrolyte interphase (SEI) as well as during cycling, the graphite anodes were pre-lithiated to ≈$Li_{0.3}C_6$ (corresponding to ≈0.7 mAh/cm^2) versus a lithium counter-electrode (450 μm, 99.9%, Rockwood Lithium) in LP57-2 electrolyte (1M $LiPF_6$ in EC:EMC = 3:7 by weight with 2% VC, BASF SE). In full-cells, two glass-fiber (GF) separators (36 × 36 mm^2, glass microfiber filter 691, VWR, Germany) with a projecting tab (10 × 10 mm^2) were used with 700 μL LP57-2 electrolyte. A piece of lithium (10 × 5 mm^2) positioned at the tab, was used as reference-electrode (RE). For a homogeneous compression of the cells at ≈2 bar, a homemade spring-loaded pouch cell holder with a 1.5 mm diameter hole as X-ray window was used, similar to that reported in our previous work.[26]

The first two formation cycles were performed at constant current (CC) at a C-rate of C/10 (based on 200 mAh/g, which corresponds to a current density of ≈1.5 mA/cm^2 at a rate of 1C). Subsequent CC cycling was carried out at C/2 (without any constant voltage hold step). The cathode voltage window was 3.0–4.5 V vs. Li^+/Li as controlled versus the Li-RE. All voltages in this work are reported vs. Li^+/Li if not stated otherwise. Initial cycling (2 cycles at C/10 and 6 cycles at C/2) was performed at the Technical University of Munich (Maccor cycler, series 4000, USA) in a thermostatic chamber at 25°C. At the long duration experiments (LDE) facility of beamline I11 at the Diamond Light Source, two nominally identical pouch cells were cycled at C/2 and ≈22°C. The following nomenclature will be used: (i) "pristine" refers to the as-received NCM-811 powder or to pristine electrode sheets (i.e., never assembled into a battery); (ii) "fresh" corresponds to data collected within the first 10 cycles (including formation cycles); (iii) "begin-of-test" (BOT) refers to a NCM-811 cathode electrode, which has gone through formation (initial 2 cycles at C/10) and 16 cycles at C/2, corresponding to our first LDE XPD data point; and, (iv) "end-of-test" (EOT) refers to a cathode at the end of the LDE test, more specifically, it refers to the LDE XPD data collected in cycle 968 for cell 1 and in cycle 975 for cell 2, although the electrochemical cycling continued until cycle 995 for cell 1 and cycle 1003 for cell 2. Subsequently, further tests were conducted (e.g., C-rate test, relaxation test), which are also denominated as EOT.

For elemental analysis, inductively coupled plasma atomic emission spectroscopy (ICP-AES) was performed at the Mikroanalytisches Labor Pascher (Remagen, Germany), for which the CAM powder was dissolved by pressurized acid digestion in aqua regia. Considering surface impurities such as Li_2SO_4, Li_2CO_3, and transition-metal carbonates, which amount in total to ≈2.2 wt% of the sample, the composition of NCM-811 was determined as $Li_{1.01}Ni_{0.79}Co_{0.10}Mn_{0.10}O_2$, giving a theoretical capacity of 280 mAh/g_{NCM} or 274 mAh/g_{CAM} (including the surface impurities) for complete Li extraction. Note that capacity values are given for the total CAM powder and that we used the latter notation throughout the entire work. The layered oxide is doped with ≈0.3 mol% Al (relative to the transition-metal amount), which is however not taken into further consideration.

X-ray powder diffraction measurements.—The in situ long-duration study of two nominally identical NCM-811/graphite pouch cells was performed using synchrotron X-ray powder diffraction on the LDE facility of beamline I11, Diamond Light Source; this will further on be referred to as "in situ S-XPD". Patterns were collected with an exposure time of 5 minutes with an X-ray beam of ≈25 keV energy (≈0.494 Å) and a 2D Pixium area detector at a distance of ≈0.25 m. NIST Standard Reference Material CeO_2 (NIST SRM 674b) was measured before every sample data collection in order to refine the wavelength and detector distance and to evaluate the instrumental broadening. Detailed information on the LDE instrument is given by Murray et al.[27] The diffraction data were reduced with the software package DAWN[28,29] and refined with the software package Topas (version 6).[30] XPD data collection was performed once a week at open circuit voltage (OCV) after 3–5 h of relaxation, both in the discharged state of the cathode at the lower cathode cut-off potential of 3.0 V vs. Li^+/Li and, after subsequent charging, in the charged state of the cathode at the upper cathode cut-off potential of 4.5 V vs. Li^+/Li. In this way, data collection was intended to be performed every ≈50 cycles at both SOCs. However, due to a beam shut-down no XPD data could be collected for several months. The cycling protocol was nevertheless continued including OCV holds every week (i.e., every ≈50 cycles).

In addition, XPD experiments were conducted at our in-house STOE STADI P diffractometer (STOE, Germany) in transmission mode using Mo-$K_{\alpha1}$ radiation (0.7093 Å, 50 kV, 40 mA) and a Mythen 1K detector with one data point every 0.015°/2θ. For the determination of instrumental broadening, a silicon standard material (NIST SRM 640c) was used. In-house measurements comprise three different types of experiments for the pristine, fresh, and harvested EOT NCM-811 materials: (i) structural information from ex situ capillary data; (ii) determination of lattice parameters and of a calibration curve correlating the lithium content x_{Li} with the c/a lattice parameter ratio ($x_{Li} = f(c/a)$), which was performed both in operando (i.e., data collection during charge-discharge cycling) and in in situ mode (i.e., data collection during intermediate OCV holds), and, (iii) relaxation tests of the (003) reflection upon the transition from CC charge to OCV. XPD experiments conducted with the Mo-$K_{\alpha1}$ laboratory XPD will further on be referred to as "L-XPD" experiments.

Ex situ L-XPD measurements were conducted over night (≈14 h) in 0.3 mm borosilicate capillaries in a 2θ range of 3–60° (with detector step size/step time of 0.15°/5 s). Cycled samples were scratched off the electrode and filled into the capillary in an argon-filled glove box.

In situ and operando L-XPD experiments were performed in pouch cells with a lithium counter-electrode and a relatively thin pouch foil (12 μm-thick Al layer). During the measurement, the cell was connected to a SP200 potentiostat (SP200, Biologic, France). For the determination of lattice parameters from the fresh NCM-811 electrode, all cycles were conducted at a C-rate of C/7.5. The first charge was limited to a maximum capacity of 180 mAh/g (corresponding to a cathode potential of ≈4.1 V vs. Li^+/Li) to avoid any side reactions of the electrolyte. By limiting the SOC window and using a Li counter-electrode, the observed irreversible capacity loss could be solely related to the NCM-811 CAM. Afterwards, the cell was cycled for several cycles at C/7.5 between cathode potentials of 3.0 and 4.6 V vs. Li^+/Li; the accumulated irreversible capacity loss caused by side reactions amounted to ≈9 mAh/g during the operando measurement, and the SOC scale in the respective figures was corrected for this value. The c/a ratio was measured operando at C/7.5 with a time resolution of 8 minutes (see below), translating to one diffractogram every ≈4 mAh/g; for in situ measurements (i.e., during a 50 min OCV hold), diffractograms were taken every 10 mAh/g. The EOT sample was cycled in situ using the cycling protocol for the LDE experiment (i.e., at C/2 between 3.0 and 4.5 V vs. Li^+/Li) with data points every 15 mAh/g. In situ L-XPD data collection was performed during intermittent OCV periods in the cycling procedure in a 2θ range of 6–48° (detector step size/step time

of 0.15°/5 s), leading to L-XPD acquisition times of 40 minutes. For operando L-XPD data collection, only small 2θ sections with non-overlapping NCM reflections were measured in repetition mode. To determine the *c*/*a* calibration curve from operando L-XPD, the (003) reflection was monitored in the 2θ range of 8.000–9.215° (0.405°/3 s), and the (110) reflection in the 2θ range of 28.500–29.715° (0.405°/3 s), with an overall acquisition time of about 8 minutes. Lattice parameter values determined by the operando L-XPD method perfectly overlap with those from in situ L-XPD data (see Figure S5 in paragraph S3 of the Supporting Information), whereby the operando method has the advantage that more data points are collected.

Finally, additional operando L-XPD lattice parameter relaxation experiments were conducted with fresh and EOT samples. After C/2 charging to a comparable state of delithiation (i.e., cathode potential cut-offs of 4.3 V vs. Li^+/Li for the fresh and of 4.5 V vs. Li^+/Li for the EOT sample), the cell was allowed to relax at OCV while monitoring only the relaxation of the (003) reflections in the 2θ range of 8.000-9.215° (0.405°/3 s), resulting in a time resolution of about 4 minutes per L-XPD pattern.

Rietveld refinement.—As the X-ray beam penetrates through the entire pouch cell, the synchrotron diffractogram contains reflections of (i) Al from the pouch foil and the cathode current collector, (ii) Cu from the anode current collector, (iii) graphite phases (graphite as conductive agent in the cathode, Li_xC_6 in the anode), and, (iv) the actual NCM reflections of interest. The scattering from the electrolyte-soaked separator and from polymers of the binder and pouch cell give rise to a complex background, which was fitted by different approaches. Initially, the background signal was defined by fitting a linear interpolation between selected data points in non-overlapping regions, as was done by Dolotko et al.[31] However, a more elegant way – because its inclusion in the refinement process is possible – is a user-defined background modeled by eight pseudo-Voigt peaks, similar to what was used by Bo et al.,[32] and which was used throughout our analysis. From the refinement of one pattern, the positions and relative intensities of the pseudo-Voigt peaks were determined and fixed across all scans with a single scale factor allowing for a free variation of the overall background intensity. Due to preferred orientation effects in the metal foils, a structure-independent Pawley fit was used for the respective phases. The peak profile was described as isotropic broadening with the Thompson-Cox-Hastings pseudo-Voigt function (TCHZ, as implemented into Topas). The instrumental contribution to the broadening was determined with the CeO_2 standard (NIST SRM 674b), giving a value of ≈0.006 for the θ-independent parameter *W* in the TCHZ function. Additional isotropic reflection broadening caused by the sample was taken into account as phase-specific micro-strain (tan θ-dependent parameter *X*) or crystallite size effects (1/cos θ-dependent parameter *Y*) in the TCHZ function of each individual phase. For a more detailed discussion see paragraph S1 in the SI.

NCM-811 is a layered transition-metal oxide known to exhibit an α-$NaFeO_2$-type structure with $R\bar{3}m$ symmetry.[33] The unit cell of NCM-811 contains Li atoms on the 3a site (fractional coordinates: 0, 0, 0) and the transition-metals randomly distributed on the 3b site (0, 0, 1/2). The oxygen atoms are on the 6c site (0, 0, $z_{6c,O}$), with $z_{6c,O}$ ranging between 0.23 and 0.24. According to literature reports[34] and our own experience, a more stable refinement is achieved if the number of refined parameters is minimized. Therefore, the following constraints were applied: (i) the site occupancy factors of Co and Mn were both fixed to 0.10 on the 3b site (as determined from the ICP-AES analysis); (ii) the overall Ni content was fixed to 0.79 per formula unit; and, (iii) for the refinement of cation disorder, the Ni distribution between 3a and 3b sites was constrained by assuming the same amount of Li on the transition-metal 3b site as the amount of Ni on the Li 3a site (≡ Li-Ni mixing, cation disorder). The chosen kind of constraints have already been applied in the literature and were found to give chemically reliable results and a stable refinement.[10,31,35–38] Furthermore, the atomic displacement parameter was constrained for all sites to be the same, because otherwise physically meaningless (sometimes negative) values were obtained. However, when refining data obtained from ex situ L-XPD capillary measurements, site-specific atomic displacement parameters could be implemented, which were in good agreement with literature values.[39,40] We used ionic scattering factors for all atoms in the structure. Generally, there is no commonly accepted rule whether to use ionic or neutral atomic form factors.[41] However, recently the advantages of the use of composite structure factors were reported.[34]

At this point, it is important to note that structure factors are a (theoretical) model of the electron density of an atom which scatters X-rays. Usually, a scattering factor of a free neutral atom deviates substantially from that of an atom in a crystal lattice. However, full charge-transfer between atoms rarely occurs, so that the actual charge density of an ion in a crystal lattice is not equal to its formal charge.[34,42,43] Accurate scattering factors therefore need to be determined for the respective structural model. As such data are not available for NCM-811, the scattering factors were chosen so that the resulting oxidation states (Li^+, Ni^{3+}, Co^{2+}, Mn^{4+}, and O^{2-}) give a chemically meaningful, neutral sum formula for the pristine material. The effects of the scattering factors might be mitigated by excluding the low 2θ region from the Rietveld refinement.[34] In our case, however, this is not possible because strong reflections are in this range and discarding them would mean a detrimental loss of information.

Any anisotropic strain introduced by changes in the lattice due to Li de-/intercalation (especially pronounced at high state-of-charge, SOC) was taken into account by the hexagonal Stephens model (see paragraph S1 in the SI for equations and Figure S3 for the Williamson-Hall plot).[44] The simultaneous refinement of the four micro-strain parameters (S_{004}, S_{004}, S_{202}, S_{301}) during the sequential Rietveld analysis of the LDE pouch cell data did not yield stable results. Therefore, only S_{004} and S_{202} were used, because these parameters had the largest effect on the fit quality. This procedure is in agreement with the literature.[45] For the refinement of the capillary data measured at the in-house diffractometer, all four strain parameters were used successfully, underlining the fact that the Stephens model is phenomenological and only helps to describe the peak shape but does not directly correspond to a physical meaning. In case of the refinement of capillary data obtained at the in-house diffractometer, absorption correction was applied. For further details on the structural parameters, constraints, and refinement results see paragraphs S1 and S2 in the SI.

In addition to the NCM phase, graphite phases of the anode were observed in the XPD patterns from NCM-811/graphite full-cells. It is known in the literature[31,46] that the lithiation of graphite is a stepwise process leading to three phases which are distinguishable by X-ray diffraction analysis: graphite (space group $P6_3/mmc$), LiC_{12} ($P6/mmm$), and LiC_6 ($P6/mmc$). The pre-lithiation of the anode results in a lithium reservoir which ensures that even in the fully discharged cell, graphite is not formed. The nevertheless observed (002) graphite reflection therefore stems from the conductive graphite additive in the NCM-811 cathode coating. Structural parameters for the refinement of the Li_xC_6 phases ($0 < x < 1$) were taken from a neutron study conducted by Dolotko et al.[47] As just the small (002) reflection of graphite appears, only the lattice parameters were refined for this phase. For the LiC_{12} phase, lattice parameters and peak broadening due to size effects could be refined. At high SOC, also LiC_6 is present, from which the lattice parameters and crystallite size broadening could be refined. Results from the structural refinement of the LDE data with respect to the different graphite phases are shown in Tables S7-S9 in the SI.

Impedance measurements and rate tests.—Electrochemical impedance spectroscopy (EIS) experiments were conducted in spring-compressed Swagelok-type T-cells (≈1 bar), in which both cathode and anode had a diameter of 11 mm. Pre-lithiated graphite was used as counter-electrode. A gold wire micro-reference (GWRE) with a Au wire diameter of 50 µm insulated with a 7 µm polyimide shrouding (Goodfellow Ltd., UK) was used as reference-electrode,[48] placed between two GF separators with 60 µL LP57-2 electrolyte. The GWRE was lithiated with a constant current of 150 nA for 1 h and yielded a constant potential of 0.31 V vs. Li^+/Li. Potential-controlled electrochemical impedance measurements (PEIS) were conducted with a potentiostat (VMP300, BioLogic, France) in a frequency range of

Journal of The Electrochemical Society, **166** (15) A3760-A3774 (2019)

100 kHz to 100 mHz with an AC voltage perturbation of 10 mV (taking 20 data points per decade and 3 period repetitions). PEIS measurements were performed during the first formation cycle, the 18th cycle, and at end-of-test during charge and discharge at intervals of 20 mAh/g. Prior to measurements, the cells were allowed to rest at OCV for 1 h. Harvested cathode material from the pouch cells of the LDE study was used for the PEIS experiments and for rate tests at EOT. For the other two cycles of interest, new cells were assembled. To fit the impedance spectra, the transmission line model (TLM) was used as described in paragraph S4 of the Supporting Information.[49]

Rate tests were done in 2325-type coin cells with cathode electrodes of 11 mm (EOT) and 14 mm (BOT) in diameter, a lithium counter-electrode (15 mm), two GF separators (16 mm), and 80 µL LP57 electrolyte (1M $LiPF_6$ in EC:EMC = 3:7 by weight, BASF SE).

X-ray photoelectron spectroscopy measurements.—X-ray photoelectron spectroscopy (XPS) measurements were conducted on pristine, BOT, and EOT electrode samples with focus on the O1s region. The electrodes were used as-received (pristine) or harvested without washing in the completely discharged state (i.e., after a constant voltage hold step at 3.0 V vs. Li^+/Li until a C/100 current cut-off). 4 mm diameter samples were cut out of the electrode sheets inside an argon-filled glove box (<0.1 ppm O_2 and H_2O, MBraun, Germany), mounted floating onto a stainless steel stub, and transferred into the loadlock of the XPS system without air exposure using the transfer device from Kratos (UK). XPS spectra were recorded with a monochromatic Al K_α source (1486.6 eV), using an Axis Supra system (Kratos, UK) with an operating pressure of $2 \cdot 10^{-8}$ Torr. A pass energy of 20 eV, step size of 0.1 eV and dwell time of 200 ms were chosen for a spot size of 800 × 300 μm^2. Binding energies were corrected based on the adventitious carbon signal at 284.8 eV in the C 1s spectrum. Fitting of the spectra was done with a mixture of Lorentzian (30%) and Gaussian (70%) shape function on top of a Shirley background.

Surface area determination.—Surface area measurements were performed on a gas sorption analyzer (Autosorb-iQ, Quantachrome, USA) at 77 K using either nitrogen or krypton as adsorbent. Beforehand, the pristine NCM-811 powder was degassed at 350°C for 3 h, whereas treated powders were degassed at 80°C for 24 h. The CAM was either treated with (i) H_2O for 30 min or (ii) LP57 + 1000 ppm H_2O for 7 days, whereby in the latter case, previous work showed that the 1000 ppm H_2O will be converted to ≈2000 ppm HF within the course of roughly 2–3 days.[50] The CAM-to-solvent ratio was 1:10 g:ml in both cases. Afterwards, the CAM was filtrated and additionally washed with dimethyl carbonate for the HF-treated sample. The specific surface area was determined from adsorption isotherms in the relative pressure range of $0.05 < p/p_0 < 0.30$ according to the Brunauer-Emmet-Teller (BET) theory. As N_2 and Kr sorption provide similar surface areas for the pristine material (N_2: 0.26 m^2/g, Kr: 0.28 m^2/g), the following experiments were only done with krypton, since it should be more accurate with a low sample amount (≈1 g).

Overview.—Figure 1 summarizes the main techniques which we have used in this study and which will be discussed in detail in the Results and Discussion section. It might be helpful for the reader to go back to this overview from time to time, especially with respect to the different XPD techniques, as it shows the targeted parameter(s) of each experiment and the different aging states of the NCM-811 CAM.

Results and Discussion

LDE electrochemical data.—Figure 2a shows the specific discharge capacity of two NCM-811/graphite full-cells cycled at the long duration experiment (LDE) facility of beamline I11 at the Diamond Light Source, UK. Initially, there is a first cycle irreversible capacity loss (ICL) of ≈25 mAh/g (not shown), which compares well with the ICL reported for NCM-111 of ≈24 mAh/g[51] and which results in a CAM stoichiometry of $Li_{0.92}Ni_{0.79}Co_{0.10}Mn_{0.10}O_2$ after the first cycle. This irreversible capacity loss of NCMs was also reported by other groups,[51–55] and Buchberger et al.[51] discussed various reasons for the ICL and were able to prove the mechanism first proposed by Kang et al.,[54,55] who suggested that the Li diffusion at the end of discharge is very sluggish because of the lack of Li-ion vacancies. These authors were able to recover the full capacity by giving the diffusion process enough time at voltages lower than 3.0 V. The capacity drops after the second cycle by ≈16 mAh/g when increasing the C-rate from C/10 to C/2 (see inset of Figure 2a), a typical rate-induced capacity loss observed for NCMs.[56] In addition, between cycle 8 and 9 there

			Pristine CAM powder	**Fresh** <10 cycles	**BOT** Cycle 18	**LDE** Cycling	**EOT** ≈1000 cycles
Technique	**Target**	**Figure**					
In situ S-XPD	$\Delta C_{Material}$ & $\Delta C_{Overpotential}$	Fig. 5			✓	✓	✓
Operando L-XPD	$c/a = f(x_{Li})$	Fig. 5a		✓			
In situ L-XPD	$c/a = f(OCV)$	Fig. 6a		✓			✓
Ex situ L-XPD	Li-Ni mixing	Fig. 3	✓				✓
Operando L-XPD	Relaxation	Fig. 9		✓			✓
In situ EIS	R_{CT}	Fig. 6b		✓	✓		✓
Rate test	$\Delta C_{Material}$	Fig. 7			✓		✓
XPS	Nature of surface layer	Fig. 8	✓		✓		✓

Figure 1. Overview of the main techniques used in this work, highlighting the targeted parameter(s), the figure where the respective results are shown in the Results and Discussion section, and the different aging states of the NCM-811 CAM which have been investigated with the respective technique.

A3764 *Journal of The Electrochemical Society*, **166** (15) A3760-A3774 (2019)

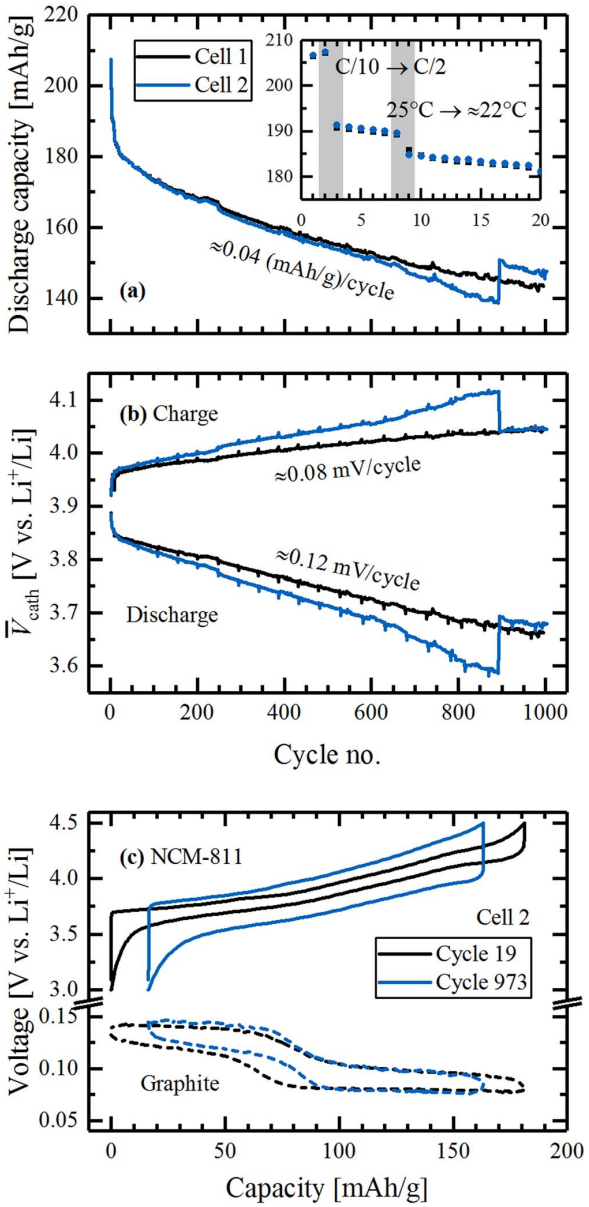

Figure 2. (a) Specific discharge capacity, (b) charge-averaged mean charge and discharge voltage of the cathode vs. Li^+/Li ($\bar{V}_{cath}$), and (c) voltage profile of anode and cathode of NCM-811/graphite full-cells cycled at ≈22°C with C/2 between 3.0–4.5 V vs. Li^+/Li at beamline I11 (Diamond Light Source, UK). The inset in panel (a) highlights the first 20 cycles, where (i) the C-rate was increased from C/10 (cycles 1 and 2) to C/2, and (ii) the cells were moved to the Diamond Light Source (between cycle 8 and 9), where the cycling temperature was ≈22°C compared to 25°C during cycles 1–8. Slight deviations from the characteristic mean voltage curves in panel (b) originate from the OCV phases for XPD data collection (every ≈50 cycles). The half-cell voltage profiles of cycle 973 in panel (c) were shifted arbitrarily along the x-axis relative to cycle 19 in order to illustrate the overpotential leading to capacity fading.

is another capacity drop of ≈3–5 mAh/g at the same C-rate, which unfortunately is due to a temperature difference between the cycling experiments conducted in our laboratory at the Technical University Munich (25°C, until cycle 8) and in the beamline hutch at the Diamond Light Source (≈22°C, from cycle 9 onwards). This difference in discharge capacity is consistent with the temperature dependence of the discharge capacity of ≈0.8 (mAh/g)/K, determined in a separate experiment (not shown) with fresh NCM-811/graphite cells cycled at C/2 at varying temperatures (19–33°C). The mean capacity drop in the subsequent cycles is ≈0.04 mAh/g per cycle (see Figure 2a), resulting in a capacity retention (at 22°C and C/2) of 77–80% after 1000 cycles, referenced to 185 mAh/g in cycle 9. The instantaneous regain of capacity for cell 2 (blue line) in cycle 893 must have been caused by a sudden improvement of the cell contact (i.e., the electrical contact between the current collector tab of the cell and the crocodile clamp of the current cable). This becomes apparent from the voltage profiles of cell 2 in cycles 892–894, which show a ≈100 mV lower charge and discharge voltage after the event in cycle 893 (corresponding to a ≈15 Ω lower resistance; see paragraph S5 and Figure S8 in the SI). However, the capacity fading rate after this event remains unchanged for the subsequent cycles.

Figure 2b shows the charge-averaged mean charge and discharge voltage of the cathode electrodes vs. Li^+/Li of cells 1 and 2 (for a given charge or discharge cycle, $\bar{V}_{cath} \equiv \int V_{cath} \times dq / \int dq$).[57] After the initial rapid increase of $\bar{V}_{cath}$ due to the increase in C-rate (from C/10 to C/2 in the 3rd cycle) and change in temperature (from 25°C to ≈22°C in cycle 9), the $\bar{V}_{cath}$ curves for charge and discharge show a relatively linear behavior, with the mean discharge voltage decreasing by ≈0.12 mV per cycle and the mean charge voltage increasing by ≈0.08 mV per cycle. The increase of the overpotential during both charge and discharge suggests an increase in cathode impedance over extended cycling. The small spikes in the $\bar{V}_{cath}$ curves every ≈50 cycles are caused by the OCV holds for XPD data collection, where the cell potential relaxes. The $\bar{V}_{cath}$ jump of cell 2 at cycle 893 is due to the above discussed change in the cell contact resistance.

Figure 2c shows a comparison of the half-cell voltage profiles of graphite and NCM-811 vs. Li^+/Li of cell 2 for the 19th cycle (black curves, after the first LDE XPD data point, BOT) and for the 973rd cycle (blue curves, close to the last LDE XPD data point in the 975th cycle, EOT). It can be seen that the overpotential of the cathode (solid lines) increases drastically with cycling, as already indicated by its mean voltage evolution. Because cycling was carried out between fixed cathode voltage limits (3.0 and 4.5 V vs. Li^+/Li), this increase of overpotential contributes significantly to the observed capacity fading, as the accessible capacity window gets narrowed from both sides.[19,58] On the other hand, the voltage profile of the graphite anode (dashed lines) shows no significant change with cycling.

In the literature, various factors are discussed which might cause the capacity fading for Ni-rich NCMs in the absence of a loss of cyclable lithium (i.e., in half-cells with lithium anodes or, as in this study, in full-cells with pre-lithiated graphite anodes), as seen in Figure 2. Amongst others, bulk structural changes such as cation disorder are identified as possible reason.[52] A notably increased fraction of Ni in the Li layer would not only reduce the number of active Li sites, but also gives rise to an increased polarization.[59] Contact loss in the CAM due to pronounced particle cracking[13] and surface instabilities,[20] however, are also reported to lead to a capacity loss due to impedance build-up. At the same time, both cracking and surface instabilities might cause a capacity loss due to material loss in the form of isolated particles or reconstructed phases, which are electrochemically inactive. In the following, the reasons for the continuous capacity fading observed in Figure 2 are analyzed by a combination of various techniques, with emphasis on the long-duration experiment XPD data.

XPD analysis with respect to bulk stability and cation mixing.— Starting our XPD analysis, we first examined whether any reversible phase transformations could be observed. For instance, for $LiNiO_2$, there are literature reports on the reversible phase transformation from a hexagonal to a monoclinic structure (H1-M transformation) and further on to new hexagonal versions (M-H2 and H2-H3 transformations) upon delithiation.[7] The H1-M transformation is accompanied by the splitting of the original (101), (012), and (104) reflections in the hexagonal symmetry, whereas the H2-H3 transformation involves an abrupt contraction of the lattice parameter *c*. In our study, no peak splitting

Journal of The Electrochemical Society, **166** (15) A3760-A3774 (2019)

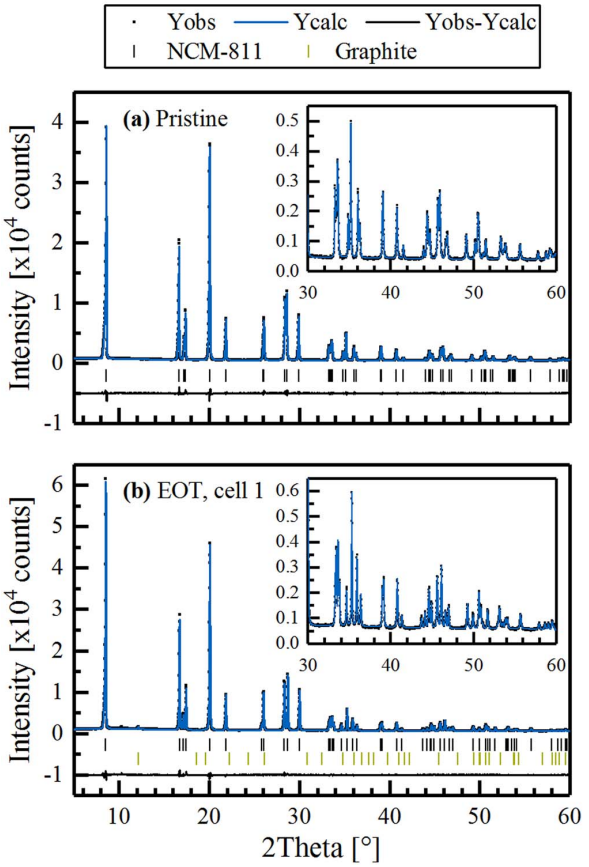

Figure 3. Refinement of ex situ L-XPD data based on capillary measurements of (a) pristine and (b) harvested EOT NCM-811 powder (from cell 1) in the common $R\bar{3}m$ space group. The data were collected at the in-house Mo-diffractometer ($\lambda = 0.7093$ Å). The observed (black points), calculated (blue lines), and difference diffraction profiles (black lines) are shown together with the position of the Bragg peaks of NCM-811 (black ticks) and graphite (green ticks). The insets show a magnification of the high-angular range. Note that the EOT NCM-811 electrode sample contains 2 wt% conductive graphite, which was included into the refinement (strongest reflection at ≈12°). The refinement results are summarized in Table I.

Table I. Refinement results of pristine NCM-811 and NCM-811 electrodes harvested at EOT, based on ex situ L-XPD capillary measurements at a Mo-diffractometer and refined in the common $R\bar{3}m$ space group. The diffractograms for pristine NCM-811 and the electrode harvested at EOT from cell 1 are shown in Figure 3. The table summarizes quality factors (*R*-values), lattice parameters and the thereof determined Li content and atomic site-specific information (including Li-Ni mixing, fractional *z*-coordinate of O, and thermal displacement parameters). The *b* values were constrained to be the same for all elements on one site. Errors given in parenthesis.

	Pristine	EOT, cell 1	EOT, cell 2
R_{wp} [%]	4.52	4.48	4.84
R_{bragg} [%]	1.14	1.04	1.49
χ^2	1.99	2.63	2.04
a [Å]	2.87212(2)	2.85945(2)	2.85931(3)
c [Å]	14.2058(2)	14.2902(2)	14.2820(3)
c/a [-]	4.94609(7)	4.99756(7)	4.9949(1)
x_{Li} [-]	1.01[a]	0.79[b]	0.80[b]
Li-Ni mixing [%][c]	3.1(1)	2.0(1)	3.1(1)
$z_{6c,O}$ [-]	0.24156(7)	0.23908(8)	0.2396(1)
$b_{3a,Li}$ [Å^2]	1.22(9)	0.7(1)	1.1(2)
$b_{3b,TM}$ [Å^2]	0.171(8)	0.298(9)	0.08(1)
$b_{6c,O}$ [Å^2]	0.62(2)	0.82(3)	0.47(3)

[a]The Li content of the pristine material was fixed to the elemental analysis results ($Li_{1.01}Ni_{0.79}Co_{0.10}Mn_{0.10}O_2$).
[b]The Li content of the EOT materials was calculated from the low-SOC *c/a* calibration curve, as shown in Figure 5a and in paragraph S1 in the SI.
[c]Li-Ni mixing gives the percentage of Ni on the 3a site of the Li layer relative to the total available occupancy of the 3a site.

and only a gradual contraction of the *c* parameter were observed. In the study of Ryu et al.,[60] these $LiNiO_2$-like transformations were only seen for NCM materials with a Ni content of 90% or higher. Other authors report on an irreversible thermal reconstruction of the rhombohedral to a spinel structure of $Li_{0.5}NiO_2$, indicated by a coalescence of the (018) and (110) reflections,[61] which we could not observe here by electrochemical cycling.

Next, we examined the XPD patterns for any sign of cation disorder between the Li and transition-metal layer, i.e., for Li-Ni mixing. The refinement of this sensitive parameter has proved to be difficult, especially in the case of in situ XPD data due to the overlapping reflections from other cell components (Al and Cu) and the complex background patterns (see paragraphs S1 and S2 in the SI). Furthermore, we observed a significant correlation between the Li occupancy and cation disorder, as it is also known from the literature.[34] The refinement of the cation disorder was therefore conducted with ex situ L-XPD data from capillary measurements with pristine NCM-811 powder and discharged NCM-811 cathodes harvested at EOT. These data are shown in Figure 3, and the refinement results are summarized in Table I, whereby the remaining Li content, x_{Li}, of the EOT samples was determined from the *c/a* calibration curves discussed in the following section (see Figure 5a). These refinements give a Li-Ni mixing of 3.1(1)% for the pristine and EOT sample of cell 2. The EOT sample of cell 1 gives a reproducible cation disorder of 2.0(1)%.

For the refinement of the in situ S-XPD data, the cation disorder was therefore fixed to the value obtained from the ex situ L-XPD capillary data, because there the parameter could be determined reliably and without any overlapping reflections. In the Rietveld refinement, the very sensitive cation disorder parameter correlates strongest to the thermal displacement parameter $b_{3a,Li}$ (≈75%) and the scale factor (≈65%). However, all *b* values are in a reasonable range.[34,39] Fixing the EOT *b* values to the pristine *b* values increases the Li-Ni disorder only by ≈0.2%. Thus, we can conclude with confidence that the Li-Ni mixing is barely affected by 1000 charge/discharge cycles and does not contribute to the observed capacity loss. Since the peak broadening of the samples is also very similar (see Table S2 in the SI for the in situ S-XPD data), all these results prove that there are no remarkable bulk structural changes observed in the NCM-811 CAM upon long-term cycling with an upper cut-off voltage of 4.5 V vs. Li^+/Li. This is in agreement with a study over 300 cycles for NCM-811/graphite full-cells including XPD data performed by Kim et al.,[62] even though it should be noted that the upper cut-off voltage in their study was only 4.2 V. Furthermore, there are literature reports (without specifically refining Li-Ni mixing) on the bulk stability of Ni-rich CAMs like $LiNi_{0.76}Co_{0.14}Al_{0.10}O_2$, which was cycled over 1000 cycles also to 4.2 V,[63] and NCM-523 cycled 50 times to a cut-off potential as high as 4.8 V vs. Li^+/Li.[58] This is in contrast to a study of Li et al.,[11] claiming the structural instability of Ni-rich CAMs, $LiNi_{0.80}Co_{0.15}Al_{0.05}O_2$ and $LiNi_{0.70}Co_{0.15}Mn_{0.15}O_2$, which showed an increase of Li-Ni disorder from 2–3% to 9–13% after cycling over 1500 charge/discharge cycles between 3.0 V and a relatively high upper cut-off voltage of 4.4 V. In our case, it can be concluded that the NCM-811 bulk structure is stable over 1000 cycles, even if a cut-off potential as high as 4.5 V vs. Li^+/Li is chosen.

A3766 *Journal of The Electrochemical Society*, **166** (15) A3760-A3774 (2019)

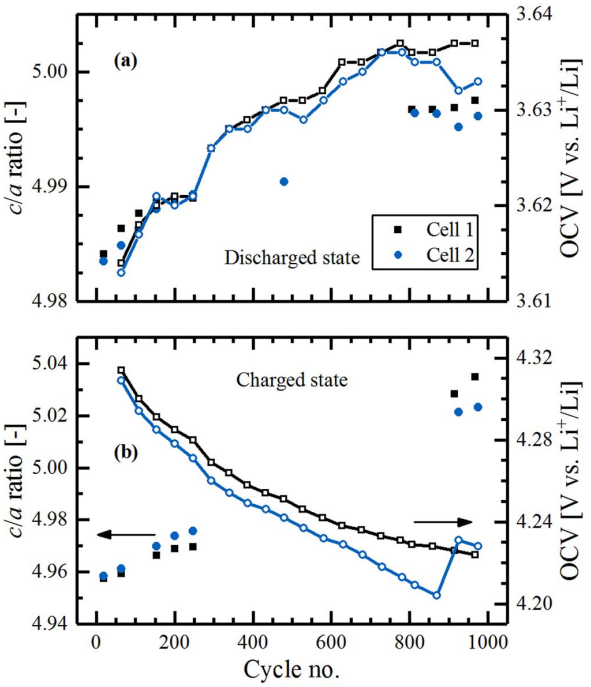

Figure 4. Evolution of the *c/a* ratio (filled symbols, left y-axes) and the OCV (line and empty symbols, right y-axes) in the (a) discharged and (b) charged state of NCM-811, determined from the in situ S-XPD data obtained from the two cells cycled at the Diamond Light Source. Missing *c/a* data points are due to a long beam shut-down.

Lattice parameter evolution monitored via XPD analysis.—From the refinement of the in situ S-XPD patterns, the lattice parameters of NCM-811 were obtained in charged and discharged state over the course of almost 1000 cycles for the two cells (more refinement results shown in paragraph S2 in the SI). The lattice parameter ratio *c/a* is shown in Figure 4 (filled symbols, left y-axes) together with the OCV at which the respective data were measured (empty symbols, right y-axes). According to literature data, the *c/a* ratio is the most reliable measure of lattice expansion (in *c*-direction) and compression (in *a*, *b* direction) induced by Li extraction and insertion in NCM materials.[64] It can be seen that in both charged and discharged state the *c/a* ratio increases during the experiment (see filled symbols). Furthermore, the OCV was found to change over the course of extended cycling, increasing in the discharged state (empty symbols in Figure 4a) and decreasing in the charged state (empty symbols in Figure 4b). For a stable bulk material – which we can assume based on the ex situ L-XPD data discussed above – it is known that the OCV scales with the SOC of the material, i.e., the higher the SOC, the higher the respective OCV value. Thus, from the OCV evolution shown in Figure 4, we can conclude that the effective SOC window becomes smaller over the course of cycling. This is in agreement with the observed capacity loss and overpotential increase of the NCM-811 electrode (see Figure 2). Here, we should note that the jump in the OCV (≈30 mV) observed for cell 2 after ≈900 cycles is related to the change in cell contacting resistance at this point and also reflected in an increase in cell capacity (see Figure 2a), as discussed above.

To understand whether this is consistent with the observed increase of the *c/a* ratio over cycling in both the charged and discharged state (filled symbols in Figures 4a, 4b), one has to consider the relationship between the *c/a* ratio and the lithium content, x_{Li}, or the SOC of NCM materials: the *c/a* ratio initially increases upon charging until it reaches a maximum at ≈60% SOC (i.e., $x_{Li} \approx 0.4$) and then decreases upon further increasing the SOC.[51,60,64,65] Thus, the observed increase in the *c/a* parameter in the discharged state (SOC << 60%) and in the charged state (SOC always >60%), clearly indicates a shrinkage in the capacity window, which at least qualitatively is consistent with the OCV evolution.

To convert the qualitative OCV and *c/a* analysis into a quantification of capacity losses in the charged and discharged state, the *c/a* curve for the first two/three cycles was measured to serve as a calibration curve of the *c/a* ratio vs. capacity (more precisely x_{Li}) or OCV, as will be described in the following. The detailed approach and the respective data sets from in situ XPD (i.e., complete XPD pattern collected at OCV conditions at different SOC steps over 2 cycles) and operando XPD (i.e., continuous data collection of (003) and (110) reflection during 3 cycles) are described in the Experimental section and are discussed in detail in paragraph S3 in the SI. The thus obtained relationship between the *c/a* ratio and the lithium content x_{Li} of NCM-811 is shown exemplarily for the 2nd discharge cycle in Figure 5a (measured in operando mode), which is in agreement with literature reports.[60,65,66]

Next, the lattice parameters obtained from the in situ S-XPD data during long-term cycling were used to compute the changes of the *c/a* ratio, from which the Li content x_{Li} in the cycled NCM-811 (i.e., in $Li_xNi_{0.79}Co_{0.10}Mn_{0.10}O_2$) could be determined, as was done by Buchberger et al.[51] The relationship between the *c/a* ratio and x_{Li} is given in Figure 5a and in paragraph S1 in the SI. Here, the advantages of using the *c/a* ratio instead of only the lattice parameters becomes evident: (i) the *c/a* ratio is close to linearity in the x_{Li} ranges of interest; and, (ii) small misalignments of the cells in the geometry of the diffractometer would not falsify the result, because the error gets cancelled out by taking the ratio of both lattice parameters. From the S-XPD analysis shown in Figure 4, we know that the *c/a* ratio in both the discharged state (low SOC) and the charged state (high SOC) increases with cycling. The grey bars in Figure 5a mark the *c/a* ratio changes over 1000 cycles in both the discharged state (left bar) and the charged state (right bar), based on the data in Figure 4 (filled symbols). With the obtained operando L-XPD calibration curve (black symbols and interpolating line in Figure 5a), a mathematical relationship between x_{Li} and *c/a* can now be established. At low SOC ($0.62 \leq x_{Li} \leq 0.91$), i.e., in the discharged state, this is best described by a quadratic equation of *c/a* as function of x_{Li} (highlighted in blue in Figure 5a, with the equation given in the figure, and also as x_{Li} as a function of *c/a* in equation (S1) in the SI). At high SOC ($0.12 \leq x_{Li} \leq 0.23$), i.e., in the charged state, there is a linear dependence between *c/a* and x_{Li} (highlighted in green, with the equation given in the figure and as equation (S2) in the SI).

With the values for *c/a* in the discharged and charged state over 1000 cycles (from Figure 4), the capacity losses at low and high SOC in the ith cycle ($\Delta C^{BOT\rightarrow i}_{Discharge}$ and $\Delta C^{BOT\rightarrow i}_{Charge}$) relative to the first in situ S-XPD data point in the 18th cycle (BOT) can now be quantified and then compared to the electrochemical capacity loss ($\Delta C^{BOT\rightarrow i}_{EC}$). The applied calculations are explained in the following, whereby a "Δ" represents a difference between two specific states. Firstly, the electrochemical capacity loss between the ith cycle and at BOT (18th cycle), $\Delta C^{BOT\rightarrow i}_{EC}$, is defined by the difference of the discharge capacity in the ith cycle, C^{i}_{EC}, and that at BOT, C^{BOT}_{EC}:

$$\Delta C^{BOT\rightarrow i}_{EC} = C^{BOT}_{EC} - C^{i}_{EC} \quad [1]$$

This can be compared to the capacity loss inferred from the in situ S-XPD data, namely to the sum of the calculated capacity losses referenced to BOT in the discharged state, $\Delta C^{BOT\rightarrow i}_{Discharge}$, and in the charged state, $\Delta C^{BOT\rightarrow i}_{Charge}$:

$$\Delta C^{BOT\rightarrow i}_{Overpotential} = \Delta C^{BOT\rightarrow i}_{Discharge} + \Delta C^{BOT\rightarrow i}_{Charge} \quad [2]$$

Both of these XPD-deduced capacity loss values can be calculated for the ith cycle relative to BOT by taking the difference between the respective x_{Li} values between the ith cycle and BOT (Δx_{Li}) in either the discharged state ($x^{i}_{Li,dis} - x^{BOT}_{Li,dis}$) or the charged state ($x^{BOT}_{Li,cha} - x^{i}_{Li,cha}$), which are obtained by the measured *c/a* ratios using the mathematical

Journal of The Electrochemical Society, **166** (15) A3760-A3774 (2019)

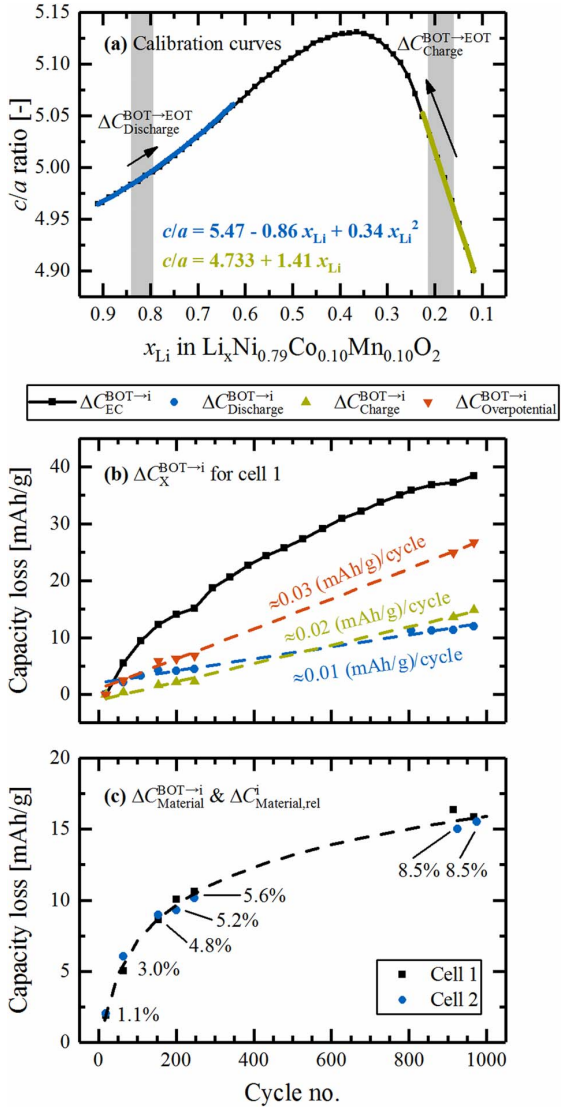

Figure 5. (a) Dependence of the *c/a* ratio on the Li content x_{Li} for the pristine NCM-811 CAM determined by operando L-XPD (black symbols and interpolating line, shown exemplarily for the 2nd discharge cycle). The quadratic and linear fits at low and high SOC are shown in blue and green, respectively (average from the first three discharge cycles, equations given in the plot and in paragraph S1 of the SI). Furthermore, the evolution of the *c/a* ratio from BOT to EOT during the long-term cycling study is indicated by the grey bars and arrows (based on the filled symbols in Figure 4). (b) Capacity loss relative to BOT calculated from electrochemical data ($\Delta C^{BOT\rightarrow i}_{EC}$, Eq. 1) and from changes of x_{Li} obtained by in situ S-XPD in the discharged ($\Delta C^{BOT\rightarrow i}_{Discharge}$, Eq. 3) and charged state ($\Delta C^{BOT\rightarrow i}_{Charge}$, Eq. 4) as well as the sum of both ($\Delta C^{BOT\rightarrow i}_{Overpotential}$, Eq. 2), (c) Capacity loss attributed to a material loss depicted in absolute values ($\Delta C^{BOT\rightarrow i}_{Material}$, Eq. 6, individual data points for cell 1 and 2) and relative to the pristine CAM ($\Delta C^{i}_{Material,rel}$, Eq. 7, percentages given for each cycle as mean value from cell 1 and 2).

relationships between the *c/a* ratio and x_{Li} (see equations (S1) and (S2) in paragraph S1 of the SI). To convert this Δx_{Li} difference into a specific capacity, the second term on the right-hand side of Equations 3 and 4 serves as a conversion factor relating 1.01 mol Li to the theoretical capacity of 274 mAh/g for complete Li extraction in the here used NCM-811 material ($Li_{1.01}Ni_{0.79}Co_{0.10}Mn_{0.10}O_2$, theoretical capacity includes surface impurities, see Experimental section).

$$\Delta C^{BOT\rightarrow i}_{Discharge} = \left(x^{i}_{Li,dis} - x^{BOT}_{Li,dis}\right) \cdot \frac{274\ mAh/g}{1.01} \quad [3]$$

$$\Delta C^{BOT\rightarrow i}_{Charge} = \left(x^{BOT}_{Li,cha} - x^{i}_{Li,cha}\right) \cdot \frac{274\ mAh/g}{1.01} \quad [4]$$

In this case, $\Delta C^{BOT\rightarrow i}_{Overpotential}$ (Equation 2) accounts for the accumulated capacity loss between BOT and the ith cycle due to an increasing overpotential, as deduced from the in situ S-XPD data. If the capacity loss over cycling were only due to an increasing NCM-811 overpotential, $\Delta C^{BOT\rightarrow i}_{Overpotential}$ would have to be identical with the electrochemically determined capacity loss $\Delta C^{BOT\rightarrow i}_{EC}$ (see Equation 1). On the other hand, if part of the NCM-811 would either become electrochemically inactive by a loss of material (e.g., by dissolution) or by the formation of an inactive phase, $\Delta C^{BOT\rightarrow i}_{EC}$ would be larger than $\Delta C^{BOT\rightarrow i}_{Overpotential}$.

The application of these calculations is shown for cell 1 in Figure 5b, where we compare the electrochemically measured capacity losses, $\Delta C^{BOT\rightarrow i}_{EC}$ (black symbols), with those calculated based on the lattice parameter changes, namely the sum of $\Delta C^{BOT\rightarrow i}_{Discharge}$ (blue symbols) and $\Delta C^{BOT\rightarrow i}_{Charge}$ (green symbols), equating to $\Delta C^{BOT\rightarrow i}_{Overpotential}$ (red symbols). The capacity loss $\Delta C^{BOT\rightarrow i}_{Overpotential}$ is caused by the increased overpotential of the NCM-811 CAM (see Figure 2c), which results in a smaller effective SOC window because the upper and lower cut-off potentials are reached earlier, corresponding to a smaller cyclable Δx_{Li}. In the lithiated state, the capacity loss calculated via $\Delta(c/a)$ is ≈0.01 (mAh/g)/cycle ($\Delta C^{BOT\rightarrow i}_{Discharge}$, blue curve in Figure 5b), while it is roughly doubled in the delithiated state ($\Delta C^{BOT\rightarrow i}_{Charge}$, green curve in Figure 5b). This corresponds to a shrinkage of the SOC window from initially $0.16 \leq x_{Li} \leq 0.84$ ($\Delta x_{Li} = 0.68$) for cell 1 in cycle 18 to $0.21 \leq x_{Li} \leq 0.79$ ($\Delta x_{Li} = 0.58$) after 1000 cycles. This shrinkage of the exchanged amount of lithium per cycle determined by in situ S-XPD translates into a capacity loss between BOT and EOT of $\Delta C^{BOT\rightarrow EOT}_{Overpotential}$ = 26.8 mAh/g (≡ value of the red curve at EOT in Figure 5b), which is substantially smaller than the electrochemically measured capacity loss from BOT to EOT of $\Delta C^{BOT\rightarrow EOT}_{EC}$ = 38.4 mAh/g (≡ value of the black curve at EOT in Figure 5b). The discrepancy between $\Delta C^{BOT\rightarrow EOT}_{Overpotential}$ and $\Delta C^{BOT\rightarrow EOT}_{EC}$ must be caused by a loss of active NCM-811, meaning that a portion of the material has either disappeared or is no longer participating in the electrochemical processes. As described in the literature, the capacity loss could be caused by the formation of an oxygen-deficient and electrochemically inactive phase formed at the surface of the NCM-811 particles, which transforms gradually into an insulating spinel/rock-salt-type layer and thereby also causes an impedance growth of the CAM.[18,19,67,68] Another possible scenario is the formation of electronically isolated particles caused by cracking phenomena, which would then become electrochemically inactive.[13] As we observe no second NCM-811 phase with shifted reflections (i.e., constant lattice parameters) in the patterns in neither discharged nor charged state, the formation of electronically isolated particles can be ruled out. Moreover, *post mortem* elemental analysis revealed only a minor amount of TMs deposited on the graphite anode at EOT (corresponding to ≈0.22 mol%$_{TM}$ when referenced to the original NCM-811 material, which would amount to a maximum capacity loss of ≈2.4 mAh/g as described in paragraph S3 of the SI), indicating that CAM dissolution is a rather negligible contribution to the overall capacity loss after ≈1000 cycles of the NCM-811 CAM between 3.0 and 4.5 V vs. Li^+/Li. This further supports the hypothesis that the loss of active material may be due to the formation of an electrochemically inactive surface layer.

To more precisely quantify the loss of electrochemically active material over cycling, one can compare the absolute electrochemically observed capacity in the ith cycle, C^{i}_{EC}, to the effective capacity window in the ith cycle expected from the Δx^{i}_{Li} range (i.e., $x^{i}_{Li,cha} - x^{i}_{Li,dis}$), as determined from the in situ S-XPD analysis and converted into a

A3768 *Journal of The Electrochemical Society*, **166** (15) A3760-A3774 (2019)

capacity, C^{i}_{XPD}:

$$C^{i}_{XPD} = \left(x^{i}_{Li,cha} - x^{i}_{Li,dis}\right) \cdot \frac{274\ mAh/g}{1.01} = \Delta x^{i}_{Li} \cdot \frac{274\ mAh/g}{1.01} \quad [5]$$

If 100% of the original NCM-811 material were active, the electrochemical capacity in the ith cycle, C^{i}_{EC}, and the capacity predicted by the Δx_{Li} range, C^{i}_{XPD}, would have to be equal. If, however, a part of the CAM becomes electrochemically inactive, the capacity expected from the XPD data, C^{i}_{XPD}, would be larger than what can be observed, C^{i}_{EC}, because the Δx_{Li} range determined from XPD is applied for the whole CAM (i.e., the CAM fraction from XPD analysis appears always as 100%). Therefore, a loss of electrochemically active material by the ith cycle, $\Delta C^{i}_{Material}$, would correspond to the difference between C^{i}_{XPD} (capacity if no cyclable material would have been lost) and the actual electrochemical capacity in the ith cycle:

$$\Delta C^{BOT\rightarrow i}_{Material} = \left(C^{i}_{XPD} - C^{i}_{EC}\right) \cdot \frac{\Delta x^{BOT}_{Li}}{\Delta x^{i}_{Li}} \quad [6]$$

The correction factor of $\Delta x^{BOT}_{Li}/\Delta x^{i}_{Li}$ takes into account that the material loss goes typically hand in hand with an increased overpotential (i.e., $\Delta x^{BOT}_{Li} > \Delta x^{i}_{Li}$). Consequently, the material loss relative to BOT has to be referred to the broader Δx^{BOT}_{Li} range and BOT should ideally be a state where no material loss has yet occurred (i.e., one of the very first cycles). More intuitively, the material loss can also be expressed in percentage terms as the electrochemically inactive phase fraction relative to the pristine CAM:

$$\Delta C^{i}_{Material,rel} = \frac{C^{i}_{XPD} - C^{i}_{EC}}{C^{i}_{XPD}} \quad [7]$$

Here, no correction is necessary since the equation only involves data from the ith cycle, with C^{i}_{XPD} being the maximum capacity, which can be achieved with the actually present overpotential of the aged CAM in the ith cycle.

The thus calculated capacity loss due to the loss of electrochemically active material, $\Delta C^{BOT\rightarrow i}_{Material}$, for both cell 1 and cell 2 as well as the average share of lost material relative to the pristine CAM, $\Delta C^{i}_{Material,rel}$, are shown in Figure 5c. The curve of the material loss shows a steep increase during the first 300 cycles and levels out afterwards, suggesting that most material losses happen in the first 300 cycles. It is known for regular NCMs[15,18] as well as for Li-rich NCMs[17,69] that a surface reconstruction is triggered by the loss of oxygen, which happens mainly in the very first cycles, especially if the cathode is charged over 80% SOC. Here, an SOC of ≈85% is reached during the first two C/10 formation cycles. On the other hand, HR-TEM images have shown that the actual reconstruction happens within 20–50 cycles for Li-rich NCMs at 25°C.[17] As vacancies in the transition-metal layer probably facilitate the reconstruction in Li-rich NCMs, it is reasonable to assume that this process takes longer for regular NCMs (here 200–300 cycles). At the end-of-test, the material loss for both cells adds up to ≈15.8 mAh/g or 8.5% (average of the data for both cells at ≈1000 cycles in Figure 5c). As we propose that this materials loss is due to the formation of a thin surface layer in the nm range with a possibly amorphous character, it is not unexpected that it is not visible as additional phase in the diffractograms, similar to the finding for aged NCMs in the literature.[18,51] For this reason, we also tried to quantify the electrochemically active NCM-811 fraction over the course of the cycling study by normalizing its scale factor (measure of the intensity of this phase) to the intensity of stable "internal standards" in the cell (see Figure S4 in the SI). For this analysis, we used the polymer peaks from the pouch foil as well as the intensity of the (111) reflection of Al and Cu, which were both refined with a structure-independent Pawley fit. As can be seen in Figure S4, the results have a relatively large scatter, but a loss of a fraction of the active NCM-811 phase from BOT to EOT can be concluded as general trend.

The above analysis has shown that we can differentiate two main contributions to the capacity loss of NCM-811, namely the overpotential-induced loss and the actual loss of cyclable material. As only the electrochemically active material can undergo a capacity loss due to an increasing overpotential, $\Delta C^{BOT\rightarrow i}_{Overpotential}$ has to be corrected by the NMC-811 phase fraction which has been lost up to the respective cycle:

$$\Delta C^{BOT\rightarrow i}_{Overpotential,corr} = \Delta C^{BOT\rightarrow i}_{Overpotential} \cdot \left(1 - \Delta C^{i}_{Material,rel}\right) \quad [8]$$

The same correction applies to the individual contributions in the discharged ($\Delta C^{BOT\rightarrow i}_{Discharge}$) and charged state ($\Delta C^{BOT\rightarrow i}_{Charge}$, see Equation 2). Since the material loss amounts to 8.5% at the end-of-test, $\Delta C^{BOT\rightarrow EOT}_{Overpotential} = 26.8$ mAh/g for cell 1 in Figure 5b reduces to 24.5 mAh/g after correction. Thus, the sum of both loss terms from BOT to EOT, $\Delta C^{BOT\rightarrow EOT}_{Overpotential,corr}$ and $\Delta C^{BOT\rightarrow EOT}_{Material}$ (15.8 mAh/g), amounts to 40.3 mAh/g for cell 1. This calculated value is slightly higher than the actual capacity loss of $\Delta C^{BOT\rightarrow EOT}_{EC} = 38.4$ mAh/g due to the material loss which was already acquired until the begin-of-test (1.9 mAh/g in the 18th cycle, see Figure 5c).

Bulk stability vs. surface instability.—In the following, XPD data from which we have inferred the stability of the bulk of NCM-811 (Figure 6a) are contrasted with impedance data from which we will get insights into the long-term stability of the NCM-811 surface (Figure 6b). Let us first focus on Figure 6a, where the *c/a* ratio is shown as a function of the open circuit voltage for the in situ L-XPD data (i) from the first two cycles of the NCM-811 cathode (black symbols/lines) and (ii) from the harvested EOT cathode of cell 1 (blue symbols/lines)

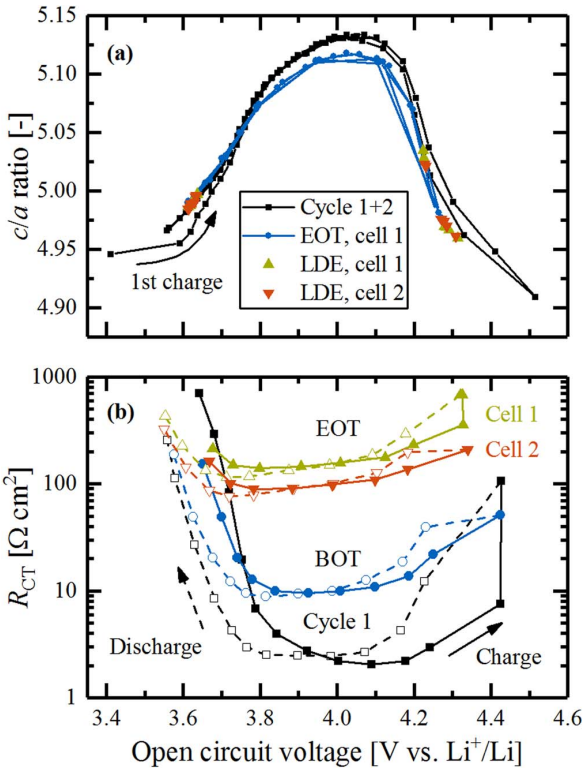

Figure 6. (a) Comparison of the in situ L-XPD *c/a* curves of a fresh NCM-811 cathode in cycle 1 and 2 (black symbols/lines) and for the EOT cathode (harvested from cell 1, blue symbols/lines) cycled vs. a lithium anode with the *c/a* data points collected during the long-term S-XPD study from cells 1 and 2 (green and red symbols, labeled as LDE, same data as in Figure 4). (b) Comparison of the charge-transfer resistance of NCM-811 cathodes in the first cycle, at BOT, and at EOT for both long-term cycled cells, measured with a GWRE in a NCM-811/pre-lithiated graphite setup at 25°C. The electrodes in cycle 1 and BOT are a different set than that at EOT. Both the *c/a* data in panel (a) and the R_{CT} data in panel (b) are shown as a function of the OCV value, at which the data points were measured.

Journal of The Electrochemical Society, **166** (15) A3760-A3774 (2019) A3769

as well as for the in situ S-XPD data from both cells over the course of cycling (green and red symbols, labeled as LDE cells). Note that the OCV values versus the Li-CE (for the L-XPD data) or the Li-RE (for the S-XPD data cycled vs. a pre-lithiated graphite CE) are exactly known from each in situ measurement, i.e., the datasets can be directly compared with each other without any correction. The Rietveld refinement of the capillary data (Figure 3) already indicated the bulk stability over the course of the 1000 cycles. The LDE S-XPD *c*/*a* data (green and red points in Figure 6a, which are the same data as in Figure 4) agree fairly well with the in situ L-XPD calibration curves of the first two cycles (black points/lines) and the EOT sample (blue points/lines). This proves that the *c*/*a* calibration curve taken for NCM-811 in the first few cycles and used to quantify the lithium content x_{Li} at low or high SOC, is also valid for NCM-811 aged over the course of 1000 cycles, so that the XPD analysis conducted in Figure 5 is feasible. The small deviation of the first *c*/*a* points in the first charge from the first discharge and the subsequent cycle is discussed in paragraph S3 in the SI and shown in more detail in Figure S6. Furthermore, the discrepancy of the EOT curve in the mid-voltage region is probably caused by a minor amount of dissolved transition-metals (≈0.22 mol% TMs detected by ICP-OES on the graphite anode at EOT). The observed discrepancy is also discussed in context with Figure S6 in paragraph S3 of the SI.

As described above, a growing overpotential on the cathode was identified to be a major reason for the observed capacity loss in NCM-811/graphite full-cells based on the XPD analysis, as shown by $\Delta C^{BOT\rightarrow i}_{Overpotential}$ in Figure 5b. It has been reported in the literature that the formation of a spinel or rock-salt-like structure at the surface of NCM cathode materials leads to a drastic increase in the charge-transfer resistance.[15,18,19] To further analyze the overpotential build-up deduced from our XPD analysis (Figure 5) and the charge/discharge curve profiles (Figure 2a and Figure S9), we determined the cathode impedance of NCM-811 cathodes after a different number of cycles, using a three-electrode setup with a micro-reference electrode. Figure S7 in the SI shows exemplary cathode impedance spectra taken at ≈4.0 V during charge of NCM-811 cathodes in the first cycle, in the 18th cycle (corresponding to BOT), and after 1000 cycles (EOT) from a harvested NCM-811 cathode. The spectra exhibit a semicircle at low frequencies, which could be assigned to the charge-transfer resistance, R_{CT}, as described in paragraph S4 in the SI. As the value of R_{CT} is SOC-dependent, these impedance measurements were conducted during OCV at different points during charge and discharge, namely at steps of 20 mAh/g, in a similar fashion as the in situ XPD measurements in Figure 6a. The resulting R_{CT} values are plotted versus OCV in Figure 6b. As was already mentioned above, there is no need to correct for any shift in capacity (x-axis) when plotting vs. OCV, because this is already a measure of the bulk state-of-charge or the lithium content. All R_{CT} curves depicted in Figure 6b have a characteristic minimum around ≈4.0 V and increasing values toward the SOC limits, analogous to what has been reported for HE-NCM.[70] A comparison of the curves during charge at ≈4.0 V is consistent with the observed increase of the NCM-811 cathode overpotential, with the charge-transfer resistance found to increase from ≈2 Ω cm^2 to ≈10 Ω cm^2 over the first 18 cycles (black vs. blue curve) and further up to ≈100–150 Ω cm^2 after 1000 cycles (green and red curve for EOT cell 1 and 2). This means that the impedance growth for cell 2 amounts to ≈90 Ω cm^2 from BOT to EOT, which at a rate of C/2 (≡ 0.75 mA/cm^2) would equate to an additional overpotential of ≈70 mV (a slightly higher impedance growth of 140 Ω cm^2 and a higher projected overpotential of ≈105 mV is obtained for cell 1). The overpotential growth calculated from the R_{CT} increase for cell 2 is reasonably consistent with what we observed from the cathode half-cell voltage profiles of cell 2 shown in Figure 2c. There, the difference between charge and discharge voltage at mid-SOC (near 4 V) increases by ≈240 mV between cycle 19 and cycle 973, compared to the R_{CT}-based prediction of ≈140 mV. A more detailed description of this overpotential build-up plotted over the whole SOC window is depicted in Figure S9 of the SI. In addition, there is also a difference plot between the cathode half-cell voltage profiles at EOT and cycle 250 versus BOT, indicating that the overpotential increase can be seen over the whole SOC window and that it is more pronounced during the discharge than during charge, an observation which for yet unknown reasons is at variance with the R_{CT} data in Figure 6b. Overall, however, the cathode potential vs. capacity curves can be used as an indicator for the impedance build-up, as they correlate reasonably well with cathode impedance based R_{CT} values. This fact is further utilized to analyze the evolution of the overpotential build-up over cycling.

While the impedance growth over the 1000 cycles shown in Figure 6b can account for a significant part of the NCM-811 capacity loss, our XPD analysis shown in Figure 5 also indicates that there must be an additional loss of cyclable material, which was found to be most pronounced during the first 300 cycles (see Figure 5c). In this context, it has been suggested that oxygen release takes place in surface-near regions of NCMs or HE-NCMs, leading to a highly disordered oxygen-deficient surface layer which during subsequent cycling transforms into a resistive spinel/rock-salt-like layer, accompanied by an impedance build-up.[15–19,71] If material at the NCM-811 particle surface were to transform directly into a resistive layer, the impedance build-up should follow the same trend over cycling as the material loss derived from the $\Delta C^{i}_{Material}$ data, namely increasing rapidly until cycle 300, followed by a more gradual increase afterwards (see Figure 5c). However, the evolution of the overpotential on the cathode half-cell voltage profile does not follow the trend of the material loss (see comparison of cycle 250 with BOT in Figure S9 in the SI). Indeed, the voltage profile in cycle 250 does not exhibit a significant overpotential (≈40 mV for cell 2 near 4.0 V during charge, highlighted by a grey bar in Figure S9 in the SI), although at the same cycle number, $\Delta C^{i}_{Material}$ shown in Figure 5c already indicates a substantial loss of cyclable material. Thus, we could further confirm the observations made in the literature[18,19] on the early transformation of the surface-near region of NCM, then followed by a subsequent, more gradual transformation into a resistive surface layer. Summarizing our findings so far: R_{CT} is the origin of the growing cathode overpotential developing gradually over the course of cycling. This, in turn, causes the cell to run earlier into its voltage limits, thereby shrinking the effective capacity window (Δx_{Li}). We showed that this capacity loss due to an increased overpotential can be monitored by XPD, as shown in Figure 5 and Figure 6a. Thus, the surface instability of the NCM-811 cathode active material is the dominant factor contributing to capacity fading.

Reversible vs. irreversible capacity losses.—To analyze the observed overpotential, which is a kinetic hindrance of the (de)lithiation process, a rate test with BOT and EOT samples was conducted to evaluate how much of the lost capacity can be recovered at very low C-rates. For a C-rate approaching zero in combination with a lithium anode, the increased NCM-811 impedance over cycling and the associated overpotential should become negligible and lead to a regain of the original capacity, except for the capacity loss which is caused by an irreversible loss of electrochemically active material. The capacity share due to the loss of active CAM would then be equal to (C_{BOT}-C_{EOT})/C_{BOT} (= $\Delta C/C_{BOT}$) at a given C-rate, as the C-rate approaches zero. The scheme in Figure 7a shows why the relative values (i.e., the comparison of BOT and EOT) should be used in this analysis. It is based on the fact that the cycling conditions, including C-rate, potential cut-offs, and temperature, determine the actual capacity that can be extracted from the CAM and which for NCMs is always below the theoretical capacity of ≈280 mAh/g_{NCM}. Let us compare two scenarios where either 100% (case A, e.g., with a very high cut-off voltage) or only 50% (case B, e.g., with an intermediate cut-off voltage) of the NCM capacity is accessed at BOT (i.e., in the absence of any loss of active material). The absolute capacity loss caused by an inactive surface layer (of the same thickness) at EOT will definitely be different for the two cases, meaning that the absolute loss for case B would only be half compared to that for case A (i.e., $\Delta C_B = 0.5 \cdot \Delta C_A$). In contrast, the BOT-normalized relative capacity loss is the same in both cases (i.e., $\Delta C/C_{BOT}$ would be identical) and is thus the correct measure for the loss of active material. However, as stated above, to quantify the irreversible capacity loss due to cyclable material loss

A3770 Journal of The Electrochemical Society, 166 (15) A3760-A3774 (2019)

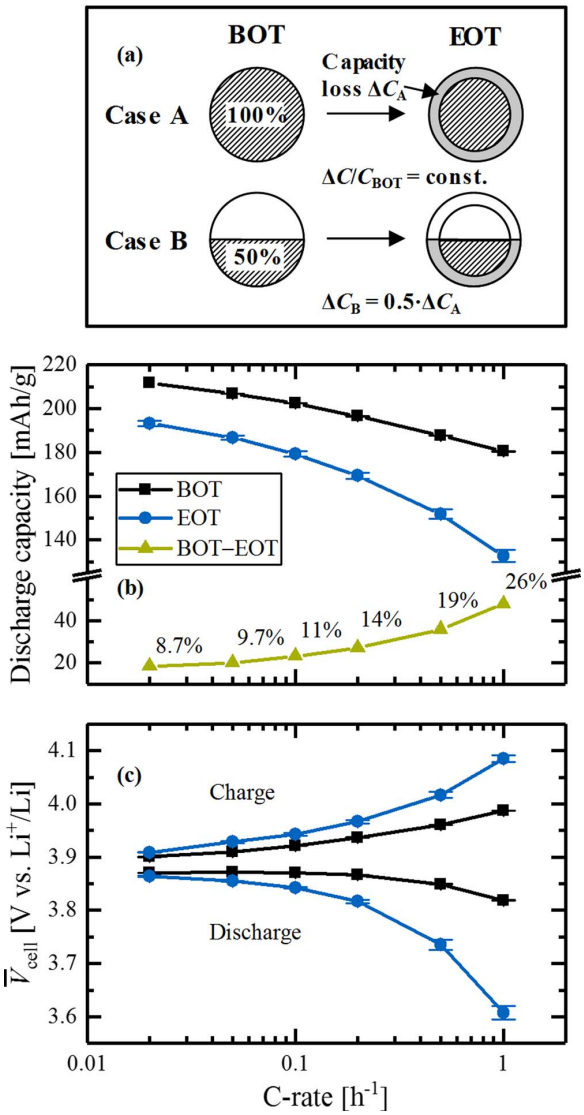

Figure 7. Rate test of BOT (i.e., test started after 18 regular cycles of the LDE protocol) and EOT NCM-811 cathodes harvested from cell 1 and 2, measured in a NCM-811/lithium coin-cell setup at 25°C. (a) Scheme illustrating the difference between absolute and relative capacity loss caused by an inactive phase. (b) Discharge capacities at BOT and EOT as well as their difference; the percentages marked on the latter are the difference between BOT and EOT capacity normalized to the BOT discharge capacity at the respective C-rate. (c) Mean charge and discharge cell voltages ($\bar{V}_{cell}$) of the NCM-811/Li cells. For EOT samples, the average capacity and $\bar{V}_{cell}$ values for the NCM-811 cathodes harvested from cell 1 and cell 2 of the long-duration experiment are shown (error bars are min/max values); for the BOT samples, two nominally identical cells were measured.

by these means, the C-rate must be small enough so that overpotentials play no role anymore. This condition should be satisfied once the charge-averaged mean charge and discharge voltages ($\bar{V}_{cell}$) for NCM-811 cathodes harvested at EOT start to become sufficiently close to that of the BOT cells. In Figure 7c, this recovery of $\bar{V}_{cell}$ during charge and discharge for the EOT cells (blue curve) is compared to the BOT cell (black curve) as the C-rate is decreased from 1C to C/50, reaching essentially identical $\bar{V}_{cell}$ values for BOT and EOT cells at C/50 (less than 10 mV difference).

The effect of a decreasing overpotential with decreasing C-rate on the discharge capacity is shown in Figure 7b. Comparing the performance of the BOT (black curve) and EOT NCM-811 cathodes (blue curve) indicates that a large fraction of the discharge capacity is regained for the EOT cells by applying a slow cycling rate of C/50. In the light of our previous analysis, the remaining (irreversible) capacity loss should arise from the NCM-811 fraction that is lost to a reconstructed and electrochemically inactive surface layer. Thus, the irreversible capacity loss of ≈18 mAh/g at C/50 (green symbols in Figure 7b) that translates into a loss of cyclable material of 8.7% (from $\Delta C/C_{BOT}$) has to be compared to the relative material loss of 8.5%, which we calculated from the XPD analysis in Figure 5c. Considering the errors, which might occur in the XPD analysis (e.g., accuracy of the calibration curves) and the rate test (e.g., weighing error of the EOT electrodes, mean voltages even at C/50 not perfectly identical), the estimates for the loss of cyclable material are reasonably close and consistent. Summarizing the presented findings: The share of the electrochemically inactive material at EOT can be calculated from both our XPD analysis and the rate test, whereby the respective reference state has to feature the same overpotential and thus the same Δx_{Li} range as at end-of-test. At a rate of C/50 at which the overpotential is minor, this reference state is the begin-of-test, whereas the overpotential build-up at C/2 during long-term cycling is significant and only the theoretical XPD capacity of the same cycle (EOT in this case) can be used as reference state (see Equations 5 and 7).

Nature of the surface layer.—XPS measurements were conducted with pristine NCM-811 electrodes as well as harvested BOT and EOT NCM-811 cathode samples to further clarify the nature of the resistive surface layer. In order to ensure a comparable SOC between the pristine and cycled electrodes (as close as possible to 0%), the latter were regularly discharged to 3.0 V vs. Li^+/Li, followed by constant voltage hold step with a C/100 current cut-off. Figure 8 is a zoom of the low-binding energy region of the O1s spectrum of pristine and aged NCM-811 samples (for the complete O1s spectrum and the used fitting parameters see Figure S10 and Table S11 in paragraph S6 of the SI). The O1s spectrum of the pristine sample shown in Figure 8a suggests the presence of a pure layered oxide with an O1s binding energy of 529.3 eV (indicated by the green line), similar to a different study conducted at our instrument.[72] After 18 charge/discharge cycles, the spectrum already shows some intensity at energies higher than the layered oxide binding energy (529.9 eV, indicated by the blue line in Figure 8b), which can be attributed to an oxygen-deficient surface layer (blue marked area). The correlation between a shift to higher binding energies and oxygen depletion in surface-near regions is established based on reference spectra of layered MnO_2, spinel Mn_3O_4, and rock-salt MnO (see paragraph S6 in the SI). It is shown there, that the O-depleted Mn-samples, i.e., spinel and rocksalt, show a peak at 0.3–0.4 eV higher energy than the layered MnO_2. After 1000 cycles (Figure 8c), the intensity of the low binding energy O1s peak shifts considerably to higher binding energy, indicating a considerable oxygen depletion at the NCM-811 surface. Therefore, at least qualitatively, the XPS analysis supports our above hypothesis that an oxygen-depleted layer is formed upon extended cycling of NCM-811 between 3.0–4.5 V vs. Li^+/Li.

Effect of the O-depleted surface layer on the SOC distribution.—Our XPD analysis showed that neither bulk structural changes, nor significant Ni-Li disorder are observable in NCM-811 over 1000 cycles (see Table I and Figure 3). However, a detailed analysis of the capacity losses indicates a loss of electrochemically active CAM (Figure 5), while the XPS analysis suggests that an oxygen-depleted surface film on the NCM-811 particles is formed upon cycling (Figure 8). Impedance data (Figure 6b) as well as rate tests (Figure 7) suggest an increased charge-transfer resistance, which is presumably caused by a resistive surface film. This poses the question whether a resistive surface layer is being formed on the external surface of each secondary NCM-811 particle with diameters of ≈5–10 µm (see Figure S11 in paragraph S8 of the SI) or whether it is being formed around each of the

Journal of The Electrochemical Society, **166** (15) A3760-A3774 (2019)

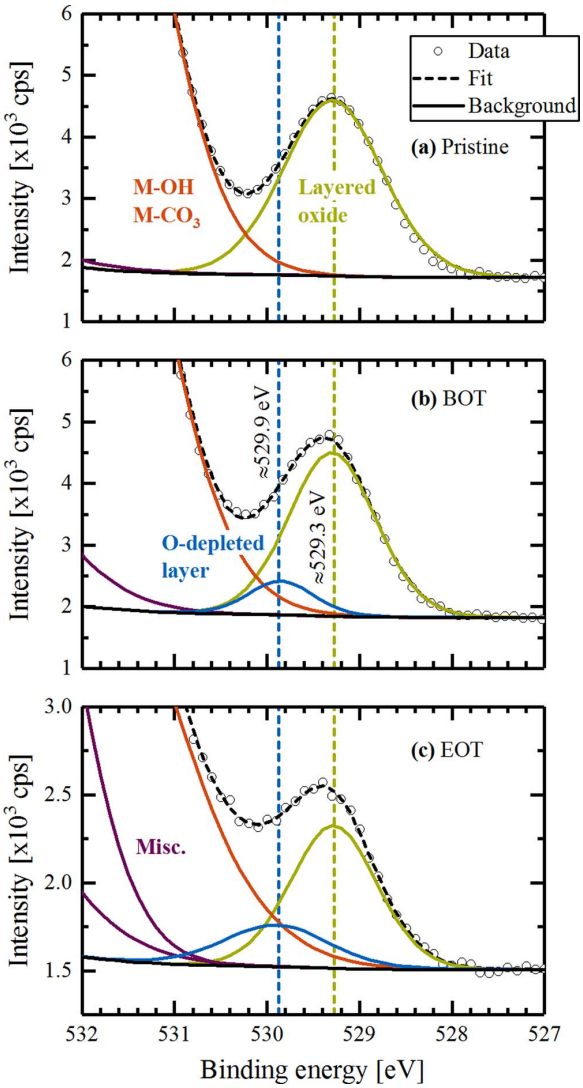

Figure 8. XPS O1s spectra of (a) pristine NCM-811 powder and of NCM-811 electrodes harvested at (b) BOT and (c) EOT. The binding energies of the layered oxide (green line) and an O-depleted surface layer (highlighted in blue) were inferred from MnO_2, Mn_3O_4, and MnO reference samples (see SI S6). Surface contaminants (hydroxides and carbonates) are fitted with one peak at higher binding energies (red line). The purple peaks referred to as miscellaneous (misc.) originate from organic surface impurities. For details on the XPS analysis and fitting procedure see paragraph S6 in the SI.

primary particles (≈0.5–1 μm in size) of which the secondary particle is composed. These two scenarios are sketched into the SEM cross-section image of a secondary NCM-811 particle shown in Figure 9a. As will be explained in the following, we will seek to examine these two scenarios by an operando XPD relaxation experiment, where the lattice parameter *c* is monitored upon the transition from a C/2 charge to OCV.

With an operando XPD relaxation experiment, the inhomogeneity of the lithium distribution (i.e., of x_{Li}) over the fresh NCM-811 electrode (after 9 cycles) and harvested EOT NCM-811 samples is compared. Thereby, the full width at half maximum (FWHM) of the reflections correlates with the homogeneity of the lattice spacing, meaning that a broader *d*-spacing distribution leads to a larger FWHM, whereas a homogenous *d*-spacing results in a sharp peak shape. Because the lattice parameters are closely linked to the lithium content x_{Li} in the NCM-811 material, the FWHM is a measure of the inhomogeneity of the SOC distribution. In this experiment, relative differences between the FWHMs of fresh and EOT samples are compared, wherefore the instrumental contribution to the broadening can be neglected (since the instrument provides a constant offset). In the relaxation experiment, selected reflections of the NCM-811 phase were monitored during the OCV period after a C/2 charge to a comparable SOC, as determined by the respective OCV (cut-off voltage of 4.3 V for fresh and 4.5 V for EOT NCM-811). The resulting OCV relaxation is shown in Figure 9b, whereby the initial potential drop from 4.3 V (fresh sample) and 4.5 V (EOT sample) to below 4.3 V occurred within the first 10 s of the OCV period. The final OCV of the fresh sample (≈4.25 V vs. Li^+/Li) is reasonably close to that of the EOT sample (≈4.23 V vs. Li^+/Li), indicating that indeed a very similar lithium content x_{Li} was established by the preceding charge at C/2. At such high SOCs (corresponding to OCV values higher than 4.2 V), the lattice parameter *a* is virtually constant, while the lattice parameter *c* depends very strongly on x_{Li} in this region (see Figure S6 in the SI). Therefore, in order to minimize the XPD data acquisition time, only the 003 reflection, which uniquely describes the lattice parameter *c*, was recorded for the data shown in Figure 9. This resulted in an acquisition time for the relevant 2θ region of ≈4 minutes (see Experimental section). Analogous relaxation measurements recording both the (110) and the (003) reflection (≈8 minutes acquisition time) were also recorded to verify that the *a* parameter indeed remains essentially constant during the OCV transients (data not shown).

As can be seen in Figure 9c, the lattice parameter *c* exhibits a slight increase during the OCV phase. In the case of the EOT sample, this could be attributed to relaxation processes within the NCM-811 material, meaning the distribution of Li ions across the bulk of the NCM-811 structure, because the FWHM (Figure 9d) also indicates such a relaxation process. Assuming a constant *a* value of ≈2.815 Å during relaxation (estimation based on data shown in Figure S6 in the SI), the SOC change can be calculated from the *c*/*a* change and the high-SOC calibration curve (shown in Figure 5a). Thus, the observed relaxation of the lattice parameter *c* for the EOT sample correlates to $\Delta x_{Li} \approx 0.015$ and $\Delta SOC \approx 4.1$ mAh/g (vs. $\Delta x_{Li} \approx 0.009$ and $\Delta SOC \approx 2.4$ mAh/g for the fresh sample). Both values show that the net capacity change during the OCV period is minor. For the fresh sample however, this process cannot be correlated to the equilibration of an initially inhomogeneous SOC distribution across the bulk of NCM-811 particles, because in this case no relaxation of the FWHM is observed. Currently, we cannot provide a solid explanation for the apparent re-lithiation of the material. One hypothesis is that electrolyte oxidation (possibly also triggered by the permanent X-ray beam) might lead to a small re-lithiation of the CAM, as suggested by Xia et al.[73] It is important to note here that the XPD data collection during the LDE study was usually performed after a 3–5 h long OCV phase, meaning that the LDE XPD data are expected to depict a well-equilibrated state.

From the FWHM of the reflections, conclusions on the heterogeneity of the lattice spacing can be drawn. Assuming a virtually constant *a* parameter, a broader FWHM of the (003) reflection thereby translates into a more pronounced inhomogeneity of the Li distribution within the NCM-811 particles. For a fresh material, no relaxation process can be seen for the FWHM (black symbols/curve in Figure 9d), and the OCV relaxation is rather small (≈30 mV between ≈5 s and ≈5 h into the OCV period, black curve in Figure 9b; initial voltage drop of ≈20 mV within the first 5 s not shown here), which we believe is due to both the relaxation of concentration gradients within the electrolyte phase and the above discussed slight extent of re-lithiation. In contrast, the EOT sample shows a significantly larger decrease in both OCV (≈50 mV between ≈10 s and ≈5 h into the OCV period, blue curve in Figure 9b; initial voltage drop of ≈220 mV in the first 10 s not shown here) and FWHM curves (blue symbols/curve in Figure 9d). The initial FWHM for the EOT NCM-811 is more than double compared to that of the fresh cathode material, indicating a severe *d*-spacing heterogeneity in the *c* direction. The final FWHM value after relaxation is the same for both samples, suggesting that an equally homogeneous Li distribution

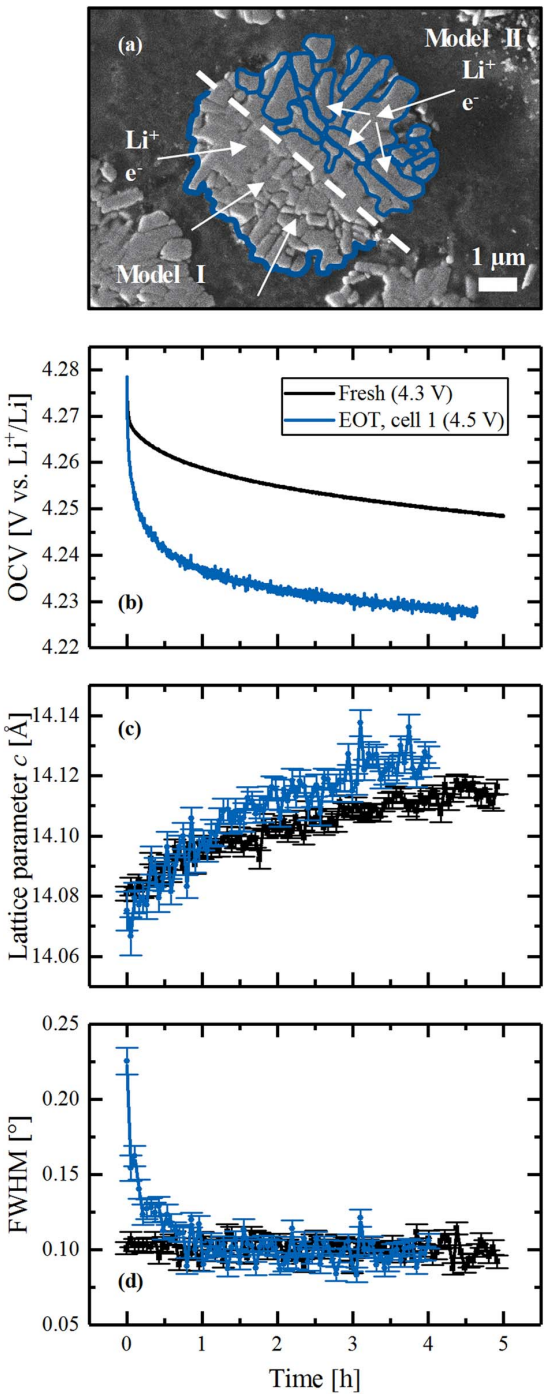

Figure 9. (a) SEM image of an NCM-811 particle, with a scheme illustrating the two discussed models for the formation of the O-deficient surface layer (sketched in blue): (i) either around the external surface of the secondary agglomerates (model I) or (ii) around each individual primary particle (model II). (b-d) Operando L-XPD relaxation experiment at the in-house diffractometer with fresh (measured in the 9th cycle, black curve) and EOT NCM-811 samples (from cell 1, blue curve) after charging to a comparable SOC with C/2: Evolution of (b) the NCM-811 cathode OCV, (c) the lattice parameter c determined from the (003) reflection, and (d) the FWHM of the (003) reflection during OCV period. The XPD data were acquired with a time resolution of ≈4 minutes.

across the bulk of the NCM-811 particles can be achieved in the EOT sample after prolonged relaxation times. This is another strong support for our above conclusion that the bulk structure of the NCM-811 material is not significantly altered by cycling over 1000 cycles.

On the other hand, the observed FWHM relaxation behavior for the EOT sample could in principle have several causes: (i) an inhomogeneous degree of NCM-811 delithiation across the cathode thickness, if the ionic resistance within the electrolyte phase (R_{ion}) were sufficiently large; (ii) an inhomogeneous lithium distribution within the bulk phase of each of the primary particles due to hindered lithium diffusion in the solid phase; and/or, (iii) different degrees of delithiation within the secondary particles.[13] Despite the increase of the ionic resistance over cycling (from initially $R_{ion} \approx 3\ \Omega\ cm^2$ to $R_{ion} \approx 9\ \Omega\ cm^2$ after 1000 cycles; see paragraph S4 in the SI), the absolute potential drop at C/2 due to R_{ion} is only ≈7 mV even after 1000 cycles, which would imply an essentially homogeneous delithiation across the cathode thickness upon charge, so that the first possible cause (i) should be negligible. With regards to the second possible cause (ii), our XPD analysis clearly indicates that there is no significant change in the Li-Ni disorder over 1000 cycles, so that one would not expect any differences in the lithium diffusion within the NCM-811 bulk phase between fresh and EOT NCM-811. This leaves the third possible cause (iii) as an explanation for the slow FWHM relaxation of the EOT NCM-811, namely an uneven degree of delithiation within the secondary particles. This must be due to the formation of the O-depleted surface layer upon cycling. Addressing our initial question, this surface layer can either be formed around (i) the secondary particles (model I in Figure 9a, sketched by the blue lines) or (ii) around the primary particles (model II) which agglomerate to the former.

For the first scenario (model I), the poor lithium ion conductivity through the resistive layer (as suggested by the large increase in R_{CT} upon cycling, see Figure 6b) around the secondary particle would be rate determining. After overcoming this barrier, the SOC distribution in the primary particles within each secondary particle would be homogeneous, in which case no initial broadening of the FWHM recorded during the OCV period following the C/2 charge would be expected for the EOT sample, contrary to what is observed in Figure 9d. For the other scenario (model II) with a resistive surface layer formed around every primary particle within a secondary particle, a homogenous degree of delithiation would also be expected within a given primary particle, but assuming that the transport of lithium ions and/or electrons is hindered by the surface film and must proceed through the NCM-811 solid phase, the degree of delithiation would be lower for primary particles deeper within the secondary particle compared to those at its outer surface. This would correspond to a SOC variation between primary particles, which would result in an initially broad FWHM in the OCV period following the C/2 charge. Over an extended OCV period, an equilibration of the different SOCs of the primary particles within a secondary particle would occur, so that the FWHM should ultimately narrow to the value observed for a fresh NCM-811 sample. This is exactly what is observed during relaxation of the EOT NCM-811 sample (see Figure 9d). Therefore, on the basis of this analysis of the operando L-XPD relaxation experiment, strong evidence is provided that the resistive O-depleted surface layer must be forming around primary particles in the cycled NCM-811 CAM.

Quite clearly, an aging mechanism according to model II is most consistent with our experimental observation so far. However, the question remains whether the delithiation of the primary particles toward the center of the secondary particles is limited by the transport of Li-ions or of electrons. Seeking to examine this question, the particle morphology of pristine and discharged EOT NCM-811 samples was analyzed by SEM, hoping that it might answer the extent of particle cracking (see paragraph S8 in the SI). Interestingly, the particle morphology at BOT compared to that at EOT shows no significant difference, indicating that NCM-811 particles are not cracked into clearly separate pieces over the 1000 cycles. However, it needs to be stressed out here that the samples were mechanically polished to obtain cross-sectional SEM images, which renders it impossible to differentiate

between small cracks and grain boundaries that are present even in the pristine NCM-811 CAM.

The formation of cracks, however, can also be examined by Kr-BET surface area measurements, as cracks would have to lead to an increase in the specific surface area. The pristine NCM-811 powder has a BET surface area of ≈0.28 m^2/g, which for non-porous spherical particles would predict a particle diameter of ≈4.5 μm (see equation (S11) in paragraph S7 of the SI). This is reasonably consistent with the secondary particle size observed by SEM (see Figure S11 in paragraph S8 of the SI), suggesting that essentially only the external surface of the pristine NCM-811 would be accessible to the electrolyte. However, it may be the case that there are simply surface impurities on the external surfaces of the secondary and/or primary particles (e.g., Li_2CO_3 or LiOH), which prevent gas (and electrolyte) access to within the secondary particles. Therefore, as these could be removed during cycling,[56] or by protons/HF formed during (electro)chemical electrolyte oxidation,[74,75] we conducted two more Kr-BET measurements to mimic this conditions in a real cell. NCM-811 was treated either with (i) water for 30 min or (ii) over a period of 7 days with LP57 electrolyte containing ≈2000 ppm HF (see Experimental section). After these treatments, the BET surface area has increased by ≈4-fold to ≈1.2 m^2/g in both cases. For the solid sphere approximation, this would correspond to a particle diameter of ≈1 μm, which is on the order of the dimensions of the primary particles (see Figure S11), indicating that the pores within the thus treated secondary NCM-811 particles become accessible for gas adsorption. Considering the known formation of protons/HF during (electro)chemical oxidation,[75] which is expected to be substantial over extensive cycling of NCM-811 to potentials of 4.5 V vs. Li^+/Li, one would also expect that the surface of the primary particles within the secondary particles gradually becomes accessible to the electrolyte over the course of cycling. The fact that the primary particles shrink by up to ≈6% when NCM-811 is charged to 4.5 V vs. Li^+/Li (see unit cell volume change in Figure S6) provides an additional argument for the electrolyte penetration into pores during cycling.

These pores would enable the release of O_2 gas from inside the secondary particles, thereby enabling the formation of an O-depleted resistive surface layer on the primary particles, ultimately leading to the morphology termed as model II in Figure 9a. The limiting transport mechanism, which leads to the initial broadening of the FWHM observed for the EOT NCM-811 sample during the OCV relaxation experiment (Figure 9d), would thus have to be due to a poor electronic conduction pathway into the aged secondary NCM-811 particle (across now loosely connected primary particles covered by a resistive O-depleted film), as a relatively fast lithium ion transport could proceed through the electrolyte within the pores.

In summary, while many literature reports claim that particle cracking is a major degradation process in NCM cathodes,[12–14] our analysis suggests that it is rather the interplay of cracks formed due to structural changes during cycling in conjunction with the dissolution of surface impurities that gradually increase the specific surface area of NCMs. As this goes along with an increasing accessibility of the electrolyte to the primary particles in the interior of the secondary particles, an O-depleted resistive surface layer can be formed on the primary particles, which in turns leads to the observed capacity fading. Based on the here proposed aging mechanism, the cycling stability of single-crystal NCMs would be predicted to be superior to poly-crystalline materials.

Estimated thickness of the O-depleted surface layer.— Assuming that the BET surface area of 1.2 m^2/g for the washed or HF-treated NCM-811 is representative for NCM-811 after 1000 cycles, the thickness of the O-depleted surface could be estimated by a similar approach as described in literature (for the calculation see paragraph S7 in the SI).[16,57] Assuming a solid sphere, a primary particle size of ≈1 μm is obtained, which is in good agreement with what can be seen in the SEM images (Figure 9a and paragraph S8 in the SI). The material loss of ≈8.5% from the XPD analysis in Figure 5c equals to the phase fraction of the O-depleted surface layer, which translates to a layer thickness of ≈15 nm. This is in good agreement with literature values, which also include transmission electron microscopy images.[67,76] Watanabe et al.[76] cycled NCA full-cells to 4.2 V for 1000 cycles and found a ≈8 nm thick NiO-like surface layer at 25°C (and ≈25 nm at 60°C), supporting our model of a surface reconstruction around primary particles. Jung et al.[67] performed half-cell cycling with NCM-523 cathodes to upper cut-off voltages of 4.5 V and 4.8 V vs. Li^+/Li, respectively, observing a gradual surface transformation from layered via spinel to rock-salt structure, with a layer thickness of ≈15–20 nm, depending on the cut-off voltage. Note, that in Figure 9a, the surface layer of model I is depicted thicker to stress that in this case, based on a smaller BET surface area of 0.28 m^2/g, the layer thickness would be around ≈66 nm, which is much thicker than the typical values reported in the literature, providing further support for model II shown in Figure 9a. We finally tried to validate the layer thickness from cross-sectional HAADF-STEM images of pristine, BOT, and EOT samples, which were prepared by focused ion beam milling (for details and images see paragraph S9 in the SI). While the pristine CAM exhibits no defects at the surface, proving its purely layered nature, transition-metals partially occupy the inter-slabs in the surface-near region of the BOT and EOT samples, as it would be the case for the spinel and/or rock-salt structure. The disordered surface layer was identified on numerous of the primary NCM-811 particles, but it was not possible to accurately quantify the surface layer thicknesses due to several reasons: (i) in many cases, the primary particles could not be tilted into the desired low-indexed zone axes, and, (ii) no clear boundary could be observed between the different phases, as they probably merge gradually into each other.[67]

Conclusions

In this work, we investigated the capacity fading in NCM-811/graphite full-cells over 1000 cycles, whereby focusing on the cathode by pre-lithiating the anode, to identify fading mechanisms with a combination of diagnostics, such as in situ and operando XPD, EIS, and XPS. From an ex situ XPD refinement of the NCM-811 before and after 1000 cycles, we concluded the bulk stability of the CAM with an unaltered Ni-Li disorder of ≈3%. Based on data from in situ XPD analysis, we were able to establish a quantitative correlation between lattice parameter changes and capacity losses in NCM-811 over the course of cycling. We concluded that the thereby identified capacity losses are caused by a shrinkage of the effective SOC window at both low and high SOC due to an increased cathode polarization. This overpotential build-up was further confirmed by cathode EIS measurements using a gold wire micro-reference electrode showing a 10-fold increase of the charge-transfer resistance. Furthermore, the difference between the capacity loss predicted by the in situ XPD analysis and that obtained from the electrochemical data reveals a CAM loss of ≈8.5%. These observations are consistent with the formation of an O-depleted resistive surface layer, which was found by XPS measurements and is assumed to show no Li intercalation. An operando XPD relaxation experiment leads us to conclude that the impedance build-up across a secondary particle is caused by the formation of a resistive O-depleted surface layer around the individual primary particles. This conclusion is further supported by BET measurements and cross-sectional SEM as well as HAADF-STEM pictures. The observed surface reconstruction on the one hand means a loss of CAM, which results in an irreversible capacity loss. On the other hand, it causes a significant overpotential thereby shrinking the apparent SOC window. This reversible capacity loss could be regained at very low C-rates. To avoid a surface reconstruction, less resistive and protective coatings for Ni-rich CAMs are essential to improve capacity retention and cycle life in future LIBs.

Acknowledgments

Financial support by BASF SE through its Scientific Network on Electrochemistry and Batteries is gratefully acknowledged. We also wish to acknowledge the Diamond Light Source for provision of beamtime at the Beamline I11 (proposal EE16866) and financial support. Further gratitude is expressed to Sophie Solchenbach for her con-

tribution to the impedance measurements, to Katia Rodewald from the Wacker-Chair of Macromolecular Chemistry at the Technical University of Munich for the SEM measurements, and to the Competence Center Material Physics of BASF SE for the STEM measurements.

ORCID

Franziska Friedrich https://orcid.org/0000-0001-9400-1212
Benjamin Strehle https://orcid.org/0000-0001-8878-1160
Michele Piana https://orcid.org/0000-0002-3310-6587

References

1. Pedro Lima, Pushevs, can be found under https://pushevs.com/2018/04/05/samsung-sdi-94-ah-battery-cell-full-specifications, accessed October 2019.
2. E. A. Olivetti, G. Ceder, G. G. Gaustad, and X. Fu, *Joule*, **1**, 229 (2017).
3. A. H. Tkaczyk, A. Bartl, A. Amato, V. Lapkovskis, and M. Petranikova, *J. Phys. D Appl. Phys.*, **51**, 203001 (2018).
4. C. B. L. Nkulu, L. Casas, V. Haufroid, T. De Putter, N. D. Saenen, T. Kayembe-Kitenge, P. M. Obadia, D. K. W. Mukoma, J.-M. L. Ilunga, T. S. Nawrot, O. L. Numbi, E. Smolders, and B. Nemery, *Nat. Sustain.*, **1**, 495 (2018).
5. M. H. Kim, H. S. Shin, D. Shin, and Y. K. Sun, *J. Power Sources*, **159**, 1328 (2006).
6. T. Ohzuku, A. Ueda, and M. Nagayama, *J. Electrochem. Soc.*, **140**, 1862 (1993).
7. H. Li, N. Zhang, J. Li, and J. R. Dahn, *J. Electrochem. Soc.*, **165**, A2985 (2018).
8. W. Li, J. Reimers, and J. Dahn, *Solid State Ionics*, **67**, 123 (1993).
9. H. Arai, S. Okada, H. Ohtsuka, M. Ichimura, and J. Yamaki, *Solid State Ionics*, **80**, 261 (1995).
10. J.-M. Kim and H.-T. Chung, *Electrochim. Acta*, **49**, 3573 (2004).
11. W. Li, X. Liu, H. Celio, P. Smith, A. Dolocan, M. Chi, and A. Manthiram, *Adv. Energy Mater.*, **8**, 1703154 (2018).
12. K. Ishidzu, Y. Oka, and T. Nakamura, *Solid State Ionics*, **288**, 176 (2016).
13. H. Liu, M. Wolf, K. Karki, Y.-S. Yu, E. A. Stach, J. Cabana, K. W. Chapman, and P. J. Chupas, *Nano Lett.*, **17**, 3452 (2017).
14. E. J. Lee, Z. Chen, H.-J. Noh, S. C. Nam, S. Kang, D. H. Kim, K. Amine, and Y.-K. Sun, *Nano Lett.*, **14**, 4873 (2014).
15. R. Jung, M. Metzger, F. Maglia, C. Stinner, and A. H. Gasteiger, *J. Electrochem. Soc.*, **164**, A1361 (2017).
16. B. Strehle, K. Kleiner, R. Jung, F. Chesneau, M. Mendez, H. A. Gasteiger, and M. Piana, *J. Electrochem. Soc.*, **164**, A400 (2017).
17. T. Teufl, B. Strehle, P. Müller, H. A. Gasteiger, and M. A. Mendez, *J. Electrochem. Soc.*, **165**, A2718 (2018).
18. D. Streich, C. Erk, A. Guéguen, P. Müller, F.-F. Chesneau, and E. J. Berg, *J. Phys. Chem. C*, **121**, 13481 (2017).
19. F. Lin, I. M. Markus, D. Nordlund, T. C. Weng, M. D. Asta, H. L. Xin, and M. M. Dieff, *Nat. Commun.*, **5**, 3529 (2014).
20. S. Sallis, N. Pereira, P. Mukherjee, N. F. Quackenbush, N. Faenza, C. Schlueter, T. L. Lee, W. L. Yang, F. Cosandey, G. G. Amatucci, and L. F. Piper, *J. Appl. Phys. Lett.*, **108**, 263902 (2016).
21. H. Zheng, Q. Sun, G. Liu, X. Song, and V. S. Battaglia, *J. Power Sources*, **207**, 134 (2012).
22. K. Amine, Z. Chen, Z. Zhang, J. Liu, W. Lu, Y. Qin, J. Lu, L. Curtis, and Y.-K. Sun, *J. Mater. Chem.*, **21**, 17754 (2011).
23. S. Solchenbach, G. Hong, A. T. S. Freiberg, R. Jung, and H. A. Gasteiger, *J. Electrochem. Soc.*, **165**, 3304 (2018).
24. USABC, USABC Goals for Advanced Batteries for EVs - CY2020 Commercialization, can be found under https://www.energy.gov/sites/prod/files/2014/05/f15/APR13_Energy_Storage_d_III_Adv_Battery_Dev_0.pdf, accessed October 2019.
25. D. Andre, S. Kim, P. Lamp, F. Lux, and F. Maglia, *J. Mater. Chem. A Mater. Energy Sustain.*, **3**, 6709 (2015).
26. K. Kleiner, B. Strehle, A. R. Baker, S. J. Day, C. C. Tang, I. Buchberger, F.-F. Chesneau, H. A. Gasteiger, and M. Piana, *Chem. Mater.*, **30**, 3656 (2018).
27. C. A. Murray, J. Potter, S. J. Day, A. R. Baker, S. P. Thompson, J. Kelly, C. G. Morris, S. Yang, and C. C. Tang, *J. Appl. Crystallogr.*, **50**, 172 (2017).
28. M. Basham, J. Filik, M. T. Wharmby, P. C. Y. Chang, B. El Kassaby, M. Gerring, J. Aishima, K. Levik, B. C. A. Pulford, I. Sikharulidze, D. Sneddon, M. Webber, S. S. Dhesi, F. Maccherozzi, O. Svensson, S. Brockhauser, G. Náray, and A. W. Ashton, *J. Synchrotron Radiat.*, **22**, 853 (2015).
29. J. Filik, A. W. Ashton, P. C. Y. Chang, S. J. Day, M. Drakopoulos, M. W. Gerring, M. L. Hart, O. V. Magdysyuk, S. Michalik, A. Smith, C. C. Tang, N. J. Terril, M. T. Wharmby, and H. Wilhem, *J. Appl. Crystallogr.*, **50**, 959 (2017).
30. A. Coelho, Coelho Software (2016).
31. O. Dolotko, A. Senyshyn, M. J. Mühlbauer, K. Nikolowski, and H. Ehrenberg, *J. Power Sources*, **255**, 197 (2014).
32. S. H. Bo, K.-W. Nam, O. J. Borkiewicz, Y.-Y. Hu, X.-Q. Yang, P. J. Chupas, K. W. Chapman, L. Wu, L. Zhang, F. Wang, C. P. Grey, and P. G. Khalifah, *Inorg. Chem.*, **53**, 6585 (2014).
33. T. A. Hewstone and B. L. Chamberland, *J. Phys. Chem. Solids*, **48**, 97 (1987).
34. H. Liu, H. Liu, S. H. Lapidus, Y. S. Meng, P. J. Chupas, and K. W. Chapman, *J. Electrochem. Soc.*, **164**, A1802 (2017).
35. Y. Arachi, H. Kobayashi, S. Emura, Y. Nakata, M. Tanaka, T. Asai, H. Sakaebe, K. Tatsumi, and H. Kageyama, *Solid State Ionics*, **176**, 895 (2005).
36. O. Sekizawa, T. Hasegawa, N. Kitamura, and Y. Idemoto, *J. Power Sources*, **196**, 6651 (2011).
37. Y. J. Gu. Y. B. chen, H. Q. Liu, Y. M. Wang, C. L. Wang, and H. K. Wu, *J. Alloys Compd.*, **509**, 7915 (2011).
38. M. Ma, N. A. Chernova, B. H. Toby, P. Y. Zavalij, and M. S. Whittingham, *J. Power Sources*, **165**, 517 (2007).
39. P. Whitfield, I. Davidson, L. Cranswick, I. Swainson, and P. Stephens, *Solid State Ionics*, **176**, 463 (2005).
40. A. Hirano, K. Kanie, T. Ichikawa, N. Imanishi, Y. Takeda, R. Kanno, T. Kamiyama, and F. Izumi, *Solid State Ionics*, **152–153**, 207 (2002).
41. L. Yin, G. S. Mattei, Z. Li, J. Zheng, W. Zhao, F. Omenya, C. Fang, W. Li, J. Li, Q. Xie, J.-G. Zhang, M. S. Whittingham, Y. S. Meng, A. Manthiram, and P. G. Khalifah, *Rev. Sci. Instrum.*, **89**, 093002 (2018).
42. S. Sasaki, K. Fujino, and Y. Takéuchi, *Proc. Japan Acad. Ser. B Phys. Biol. Sci.*, **55**, 43 (1979).
43. S. Sasaki, K. Fujino, Y. Takéuchi, and R. Sadanaga, *Acta Crystallogr. Sect. A*, **36**, 904 (1980).
44. P. W. Stephens, *J. Appl. Crystallogr.*, **32**, 281 (1999).
45. A. O. Kondrakov, H. Geßwein, K. Galdina, L. de Biasi, V. Meded, E. O. Filatova, G. Schumacher, W. Wenzel, P. Hartmann, T. Brezesinski, and J. Janek, *J. Phys. Chem. C*, **121**, 24381 (2017).
46. A. Senyshyn, O. Dolotko, M. J. Mühlbauer, K. Nikolowski, H. Fuess, and H. Ehrenberg, *J. Electrochem. Soc.*, **160**, A3198 (2013).
47. O. Dolotko, A. Senyshyn, M. J. Mühlbauer, K. Nikolowski, F. Scheiba, and H. Ehrenberg, *J. Electrochem. Soc.*, **159**, A2082 (2012).
48. S. Solchenbach, D. Pritzl, E. J. Y. Kong, J. Landesfeind, and H. A. Gasteiger, *J. Electrochem. Soc.*, **163**, A2265 (2016).
49. J. Landesfeind, D. Pritzl, and H. A. Gasteiger, *J. Electrochem. Soc.*, **164**, A1773 (2017).
50. D. Strmcnik, I. E. Castelli, J. G. Connell, D. Haering, M. Zorko, P. Martins, P. P. Lopes, B. Genorio, T. Østergaard, H. A. Gasteiger, F. Maglia, B. K. Antonopoulos, V. R. Stamenkovic, J. Rossmeisl, and N. M. Markovic, *Nat. Catal.*, **1**, 255 (2018).
51. I. Buchberger, S. Seidlmayer, A. Pokharel, M. Piana, J. Hattendorff, P. Kudejova, R. Gilles, and H. A. Gasteiger, *J. Electrochem. Soc.*, **162**, A2737 (2015).
52. J. Choi and A. Manthiram, *Solid State Ionics*, **176**, 2251 (2005).
53. F. German, A. Hintennach, A. LaCroix, D. thiemig, S. Oswald, F. Scheiba, M. J. Hoffmann, and H. Ehrenberg, *J. Power Sources*, **264**, 100 (2014).
54. S. H. Kang, D. P. Abraham, W. S. Yoon, K. W. Nam, and X. Q. Yang, *Electrochim. Acta*, **54**, 684 (2008).
55. S. H. Kang, W. S. Yoon, K. W. Nam, X. Q. Yang, and D. P. Abraham, *J. Mater. Sci.*, **43**, 4701 (2008).
56. R. Jung, R. Morasch, P. Karayaylali, K. Philips, F. Maglia, C. Stinner, Y. Shao-Horn, and H. A. Gasteiger, *J. Electrochem. Soc.*, **165**, A132 (2018).
57. R. Jung, M. Metzger, F. Maglia, C. Stinner, and H. A. Gasteiger, *J. Phys. Chem. Lett.*, **8**, 4820 (2017).
58. S.-K. Jung, H. Gwon, J. Hong, K.-Y. Park, D.-H. Seo, H. Kim, J. Hyun, W. Yang, and K. Kang, *Adv. Energy Mater.*, **4**, 1300787 (2014).
59. Y. Makimura, T. Sasaki, T. Nonaka, Y. F. Nishimura, T. Uyama, C. Okuda, Y. Itou, and Y. Takeuchi, *J. Mater. Chem. A*, **4**, 8350 (2016).
60. H. H. Ryu, K. J. Park, C. S. Yoon, and Y. K. Sun, *Chem. Mater.*, **30**, 1155 (2018).
61. S. Choi and A. Manthiram, *J. Electrochem. Soc.*, **149**, A1157 (2002).
62. H. R. Kim, S. G. Woo, J. H. Kim, W. Cho, and Y. J. Kim, *J. Electroanal. Chem.*, **782**, 168 (2016).
63. S. Watanabe, T. Hosokawa, K. Morigaki, M. Kinoshita, and K. Nakura, *ECS Trans.*, **41**, 65 (2012).
64. N. Yabuuchi, Y. Makimura, and T. Ohzuku, *J. Electrochem. Soc.*, **154**, A314 (2007).
65. L. de Biasi, A. O. Kondrakov, H. Geßwein, T. Brezesinski, P. Hartmann, and J. Janek, *J. Phys. Chem. C*, **121**, 26163 (2017).
66. A. O. Kondrakov, A. Schmidt, J. Xu, H. Geßwein, R. Mönig, P. Hartmann, H. Sommer, T. Brezesinski, and J. Janek, *J. Phys. Chem. C*, **121**, 3286 (2017).
67. S. K. Jung, H. Gwon, J. Hong, K.-Y. Park, D.-H. Seo, H. Kim, J. Hyun, W. Yang, and K. Kang, *Adv. Energy Mater.*, **4**, 1300787 (2014).
68. D. Mohanty, K. Dahlberg, D. M. King, L. A. David, A. S. Sefat, D. L. Wood, C. Daniel, S. Shar, V. Mahajan, M. Lee, and F. Albano, *Sci. Rep.*, **6**, 26532 (2016).
69. K. Luo, M. R. Roberts, R. Hao, N. Guerrini, D. M. Pickup, Y.-S. Liu, K. Edström, J. Guo, A. V. Chadwick, L. C. Duda, and P. G. Bruce, *Nat. Chem.*, **8**, 684 (2016).
70. T. Teufl, D. Pritzl, S. Solchenbach, H. A. Gasteiger, and M. A. Mendez, *J. Electrochem. Soc.*, **166**, A1275 (2019).
71. H. Koga, L. Croguennec, M. Ménétrier, P. Mannessiez, F. Weill, and C. Delmas, *J. Power Sources*, **236**, 250 (2013).
72. H. Sclar, J. Sicklinger, E. M. Ericson, S. Maiti, J. Grinblat, M. Talianker, L. Burstein, H. Beyer, G. Avruschenko, H. A. Gasteiger, B. Markovsky, and D. Aurback, *to be submitted*.
73. J. Xia, K. J. Nelson, Z. Lu, and J. R. Dahn, *J. Power Sources*, **329**, 387 (2016).
74. M. Metzger, B. Strehle, S. Solchenbach, and H. A. Gasteiger, *J. Electrochem. Soc.*, **163**, 798 (2016).
75. J. Wandt, A. T. S. Freiberg, A. Ogrodnik, and H. A. Gasteiger, *Mater. Today*, **21**, 825 (2018).
76. S. Watanabe, M. Kinoshita, T. Hosokawa, K. Morigaki, and K. Nakura, *J. Power Sources*, **258**, 210 (2014).

Supporting Information

Capacity Fading Mechanisms of NCM-811 Cathodes in Lithium-Ion Batteries Studied by X-ray Diffraction and Other Diagnostics

Franziska Friedrich,[1,=] Benjamin Strehle,[1,=] Anna T. S. Freiberg,[1] Karin Kleiner,[1,2] Sarah J. Day,[2] Christoph Erk,[3] Michele Piana,[1] and Hubert A. Gasteiger[1]

[1] *Chair of Technical Electrochemistry, Department of Chemistry and Catalysis Research Center, Technical University of Munich, D-85748 Garching, Germany*

[2] *Harwell Science and Innovation Campus, Diamond Light Source, Didcot, Oxfordshire OX11 0DE, UK*

[3] *BASF SE Ludwigshafen, Lithium-Ion Battery Research, D-67056 Ludwigshafen, Germany*

[=] *These authors contributed equally to this work.*

Contents

S1: Supplementary Information on Refinement Strategy

Background fit.— As mentioned in the Experimental section of the main text, two different approaches were applied to fit the complex background. In the following, both fits are compared. One option is fitting a linear interpolation between selected data points, which results in an approximately linear background for single reflections, even for the (003) reflection which is located in the 2θ range with a clearly apparent nonlinear background. Therefore, the integrated area of the peaks and the structural information derived from them is assumed to be rather reproducible. On the other hand, this fit gives rise to an irregular background curve as can be seen in the following figure. The limited amount of data points, which are manually selected for the background fit, is the reason for this poor fit quality. Therefore, another method was applied to fit the complex background. A combination of eight pseudo-Voigt peaks was used to model the broad and high background of the cell components diffracting in the 2θ range below 12°. In addition, the standard background functions implemented in Topas (polynomial and 1/X) are used. The thereby obtained background is smooth in comparison to the linear interpolated background. Although the fit of the complex background below 12° 2θ is not perfect, the reflections of interest can be refined based on a continuous and smooth background, which improves the quality of the refinement.

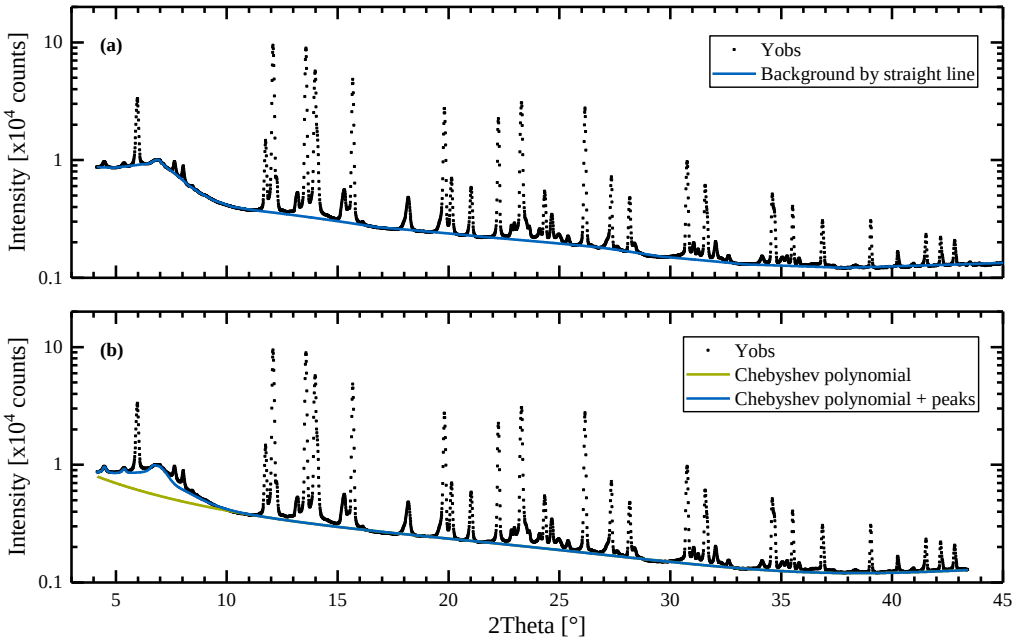

Figure S1. In situ S-XPD of an NCM-811/graphite full-cell (LDE cell 1 in the charged state in the 968th cycle) measured at beamline I11 of the Diamond Light Source, showing the measured data points and the fitted background: (a) a straight-line background fit in comparison to (b) a combination of pseudo-Voigt peaks and standard Topas background functions (polynomials and 1/X).

Applied constraints and calculation of Li occupancy in $Li_xNi_{0.79}Co_{0.1}Mn_{0.1}O_2$.— Underlying structural parameters and constraints for the refinement of the NCM phase are summarized in **Table S1**. An example of a refinement of an NCM-811/graphite pattern is given in **Figure S2**.

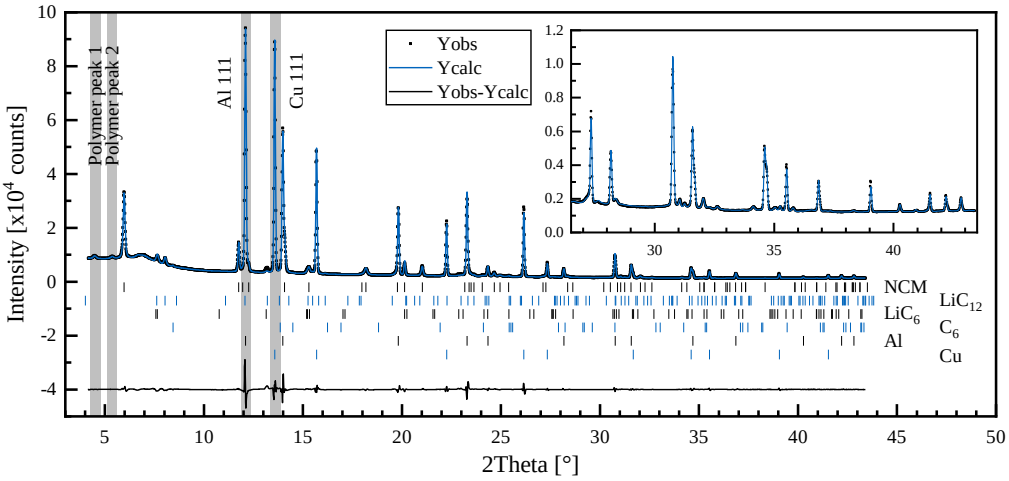

Figure S2. In situ S-XPD pattern of an NCM-811/graphite full-cell (LDE cell 1 in the charged state in the 968th cycle) with the experimental data points (points), the calculated fit (blue line), and the difference plot (black line). The inset shows the reflections at high angles. The reflection positions of NCM-811, LiC_{12}, LiC_6, C_6, Al, and Cu phases are shown as ticks below the diffractogram. Highlighted peaks were used as "internal standards" for the quantification of the material loss discussed in paragraph S2.

The parameter x_{Li} stands for the Li occupancy, calculated based on the fit of the operando L-XPD *c*/*a* calibration curve as discussed in the main text. For the low SOC range ($0.62 \leq x_{Li} \leq 0.91$), the quadratic fit gives the following equation when solved for x_{Li}:

$$x_{Li} = \frac{73.80 - \sqrt{c/a \cdot 10^4 - 49222}}{58.36} \quad \text{(S1)}$$

The linear fit for the high SOC range ($0.12 \leq x_{Li} \leq 0.23$) results in the following equation for x_{Li}:

$$x_{Li} = \frac{c/a - 4.733}{1.41} \quad \text{(S2)}$$

With equations (S1) and (S2), the occupancy of Li on the Li site can be calculated. However, the cation disorder between Ni and Li has to be taken into account to get the true number of Li atoms on the Li site and, in turn, also the number of Ni atoms on the Li site. Therefore, the parameter *dis* in **Table S1** stands for the amount of Li (Ni) which was found to be on the TM (Li) site by refining pristine and EOT samples from ex situ L- XPD measurements at our in-house diffractometer. A disorder (Li-Ni mixing) of 3% equals to a *dis* parameter of 0.03.

Table S1. Structural parameters from the Rietveld refinement of the NCM-811 phase with Wyckoff positions, fractional coordinates, and site occupancy factors. The thermal displacement parameter was constrained for all sites in case of the in situ S-XPD data and refined site-specific for the ex situ L-XPD data collected at the in-house diffractometer. Refined values for z_O are given in paragraph S2.

$Li_xNi_{0.79}Co_{0.10}Mn_{0.10}O_2$: Space group $R\bar{3}m$ (166) with x_{Li} = Li content and *dis* = disorder					
Atom	Wyckoff position	*x*	*y*	*z*	S.O.F.
Li(1)	3a, Li	0	0	0	x_{Li} - *dis*
Li(2)	3b, TM	0	0	0.5	*dis*
Ni(1)	3b, TM	0	0	0.5	0.79 - *dis*
Ni(2)	3a, Li	0	0	0	*dis*
Co	3b, TM	0	0	0.5	0.10
Mn	3b, TM	0	0	0.5	0.10
O	6c, O	0	0	$z_{6c,O} \approx 0.24$	1

Stephens model.— In agreement with the literature,[S1,S2] anisotropic reflection broadening was also observed in this study for samples at high degrees of delithiation. The anisotropy can be caused by inhomogeneous Li (de)intercalation, oxygen deficiency and lattice distortions. For perfectly isotropic samples, the FWHM (Γ_{total}) is supposed to be the sum of the particle size broadening Γ_{size} and the micro-strain broadening Γ_{strain}, as described by the following equations:

$$\Gamma_{total} = \Gamma_{strain} + \Gamma_{size} \tag{S3}$$

$$\Gamma_{total} = 4\,\varepsilon \tan\theta + \frac{K\lambda}{L\cos\theta} \tag{S4}$$

where ε = strain, K = Scherrer constant ($0.89 < K < 1$; usually $K = 0.9$ for spherical particles),[S3] λ = wavelength of the X-rays in nm, L = diameter of the (spherical) particles in nm, and 2θ = Bragg angle of the respective reflection.

By the following transformation, a linear correlation (the so-called Williamson-Hall plot) between $\Gamma_{total} \cdot \cos\theta$ and $\sin\theta$ can be established, with the micro-strain broadening as slope and the apparent particle size as intercept.

$$\Gamma_{total} \cdot \cos\theta = 4\,\varepsilon\,\sin\theta + \frac{K\lambda}{L} \tag{S5}$$

For an ideal material with isotropic broadening, like the herein used CeO_2 standard material, the Williamson-Hall plot gives a straight line as can be seen in **Figure S3** ($R^2 = 0.84$). The data points of

the discharged NCM-811 are also reasonably close to a straight line (R^2 = 0.07). However, the reflections of the charged NCM-811 do not follow a Williamson-Hall behavior.

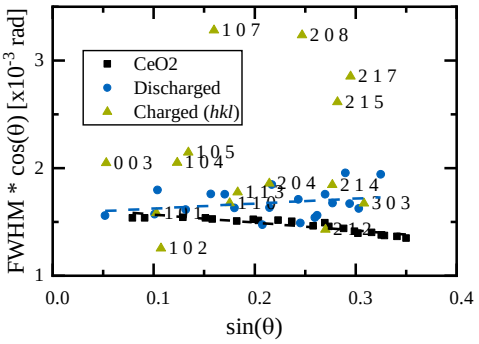

Figure S3. Williamson-Hall plot of the NCM-811 phase (from in situ S-XPD at BOT in the discharged and charged state) compared to the CeO_2 standard material, as determined by single reflection fitting with a pseudo-Voigt function. For the charged state, the reflections are labeled with the corresponding *hkl* indices.

This so-called anisotropic line shape broadening is accommodated by a phenomenological model of the multi-dimensional distribution of lattice metrics within a sample. It was first introduced by Peter Stephens in 1999 and is therefore called Stephens model.[S4] The investigated samples belong to the $R\bar{3}m$ space group. According to the literature, a trigonal Bravais lattice with hexagonal indexing was employed, leading to four independent anisotropic strain parameters S_{400}, S_{202}, S_{004}, and S_{301},[S2,S4,S5] of which only S_{004} and S_{202} were used for fitting the in situ S-XPD data. The anisotropic broadening contribution is thereby given by

$$\Gamma_A(hkl) = \left[\sum_{HKL} S_{HKL}\, h^H k^K l^L \right]^{1/2} d^2 \tan\theta \qquad \text{(S6)}$$

with

$$\sum_{HKL} S_{HKL}\, h^H k^K l^L = S_{400}\left(h^4 + k^4 + 3h^2k^2 + 2h^3k + 2hk^3\right) + \qquad \text{(S7)}$$

$$S_{004}\, l^4 +$$

$$S_{202}\, 3\left(h^2l^2 + k^2l^2 + hkl^2\right) +$$

$$S_{301}\left(3h^2kl - 3hk^2l + 2h^3l - 2k^3l\right)$$

It is important to note that Γ_A is given in radians. For a conversion to degrees, as used in the Topas software, the factor 180°/π must be applied. For an easier handling of the strain parameters, another factor of 10^{-5} is implemented in the Topas macros. The Gaussian and Lorentzian contributions of Γ_A are implemented into the pseudo-Voigt function (TCHZ) describing the overall reflection shape as follows:

$$\Gamma_G = [U \tan^2\theta + V \tan\theta + W + Z/\cos^2\theta + (1 - \xi)^2\, \Gamma_A^2(hkl)]^{1/2} \qquad \text{(S8)}$$

$$\Gamma_L = X \tan\theta + Y/\cos\theta + \xi\,\Gamma_A\,(hkl) \quad \text{(S9)}$$

where ξ is a mixing parameter to interpolate between the Gaussian and Lorentzian line shape. In the following tables, the refinement results of the LDE data for the anisotropic strain parameters S_{004} and S_{202} are shown. The mixing parameter ξ always converges to 1 (i.e., mainly Lorentzian line shape). The isotropic strain parameter of the TCHZ function (X) was set to zero when the Stephens model was applied. The evolution of the S_{004} and S_{202} strain parameters in the charged state of the LDE cells is summarized in **Table S2**, which shows that the line shape broadening of the NCM-811 phase stays basically constant over the course of almost 1000 cycles.

Table S2. Anisotropic strain parameters used in the Stephens model in the refinement of the LDE data of cell 1 and 2 in the charged state. Errors are given in parenthesis.

Cell 1			Cell 2		
Cycle	S_{004}	S_{202}	Cycle	S_{004}	S_{202}
18	95(6)	270(50)	18	99(6)	280(50)
64	82(5)	250(50)	64	83(5)	230(50)
155	69(5)	240(50)	155	68(5)	200(50)
201	64(5)	260(50)	201	62(5)	210(50)
248	64(5)	260(50)	248	58(5)	230(50)
915	63(5)	280(50)	926	64(6)	290(60)
969	57(5)	320(50)	976	56(6)	310(60)

S2: Rietveld Refinement Results

Refinement results of the NCM-811 phase.— The results from the in situ S-XPD refinement of the NCM-811 phase during the LDE study are summarized in the following tables sorted by cell number (cell 1 and 2) and SOC (first in the discharged state and then in the charged state). During the refinement, the Li-Ni disorder was fixed to the value determined from the ex situ L-XPD data (3.1%) as is described in the main text.

Table S3. Refined structural parameters for $Li_xNi_{0.79}Co_{0.10}Mn_{0.10}O_2$ in the discharged state (cell 1) with errors given in parenthesis.

Cycle	*a* [Å]	*c* [Å]	*V* [Å^3]	*c*/*a* [-]	x_{Li} [-]	$z_{6c,O}$ [-]	b_{all} [Å^2]	R_{bragg} [%]
18	2.8618(1)	14.2641(7)	101.169(8)	4.9841(3)	0.838	0.2397(3)	1.31(6)	1.24
63	2.8613(1)	14.2675(7)	101.161(8)	4.9863(3)	0.831	0.2396(3)	1.33(6)	1.31
108	2.8613(1)	14.2711(7)	101.185(9)	4.9876(3)	0.826	0.2389(3)	1.33(7)	1.83
154	2.8611(1)	14.2735(7)	101.185(9)	4.9887(3)	0.823	0.2394(3)	1.49(7)	1.41
200	2.8620(1)	14.2775(7)	101.281(8)	4.9886(3)	0.823	0.2386(3)	1.20(6)	2.00
247	2.8620(1)	14.2782(7)	101.284(8)	4.9890(3)	0.822	0.2389(3)	1.30(6)	1.68
806	2.8654(1)	14.3171(7)	101.799(8)	4.9967(3)	0.797	0.2387(3)	1.34(6)	1.60
859	2.8654(1)	14.3174(7)	101.804(8)	4.9967(3)	0.797	0.2384(3)	1.27(6)	1.92
914	2.8653(1)	14.318(7)	101.800(9)	4.9969(3)	0.796	0.2382(3)	1.28(7)	2.14
968	2.8651(1)	14.3183(7)	101.788(9)	4.9975(3)	0.794	0.2385(3)	1.32(7)	1.77

Table S4. Refined structural parameters for $Li_xNi_{0.79}Co_{0.10}Mn_{0.10}O_2$ in the discharged state (cell 2) with errors given in parenthesis.

Cycle	a [Å]	c [Å]	V [Å^3]	c/a [-]	x_{Li} [-]	$z_{6c,O}$ [-]	b_{all} [Å^2]	R_{bragg} [%]
18	2.8682(1)	14.2937(6)	101.831(8)	4.9835(3)	0.840	0.2401(3)	1.37(6)	1.38
63	2.8682(1)	14.2977(7)	101.859(8)	4.9848(3)	0.836	0.2397(3)	1.35(7)	1.27
108	2.8681(1)	14.3011(7)	101.877(9)	4.9863(3)	0.831	0.2392(3)	1.32(7)	1.45
154	2.8676(1)	14.3031(7)	101.855(8)	4.9880(3)	0.825	0.2399(3)	1.53(7)	1.17
200	2.8673(1)	14.3050(8)	101.85(1)	4.9891(3)	0.821	0.2399(3)	1.37(8)	1.51
247	2.8674(1)	14.306(1)	101.86(1)	4.9893(4)	0.821	0.2402(3)	1.5(1)	1.71
814	2.8658(1)	14.3179(7)	101.834(9)	4.9964(3)	0.798	0.2398(3)	1.42(7)	1.29
869	2.8657(1)	14.3179(7)	101.830(9)	4.9963(3)	0.799	0.2395(3)	1.31(7)	1.30
925	2.8661(1)	14.3166(8)	101.85(1)	4.9952(3)	0.802	0.2395(3)	1.34(7)	1.28
975	2.8658(1)	14.3175(7)	101.835(9)	4.9961(3)	0.799	0.2398(3)	1.35(7)	1.52

Table S5. Refined structural parameters for $Li_xNi_{0.79}Co_{0.10}Mn_{0.10}O_2$ in the charged state (cell 1) with errors given in parenthesis.

Cycle	a [Å]	c [Å]	V [Å^3]	c/a [-]	x_{Li} [-]	$z_{6c,O}$ [-]	b_{all} [Å^2]	R_{bragg} [%]
18	2.81434(8)	13.952(1)	95.701(9)	4.9576(4)	0.159	0.2337(3)	1.66(6)	1.66
63	2.81472(8)	13.960(1)	95.779(9)	4.9595(4)	0.161	0.2335(3)	1.72(6)	1.50
154	2.81532(8)	13.982(1)	95.973(8)	4.9663(4)	0.165	0.2340(3)	1.86(6)	1.29
200	2.81625(8)	13.994(1)	96.118(9)	4.9689(4)	0.167	0.2337(3)	1.68(5)	1.52
247	2.81643(8)	13.997(1)	96.150(9)	4.9695(4)	0.168	0.2338(3)	1.70(6)	1.57
914	2.82367(9)	14.199(1)	98.04(1)	5.0282(4)	0.209	0.2330(3)	1.80(6)	1.45
968	2.82389(8)	14.218(1)	98.189(9)	5.0347(4)	0.214	0.2332(3)	1.75(6)	1.63

Table S6. Refined structural parameters for $Li_xNi_{0.79}Co_{0.10}Mn_{0.10}O_2$ in the charged state (cell 2) with errors given in parenthesis.

Cycle	a [Å]	c [Å]	V [Å^3]	c/a [-]	x_{Li} [-]	$z_{6c,O}$ [-]	b_{all} [Å^2]	R_{bragg} [%]
18	2.82028(8)	13.985(1)	96.330(9)	4.9584(4)	0.160	0.2339(3)	1.78(6)	1.44
63	2.82074(8)	13.995(1)	96.435(9)	4.9612(4)	0.162	0.2336(3)	1.79(6)	1.42
154	2.82141(8)	14.022(1)	96.668(9)	4.9699(4)	0.168	0.2341(3)	2.08(6)	1.38
200	2.82164(9)	14.035(1)	96.77(1)	4.9739(5)	0.171	0.2337(3)	1.80(7)	1.74
247	2.82187(9)	14.040(1)	96.82(1)	4.9756(4)	0.172	0.2339(3)	1.77(7)	1.76
925	2.8302(1)	14.212(1)	98.59(1)	5.0214(5)	0.205	0.2336(3)	1.87(7)	1.46
975	2.82380(9)	14.184(1)	97.95(1)	5.0233(5)	0.206	0.2343(3)	1.89(7)	1.47

Refinement results of the Li_xC_6 phases.— Refinement results from the graphite phases are shown in **Table S7** (C), **Table S8** (LiC_{12}), and **Table S9** (LiC_6). Starting values were taken from Dolotko *et al.*,[S6] and the thermal displacement parameters were kept constant at their respective values. For graphite, only the lattice parameters were refined. For the LiC_{12} and the LiC_6 phase, lattice parameters and peak broadening due to size effects and fractional coordinates of carbon could be refined.

Table S7. Structural data of graphite added as conductive agent to the cathode coating. Exemplary data for cell 1 in cycle 968 in the charged state.

Graphite: Space group $P6_3/mmc$ (194), a = 2.49(1) Å, c = 6.68(1) Å, R_{bragg} = 2.0%					
Atom	Wyckoff position	x	y	z	b_{all} [Å^2] [S6]
C(1)	2b	0	0	1/4	1.62
C(2)	2c	1/3	2/3	1/4	1.62

Table S8. Structural data of LiC_{12} determined by Rietveld refinement of cell 1 in cycle 968 in the charged state.

LiC_{12}: Space group P6/mmm (191), a = 4.293(3) Å, c = 7.038(2) Å, R_{bragg} = 4.8%					
Atom	Wyckoff position	x	y	z	b_{all} [Å^2] [S6]
Li	1a	0	0	0	1.49
C	12n	0.361(6)	0	0.165(2)	1.49

Table S9. Structural data of LiC_6 determined by Rietveld refinement of cell 1 in cycle 968 in the charged state.

LiC_6: Space group P6/*mmc* (191), a = 4.315(3) Å, c = 3.700(2) Å, R_{bragg} = 4.9%					
Atom	Wyckoff position	*x*	*y*	*z*	b_{all} [Å^2] [S6]
Li	1a	0	0	0	1.65
C	12n	0	0.34(1)	1/2	1.65

Quantitative phase analysis.— For a quantitative phase analysis using XPD data, an internal standard is necessary. In order to quantify the CAM phase loss, the NCM-811 scale factor was normalized to the intensity of different reflections. The respective reflection intensity is assumed to correlate solely with the beam intensity and to show no change in the phase fraction. This is why no Li_xC_6 phases were used. However, due to preferred orientation, the Al and Cu phases were refined structure-independent as Pawley fits. Therefore, no classical phase quantification by Rietveld refinement was possible. For this reason, the small polymer reflections at 4.5° 2θ and 5.4° 2θ as well as the 111 reflections from Al and Cu were chosen as "internal standards" (see highlighted reflections in **Figure S2**). The polymer reflections arise from the pouch foil. As can be seen in **Figure S2**, the 111 reflection of Cu is most suitable for such an analysis because there is no significant overlap with any reflections of the NCM-811 phase. In **Figure S4**, the results of the performed estimation are shown for cell 1 and 2 in the discharged and charged state. All three different normalization methods have in common that an NCM-811 material loss over the course of cycling becomes evident (despite for cell 1 when normalized to the Cu 111 reflection). However, the resulting absolute values scatter substantially. From the analysis in **Figure 5c**, a material loss of 8.5% is expected. Small changes in the NCM-811 phase fraction are expected to give rise to minor intensity changes and they proved to be very hard to quantify with the herein applied "internal standards". In conclusion, we can say that a quantitative analysis of the NCM-811 phase fraction was not possible using a ratio between scale factors and reflection intensities, but the results at least qualitatively follow the observed trend for the NCM-811 material loss.

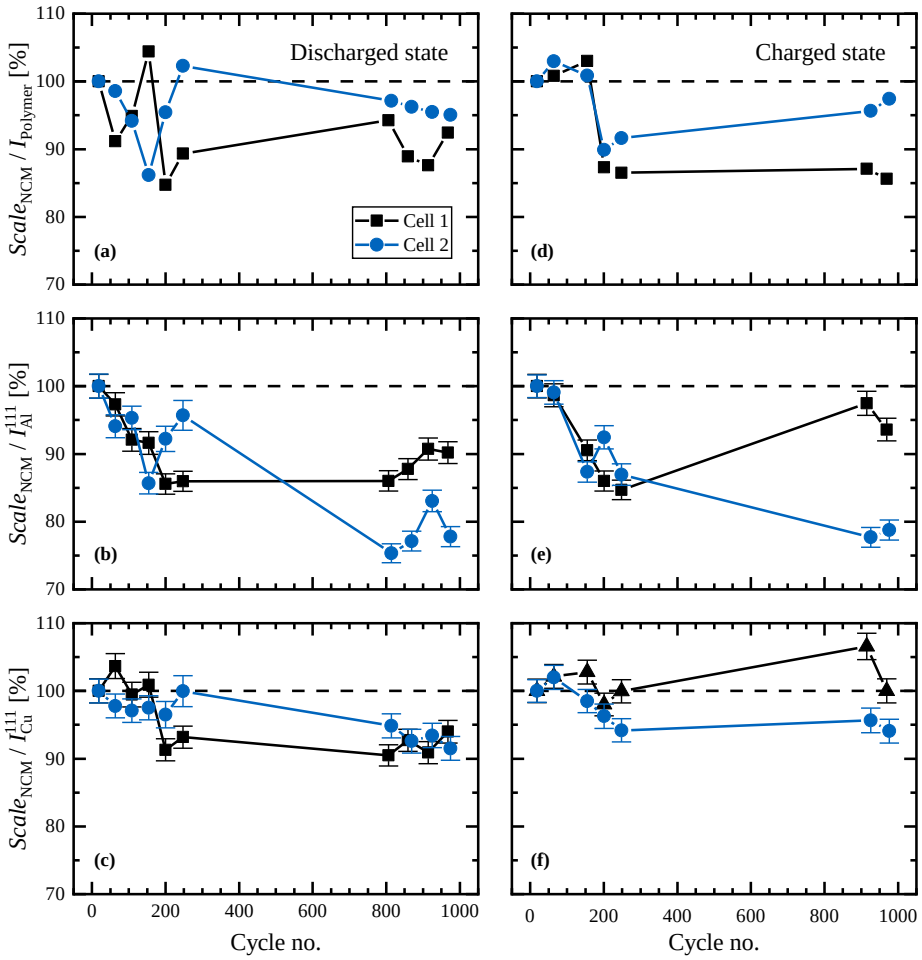

Figure S4. Results of the NCM-811 phase quantification from the in situ S-XPD data for both cells in the discharged (left panels) and charged state (right panels) over the course of cycling, making use of different "internal standards": (a,d) the intensity of the polymer peaks; (b,e) the intensity of the 111 reflection of the Al current collector; (c,f) the intensity of the 111 reflection of the Cu current collector. The error bars for the polymer-based normalization are not shown because they are too large for the chosen scale.

S3: Lattice Parameter and *c*/*a* Calibration Curves

To obtain a calibration curve for the *c*/*a* ratio, diffraction data over the whole charge/discharge cycle are necessary. We tried two different approaches to collect this data:

(a) In situ L-XPD measurements: The cell is cycled at C/7.5 and at defined capacity steps (e.g., every 10 or 15 mAh/g), XPD data are collected during OCV periods. The main advantage is that data over a large 2θ range are collected, thus most NCM reflections contribute to the refinement. A disadvantage is that just a limited amount of *c*/*a* data points are collected during cycling, especially at high SOC, where the *c*/*a* curve is very steep. Thus, the intervals between the *c*/*a* data points in this region are rather large.

(b) Operando L-XPD measurements: The cell is cycled at a rate of C/7.5 while a small part of the 2θ range is measured continuously. Thereby, selected non-overlapping reflections of the NCM-811 phase, namely 003 and 110, are monitored alternatingly during cycling. The main advantage is that a time resolution of ≈8 minutes (corresponding to SOC intervals of ≈4 mAh/g) allows for a sufficient amount of *c*/*a* data points for interpolation of the *c*/*a* curve. A disadvantage is that only two reflections contribute to the refinement, so that the accuracy of the obtained lattice parameter values has to be verified.

Figure S5 compares the two differently obtained data sets, showing that the lattice parameter values obtained by the operando L-XPD technique (ΔSOC ≈ 4 mAh/g) are in good agreement with those obtained by in situ L-XPD (ΔSOC = 10 mAh/g). While no actual structural information can be obtained from the single reflection fits, the operando L-XPD method can be used to track the evolution of the lattice parameter with rather short acquisition times, so that we could use it also to monitor the evolution of the *c* parameter upon a transition from constant-current charge to OCV (see **Figure 8** in the main text).

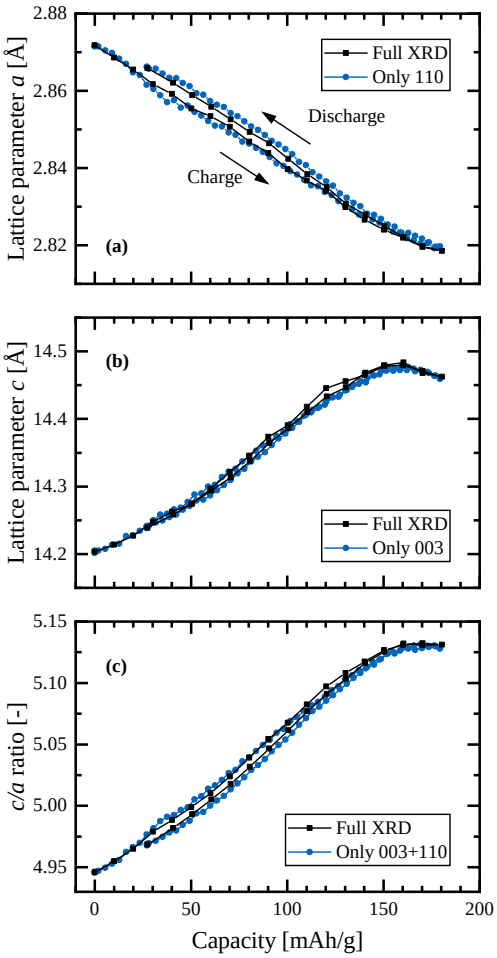

Figure S5. Comparison of lattice parameter values vs. capacity of NCM-811/lithium cells obtained by refining in situ L-XPD data (i.e., fitting the full XPD pattern measured during intermediate OCV phases) versus those obtained by refining operando L-XPD data (i.e., continuous measurements of the 003 and 110 reflections, determining *a* and *c* by single reflection fitting). Data were collected at the in-house Mo-diffractometer and show the first cycle at C/7.5 charged to 180 mAh/g and then discharged to 3.0 V.

Next, we will use in situ L-XPD data to examine the evolution of the lattice parameters over the first two formation cycles (cycle 1 and 2) at C/7.5 and compare them to the lattice parameter values which are obtained by in situ L-XPD with an NCM-811 cathode harvested from cell 1 at EOT (both cells are assembled with metallic lithium anodes). The determined lattice parameters and the unit cell volume versus OCV are shown in **Figure S6**, whereby the observed evolution of structural parameters is in agreement with literature reports.[S2,S7–S10] With increasing OCV of the fresh NCM-811 cathode, i.e., with increasing extent of delithiation, the lattice parameter *a* drops from ≈2.87 Å to ≈2.81 Å, and then remains essentially constant at OCV values exceeding ≈4.2 V (see **Figure S6a**). It is reported that the TM-O distance closely follows the behavior of the lattice parameter *a* upon delithiation, because both values directly depend on the oxidation states and the ionic radii of the transition metals. When Li-ions are removed from the structure, this charge is compensated for by the oxidation of TMs, resulting in decreased ionic radii and hence a decrease in the lattice parameter *a*.

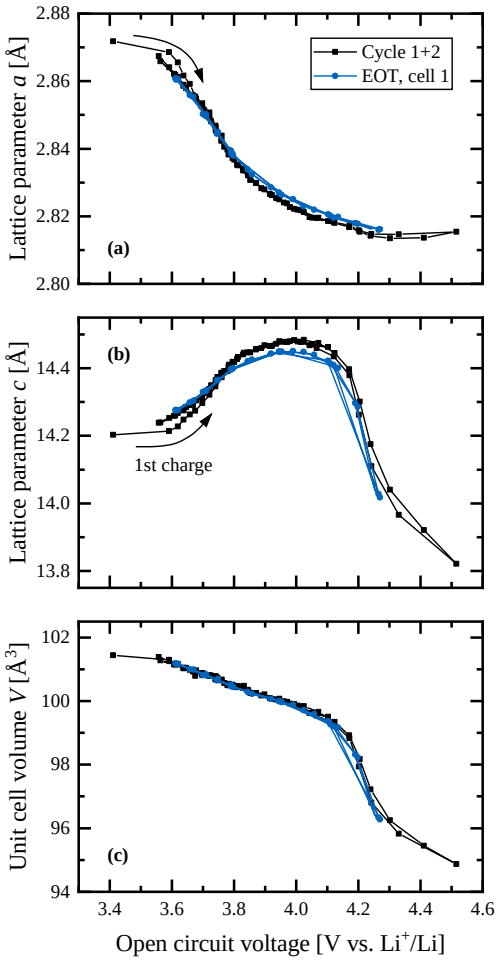

Figure S6. Dependence of (a) lattice parameter *a*, (b) lattice parameter *c*, and (c) unit cell volume *V* on the OCV of NCM-811 during charge/discharge, as determined by in situ L-XPD. The black lines/symbols are obtained with fresh NCM-811 (cycle 1+2, C/7.5, ΔSOC = 10 mAh/g) and the blue lines/symbols are obtained with an EOT sample harvested from the LDE cell 1 (C/2, ΔSOC = 15 mAh/g). The counter-electrode is metallic lithium.

The lattice parameter *c*, which correlates to the Li-O distance, exhibits a more complex behavior. After an initial increase from ≈14.2 Å to ≈14.5 Å, a broad maximum is reached at an OCV of ≈4.0 V, followed by a steep decrease to ≈13.8 Å upon further delithiation (see **Figure S6b**). The initial rise is interpreted as a result of the increasing coulombic repulsion between negatively charged oxygen anions remaining in the layered structure upon removal of the Li-ions between them. The interaction of Li with lattice oxygen is reported to be accompanied with a partial charge transfer from oxygen to lithium, resulting in a screening effect that diminishes the inter-slab repulsion. Upon delithiation, this screening effect is minimized and thereby leads to an increase in *c*. On the other hand, the observation of a decreasing *c* at an OCV exceeding ≈4.0 V must imply a decrease in the inter-slab repulsion. It is known in the literature[S11] that TM 3d and O 2p states are highly hybridized in layered Ni-rich compounds. This means that electrons can be extracted from both TM and O states, which decreases the effective charge of the oxygen atoms and thereby the inter-slab repulsion, resulting in a decrease in *c*. While the decreasing

screening effect by Li should induce an elongation in the *c* direction, the decreasing effective oxygen charge due to TM-O hybridization would cause a shrinkage. Both effects seem to be present, with the elongation in the *c* direction being dominant until an OCV of ≈4.0 V, and the shrinkage in the *c* direction occurring at higher degrees of delithiation. At the beginning of charge, the change in the unit cell volume is dominated by the changes in *a*, which contributes to the cell volume by the second power. At high OCV values, i.e., at low lithium contents, where the lattice parameter *a* remains essentially constant and *c* shows a steep decrease with OCV, the change in the unit cell volume is mostly dominated by the changes in *c*.

When we now compare the evolution of the lattice parameters of fresh NCM-811 upon cycling with that of the harvested EOT sample (black vs. blue lines/symbols in **Figure S6**), the advantage of the ability to plot the structural parameters versus the NCM-811 OCV becomes clear: In operando XPD, the degree of (de)lithiation at a given SOC is not anymore defined, as it changes due to capacity losses upon aging (e.g., by increased polarization, CAM loss, and/or loss of cyclable lithium if used in a full-cell without a pre-lithiated anode). In contrast, for in situ XPD data taken at OCV, the degree of (de)lithiation at a given OCV value is identical for fresh and aged samples. The first data points of the first charge in **Figure S6** indicate that the structural evolution of a material with a full Li site and no cycling history deviates slightly from that of a cycled CAM. This, however, has no influence on our analysis. Apart from that, lattice parameter *a* shows the same trend for the aged NCM-811 harvested at EOT as for the fresh material, although its absolute value is slightly higher for the EOT material at OCV values >3.8 V (see **Figure S6a**). An increased *a* for the aged NCM-811 would suggest a lower oxidation state of the transition-metals compared to the fresh NCM-811. Lattice parameter *c* for the aged NCM-811 is slightly decreased at OCV values of >3.8 V (see **Figure S6b**) compared to fresh NCM-811, indicating that the observed repulsion between the negatively charged oxygen layers is less severe. This might be caused by a more covalent TM-O bond, with significant charge transfer from O to the transition-metals. The resulting decreased TM oxidation state is in agreement with the results for the lattice parameter *a*. Although there are literature reports on a small lowering of the Co and Mn oxidation states upon extended cycling,[S12] it has to be noted that so far these observations were only made on the near-surface region of cathodes. Interestingly, the deviations of the lattice parameters between the fresh and the EOT sample do not affect the net cell volume, as the values for the unit cell volume before and after 1000 cycles agree almost perfectly over the entire OCV range (see **Figure S6c**).

To get an idea of what might have happened to the transition-metals of the cathode, we conducted ICP-AES measurements of the graphite anode at EOT and found that over the course of the ≈1000 cycles, an amount of transition-metals corresponding to 0.22 $mol\%_{TM}$ of the NCM-811 material was deposited on the anode. The relative distribution of Ni, Co, and Mn amongst the metals deposited on the anode is 84%, 2%, and 14%, which at least for Ni and Mn is close to the stoichiometric metal ratio in the fresh NCM-811, suggesting that there is no strong indication for a preferential metal loss (e.g., of Mn).

Different mechanisms are reported for the transition metal dissolution from NCM CAMs.[S9] The possible extent of dissolution of Ni and Mn out of the pouch cell components (pouch foil, current collector and tabs) is not known. However, Al current collectors generally have a Mn contamination on the order of 100 ppm due to production processes. Assuming that a loss of one transition-metal in NCM-811 will result in a maximum loss of 4 cyclable lithium due to charge compensation (e.g., for 1 removed Mn^{4+}, 4 Li^{+} would have to remain in the structure), the maximum capacity loss based on a transition-metal loss of 0.22 $mol\%_{TM}$ would be ≈2.4 mAh/g, similar values as those suggested by Buchberger *et al.* for NCM-111.[S9]

S4: Impedance Measurements

To fit the cathode impedance spectra obtained with a gold wire micro-reference electrode (GWRE), the transmission line model (TLM) was used as described in the literature.[S13] The fitted equivalent circuit is described by R_{HF} + TLM[R_{ion}, R_{CT}/Q_{CT}] + $R_{contact}/Q_{contact}$ + W, with R_{HF} as the high-frequency resistance, TLM as a transmission line model with ionic resistance R_{ion} and an R_{CT}/Q_{CT} parallel circuit element of the charge transfer resistance R_{CT} and a constant phase element (CPE; $Z_{CPE} = [Q\cdot(i\omega)^{\alpha}]^{-1}$) denoted with Q_{CT}, the $R_{contact}/Q_{contact}$ parallel circuit element of the contact resistance $R_{contact}$ and a $Q_{contact}$ CPE, and, finally a Warburg diffusion element W. W and $R_{contact}/Q_{contact}$ were only used when appropriate. The fitted value for the ionic resistance was $R_{ion} \approx 3\ \Omega\ cm^2$ during the first and 18th cycle and $R_{ion} \approx 9\ \Omega\ cm^2$ at EOT. **Figure S7** shows three representative cathode impedance spectra of NCM-811 measured in NCM-811/graphite full-cells (with a GWRE) during charge at an OCV of ≈4.0 V in the first, the 18th cycle, and after 1000 cycles.

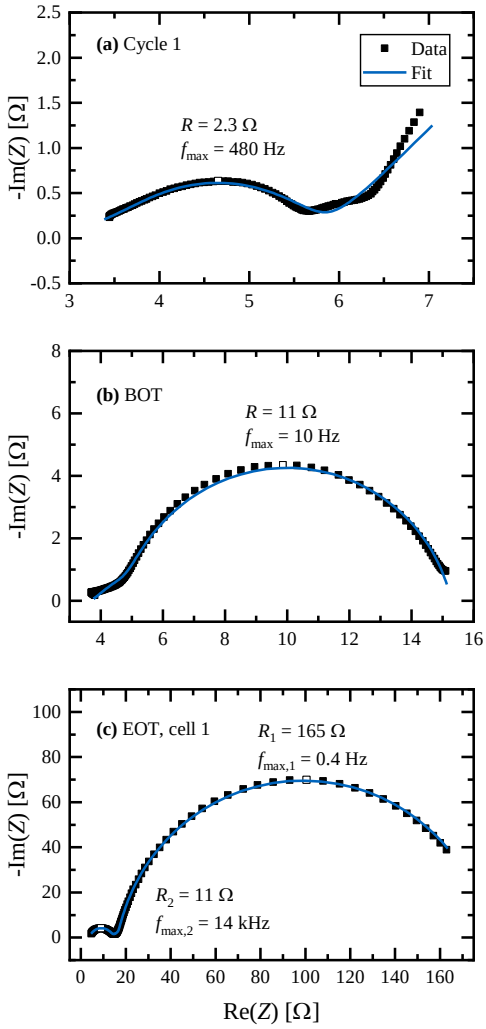

Figure S7. Exemplary cathode impedance spectra of NCM-811/graphite full-cells with a micro-reference electrode (GWRE) measured after a C/10 charge to an OCV of ≈4.0 V: (a) in the first charging cycle; (b) in the

18th cycle (BOT); and, (c) for the harvested NCM-811 cathode from the LDE experiment after 1000 cycles (EOT). The data (black symbols) were fitted (blue lines) to: R_{HF} + TLM[R_{ion}, R_{CT}/Q_{CT}] (+ $R_{contact}/Q_{contact}$) (+ W) (see text for assignments). Spectra were recorded from 100 kHz to 100 mHz with a voltage perturbation of 10 mV at 25°C.

For both the fresh NCM-811 and the NCM-811 at BOT (18th cycle), no feature indicating a contact resistance could be observed (see **Figure S7a,b**) and the fit was conducted without the $R_{contact}/Q_{contact}$ element. On the other hand, an apparent contact resistance feature was observed at high frequencies for the EOT sample (see **Figure S7c**). A rough order-of-magnitude estimation of the capacitances related to charge transfer and to the contact resistance by neglecting the constant phase exponent α was conducted to verify the assignment of the fitting parameters to the semicircles:[S13–S15]

$$C_{calc} = \frac{1}{R\,2\pi f_{max}} \tag{S10}$$

This calculation yields values of $C_{calc,CT} \approx 0.14$ mF for the first charge cycle, $C_{calc,CT} \approx 1.5$ mF for the BOT sample, and $C_{calc,CT} \approx 2.4$ mF and $C_{calc,contact} \approx 1.0$ µF for the EOT sample. An overview of the all values is shown in **Table S10**.

Table S10: Overview of the resistances (R) and the maximum frequencies (f_{max}) of the R/Q elements determined from the Nyquist plots in Fig. S7, together with the calculated capacitances (C_{calc}) according to eq. S10. Based on the assigned interfaces, the calculated capacitances were normalized to the total surface area (A_{total}) to calculate an estimated capacitance (C_{est}), for which different NCM-811 BET surface areas ($A_{BET,CAM}$) were used as described in the text. Note that for the EOT sample (from cell 1), two clearly pronounced semicircles were observed (denoted below as low-f and high-f).

Sample	R [Ω]	f_{max} [Hz]	C_{calc} [mF]	Assigned interface	$A_{BET,CAM}$ [m²/g]	A_{total} [cm²]	C_{est} [µF/cm²]
Cycle 1	2.3	480	0.14	Electrode/electrolyte	0.27	95	≈1.5
BOT	11	10	1.5	Electrode/electrolyte	1.2	160	≈9.4
EOT (low-f)	165	0.4	2.4	Electrode/electrolyte	1.2	160	≈15
EOT (high-f)	11	$14\cdot10^{3}$	$1.0\cdot10^{-3}$	Al foil/electrode	-	0.95	≈1.1

The C_{calc} values of the BOT and EOT samples were normalized to the total surface area of the cathode electrode, including the BET surface area of SFG6L (≈20 m²/g), C65 (≈62 m²/g), and of either the fresh NCM-811 (≈0.27 m²/g) or of aged NCM-811 after removal of the surface impurities with the HF treatment (≈1.2 m²/g, see discussion in context of Figure 8 in the main text). This results in an estimated total cathode electrode surface area of either ≈95 cm² for fresh or of ≈160 cm² for aged NCM-811. When normalizing the C_{calc} values by the total electrode surface area and when neglecting the α exponent of the CPE elements, one would expect to obtain estimated specific capacitances (C_{est}), which are comparable to the typical double layer capacitance of ≈10 µF/cm².[S13,S16] For the BOT and EOT samples, $C_{est,CT}$ is ≈9.4 µF/cm² and ≈15 µF/cm², respectively, which is consistent with the expected value and suggests that our assignment is correct. On the other hand, $C_{est,CT}$ for the NCM-811 in the first cycle is only ≈1.5 µF/cm², which must be due to the fact that the "semicircle" seen in the Nyquist plot for the

first cycle (**Figure S7a**) must contain at least two different processes, as indicated by the very low α value of 0.6 (vs. 0.9 for the other semicircles in the BOT and EOT samples), so that the associated $Q_{est,CT}$ value can only be taken as an order-of-magnitude estimate. A reason for this relatively small capacitance might be the fact that this electrode has never been cycled to voltages above 4.0 V where this impedance spectrum was recorded. As mentioned in the main text in context with the shift of the R_{CT} vs. OCV curve of the first charge (**Figure 5**), it is known from the literature[S17] that surface species, such as Li_2CO_3, are removed upon the first charge, a process which might not be completed at this point and their continuous slow removal during the first-cycle impedance measurements at 4.0 V might lead to artefacts as the surface might be changing while recording the impedance data.

Finally, let us examine the high-frequency semicircle clearly apparent in the EOT sample, which is likely related to a contact resistance at the interface between the Al current collector and the cathode electrode. This can be verified by normalizing C_{calc} to the exposed area of the Al current collector ($\equiv$0.95 cm^2), yielding an estimated capacitance of $C_{est,contact}$ $\approx$1.1 µF/cm^2, which is on the same order of magnitude than a double layer capacitance,[S13,S16] thus proving that the assignment of this impedance feature to a contact resistance is correct.

S5: Selected Cathode Half-Cell Voltage Profiles

Figure S8 shows cathode voltage profiles of cell 2 at C/2 (≡ 0.72 mA/cm^2 or 6.46 mA), for which a sudden jump in capacity and in the average charge and discharge voltages is observed during cycle 893 (see **Figure 1a** and **b**), plotting the voltage profiles before and after this event. Quite clearly, both the charge and the discharge voltages between cycle 892 (black line) and cycle 894 (green line) differ by ≈100 mV along the entire capacity range, which corresponds to a resistance decrease of ≈15 Ω (from 100 mV/6.46 mA, ≈140 Ω cm^2). As evident from the voltage profile of cycle 893 (blue symbols), this decrease in potential, i.e., this drop in resistance, occurred instantaneously, indicating that it cannot be caused by any structural change within the cathode, but must be related to a sudden improvement of the electronic contacting of the cell. This was likely caused by obtaining a better electronic contact between the current collector tabs of the pouch cell and the crocodile clamp by some random movement. While we cannot prove this hypothesis, due to the fact that both cells showed again rather similar capacities and average charge/discharge voltages after cycle 893 (see **Figure 1a** and **b**), we are very confident that this contacting issue does not influence the observations and conclusions made in our work.

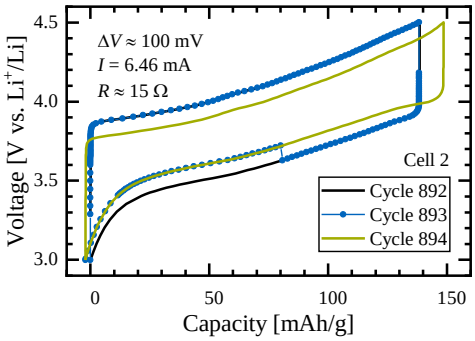

Figure S8. Cathode half-cell voltage profiles at C/2 of the LDE cell 2 during cycles 892 (black line), 893 (blue line/symbols), and 894 (green line), where a sudden jump in capacity and average charge/discharge voltage occurred.

An additional figure of cathode half-cell voltage profiles serves to support the line of argument that the impedance build-up happens with a considerable time delay compared to the material loss, because the surface oxygen-depleted surface layer restructures only gradually into a resistive surface layer. To show this, the cathode voltage profiles and the respective difference plots of the 250th cycle, at EOT, and at BOT are shown for cell 1 and 2 in **Figure S9**. Here, the capacity axis used in **Figure 1c** in the main text is converted into the lithium content (x_{Li}) scale for the NCM-811 bulk material, as determined by the XPD analysis (see **Figure 4**). Independent of the degree of material loss, this visualization allows the best comparison between voltage curves of the retained bulk material over the course of extended cycling (assuming that the surface layer is electrochemically inactive and does not contribute to the obtained capacities). The increase of cathode overpotential observable in the 250th cycle is slightly higher than at BOT (cycle 19), but much lower than at EOT (cycle 970/973), while in the 250th cycle

the material loss at the surface was found to be already ≈65% of that at EOT (5.6% after 250 cycles vs. 8.5% at EOT, see **Figure 4c**). In **Figure S9**, the grey bars highlight the x_{Li} region where the OCV is ≈4.0 V, i.e., the region from which the overpotential estimates are derived in the main text. It can therefore be concluded that the loss of active material by the formation of the oxygen-depleted surface layer initially does not substantially increase the cathode impedance (i.e., the surface layer has a relatively low resistance), but that it gradually transforms into a substantially more resistive structure which gives rise to the observed impedance build up (see **Figure 5b**).

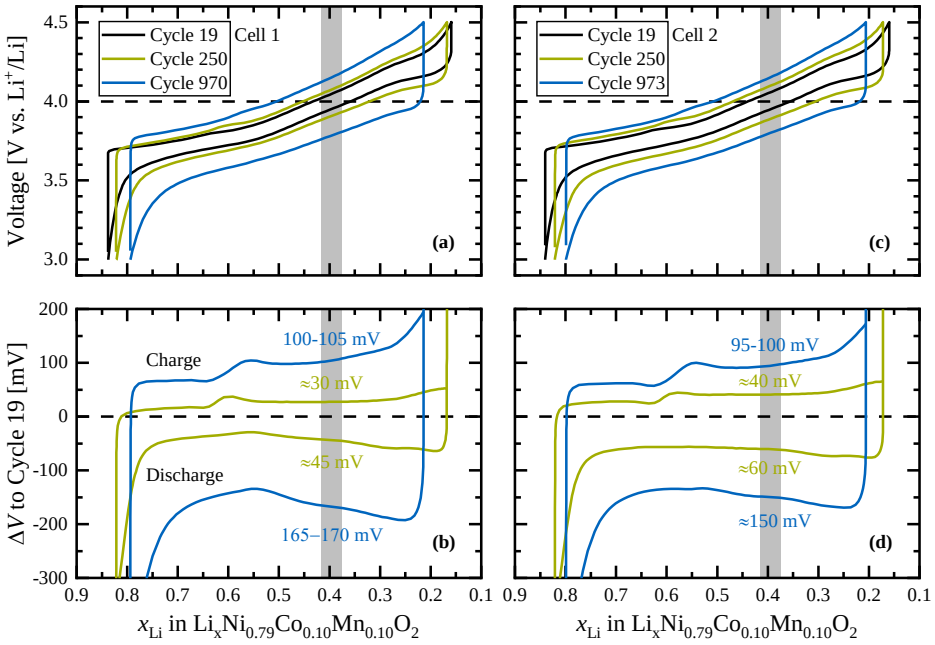

Figure S9. (a,c) Cathode voltage profiles of both LDE cells from the 19th (close to BOT, black line), the 250th (green line), and the 970th/973rd cycle (close to EOT, blue line) plotted vs. the lithium content (x_{Li}) of the retained bulk material, which was determined by the *c*/*a* ratio from the charged and discharged state of the respective in situ S-XPD data. (b,d) Voltage difference of the curves from the 250th and 970th/973rd cycle relative to the 19th cycle. The grey bars highlight the overpotential increase for the x_{Li} region at which the OCV of ≈4.0 V vs Li^+/Li is expected.

S6: XPS Reference Data

To establish a correlation between intensity shifts in the O1s XPS spectrum of our sample and structural information, reference spectra are necessary. For this purpose, layered MnO_2 (purity >99%), spinel Mn_3O_4 (purity >97%) and rock-salt MnO samples (purity >99%, all samples from Sigma-Aldrich) were analyzed by X-ray photoelectron spectroscopy. The focus thereby lies on the peak at lower binding energies (green and blue fits in **Figure S10**) because the one at higher energies derives from surface impurities like carbonates and hydroxides (red fits in **Figure S10**). A comparison of the reference spectra (**Figure S10g-i**) shows that the low-energy O1s peak shifts to higher binding energy as the oxygen content of the materials decreases, namely from 529.3 eV for layered MnO_2 (panel g) to 529.6 eV for spinel Mn_3O_4 (panel h) and to 529.7 eV for rock-salt MnO (panel i). Based on this observation, a correlation between the shifts of the low-energy O1s peaks towards higher binding energies upon cycling of the NCM-811 sample (pristine → BOT → EOT) deduced from the fits in **Figure S10d-f** is consistent with an increasing oxygen deficiency in the surface-near regions upon cycling. The detailed fitting values and applied constraints for peak energy and FWHM are listed in **Table S11**. The position of the peak of the O-depleted layer in NCM-811 (≈529.9 eV, marked by the dashed blue lines in **Figure S10d-f**) likely deviates from the reference samples because of the different local environment around the oxygen (only Mn in reference samples vs. Ni, Co and Mn in NCM-811).

In addition, the intensity of the peak around ≈533.5 eV (and an additional peak for the EOT sample at ≈532.8 eV) is evolving with cycling (**Figure S10a-c**), which we denominated as "miscellaneous". In the literature,[S18,S19] a similar feature is reported in the O1s XPS spectra of cycled NCA cathodes and ascribed to a CEI-type (cathode electrolyte interphase) film forming on the cathode by electrolyte decomposition (e.g., lithium alkyl carbonates, Li-O-CO-O-R), which is also possible in our case.

Table S11: XPS fitting parameters for the fits in **Figure S10** for pristine, BOT, and harvested EOT NCM-811 as well as for three reference compounds: peak energy with constrained deviation and FWHM with respective range constraint. Additionally, parameters for the main surface impurity peak are shown.

Sample (panel)	Assigned species	Energy [eV] (constrained deviation)	FWHM [eV] (constrained range)
Pristine (a,d)	Layered (green)	529.3 (±0.1)	1.26 (0.8-1.35)
	M-OH/M-CO_3 (red)	531.9 (±0.1)	1.62 (0.8-2.35)
BOT (b,e)	Layered (green)	529.3 (±0.1)	1.10 (0.8-1.35)
	O-depleted (blue)	529.9 (fixed)	1.08 (0.8-1.35)
	M-OH/M-CO_3 (red)	531.9 (±0.1)	1.66 (0.8-2.35)
EOT (c,f)	Layered (green)	529.3 (±0.1)	1.10 (0.8-1.35)
	O-depleted (blue)	529.9 (fixed)	1.24 (0.8-1.35)
	M-OH/M-CO_3 (red)	531.9 (±0.1)	2.26 (0.8-2.35)
MnO_2 (g)	Layered (green)	529.3 (-)	0.88 (0.8-1.35)
Mn_3O_4 (h)	Spinel (blue)	529.6 (-)	1.17 (0.8-1.35)
MnO (i)	Rock-salt (blue)	529.7 (-)	0.95 (0.8-1.35)

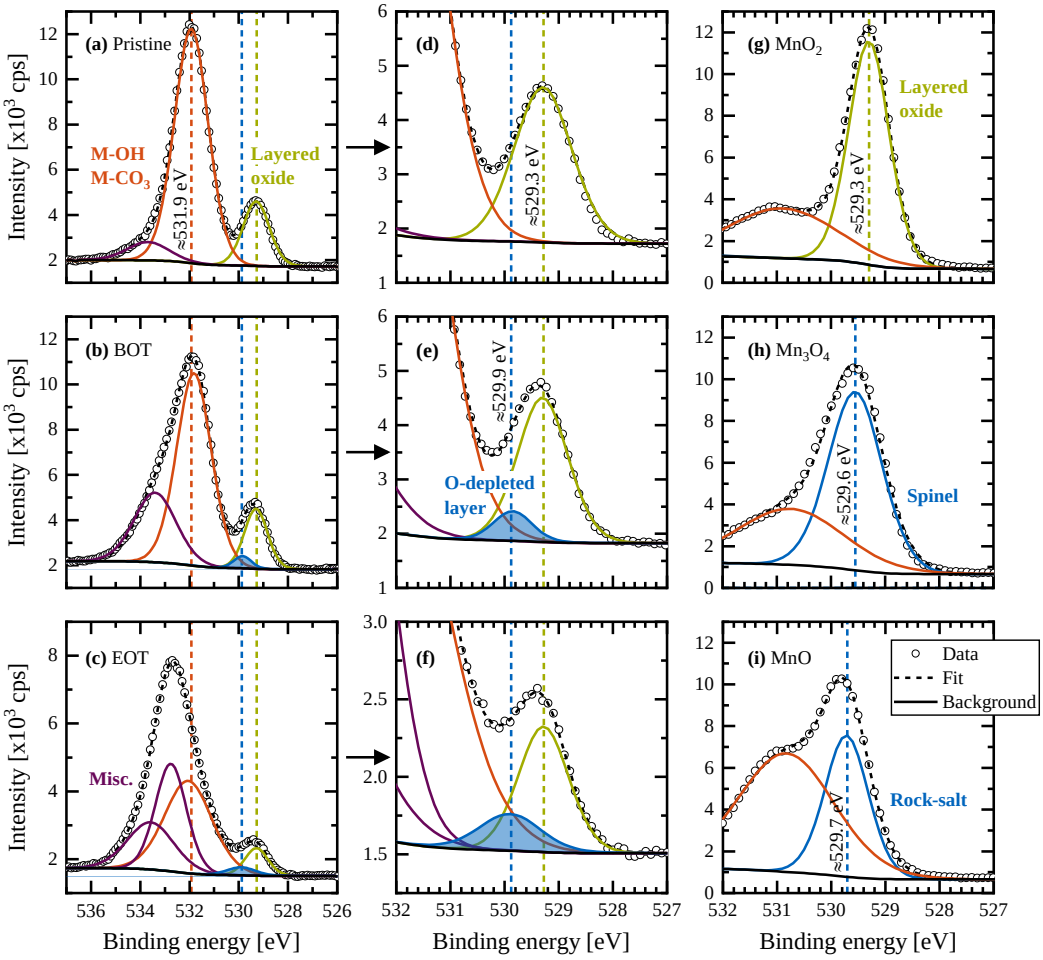

Figure S10. XPS O1s spectra of pristine, BOT, and EOT NCM-811 samples with surface hydroxide and carbonate impurities highlighted by a red dashed line in panels a-c; close-ups of the peak at lower binding energies are shown in panels d-f. Reference XPS O1s spectra of layered (MnO_2), spinel (Mn_3O_4), and rock-salt (MnO) manganese reference compounds are shown in panels g-i. The peak position of a layered and an oxygen-deficient (spinel and rock-salt) structure are highlighted by green and blue dashed lines in panels d-i. All spectra are shown with Shirley background in black line, data points as empty symbols, and the overall fit as black dashed line. The colored lines corresponding to the respective surface species as indicated in the plots give a deconvolution of the overall fitting. The fitting parameters and their constrained values for the low-energy O1s peaks (green and blue) and for the main surface impurity peak (red) are listed in **Table S12**.

S7: Calculation of O-depleted Surface Layer Thickness

Based on the discrepancy between the absolute capacity losses observed by electrochemical measurement (C_{EC}^{EOT}) and calculated from the change in lattice parameters ($C_{Material}^{EOT}$), we deduced a loss of cyclable CAM as is discussed in context with **Figure 5c** in the main text. This evaluation provides the capacity loss due to material loss, $\Delta C_{Material}^{BOT \rightarrow EOT}$ = 15.8 mAh/g, or in percentage terms relative to the pristine CAM, $\Delta C_{Material,rel}^{EOT}$ = 8.5%. This ratio gives the estimated molar fraction of NCM-811, which is no longer taking part in Li intercalation ($x_{surface\text{-}layer}$). To translate the molar fraction into a surface layer thickness, the approximate particle radius is estimated from the BET surface area (A_{BET}) and the crystallographic density of the CAM (ρ_{cryst}) as given in equation (S11) and **Table S13**. For this calculation, the surface area of the aged NCM-811 is used (1.2 m^2/g after HF treatment, as discussed in context with **Figure 8** in the main text), because this is the actual surface area, on which the layer will form upon extended cycling. The surface layer thickness ($t_{surface\text{-}layer}$) can then be estimated from the particle radius and the molar fraction using equations (S12) and (S13). All calculated values and measurement data are summarized in **Table S13**. Detailed information about these calculations are reported in the literature.[S20,S21]

$$r = \frac{3}{A_{BET}\,\rho_{cryst}} \tag{S11}$$

$$r' = r\,(1 - x_{surface\text{-}layer})^{1/3} \tag{S12}$$

$$t_{surface\text{-}layer} = r - r' \tag{S13}$$

Table S13. Parameters for calculating the thickness of a presumably inactive surface layer formed upon ≈1000 cycles. The BET surface area (A_{BET}) was measured by both Kr and N_2 physisorption (yielding identical values) after exposure of the NCM-811 CAM to 1000 ppm HF in LP57 (see main text); the crystallographic density (ρ) was obtained from Rietveld refinement. The average radius of the NCM-811 particles was based on a spherical approximation using (S10), while the molar fraction of material lost in the surface layer ($x_{surface\text{-}layer}$) is based on the EOT value given in **Figure 5c**. The approximate surface layer thickness ($t_{surface\text{-}layer}$) then follows from (S11) and (S12).

Parameter	Value
A_{BET} [m^2/g]	1.2
ρ_{cryst} [g/cm^3]	4.75
r [nm]	526
$x_{surface\text{-}layer}$ [%]	8.5
$t_{surface\text{-}layer}$ [nm]	15

S8: SEM Cross-Sectional Images of Pristine and EOT NCM-811

The morphology of CAM secondary particles was evaluated from cross-sectional SEM images. For that purpose, 1 x 1 cm^2 pieces were punched out of pristine and end-of-test electrodes in their fully lithiated state. The samples were fixed in a Teflon holder, embedded in epoxy resin (EpoThin 2 resin and hardener, Buehler, USA), and subjected to reduced pressure in order to remove gas bubbles. After hardening overnight at 40°C, the resin block was removed from the holder, ground on SiC paper in two steps (grade P320 and P1200, CarbiMet S, Buehler), and subsequently polished with 9 and 3 µm diamond polishing pastes (MetaDi Supreme Polycrystalline Diamond Suspension, Buehler) on a micro cloth (MicroCloth, Buehler). The final polishing step was done with a 0.05 µm Al_2O_3 agent (MasterPrep Alumina Suspension, Buehler) on a micro cloth (ChemoMet, Buehler). The contact pressure was set to 5 N for every step. SEM analysis was performed with a JEOL scanning electron microscope (JSM-7500F, JEOL, Japan) in the backscattering mode at an accelerating voltage of 5 kV.

In context with **Figure 8** in the main text, the SEM images presented in **Figure S11** indicate that the contact area between electrolyte and primary particles is quite large and that most primary particles indeed are in direct contact with the electrolyte.

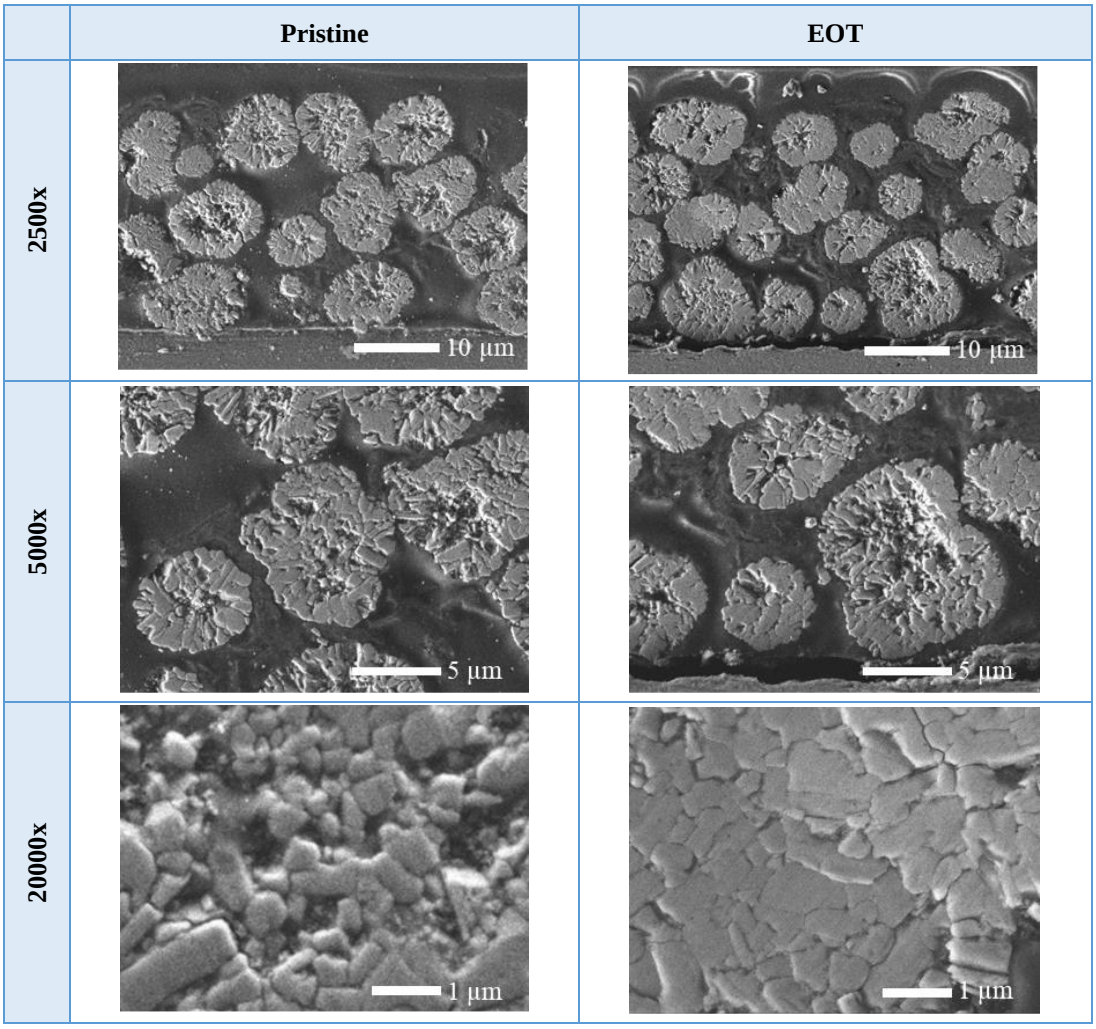

Figure S11: Cross-sectional SEM pictures of pristine (calandered electrode sheets, left) and EOT NCM-811 (discharged state, right) at different magnifications measured in backscattering mode at an accelerating voltage of 5 kV.

S9: HAADF-STEM Images of Pristine, BOT and EOT NCM-811

High Angle Annular Dark Field – Scanning Transmission Electron Microscopy (HAADF-STEM) images were measured from a pristine NCM-811 electrode, a BOT electrode which was cycled according to the LDE protocol, and a harvested EOT electrode. The BOT and EOT electrodes (in the discharged state) were first washed thoroughly with dimethyl carbonate (DMC, BASF SE) in an argon-filled glove box to remove $LiPF_6$ salt residuals and then dried overnight at room temperature. Afterwards, all samples were prepared by focused ion beam (FIB) milling using a Helios G4 CX dualbeam machine (Thermo Fisher Scientific, USA). The samples were immediately imaged at 300 keV by HAADF-STEM using a Thermo Fisher Themis Z 3.1 microscope.

The HAADF-STEM images are summarized in **Figure S12**. The two primary particles of the pristine NCM-811 in the left picture are imaged in the desired low-indexed zone axes in order to differentiate any disordered spinel/rock-salt structure from the regular layered structure. The pristine particle on the left (as well as in the right picture) seems to be imaged along the *ab* plane, highlighting the hexagonal arrangement of the transition-metals within their layer (which appear as bright spots due to the high *Z* number). In contrast, the pristine particle on the right shows the layered structure along the *c* direction, highlighting the alternating stacking of the transition-metal (bright lines) and lithium layers (inter-slab, dark lines). If transition-metals (partially) occupy the lithium layers, the intensity of these atomic columns would be increased and the region would therefore appear brighter in the image. This is however not the case for the pristine NCM-811, i.e., the layered structure ranges from the bulk of the particles to their surface without any defects. On the other hand, the BOT and EOT primary NCM-811 particles feature inter-slabs in the surface-near region (as indicated either (i) with arrows for the representation along the *c* direction in the left pictures or (ii) by dashed lines for the representation along the *ab* plane in the right figures), which are partially occupied with transition-metals, as it would be expected for spinel/rock-salt structures. However, no clear boundary between the layered bulk structure and the disordered spinel/rock-salt surface structure can be discerned from these images. The phases seem to merge gradually into each other, which makes it difficult to quantify the surface layer thickness.

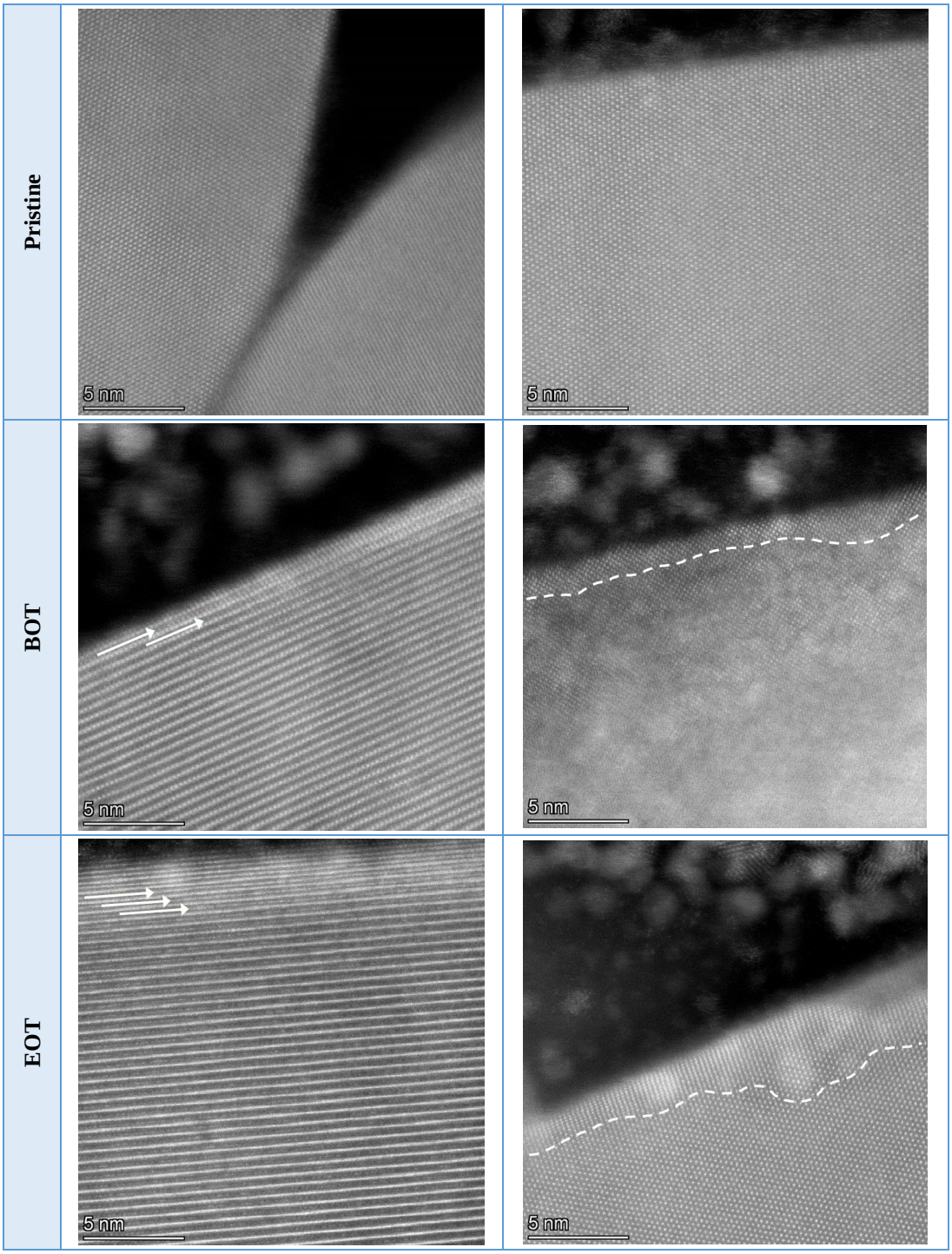

Figure S12: HAADF-STEM pictures of pristine (top), BOT (18th cycle, middle), and EOT NCM-811 particles (after 1000 cycles, bottom). The arrows/dashed lines in the BOT and EOT images exemplary indicate surface-near inter-slabs/regions which are partially populated with transition-metals (and which appear as bright spots/lines in these images).

S10: Literature

S1. K. Kleiner, B. Strehle, A. R. Baker, S. J. Day, C. C. Tang, I. Buchberger, F.-F. Chesneau, H. A. Gasteiger, and M. Piana, *Chem. Mater.*, **30**, 3656 (2018).

S2. A. O. Kondrakov, A. Schmidt, J. Xu, H. Geßwein, R. Mönig, P. Hartmann, H. Sommer, T. Brezesinski, and J. Janek, *J. Phys. Chem. C*, **121**, 3286 (2017).

S3. V. K. Pecharsky and P. Y. Zavalij, *Fundamentals of Powder Diffraction and Structural Characterization of Materials*, Springer, New York (2005).

S4. P. W. Stephens, *J. Appl. Crystallogr.*, **32**, 281 (1999).

S5. J. Frantti, S. Eriksson, S. Hull, V. Lantto, H. Rundlöf, and M. Kakihana, *J. Phys. Condens. Matter*, **15**, 6031 (2003).

S6. O. Dolotko, A. Senyshyn, M. J. Mühlbauer, K. Nikolowski, F. Scheiba, and H. Ehrenberg, *J. Electrochem. Soc.*, **159**, A2082 (2012).

S7. A. O. Kondrakov, H. Geßwein, K. Galdina, L. de Biasi, V. Meded, E. O. Filatova, G. Schuhmacher, W. Wenzel, P. Hartmann, T. Brezesinski, and J. Janek, *J. Phys. Chem. C*, **121**, 24381 (2017).

S8. L. de Biasi, A. O. Kondrakov, H. Geßwein, P. Hartmann, T. Brezesinski, and J. Janek, *J. Phys. Chem. C*, **121**, 26163 (2017).

S9. I. Buchberger, S. Seidlmayer, A. Pokharel, M. Piana, J. Hattendorff, P. Kudejova, R. Gilles, and H. A. Gasteiger, *J. Electrochem. Soc.*, **162**, A2737 (2015).

S10. O. Dolotko, A. Senyshyn, M. J. Mühlbauer, K. Nikolowski, and H. Ehrenberg, *J. Power Sources*, **255**, 197 (2014).

S11. D.-H. Seo, A. Urban, and G. Ceder, *Phys. Rev. B Condens. Matter Mater. Phys.*, 115118 (1998).

S12. F. Lin, I. M. Markus, D. Nordlund, T.-C. Weng, M. D. Asta, H. L. Xin, and M. M. Doeff, *Nat. Commun.*, **5**, 1 (2014).

S13. J. Landesfeind, D. Pritzl, and H. A. Gasteiger, *J. Electrochem. Soc.*, **164**, A1773 (2017).

S14. J. Landesfeind, J. Hattendorff, A. Ehrl, W. A. Wall, and H. A. Gasteiger, *J. Electrochem. Soc.*, **163**, A1373 (2016).

S15. T. Teufl, D. Pritzl, S. Solchenbach, H. A. Gasteiger, and M. A. Mendez, *J. Electrochem. Soc.*, **166**, A1275 (2019).

S16. T. Teufl, B. Strehle, P. Müller, H. A. Gasteiger, and M. A. Mendez, *J. Electrochem. Soc.*, **165**, A2718 (2018).

S17. A. Grenier, H. Liu, K. M. Wiaderek, Z. W. Lebens-Higgins, O. J. Borkiewicz, L. F. J. Piper, P. J. Chupas, and K. W. Chapman, *Chem. Mater.*, **29**, 7345 (2017).

S18. S. Watanabe, M. Kinoshita, T. Hosokawa, K. Morigaki, and K. Nakura, *J. Power Sources*, **258**, 210 (2014).

S19. M. Shikano, H. Kobayashi, S. Koike, H. Sakaebe, E. Ikenaga, K. Kobayashi, and K. Tatsumi, *J. Power Sources*, **174**, 795 (2007).

S20. B. Strehle, K. Kleiner, R. Jung, F. Chesneau, M. Mendez, H. A. Gasteiger, and M. Piana, *J. Electrochem. Soc.*, **164**, A400 (2017).

S21. R. Jung, M. Metzger, F. Maglia, C. Stinner, and A. H. Gasteiger, *J. Electrochem. Soc.*, **164**, A1361 (2017).

3.4.2 Comparative *Ex Situ* Study Performed at Elevated Temperature

The article entitled "A Comparative Study on Structural Changes during Long-Term Cycling of NCM-811 at Ambient and Elevated Temperatures" was submitted in February 2021 to the peer-reviewed *Journal of The Electrochemical Society* and published in May 2021.[209] It is available as "open access" article and distributed under the terms of the Creative Commons Attribution Non-Commercial No Derivatives 4.0 License. The study was presented by Franziska Friedrich at the PRiME Meeting in Honolulu, Hawaii, USA (October 4-9, 2020, Abstract Number 254). The permanent weblink of this article can be found under: https://iopscience.iop.org/article/10.1149/1945-7111/abf780.

There is a growing demand for Li-ion batteries to operate and survive under extreme thermal conditions,[263] which is why cycle-life studies are more and more performed at elevated temperatures (in the range of ≈40-60°C).[82,89,94,176] Such accelerated stress tests can be applied for the screening of a large number of materials, but it requires facile characterization methods to monitor the evolution of important material properties upon cycling.

Based on the NCM-811 degradation study conducted at ambient temperature (see section 3.4.1), we present here our follow-up work, which investigates the capacity fading of the Ni-rich NCM-811 over 700 cycles at the elevated temperature of 45°C. Keeping most of the cycling conditions constant, the capacity loss at C/2 is more than doubled at 45°C compared to 22°C. In contrast to our former study, where the underlying degradation mechanisms were examined by in-depth, but cumbersome *in situ* techniques, we now cycle six pouch cells to different cycle numbers and subject the harvested cathode electrodes to a series of simple *ex situ* techniques. For example, the charge-transfer resistance of the NCM-811 CAM is measured in a modified half-cell setup, which does not require the use of a µ-RE for impedance measurements. The resistance build-up is further monitored by current pulses in the full-cells (also referred to as direct current internal resistance (DCIR) method[145]). The fraction of lost cyclable CAM is determined by the afore-mentioned XPD analysis and purely electrochemically by slow cycling in the half-cells. At a C-rate of C/50, the resistance build-up becomes negligible and any capacity

difference compared to the initial performance originates solely from the cathode active material loss.

Comparing bulk versus surface degradation modes, we observe this time an increase of the Li-Ni mixing on the order of ≈1-2%, which could decrease the lithium bulk diffusivity, but its quantitative contribution to the capacity fading remains elusive. After 700 cycles at 45°C, we could ascribe ≈60% of the observed capacity fading to the loss of electrochemically active CAM (compared to ≈40% material loss after 1000 cycles at 22°C), which is caused by the formation of a reconstructed, rock-salt-like surface.[89,264] Surface area measurements by Kr-BET show that virtually all primary NCM-811 particles are exposed to the electrolyte in the charged state, because their large volume contraction leads to intergranular cracking.[24,88] Thus, the surface layer thickness around the primary crystallites is estimated to be ≈6 nm at 22°C and ≈12-14 nm at 45°C until the end-of-test. Since these surface instabilities depend predominantly on the lithium utilization of the layered oxides, they are an intrinsic challenge for Ni-rich poly-crystalline CAMs,[85,86] and a lot of research efforts are invested into alternative synthesis strategies such as micro-structured and single-crystalline cathodes (reducing the available surface area)[265] as well as into the washing of CAMs (reducing the oxygen release).[257] In this respect, the Dahn group could already show that single-crystalline NCM-523 experiences barely any material loss, even if cycled for 2500 cycles until 4.3 V at 55°C.[94]

Author contributions

F.F. built the pouch cells and was in charge of the EIS and Kr-BET measurements. B.S. carried out the rate tests and the structural analysis. B.S. wrote the manuscript. All authors discussed the results and commented on the manuscript. B.S. and F.F. contributed equally to this work as co-shared first authors.

Journal of The Electrochemical Society, 2021 **168** 050512

A Comparative Study of Structural Changes during Long-Term Cycling of NCM-811 at Ambient and Elevated Temperatures

Benjamin Strehle,[=,*,z] Franziska Friedrich,[=,*] and Hubert A. Gasteiger[**]

Chair of Technical Electrochemistry, Department of Chemistry and Catalysis Research Center, Technical University of Munich, D-85748 Garching, Germany

Lithium-ion batteries operate predominantly at room temperature, but some applications such as electric vehicles also demand operation at higher temperature. This is especially challenging for cathode active materials (CAMs), which undergo an accelerated failure at elevated temperature. Here, we systematically compare the capacity fading of the Ni-rich NCM-811 at two different temperatures. The first dataset over 1000 cycles at 22 °C stems from a former study, while the NCM-811/graphite full-cells are investigated now under similar conditions at 45 °C for 700 cycles. We focus on the CAM by using pre-lithiated graphite anodes. The capacity loss due to NCM-811 degradation at 45 °C is more than doubled compared to 22 °C. The underlying mechanisms related to the bulk and the surface of the CAM are quantified by several ex situ techniques such as X-ray powder diffraction, half-cell cycling with impedance spectroscopy, and Kr-BET. The aging happens mainly at the surface of the primary particles, forming a resistive, disordered surface layer, whose thickness is estimated to reach ≈6 nm at 22 °C and ≈12–14 nm at 45 °C by the end-of-test. Furthermore, the Li-Ni mixing in the bulk increases by ≈1%–2% at elevated temperature, but its contribution to the capacity loss remains elusive.

 [DOI: 10.1149/1945-7111/abf780]

Manuscript submitted February 25, 2021; revised manuscript received March 29, 2021. Published May 13, 2021. *This was Paper 254 presented during PRiME 2020, October 4–9, 2020.*

Layered transition-metal oxides are the most widely applied class of cathode active materials (CAMs) in lithium-ion batteries (LIBs). They dominate the fast-growing market of electric vehicles (EVs), combining high energy and power density with long cycle-life.[1] On a structural level, layered oxides can be written as $Li_{1+\delta}[TM]_{1-\delta}O_2$, with alternating layers of lithium and transition-metals (TMs) in octahedral coordination and with a small degree of over-lithiation (typically $0 < \delta < 0.05$). Depending on the choice of transition-metals, layered oxides are referred to as NCMs (combining Ni, Co, and Mn) or NCAs (replacing Mn by Al, which is actually not a TM). Making efforts to reduce the cobalt content due to sustainability and geopolitical aspects,[2,3] there is an ongoing trend to increase the nickel content as much as possible. This strategy goes along with a higher specific capacity at a given cell voltage compared to less Ni-rich counterparts, but Ni-rich CAMs are also prone to structural and thermal instabilities.[4,5] In this respect, NCM-811 ($Li_{1+\delta}[Ni_{0.8}Co_{0.1}Mn_{0.1}]_{1-\delta}O_2$) is currently one of the most Ni-rich NCM materials with proven cycling stability.[6–8]

In a recent study from 2019, we investigated the long-term cycling stability of NCM-811 at ambient temperature (≈22 °C).[9] Using in situ X-ray powder diffraction (XPD) in combination with other diagnostics such as electrochemical impedance spectroscopy (EIS) and X-ray photoelectron spectroscopy (XPS), we elucidated the capacity fading mechanism of an NCM-811 cathode active material and quantified its main contributions to cell capacity fading over the duration of 1000 cycles. We provided evidence that the high-voltage operation until 4.5 V vs Li^+/Li leads to the formation of a resistive, oxygen-depleted surface layer around the primary particles. Consequently, the capacity fading intrinsic to the NCM-811 CAM can be divided into two contributions, one originating from the irreversible cathode active material loss (due to the surface reconstruction of the CAM) and one originating from the growing charge-transfer resistance and the associated overpotential loss (due to the resistive nature of the surface layer). The latter is particularly pronounced at high charge/discharge rates.

Even though the majority of applications are designed to operate at/near room temperature, there is a growing demand for lithium-ion batteries to operate and survive also under more extreme thermal conditions.[10,11] Electric vehicles, e.g., should run both in colder and hotter regions. The United States Advanced Battery Consortium (USABC) aims at a survival temperature ranging from −40 °C to +66 °C for 24 h.[12] This goal for EV applications might be one of the reasons why the focus of academic research is increasingly placed on performing cycling studies at elevated temperatures (in the range of ≈40 °C–60 °C).[13–16] Furthermore, high-temperature cycling accelerates the battery failure and can thus be used as an accelerated stress test (AST) to evaluate new or optimized CAMs. Alternative AST strategies that have been reported are potential hold or open circuit voltage (OCV) rest phases at high voltages as well as cycling with low salt concentrations.[17]

On the other hand, the evaluation of ASTs requires facile characterization methods to extract important battery parameters over the course of (long-term) cycling. With respect to CAM evaluation, such parameters are the percentage of active material loss and the increase of the charge-transfer resistance, which were deduced from in situ XPD and EIS in our former work. In situ and operando techniques can generate much more authoritative information than ex situ (or post-mortem) experiments, because they characterize the material under real operating conditions. At the same time, they are often cumbersome and need advanced instrumentation (e.g., custom-made cell designs or synchrotron radiation), which is not readily available in every laboratory. Thus, high-throughput ASTs should be accompanied by some basic ex situ techniques.

In the present work, we want to systematically compare the long-term cycling performance of NCM-811 at ambient and elevated temperatures. Using the cycle-life analysis over 1000 cycles at 22 °C from our precedent study as Ref. 9, the same NCM-811 cathode active material is cycled here at 45 °C for up to 700 cycles. To ensure comparability, the other cycling conditions are kept constant. As in our previous study, the graphite counter-electrode (CE) is pre-lithiated to eliminate cell capacity fading contributions from the anode and the NCM-811 potential is controlled vs the lithium reference-electrode (RE). Every ≈150 cycles, one of the pouch cells is stopped and the harvested cathode electrode is subjected to several ex situ techniques such as XPD, EIS, and surface area determination

[=]These authors contributed equally to this work.
[*]Electrochemical Society Student Member.
[**]Electrochemical Society Fellow.
[z]E-mail: benjamin.strehle@tum.de

by Kr-BET. Here, the NCM-811 cathode active material loss is quantified by two independent approaches, either by XPD or purely by electrochemical means, while the charge-transfer resistance from EIS is compared to direct current internal resistance (DCIR) measurements in the pouch cells. Furthermore, we are seeking to clarify whether the NCM-811 CAM aging at elevated temperature is mechanistically similar, or different, to its fading at ambient temperature. This question addresses the relative importance of bulk vs surface related degradation phenomena, in particular Li-Ni mixing in the bulk vs surface reconstruction.

Experimental

Battery assembly and cycling.—The materials and battery design used here are identical to our previous aging study of NCM-811 at ambient temperature and can be looked up in detail there.[9] Briefly, the CAM composition was determined to be $Li_{1.01}Ni_{0.79}Co_{0.10}Mn_{0.10}O_2$ by elemental analysis, which gives a theoretical capacity of 274 mAh g^{-1} (including ≈2.2 wt% surface impurities). Cathode electrode sheets with 94 wt% CAM, 2 wt% Timcal SFG6L graphite, 1 wt% Timcal C65 conductive carbon, and 3 wt% Kynar PVDF binder (HSV900) were provided by BASF SE (Germany). The electrode sheets were calendered to a porosity of ≈30% and have a CAM loading of ≈7.0 mg_{CAM} cm^{-2} (±1%), corresponding to ≈1.4 mAh cm^{-2} for a practical capacity of 200 mAh g^{-1}. The CAM loading is lower than the previously reported value of ≈7.4 mg_{CAM} cm^{-2}, probably due to a small variation along the electrode spool. Single-layer pouch cells with 9 cm^2 cathode area (30 × 30 mm^2) were manufactured with a geometrically as well as capacitively over-sized graphite counter-electrode (CE, 33 × 33 mm^2, ≈7.1 $mg_{graphite}$ cm^{-2}, corresponding to ≈2.3 mAh cm^{-2}, BASF SE), two glass-fiber (GF) separators (36 × 36 mm^2, glass microfiber filter 691, VWR, Germany), a lithium metal reference-electrode (RE), and 700 μL LP57 electrolyte (1M $LiPF_6$ in EC:EMC = 3:7 by weight; electrolyte-to-CAM mass ratio of ≈13/1). In contrast to our former study that used LP57-2 with 2% vinylene carbonate (VC), the VC additive was omitted in the full-cells in this work due to its oxidative instability at elevated temperatures.[18] To ensure a stable solid electrolyte interface (SEI), the graphite counter-electrode was however pre-formed and pre-lithiated in a half-cell configuration at 45 °C in LP57-2 electrolyte. The pre-lithiation to ≈$Li_{0.24}C_6$ (corresponding to ≈0.55 mAh cm^{-2}) provides a sufficiently large lithium reservoir for the full-cells (0.55/1.4 ≈ 40% of the cathode capacity). This approach avoids any capacity fading due to the loss of cyclable lithium and thus, the Li-RE can be used for the potential control of the cathode. Furthermore, the anode/cathode balancing after pre-lithiation amounts to (2.3-0.55)/1.4 ≈ 1.25/1, i.e., the remaining storage capability of the anode does not pose a risk for lithium plating during charge. The pouch cells were compressed in a spring-loaded holder at a homogeneous pressure of ≈2 bar.

The pouch cells were tested at 45 °C in a temperature-controlled chamber (Binder, Germany) with a battery cycler (Series 4000, Maccor, USA). The cycling protocol consists of a loop of 50 cycle segments, which are further divided into three sequential steps:

(i) The first two cycles were done at constant-current (CC) mode at a C-rate of C/10 and in the cathode potential window of 3.0–4.5 V vs Li^+/Li, as controlled vs the Li-RE. All C-rates throughout this study are based on a nominal specific capacity of 200 mAh g^{-1} and the unit "V" refers to 'V vs Li^+/Li', unless stated otherwise.

(ii) The third cycle is a direct current internal resistance (DCIR) measurement at a relative state of charge (SOC) of 65%, as referenced to the discharge capacity of the preceding C/10 cycle. The partial charge to 65% SOC, where the DCIR measurement was taken, and the subsequent discharge back to a cathode potential of 3.0 V were also carried out at C/10. The DCIR measurement itself was done after a 2 h rest period at open circuit voltage (OCV, ≈4.0 V), applying a discharge pulse of C/5 for 10 s. The area specific resistance (R_{DCIR} in Ω cm^2) was computed by the Maccor MIMS Client according to:[19]

$$R_{DCIR} = \frac{\frac{V_1 + V_3}{2} - V_2}{j_2} \quad [1]$$

Here, V_1 is the OCV right before the pulse, V_2 is the voltage at the end of the 10 s pulse, V_3 is the OCV 10 s after the pulse, and j_2 is the current density of the C/5 discharge pulse (≈0.28 mA cm^{-2}). Please note that the induced change of ≈0.1 mAh g^{-1} (corresponding to an SOC variation of ≈0.05%) is negligible and that R_{DCIR} relates solely to the resistance of the cathode due to the potential control vs the Li-RE.

(iii) The remaining 47 cycles were done in CC mode at C/2 between cathode potentials of 3.0–4.5 V, which are, for the sake of comparability, the same cycling conditions than in our previous study at ≈22 °C.[9]

This iterative protocol of 50 cycle segments was applied to six cells, which passed through an increasing total number of cycles, ranging from only six cycles (i.e., two cycles at C/10, one DCIR test cycle, and three cycles at C/2; referred to as begin-of-test, BOT), to 100 cycles and then in steps of 150 cycles to a maximum of 700 cycles (end-of-test, EOT). Each cell was stopped in the discharged state (i.e., after a final C/2 cycle until 3.0 V) and the cathode OCV was measured for ≈5 h at 45 °C and finally for another ≈5 h at 25 °C. The final OCV values taken at 45 °C and 25 °C agree within less than ±10 mV for a given cell. After cell disassembly, the NCM-811 cathode electrodes were stored for further ex situ analyses in an argon-filled glove box.

X-ray powder diffraction and Rietveld refinement.—XPD measurements aimed at monitoring the evolution of the lithium content (x_{Li} in $Li_xNi_{0.79}Co_{0.10}Mn_{0.10}O_2$) and the Li-Ni mixing ($Ni_{Li}$) in the NCM-811 CAM upon cycling. The experiments were conducted at our in-house STOE STADI P diffractometer (STOE, Germany) in transmission mode, using Mo-$K_{\alpha 1}$ radiation (0.7093 Å, 50 kV, 40 mA), a Ge(111) monochromator, and a Mythen 1K detector with one data point every 0.015°/2θ. A silicon standard material was used for the determination of the instrumental broadening. The CAM powder was measured ex situ in air-tight sealed 0.3 mm borosilicate capillaries in the 2θ range of 5°–90° for ≈17 h. For measurements with the discharged CAM, the material was scratched off with a scalpel from the harvested electrodes of each of the six pouch cells and loaded into two capillaries without further washing (for two independent XPD repeat measurements). On the other hand, for measurements with the charged CAM, the 30 × 30 mm^2 cathodes harvested from the cycled pouch cells were punched out into disk-shaped electrodes with a diameter of 14 mm. These smaller electrodes were assembled with a Ø 15 mm Li-CE, two Ø 16 mm GF separators, and 80 μl LP57 electrolyte in CR2032-type coin cells, which were cycled at C/2 and 45 °C for 1.5 cycles between 3.0–4.5 V and then stopped at 4.5 V. Due to electrolyte residuals, the CAM mass could not properly be determined and we used the average loading of the pristine electrodes instead, which leads to an uncertainty of ≈1% for the applied current and the extracted capacity. In order to minimize self-discharge effects, which would lead to an apparently erroneous increase of the determined x_{Li} value in the charged state at 4.5 V, the OCV periods at 45 °C and 25 °C that followed these 1.5 cycles were not longer than 30 min each (change in the OCV at 25 °C of less than 15 mV over the max. 30 min). Afterwards, the coin cells were immediately opened and the charged CAM was prepared for the XPD measurement at the same day.

The Rietveld refinements were performed with the software package Topas.[20] NCM-811 exhibits a layered α-$NaFeO_2$-type

Journal of The Electrochemical Society, 2021 **168** 050512

structure with $R\bar{3}m$ symmetry and we therefore used the following structural model: $[Li_{x-v}Ni_v]_{3a}[Li_vNi_{0.79-v}Co_{0.10}Mn_{0.10}]_{3b}[O]_{6c}$. Here, the overall lithium content (x_{Li}) was calculated according to the *c*/*a* lattice parameter ratio of the cycled samples. The calibration curves, $x_{Li} = f(c/a)$, were determined by operando XPD from the initial cycles of this particular CAM in our previous publication and they look as follows in the discharged (i.e., at low SOC, $0.62 \leqslant x_{Li,dis} \leqslant 0.91$) and charged state (i.e., at high SOC, $0.12 \leqslant x_{Li,cha} \leqslant 0.23$):[9]

$$x_{Li,dis} = \frac{73.80 - \sqrt{c/a \cdot 10^4 - 49222}}{58.36}, \quad \text{for } 0.62 \leqslant x_{Li,dis} \leqslant 0.91 \qquad [2]$$

$$x_{Li,cha} = \frac{c/a - 4.733}{1.41}, \text{ for } 0.12 \leqslant x_{Li,cha} \leqslant 0.23 \qquad [3]$$

The Li-Ni mixing was treated as a paired anti-site defect ($v_{Li} = v_{Ni}$). This means that the amount of Ni in the Li layer (Ni_{Li}) is the same as the amount of Li in the TM layer (Li_{TM}). Please note that in the special case of the pristine CAM, v_{Li} equals $v_{Ni} + 0.01$ due to full occupation of all layers (at $x_{Li} = 1.01$). The Li-Ni mixing is reported in percentage terms as $Ni_{Li} = v_{Ni} \cdot 100\%$.

The refinements included the following non-structural parameters:

- background: Chebyshev polynomial with 15 parameters
- instrument: zero shift and axial divergence
- absorption: cylindrical absorption correction ($\mu R \approx 0.75$, assuming a packing density of 40%)

The structure-related refinement parameters are the following:

- scale factor
- broadening: isotropic contribution from crystallite size and anisotropic contribution from microstrain using the hexagonal Stephens model[21]
- lattice parameters: *a* and *c*
- fractional coordinate: $z_{6c,O}$
- atomic displacement parameters: three site-specific and isotropic parameters ($b_{3a,Li}$, $b_{3b,TM}$, and $b_{6c,O}$)
- site occupancy factors: v_{Ni} (and x_{Li}) as outline above, using ionic scattering factors for all elements (Li^+, Ni^{3+}, Co^{2+}, Mn^{4+}, and O^{2-})

Furthermore, the 2 wt% of conductive graphite (Timcal SFG6L) in the cathode electrode sheet were included into the Rietveld fits by refining its scale factor, crystallite size broadening, and lattice parameters, while fixing the other structural parameters of the $P6_3/mmc$ graphite phase to the values from Dolotko et al.[22] Due to the high intensity of the freshly replaced Mo source, we also noticed tiny reflections of the borosilicate capillary in some of the diffractograms, which were treated as additional reflections based on an empty capillary measurement.

Rate test and impedance analysis.—We punched out another Ø 14 mm electrode from each of the pouch cell cathodes harvested after cycling, reassembling them into coin cells with a lithium metal counter-electrode (separator and electrolyte as described above). These were used to perform a rate test towards slow C-rates in combination with electrochemical impedance spectroscopy (EIS). Since a conventional lithium metal foil would have a large contribution to the EIS response of the NCM-811 half-cells, we placed a free-standing graphite (FSG) electrode on top of the lithium metal foil (i.e., between the lithium metal and the separator), as it was described by Morasch et al.[23] Using this Li/FSG composite as counter-electrode, its impedance contribution (imaginary and real part of $<5\ \Omega\ cm^2$ over the measured frequency range[23]) to the half-cell impedance is comparably small compared to that of the NCM-811 cathode. Consequently, the measured cell impedance can be reasonably well approximated to correspond to that of the NCM-811 cathode. The coin cells were cycled between 3.0–4.5 V at 45 °C for two cycles each at C/2, C/10, C/50, and finally again at C/2. The two C/10 cycles over the entire voltage range were completed by a third DCIR-like cycle to 65% SOC (OCV of ≈4.0 V, see full-cells), at which we conducted potential-controlled EIS measurements with a potentiostat (VMP300, BioLogic, France) in the frequency range of 100 kHz to 100 mHz with an AC voltage perturbation of 15 mV (taking eight data points per decade and three repetitions per point).

To fit the impedance spectra acquired at 65% SOC and 45 °C, we used an equivalent circuit described by R_{HF} + TLM[R_{ion}, R_{CT}/Q_{CT}] + $R_{contact}/Q_{contact}$, with the elements defined as follows: (i) R_{HF} being the high-frequency resistance of the half-cell; (ii) TLM representing a transmission line model with the ionic resistance in the electrolyte phase between the pores of the electrode (R_{ion}), and a parallel circuit element of the charge-transfer resistance (R_{CT}) and a constant phase element (CPE, Q_{CT}); and, (iii) another parallel circuit element of the contact resistance ($R_{contact}$) and a $Q_{contact}$ CPE that is generally observed as an interfacial resistance between the cathode electrode and the aluminum current collector.[9,24] The last discharge of the half-cells at C/2 was to a cell voltage of 2.55 V, followed by constant voltage hold for 1–6 h before cell disassembly. The harvested electrodes were used for surface area measurements that are described in the following.

Surface area determination.—After the rate test, the discharged NCM-811 cathodes were subjected to Kr-BET measurements. Before that, the electrodes were thoroughly washed in three steps with an EC/EMC mixture and twice with DMC to remove any residuals from the conductive salt, as described by Oswald et al.,[25] and then dried at 120 °C under dynamic vacuum for at least 6 h. Surface area measurements were performed on a gas sorption analyzer (Autosorb-iQ, Quantachrome, USA) at 77 K using krypton as adsorbate and the obtained surface areas are referenced to the mass of the washed electrodes. Kr has the advantage over N_2 to be much more sensitive due to its ≈300 times lower saturation pressure (p_0), which minimizes the void volume correction and thus enables the analysis of low surface area samples. The specific surface area of the NCM-811 CAM ($A_{BET,CAM}$ in m^2/g_{CAM}) was determined from adsorption isotherms in the relative pressure range of $\approx 0.13 < p/p_0 < 0.29$ with seven data points according to the Brunauer-Emmet-Teller (BET) theory. The actually measured surface area of the entire electrode ($A_{BET,elec}$ in m^2/g_{elec}), consisting of 94 wt% CAM and 6 wt % inactive electrode additives (viz., 2 wt% SFG6L conductive graphite, 1 wt% C65 conductive carbon, and 3 wt% PVDF binder), was converted into $A_{BET,CAM}$ by subtracting the contribution of the inactive electrode additives ($A_{BET,add}$ in m^2/g_{add}):

$$A_{BET,CAM} = \frac{A_{BET,elec} - 0.06 \cdot A_{BET,add}}{0.94} \qquad [4]$$

Here, $A_{BET,add}$ of the overall 6 wt% inactive electrode additives was measured separately, using electrodes comprising only the additives in the same ratio as in the actual NCM-811 electrodes. The pristine additives-only electrode yielded a specific surface area of 5.10 ± 0.11 m^2/g_{add} (average from two electrodes). To evaluate a possible change of $A_{BET,add}$ during cycling, we tried to mimic the full-cell conditions by cyclic voltammetry at a scan rate of 0.2 mV s^{-1} between 2.55–4.5 V (requiring a time comparable to that for C/2 cycling). After 10 or 20 cyclic voltammetry cycles at 45 °C vs a Li/FSG-CE, $A_{BET,add}$ rises by ≈9% to 5.56 ± 0.01 m^2/g_{add} (average from these two cells). Using the specific surface area of the conductive additive powders (SFG6L: ≈20 m^2/g, C65: ≈62 m^2/g), one would expect $A_{BET,add}$ to be ≈17 m^2/g_{add} for the additives-only electrode. This discrepancy is explained by prior observations that pore blocking by the PVDF binder can substantially lower the electrode surface area, depending on the type of conductive additives and the binder content.[25,26] In Eq. 4, the first $A_{BET,add}$ value

(5.10 m^2/g_{add}) was used for the pristine NCM-811 electrode, while the latter (5.56 m^2/g_{add}) was used for any cycled electrode. The inactive electrode additives contribute with ≈15%–20% to the total surface area of the cycled electrodes.

Results and Discussion

Electrochemical full-cell data.—To focus solely on the intrinsic degradation mechanisms of the NCM-811 cathode active material at elevated temperature, we designed the full-cells in such a way that common degradation processes originating from the anode and from the electrolyte are effectively suppressed during battery operation. Since the graphite anode is pre-lithiated to a cathode capacity of ≈40% (see Experimental section), the loss of cyclable lithium on the anode side does not contribute to the observed capacity fading.[27] This approach allows the NCM-811 cathode to be operated between fixed cut-off potentials of 3.0 and 4.5 V vs Li^+/Li, as controlled vs a Li-RE. Furthermore, electrolyte changes such as oxidation reactions at the cathode side and $LiPF_6$ salt depletion could deteriorate the cell performance[28] at realistic mass ratios of $m_{electrolyte}/m_{CAM} \approx 1/1$.[29] Therefore, we employ highly porous glass-fiber separators in our full-cells, which enable a large electrolyte excess of $m_{electrolyte}/m_{CAM} \approx 13/1$, so that the bulk electrolyte properties remain unaltered. Assuming that electrolyte degradation is relevant under the applied conditions, the thereby released protic species could lead to transition-metal dissolution from the CAM surface;[27] however, the SiO_2-containing GF separator acts as a proton scavenger.[30,31] We want to stress that all these modifications distinguish this work from other studies using more realistic cell setups (i.e., graphite anode not pre-lithiated, less electrolyte volume, and polyolefin separators), but they are done on purpose to obtain an in-depth and quantitative understanding of the CAM degradation. To enhance its degradation processes, the NCM-811 CAM is further subjected to an accelerated stress test, because the upper cut-off potential of 4.5 V vs Li^+/Li is chosen deliberately higher than in commercial NCM/graphite cells. Here, the upper full-cell voltage (V_{FC}) typically amounts to 4.2–4.3 V_{FC},[12,16] corresponding only to ≈4.3–4.4 V vs Li^+/Li.

Figure 1 shows from top to bottom the evolution of the discharge capacity at C/2 (including checkup cycles at C/10), the charge-averaged mean charge and discharge voltage, and the DCIR resistance measured at a relative state of charge (SOC) of 65% (based on the preceding C/10 cycle). For all six cells, the first charge at C/10 to 4.5 V yields ≈237 mAh g^{-1} (not shown), corresponding to an absolute SOC of ≈86% (referenced to the total amount of lithium in the NCM-811 CAM). This is well beyond the onset of oxygen evolution from the layered oxide surface at ≈80%.[32,33] The following C/10 discharge yields a capacity of ≈221 mAh g^{-1}, which decreases to an initial discharge capacity of ≈207 mAh g^{-1} at the faster rate of C/2 (see Fig. 1a). The capacity fading is very reproducible among the six cells, which were tested for an increasing number of cycles ranging from 6 to 700 cycles (see differently colored symbols in Fig. 1a). In the overlapping cycling segments, the average standard deviation between the cells amounts to ±2 mAh g^{-1}.

Focusing first on the C/2 cycling, Table I compares the begin-of-test (BOT) discharge capacity values at 45 °C with those from our previous study with the same CAM at 22 °C as well as their end-of-test (EOT) values after 1000 and 750 cycles, respectively. The BOT capacity increases by ≈24 mAh g^{-1} when comparing the BOT value after 18 cycles at 22 °C and after 6 cycles at 45 °C (for an explanation why BOT was defined after 18 cycles in our previous study, see Ref. 9) or by ≈17 mAh g^{-1} when comparing cycle 6, which we ascribe to the enhanced kinetics at elevated temperature. However, the higher initial capacity at 45 °C goes along with a faster degradation upon cycling, with the capacity fading of ≈0.04 mAh g^{-1} per cycle at 22 °C being more than doubled at 45 °C (≈0.10 mAh g^{-1} per cycle). Consequently, the EOT capacity of ≈139 mAh g^{-1} after 700 cycles at 45 °C is already ≈6 mAh g^{-1} lower than that after 1000 cycles at 22 °C.

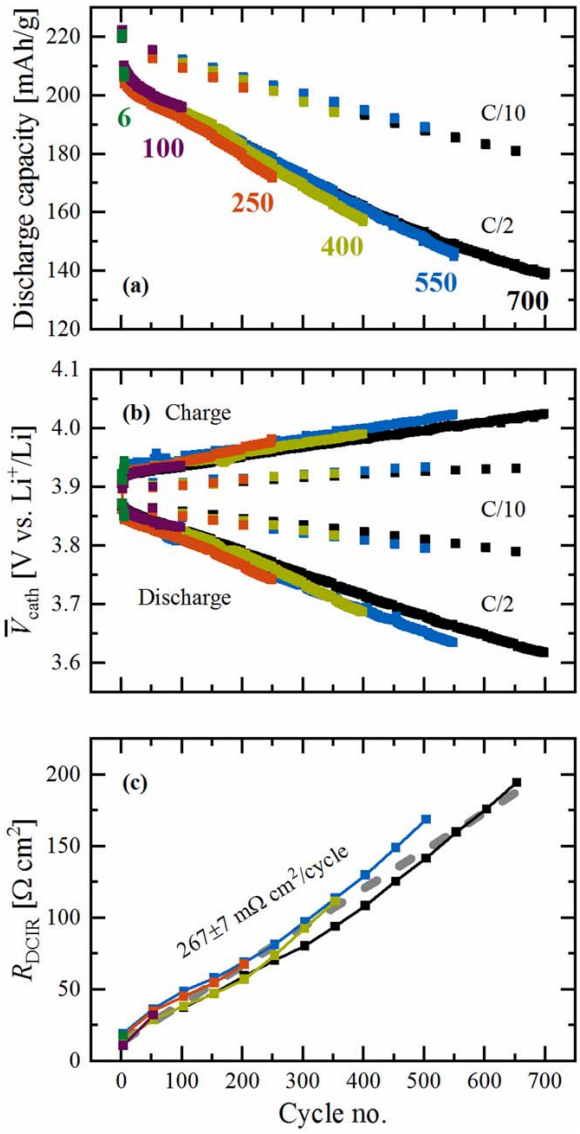

Figure 1. Cycle-life degradation of the NCM-811 CAM evaluated in NCM-811/graphite full-cells with a partially pre-lithiated graphite CE, which were cycled at 45 °C and C/2 (with intermittent C/10 checkup cycles) between cathode potentials of 3.0–4.5 V measured vs a Li-RE. (a) Specific discharge capacities. (b) Charge-averaged mean charge and discharge cathode voltages vs Li^+/Li ($\bar{V}_{cath} \equiv \int V_{cath}\, dq / \int dq$). (c) Cathode resistance measured by a DCIR pulse at 65% SOC with respect to the preceding C/10 cycle (R_{DCIR} calculated according to Eq. 1). The discharge capacities and the mean voltages are shown for both the regular C/2 cycles and the intermittent C/10 checkup cycles, while the DCIR cycles to 65% SOC are excluded from these panels. Slight deviations from the characteristic mean voltage curves due to the change of C-rate or OCV periods were further omitted from panel (b). The numbers in panel (a) give the total number of cycles for each of the six cells. The increase of R_{DCIR} in panel (c) was determined to be 267 ± 7 mΩ cm^2/cycle by a linear fit through all data points, as marked by the dashed gray line ($R^2 = 0.975$).

Even though there is no study which investigates NCM-811 under similar conditions, it is useful to compare our results with literature data in order to validate that the performance degradation shown in Fig. 1a is reasonable. Li et al. tested $LiNi_{0.80}Co_{0.15}Al_{0.05}O_2$ (NCA) in multi-layer pouch cells at 40 °C and various full-cell (FC)

Journal of The Electrochemical Society, 2021 **168** 050512

Table I. Comparison of the C/2 discharge capacity, as reported in our previous publication at 22 °C[9] and as measured in this work at 45 °C. The NCM-811/graphite full-cells were cycled between cathode potentials of 3.0–4.5 V vs Li^+/Li and analyzed from the respective begin-of-test (BOT) to end-of-test (EOT).

C/2 capacity [mAh g^{-1}]	Ambient temperature (22 °C)	Elevated temperature (45 °C)
BOT → EOT	Cycle 18 → 1000	Cycle 6 → 700
BOT	≈183	≈207
EOT	≈145	≈139
Capacity loss ($\Delta C_{EC}^{BOT \rightarrow EOT}$)	≈38 (≈0.04 per cycle)	≈68 (≈0.10 per cycle)
Capacity retention	≈79%	≈67%

cut-off conditions, including C/2 cycling between 3.0–4.2 V_{FC} and 3.0–4.3 V_{FC} with a constant voltage (CV) hold at the upper cut-off.[13] Please note that the full-cell voltage (V_{FC}) is roughly 0.1 V lower than the cathode potentials vs Li^+/Li given in our study and that we use a partially pre-lithiated graphite CE. After 700 cycles of these NCA/graphite full-cells, the capacity retention amounts to ≈86% (at an upper cathode potential of ≈4.3 V vs Li^+/Li) and ≈78% (≈4.4 V vs Li^+/Li), which is more than the ≈67% obtained for our NCM-811/graphite full-cells under the slightly harsher conditions of 45 °C and an upper cathode potential of 4.5 V vs Li^+/Li (see Table I). Schweidler et al. investigated NCM-851005/graphite single-layer pouch cells at 45 °C and 1C between 2.8 and 4.2 V_{FC} (also with CV hold, CE not pre-lithiated).[15] They report an initial capacity of ≈195 mAh g^{-1} and a fairly linear fading of ≈0.07 mAh g^{-1} per cycle. Since the capacity loss is again smaller than in our present work, it is reasonable to assume that the CAM aging, which strongly increases with increasing upper cathode potentials, is the dominant factor in all cases, and that any lithium inventory loss at the anode does not contribute much to the reported fading. In realistic full-cells, the amount of cyclable lithium could be reduced, e.g., due to TM dissolution from the cathode and the consequent attack of the SEI,[34] which potentially limits the lithiation of the CAM during discharge.[35] Here, the pre-lithiation of the graphite anode deliberately eliminates this effect in order to focus on the degradation of the NCM-811 CAM.

The ex situ diagnostic analyses presented later will try to answer the question if the aging mechanism of the NCM-811 CAM is mostly due to its surface reconstruction, as it was the case in our previous degradation study with the same CAM conducted at 22 °C,[9] or if other (bulk) phenomena come into play at an elevated temperature. The reduced fading of ≈0.06 mAh g^{-1} per cycle during the C/10 checkup cycles compared to ≈0.10 mAh g^{-1} per cycle at C/2 (both taken from Fig. 1a) already points towards an overpotential-induced capacity loss, which might be caused by the formation of a resistive surface layer and/or by an increase of the bulk resistance of the CAM (e.g., due to sluggish lithium diffusion kinetics). Such a resistance build-up is further suggested by the evolution of the mean charge and discharge cathode voltages shown in Fig. 1b. Inspecting their average changes over cycling (see Table II), the decrease of the mean discharge voltage is always higher than the increase of the mean charge voltage (by a factor of 1.5–2.5). This discrepancy could potentially be ascribed to a path dependence of the cathode resistance (or one of its components) between charge and discharge. In this context, Pan et al. reported the chemical diffusion coefficient of Li ($\tilde{D}_{Li}$) to be up to four times higher during delithiation (i.e., during charge) than during lithiation (i.e., during discharge) of $LiCoO_2$ thin-film electrodes at the H1-H2 phase transition.[36] This initial phase transition takes place at low SOCs, where also NCM layered oxides exhibit largely different resistances: while the voltage vs capacity curve is relatively flat at the beginning of charge, indicating small overpotentials, it drops steeply at the end of discharge, i.e., the cathode resistance is much higher for the same lithium content during discharge.[9,13] Besides the lithium diffusion kinetics in the bulk of the CAM, the charge-transfer resistance at its surface might also contribute to the different changes of the cathode mean voltage during charge vs discharge (see Table II). The charge-transfer rises strongly towards the voltage cut-offs, especially at the low-SOC limit, which makes it however difficult to clearly resolve differences between charge and discharge under common measurement conditions (e.g., for EIS measurements with a capacity spacing of 20 mAh g^{-1}).[9]

Finally, Fig. 1c shows the evolution of the direct current internal resistance (R_{DCIR}) of the cathode, which was measured in the mid-SOC range (65% SOC based on the preceding C/10 cycle), so that it is only marginally affected by slight variations of the lithium content (x_{Li}) upon cycling: this relative SOC of 65% occurs within the narrow OCV range of 3.98–4.00 V over all cycles, indicating a small variation of x_{Li}, and furthermore lies in a region where the charge-transfer resistance varies little with x_{Li} (note that R_{CT} is at/near its minimum at an OCV of ≈4.0 V for any given cycle, as shown in Fig. 6 of our previous study with the same CAM[9]). Here, R_{DCIR} rises almost linearly for all six cells (see Fig. 1c), with an average slope of 267 ± 7 mΩ cm^2 per cycle. This resistance increase can also be translated into a voltage change by multiplying the slope with the current densities applied at C/2 and C/10, respectively. Doing so in Table II, the calculated voltage changes of ≈0.19 and ≈0.04 mV/cycle resemble the evolution of the mean charge voltage, amounting to ≈0.14 mV/cycle at C/2 and ≈0.05 mV/cycle at C/10, whereas the evolution of the mean discharge voltages stays higher. This might be due to the fact that the mean discharge voltage is dominated by the very high R_{CT} (and/or very low $\tilde{D}_{Li}$) at low SOCs, so that R_{DCIR} taken near the minimum of the R_{CT} vs SOC curve is not representative of the much higher resistance toward the end of discharge.

Validation of the DCIR measurement by EIS.—Since the DCIR measurement does not tell us which component(s) of the cathode resistance increases upon cycling, we performed an ex situ EIS analysis with the harvested pouch cell electrodes. To enable this analysis in a coin cell setup, i.e., in the absence of a μ-RE, the Li-CE was extended by a free-standing graphite (FSG) electrode in contact with metallic lithium, which drastically lowers the impedance of the counter-electrode.[23] The coin cells with such a Li/FSG-CE ran through a multi-step cycling procedure, which includes an EIS measurement at a relative SOC of 65% within a DCIR-like cycle, analogous to that conducted with the full-cells (see Experimental section for more details). The results of the EIS analysis are illustrated in Fig. 2.

First, the feasibility of this approach was tested with a symmetrical cell of two Li/FSG electrodes, which was cycled similarly to the actual coin cells (by applying the same current densities and charging times). As shown in Fig. 2a, the imaginary part of the impedance of such a symmetrical Li/FSG cell is below ≈1 Ω cm^2 and the HFR-corrected real part of its impedance is below ≈5 Ω cm^2 (sum of both electrodes), consistent with the values reported in Ref. 23. As will be shown below, these impedances are very small compared to the HFR-corrected impedances of the coin cells composed of harvested NCM-811 cathodes and a Li/FSG-CE, so that the HFR-corrected impedance response of the latter closely corresponds to the impedance of the harvested NCM-811 electrodes.

Table II. Comparison of the mean voltage change of the NCM-811 cathode ($\bar{V}_{cath}$) during C/2 and C/10 cycling at either 22 °C over 1000 cycles or at 45 °C over 700 cycles. For charge and discharge, the slope from linear fits of the mean voltages presented in our previous publication[9] and in Fig. 1b is given in absolute values. Furthermore, the mean voltage change was calculated from R_{DCIR} in Fig. 1c according to $\frac{d\bar{V}_{cath}}{dcycle} = \frac{dR_{DCIR}}{dcycle}\Delta j$, with $\frac{dR_{DCIR}}{dcycle} = 267\ m\Omega\ cm^2/cycle$ and j = 0.7 mA cm^{-2} at C/2 and 0.14 mA cm^{-2} at C/10, respectively.

$\frac{d\bar{V}_{cath}}{dcycle}$ [mV/cycle]	Ambient temperature (22 °C) C/2 cycling	Elevated temperature (45 °C) C/2 cycling	Elevated temperature (45 °C) C/10 cycling
Charge	≈0.08	≈0.14	≈0.05
Discharge	≈0.12	≈0.35	≈0.11
Discharge/charge ratio	≈1.5	≈2.5	≈2.2
From R_{DCIR}	n.d.	≈0.19	≈0.04

More precisely, the contribution of the Li/FSG-CE to the overall impedance would even be lower since the symmetric Li/FSG cell impedance represents the impedance of two rather than one Li/FSG electrodes.

The spectra in Fig. 2 feature two semicircles: (i) a small semicircle at high frequencies (with a frequency maximum of $f_{max} \approx$ 2.2–5.4 kHz between 6 and 700 cycles), and (ii) another semicircle at low frequencies (with $f_{max} \approx$ 14.8-0.18 Hz between 6 and 700 cycles), whose diameter increases significantly upon cycling. As illustrated in our previous publications,[9,37] the underlying processes that are represented by each of the two R/Q elements in our impedance model (see caption of Fig. 2) can be deduced from an estimate of the associated double layer capacitance, which normalized to the proper interface should be on the order of 10 μF cm^{-2}.[24] Doing so, the high-frequency semicircle must correspond to the contact resistance between the cathode electrode coating and the current collector, since its capacitance when normalized to the geometric surface area of the current collector results in 2–4 μF/cm$^2_{geom}$. The low-frequency semicircle on the other hand is described by a transmission line model (TLM) that represents a complex convolution of the ion conduction in the electrolyte phase within the porous electrode (R_{ion}) and the charge-transfer resistance (R_{CT}). Its capacitance should thus reflect the double layer capacitance of the CAM and the conductive additives, consistent with the fact that the capacitance normalized by the BET surface area of the cycled cathode electrodes results in 10–25 μF/cm$^2_{BET}$. Here, the surface area of the cycled electrodes amounts to $A_{BET,elec} \approx$ 1.6–2.8 m^2/g$_{elec}$, as determined by Kr-BET (see Experimental section).

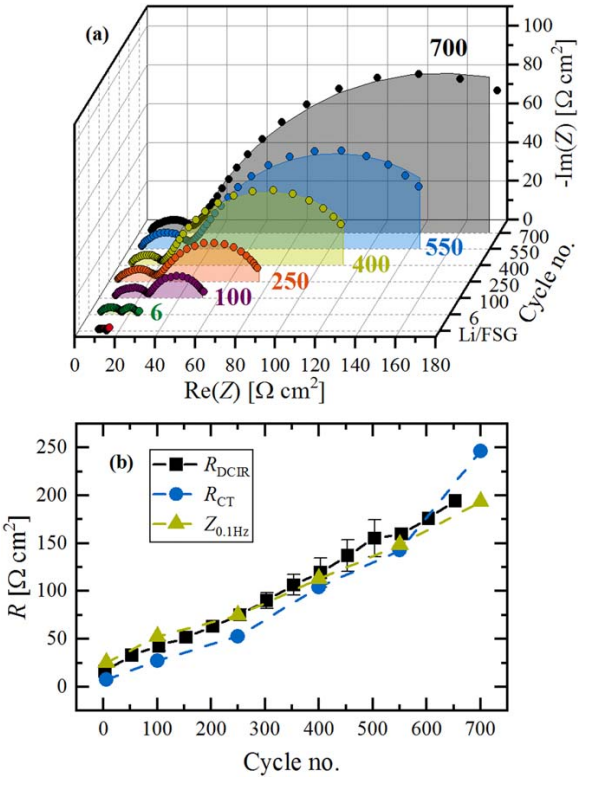

Figure 2. Ex situ EIS analysis of the harvested pouch cell cathodes, from which 14 mm diameter electrodes were punched out and re-assembled as working-electrode (WE) vs a Li/FSG-CE in a coin cell. (a) Impedance spectra were measured at the same conditions as the DCIR pulse in the full-cells (45 °C, 65% SOC, OCV ≈ 4.0 V). The data points (symbols) were fitted (lines) to: R_{HF} + TLM[R_{ion}, R_{CT}/Q_{CT}] + $R_{contact}/Q_{contact}$. The spectrum of a symmetrical Li/FSG cell, which underwent the same cycling procedure than the other coin cells prior to the EIS measurement, is also shown, demonstrating the negligible contribution of the Li/FSG-CE to the overall impedance beyond the high-frequency resistance. (b) Comparison of the averaged R_{DCIR} from Fig. 1c with the cathode charge-transfer resistance (R_{CT}) determined from the above fit of the EIS data and the low-frequency impedance at 0.1 Hz ($Z_{0.1Hz}$).

The contact resistance ($R_{contact}$) deduced from the high-frequency semicircle is in the range of ≈12–26 Ω cm^2. The observed small variation of this value might be caused by artifacts from the assembly of the coin cells with harvested cathodes. The α value of the corresponding constant phase element ($Q_{contact}$) is on the order of ≈0.7. The low-frequency semicircle was fitted by a transmission line model, consisting of R_{ion} and R_{CT}/Q_{CT}.[24] The values for R_{ion} are ≈0.75–1.5 Ω cm^2 for the samples up to 250 cycles. Afterwards, as the charge-transfer resistance becomes very large, the deconvolution of R_{ion} and R_{CT} becomes rather error-prone, resulting in fitted R_{ion} values of ≈10–20 Ω cm^2, which is likely incorrect. For cathode electrodes with ≈30% porosity, as used in this study, we do not expect that R_{ion} significantly increases over cycling. Thus, for the fitting of the impedance spectra where a reasonable value for R_{ion} could not be determined due to the dominance of R_{CT} (after 400–700 cycles), we used a fixed value of 1.5 Ω cm^2 for R_{ion}. The α value of Q_{CT} evolves gradually from 0.93 to 0.75. For these cycling data at 45 °C, R_{CT} increases from ≈7 Ω cm^2 after 6 cycles to ≈246 Ω cm^2 after 700 cycles. This is considerably higher than at 22 °C, where R_{CT} for the same CAM amounted to ≈100–150 Ω cm^2 after 1000 cycles,[9] which indicates the formation of a thicker resistive surface layer at elevated temperature.

In Fig. 2b, the R_{CT} values obtained from the fit of the EIS data of the harvested NCM-811 cathodes (see Fig. 2a) are compared to the averaged R_{DCIR} values of the six full-cells (data taken from Fig. 1c). Note that the DCIR pulse was conducted every 50 cycles at the beginning of the full-cell cycling loop, so that the last measurement was taken after 650 cycles, while the ex situ EIS measurements are taken up to 700 cycles. The charge-transfer resistance of the NCM-811 cathode fully describes the observed R_{DCIR} trend, with R_{CT} increasing in a similar fashion as R_{DCIR}. The observation that R_{CT} is consistently lower than R_{DCIR} is due to the fact that the latter also includes contributions from R_{HF}, $R_{contact}$, and R_{ion}. Therefore, a more rigorous comparison of the DCIR resistance with the EIS data would be to compare it with the EIS-derived low-frequency resistance, which corresponds to the magnitude of the impedance

Journal of The Electrochemical Society, 2021 **168** 050512

Table III. Rietveld refinement results of the NCM-811 CAM (pristine CAM powder, pristine electrode, as well as cycled and discharged electrodes). For the cycled electrodes, one of the two separately measured capillaries of the same electrode is exemplary given in the table (viz., the measurement with the lower Ni_{Li} value). The table summarizes quality factors (*R*-values), lattice parameters, and the therefrom determined Li content (according to Eq. 2 for the cycled electrodes), atomic site-specific information (including Li-Ni mixing, fractional z-coordinate of O, and atomic displacement parameters), and the fitted weight fraction of conductive graphite (nominally 2 wt%). Errors are given in parenthesis.

	Pristine powder	Pristine electrode	6	100	250	400	550	700
R_{wp} [%]	3.68	2.45	4.09	4.01	3.94	4.19	4.11	4.38
R_{bragg} [%]	0.906	0.648	0.898	0.989	1.06	1.30	1.12	1.55
χ^2	2.46	1.35	3.79	3.61	3.49	4.16	4.41	4.48
a [Å]	2.87214(1)	2.87246(1)	2.86888(2)	2.86873(2)	2.86738(2)	2.86690(2)	2.86606(2)	2.86693(2)
c [Å]	14.2081(1)	14.2080(1)	14.2409(1)	14.2516(1)	14.2622(2)	14.2712(2)	14.2735(2)	14.2756(2)
c/*a* [–]	4.94685(5)	4.94629(5)	4.96391(5)	4.96790(6)	4.97395(6)	4.97792(6)	4.98017(6)	4.97939(7)
x_{Li} [–]	1.01	1.01	0.915	0.898	0.875	0.861	0.852	0.855
Ni_{Li} [%]	1.98(7)	1.84(7)	1.71(8)	2.13(8)	2.54(8)	3.07(8)	2.75(8)	3.54(9)
$z_{6c,O}$ [–]	0.24113(5)	0.24092(5)	0.24029(6)	0.24016(6)	0.24011(6)	0.24000(7)	0.23993(6)	0.24006(7)
$b_{3a,Li}$ [Å^2]	0.73(5)	0.68(6)	0.76(8)	0.73(7)	0.80(8)	0.80(8)	0.85(8)	0.81(8)
$b_{3b,TM}$ [Å^2]	0.310(4)	0.473(5)	0.462(6)	0.482(6)	0.479(6)	0.432(7)	0.489(7)	0.445(7)
$b_{6c,O}$ [Å^2]	0.81(1)	0.97(2)	1.07(2)	1.12(2)	1.18(2)	1.23(2)	1.16(2)	1.25(2)
Graphite [wt%]	n.d.	1.9(1)	1.56(8)	1.44(8)	1.29(9)	1.47(9)	1.32(9)	1.30(9)

($|Z| = \sqrt{\mathrm{Re}(Z)^2 + \mathrm{Im}(Z)^2}$) at the nominal equivalent frequency than the DCIR pulse duration. For the here used 10 s DCIR pulse, this translates into 100 mHz, which is the lowest frequency measured during EIS analysis shown in Fig. 2a. Therefore, the magnitude of the impedance at 100 mHz ($Z_{0.1Hz}$) is compared with R_{DCIR} in Fig. 2b. R_{DCIR} and $Z_{0.1Hz}$ agree within ±10 Ω cm^2 throughout cycling, which is quite reasonable. For the first data points after 6 and 100 cycles, $Z_{0.1Hz}$ is slightly higher than R_{DCIR}, which most likely is due to the fact that the two more cycles at C/2 and C/10 that were applied to the harvested cathode electrodes prior to the ex situ EIS measurements might add some additional aging to the relatively fresh NCM-811 CAM.

Even though we believe that the here measured charge-transfer resistance predominantly originates from a reconstructed, spinel/rock-salt-type surface layer, which is caused by oxygen release and which grows from the CAM surface gradually into its interior, there is also the possibility that electrolyte decomposition products might form a resistive surface film, which is often referred to as cathode-electrolyte interphase (CEI).[11] This CEI-type surface film would grow on top of the CAM surface. The high-frequency semicircle obviously does not allow for discerning the occurrence of two different types of surface layers; however, we can try to evaluate the importance of the CEI on the basis of (i) the electrochemical stability of the electrolyte towards anodic oxidation and (ii) its chemical stability towards reactive lattice oxygen.[38] Regarding the first point, Metzger et al. have shown that EC-based electrolytes are oxidatively stable at potentials greater than 4.5 V vs Li^+/Li, even at an elevated temperature of 50 °C.[39] This is further supported by an LNMO study by Pritzl et al.,[18] where LNMO/graphite full-cells were cycled at 40 °C and with an LP57 electrolyte containing different concentrations of VC. LNMO is an ideal model electrode, because the spinel structure is inherently stable against oxygen release and the concomitant surface reconstruction.[33,38] At the same time, it operates at a high potential of ≈4.7 V vs Li^+/Li, which enables to study exclusively the influence of electrolyte oxidation on the cathode resistance. For the EC/EMC/$LiPF_6$ base electrolyte without VC, the cathode resistance remained constant over the duration of 100 cycles, i.e., we can exclude the formation of a resistive CEI-type surface layer. If VC was added in high concentrations, the cathode resistance however increased because VC gets already oxidized at ≈4.3 V vs Li^+/Li, so that an organic film of poly(VC) deposits on the LNMO surface. For this reason, VC was omitted in our NCM-811/graphite full-cells.

The oxygen release from the CAM surface is accompanied by the chemical degradation of the electrolyte.[40] In case of EC, the attack of singlet oxygen leads to the in situ formation of VC at an intermediate stage of the decomposition cascade. When NCM-622/graphite full-cells are cycled above the onset potential of oxygen release (until 4.6 V_{FC} at 25 °C), Teufl et al. reported a rapid rollover failure within ≈25 cycles using an EC-based electrolyte and a low $m_{electrolyte}/m_{CAM}$ ratio of ≈1.6/1.[41] The authors suggested that the cell resistance build-up that leads to this rollover failure is due to an increase of the cathode resistance, caused by the oxidation of VC at these high potentials. On the other hand, the capacity fading of very similar NCM-622/graphite cells with LP57 electrolyte (also cycled until 4.6 V_{FC} at 25 °C) is considerably less using a $m_{electrolyte}/m_{CAM}$ ratio of ≈8/1.[14] Here, the cells last for ≈300 cycles until they reach the same capacity drop than after the above rollover failure. In summary, we cannot entirely exclude the formation of a resistive CEI-type surface film also in our case, especially at the elevated temperature of 45 °C, where both the oxygen release and the electrolyte decomposition are increased compared to 25 °C operation.[14] However, the here used ≈0.2 V lower upper cut-off potential of 4.5 V vs Li^+/Li and the higher $m_{electrolyte}/m_{CAM}$ ratio of ≈13/1 probably counteract these effects. Furthermore, we think that such an organic surface film, if present, does not contribute to the observed capacity losses, because its share in R_{CT} is expected to be independent of the state of charge (and thus not larger than measured for the medium SOC of 65% in Fig. 2). On the other hand, R_{CT} significantly increases towards the lower and upper SOC limit at the cut-off voltages,[9] which is believed to be caused by the slowed Li diffusion within the reconstructed, spinel/rock-salt-type surface layer.[42]

Bulk stability and Li-Ni mixing analyzed via XPD.—The bulk stability of layered oxides typically refers to the level of cation mixing, where a transition-metal moves irreversibly from the native TM layer into the Li layer. Due to similar ionic radii of Li^+ and Ni^{2+}, Ni is mainly believed to be the moving TM,[4,43,44] but X-ray diffraction does not allow any distinction among the three TMs and Ni is just the most favorable representative in the investigated Ni-rich NCM-811. Refining the Li-Ni mixing as a paired anti-site defect of Ni_{Li} and Li_{TM} in the common $R\bar{3}m$ space group, we observed no systematic change in the extent of Li-Ni mixing between the pristine and EOT samples after 1000 cycles in our prior study with the same CAM at 22 °C.[9] We thus concluded that the freely refined Ni_{Li} stays constant at a level of ≈3%, which was recently supported by Xu et al. for NCM-811 also cycled at room temperature.[45] The Rietveld refinement results of the present study at 45 °C are summarized in Fig. 3 and Table III.

Figure 3a shows exemplarily the XPD pattern of the discharged cathode at EOT after 700 cycles and the corresponding Rietveld

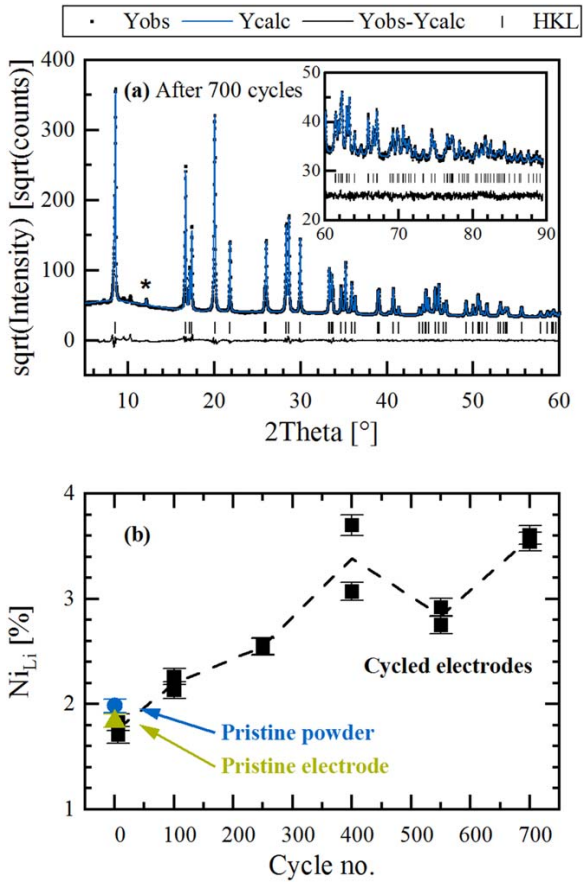

Figure 3. Determination of the Li-Ni mixing from ex situ XPD data of the harvested NCM-811 electrodes in the discharged state. (a) Rietveld refinement of the EOT NCM-811 CAM after 700 cycles. The data were collected at our in-house Mo-diffractometer ($\lambda = 0.7093$ Å) in the 2θ range of 5°–90°. The observed (black points), calculated (blue line), and difference diffraction profile (black line) are shown together with the position of the Bragg peaks of NCM-811 (black ticks). The asterisk at ≈12° indicates the strongest (002) reflection of conductive graphite, which was also included into the refinement. The inset shows the high-angular range from 60° to 90°. To visualize the increasingly smaller reflections at higher 2θ, the intensity is displayed on a square root scale on the y-axis. (b) Evolution of the Li-Ni mixing, labeled as Ni_{Li}, over the course of 700 cycles. The cycled electrodes were measured twice in two separate capillaries and are further compared with the pristine CAM powder and the pristine electrode (both heated at 120 °C prior to loading the material into the capillaries). The dashed black line shows the average trend of the cycled electrodes.

refinement fit. Apart from 2 wt% conductive graphite in the electrode formulation, whose most intense peak is highlighted by an asterisk, there is no crystallographic side phase visible in the pattern. Regarding the NCM-811 material, its layered structure is well preserved and the applied model satisfactorily describes the bulk material, as can be also seen from the fairly constant *R*-values in Table III. Other structural parameters such as the atomic displacement parameters scatter in a sufficiently narrow range, which gives further confidence about the validity of the refined Ni_{Li} values (see Fig. 3b).

Ni_{Li} was determined from two separate capillaries of the same harvested cathodes, together with the pristine CAM powder and the pristine electrode. The deviation between the duplicate measurements amounts to less than 0.2%, which is close to the estimated standard uncertainty from the Rietveld fit of ≈0.1%. Only the XPD data from the cathode harvested after 400 cycles differ in this respect with a deviation of ≈0.6%. Starting with the pristine CAM, its Li-Ni mixing of ≈1.8%–2.0% turns out to be lower than the ≈3.1% reported in our previous study, despite using the identical NCM-811 sample and the same electrode sheets that had been stored under inert conditions in an argon-filled glove box. In comparison to the former study, we extended the 2θ range from 60° to 90°, but this does not alter the refinement outcome (within the margin of uncertainty); it only slightly reduces the extent of correlations for the sensitive Ni_{Li} parameter (≈70% to the scale factor and to $b_{3a,Li}$). Unfortunately, we cannot provide a solid explanation for this discrepancy. We speculate that the replacement of the Mo-source and the following re-adjustment of the diffractometer might have caused this difference in the refinement-based value of Ni_{Li}. To avoid any artefacts which might be caused by instrumental variations, we consequently tried to measure the samples in this study under fairly constant conditions within a short period of time. Yin et al. investigated 17 pristine NCM samples by high-resolution X-ray and neutron powder diffraction and they established a linear correlation between the Ni_{Li} amount and the Ni content of the NCM (more specifically, between % Ni_{Li} and Ni^{2+}).[46] For NCM-811, this correlation projects a Ni_{Li} amount of 3.4 ± 0.5%, which would match the value reported in our earlier study.[9] However, as discussed by the authors, the Li-Ni mixing further depends on the calcination temperature and the activation energy of defect formation (on the order of 200–300 meV), so the here reported value of ≈1.8%–2.0% is not unreasonable.

Analyzing the cycled NCM-811 electrodes with regards to Ni_{Li}, we find that for the cathode harvested after only 6 cycles, the extent of Li-Ni mixing agrees with that of the pristine CAM powder and the pristine electrode (see Fig. 3b). After increasingly more cycles, the Li-Ni mixing rises by ≈1%–2% until the end-of-test (700 cycles), depending on how one interprets the scatter of the Ni_{Li} values between 400, 550, and 700 cycles. At this point, we want to discuss shortly some aspects of the structural model: $[Li_{x-v}Ni_v]_{3a}[Li_vNi_{0.79-v}Co_{0.10}Mn_{0.10}]_{3b}[O]_{6c}$ (see also Experimental section). Here, x_{Li} was deduced from the *c*/*a* lattice parameter ratio according to Eq. 2, whereby x_{Li} of the discharged cathodes decreases upon cycling (see Table III). If x_{Li} would have been fixed to the pristine value of 1.01 for all samples (e.g., in default of a proper method to determine x_{Li} of cycled samples), the fitted value of Ni_{Li}, e.g., at EOT (700 cycles) would be reduced from ≈3.6% to ≈2.4% (so that one might mistakenly conclude there is hardly any change in comparison to ≈1.8%–2.0% of the pristine NCM-811). This is due to the fact that the required electron density of the Li layer would mainly be compensated by Li itself, so that there would be no need in the refinement routine to place additional Ni there. Alternatively, refining the Li-Ni mixing not as a paired anti-site defect of Ni_{Li} and Li_{TM}, but purely as Ni_{Li} (i.e., $v_{Li} = 0$), has not such a big impact: the absolute amount of Ni_{Li} would shift to lower values by a maximum of only ≈0.3% after 700 cycles (because the remaining Li again partially provides the required electron density of the Li layer). It is thus very important to report all relevant aspects of the refinement, including a clear description what x_{Li} value was used for a given fit), in order to enable a comparison of the structural data reported in different publications.

Even though the absolute values of Ni_{Li} have to be treated with caution, we are quite confident that the observed trend of an increasing Li-Ni mixing by ≈1%–2% while cycling NCM-811 for 700 cycles at 45 °C between cathode potentials of 3.0–4.5 V is correct. The trickier question, however, addresses the impact of an increasing extent of Li-Ni mixing on the electrochemical performance of the NCM-811 CAM. How would it affect the cathode resistance and finally the achievable capacity? Makimura et al. synthesized a series of $[Li_{1-y}Ni_y][Ni,Co,Al]O_2$ samples ($0 \leqslant y \leqslant 0.13$) and they found a perfectly linear correlation between the capacity (*C*) and *y* for C/10 cycling at 20 °C between cathode potentials of 2.5 and 4.2 V, namely C [mAh g^{-1}] = 181.4 – 725.5·*y*.[47] When normalized to the highest capacity for $y = 0$ (C_0), this

Journal of The Electrochemical Society, 2021 **168** 050512

equates to C/C_0 [%] = 100 – 400·y, so that the observed capacity loss is four times higher than the loss that would be simply expected by the blocking of free Li sites by inactive Ni. The authors confirmed a strong polarization effect originating from slowed Li diffusion kinetics. This generalized $C/C_0 = f(y)$ correlation can be used to estimate the impact of a maximum of 2% increase in Ni_{Li} over 700 cycles (see Fig. 3b) on the capacity, since y equals approximately ν_{Ni} in the structural model of NCM-811 (please note that $Ni_{Li} = \nu_{Ni} \cdot 100\%$). For a maximum increase of Ni_{Li} by 2% from BOT to EOT, the capacity fading predicted by the above relationship observed by Makimura et al. would amount to 8% or ≈18 mAh g^{-1} (based on an initial capacity of ≈221 mAh g^{-1} at C/10, see Fig. 1a). This is ≈45% of the overall capacity loss of ≈40 mAh g^{-1} at C/10 (same C-rate as applied by Makimura et al.[47]). It is difficult to make any statement about the Li diffusion kinetics of NCM-811. The cathode mean charge voltage could be fully explained by the increase of R_{DCIR} at ≈4.0 V (see Table II), which in turn is a direct measure of R_{CT} (see Fig. 2), but $\tilde{D}_{Li}$ might potentially have an impact on the more pronounced change of the cathode mean discharge voltage. In this context, Makimura et al. observed a higher polarization during discharge than during charge with increasing y, but at the same time the capacity was more limited in the charge than discharge endpoint (ratio of ≈2/1).[47] In summary, the cycling-induced increase of the Li-Ni mixing by ≈1%–2% over 700 cycles might appear negligible, but its contribution to the capacity fading due to the slowed Li diffusion kinetics in the bulk phase could indeed be relevant. Since the correlation reported for NCA samples by Makimura et al. might not be fully applicable to our NCM-811 CAM, however, the precise quantification of the capacity loss caused by increasing Li–Ni mixing remains elusive.

Finally, we want to look at a recent study of Li et al., where NCM-811 was cycled for 1000 cycles at 25 °C to different upper cut-off voltages in NCM-811/graphite full-cells.[44] For cycling until 4.2 and 4.4 V_{FC}, which translates into ≈4.3 and ≈4.5 V vs Li^+/Li, the authors report the Li-Ni mixing to increase vastly by 6.7% and 11.9%, respectively. Unfortunately, their structural model is barely described in the publication, which makes it difficult to compare their results to ours. According to the $C/C_0 = f(y)$ correlation by Makimura et al.,[47] the Li-Ni mixing has to account completely (and beyond) for the observed capacity fading (78% and 52% capacity retention). This refinement result seems to be quite unlikely, because Li et al. also identified other important degradation mechanisms such as TM dissolution and deposition on the anode, surface NiO formation, and particle cracking.[44]

Lithium content via XPD analysis.—The above evaluation of the XPD data from the cathodes harvested in the discharged state already indicated a steady decrease of the lithium content of the discharged NCM-811 CAM upon cycling (see x_{Li} in Table III). This behavior can be easily rationalized by the increasing overpotential (e.g., reflected by the changes in the mean charge/discharge cathode voltage, see Fig. 1b), which narrows the accessible SOC window from both sides in the completely discharged and charged states when cycling the NCM-811 electrode in the fixed cathode voltage window of 3.0–4.5 V. In our study conducted at 22 °C,[9] the x_{Li} data from in situ XPD were the centerpiece to deconvolute the capacity loss into its contributions originating from the increase of R_{CT} related overpotentials and from a loss of cyclable cathode active material. This analysis shall also be applied here based on ex situ XPD data. Since the full-cells were stopped during C/2 cycling after running into the lower cut-off voltage, XPD data in the discharged state of the harvested NCM-811 cathodes could be acquired immediately. For XPD analysis in the charged state, we punched out smaller electrodes, which were cycled in half-cells at C/2 for 1.5 more cycles and which were then disassembled after running into the upper cut-off cathode voltage of 4.5 V. The *c*/*a* lattice parameter ratio from the diffractograms and the thereof determined lithium content are summarized in Fig. 4.

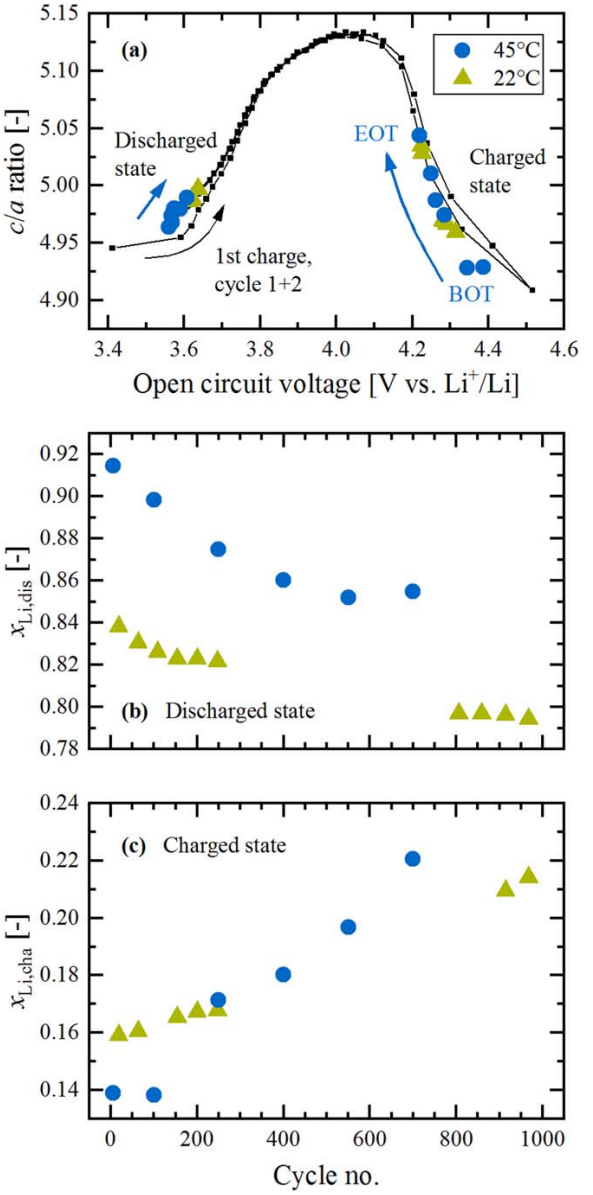

Figure 4. Determination of the lithium content in the discharged and charged state of NCM-811 electrodes operated between cathode potentials of 3.0–4.5 V at C/2 and different cycling temperatures. (a) Evolution of the underlying c/a lattice parameter ratio vs OCV and comparison to the c/a curve of a fresh NCM-811 cathode in cycle 1 and 2 (black squares/lines). The cycle 1 + 2 curve and the in situ XPD data for cycling at 22 °C (green triangles) were taken from our previous publication (see curves labeled "Cycle 1 + 2" and "LDE, cell 1" in Fig. 6a of Friedrich et al.,[9] published by ECS, licensed as CC BY 4.0). The ex situ XPD data at 45 °C (blue circles) originate directly from the harvested full-cell electrodes (discharged state) or from harvested electrodes that were subjected to another 1.5 half-cell cycles (charged state) and are shown vs the final OCV value at 25 °C (see Experimental section). The c/a data points are converted into the lithium content: (b) in the discharged state via Eq. 2, referred to as $x_{Li,dis}$; (c) in the charged state via Eq. 3, referred to as $x_{Li,cha}$. At 45 °C, the BOT value of $x_{Li,dis} \approx 0.915$ slightly exceeds the margin of the c/a calibration curve, but additional ex situ points of fresh NCM-811 cathodes showed that Eq. 2 holds true until ≈0.95.

The $x_{Li} = f(c/a)$ calibration curves were measured within the first cycles of a fresh NCM-811 cathode,[9] where the lithium content (x_{Li}) can be deduced fairly accurately from the exchanged capacity (assuming purely faradaic currents from lithium de-/intercalation into the CAM). This approximation is not true anymore during prolonged cycling, due to the charge accumulation caused by tiny parasitic currents. Consequently, it is difficult to prove if the initially determined calibration curves and the extracted x_{Li} values are still valid, because there is no direct measure of the CAM's state of charge. On the other side, we continuously tracked the open circuit voltage (at 45 °C and finally also at 25 °C), and the c/a ratio is shown as a function of the OCV at 25 °C in Fig. 4a. Here, the c/a data from 45 °C cycling (blue circles in Fig. 4a) are contrasted with the data from 22 °C cycling (green triangles) and with the full $c/a = f(OCV)$ curve of a fresh NCM-811 cathode (black squares/lines). Note that the OCV values are known for every measurement, i.e., all datasets can be compared with each other without any correction. We see that, independent of the cycling temperature, the c/a data in the completely discharged and charged state coincide nicely with the initial calibration curve. The c/a values increase with cycling in both the discharged and charged state, indicating a shrinking OCV window. Since the $c/a = f(OCV)$ correlation is maintained upon cycling and since the OCV is an indirect measure of the absolute SOC (i.e., the SOC referenced to x_{Li}), we can continue to convert the c/a ratio into the lithium content. This is done by applying Eq. 2 for the discharged state (see $x_{Li,dis}$ in Fig. 4b) and by applying Eq. 3 for the charged state (see $x_{Li,cha}$ in Fig. 4c), respectively. For a more detailed explanation of this procedure see the Experimental section and Friedrich et al.[9]

Let us first look at the BOT values, where the 45 °C capacity is ≈24 mAh g^{-1} higher than at 22 °C (see Table I). This capacity gain predominantly occurs in the discharged state, because $x_{Li,dis}$ is higher by ≈0.08 in the discharged state (see Fig. 4b), while $x_{Li,cha}$ is only lower by ≈0.02 in the charged state (see Fig. 4c), corresponding to a ratio in Δx_{Li} of ≈4/1. Based on dQ/dV plots, Li et al. also reported that the low-SOC capacity (i.e., towards the discharged state) of NCA depends strongly on temperature (and mildly on C-rate), but the high-SOC limit (i.e., towards the charged state) is hardly affected by neither temperature nor C-rate.[13] They explain this behavior by the kinetic hindrance from solid-state lithium diffusion, which hampers the lithium intercalation back into the layered oxide during discharge. In the following, $x_{Li,dis}$ continuously decreases while $x_{Li,cha}$ increases with cycling, as already anticipated from the $c/a = f(OCV)$ raw data (see Fig. 4a). The changes are quite uniform, except for the $x_{Li,cha}$ value after 100 cycles at 45 °C that remains at the value of ≈0.14 obtained after 6 cycles (see Fig. 4c). Furthermore, $x_{Li,dis}$ does not continue to decrease anymore between 550 and 700 cycles (see Fig. 4b). Comparing the changes in x_{Li} from BOT to EOT between both temperatures, $\Delta x_{Li,dis}$ and $\Delta x_{Li,cha}$ are by a factor of ≈1.4–1.5 higher after 700 cycles at 45 °C compared to 1000 cycles at 22 °C ($|\Delta x_{Li,dis}|$: ≈0.044 at 22 °C vs ≈0.060 at 45 °C; $\Delta x_{Li,cha}$: ≈0.055 at 22 °C vs ≈0.081 at 45 °C). This result is in line with the more strongly increasing overpotential at the higher temperature, as outlined in the previous paragraphs. However, it is difficult to relate the Δx_{Li} differences quantitatively to the mean cathode voltages (Fig. 1b) or to the R_{DCIR}/R_{CT} evolution (Fig. 2b), because only the resistances in the low- and high-SOC region towards the voltage cut-offs matter for the overpotential-induced capacity loss (but these resistances are not directly addressed by the former measures).

In light of the results from Figs. 3 and 4, we want to emphasize that the aged NCM-811 CAM could be always refined as a single phase based on the Rietveld refinement of the ex situ XPD data. This is in contrast to some operando studies about Ni-rich NCMs and NCAs (with 80%–85%$_{Ni}$), which detected the emergence of two to three simultaneously present layered phases over the course of long-term cycling, especially in the charged (delithiated) state.[15,45,48,49] Xu et al. observed a so-called "fatigued" phase of NCM-811 (together with an "active" and "intermediate" phase), whose upper SOC limit was fixed at approximately 75% (corresponding to $x_{Li,cha} \approx 0.25$).[45] They assign this threshold to the increasing interfacial lattice strain between the reconstructed rock-salt surface layer (caused by lattice oxygen release at high SOCs) and the bulk layered structure beyond ≈75% SOC. The segregation into several phases might however disappear in the charged state when the CAM is held long enough under constant voltage[15] or open circuit voltage.[49] Despite forming a reconstructed surface layer, we could operate NCM-811 continuously to $x_{Li,cha}$ values below 0.25 (see Fig. 4c) without any evidence for an additional "fatigued" layered phase in the XPD data, contrary to the up to ≈70% observed by Xu et al.[45] This is perhaps due to the observation that such a fatigued phase may only occur upon extensive particle cracking, in which case Schweidler et al. observed the occurrence of a fatigued phase that nevertheless could be fully accessed at very low currents.[15]

Capacity loss analysis.—With the XPD-derived x_{Li} data, we can now proceed to perform the capacity loss analysis. Here, the material loss is probably the most interesting parameter, which quantifies the fraction of the electrochemically active CAM lost and/or converted into an electrochemically inactive phase upon cycling. In the former 22 °C study, the material loss could be explained by the formation of a resistive, oxygen-deficient surface layer around the primary particles, and this loss of electrochemically active material was calculated in percentage terms relative to the pristine CAM as follows:[9]

$$\Delta C^{i}_{Material,rel} = \frac{C^{i}_{XPD} - C^{i}_{EC}}{C^{i}_{XPD}} \quad [5]$$

where C^{i}_{EC} (in mAh g^{-1}) is the electrochemically measured discharge capacity in the ith cycle and C^{i}_{XPD} (also in mAh g^{-1}) is the theoretically expected capacity inferred from XPD:

$$C^{i}_{XPD} = (x^{i}_{Li,dis} - x^{i}_{Li,cha}) \cdot \frac{274\ \text{mAh g}^{-1}}{1.01} \quad [6]$$

C^{i}_{XPD} is applied to the whole CAM and thus assumes no material to be lost while aging, but it considers the narrowed SOC window during C/2 cycling due to the actually present overpotential in the ith cycle. Thus, the difference between C^{i}_{XPD} and C^{i}_{EC} represents the loss of electrochemically active material in the ith cycle (in mAh g^{-1}); if this difference is normalized by C^{i}_{XPD}, it reflects the relative loss of electrochemically active material. Please note that 274 mAh g^{-1} correspond to the theoretical capacity for complete lithium extraction of 1.01 from the pristine CAM (see Experimental section).

Even though providing quantitative insights into CAM degradation, we admit that the XPD analysis is not really practical to be applied on a routine basis, since it requires a precise $x_{Li} = f(c/a)$ calibration curve for every CAM and that the bulk of the CAM stays fairly unaltered under the testing conditions (e.g., extensive Li-Ni mixing[44] or lattice dislocations[50] could potentially modify the $x_{Li} = f(c/a)$ relationship). These drawbacks call for alternative methods. Relying solely on electrochemical data, Dahn's group developed a differential voltage analysis software (which also requires that the bulk of the CAM does not change upon cycling).[51] Here, dV/dQ vs Q curves of the cycled full-cell are compared to reference half-cells from anode and cathode. They are matched with each other by adjusting two parameters for each electrode: the electrochemically active mass of the electrodes and their capacity slippage. Other diagnostic and prognostic tools use a similar set of parameters to model battery aging from experimental data.[52,53] The loss of electrochemically active material can then be calculated from the decrease of the cathode mass.

In our previous publication, we also tried to estimate the material loss by applying a C-rate test and comparing the electrochemical

Journal of The Electrochemical Society, 2021 **168** 050512

capacity in the ith cycle (C^{i}_{EC}) to an adequate reference state (C^{0}_{EC}):

$$\Delta C^{i}_{Material,rel} = \frac{C^{0}_{EC} - C^{i}_{EC}}{C^{0}_{EC}} \quad [7]$$

There are two important requirements to be fulfilled by the reference state: (i) it must not yet have experienced an electrochemically active material loss, which limits the reference state to the initial cycles; and, (ii) the overpotential must be negligible, which demands that C^{0}_{EC} and C^{i}_{EC} are measured at a very slow C-rate. Under these conditions, any reversible capacity loss can be compensated for and only the irreversible loss of electrochemically active material remains. In our previous work with the same NCM-811 CAM, it turned out that a C-rate of C/50 was sufficiently slow to minimize the impact of overpotentials on the attained capacity.[9] C/50 cycling at 45 °C between cathode potentials of 3.0–4.5 V delivers a discharge capacity of $C^{0}_{EC} = 228 \pm 1$ mAh g^{-1} within the first two cycles of a pristine NCM-811 cathode (which is quite close to the 221 ± 1 mAh g^{-1} obtained a C/10, see Fig. 1a). Electrodes that were punched out from the cathodes harvested from the cycled pouch cells were also subjected to two C/50 cycles (following EIS at C/10, see Experimental section). The cathode mean discharge voltage of the cycled electrodes agrees within less than 35 mV (lower) with that of the pristine cathode, even though the mean discharge voltage after 700 cycles has decreased by ≈80 mV at C/10 and ≈250 mV at C/2 (see Fig. 1b). This implies that the resistance increase over cycling does not result in any significant overpotential at this very low C-rate of C/50, i.e., the above requirements for this analysis are satisfied.

Figure 5 compares the relative material loss of the electrodes cycled at 45 °C and calculated by this EC method (black squares, acc. to Eq. 7) to that calculated by the XPD analysis (acc. to Eq. 5) for the electrodes cycled at 45 °C (blue circles) and those cycled at 22 °C in our previous study (green triangles). Focusing first on the electrodes cycled at 45 °C, Fig. 5 shows that the electrochemically active material loss obtained by the EC vs the XPD method, both independent datasets, match extremely well within ±1 percentage points. The only exception is the EOT sample after 700 cycles, where the XPD-derived material loss (≈18.2%) exceeds that obtained from the EC method (≈15.6%) by ≈2.6 percentage points. This difference could potentially be explained by a slightly too high $x_{Li,dis}$ value (see Fig. 4b), which in turn would increase C^{i}_{XPD} and thus the XPD-based $\Delta C^{i}_{Material,rel}$ value (see Eqs. 5 and 6).

For the electrodes cycled at 22 °C, most of the electrochemically active material get lost within the first 200–300 cycles, then leveling off and reaching ≈8.5% after 1000 cycles. For the electrodes cycled at 45 °C, the progress of the material loss shows a similar trend in the beginning, but contrary to the 22 °C data, it does not diminish until 700 cycles. Even though the trend is not exactly clear, either possessing a sharp rise from 550 to 700 cycles (as indicated by the XPD method) or a more uniform increase (as suggested by the EC method), the EOT value after 700 cycles at 45 °C amounts to ≈15.6%–18.2% and is thus twice as big than after 1000 cycles at 22 °C. Using the d*V*/d*Q* analysis software,[51] Li et al. tracked the CAM loss of their NCA/graphite full-cells cycled at 40 °C.[13] For the upper cut-off voltage of 4.3 V_{FC} (corresponding to ≈4.4 V vs Li^{+}/Li), the calculated CAM loss amounts to 4.3 ± 0.5% and 10.1 ± 0.5% after 400 and 800 cycles, respectively. While these losses for NCA are ≈2-fold lower than those in this study for NCM-811, this may not only be due to the different active materials but also due to the here used ≈0.1 V higher upper cathode potential and the 5 °C higher temperature. In an earlier publication from the Dahn group, they reported ≈8% of lost NCM-811 after only 83 cycles under very similar conditions (again 40 °C and 4.3 V_{FC}),[54] which seems quite large compared to our data. All these datasets point towards the influence of the cycling conditions (e.g., temperature, upper cut-off voltage, and depth of discharge) and the nature of the CAM (e.g., NCM vs NCA) on the extent of material loss, so that a quantitative comparison with other work in the literature is typically not possible.

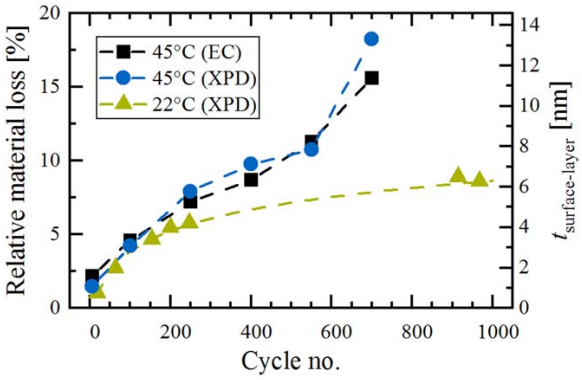

Figure 5. Determination of the NCM-811 material loss ($\Delta C^{i}_{Material,rel}$) upon extended cycling at 45 °C between cathode potentials of 3.0–4.5 V, either determined from slow C/50 cycling of the harvested cathodes (EC method using Eq. 7; black squares), or from our XPD analysis (using Eqs. 5 and 6; blue circles). The XPD data at 22 °C (green triangles) were taken from our previous publication (see data labeled "Cell 1" in Fig. 5c of Friedrich et al.,[9] published by ECS, licensed as CC BY 4.0). The material loss in percentage terms is converted into the thickness of a resistive, O-depleted surface layer on the right. Here, we assumed spherical primary particles, whose average diameter of ≈410 nm was estimated from the BET surface area of a charged electrode (≈3.1 m^2/g_{CAM}, see later discussion); for details of this calculation see the supporting information of Ref. 9.

But what causes the temperature dependence in this work? The more pronounced material loss at elevated temperature suggests a thicker reconstructed, oxygen-depleted surface layer. However, the upper SOC limit is almost not affected by the temperature rise, as was already seen for the BOT values of $x_{Li,cha}$ at C/2 (see Fig. 4c) as well as for the C/10 formation cycles (absolute SOC values of ≈85% vs ≈86%). Since the oxygen release that leads to the surface transformation predominantly depends on the maximum SOC (i.e., the extent of delithiation),[32,33] one would expect a similar driving force for oxygen release for the cycling conditions at both temperatures. On the other hand, the kinetics of the surface reconstruction would be expected to be faster (e.g., for oxygen transport and TM rearrangement), by which the O-depleted, spinel/rock-salt-like layer would be able to penetrate deeper into the primary particles. The temperature dependence of the initial oxygen release was studied by Jung et al. for an NCM-622 CAM.[14] Taking the sum of evolved O_2, CO, and CO_2 within the first four cycles until 4.8 V_{FC}, the gassing caused by oxygen release increased by a factor of ≈1.5 and ≈1.9 when increasing the temperature from 25 °C to 40 °C or to 50 °C, respectively. In our case, the NCM-811 CAM operates for most of the time above the SOC threshold for oxygen release at ≈80%, corresponding to an $x_{Li,cha}$ value of ≈0.20 at the upper cut-off potential. As shown in Fig. 4c, $x_{Li,cha}$ remains below 0.20 for the first ≈750 cycles during 22 °C operation (interpolated from a linear fit through the existing data) and for ≈550 cycles during 45 °C operation. Consequently, the oxygen release could proceed almost unlimited; however, Jung et al. further showed that the oxygen release diminishes from cycle to cycle.[14] At 40 °C, e.g., the gassing of the NCM-622 CAM in cycle 2–4 reduced by a factor of ≈2.2, ≈3.7, and ≈4.0 compared to the first cycle. Even though we cannot finally say for how long oxygen is released from the CAM surface, we want to emphasize that the here quantified fraction of lost CAM does not directly correspond to the accumulated amount of evolved lattice oxygen until the respective cycle number. The transformation of the electrochemically active, layered structure into an electrochemically inactive, resistive surface layer is assumed to be a two-step process.[9] After the initial oxygen release, the

Journal of The Electrochemical Society, 2021 168 050512

Table IV. Deconvolution of the electrochemically measured capacity loss from BOT to EOT ($\Delta C_{EC}^{BOT\rightarrow EOT}$) into its contributions originating from the loss of cyclable CAM ($\Delta C_{Material}^{BOT\rightarrow EOT}$) and the overpotential-induced loss ($\Delta C_{Overpotential}^{BOT\rightarrow EOT}$). $\Delta C_{Overpotential}^{BOT\rightarrow EOT}$ can be further divided into capacity losses in the discharged ($\Delta C_{Discharge}^{BOT\rightarrow EOT}$) and charged state ($\Delta C_{Charge}^{BOT\rightarrow EOT}$), respectively. The underlying equations of the XPD analysis are provided in the Appendix and the values at ambient temperature stem from our previous publication of the same material.[9] The sum of $\Delta C_{Material}^{BOT\rightarrow EOT}$ and $\Delta C_{Overpotential}^{BOT\rightarrow EOT}$ exceeds $\Delta C_{EC}^{BOT\rightarrow EOT}$ due to rounding errors and due to the fact that some material loss was already acquired until BOT.

C/2 capacity loss [mAh g^{-1}]	Equation	Ambient temperature (22 °C)	Elevated temperature (45 °C)
BOT → EOT		Cycle 18 → 1000	Cycle 6 → 700
$\Delta C_{EC}^{BOT\rightarrow EOT}$	(A·1)	≈38	≈68
$\Delta C_{Material}^{BOT\rightarrow EOT}$	(A·2)	≈16	≈40
$\Delta C_{Overpotential}^{BOT\rightarrow EOT}$	(A·3)	≈25	≈31
- $\Delta C_{Discharge}^{BOT\rightarrow EOT}$	(A·4)	≈11	≈13
- $\Delta C_{Charge}^{BOT\rightarrow EOT}$	(A·5)	≈14	≈18

transition-metals in the then O-depleted structure have to rearrange to form a spinel/rock-salt-type surface layer, which is incapable of reversibly de-/intercalating a significant amount of lithium-ions. While both steps run basically in parallel during the thermal decomposition of charged NCM/NCA CAMs,[5,55] the TM rearrangement is expected to be retarded during electrochemical cycling. For Li-rich NCMs at 25 °C, HR-TEM images have shown that the actual reconstruction happens within 20–50 cycles.[56] As vacancies in the TM layer probably facilitate the rearrangement in Li-rich NCMs, it is reasonable to assume that this process takes longer for regular NCMs (here >100 cycles).

Using the set of XPD-based equations introduced in our former study,[9] which are shortly summarized in the Appendix of this work, Table IV deconvolutes the BOT-to-EOT capacity losses measured at 22 °C and 45 °C. Here, the electrochemically measured capacity losses at C/2 ($\Delta C_{EC}^{BOT\rightarrow EOT}$, see Eq. A·1) amount to ≈38 mAh g^{-1} for cycling at 22 °C (cycles 18 to 1000) and to ≈68 mAh g^{-1} for cycling at 45 °C (cycles 6 to 700; see also Table I). As already anticipated by the relative material losses in Fig. 5, this difference of ≈30 mAh g^{-1} is largely dominated by the extent of surface reconstruction at ambient vs elevated temperature, which translates into absolute capacity losses ($\Delta C_{Material}^{BOT\rightarrow EOT}$, see Eq. A·2) of ≈16 mAh g^{-1} for cycling at 22 °C and ≈40 mAh g^{-1} for cycling at 45 °C, respectively. This is a ≈2.5-fold increase caused by the enhanced loss of cyclable NCM-811 CAM when increasing the cycling temperature. On the other hand, the overpotential-induced capacity loss ($\Delta C_{Overpotential}^{BOT\rightarrow EOT}$, see Eq. A·3) increases only by factor of ≈1.2 (from ≈25 mAh g^{-1} at 22 °C to ≈31 mAh g^{-1} at 45 °C), which is composed of contributions from the discharged state ($\Delta C_{Discharge}^{BOT\rightarrow EOT}$, see Eq. A·4) and from the charged state ($\Delta C_{Charge}^{BOT\rightarrow EOT}$, see A·5). At the first glance, this moderate rise of the overpotential-related losses is less than that projected from the underlying x_{Li} data: $\Delta x_{Li,dis}^{BOT\rightarrow EOT}$ (see Fig. 4b) and $\Delta x_{Li,cha}^{BOT\rightarrow EOT}$ (see Fig. 4c) increase by a factor of ≈1.4–1.5 when increasing the cycling temperature from 22 to 45 °C. This discrepancy is due to the fact that $\Delta C_{Overpotential}^{BOT\rightarrow EOT}$ (and its individual components in the discharged and charged state) have to be corrected by the phase fraction of lost NCM-811 CAM, because only the cyclable CAM can experience a capacity loss due to an increasing overpotential. Consequently, as the relative material loss is doubled after 700 cycles at 45 °C compared to 1000 cycles at 22 °C (see Fig. 5), the overpotential-induced capacity losses in units of mAh g^{-1} turn out to be smaller than the shrinkage of the accessible Δx_{Li} window of the retained NCM-811 CAM.

Cracking and surface layer thickness.—Finally, we want to estimate the thickness of the reconstructed surface layer formed over extended cycling. This question requires to determine the surface area of the CAM, which will change upon cycling due to particle cracking.[9,25] Figure 6 shows the evolution of the specific NCM-811 surface area of the cycled electrodes harvested in the discharged state (black data points), as determined by Kr-BET measurements. Here, the contribution of the NCM-811 CAM was calculated according to Eq. 4 by subtracting the share of the electrode additives (2 wt% SFG6L graphite, 1 wt% C65 carbon black, and 3 wt% PVDF binder) in the composite cathode. Their surface area was determined from additives-only electrodes, consisting only of the inert components with the same weight ratio as in the actual cathodes, yielding $A_{BET,add}$ = 5.10 m^2/g_{add} for fresh and 5.56 m^2/g_{add} for cycled additives-only electrodes (see Experimental section). This approach assumes that the binder does not significantly alter the accessible surface area of the CAM in the cathode electrodes, even though the binder was found to reduce the surface area of the conductive agents by a factor of ≈3 in the additives-only electrodes (see Experimental section). To prove this assumption, we can compare the surface area of the pristine NCM-811 CAM in its form as pure powder of 0.28 m^2/g_{CAM} (blue line in Fig. 6) with that obtained for the CAM in the fresh cathode electrode of 0.30 ± 0.02 m^2/g_{CAM} (determined from the electrode specific surface area of $A_{BET,elec}$ = 0.58 ± 0.01 m^2/g_{elec} by subtracting the weight-fraction-normalized value of $A_{BET,add}$ acc. to Eq. 4; average from two measurements). Since the CAM specific

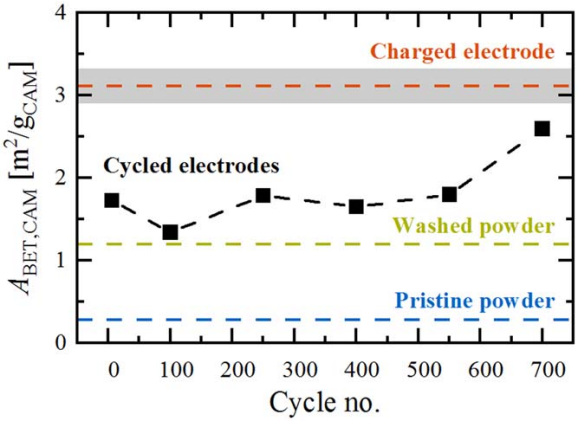

Figure 6. Evolution of the NCM-811 surface area ($A_{BET,CAM}$) during long-term cycling at 45 °C. The cycled electrodes (black data points) were measured in the discharged state by Kr-BET (following the rate test and washing steps with aprotic solvents; see Experimental section), whereby the surface area contribution of the CAM was calculated according to Eq. 4. In order to provide some reference points (depicted as horizontal lines), the $A_{BET,CAM}$ values of the cycled electrodes are compared to those of the pristine NCM-811 powder (blue line), of washed NCM-811 powder (either in water or HF-containing electrolyte; green line), and of a charged electrode (after a first charge at C/10 to a cathode potential of 4.5 V at 45 °C; red line).

Journal of The Electrochemical Society, 2021 168 050512

surface areas of the pristine NCM-811 powder and cathode electrode agree nicely with each other, we can now continue with the surface area analysis of the cycled electrodes (black data points in Fig. 6).

In the cycled electrodes, the surface area of the NCM-811 CAM is on a rather constant level of ≈1.8 m^2/g_{CAM} and only increases to ≈2.6 m^2/g_{CAM} at the end-of-test after 700 cycles. To evaluate these numbers, some important reference points are shown as horizontal lines in Fig. 6. The afore-mentioned pristine CAM powder (blue line) has a significantly lower surface area of 0.28 m^2/g_{CAM}. Assuming solid spheres and using the crystallographic density of 4.75 g cm^{-3}, this value translates into an average particle diameter of $d_{avg} \approx 4.5$ μm ($d_{avg} = 6/(\rho_{cryst} \cdot A_{BET,CAM})$), which is on the order of the secondary agglomerates (d_{50} value of 10.2 μm determined by laser scattering). Consequently, we predominantly see the outer surface of the secondary agglomerates, while the inner surface of the primary particles is not accessible for two reasons: (i) the crystallites are closely packed after calcination with little pore volume in between and (ii) the pore space between the primary crystallites is blocked due to the presence of surface impurities such Li_2CO_3 and LiOH. As shown in our first publication for the same NCM-811 CAM,[9] these impurities can be removed by washing the CAM powder in water or by storing it in an HF-containing electrolyte, yielding in both cases 1.2 m^2/g_{CAM} (green line). The surface area of the cycled electrodes is still higher (≈1.3–2.6 m^2/g_{CAM}; see black squares in Fig. 6), because the crystallites experience a continuous contraction/expansion during charge/discharge cycling. Under the given conditions (C/2 cycling at 45 °C between cathode potentials of 3.0–4.5 V), the change of the unit cell volume, $\Delta V/V_{dis}$, evolves from −6.1% at BOT to −3.1% at EOT. Since the unit cell volume shrinks predominantly at high SOCs ($x_{Li} < 0.35$ for NCM materials),[57] $\Delta V/V_{dis}$ gets smaller over the course of cycling due to the gradual increase of $x_{Li,cha}$ at the upper cut-off voltage (see Fig. 4c). The reversible "breathing" in every single cycle accumulates a mismatch between the primary particles, so that their packing in the discharged state is not as dense as it was in the pristine state, exposing additional inner surface area.

When we develop this argument further, the contracted crystallites in the charged state should exhibit the highest surface area. For this reason, we also measured Kr-BET of the charged electrodes after the first charge at C/10 to a cathode potential of 4.5 V at 45 °C, yielding a specific surface area of the CAM of 3.1 ± 0.2 m^2/g_{CAM} (average from two electrodes; red line). For solid spheres, this gives an average diameter of $d_{avg} \approx 0.41 \pm 0.03$ μm, which indeed reflects the size of the primary particles (see Fig. S11 -in our former study[9]). Oswald et al. have visualized these alternating phenomena by cross-sectional FIB-SEM images of NCM-622, illustrating (i) the separation of primary particles in the charged state and (ii) their subsequent compaction in the discharged state.[25] After 303 cycles to a cathode potential of 4.5 V at 25 °C, they reported a surface area of ≈3.1 m^2/g_{CAM} in the discharged state, which resembles that of our NCM-811 CAM in the charged state of the first cycle.

Alternatively, Oswald et al. introduced an EIS-based method to monitor the surface area of electrodes by utilizing its correlation to the electrochemical double layer capacitance.[25] Kr-BET and EIS have some intrinsic differences. Most importantly, krypton atoms can access pores as small as ≈0.2 nm, while the penetration of solvated lithium-ions into pores requires pore diameters of greater than ≈1 nm, so that only pores above this value will contribute to the capacitance determined by EIS. This might explain why the here reported surface area changes determined by Kr-BET (see Fig. 6) occur mainly from the pristine state to BOT (6 cycles): after the initial few cycles, the surface impurities seem to be already removed and the particle disintegration seems to have already created permanent pores at least on the sub-nm scale, which can be detected right away by Kr-BET. In Oswald's EIS data, there is also a sharp but less extensive rise in the first cycles and the capacitance increases notably in the later cycles as well. This is rationalized by the steady expansion of pores (or cracks) in the discharged state (due to the accumulating mismatch between the primary crystallites), so that the further increase of CAM surface area only becomes detectable by EIS after a certain pore/crack size threshold has been reached.

The above discussion highlights the coexistence of solid/solid, solid/liquid, and solid/gas interfaces within the secondary agglomerates. As their relative ratio will change during cycling, we have to select a proper surface area for the calculation of the surface layer thickness. In this respect, recent publications address the question if the surface reconstruction requires the exposure of the surface to the electrolyte.[15,58,59] In the work of Schweidler et al.[15] and Zou et al.,[58] STEM imaging of cycled Ni-rich CAMs revealed reconstruction layers on open surfaces (exposed to the electrolyte), while the layered structure was maintained on sealed surfaces (not in contact with the electrolyte). For solid/solid interfaces, Zou et al. further differentiate between incoherent boundaries (stable against phase transitions) and twin boundaries (prone to phase transitions). All these different modes of surface reconstruction can be ascribed to intergranular cracking. In contrast, Ahmed et al. reported on the growth of rock-salt-like regions at the boundary of intragranular nanopores, which are encapsulated in the bulk of the CAM and thus not exposed to the electrolyte.[59] Yan et al. identified intragranular cracks, which are initiated from the grain interior and can generate completely new surfaces (in contrast to sealed surfaces, which are already present, but buried).[50] We conclude that the surface reconstruction depends on the type of grain boundary and its exposure to the electrolyte. Consequently, the calculated thickness can just provide an estimate, which averages over the heterogeneous surfaces. We decided to proceed with the ≈3.1 m^2/g_{CAM} of the charged electrode, because this value represents in good approximation all available surfaces of the crystallites, which might potentially be exposed to the electrolyte (due to intergranular cracking, particularly in the charged state). Furthermore, the layered-to-spinel/rock-salt transformation is initiated by the release of lattice oxygen at these high SOCs.

Using the equations described in our former work,[9] the relative material loss (left axis in Fig. 5) is converted into the average thickness, $t_{surface\text{-}layer}$ (right axis in Fig. 5). As already discussed beforehand, we want to mention that the here calculated thickness represents the electrochemically inactive surface layer, which yet might be thinner than the O-depleted surface layer at a given cycle number. The initial oxygen release has to be completed by the rearrangement of the transition-metals in order to be become detectable as lost CAM. Therefore, we assume several reaction fronts, which gradually grow from the surface of the primary particles into their interior, but only the fully reconstructed and non-intercalating layer can be measured by our approach. With the ≈3.1 m^2/g_{CAM} of the charged electrode, the re-calculation of the EOT value after 1000 cycles at 22 °C now gives ≈6 nm, which agrees much better to the HAADF-STEM images in our previous study than the back then estimated ≈15 nm on the basis of the 1.2 m^2/g_{CAM} of the washed CAM. At 45 °C, the surface layer thickness amounts to ≈12–14 nm after 700 cycles. Even though all quantification methods, either XPD and Kr-BET (as applied here) or STEM imaging, should be taken with a grain of salt, the 45 °C trend line is in good agreement to the STEM data of Schweidler et al.[15] Similar to our NCM-811, they cycled their NCM-851005 at 45 °C to 4.2 V_{FC} (corresponding to ≈4.3 V vs Li^+/Li) and reported a rock-salt-like phase of ≈2 nm after 100 cycles and ≈14 nm after 500 cycles, respectively. In light of the above arguments, the observed surface layer is however not perfectly uniform around the individual primary particles.[15] Consequently, the average thickness of ≈14 nm after 500 cycles reported by Schweidler et al.[15] is in a reasonably good agreement with the here estimated ≈8 nm for the NCM-811 electrode cycled for 550 cycles (see Fig. 5). In summary, the CAM surface area and the thickness of the reconstruction layer can be accessed by various methods, including microscopy, BET, and EIS. In order to evaluate how quantitative their agreement can be in the best case, all these methods have to be applied to the same material in a complementary manner.

Journal of The Electrochemical Society, 2021 168 050512

Our data as well as all the discussed data and findings from other groups are based on poly-crystalline CAMs, but there is an ongoing trend to switch to single-crystalline layered oxides.[16,60–62] In that case, the crystallites have a size in the μm range. As long as intragranular cracking of individual crystallites does not generate new surfaces, e.g., due to real particle fracture, we would expect the surface area of single-crystalline CAMs to stay below 1 m^2/g_{CAM} also during cycling. The lower surface-to-bulk ratio would substantially decrease the loss of electrochemically active material (assuming that it is occurring mostly on CAM surfaces exposed to the electrolyte) and the associated degradation mechanism. This is an interesting working hypothesis for single-crystalline CAMs to look at in the future.

Conclusions

In the present work, we investigated in a comparative manner the degradation mechanisms of the Ni-rich layered oxide NCM-811 at ambient (22 °C) and elevated temperatures (45 °C). Apart from the temperature variation, the NCM-811/graphite full-cells were cycled in a very similar fashion at a constant-current of C/2 between cathode potentials of 3.0 and 4.5 V. In order to focus solely on the CAM degradation and to exclude any effects due to a lithium loss at the anode, the graphite CE was partially pre-lithiated and the potential was controlled vs the Li-RE. Furthermore, the large electrolyte excess prevents any capacity fading caused by the potential electrolyte breakdown.

The capacity loss during C/2 cycling was more than doubled at 45 °C operation (data generated in this work) compared to 22 °C operation (data acquired in our first study[9]). To elucidate the underlying degradation mechanisms, we switched from time-consuming in situ techniques to their simplified ex situ counterparts, including X-ray powder diffraction, electrochemical impedance spectroscopy, and Kr-BET. We could ascribe ≈60% of the observed capacity loss after 700 cycles at 45 °C to the loss of electrochemically active material, which is caused by the formation of a reconstructed, electrochemically inactive surface. This compares to only ≈40% material loss after 1000 cycles at 22 °C.

The formation of the reconstructed, oxygen-depleted surface results in a growth of the charge-transfer resistance of the NCM-811 CAM, which is also reflected by an analogous increase of the DCIR resistance and further leads to overpotential-induced capacity losses. After 700 cycles at 45 °C, the layer thickness around the primary particles exposed to the electrolyte is estimated to be ≈12–14 nm, reasonably consistent with the literature, while only ≈6 nm are estimated after 1000 cycles at 25 °C. We attribute this difference to the faster kinetics for oxygen removal and/or transition-metal rearrangement at the higher temperature.

The overpotential-induced capacity losses occur in a similar ratio both in the discharged state (i.e., during lithiation of the CAM) and the charged state (i.e., during delithiation of the CAM). Whether these losses are predominantly caused by the increased charge-transfer resistance or by a decreased lithium diffusivity in the bulk phase cannot be finally answered. However, the extent of Li-Ni mixing stays constant at 22 °C and increases only by ≈1%–2% after 700 cycles after 45 °C. Furthermore, we could not observe the emergence of a so-called fatigued phase with a layered structure.

Acknowledgments

Financial support by BASF SE through its Scientific Network on Electrochemistry and Batteries is gratefully acknowledged.

Appendix

Equations used for the capacity loss analysis.—The XPD-derived variation of the lithium content (x_{Li}) over the course of cycling (see Fig. 4) enables the deconvolution of the electrochemically measured capacity loss, $\Delta C_{EC}^{BOT\rightarrow i}$ (in mAh g^{-1}):

$$\Delta C_{EC}^{BOT\rightarrow i} = C_{EC}^{BOT} - C_{EC}^{i} \quad [A\cdot1]$$

which is defined by the difference of the discharge capacity in the ith cycle (C_{EC}^{i}) relative to that at the begin-of-test (C_{EC}^{BOT}). Please note that the following equations were established in our former publication by Friedrich et al., where they are explained in great detail.[9]

The first contribution is the absolute loss of electrochemically active material in the form of a reconstructed, O-depleted surface layer, which can be quantified as $\Delta C_{Material}^{BOT\rightarrow i}$ (in mAh g^{-1}, just like the other loss terms) by the following equation:

$$\Delta C_{Material}^{BOT\rightarrow i} = (C_{XPD}^{i} - C_{EC}^{i}) \cdot \Delta\frac{\Delta x_{Li}^{BOT}}{\Delta x_{Li}^{i}} \quad [A\cdot2]$$

Here, the material loss corresponds to the difference between the theoretically expected capacity inferred from XPD (C_{XPD}^{i}, see Eq. 6) and the actually measured discharge capacity in the ith cycle (C_{EC}^{i}). To reference this difference to BOT, it has to be corrected by the accessible Δx_{Li} ranges between the discharged and charged state (e.g., $\Delta x_{Li}^{i} = x_{Li,dis}^{i} - x_{Li,cha}^{i}$), which typically shrink upon cycling due to the increasing overpotential (i.e., $\Delta x_{Li}^{BOT} > \Delta x_{Li}^{i}$).

The overpotential-induced loss ($\Delta C_{Overpotential}^{BOT\rightarrow i}$) is the second contribution, which can be further divided into capacity losses in the discharged ($\Delta C_{Discharge}^{BOT\rightarrow i}$) and in the charged state ($\Delta C_{Charge}^{BOT\rightarrow i}$):

$$\Delta C_{Overpotential}^{BOT\rightarrow i} = \Delta C_{Discharge}^{BOT\rightarrow i} + \Delta C_{Charge}^{BOT\rightarrow i} \quad [A\cdot3]$$

where by the two individual contributions are calculated according to:

$$\Delta C_{Discharge}^{BOT\rightarrow i} = (x_{Li,dis}^{BOT} - x_{Li,dis}^{i}) \cdot \frac{274\ \text{mAh g}^{-1}}{1.01} \cdot (1 - \Delta C_{Material,rel}^{i}) \quad [A\cdot4]$$

$$\Delta C_{Charge}^{BOT\rightarrow i} = (x_{Li,cha}^{i} - x_{Li,cha}^{BOT}) \cdot \frac{274\ \text{mAh g}^{-1}}{1.01} \cdot (1 - \Delta C_{Material,rel}^{i}) \quad [A\cdot5]$$

by taking the difference of the respective x_{Li} values between BOT and the ith cycle in either the discharged ($x_{Li,dis}^{BOT} - x_{Li,dis}^{i}$) or charged state ($x_{Li,cha}^{i} - x_{Li,cha}^{BOT}$). Note that for this analysis it is irrelevant whether the difference in x_{Li} is due to an increase of the CAM's R_{CT} (caused by the formation of a resistive surface layer) or a decrease of the lithium diffusivity in the bulk of the CAM (caused by transition-metal migration into the lithium layer). Since only the electrochemically active material can undergo a capacity loss due to an increasing overpotential, Eqs. A·3–A·5 include a correction term that considers the NCM-811 phase fraction which has already been lost until the ith cycle ($\Delta C_{Material,rel}^{i}$, see Eq. 5).

ORCID

Benjamin Strehle https://orcid.org/0000-0001-8878-1160
Franziska Friedrich https://orcid.org/0000-0001-9400-1212
Hubert A. Gasteiger https://orcid.org/0000-0001-8199-8703

References

1. G. Zubi, R. Dufo-López, M. Carvalho, and G. Pasaoglu, *Renew. Sustain. Energy Rev.*, **89**, 292 (2018).
2. E. A. Olivetti, G. Ceder, G. G. Gaustad, and X. Fu, *Joule*, **1**, 229 (2017).
3. C. Banza Lubaba Nkulu et al., *Nat. Sustain.*, **1**, 495 (2018).
4. H.-J. Noh, S. Youn, C. S. Yoon, and Y.-K. Sun, *J. Power Sources*, **233**, 121 (2013).

5. S.-M. Bak, E. Hu, Y. Zhou, X. Yu, S. D. Senanayake, S.-J. Cho, K.-B. Kim, K. Y. Chung, X.-Q. Yang, and K.-W. Nam, *ACS Appl. Mater. Interfaces*, **6**, 22594 (2014).
6. S.-T. Myung, F. Maglia, K.-J. Park, C. S. Yoon, P. Lamp, S.-J. Kim, and Y.-K. Sun, *ACS Energy Lett.*, **2**, 196 (2017).
7. H.-H. Ryu, K.-J. Park, C. S. Yoon, and Y.-K. Sun, *Chem. Mater.*, **30**, 1155 (2018).
8. W. Li, E. M. Erickson, and A. Manthiram, *Nat. Energy*, **5**, 26 (2020).
9. F. Friedrich, B. Strehle, A. T. S. Freiberg, K. Kleiner, S. J. Day, C. Erk, M. Piana, and H. A. Gasteiger, *J. Electrochem. Soc.*, **166**, A3760 (2019).
10. M.-T. F. Rodrigues, G. Babu, H. Gullapalli, K. Kalaga, F. N. Sayed, K. Kato, J. Joyner, and P. M. Ajayan, *Nat. Energy*, **2**, 17108 (2017).
11. G. Xu, X. Liu, A. Daali, R. Amine, Z. Chen, and K. Amine, *Adv. Funct. Mater.*, **30**, 2004748 (2020).
12. USABC, USABC Goals for Advanced Batteries for EVs (2020), https//www.energy.gov/sites/prod/files/2014/05/f15/APR13_Energy_Storage_d_III_Adv_Battery_Dev_0.pdf.
13. J. Li, J. Harlow, N. Stakheiko, N. Zhang, J. Paulsen, and J. Dahn, *J. Electrochem. Soc.*, **165**, A2682 (2018).
14. R. Jung, P. Strobl, F. Maglia, C. Stinner, and H. A. Gasteiger, *J. Electrochem. Soc.*, **165**, A2869 (2018).
15. S. Schweidler, L. de Biasi, G. Garcia, A. Mazilkin, P. Hartmann, T. Brezesinski, and J. Janek, *ACS Appl. Energy Mater.*, **2**, 7375 (2019).
16. J. E. Harlow et al., *J. Electrochem. Soc.*, **166**, A3031 (2019).
17. C. P. Aiken, J. E. Harlow, R. Tingley, T. Hynes, E. R. Logan, S. L. Glazier, A. S. Keefe, and J. R. Dahn, *J. Electrochem. Soc.*, **167**, 130541 (2020).
18. D. Pritzl, S. Solchenbach, M. Wetjen, and H. A. Gasteiger, *J. Electrochem. Soc.*, **164**, A2625 (2017).
19. *MIMS Client, Version 1.4* (Maccor Inc, Tulsa, United States of America) (2019).
20. *TOPAS-Academic* V6 (Coelho Software, Brisbane, Australia) (2016).
21. P. W. Stephens, *J. Appl. Crystallogr.*, **32**, 281 (1999).
22. O. Dolotko, A. Senyshyn, M. J. Muhlbauer, K. Nikolowski, F. Scheiba, and H. Ehrenberg, *J. Electrochem. Soc.*, **159**, A2082 (2012).
23. R. Morasch, B. Suthar, and H. A. Gasteiger, *J. Electrochem. Soc.*, **167**, 100540 (2020).
24. J. Landesfeind, D. Pritzl, and H. A. Gasteiger, *J. Electrochem. Soc.*, **164**, A1773 (2017).
25. S. Oswald, D. J. Pritzl, M. Wetjen, and H. Gasteiger, *J. Electrochem. Soc.* (2020).
26. S. Meini, M. Piana, H. Beyer, J. Schwämmlein, and H. A. Gasteiger, *J. Electrochem. Soc.*, **159**, A2135 (2012).
27. I. Buchberger, S. Seidlmayer, A. Pokharel, M. Piana, J. Hattendorff, P. Kudejova, R. Gilles, and H. A. Gasteiger, *J. Electrochem. Soc.*, **162**, A2737 (2015).
28. L. M. Thompson, W. Stone, A. Eldesoky, N. K. Smith, C. R. M. McFarlane, J. S. Kim, M. B. Johnson, R. Petibon, and J. R. Dahn, *J. Electrochem. Soc.*, **165**, A2732 (2018).
29. F. T. Wagner, B. Lakshmanan, and M. F. Mathias, *J. Phys. Chem. Lett.*, **1**, 2204 (2010).
30. R. Sharabi, E. Markevich, V. Borgel, G. Salitra, D. Aurbach, G. Semrau, M. A. Schmidt, N. Schall, and C. Stinner, *Electrochem. Commun.*, **13**, 800 (2011).
31. T. Yim, H.-J. Ha, M.-S. Park, K. J. Kim, J.-S. Yu, and Y.-J. Kim, *RSC Adv.*, **3**, 25657 (2013).
32. R. Jung, M. Metzger, F. Maglia, C. Stinner, and H. A. Gasteiger, *J. Electrochem. Soc.*, **164**, A1361 (2017).
33. J. Wandt, A. T. S. Freiberg, A. Ogrodnik, and H. A. Gasteiger, *Mater. Today*, **21**, 825 (2018).
34. S. Solchenbach, G. Hong, A. T. S. Freiberg, R. Jung, and H. A. Gasteiger, *J. Electrochem. Soc.*, **165**, A3304 (2018).
35. R. Jung, F. Linsenmann, R. Thomas, J. Wandt, S. Solchenbach, F. Maglia, C. Stinner, M. Tromp, and H. A. Gasteiger, *J. Electrochem. Soc.*, **166**, A378 (2019).
36. R. Pan, D. Rau, Y. Moryson, J. Sann, and J. Janek, *ACS Appl. Energy Mater.*, **3**, 6065 (2020).
37. T. Teufl, D. Pritzl, S. Solchenbach, H. A. Gasteiger, and M. A. Mendez, *J. Electrochem. Soc.*, **166**, A1275 (2019).
38. R. Jung, M. Metzger, F. Maglia, C. Stinner, and H. A. Gasteiger, *J. Phys. Chem. Lett.*, **8**, 4820 (2017).
39. M. Metzger, P. Walke, S. Solchenbach, G. Salitra, D. Aurbach, and H. A. Gasteiger, *J. Electrochem. Soc.*, **167**, 160522 (2020).
40. A. T. S. Freiberg, M. K. Roos, J. Wandt, R. de Vivie-Riedle, and H. A. Gasteiger, *J. Phys. Chem. A*, **122**, 8828 (2018).
41. T. Teufl, D. Pritzl, P. Krieg, B. Strehle, M. A. Mendez, and H. A. Gasteiger, *J. Electrochem. Soc.*, **167**, 110505 (2020).
42. R. Weber, A. J. Louli, K. P. Plucknett, and J. R. Dahn, *J. Electrochem. Soc.*, **166**, A1779 (2019).
43. H. Li, M. Cormier, N. Zhang, J. Inglis, J. Li, and J. R. Dahn, *J. Electrochem. Soc.*, **166**, A429 (2019).
44. W. Li, X. Liu, Q. Xie, Y. You, M. Chi, and A. Manthiram, *Chem. Mater.*, **32**, 7796 (2020).
45. C. Xu et al., *Nat. Mater.*, **20**, 84 (2020).
46. L. Yin et al., *Chem. Mater.*, **32**, 1002 (2020).
47. Y. Makimura, T. Sasaki, T. Nonaka, Y. F. Nishimura, T. Uyama, C. Okuda, Y. Itou, and Y. Takeuchi, *J. Mater. Chem. A*, **4**, 8350 (2016).
48. K. Kleiner, D. Dixon, P. Jakes, J. Melke, M. Yavuz, C. Roth, K. Nikolowski, V. Liebau, and H. Ehrenberg, *J. Power Sources*, **273**, 70 (2015).
49. H. Liu, M. Wolf, K. Karki, Y.-S. Yu, E. A. Stach, J. Cabana, K. W. Chapman, and P. J. Chupas, *Nano Lett.*, **17**, 3452 (2017).
50. P. Yan, J. Zheng, M. Gu, J. Xiao, J.-G. Zhang, and C.-M. Wang, *Nat. Commun.*, **8**, 14101 (2017).
51. H. M. Dahn, A. J. Smith, J. C. Burns, D. A. Stevens, and J. R. Dahn, *J. Electrochem. Soc.*, **159**, A1405 (2012).
52. M. Dubarry, C. Truchot, and B. Y. Liaw, *J. Power Sources*, **219**, 204 (2012).
53. F. Wang, Z. Lin, L. Liu, X. Wei, S. Lin, L. Dai, Y. Wei, C. Liang, and B. Liaw, *J. Electrochem. Soc.*, **167**, 090549 (2020).
54. J. Li, H. Liu, J. Xia, A. R. Cameron, M. Nie, G. A. Botton, and J. R. Dahn, *J. Electrochem. Soc.*, **164**, A655 (2017).
55. S.-M. Bak, K.-W. Nam, W. Chang, X. Yu, E. Hu, S. Hwang, E. A. Stach, K.-B. Kim, K. Y. Chung, and X.-Q. Yang, *Chem. Mater.*, **25**, 337 (2013).
56. T. Teufl, B. Strehle, P. Müller, H. A. Gasteiger, and M. A. Mendez, *J. Electrochem. Soc.*, **165**, A2718 (2018).
57. L. de Biasi, A. O. Kondrakov, H. Geßwein, T. Brezesinski, P. Hartmann, and J. Janek, *J. Phys. Chem. C*, **121**, 26163 (2017).
58. L. Zou, W. Zhao, H. Jia, J. Zheng, L. Li, D. P. Abraham, G. Chen, J. R. Croy, J.-G. Zhang, and C. Wang, *Chem. Mater.*, **32**, 2884 (2020).
59. S. Ahmed et al., *ACS Nano*, **13**, 10694 (2019).
60. J. Li, H. Li, W. Stone, R. Weber, S. Hy, and J. R. Dahn, *J. Electrochem. Soc.*, **164**, A3529 (2017).
61. J. Li, A. R. Cameron, H. Li, S. Glazier, D. Xiong, M. Chatzidakis, J. Allen, G. A. Botton, and J. R. Dahn, *J. Electrochem. Soc.*, **164**, A1534 (2017).
62. H. H. Sun, H.-H. Ryu, U.-H. Kim, J. A. Weeks, A. Heller, Y.-K. Sun, and C. B. Mullins, *ACS Energy Lett.*, **5**, 1136 (2020).

4 Conclusions

This PhD thesis investigated important degradation mechanisms of layered oxides used as cathode active materials in Li-ion batteries. By employing primarily on-line electrochemical mass spectrometry and diffraction methods, we did not only manage to identify degradation processes happening both at the surface and within the bulk of the materials, but we successfully aimed at quantifying and monitoring their extent during battery operation. In this manner, we could correlate the observed processes to the electrochemical performance and the capacity fading of the cathode active materials. The key findings of this thesis are summarized in Figure 19, whereby Li- and Mn-rich layered oxides are addressed in the sections 3.1, 3.2, and 3.3, while section 3.4 focused on the Ni-rich NCM-811 CAM.

At the beginning, we examined a series of differently synthesized Li- and Mn-rich layered oxides in section 3.1, which differ with respect to their morphology and transition-metal composition. In order to increase the energy density and to further reduce the cost of over-lithiated CAMs, this work is motivated by the goal to replace the loosely packed and Co-containing state-of-the-art materials, which are also the main object of investigation in the following sections (see cross-sectional SEM image in Figure 19), by more densely packed and Co-free materials. However, the dense CAMs still suffer from a poor electrochemical performance, as evidenced during a rate test, where they provide ≈70-140 mAh/g less capacity at 1C than the porous reference material. By performing a detailed material characterization of the as-received CAM powders, including gas sorption measurements and a size/strain analysis of X-ray powder diffraction data, we could correlate the accessible capacity quantitatively to two material properties: (i) the specific surface area and (ii) the microstrain in the bulk of the CAMs. These metrics can be readily quantified for newly synthesized materials and might thus serve as figures of merit to estimate their electrochemical performance prior to any battery testing.

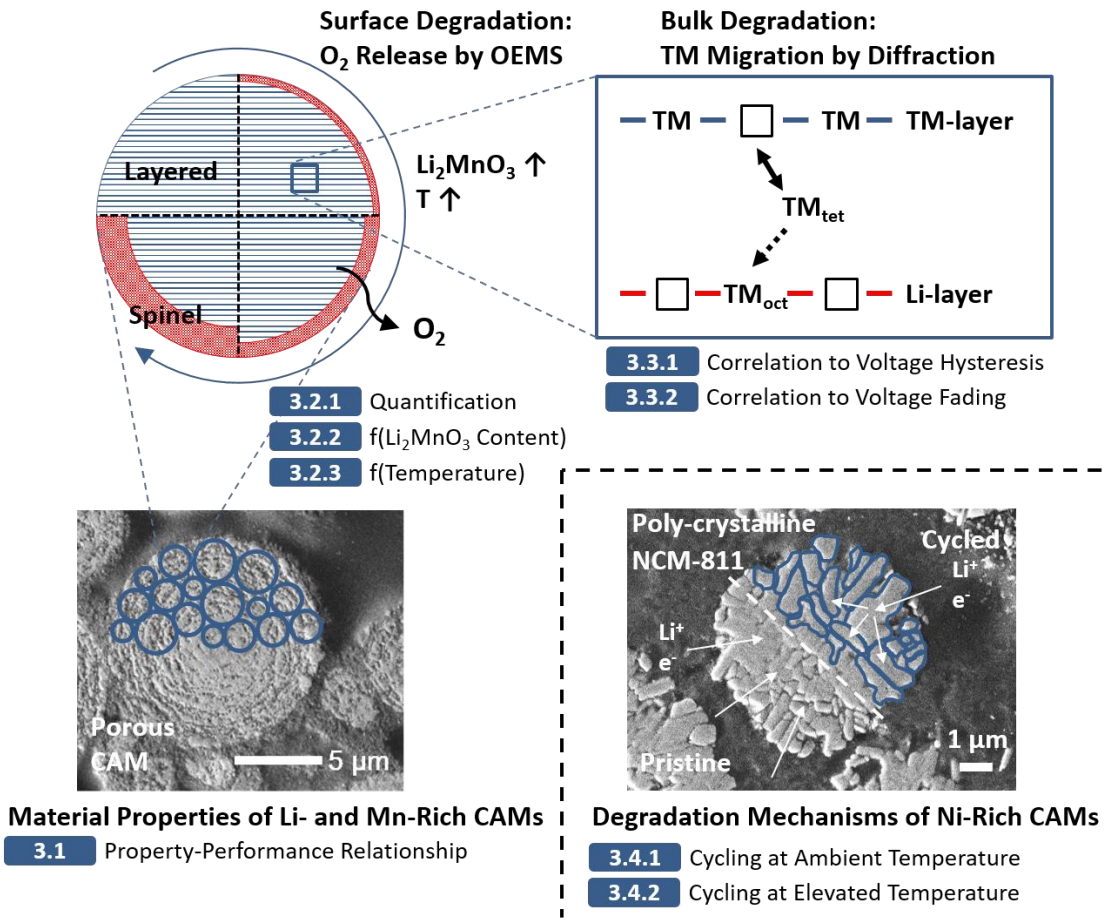

Figure 19. Graphical summary of the key results of this PhD thesis. Section 3.1 elucidated the property-performance relationship of Li- an Mn-rich layered oxides by comparing differently synthesized CAMs. Their surface-related degradation was investigated by OEMS in section 3.2. After a first quantification of the underlying oxygen release (section 3.2.1), we further studied its dependence on the Li_2MnO_3 content (sections 3.2.2) and on the cycling temperature (section 3.2.3), respectively. In the following, several diffraction methods were applied to examine the bulk-related degradation of Li- and Mn-rich CAMs in section 3.3, whereby we were primarily seeking to find a correlation of the transition-metal migration to the voltage hysteresis (section 3.3.1) and the voltage fading (section 3.3.2). Finally, we had a look on the long-term degradation of Ni-rich CAMs in section 3.4. The capacity fading mechanisms of a NCM-811 CAM were thoroughly quantified for up to 1000 cycles at ambient temperature (section 3.4.1) and for up to 700 cycles at elevated temperature (section 3.4.2), respectively.

After identifying important properties of the pristine materials, section 3.2 studied the gas evolution during the initial cycles by OEMS. The oxygen release from Li- and Mn-rich layered oxides is well-known,[151,152] but its origin remained controversially discussed in the literature.[142,266] For a material with a nominal Li_2MnO_3 content of 0.42, a detailed quantification of the evolved gases in section 3.2.1 showed that oxygen is released from a thin layer on the particle surface rather than from a bulk conversion of the Li_2MnO_3 phase. The thickness of the hypothesized disordered spinel-type surface layer is estimated from the evolved amounts of O_2 and CO_2

within the first two cycles to be on the order of ≈2-3 nm, which is in good agreement with previous (S)TEM studies.[161,162]

Based on the above observation, we carried out a second comparative study in section 3.2.2, where the oxygen release and the emergence of disordered surface phases was investigated in dependence of the Li_2MnO_3 content of three LMR-NCMs (ranging from 0.33 to 0.50). The oxygen release increased by two orders of magnitude with increasing Li_2MnO_3 content and the thereof calculated mole fractions of the spinel-type phase agreed with the quantification independently derived from the electrochemical analysis of the capacities in dQ/dV plots. Furthermore, the estimated layer thicknesses from the gas analysis were in good agreement with HRTEM measurements conducted on cycled electrodes, which also verified the spinel-type nature. The only exception was the material with the highest Li_2MnO_3 content, where the spinel phase also grew into the bulk of material, while the spinel formation was restricted to the near-surface region for the other two materials with lower Li_2MnO_3 content. Despite these differences with respect to the surface degradation caused by oxygen release, we could not observe a clear correlation to the capacity retention and voltage fading of full-cells.

Finally, we had a look on the temperature dependence of the oxygen release in section 3.2.3. By analogy with the variation of the Li_2MnO_3 content (measured at 25°C), increasing the activation temperature from 0 to 45°C substantially enhanced the oxygen release. Furthermore, the dQ/dV plots showed that the rate of surface reconstruction into a spinel phase is accelerated with increasing temperature. The combination of both effects could explain why the low-temperature at 0°C provided ≈25 mAh/g more capacity than the high-temperature activation at 45°C,[255] while also releasing more CO_2 into the following cycles.

In summary, this section revealed that a Li- and Mn-rich CAM with a limited Li_2MnO_3 content of 0.33 would be the preferred choice for real applications, because it showed a similar full-cell performance but the lowest oxygen release in comparison to the other CAMs with higher Li_2MnO_3 content. At the expense of limiting the capacity, a high-temperature activation might be applied in large-format cells in order to shift as much gassing as possible into the formation cycle before venting and finally sealing the cell.[166]

While the previous section suggested strategies how the oxygen release and its implications can be minimized, the voltage hysteresis and the voltage fading remain a serious problem of Li- and Mn-rich layered oxides.[29] These phenomena have their roots in the bulk structure of the material and were thus studied by diffraction methods in section 3.3. By using *in situ* laboratory XPD in section 3.3.1, we monitored the lattice parameters within the initial cycles as a function of the Li_2MnO_3 content and the cycling conditions. When plotted versus the state of charge, the lattice parameters experienced the same hysteresis between the charge and discharge reaction as the open circuit voltage, which allowed conclusions about the path dependence of the underlying redox processes. However, the hysteresis of the unit cell volume vanished when correlated to the open circuit voltage, resulting in a universal curve for all three tested materials, which describes them independent of the lithium content. To clarify the role of transition-metal migration between the Li and TM layer, we carried out joint Rietveld refinements of *ex situ* L-XPD and NPD data. The applied structural models had to be simple in order to avoid erroneous results, so that only the distribution of Li and Ni on the two metal layers could be refined at the same time. Even though we determined a difference of up to ≈2.4% migrated Ni between charge and discharge within the second cycle, we could not prove any direct correlation to the voltage and lattice parameter hysteresis.

In contrast, we proposed a causal relationship between the voltage fading and the TM migration in section 3.3.2. Here, the TM distribution was determined by *in situ* synchrotron XPD. Over the duration of ≈100 cycles, the amount of transition-metals irreversibly captured on octahedral Li-sites increased by ≈3% in the discharged state, while the mean discharge voltage decreased by ≈250 mV. In the charged state, we detected in addition a constantly high level of ≈8-9% TMs on tetrahedral Li-sites, which might explain the high capacities of Li- and Mn-rich layered oxides due to the stabilizing effect in the delithiated state.

Despite their potential as cost-effective cathode active material for Li-ion batteries, this thesis addressed several challenges of Li- and Mn-rich layered oxides and we revealed the underlying degradation mechanisms. Since over-lithiated CAMs could not be commercialized yet, Ni-rich materials are the dominating class of CAMs,

especially for EV applications.[6,9] For this reason, we finally studied the long-term capacity fading of a poly-crystalline NCM-811 CAM in section 3.4, which was cycled for several hundreds of cycles either at the ambient temperature of 22°C (section 3.4.1) or at the elevated temperature of 45°C (section 3.4.2). The capacity loss during C/2 cycling to an upper cut-off potential of 4.5 V vs. Li^+/Li was more than doubled at 45°C operation compared to 22°C operation. By recording XPD patterns in regular cycle number intervals both in the completely discharged and charged state, we could establish a quantitative relationship between the NCM-811 lattice parameters and the observed capacity fading. The formation of a reconstructed, electrochemically inactive surface layer leads to two capacity loss terms: (i) an irreversible loss due to the active material lost for its formation and (ii) an overpotential-induced loss due to the increasing charge-transfer resistance. The percentage of lost material is an important parameter to evaluate the aging behavior of different CAMs and/or under different cycling conditions,[94,176] which can be either inferred from the XPD analysis or purely electrochemically by slow half-cell cycling. Further measurements provided evidence that the resistive surface layer is gradually formed around the primary crystallites (see cross-sectional SEM image in Figure 19), which are virtually all exposed to the electrolyte in the charged state. The layer thickness is estimated to be ≈6 nm after 1000 cycles at 22°C and ≈12-14 nm after 700 cycles after 45°C, consistent with STEM studies.[84,89] On the other hand, the bulk structure remained reasonably stable, as the Li-Ni mixing increased by a maximum of ≈1-2% at 45°C and was even constant at 22°C. Consequently, surface instabilities are the main degradation mechanism of Ni-rich poly-crystalline CAMs,[86,87] which could be addressed either by minimizing the initial oxygen release (e.g., washing of the CAMs[257]) or by reducing the surface-to-bulk ration (e.g., using single-crystalline CAMs[265]).

Future work should have a focus on the optimization of Li- and Mn-rich layered oxides. With respect to their bulk properties, this requires the understanding of the microstrain, e.g., by the use of advanced (S)TEM techniques, which are capable of visualizing even light atoms such as lithium and oxygen in layered transition-metal oxides.[267] In so doing, the possible impact of oxygen vacancies and the displacement of individual atoms or layers can be examined on an atomic level for the different CAMs investigated within this thesis. Furthermore, first experiments have shown

that an additional post-calcination step at ≥1000°C (which intentionally goes beyond the original calcination temperature of ≈930°C) can more than halve the microstrain of the dense and Co-free CAM that was studied in section 3.1 (see as-received D-woCo-6 versus post-calcined D-woCo-6-1000C CAM). In order to improve substantially the accessible capacity and energy density, however, the desired reduction of microstrain has to be delicately balanced with the concomitant decrease of specific surface area (due to agglomerate growth and the loss of internal porosity), which adversely affects the electrochemical performance during a rate test. After identifying a promising candidate, it would be also interesting to investigate its gassing behavior by OEMS, because the oxygen release from a dense CAM with ≈1 m^2/g is expected to be less problematic than from a state-of-the-art porous CAM with ≈5 m^2/g. Long-term cycling experiments in full-cells would complete the required dataset to evaluate the feasibility of such a post-calcined and optimized CAM on a laboratory scale.

References

1. Nishi, Y. The Dawn of Lithium-Ion Batteries. *Interface Mag.* **25**, 71–74 **(2016)**.

2. Liang, Y., Zhao, C., Yuan, H., Chen, Y., Zhang, W., Huang, J., Yu, D., Liu, Y., Titirici, M., Chueh, Y., Yu, H. & Zhang, Q. A review of rechargeable batteries for portable electronic devices. *InfoMat* **1**, 6–32 **(2019)**.

3. The Royal Swedish Academy of Science. The Nobel Prize in Chemistry 2019 - Press Release. *accessed March 10, 2021,* https://www.nobelprize.org/prizes/chemistry/2019/press-release/.

4. Whittingham, M. S. Electrical Energy Storage and Intercalation Chemistry. *Science* **192**, 1126–1127 **(1976)**.

5. Mizushima, K., Jones, P. C., Wiseman, P. J. & Goodenough, J. B. Li_xCoO_2 ($0<x\leq1$): A new cathode material for batteries of high energy density. *Mater. Res. Bull.* **15**, 783–789 **(1980)**.

6. Blomgren, G. E. The Development and Future of Lithium Ion Batteries. *J. Electrochem. Soc.* **164**, A5019–A5025 **(2017)**.

7. Schmuch, R., Wagner, R., Hörpel, G., Placke, T. & Winter, M. Performance and cost of materials for lithium-based rechargeable automotive batteries. *Nat. Energy* **3**, 267–278 **(2018)**.

8. Dunn, B., Kamath, H. & Tarascon, J.-M. Electrical Energy Storage for the Grid: A Battery of Choices. *Science* **334**, 928–935 **(2011)**.

9. Ding, Y., Cano, Z. P., Yu, A., Lu, J. & Chen, Z. Automotive Li-Ion Batteries: Current Status and Future Perspectives. *Electrochem. Energy Rev.* **2**, 1–28 **(2019)**.

10. Deutschland überholt USA bei Neuzulassungen von E-Autos. *accessed March 19, 2021,* https://www.spiegel.de/auto/elektromobilitaet-deutschland-ueberholt-usa-bei-e-auto-neuzulassungen-a-70cc9f19-5904-4ffa-964a-75db553a41b5?sara_ecid=soci_upd_KsBF0AFjflf0DZCxpPYDCQgO1dEMph.

11. Global EV Outlook 2020. *accessed March 18, 2021,* https://www.iea.org/reports/global-ev-outlook-2020.

12. UNFCCC. The Paris Agreement on Climate Change. *accessed March 18, 2021,* https://unfccc.int/sites/default/files/english_paris_agreement.pdf.

13. Rogelj, J., den Elzen, M., Höhne, N., Fransen, T., Fekete, H., Winkler, H., Schaeffer, R., Sha, F., Riahi, K. & Meinshausen, M. Paris Agreement climate proposals need a boost to keep warming well below 2 °C. *Nature* **534**, 631–639 **(2016)**.

14. So planen VW, BMW, Daimler und Co. den Abschied vom Verbrennungsmotor. *accessed March 18, 2021,* https://www.spiegel.de/auto/vw-bmw-mercedes-und-co-wie-sich-die-autohersteller-vom-verbrennungsmotor-verabschieden-a-5af42a43-26b3-418e-8d83-421f223dec50?sara_ecid=soci_upd_KsBF0AFjflf.

15. Electric Vehicle Database. Tesla Model 3 Standard Plus. *accessed March 19, 2021,* https://ev-database.de/pkw/1320/Tesla-Model-3-Standard-Plus.

16. Andre, D., Kim, S.-J., Lamp, P., Lux, S. F., Maglia, F., Paschos, O. & Stiaszny, B. Future generations of cathode materials: an automotive industry perspective. *J. Mater. Chem. A* **3**, 6709–6732 **(2015)**.

17. Gröger, O., Gasteiger, H. A. & Suchsland, J.-P. Review—Electromobility: Batteries or Fuel Cells? *J. Electrochem. Soc.* **162**, A2605–A2622 **(2015)**.

18. Li, W., Erickson, E. M. & Manthiram, A. High-nickel layered oxide cathodes for lithium-based automotive batteries. *Nat. Energy* **5**, 26–34 **(2020)**.

19. London Metal Exchange. Cobalt and nickel prices. *accessed March 19, 2021,* https://www.lme.com/.

20. Olivetti, E. A., Ceder, G., Gaustad, G. G. & Fu, X. Lithium-Ion Battery Supply Chain Considerations: Analysis of Potential Bottlenecks in Critical Metals. *Joule* **1**, 229–243 **(2017)**.

21. Banza Lubaba Nkulu, C., Casas, L., Haufroid, V., De Putter, T., Saenen, N. D., Kayembe-Kitenge, T., Musa Obadia, P., Kyanika Wa Mukoma, D., Lunda Ilunga, J.-M., Nawrot, T. S., Luboya Numbi, O., Smolders, E. & Nemery, B. Sustainability of artisanal mining of cobalt in DR Congo. *Nat. Sustain.* **1**, 495–504 **(2018)**.

22. Tkaczyk, A. H., Bartl, A., Amato, A., Lapkovskis, V. & Petranikova, M. Sustainability evaluation of essential critical raw materials: cobalt, niobium, tungsten and rare earth elements. *J. Phys. D. Appl. Phys.* **51**, 203001 **(2018)**.

23. Noh, H.-J., Youn, S., Yoon, C. S. & Sun, Y.-K. Comparison of the structural and electrochemical properties of layered $Li[Ni_xCo_yMn_z]O_2$ (x = 1/3, 0.5, 0.6, 0.7, 0.8 and 0.85) cathode material for lithium-ion batteries. *J. Power Sources* **233**, 121–130 **(2013)**.

24. de Biasi, L., Kondrakov, A. O., Geßwein, H., Brezesinski, T., Hartmann, P. & Janek, J. Between Scylla and Charybdis: Balancing Among Structural Stability and Energy Density of Layered NCM Cathode Materials for Advanced Lithium-Ion Batteries. *J. Phys. Chem. C* **121**, 26163–26171 **(2017)**.

25. Jung, R., Metzger, M., Maglia, F., Stinner, C. & Gasteiger, H. A. Oxygen Release and Its Effect on the Cycling Stability of $LiNi_xMn_yCo_zO_2$ (NMC) Cathode Materials for Li-Ion Batteries. *J. Electrochem. Soc.* **164**, A1361–A1377 **(2017)**.

26. Metalary. Iron and manganese prices. *accessed March 19, 2021,* https://www.metalary.com/.

27. Teufl, T., Strehle, B., Müller, P., Gasteiger, H. A. & Mendez, M. A. Oxygen Release and Surface Degradation of Li- and Mn-Rich Layered Oxides in Variation of the Li_2MnO_3 Content. *J. Electrochem. Soc.* **165**, A2718–A2731 **(2018)**.

28. Rozier, P. & Tarascon, J. M. Review—Li-Rich Layered Oxide Cathodes for Next-Generation Li-Ion Batteries: Chances and Challenges. *J. Electrochem. Soc.* **162**, A2490–A2499 **(2015)**.

29. Zheng, J., Myeong, S., Cho, W., Yan, P., Xiao, J., Wang, C., Cho, J. & Zhang, J. Li- and Mn-Rich Cathode Materials: Challenges to Commercialization. *Adv. Energy Mater.* **7**, 1601284 **(2017)**.

30. Xu, K. Nonaqueous Liquid Electrolytes for Lithium-Based Rechargeable Batteries. *Chem. Rev.* **104**, 4303–4418 **(2004)**.

31. Landesfeind, J. & Gasteiger, H. A. Temperature and Concentration Dependence of the Ionic Transport Properties of Lithium-Ion Battery Electrolytes. *J. Electrochem. Soc.* **166**, A3079–A3097 **(2019)**.

32. Aurbach, D., Gofer, Y., Ben-Zion, M. & Aped, P. The behaviour of lithium electrodes in propylene and ethylene carbonate: The major factors that influence Li cycling efficiency. *J. Electroanal. Chem.* **339**, 451–471 **(1992)**.

33. Nie, M., Chalasani, D., Abraham, D. P., Chen, Y., Bose, A. & Lucht, B. L. Lithium Ion Battery Graphite Solid Electrolyte Interphase Revealed by Microscopy and Spectroscopy. *J. Phys. Chem. C* **117**, 1257–1267 **(2013)**.

34. Strehle, B., Solchenbach, S., Metzger, M., Schwenke, K. U. & Gasteiger, H. A. The Effect of CO_2 on Alkyl Carbonate Trans-Esterification during Formation of Graphite Electrodes in Li-Ion Batteries. *J. Electrochem. Soc.* **164**, A2513–A2526 **(2017)**.

35. Peled, E. The Electrochemical Behavior of Alkali and Alkaline Earth Metals in Nonaqueous Battery Systems—The Solid Electrolyte Interphase Model. *J. Electrochem. Soc.* **126**, 2047–2051 **(1979)**.

36. Xu, K. Electrolytes and Interphases in Li-Ion Batteries and Beyond. *Chem. Rev.* **114**, 11503–11618 **(2014)**.

37. Takeuchi, E. S., Gan, H., Palazzo, M., Leising, R. A. & Davis, S. M. Anode Passivation and Electrolyte Solvent Disproportionation: Mechanism of Ester Exchange Reaction in Lithium-Ion Batteries. *J. Electrochem. Soc.* **144**, 1944 **(1997)**.

38. Yoshida, H., Fukunaga, T., Hazama, T., Terasaki, M., Mizutani, M. & Yamachi, M. Degradation mechanism of alkyl carbonate solvents used in lithium-ion cells during initial charging. *J. Power Sources* **68**, 311–315 **(1997)**.

39. Burns, J. C., Kassam, A., Sinha, N. N., Downie, L. E., Solnickova, L., Way, B. M. & Dahn, J. R. Predicting and Extending the Lifetime of Li-Ion Batteries. *J. Electrochem. Soc.* **160**, A1451–A1456 **(2013)**.

40. Zhang, S. S. A review on electrolyte additives for lithium-ion batteries. *J. Power Sources* **162**, 1379–1394 **(2006)**.

41. Nie, M., Demeaux, J., Young, B. T., Heskett, D. R., Chen, Y., Bose, A., Woicik, J. C. & Lucht, B. L. Effect of Vinylene Carbonate and Fluoroethylene Carbonate on SEI Formation on Graphitic Anodes in Li-Ion Batteries. *J. Electrochem. Soc.* **162**, A7008–A7014 **(2015)**.

42. Schwenke, K. U., Solchenbach, S., Demeaux, J., Lucht, B. L. & Gasteiger, H. A. The Impact of CO_2 Evolved from VC and FEC during Formation of Graphite Anodes in Lithium-Ion Batteries. *J. Electrochem. Soc.* **166**, A2035–A2047 **(2019)**.

43. Petibon, R., Henry, E. C., Burns, J. C., Sinha, N. N. & Dahn, J. R. Comparative Study of Vinyl Ethylene Carbonate (VEC) and Vinylene Carbonate (VC) in $LiCoO_2$/Graphite Pouch Cells Using High Precision Coulometry and Electrochemical Impedance Spectroscopy Measurements on Symmetric Cells. *J. Electrochem. Soc.* **161**, A66–A74 **(2013)**.

44. Pritzl, D., Solchenbach, S., Wetjen, M. & Gasteiger, H. A. Analysis of Vinylene Carbonate (VC) as Additive in Graphite/$LiNi_{0.5}Mn_{1.5}O_4$ Cells. *J. Electrochem. Soc.* **164**, A2625–A2635 **(2017)**.

45. Wang, D. Y., Sinha, N. N., Burns, J. C., Aiken, C. P., Petibon, R. & Dahn, J. R. A Comparative Study of Vinylene Carbonate and Fluoroethylene Carbonate Additives for $LiCoO_2$/Graphite Pouch Cells. *J. Electrochem. Soc.* **161**, A467–A472 **(2014)**.

46. Teufl, T., Pritzl, D., Krieg, P., Strehle, B., Mendez, M. A. & Gasteiger, H. A. Operating EC-based Electrolytes with Li- and Mn-Rich NCMs: The Role of O_2-Release on the Choice of the Cyclic Carbonate. *J. Electrochem. Soc.* **167**, 110505 **(2020)**.

47. Wandt, J., Freiberg, A. T. S., Ogrodnik, A. & Gasteiger, H. A. Singlet oxygen evolution from layered transition metal oxide cathode materials and its implications for lithium-ion batteries. *Mater. Today* **21**, 825–833 **(2018)**.

48. Jung, R., Metzger, M., Maglia, F., Stinner, C. & Gasteiger, H. A. Chemical versus Electrochemical Electrolyte Oxidation on NMC111, NMC622, NMC811, LNMO, and Conductive Carbon. *J. Phys. Chem. Lett.* **8**, 4820–4825 **(2017)**.

49. Freiberg, A. T. S., Roos, M. K., Wandt, J., de Vivie-Riedle, R. & Gasteiger, H. A. Singlet Oxygen Reactivity with Carbonate Solvents Used for Li-Ion Battery Electrolytes. *J. Phys. Chem. A* **122**, 8828–8839 **(2018)**.

50. Ma, L., Glazier, S. L., Petibon, R., Xia, J., Peters, J. M., Liu, Q., Allen, J., Doig, R. N. C. & Dahn, J. R. A Guide to Ethylene Carbonate-Free Electrolyte Making for Li-Ion Cells. *J. Electrochem. Soc.* **164**, A5008–A5018 **(2017)**.

51. Nishi, Y. Lithium ion secondary batteries; past 10 years and the future. *J. Power Sources* **100**, 101–106 **(2001)**.

52. Schweidler, S., de Biasi, L., Schiele, A., Hartmann, P., Brezesinski, T. & Janek, J. Volume Changes of Graphite Anodes Revisited: A Combined Operando X-ray Diffraction and In Situ Pressure Analysis Study. *J. Phys. Chem. C* **122**, 8829–8835 **(2018)**.

53. Wandt, J., Jakes, P., Granwehr, J., Eichel, R.-A. & Gasteiger, H. A. Quantitative and time-resolved detection of lithium plating on graphite anodes in lithium ion batteries. *Mater. Today* **21**, 231–240 **(2018)**.

54. Qiu, B., Zhang, M., Wu, L., Wang, J., Xia, Y., Qian, D., Liu, H., Hy, S., Chen, Y., An, K., Zhu, Y., Liu, Z. & Meng, Y. S. Gas–solid interfacial modification of oxygen activity in layered oxide cathodes for lithium-ion batteries. *Nat. Commun.* **7**, 12108 **(2016)**.

55. Jung, H.-G., Jang, M. W., Hassoun, J., Sun, Y.-K. & Scrosati, B. A high-rate long-life $Li_4Ti_5O_{12}$/$Li[Ni_{0.45}Co_{0.1}Mn_{1.45}]O_4$ lithium-ion battery. *Nat. Commun.* **2**, 516 **(2011)**.

56. Nitta, N., Wu, F., Lee, J. T. & Yushin, G. Li-ion battery materials: present and future. *Mater. Today* **18**, 252–264 **(2015)**.

57. Bernhard, R., Meini, S. & Gasteiger, H. A. On-Line Electrochemical Mass Spectrometry Investigations on the Gassing Behavior of $Li_4Ti_5O_{12}$ Electrodes and Its Origins. *J. Electrochem. Soc.* **161**, A497–A505 **(2014)**.

58. Nitta, N. & Yushin, G. High-Capacity Anode Materials for Lithium-Ion Batteries: Choice of Elements and Structures for Active Particles. *Part. Part. Syst. Charact.* **31**, 317–336 **(2014)**.

59. Wetjen, M., Pritzl, D., Jung, R., Solchenbach, S., Ghadimi, R. & Gasteiger, H. A. Differentiating the Degradation Phenomena in Silicon-Graphite Electrodes for Lithium-Ion Batteries. *J. Electrochem. Soc.* **164**, A2840–A2852 **(2017)**.

60. Wetjen, M., Solchenbach, S., Pritzl, D., Hou, J., Tileli, V. & Gasteiger, H. A. Morphological Changes of Silicon Nanoparticles and the Influence of Cutoff Potentials in Silicon-Graphite Electrodes. *J. Electrochem. Soc.* **165**, A1503–A1514 **(2018)**.

61. Whittingham, M. S. Lithium Batteries and Cathode Materials. *Chem. Rev.* **104**, 4271–4302 **(2004)**.

62. Manthiram, A. A reflection on lithium-ion battery cathode chemistry. *Nat. Commun.* **11**, 1550 **(2020)**.

63. Delmas, C., Fouassier, C. & Hagenmuller, P. Structural classification and properties of the layered oxides. *Phys. B+C* **99**, 81–85 **(1980)**.

64. Wang, K., Wan, J., Xiang, Y., Zhu, J., Leng, Q., Wang, M., Xu, L. & Yang, Y. Recent advances and historical developments of high voltage lithium cobalt oxide materials for rechargeable Li-ion batteries. *J. Power Sources* **460**, 228062 **(2020)**.

65. Venkatraman, S., Shin, Y. & Manthiram, A. Phase Relationships and Structural and Chemical Stabilities of Charged $Li_{1-x}CoO_{2-\delta}$ and $Li_{1-x}Ni_{0.85}Co_{0.15}O_{2-\delta}$ Cathodes. *Electrochem. Solid-State Lett.* **6**, A9 **(2003)**.

66. Thackeray, M. M., David, W. I. F., Bruce, P. G. & Goodenough, J. B. Lithium insertion into manganese spinels. *Mater. Res. Bull.* **18**, 461–472 **(1983)**.

67. Thackeray, M. M. Manganese oxides for lithium batteries. *Prog. Solid State Chem.* **25**, 1–71 **(1997)**.

68. Jang, D. H., Shin, Y. J. & Oh, S. M. Dissolution of Spinel Oxides and Capacity Losses in 4 V $Li/Li_xMn_2O_4$ Cells. *J. Electrochem. Soc.* **143**, 2204–2211 **(1996)**.

69. Solchenbach, S., Hong, G., Freiberg, A. T. S., Jung, R. & Gasteiger, H. A. Electrolyte and SEI Decomposition Reactions of Transition Metal Ions Investigated by On-Line Electrochemical Mass Spectrometry. *J. Electrochem. Soc.* **165**, A3304–A3312 **(2018)**.

70. Amine, K., Tukamoto, H., Yasuda, H. & Fujita, Y. Preparation and electrochemical investigation of $LiMn_{2-x}Me_xO_4$ (Me: Ni, Fe, and x = 0.5, 1) cathode materials for secondary lithium batteries. *J. Power Sources* **68**, 604–608 **(1997)**.

71. Zhong, Q., Bonakdarpour, A., Zhang, M., Gao, Y. & Dahn, J. R. Synthesis and Electrochemistry of $LiNi_xMn_{2-x}O_4$. *J. Electrochem. Soc.* **144**, 205–213 **(1997)**.

72. Qiao, R., Wray, L. A., Kim, J.-H., Pieczonka, N. P. W., Harris, S. J. & Yang, W. Direct Experimental Probe of the Ni(II)/Ni(III)/Ni(IV) Redox Evolution in $LiNi_{0.5}Mn_{1.5}O_4$ Electrodes. *J. Phys. Chem. C* **119**, 27228–27233 **(2015)**.

73. Padhi, A. K., Nanjundaswamy, K. S. & Goodenough, J. B. Phospho-olivines as Positive-Electrode Materials for Rechargeable Lithium Batteries. *J. Electrochem. Soc.* **144**, 1188–1194 **(1997)**.

74. Julien, C., Mauger, A., Zaghib, K. & Groult, H. Comparative Issues of Cathode Materials for Li-Ion Batteries. *Inorganics* **2**, 132–154 **(2014)**.

75. Sides, C. R., Croce, F., Young, V. Y., Martin, C. R. & Scrosati, B. A High-Rate, Nanocomposite $LiFePO_4$/Carbon Cathode. *Electrochem. Solid-State Lett.* **8**, A484 **(2005)**.

76. Chen, Z., Zhu, H., Ji, S., Fakir, R. & Linkov, V. Influence of carbon sources on electrochemical performances of $LiFePO_4$/C composites. *Solid State Ionics* **179**, 1810–1815 **(2008)**.

77. Ahmed, S., Nelson, P. A., Gallagher, K. G., Susarla, N. & Dees, D. W. Cost and energy demand of producing nickel manganese cobalt cathode material for lithium ion batteries. *J. Power Sources* **342**, 733–740 **(2017)**.

78. Liu, Z., Yu, A. & Lee, J. Y. Synthesis and characterization of $LiNi_{1-x-y}Co_xMn_yO_2$ as the cathode materials of secondary lithium batteries. *J. Power Sources* **81**–

82, 416–419 **(1999)**.

79. Jang, Y.-I., Huang, B., Wang, H., Maskaly, G. R., Ceder, G., Sadoway, D. R., Chiang, Y.-M., Liu, H. & Tamura, H. Synthesis and characterization of $LiAl_yCo_{1-y}O_2$ and $LiAl_yNi_{1-y}O_2$. *J. Power Sources* **81–82**, 589–593 **(1999)**.

80. Myung, S.-T., Maglia, F., Park, K.-J., Yoon, C. S., Lamp, P., Kim, S.-J. & Sun, Y.-K. Nickel-Rich Layered Cathode Materials for Automotive Lithium-Ion Batteries: Achievements and Perspectives. *ACS Energy Lett.* **2**, 196–223 **(2017)**.

81. Yoon, C. S., Park, K.-J., Kim, U.-H., Kang, K. H., Ryu, H.-H. & Sun, Y.-K. High-Energy Ni-Rich $Li[Ni_xCo_yMn_{1-x-y}]O_2$ Cathodes via Compositional Partitioning for Next-Generation Electric Vehicles. *Chem. Mater.* **29**, 10436–10445 **(2017)**.

82. Jung, R., Strobl, P., Maglia, F., Stinner, C. & Gasteiger, H. A. Temperature Dependence of Oxygen Release from $LiNi_{0.6}Mn_{0.2}Co_{0.2}O_2$ (NMC622) Cathode Materials for Li-Ion Batteries. *J. Electrochem. Soc.* **165**, A2869–A2879 **(2018)**.

83. Abraham, D. P., Twesten, R. D., Balasubramanian, M., Kropf, J., Fischer, D., McBreen, J., Petrov, I. & Amine, K. Microscopy and Spectroscopy of Lithium Nickel Oxide-Based Particles Used in High Power Lithium-Ion Cells. *J. Electrochem. Soc.* **150**, A1450 **(2003)**.

84. Watanabe, S., Kinoshita, M., Hosokawa, T., Morigaki, K. & Nakura, K. Capacity fade of $LiAl_yNi_{1-x-y}Co_xO_2$ cathode for lithium-ion batteries during accelerated calendar and cycle life tests (surface analysis of $LiAl_yNi_{1-x-y}Co_xO_2$ cathode after cycle tests in restricted depth of discharge ranges). *J. Power Sources* **258**, 210–217 **(2014)**.

85. Li, W., Asl, H. Y., Xie, Q. & Manthiram, A. Collapse of $LiNi_{1-x-y}Co_xMn_yO_2$ Lattice at Deep Charge Irrespective of Nickel Content in Lithium-Ion Batteries. *J. Am. Chem. Soc.* **141**, 5097–5101 **(2019)**.

86. Li, H., Liu, A., Zhang, N., Wang, Y., Yin, S., Wu, H. & Dahn, J. R. An Unavoidable Challenge for Ni-Rich Positive Electrode Materials for Lithium-Ion Batteries. *Chem. Mater.* **31**, 7574–7583 **(2019)**.

87. Park, K.-J., Hwang, J.-Y., Ryu, H.-H., Maglia, F., Kim, S.-J., Lamp, P., Yoon, C. S. & Sun, Y.-K. Degradation Mechanism of Ni-Enriched NCA Cathode for Lithium Batteries: Are Microcracks Really Critical? *ACS Energy Lett.* **4**, 1394–1400 **(2019)**.

88. Liu, H., Wolf, M., Karki, K., Yu, Y.-S., Stach, E. A., Cabana, J., Chapman, K. W. & Chupas, P. J. Intergranular Cracking as a Major Cause of Long-Term Capacity Fading of Layered Cathodes. *Nano Lett.* **17**, 3452–3457 **(2017)**.

89. Schweidler, S., de Biasi, L., Garcia, G., Mazilkin, A., Hartmann, P., Brezesinski, T. & Janek, J. Investigation into Mechanical Degradation and Fatigue of High-Ni NCM Cathode Material: A Long-Term Cycling Study of Full Cells. *ACS Appl. Energy Mater.* **2**, 7375–7384 **(2019)**.

90. Oswald, S., Pritzl, D., Wetjen, M. & Gasteiger, H. A. Novel Method for Monitoring the Electrochemical Capacitance by In Situ Impedance Spectroscopy as Indicator for Particle Cracking of Nickel-Rich NCMs: Part I. Theory and Validation. *J. Electrochem. Soc.* **167**, 100511 **(2020)**.

91. Makimura, Y., Sasaki, T., Nonaka, T., Nishimura, Y. F., Uyama, T., Okuda, C., Itou, Y. & Takeuchi, Y. Factors affecting cycling life of $LiNi_{0.8}Co_{0.15}Al_{0.05}O_2$ for lithium-ion batteries. *J. Mater. Chem. A* **4**, 8350–8358 **(2016)**.

92. Liu, W., Oh, P., Liu, X., Lee, M.-J., Cho, W., Chae, S., Kim, Y. & Cho, J. Nickel-Rich Layered Lithium Transition-Metal Oxide for High-Energy Lithium-Ion Batteries. *Angew. Chemie Int. Ed.* **54**, 4440–4457 **(2015)**.

93. Li, W., Liu, X., Xie, Q., You, Y., Chi, M. & Manthiram, A. Long-Term Cyclability of NCM-811 at High Voltages in Lithium-Ion Batteries: an In-Depth Diagnostic Study. *Chem. Mater.* **32**, 7796–7804 **(2020)**.

94. Harlow, J. E., Ma, X., Li, J., Logan, E., Liu, Y., Zhang, N., Ma, L., Glazier, S. L., Cormier, M. M. E., Genovese, M., Buteau, S., Cameron, A., Stark, J. E. & Dahn, J. R. A Wide Range of Testing Results on an Excellent Lithium-Ion Cell Chemistry to be used as Benchmarks for New Battery Technologies. *J. Electrochem. Soc.* **166**, A3031–A3044 **(2019)**.

95. Pillot, C. The Rechargeable Battery Market and Main Trends 2018-2030. *accessed April 9, 2021,* https://www.google.com/url?sa=t&rct=j&q=&esrc=s&source=web&cd=&ved=2ahUKEwiO3uqaxPHvAhUQgP0HHauXATIQFjABegQIBBAD&url=https%253A%252F%252Fwww.bpifrance.fr%252Fcontent%252Fdownload%252F76854%252F831358%252Ffile%252F02%252520-%252520Presentation%252520Avicen.

96. LG to supply NCMA battery for Tesla next year. *accessed April 10, 2021,* https://m.koreatimes.co.kr/pages/article.asp?newsIdx=301037.

97. Kim, U.-H., Kuo, L.-Y., Kaghazchi, P., Yoon, C. S. & Sun, Y.-K. Quaternary Layered Ni-Rich NCMA Cathode for Lithium-Ion Batteries. *ACS Energy Lett.* **4**, 576–582 **(2019)**.

98. Dahn, J. Structure and electrochemistry of $Li_{1\pm y}NiO_2$ and a new Li_2NiO_2 phase with the $Ni(OH)_2$ structure. *Solid State Ionics* **44**, 87–97 **(1990)**.

99. Bianchini, M., Roca-Ayats, M., Hartmann, P., Brezesinski, T. & Janek, J. There and back again - The journey of $LiNiO_2$ as cathode active material. *Angew. Chemie Int. Ed.* **58**, 10434-10458 **(2018)**.

100. Li, H., Cormier, M., Zhang, N., Inglis, J., Li, J. & Dahn, J. R. Is Cobalt Needed in Ni-Rich Positive Electrode Materials for Lithium Ion Batteries? *J. Electrochem. Soc.* **166**, A429–A439 **(2019)**.

101. Kitsche, D., Schweidler, S., Mazilkin, A., Geßwein, H., Fauth, F., Suard, E., Hartmann, P., Brezesinski, T., Janek, J. & Bianchini, M. The effect of gallium substitution on the structure and electrochemical performance of $LiNiO_2$ in

lithium-ion batteries. *Mater. Adv.* **1**, 639-647 **(2020)**.

102. Volkswagen Power Day. *accessed April 10, 2021,* https://www.volkswagenag.com/presence/investorrelation/publications/presentations/2021/03/2021-03-15_PowerDayVWGroup.pdf.

103. Manganese-rich cathode chemistries: The once and future king? *accessed April 10, 2021,* https://cellsiders.substack.com/p/manganese-rich-cathode-chemistries.

104. Xiao, J., Chernova, N. A. & Whittingham, M. S. Layered Mixed Transition Metal Oxide Cathodes with Reduced Cobalt Content for Lithium Ion Batteries. *Chem. Mater.* **20**, 7454–7464 **(2008)**.

105. Monconduit, L., Croguennec, L. & Dedryvère, R. *Electrodes for Li-Ion Batteries*. **(John Wiley & Sons, Inc., 2015)**.

106. Chappel, E., Núñez-Regueiro, M. ., Chouteau, G., Sulpice, A. & Delmas, C. Low field magnetism and cationic distribution in quasi-stoichiometric $Li_{1-x}Ni_{1+x}O_2$. *Solid State Commun.* **119**, 83–87 **(2001)**.

107. Kurzhals, P., Riewald, F., Bianchini, M., Sommer, H., Gasteiger, H. & Janek, J. The $LiNiO_2$ Cathode Active Material: A Comprehensive Study of Calcination Conditions and their Correlation with Physicochemical Properties. Part I. Structural Chemistry. *J. Electrochem. Soc.* **(2021)**.

108. Yin, L., Li, Z., Mattei, G. S., Zheng, J., Zhao, W., Omenya, F., Fang, C., Li, W., Li, J., Xie, Q., Erickson, E. M., Zhang, J.-G., Whittingham, M. S., Meng, Y. S., Manthiram, A. & Khalifah, P. G. Thermodynamics of Antisite Defects in Layered NMC Cathodes: Systematic Insights from High-Precision Powder Diffraction Analyses. *Chem. Mater.* **32**, 1002–1010 **(2020)**.

109. Thackeray, M. M., Kang, S.-H., Johnson, C. S., Vaughey, J. T., Benedek, R. & Hackney, S. A. Li_2MnO_3-stabilized $LiMO_2$ (M = Mn, Ni, Co) electrodes for lithium-ion batteries. *J. Mater. Chem.* **17**, 3112 **(2007)**.

110. Bianchini, M., Schiele, A., Schweidler, S., Sicolo, S., Fauth, F., Suard, E., Indris, S., Mazilkin, A., Nagel, P., Schuppler, S., Merz, M., Hartmann, P., Brezesinski, T. & Janek, J. From $LiNiO_2$ to Li_2NiO_3 : Synthesis, Structures and Electrochemical Mechanisms in Li-Rich Nickel Oxides. *Chem. Mater.* **32**, 9211–9227 **(2020)**.

111. Sathiya, M., Rousse, G., Ramesha, K., Laisa, C. P., Vezin, H., Sougrati, M. T., Doublet, M.-L., Foix, D., Gonbeau, D., Walker, W., Prakash, A. S., Ben Hassine, M., Dupont, L. & Tarascon, J.-M. Reversible anionic redox chemistry in high-capacity layered-oxide electrodes. *Nat. Mater.* **12**, 827–835 **(2013)**.

112. Hong, J., Gent, W. E., Xiao, P., Lim, K., Seo, D.-H., Wu, J., Csernica, P. M., Takacs, C. J., Nordlund, D., Sun, C.-J., Stone, K. H., Passarello, D., Yang, W., Prendergast, D., Ceder, G., Toney, M. F. & Chueh, W. C. Metal–oxygen decoordination stabilizes anion redox in Li-rich oxides. *Nat. Mater.* **18**, 256–265 **(2019)**.

113. Rossouw, M. & Thackeray, M. Lithium manganese oxides from Li_2MnO_3 for rechargeable lithium battery applications. *Mater. Res. Bull.* **26**, 463–473 **(1991)**.

114. Kalyani, P., Chitra, S., Mohan, T. & Gopukumar, S. Lithium metal rechargeable cells using Li_2MnO_3 as the positive electrode. *J. Power Sources* **80**, 103–106 **(1999)**.

115. Robertson, A. D. & Bruce, P. G. Mechanism of Electrochemical Activity in Li_2MnO_3. *Chem. Mater.* **15**, 1984–1992 **(2003)**.

116. Bréger, J., Jiang, M., Dupré, N., Meng, Y. S., Shao-Horn, Y., Ceder, G. & Grey, C. P. High-resolution X-ray diffraction, DIFFaX, NMR and first principles study of disorder in the Li_2MnO_3–$Li[Ni_{1/2}Mn_{1/2}]O_2$ solid solution. *J. Solid State Chem.* **178**, 2575–2585 **(2005)**.

117. Yu, D. Y. W., Yanagida, K., Kato, Y. & Nakamura, H. Electrochemical Activities in Li_2MnO_3. *J. Electrochem. Soc.* **156**, A417 **(2009)**.

118. Serrano-Sevillano, J., Carlier, D., Saracibar, A., Lopez del Amo, J. M. & Casas-Cabanas, M. DFT-Assisted Solid-State NMR Characterization of Defects in Li_2MnO_3. *Inorg. Chem.* **58**, 8347–8356 **(2019)**.

119. Rana, J., Papp, J. K., Lebens-Higgins, Z., Zuba, M., Kaufman, L. A., Goel, A., Schmuch, R., Winter, M., Whittingham, M. S., Yang, W., McCloskey, B. D. & Piper, L. F. J. Quantifying the Capacity Contributions during Activation of Li_2MnO_3. *ACS Energy Lett.* **5**, 634–641 **(2020)**.

120. Numata, K., Sakaki, C. & Yamanaka, S. Synthesis of Solid Solutions in a System of $LiCoO_2$-Li_2MnO_3 for Cathode Materials of Secondary Lithium Batteries. *Chem. Lett.* **26**, 725–726 **(1997)**.

121. Numata, K. Synthesis and characterization of layer structured solid solutions in the system of $LiCoO_2$–Li_2MnO_3. *Solid State Ionics* **117**, 257–263 **(1999)**.

122. Lu, Z., MacNeil, D. D. & Dahn, J. R. Layered Cathode Materials $Li[Ni_xLi_{(1/3-2x/3)}Mn_{(2/3-x/3)}]O_2$ for Lithium-Ion Batteries. *Electrochem. Solid-State Lett.* **4**, A191 **(2001)**.

123. Lu, Z., Beaulieu, L. Y., Donaberger, R. A., Thomas, C. L. & Dahn, J. R. Synthesis, Structure, and Electrochemical Behavior of $Li[Ni_xLi_{1/3-2x/3}Mn_{2/3-x/3}]O_2$. *J. Electrochem. Soc.* **149**, A778 **(2002)**.

124. Lu, Z. & Dahn, J. R. Understanding the Anomalous Capacity of $Li/Li[Ni_xLi_{(1/3-2x/3)}Mn_{(2/3-x/3)}]O_2$ Cells Using In Situ X-Ray Diffraction and Electrochemical Studies. *J. Electrochem. Soc.* **149**, A815 **(2002)**.

125. Lu, Z. & Dahn, J. R. In Situ and Ex Situ XRD Investigation of $Li[Cr_xLi_{1/3-x/3}Mn_{2/3-2x/3}]O_2$ (x=1/3) Cathode Material. *J. Electrochem. Soc.* **150**, A1044 **(2003)**.

126. Park, Y. J., Hong, Y.-S., Wu, X., Kim, M. G., Ryu, K. S. & Chang, S. H. Synthesis and Electrochemical Characteristics of $Li[Co_xLi_{(1/3-x/3)}Mn_{(2/3-2x/3)}]O_2$ Compounds. *J. Electrochem. Soc.* **151**, A720 **(2004)**.

127. Ammundsen, B. & Paulsen, J. Novel Lithium-Ion Cathode Materials Based on Layered Manganese Oxides. *Adv. Mater.* **13**, 943–956 **(2001)**.

128. Yu, L., Yang, H., Ai, X. & Cao, Y. Structural and Electrochemical Characterization of Nanocrystalline $Li[Li_{0.12}Ni_{0.32}Mn_{0.56}]O_2$ Synthesized by a Polymer-Pyrolysis Route. *J. Phys. Chem. B* **109**, 1148–1154 **(2005)**.

129. Johnson, C. S., Kim, J.-S., Lefief, C., Li, N., Vaughey, J. T. & Thackeray, M. M. The significance of the Li_2MnO_3 component in 'composite' x $Li_2MnO_3 \cdot (1-x)$ $LiMn_{0.5}Ni_{0.5}O_2$ electrodes. *Electrochem. commun.* **6**, 1085–1091 **(2004)**.

130. Lu, Z., Chen, Z. & Dahn, J. R. Lack of Cation Clustering in $Li[Ni_xLi_{1/3-2x/3}Mn_{2/3-x/3}]O_2$ ($0 < x \leq 1/2$) and $Li[Cr_xLi_{(1-x)/3}Mn_{(2-2x)/3}]O_2$ ($0 < x < 1$). *Chem. Mater.* **15**, 3214–3220 **(2003)**.

131. Hu, S., Pillai, A. S., Liang, G., Pang, W. K., Wang, H., Li, Q. & Guo, Z. Li-Rich Layered Oxides and Their Practical Challenges: Recent Progress and Perspectives. *Electrochem. Energy Rev.* **2**, 277–311 **(2019)**.

132. Mohanty, D., Kalnaus, S., Meisner, R. A., Rhodes, K. J., Li, J., Payzant, E. A., Wood, D. L. & Daniel, C. Structural transformation of a lithium-rich $Li_{1.2}Co_{0.1}Mn_{0.55}Ni_{0.15}O_2$ cathode during high voltage cycling resolved by in situ X-ray diffraction. *J. Power Sources* **229**, 239–248 **(2013)**.

133. Pan, C., Lee, Y. J., Ammundsen, B. & Grey, C. P. ^{6}Li MAS NMR Studies of the Local Structure and Electrochemical Properties of Cr-doped Lithium Manganese and Lithium Cobalt Oxide Cathode Materials for Lithium-Ion Batteries. *Chem. Mater.* **14**, 2289–2299 **(2002)**.

134. Yoon, W.-S., Kim, N., Yang, X.-Q., McBreen, J. & Grey, C. P. ^{6}Li MAS NMR and in situ X-ray studies of lithium nickel manganese oxides. *J. Power Sources* **119–121**, 649–653 **(2003)**.

135. Bareño, J., Balasubramanian, M., Kang, S. H., Wen, J. G., Lei, C. H., Pol, S. V., Petrov, I. & Abraham, D. P. Long-Range and Local Structure in the Layered Oxide $Li_{1.2}Co_{0.4}Mn_{0.4}O_2$. *Chem. Mater.* **23**, 2039–2050 **(2011)**.

136. Jarvis, K. A., Deng, Z., Allard, L. F., Manthiram, A. & Ferreira, P. J. Atomic Structure of a Lithium-Rich Layered Oxide Material for Lithium-Ion Batteries: Evidence of a Solid Solution. *Chem. Mater.* **23**, 3614–3621 **(2011)**.

137. Yu, H., Ishikawa, R., So, Y.-G., Shibata, N., Kudo, T., Zhou, H. & Ikuhara, Y. Direct Atomic-Resolution Observation of Two Phases in the $Li_{1.2}Mn_{0.567}Ni_{0.166}Co_{0.067}O_2$ Cathode Material for Lithium-Ion Batteries. *Angew. Chemie Int. Ed.* **52**, 5969–5973 **(2013)**.

138. McCalla, E., Lowartz, C. M., Brown, C. R. & Dahn, J. R. Formation of Layered–

Layered Composites in the Li–Co–Mn Oxide Pseudoternary System during Slow Cooling. *Chem. Mater.* **25**, 912–918 **(2013)**.

139. McCalla, E., Rowe, A. W., Shunmugasundaram, R. & Dahn, J. R. Structural Study of the Li–Mn–Ni Oxide Pseudoternary System of Interest for Positive Electrodes of Li-Ion Batteries. *Chem. Mater.* **25**, 989–999 **(2013)**.

140. McCalla, E., Rowe, A. W., Camardese, J. & Dahn, J. R. The Role of Metal Site Vacancies in Promoting Li–Mn–Ni–O Layered Solid Solutions. *Chem. Mater.* **25**, 2716–2721 **(2013)**.

141. Hong, J., Gwon, H., Jung, S.-K., Ku, K. & Kang, K. Review—Lithium-Excess Layered Cathodes for Lithium Rechargeable Batteries. *J. Electrochem. Soc.* **162**, A2447–A2467 **(2015)**.

142. Luo, K., Roberts, M. R., Hao, R., Guerrini, N., Pickup, D. M., Liu, Y.-S., Edström, K., Guo, J., Chadwick, A. V., Duda, L. C. & Bruce, P. G. Charge-compensation in 3d-transition-metal-oxide intercalation cathodes through the generation of localized electron holes on oxygen. *Nat. Chem.* **8**, 684–691 **(2016)**.

143. Assat, G., Foix, D., Delacourt, C., Iadecola, A., Dedryvère, R. & Tarascon, J.-M. Fundamental interplay between anionic/cationic redox governing the kinetics and thermodynamics of lithium-rich cathodes. *Nat. Commun.* **8**, 2219 **(2017)**.

144. Croy, J. R., Gallagher, K. G., Balasubramanian, M., Chen, Z., Ren, Y., Kim, D., Kang, S.-H., Dees, D. W. & Thackeray, M. M. Examining Hysteresis in Composite x $Li_2MnO_3 \cdot$ (1–x) $LiMO_2$ Cathode Structures. *J. Phys. Chem. C* **117**, 6525–6536 **(2013)**.

145. Teufl, T., Pritzl, D., Solchenbach, S., Gasteiger, H. A. & Mendez, M. A. Editors' Choice—State of Charge Dependent Resistance Build-Up in Li- and Mn-Rich Layered Oxides during Lithium Extraction and Insertion. *J. Electrochem. Soc.* **166**, A1275–A1284 **(2019)**.

146. Radin, M. D., Vinckeviciute, J., Seshadri, R. & Van der Ven, A. Manganese oxidation as the origin of the anomalous capacity of Mn-containing Li-excess cathode materials. *Nat. Energy* **4**, 639–646 **(2019)**.

147. Muhammad, S., Kim, H., Kim, Y., Kim, D., Song, J. H., Yoon, J., Park, J.-H., Ahn, S.-J., Kang, S.-H., Thackeray, M. M. & Yoon, W.-S. Evidence of reversible oxygen participation in anomalously high capacity Li- and Mn-rich cathodes for Li-ion batteries. *Nano Energy* **21**, 172–184 **(2016)**.

148. Yu, H., Kim, H., Wang, Y., He, P., Asakura, D., Nakamura, Y. & Zhou, H. High-energy 'composite' layered manganese-rich cathode materials via controlling Li_2MnO_3 phase activation for lithium-ion batteries. *Phys. Chem. Chem. Phys.* **14**, 6584 **(2012)**.

149. Hy, S., Felix, F., Rick, J., Su, W.-N. & Hwang, B. J. Direct In situ Observation of Li_2O Evolution on Li-Rich High-Capacity Cathode Material,

$Li[Ni_xLi_{(1-2x)/3}Mn_{(2-x)/3}]O_2$ ($0 \leq x \leq 0.5$). *J. Am. Chem. Soc.* **136**, 999–1007 **(2014)**.

150. Mohanty, D., Li, J., Abraham, D. P., Huq, A., Payzant, E. A., Wood, D. L. & Daniel, C. Unraveling the Voltage-Fade Mechanism in High-Energy-Density Lithium-Ion Batteries: Origin of the Tetrahedral Cations for Spinel Conversion. *Chem. Mater.* **26**, 6272–6280 **(2014)**.

151. Armstrong, A. R., Holzapfel, M., Novák, P., Johnson, C. S., Kang, S.-H., Thackeray, M. M. & Bruce, P. G. Demonstrating Oxygen Loss and Associated Structural Reorganization in the Lithium Battery Cathode $Li[Ni_{0.2}Li_{0.2}Mn_{0.6}]O_2$. *J. Am. Chem. Soc.* **128**, 8694–8698 **(2006)**.

152. La Mantia, F., Rosciano, F., Tran, N. & Novák, P. Direct evidence of oxygen evolution from $Li_{1+x}(Ni_{1/3}Mn_{1/3}Co_{1/3})_{1-x}O_2$ at high potentials. *J. Appl. Electrochem.* **38**, 893–896 **(2008)**.

153. Zheng, J. M., Zhang, Z. R., Wu, X. B., Dong, Z. X., Zhu, Z. & Yang, Y. The Effects of AlF_3 Coating on the Performance of $Li[Li_{0.2}Mn_{0.54}Ni_{0.13}Co_{0.13}]O_2$ Positive Electrode Material for Lithium-Ion Battery. *J. Electrochem. Soc.* **155**, A775 **(2008)**.

154. Castel, E., Berg, E. J., El Kazzi, M., Novák, P. & Villevieille, C. Differential Electrochemical Mass Spectrometry Study of the Interface of x $Li_2MnO_3 \cdot$ (1-x) $LiMO_2$ (M = Ni, Co, and Mn) Material as a Positive Electrode in Li-Ion Batteries. *Chem. Mater.* **26**, 5051–5057 **(2014)**.

155. Strehle, B., Kleiner, K., Jung, R., Chesneau, F., Mendez, M., Gasteiger, H. A. & Piana, M. The Role of Oxygen Release from Li- and Mn-Rich Layered Oxides during the First Cycles Investigated by On-Line Electrochemical Mass Spectrometry. *J. Electrochem. Soc.* **164**, A400–A406 **(2017)**.

156. Assat, G. & Tarascon, J.-M. Fundamental understanding and practical challenges of anionic redox activity in Li-ion batteries. *Nat. Energy* **3**, 373–386 **(2018)**.

157. Seo, D.-H., Lee, J., Urban, A., Malik, R., Kang, S. & Ceder, G. The structural and chemical origin of the oxygen redox activity in layered and cation-disordered Li-excess cathode materials. *Nat. Chem.* **8**, 692–697 **(2016)**.

158. Xie, Y., Saubanère, M. & Doublet, M.-L. Requirements for reversible extra-capacity in Li-rich layered oxides for Li-ion batteries. *Energy Environ. Sci.* **10**, 266–274 **(2017)**.

159. Gent, W. E., Lim, K., Liang, Y., Li, Q., Barnes, T., Ahn, S.-J., Stone, K. H., McIntire, M., Hong, J., Song, J. H., *et al.* Coupling between oxygen redox and cation migration explains unusual electrochemistry in lithium-rich layered oxides. *Nat. Commun.* **8**, 2091 **(2017)**.

160. Qian, D., Xu, B., Chi, M. & Meng, Y. S. Uncovering the roles of oxygen vacancies in cation migration in lithium excess layered oxides. *Phys. Chem. Chem. Phys.* **16**, 14665–14668 **(2014)**.

161. Boulineau, A., Simonin, L., Colin, J.-F., Bourbon, C. & Patoux, S. First Evidence of Manganese–Nickel Segregation and Densification upon Cycling in Li-Rich Layered Oxides for Lithium Batteries. *Nano Lett.* **13**, 3857–3863 **(2013)**.

162. Genevois, C., Koga, H., Croguennec, L., Ménétrier, M., Delmas, C. & Weill, F. Insight into the Atomic Structure of Cycled Lithium-Rich Layered Oxide $Li_{1.20}Mn_{0.54}Co_{0.13}Ni_{0.13}O_2$ Using HAADF STEM and Electron Nanodiffraction. *J. Phys. Chem. C* **119**, 75–83 **(2015)**.

163. Shukla, A. K., Ramasse, Q. M., Ophus, C., Duncan, H., Hage, F. & Chen, G. Unravelling structural ambiguities in lithium- and manganese-rich transition metal oxides. *Nat. Commun.* **6**, 8711 **(2015)**.

164. Carroll, K. J., Qian, D., Fell, C., Calvin, S., Veith, G. M., Chi, M., Baggetto, L. & Meng, Y. S. Probing the electrode/electrolyte interface in the lithium excess layered oxide $Li_{1.2}Ni_{0.2}Mn_{0.6}O_2$. *Phys. Chem. Chem. Phys.* **15**, 11128 **(2013)**.

165. Jung, R., Morasch, R., Karayaylali, P., Phillips, K., Maglia, F., Stinner, C., Shao-Horn, Y. & Gasteiger, H. A. Effect of Ambient Storage on the Degradation of Ni-Rich Positive Electrode Materials (NMC811) for Li-Ion Batteries. *J. Electrochem. Soc.* **165**, A132–A141 **(2018)**.

166. Schreiner, D., Zünd, T., Günter, F. J., Kraft, L., Stumper, B., Linsenmann, F., Schüßler, M., Wilhelm, R., Jossen, A., Reinhart, G. & Gasteiger, H. A. Comparative Evaluation of LMR-NCM and NCA Cathode Active Materials in Multilayer Lithium-Ion Pouch Cells: Part I. Production, Electrode Characterization, and Formation. *J. Electrochem. Soc.* **168**, 030507 **(2021)**.

167. Kraft, L., Zünd, T., Schreiner, D., Wilhelm, R., Günter, F. J., Reinhart, G., Gasteiger, H. A. & Jossen, A. Comparative Evaluation of LMR-NCM and NCA Cathode Active Materials in Multilayer Lithium-Ion Pouch Cells: Part II. Rate Capability, Long-Term Stability, and Thermal Behavior. *J. Electrochem. Soc.* **168**, 020537 **(2021)**.

168. Hong, J., Lim, H.-D., Lee, M., Kim, S.-W., Kim, H., Oh, S.-T., Chung, G.-C. & Kang, K. Critical Role of Oxygen Evolved from Layered Li–Excess Metal Oxides in Lithium Rechargeable Batteries. *Chem. Mater.* **24**, 2692–2697 **(2012)**.

169. Guéguen, A., Streich, D., He, M., Mendez, M., Chesneau, F. F., Novák, P. & Berg, E. J. Decomposition of $LiPF_6$ in High Energy Lithium-Ion Batteries Studied with Online Electrochemical Mass Spectrometry. *J. Electrochem. Soc.* **163**, A1095–A1100 **(2016)**.

170. Kim, K., Park, I., Ha, S.-Y., Kim, Y., Woo, M.-H., Jeong, M.-H., Shin, W. C., Ue, M., Hong, S. Y. & Choi, N.-S. Understanding the thermal instability of fluoroethylene carbonate in $LiPF_6$-based electrolytes for lithium ion batteries. *Electrochim. Acta* **225**, 358–368 **(2017)**.

171. Buchberger, I., Seidlmayer, S., Pokharel, A., Piana, M., Hattendorff, J., Kudejova, P., Gilles, R. & Gasteiger, H. A. Aging Analysis of Graphite/$LiNi_{1/3}Mn_{1/3}Co_{1/3}O_2$ Cells Using XRD, PGAA, and AC Impedance. *J. Electrochem. Soc.* **162**, A2737–

A2746 **(2015)**.

172. Wandt, J., Freiberg, A., Thomas, R., Gorlin, Y., Siebel, A., Jung, R., Gasteiger, H. A. & Tromp, M. Transition metal dissolution and deposition in Li-ion batteries investigated by operando X-ray absorption spectroscopy. *J. Mater. Chem. A* **4**, 18300–18305 **(2016)**.

173. Gilbert, J. A., Shkrob, I. A. & Abraham, D. P. Transition Metal Dissolution, Ion Migration, Electrocatalytic Reduction and Capacity Loss in Lithium-Ion Full Cells. *J. Electrochem. Soc.* **164**, A389–A399 **(2017)**.

174. Jung, R., Linsenmann, F., Thomas, R., Wandt, J., Solchenbach, S., Maglia, F., Stinner, C., Tromp, M. & Gasteiger, H. A. Nickel, Manganese, and Cobalt Dissolution from Ni-Rich NMC and Their Effects on NMC622-Graphite Cells. *J. Electrochem. Soc.* **166**, A378–A389 **(2019)**.

175. Pan, H., Zhang, S., Chen, J., Gao, M., Liu, Y., Zhu, T. & Jiang, Y. Li- and Mn-rich layered oxide cathode materials for lithium-ion batteries: a review from fundamentals to research progress and applications. *Mol. Syst. Des. Eng.* **3**, 748–803 **(2018)**.

176. Li, J., Harlow, J., Stakheiko, N., Zhang, N., Paulsen, J. & Dahn, J. Dependence of Cell Failure on Cut-Off Voltage Ranges and Observation of Kinetic Hindrance in $LiNi_{0.8}Co_{0.15}Al_{0.05}O_2$. *J. Electrochem. Soc.* **165**, A2682–A2695 **(2018)**.

177. Friedrich, F., Strehle, B., Freiberg, A. T. S., Kleiner, K., Day, S. J., Erk, C., Piana, M. & Gasteiger, H. A. Capacity fading mechanisms of NCM-811 cathodes in lithium-ion batteries studied by X-ray diffraction and other diagnostics. *J. Electrochem. Soc.* **166**, **(2019)**.

178. Liu, H., Chen, Y., Hy, S., An, K., Venkatachalam, S., Qian, D., Zhang, M. & Meng, Y. S. Operando Lithium Dynamics in the Li-Rich Layered Oxide Cathode Material via Neutron Diffraction. *Adv. Energy Mater.* **6**, 1502143 **(2016)**.

179. Metzger, M., Strehle, B., Solchenbach, S. & Gasteiger, H. A. Hydrolysis of Ethylene Carbonate with Water and Hydroxide under Battery Operating Conditions. *J. Electrochem. Soc.* **163**, A1219–A1225 **(2016)**.

180. Sicklinger, J., Beyer, H., Hartmann, L., Riewald, F., Sedlmeier, C. & Gasteiger, H. A. SO_3 Treatment of Lithium- and Manganese-Rich NCMs for Li-Ion Batteries: Enhanced Robustness towards Humid Ambient Air and Improved Full-Cell Performance. *J. Electrochem. Soc.* **167**, 130507 **(2020)**.

181. Ren, D., Shen, Y., Yang, Y., Shen, L., Levin, B. D. A., Yu, Y., Muller, D. A. & Abruña, H. D. Systematic Optimization of Battery Materials: Key Parameter Optimization for the Scalable Synthesis of Uniform, High-Energy, and High Stability $LiNi_{0.6}Mn_{0.2}Co_{0.2}O_2$ Cathode Material for Lithium-Ion Batteries. *ACS Appl. Mater. Interfaces* **9**, 35811–35819 **(2017)**.

182. Hy, S., Liu, H., Zhang, M., Qian, D., Hwang, B.-J. & Meng, Y. S. Performance and design considerations for lithium excess layered oxide positive electrode

materials for lithium ion batteries. *Energy Environ. Sci.* **9**, 1931–1954 **(2016)**.

183. Zhang, Y., Hou, P., Zhou, E., Shi, X., Wang, X., Song, D., Guo, J. & Zhang, L. Pre-heat treatment of carbonate precursor firstly in nitrogen and then oxygen atmospheres: A new procedure to improve tap density of high-performance cathode material $Li_{1.167}(Ni_{0.139}Co_{0.139}Mn_{0.556})O_2$ for lithium ion batteries. *J. Power Sources* **292**, 58–65 **(2015)**.

184. Mao, W., Ai, G., Dai, Y., Fu, Y., Song, X., Lopez, H. & Battaglia, V. Nature of the Impedance at Low States of Charge for High-Capacity, Lithium and Manganese-Rich Cathode Materials. *J. Electrochem. Soc.* **163**, A3091–A3098 **(2016)**.

185. Dees, D. W., Abraham, D. P., Lu, W., Gallagher, K. G., Bettge, M. & Jansen, A. N. Electrochemical Modeling and Performance of a Lithium- and Manganese-Rich Layered Transition-Metal Oxide Positive Electrode. *J. Electrochem. Soc.* **162**, A559–A572 **(2015)**.

186. Ohzuku, T., Nagayama, M., Tsuji, K. & Ariyoshi, K. High-capacity lithium insertion materials of lithium nickel manganese oxides for advanced lithium-ion batteries: toward rechargeable capacity more than 300 mA h g^{-1}. *J. Mater. Chem.* **21**, 10179 **(2011)**.

187. Dogan, F., Long, B. R., Croy, J. R., Gallagher, K. G., Iddir, H., Russell, J. T., Balasubramanian, M. & Key, B. Re-entrant Lithium Local Environments and Defect Driven Electrochemistry of Li- and Mn-Rich Li-Ion Battery Cathodes. *J. Am. Chem. Soc.* **137**, 2328–2335 **(2015)**.

188. Gallagher, K. G., Croy, J. R., Balasubramanian, M., Bettge, M., Abraham, D. P., Burrell, A. K. & Thackeray, M. M. Correlating hysteresis and voltage fade in lithium- and manganese-rich layered transition-metal oxide electrodes. *Electrochem. commun.* **33**, 96–98 **(2013)**.

189. Croy, J. R., Balasubramanian, M., Gallagher, K. G. & Burrell, A. K. Review of the U.S. Department of Energy's "Deep Dive" Effort to Understand Voltage Fade in Li- and Mn-Rich Cathodes. *Acc. Chem. Res.* **48**, 2813–2821 **(2015)**.

190. Sathiya, M., Abakumov, A. M., Foix, D., Rousse, G., Ramesha, K., Saubanère, M., Doublet, M. L., Vezin, H., Laisa, C. P., Prakash, A. S., Gonbeau, D., VanTendeloo, G. & Tarascon, J.-M. Origin of voltage decay in high-capacity layered oxide electrodes. *Nat. Mater.* **14**, 230–238 **(2015)**.

191. Strehle, B., Zünd, T., Sicolo, S., Kiessling, A., Baran, V. & Gasteiger, H. A. Correlating the Voltage Hysteresis in Li- and Mn-Rich Layered Oxides to Reversible Structural Changes by Using X-ray and Neutron Powder Diffraction. *J. Electrochem. Soc.* **169**, 020554 **(2022)**.

192. Kleiner, K., Strehle, B., Baker, A. R., Day, S. J., Tang, C. C., Buchberger, I., Chesneau, F.-F., Gasteiger, H. A. & Piana, M. Origin of High Capacity and Poor Cycling Stability of Li-Rich Layered Oxides: A Long-Duration in Situ Synchrotron Powder Diffraction Study. *Chem. Mater.* **30**, 3656–3667 **(2018)**.

193. Hong, J., Seo, D.-H., Kim, S.-W., Gwon, H., Oh, S.-T. & Kang, K. Structural evolution of layered $Li_{1.2}Ni_{0.2}Mn_{0.6}O_2$ upon electrochemical cycling in a Li rechargeable battery. *J. Mater. Chem.* **20**, 10179 **(2010)**.

194. Gu, M., Belharouak, I., Zheng, J., Wu, H., Xiao, J., Genc, A., Amine, K., Thevuthasan, S., Baer, D. R., Zhang, J.-G., Browning, N. D., Liu, J. & Wang, C. Formation of the Spinel Phase in the Layered Composite Cathode Used in Li-Ion Batteries. *ACS Nano* **7**, 760–767 **(2013)**.

195. Phattharasupakun, N., Geng, C., Johnson, M. B., Väli, R., Sawangphruk, M. & Dahn, J. R. Impact of Cr Doping on the Voltage Fade of Li-Rich Mn-Rich $Li_{1.11}Ni_{0.33}Mn_{0.56}O_2$ and $Li_{1.2}Ni_{0.2}Mn_{0.6}O_2$ Positive Electrode Materials. *J. Electrochem. Soc.* **167**, 160545 **(2020)**.

196. Tsiouvaras, N., Meini, S., Buchberger, I. & Gasteiger, H. A. A Novel On-Line Mass Spectrometer Design for the Study of Multiple Charging Cycles of a Li-O_2 Battery. *J. Electrochem. Soc.* **160**, A471–A477 **(2013)**.

197. Metzger, M., Marino, C., Sicklinger, J., Haering, D. & Gasteiger, H. A. Anodic Oxidation of Conductive Carbon and Ethylene Carbonate in High-Voltage Li-Ion Batteries Quantified by On-Line Electrochemical Mass Spectrometry. *J. Electrochem. Soc.* **162**, A1123–A1134 **(2015)**.

198. Metzger, M., Strehle, B., Solchenbach, S. & Gasteiger, H. A. Origin of H_2 Evolution in LIBs: H_2O Reduction vs. Electrolyte Oxidation. *J. Electrochem. Soc.* **163**, A798–A809 **(2016)**.

199. Sicklinger, J., Metzger, M., Beyer, H., Pritzl, D. & Gasteiger, H. A. Ambient Storage Derived Surface Contamination of NCM811 and NCM111: Performance Implications and Mitigation Strategies. *J. Electrochem. Soc.* **166**, A2322–A2335 **(2019)**.

200. Solchenbach, S., Metzger, M., Egawa, M., Beyer, H. & Gasteiger, H. A. Quantification of PF_5 and POF_3 from Side Reactions of $LiPF_6$ in Li-Ion Batteries. *J. Electrochem. Soc.* **165**, A3022–A3028 **(2018)**.

201. Metzger, M. PhD Thesis: Studies on Fundamental Materials Degradation Mechanisms in Lithium-ion Batteries via On-line Electrochemical Mass Spectrometry. **(Technical University of Munich, 2017)**.

202. Bianchini, M., Fauth, F., Hartmann, P., Brezesinski, T. & Janek, J. An in situ structural study on the synthesis and decomposition of $LiNiO_2$. *J. Mater. Chem. A* **8**, 1808–1820 **(2020)**.

203. Kondrakov, A. O., Geßwein, H., Galdina, K., de Biasi, L., Meded, V., Filatova, E. O., Schumacher, G., Wenzel, W., Hartmann, P., Brezesinski, T. & Janek, J. Charge-Transfer-Induced Lattice Collapse in Ni-Rich NCM Cathode Materials during Delithiation. *J. Phys. Chem. C* **121**, 24381–24388 **(2017)**.

204. Li, H., Zhang, N., Li, J. & Dahn, J. R. Updating the Structure and Electrochemistry of Li_xNiO_2 for $0 \leq x \leq 1$. *J. Electrochem. Soc.* **165**, A2985–A2993 **(2018)**.

205. Kleiner, K., Dixon, D., Jakes, P., Melke, J., Yavuz, M., Roth, C., Nikolowski, K., Liebau, V. & Ehrenberg, H. Fatigue of $LiNi_{0.8}Co_{0.15}Al_{0.05}O_2$ in commercial Li ion batteries. *J. Power Sources* **273**, 70–82 **(2015)**.

206. Xu, C., Märker, K., Lee, J., Mahadevegowda, A., Reeves, P. J., Day, S. J., Groh, M. F., Emge, S. P., Ducati, C., Layla Mehdi, B., Tang, C. C. & Grey, C. P. Bulk fatigue induced by surface reconstruction in layered Ni-rich cathodes for Li-ion batteries. *Nat. Mater.* **20**, 84–92 **(2021)**.

207. Konishi, H., Hirano, T., Takamatsu, D., Gunji, A., Feng, X., Furutsuki, S., Okumura, T., Terada, S. & Tamura, K. Electrochemical reaction mechanisms under various charge-discharge operating conditions for $Li_{1.2}Ni_{0.13}Mn_{0.54}Co_{0.13}O_2$ in a lithium-ion battery. *J. Solid State Chem.* **262**, 294–300 **(2018)**.

208. Friedrich, F., Strehle, B., Freiberg, A. T. S., Kleiner, K., Day, S. J., Erk, C., Piana, M. & Gasteiger, H. A. Editors' Choice—Capacity Fading Mechanisms of NCM-811 Cathodes in Lithium-Ion Batteries Studied by X-ray Diffraction and Other Diagnostics. *J. Electrochem. Soc.* **166**, A3760–A3774 **(2019)**.

209. Strehle, B., Friedrich, F. & Gasteiger, H. A. A Comparative Study of Structural Changes during Long-Term Cycling of NCM-811 at Ambient and Elevated Temperatures. *J. Electrochem. Soc.* **168**, 050512 **(2021)**.

210. Dinnebier, R. E., Leineweber, A. & Evans, J. S. O. *Rietveld Refinement Practical Powder Diffraction Pattern Analysis Using Topas*. *Rietveld Refinement* **(De Gruyter, 2019)**.

211. Williamson, G. . & Hall, W. X-ray line broadening from filed aluminium and wolfram. *Acta Metall.* **1**, 22–31 **(1953)**.

212. Gent, W. E., Li, Y., Ahn, S., Lim, J., Liu, Y., Wise, A. M., Gopal, C. B., Mueller, D. N., Davis, R., Weker, J. N., Park, J.-H., Doo, S.-K. & Chueh, W. C. Persistent State-of-Charge Heterogeneity in Relaxed, Partially Charged $Li_{1-x}Ni_{1/3}Co_{1/3}Mn_{1/3}O_2$ Secondary Particles. *Adv. Mater.* **28**, 6631–6638 **(2016)**.

213. Fell, C. R., Qian, D., Carroll, K. J., Chi, M., Jones, J. L. & Meng, Y. S. Correlation Between Oxygen Vacancy, Microstrain, and Cation Distribution in Lithium-Excess Layered Oxides During the First Electrochemical Cycle. *Chem. Mater.* **25**, 1621–1629 **(2013)**.

214. Robert, R. & Novák, P. Structural Changes and Microstrain Generated on $LiNi_{0.80}Co_{0.15}Al_{0.05}O_2$ during Cycling: Effects on the Electrochemical Performance. *J. Electrochem. Soc.* **162**, A1823–A1828 **(2015)**.

215. Kondrakov, A. O., Schmidt, A., Xu, J., Geßwein, H., Mönig, R., Hartmann, P., Sommer, H., Brezesinski, T. & Janek, J. Anisotropic Lattice Strain and Mechanical Degradation of High- and Low-Nickel NCM Cathode Materials for Li-Ion Batteries. *J. Phys. Chem. C* **121**, 3286–3294 **(2017)**.

216. Stephens, P. W. Phenomenological model of anisotropic peak broadening in

powder diffraction. *J. Appl. Crystallogr.* **32**, 281–289 **(1999)**.

217. Rietveld, H. M. A profile refinement method for nuclear and magnetic structures. *J. Appl. Crystallogr.* **2**, 65–71 **(1969)**.

218. Liu, H., Liu, H., Lapidus, S. H., Meng, Y. S., Chupas, P. J. & Chapman, K. W. Sensitivity and Limitations of Structures from X-ray and Neutron-Based Diffraction Analyses of Transition Metal Oxide Lithium-Battery Electrodes. *J. Electrochem. Soc.* **164**, A1802–A1811 **(2017)**.

219. Yin, L., Mattei, G. S., Li, Z., Zheng, J., Zhao, W., Omenya, F., Fang, C., Li, W., Li, J., Xie, Q., Zhang, J.-G., Whittingham, M. S., Meng, Y. S., Manthiram, A. & Khalifah, P. G. Extending the limits of powder diffraction analysis: Diffraction parameter space, occupancy defects, and atomic form factors. *Rev. Sci. Instrum.* **89**, 093002 **(2018)**.

220. McCusker, L. B., Von Dreele, R. B., Cox, D. E., Louër, D. & Scardi, P. Rietveld refinement guidelines. *J. Appl. Crystallogr.* **32**, 36–50 **(1999)**.

221. Toby, B. H. R factors in Rietveld analysis: How good is good enough? *Powder Diffr.* **21**, 67–70 **(2006)**.

222. Schwarzenbach, D., Abrahams, S. C., Flack, H. D., Prince, E. & Wilson, A. J. C. Statisical descriptions in crystallography. II. Report of a Working Group on Expression of Uncertainty in Measurement. *Acta Crystallogr. Sect. A Found. Crystallogr.* **51**, 565–569 **(1995)**.

223. Rodríguez-Carvajal, J. Recent advances in magnetic structure determination by neutron powder diffraction. *Phys. B Condens. Matter* **192**, 55–69 **(1993)**.

224. Rodríguez-Carvajal, J. Recent Developments of the Program FULLPROF. *IUCr Newsl.* **26**, 12–19 **(2001)**.

225. TOPAS-Academic V6, Coelho Software, Brisbane, Australia, 2016.

226. TOPAS 6 Technical Reference, Bruker AXS GmbH, Karlsruhe, Germany, 2014.

227. Ryu, H.-H., Park, K.-J., Yoon, C. S. & Sun, Y.-K. Capacity Fading of Ni-Rich $Li[Ni_xCo_yMn_{1-x-y}]O_2$ ($0.6 \leq x \leq 0.95$) Cathodes for High-Energy-Density Lithium-Ion Batteries: Bulk or Surface Degradation? *Chem. Mater.* **30**, 1155–1163 **(2018)**.

228. Herklotz, M., Scheiba, F., Hinterstein, M., Nikolowski, K., Knapp, M., Dippel, A.-C., Giebeler, L., Eckert, J. & Ehrenberg, H. Advances in in situ powder diffraction of battery materials: a case study of the new beamline P02.1 at DESY, Hamburg. *J. Appl. Crystallogr.* **46**, 1117–1127 **(2013)**.

229. Borkiewicz, O. J., Shyam, B., Wiaderek, K. M., Kurtz, C., Chupas, P. J. & Chapman, K. W. The AMPIX electrochemical cell: a versatile apparatus for in situ X-ray scattering and spectroscopic measurements. *J. Appl. Crystallogr.* **45**, 1261–1269 **(2012)**.

230. Buchberger, I. H. PhD Thesis: Electrochemical and structural investigations on lithium-ion battery materials and related degradation processes. **(Technical University of Munich, 2016)**.

231. Aiken, C. P., Harlow, J. E., Tingley, R., Hynes, T., Logan, E. R., Glazier, S. L., Keefe, A. S. & Dahn, J. R. Accelerated Failure in $Li[Ni_{0.5}Mn_{0.3}Co_{0.2}]O_2$/Graphite Pouch Cells Due to Low $LiPF_6$ Concentration and Extended Time at High Voltage. *J. Electrochem. Soc.* **167**, 130541 **(2020)**.

232. Murray, C. A., Potter, J., Day, S. J., Baker, A. R., Thompson, S. P., Kelly, J., Morris, C. G., Yang, S. & Tang, C. C. New synchrotron powder diffraction facility for long-duration experiments. *J. Appl. Crystallogr.* **50**, 172–183 **(2017)**.

233. Friedrich, F. Master Thesis: Investigation of structural changes over long-term cycling in Ni-rich layered oxides used as Li-ion battery cathodes. **(Technical University of Munich, 2017)**.

234. Llewellyn, A. V., Matruglio, A., Brett, D. J. L., Jervis, R. & Shearing, P. R. Using In-Situ Laboratory and Synchrotron-Based X-ray Diffraction for Lithium-Ion Batteries Characterization: A Review on Recent Developments. *Condens. Matter* **5**, 75 **(2020)**.

235. Li, Z., Yin, L., Mattei, G. S., Cosby, M. R., Lee, B.-S., Wu, Z., Bak, S.-M., Chapman, K. W., Yang, X.-Q., Liu, P. & Khalifah, P. G. Synchrotron Operando Depth Profiling Studies of State-of-Charge Gradients in Thick $Li(Ni_{0.8}Mn_{0.1}Co_{0.1})O_2$ Cathode Films. *Chem. Mater.* **32**, 6358–6364 **(2020)**.

236. Strehle, B., Yoon, J., Friedrich, F. & Gasteiger, H. A. Specific Surface Area and Bulk Strain: Important Material Metrics Determining the Electrochemical Performance of Li- and Mn-Rich Layered Oxides. *J. Electrochem. Soc.* **169**, 060521 **(2022)**.

237. Liu, J., Yin, L., Wu, L., Bai, J., Bak, S.-M., Yu, X., Zhu, Y., Yang, X.-Q. & Khalifah, P. G. Quantification of Honeycomb Number-Type Stacking Faults: Application to $Na_3Ni_2BiO_6$ Cathodes for Na-Ion Batteries. *Inorg. Chem.* **55**, 8478–8492 **(2016)**.

238. Whitfield, P. S., Davidson, I. J., Mercier, P. H. J., Le Page, Y., Mitchell, L. D., Stephens, P. W., Cranswick, L. M. D. & Swainson, I. P. Simultaneous refinements with complex compositional constraints—example of singular value decomposition to diagnose poor matrix conditioning. *Powder Diffr.* **21**, 172–172 **(2006)**.

239. Koga, H., Croguennec, L., Mannessiez, P., Ménétrier, M., Weill, F., Bourgeois, L., Duttine, M., Suard, E. & Delmas, C. $Li_{1.20}Mn_{0.54}Co_{0.13}Ni_{0.13}O_2$ with Different Particle Sizes as Attractive Positive Electrode Materials for Lithium-Ion Batteries: Insights into Their Structure. *J. Phys. Chem. C* **116**, 13497–13506 **(2012)**.

240. Jiang, M., Key, B., Meng, Y. S. & Grey, C. P. Electrochemical and Structural Study of the Layered, "Li-Excess" Lithium-Ion Battery Electrode Material

Li[$Li_{1/9}Ni_{1/3}Mn_{5/9}$]O_2. *Chem. Mater.* **21**, 2733–2745 **(2009)**.

241. Atomic form factors. *accessed April 2, 2021,* http://lampx.tugraz.at/~hadley/ss1/crystaldiffraction/atomicformfactors/formfactors.php.

242. Chen, C.-J., Pang, W. K., Mori, T., Peterson, V. K., Sharma, N., Lee, P.-H., Wu, S., Wang, C.-C., Song, Y.-F. & Liu, R.-S. The Origin of Capacity Fade in the $Li_2MnO_3 \cdot LiMO_2$ (M = Li, Ni, Co, Mn) Microsphere Positive Electrode: An Operando Neutron Diffraction and Transmission X-ray Microscopy Study. *J. Am. Chem. Soc.* **138**, 8824–8833 **(2016)**.

243. Chen, W.-C., Song, Y.-F., Wang, C.-C., Liu, Y., Morris, D. T., Pianetta, P. A., Andrews, J. C., Wu, H.-C. & Wu, N.-L. Study on the synthesis–microstructure-performance relationship of layered Li-excess nickel–manganese oxide as a Li-ion battery cathode prepared by high-temperature calcination. *J. Mater. Chem. A* **1**, 10847 **(2013)**.

244. Chen, Z., Wang, J., Huang, J., Fu, T., Sun, G., Lai, S., Zhou, R., Li, K. & Zhao, J. The high-temperature and high-humidity storage behaviors and electrochemical degradation mechanism of $LiNi_{0.6}Co_{0.2}Mn_{0.2}O_2$ cathode material for lithium ion batteries. *J. Power Sources* **363**, 168–176 **(2017)**.

245. Chernova, N. A., Nolis, G. M., Omenya, F. O., Zhou, H., Li, Z. & Whittingham, M. S. What can we learn about battery materials from their magnetic properties? *J. Mater. Chem.* **21**, 9865 **(2011)**.

246. Ahmed, S., Pokle, A., Schweidler, S., Beyer, A., Bianchini, M., Walther, F., Mazilkin, A., Hartmann, P., Brezesinski, T., Janek, J. & Volz, K. The Role of Intragranular Nanopores in Capacity Fade of Nickel-Rich Layered $Li(Ni_{1-x-y}Co_xMn_y)O_2$ Cathode Materials. *ACS Nano* **13**, 10694–10704 **(2019)**.

247. Kitada, K., Murayama, H., Fukuda, K., Arai, H., Uchimoto, Y., Ogumi, Z. & Matsubara, E. Factors determining the packing-limitation of active materials in the composite electrode of lithium-ion batteries. *J. Power Sources* **301**, 11–17 **(2016)**.

248. Froboese, L., Titscher, P., Westphal, B., Haselrieder, W. & Kwade, A. Mercury intrusion for ion- and conversion-based battery electrodes – Structure and diffusion coefficient determination. *Mater. Charact.* **133**, 102–111 **(2017)**.

249. Giesche, H. Mercury Porosimetry: A General (Practical) Overview. *Part. Part. Syst. Charact.* **23**, 9–19 **(2006)**.

250. Gallagher, K. G., Trask, S. E., Bauer, C., Woehrle, T., Lux, S. F., Tschech, M., Lamp, P., Polzin, B. J., Ha, S., Long, B., Wu, Q., Lu, W., Dees, D. W. & Jansen, A. N. Optimizing Areal Capacities through Understanding the Limitations of Lithium-Ion Electrodes. *J. Electrochem. Soc.* **163**, A138–A149 **(2016)**.

251. Kwade, A., Haselrieder, W., Leithoff, R., Modlinger, A., Dietrich, F. & Droeder, K. Current status and challenges for automotive battery production technologies. *Nat. Energy* **3**, 290–300 **(2018)**.

252. Bak, S.-M., Nam, K.-W., Chang, W., Yu, X., Hu, E., Hwang, S., Stach, E. A., Kim, K.-B., Chung, K. Y. & Yang, X.-Q. Correlating Structural Changes and Gas Evolution during the Thermal Decomposition of Charged $Li_xNi_{0.8}Co_{0.15}Al_{0.05}O_2$ Cathode Materials. *Chem. Mater.* **25**, 337–351 **(2013)**.

253. Bak, S.-M., Hu, E., Zhou, Y., Yu, X., Senanayake, S. D., Cho, S.-J., Kim, K.-B., Chung, K. Y., Yang, X.-Q. & Nam, K.-W. Structural Changes and Thermal Stability of Charged $LiNi_xMn_yCo_zO_2$ Cathode Materials Studied by Combined In Situ Time-Resolved XRD and Mass Spectroscopy. *ACS Appl. Mater. Interfaces* **6**, 22594–22601 **(2014)**.

254. Streich, D., Erk, C., Guéguen, A., Müller, P., Chesneau, F.-F. & Berg, E. J. Operando Monitoring of Early Ni-mediated Surface Reconstruction in Layered Lithiated Ni–Co–Mn Oxides. *J. Phys. Chem. C* **121**, 13481–13486 **(2017)**.

255. Erickson, E. M., Schipper, F., Tian, R., Shin, J.-Y., Erk, C., Chesneau, F. F., Lampert, J. K., Markovsky, B. & Aurbach, D. Enhanced capacity and lower mean charge voltage of Li-rich cathodes for lithium ion batteries resulting from low-temperature electrochemical activation. *RSC Adv.* **7**, 7116–7121 **(2017)**.

256. Freiberg, A. T. S., Sicklinger, J., Solchenbach, S. & Gasteiger, H. A. Li_2CO_3 decomposition in Li-ion batteries induced by the electrochemical oxidation of the electrolyte and of electrolyte impurities. *Electrochim. Acta* **346**, 136271 **(2020)**.

257. Pritzl, D., Teufl, T., Freiberg, A. T. S., Strehle, B., Sicklinger, J., Sommer, H., Hartmann, P. & Gasteiger, H. A. Editors' Choice—Washing of Nickel-Rich Cathode Materials for Lithium-Ion Batteries: Towards a Mechanistic Understanding. *J. Electrochem. Soc.* **166**, A4056–A4066 **(2019)**.

258. Friedrich, F., Pieper, S. & Gasteiger, H. A. Entropy Measurements of Li-Ion Battery Cells with Li- and Mn-Rich Layered Transition Metal Oxides via Linear Temperature Variation. *J. Electrochem. Soc.* **168**, 120502 **(2021)**.

259. Kim, S., Ma, X., Ong, S. P. & Ceder, G. A comparison of destabilization mechanisms of the layered Na_xMO_2 and Li_xMO_2 compounds upon alkali de-intercalation. *Phys. Chem. Chem. Phys.* **14**, 15571 **(2012)**.

260. Vinckevičiūtė, J., Radin, M. D., Faenza, N. V., Amatucci, G. G. & Van der Ven, A. Fundamental insights about interlayer cation migration in Li-ion electrodes at high states of charge. *J. Mater. Chem. A* **7**, 11996–12007 **(2019)**.

261. Lin, F., Markus, I. M., Nordlund, D., Weng, T.-C., Asta, M. D., Xin, H. L. & Doeff, M. M. Surface reconstruction and chemical evolution of stoichiometric layered cathode materials for lithium-ion batteries. *Nat. Commun.* **5**, 3529 **(2014)**.

262. Li, W., Liu, X., Celio, H., Smith, P., Dolocan, A., Chi, M. & Manthiram, A. Mn versus Al in Layered Oxide Cathodes in Lithium-Ion Batteries: A Comprehensive Evaluation on Long-Term Cyclability. *Adv. Energy Mater.* **8**, 1703154 **(2018)**.

263. Rodrigues, M.-T. F., Babu, G., Gullapalli, H., Kalaga, K., Sayed, F. N., Kato, K.,

Joyner, J. & Ajayan, P. M. A materials perspective on Li-ion batteries at extreme temperatures. *Nat. Energy* **2**, 17108 **(2017)**.

264. Zou, L., Zhao, W., Jia, H., Zheng, J., Li, L., Abraham, D. P., Chen, G., Croy, J. R., Zhang, J.-G. & Wang, C. The Role of Secondary Particle Structures in Surface Phase Transitions of Ni-Rich Cathodes. *Chem. Mater.* **32**, 2884–2892 **(2020)**.

265. Sun, H. H., Ryu, H.-H., Kim, U.-H., Weeks, J. A., Heller, A., Sun, Y.-K. & Mullins, C. B. Beyond Doping and Coating: Prospective Strategies for Stable High-Capacity Layered Ni-Rich Cathodes. *ACS Energy Lett.* **5**, 1136–1146 **(2020)**.

266. Yabuuchi, N., Yoshii, K., Myung, S.-T., Nakai, I. & Komaba, S. Detailed Studies of a High-Capacity Electrode Material for Rechargeable Batteries, Li_2MnO_3-$LiCo_{1/3}Ni_{1/3}Mn_{1/3}O_2$. *J. Am. Chem. Soc.* **133**, 4404–4419 **(2011)**.

267. Ahmed, S., Bianchini, M., Pokle, A., Munde, M. S., Hartmann, P., Brezesinski, T., Beyer, A., Janek, J. & Volz, K. Visualization of Light Elements using 4D STEM: The Layered-to-Rock Salt Phase Transition in $LiNiO_2$ Cathode Material. *Adv. Energy Mater.* **10**, 2001026 **(2020)**.

Acknowledgements

The content of this PhD thesis was accomplished between October 2015 and May 2021 at the Chair of Technical Electrochemistry at the Technical University of Munich (TUM) in the group of Prof. Dr. Hubert A. Gasteiger.

First of all, I would like to thank my PhD advisor **Hubert A. Gasteiger**: For the wonderful opportunity to work and learn in your group! Thank you for the truly excellent support and inspirational guidance during the last years. In an unmistakable manner, you share your unlimited knowledge about electrochemistry and teach us to become passionate and honest scientists, who should not choose the simple way, but think outside the box, while always having fun during work. I especially like the way how you create an atmosphere which is carried by mutual trust and where we can develop our own ideas. At the same time, you are always on hand with help and technical input if necessary. My PhD time was a joyful journey which taught me a lot, both scientifically and personally, and for which I will always be very grateful.

Many thanks go to our administrative assistant **Veronika Pichler** who keeps the chair running by supporting all employees in administrative and organizational questions. But beyond that, you are always in a good mood and I particularly liked all our funny, non-scientific discussions.

I would also like to express my gratitude to **all current and former members** of the Chair of Technical Electrochemistry for the very pleasant working atmosphere. You all together make this group to a great place of curiosity and collaboration and I am really proud to have been a part of this community. Among them, special thanks go to **Franziska Friedrich**, **Tanja Zünd**, **Anna Freiberg**, **Tobias Teufl**, **Roland Jung**, and **Karin Kleiner** for their active support and our fruitful discussions in shared projects.

My starting point into the field of lithium-ion batteries was my Master's thesis, for which **Sophie Solchenbach** and **Michael Metzger** were the best supervisors I could imagine. Thank you for sharing your knowledge and approach to science with me. On that note, I also want to thank my former students **Daniel Rutz**, **Franziska Friedrich**, **Ying Ying Kang**, **Degenhart Hochfilzer**, **Tobias Käter**, and **Askin Eldiven**, for their support, enthusiasm, and challenging questions.

I acknowledge the financial support and scientific exchange provided by BASF SE through its "Network on Electrochemistry and Batteries". Furthermore, I greatly acknowledge our BASF team at TUM with the former members **K. Uta Schwenke**, **Michael Metzger**, **Hans Beyer**, **Sophie Solchenbach**, **Daniel Pritzl**, and **Johannes Sicklinger** and the current members **Michele Piana**, **Franziska Friedrich**, **Stefan Oswald**, **Louis Hartmann**, and **Jiyoung Yoon**. I really enjoyed our team spirit and I have learned a lot from you.

I want to thank the beamline scientists I was collaborating with in several projects, especially at the beamline I11 of the Diamond Light Source, because you measured the long-duration experiments and always provided support during this time. Moreover, I thank the German Academic Exchange Service (DAAD) for the travel scholarship to the 236th ECS meeting in Atlanta (USA).

Zuallerletzt möchte ich ein ganz großes Dankeschön an meine **Familie und Freunde** aussprechen, die mich tatkräftig und vorbehaltlos während meiner Doktorarbeit und weit darüber hinaus unterstützt haben.

Scientific Contributions

Articles

1. **B. Strehle**, J. Yoon, F. Friedrich, and H. A. Gasteiger, "Specific Surface Area and Bulk Strain: Important Material Metrics Determining the Electrochemical Performance of Li- and Mn-Rich Layered Oxides", *J. Electrochem. Soc.*, **169**, 060521 (2022).

2. **B. Strehle**,[=] T. Zünd,[=] S. Sicolo, A. Kiessling, V. Baran, and H. A. Gasteiger, "Correlating the Voltage Hysteresis in Li- and Mn-Rich Layered Oxides to Reversible Structural Changes by Using X-Ray and Neutron Powder Diffraction", *J. Electrochem. Soc.*, **169**, 020554 (2022).

3. **B. Strehle**,[=] F. Friedrich,[=] and H. A. Gasteiger, "A Comparative Study of Structural Changes during Long-Term Cycling of NCM-811 at Ambient and Elevated Temperatures", *J. Electrochem. Soc.*, **168**, 050512 (2021).

4. T. Teufl, D. Pritzl, P. Krieg, **B. Strehle**, M. A. Mendez, and H. A. Gasteiger, "Operating EC-based Electrolytes with Li- and Mn-Rich NCMs: The Role of O_2-Release on the Choice of Cyclic Carbonate", *J. Electrochem. Soc.*, **167**, 110505 (2020).

5. D. Pritzl,[=] T. Teufl,[=] A. T. S. Freiberg, **B. Strehle**, J. Sicklinger, H. Sommer, P. Hartmann, and H. A. Gasteiger, "Editors' Choice—Washing of Nickel-Rich Cathode Materials for Lithium-Ion Batteries: Towards a Mechanistic Understanding", *J. Electrochem. Soc.*, **166**, A4056-A4066 (2019).

6. F. Friedrich,[=] **B. Strehle**,[=] A. T. S. Freiberg, K. Kleiner, S. J. Day, C. Erk, M. Piana, and H. A. Gasteiger, "Editors' Choice—Capacity Fading Mechanisms of NCM-811 Cathodes in Lithium-Ion Batteries Studied by X-ray Diffraction and Other Diagnostics", *J. Electrochem. Soc.*, **166**, A3760-A3774 (2019).

7. T. Teufl, **B. Strehle**, P. Müller, H. A. Gasteiger, and M. Mendez, "Oxygen Release and Surface Degradation of Li- and Mn-Rich Layered Oxides in Variation of the Li_2MnO_3 Content", *J. Electrochem. Soc.*, **165**, A2718-A2731 (2018).

8. K. Kleiner, **B. Strehle**, A. R. Baker, S. J. Day, C. C. Tang, I. Buchberger, F.-F. Chesneau, H. A. Gasteiger, and M. Piana, "Origin of High Capacity and Poor Cycling Stability of Li-Rich Layered Oxides: A Long-Duration in Situ Synchrotron Powder Diffraction Study", *Chem. Mater.*, **30**, 3656-3667 (2018).

9. **B. Strehle**, S. Solchenbach, M. Metzger, K. U. Schwenke, and H. A. Gasteiger, "The Effect of CO_2 on Alkyl Carbonate Trans-Esterification during Formation of Graphite Electrodes in Li-Ion Batteries", *J. Electrochem. Soc.*, **164**, A2513-A2526 (2017).

10. **B. Strehle**, K. Kleiner, R. Jung, F. Chesneau, M. Mendez, H. A. Gasteiger, and M. Piana, "The Role of Oxygen Release from Li- and Mn-Rich Layered Oxides during the First Cycles Investigated by On-Line Electrochemical Mass Spectrometry", *J. Electrochem. Soc.*, **164**, A400-A406 (2017).

11. M. Metzger, **B. Strehle**, S. Solchenbach, and H. A. Gasteiger, "Hydrolysis of Ethylene Carbonate with Water and Hydroxide under Battery Operating Conditions", *J. Electrochem. Soc.*, **163**, A1219-A1225 (2016).

12. M. Metzger, **B. Strehle**, S. Solchenbach, and H. A. Gasteiger, "Origin of H_2 Evolution in LIBs: H_2O Reduction vs. Electrolyte Oxidation", *J. Electrochem. Soc.*, **163**, A798-A809 (2016).

Oral presentations

1. **B. Strehle**, T. Zünd, and H. A. Gasteiger, "Lattice Parameter Hysteresis in Li- and Mn-Rich Layered Oxides and Its Dependence on State of Charge and Open Circuit Voltage", Abstract #A05-0346, 236th ECS Meeting, Atlanta (USA), 2019.

2. **B. Strehle**, F. Friedrich, A. T. S. Freiberg, M. Piana, and H. A. Gasteiger, "Investigation of Structural Changes during Long-Term Cycling of NCM-811 Used As Cathode Active Material in Li-Ion Batteries", Abstract #A05-0559, 235th ECS Meeting, Dallas (USA), 2019.

3. **B. Strehle**, M. Metzger, S. Solchenbach, S. Meini, and H. A. Gasteiger, "The Effect of CO_2 on Alkyl Carbonate Trans-Esterification during Formation of Graphite Electrodes in Li-Ion Batteries", Abstract #A05-0369, 228th ECS Meeting, Phoenix (USA), 2015.

Poster presentations

1. **B. Strehle**, F. Friedrich, K. Kleiner, M. Piana, and H. A. Gasteiger, "Investigation of Structural Changes Over Long-Term Cycling of NCM-811 Used as Cathode Active Material in Li-Ion Batteries", 16th Ulm ElectroChemical Talks, Ulm (Germany), 2018.